TECHNISCHE UNIVERSITÄT MÜNCHEN

TUM School of Engineering and Design

Oscillatory flow through porous media

Lukas Maximilian Unglehrt

Vollständiger Abdruck der von der TUM School of Engineering and Design der Technischen Universität München zur Erlangung eines

Doktors der Ingenieurwissenschaften (Dr.-Ing.)

genehmigten Dissertation.

Vorsitz:	Prof. Dr.-Ing. Roberto Cudmani
Prüfer der Dissertation:	1. Prof. Dr.-Ing. Michael Manhart 2. Priv.-Doz. Dr. rer. nat. Gabriele Chiogna 3. Prof. Dr. Dominik Obrist

Die Dissertation wurde am 18.12.2023 bei der Technischen Universität München eingereicht und durch die TUM School of Engineering and Design am 08.04.2024 angenommen.

Zusammenfassung

Oszillierende Strömungen durch poröse Medien treten bei welleninduzierten Strömungen durch den Meeresboden, Korallenriffe und Wellenbrecher auf und können die Wärme- und Stoffübertragung in Wärmetauschern und chemischen Reaktoren verbessern. In dieser Arbeit wird die von einem sinusförmigen makroskopischen Druckgradienten getriebene Strömung durch eine hexagonale Kugelpackung mittels direkter numerischer Simulation untersucht. Das Strömungsproblem wird durch die Hagen- und Womersleyzahlen (Hg und Wo) bestimmt, welche die Amplitude bzw. Frequenz des Druckgradienten mit den viskosen Kräften ins Verhältnis setzen. Ziel der Arbeit ist es, den Strömungszustand auf der Porenskala für gegebene Hg und Wo zu bestimmen und bestehende Modelle für die Abhängigkeit der Filtergeschwindigkeit vom Druckgradienten zu bewerten und zu verbessern.
Nichtlineare Strömungen werden in laminar, transitionell und chaotisch/turbulent unterteilt. Die nichtlinearen Effekte bei laminarer Strömung werden durch die Energie der höheren Harmonischen und durch die Abweichung des Geschwindigkeitsfelds von der Vorwärts-Rückwärts-Symmetrie quantifiziert. Sie treten bei kleiner Wo in Phase mit und bei großer Wo verzögert gegenüber der Filtergeschwindigkeit auf. Auf der Porenskala bilden sich mit zunehmender Hg Trägheitskerne und Rezirkulationszonen und mit zunehmender Wo Grenzschichten aus. Der Übergang von laminarer zu chaotischer Strömung wird durch den Symmetriebruch des Geschwindigkeitsfelds markiert. Bei turbulenter Strömung ist die turbulente kinetische Energie während der Beschleunigungsphase am niedrigsten und während der Verzögerungsphase am höchsten. Die Dissipationsrate zeigt eine Hysterese gegenüber der kinetischen Energie, die mittels der Reynolds-Zerlegung erklärt werden kann. Abschließend wird ein Gesamtbild der Strömungsregime skizziert und mögliche Transitionsszenarien werden diskutiert.
Unter den bestehenden Modellen für instationäre Strömungen durch poröse Medien können die dynamischen Permeabilitätsmodelle das Verhalten linearer Strömungen im gesamten Wo-Bereich abbilden. Die instationäre Forchheimer-Gleichung ist für niedrige Wo und für stark nichtlineare Strömungen geeignet, aber es treten große Fehler für lineare Strömungen bei mittleren und hohen Wo auf. Mithilfe einer Druckzerlegung (Graham, J. Fluid Mech., 2019) wird der Widerstand in stationärer und oszillierender Strömung untersucht. Der Beschleunigungsdruckwiderstand ist proportional zum makroskopischen Druckgradienten. Der Reibungs- und der viskose Druckwiderstand zeigen eine $Re^{3/2}$-Grenzschichtskalierung für große Reynoldszahlen (Re). Der konvektive Druckwiderstand zeigt ein Re^3-Verhalten bei kleinen Re, aber das Verhalten bei großen Re ist unklar. Es wird ein neues Modell für den Reibungs- und den viskosen Druckwiderstand vorgeschlagen, welches das lineare Modell von Pride et al. (Phys. Rev. B, 1993) mit einer $Re^{3/2}$-Skalierung verbindet und über einen großen Bereich des Parameterraums zutreffende Vorhersagen liefert. Desweiteren wird ein neues Modell der Dissipationsrate in linearen instationären Strömungen vorgeschlagen, welches das Grenzschichtverhalten in Anfahrströmungen mit dem Verhalten quasi-stationärer Strömungen verbindet.

Abstract

Oscillatory flow through porous media occurs in wave-induced flow through the seabed, coral reefs and breakwaters, and can improve heat and mass transfer in heat exchangers and chemical reactors. In this study, flow through a hexagonal sphere pack driven by a sinusoidal macroscopic pressure gradient is investigated by means of direct numerical simulation. The flow problem is determined by the Hagen and Womersley numbers (Hg and Wo), which relate the amplitude and frequency of the pressure gradient, respectively, to the viscous forces. The aim of the study is to determine the flow state on the pore scale for given Hg and Wo and to evaluate and improve existing models for the dependency of the superficial velocity on the pressure gradient.

Nonlinear flow is categorised as laminar, transitional or chaotic/turbulent. The nonlinear effects in laminar flow are quantified by the energy of the higher harmonics and the deviation of the velocity field from a fore-aft symmetry. They occur in phase with the superficial velocity for small Wo and lag behind the superficial velocity for large Wo. At the pore scale, inertial cores and recirculation regions appear with increasing Hg, and boundary layers form with increasing Wo. The transition from laminar to chaotic flow is characterised by the symmetry breaking of the velocity field. In turbulent flow, the turbulent kinetic energy is lowest during the acceleration phase and highest during the deceleration phase. The dissipation rate shows a hysteresis with respect to the kinetic energy, which can be explained by the Reynolds decomposition. Finally, an overall picture of the flow regimes is outlined and possible transition scenarios are discussed.

Among the existing models for unsteady flow through porous media, the dynamic permeability models can reproduce the linear flow behaviour over the entire Wo range. The unsteady Forchheimer equation is suitable for low Wo and for strongly nonlinear flow, but large errors are observed in linear flow for medium and high Wo. The drag force in stationary and oscillatory flow is investigated using Graham's pressure decomposition (J. Fluid Mech., 2019). The accelerative pressure drag is proportional to the macroscopic pressure gradient. The friction and the viscous pressure drag show a $Re^{3/2}$ boundary layer scaling for large Reynolds numbers (Re). The convective pressure drag shows a Re^3 behaviour at small Re, but the large Re behaviour is unclear. A new model for the friction and the viscous pressure drag is proposed that combines the linear model of Pride et al. (Phys. Rev. B, 1993) with a $Re^{3/2}$ scaling and results in accurate predictions over a large region of the parameter space. A new model is also proposed for the dissipation rate in linear unsteady flow, which combines the boundary layer behaviour in starting flow with the behaviour of quasi-steady flow.

Preface

I am glad to have spent the past five years writing this thesis at the Professorship for Hydromechanics. The welcoming, open, curious and familiar atmosphere at the chair is perhaps best embodied by the morning coffee break that sets the stage for challenging scientific and political discussions, which I have very much enjoyed. It is also represented by the traditional Spitzingsee seminar, the celebration after the doctoral defense and the Christmas party, which have made it easy to become a part of the team. This cohesion was especially important during difficult times such as the death of our colleague Alex and the Corona pandemic.

I would like to thank Michael for the opportunity of writing this dissertation in the first place, for advising me during my thesis and for the freedom and support to follow my curiosity instead of insisting on the work plan. I would also like to express my gratitude to my mentor Helge Andersson, to the reviewers of my thesis, Gabriele Chiogna and Dominik Obrist, and the chair of the doctoral committee, Roberto Cudmani. A big thank you goes to my colleagues Alex, Ante, Ash, Chantel, Daniel, Hao, Julian, Kuiju, Simon, Uli, Xinyi and Yoshi, who have made my time at this chair a great experience and who have helped and supported me a lot along the way. I would also like to thank Evelyn, Christian, Jan and Philip for running the chair behind the scenes, and Florian, Håkon and Johannes at KM Turbulenz for their brilliant work on MGLET that made this thesis possible.

I would like to thank my family, especially my parents, and my friends for their support and encouragement and I would like to particularly thank Sebastian, Markus and Theresa for proofreading this thesis. Finally, I would like to thank my wonderful girlfriend Julia, who has supported me throughout the sometimes taxing last years of my doctorate and to whom I dedicate this thesis.

I gratefully acknowledge the financial support of the German Research Foundation (DFG) under grant no. MA2062/13-1 and the computing time provided by the Leibniz Supercomputing Centre (LRZ) of the Bavarian Academy of Sciences on its Linux Cluster.

Contents

List of Tables

List of Figures

Nomenclature

In the following, the recurring abbreviations and symbols are defined. Definitions of the other symbols are given at the point of use. The mathematical notation is based on the ISO 80000-2:2019 standard; a deviating notation is used for the real and imaginary part of a complex number and for the Fourier transform. The notation is given in the following order: abbreviations, dimensionless numbers, mathematical operators, upper-case and lower-case Greek letters, and upper-case and lower-case Roman letters.

Abbreviations

cpd	cells per diameter
CPU-h	(wall-clock time of simulation) $\cdot$ (number of processes) in hours
DNS	Direct numerical simulation
hcp	hexagonal close-packing
LES	Large-eddy simulation
MKE	Mean kinetic energy
REV	Representative elementary volume
SGS	Sub-grid scale
TKE	Turbulent kinetic energy

Dimensionless Numbers

$Gö$	Görtler number
Hg	Hagen number
KC	Keulegan-Carpenter number
St	Strouhal number
Re	Reynolds number for flow through porous media $Re = \lvert\langle \boldsymbol{u} \rangle_\mathrm{s}\rvert \, d/\nu$
Re_crit	Critical Reynolds number for the onset of instability
Re_0	Reynolds number for flow around a sphere $Re_0 = U_0 \, d/\nu$
$Re_{0,\mathrm{crit}}$	Critical Reynolds number for the onset of instability
Re_δ	Reynolds number for the Stokes boundary layer $Re_\delta = U_0 \, \delta_\mathrm{s}/\nu$
$Re_{\delta,\mathrm{crit}}$	Critical Reynolds number for the onset of instability
Wo	Womersley number

Mathematical Operators

$\cdot$	Inner product $\boldsymbol{a} \cdot \boldsymbol{b} = a_i b_i$
$\otimes$	Outer product $(\boldsymbol{a} \otimes \boldsymbol{b})_{ij} = a_i b_j$
$\times$	Cross product $(\boldsymbol{a} \times \boldsymbol{b})_i = \epsilon_{ijk} a_j b_k$
:	Double inner product $\boldsymbol{A} : \boldsymbol{B} = A_{ij} B_{ij}$
d	Total differential
∂	Partial differential
$\boldsymbol{\nabla}$	Nabla operator
Δ	Laplace operator
$O(.)$	Landau symbol (order of magnitude)
$\Re(.)$	Real part
$\Im(.)$	Imaginary part
$\langle . \rangle_{\mathrm{i}}$	Intrinsic volume average
$\langle . \rangle_{\mathrm{s}}$	Superficial volume average
$\overline{(.)}$	Phase average
$\tilde{(.)}$	Deviation from the intrinsic volume average
$(.)'$	Deviation from the phase average
$(.)''$	Deviation from the base flow
$\hat{(.)}$	Nondimensionalised quantity
$\mathcal{F}\{.\}(\omega)$	Fourier transform
$\mathcal{F}^{-1}\{.\}(t)$	Inverse Fourier transform

Upper-case Greek Letters

Δt	Time step
Δx, Δy, Δz	Grid spacing in the x-, y and z-directions
Λ	Viscous length scale $\Lambda = 2 \int_{V_{\mathrm{f}}} \lvert\boldsymbol{u}_{\mathrm{pot}}\rvert^2 \, \mathrm{d}V / \int_{A_{\mathrm{fs}}} \lvert\boldsymbol{u}_{\mathrm{pot}}\rvert^2 \, \mathrm{d}A$
$\boldsymbol{\Phi}$	Auxiliary potential (eq. B.26)
Ω	Angular frequency of oscillation
Ω_0	Characteristic frequency of the porous medium $\Omega_0 = \epsilon\nu/(\alpha_\infty K)$

Lower-case Greek Letters

α_0	Static viscous tortuosity $\alpha_0 = \langle \boldsymbol{u}^2_{\mathrm{Stokes}} \rangle_{\mathrm{i}} \,/\, \langle \boldsymbol{u}_{\mathrm{Stokes}} \rangle^2_{\mathrm{i}}$

α_∞	High-frequency limit of the dynamic tortuosity $\alpha_\infty = \left\langle \boldsymbol{u}_{\mathrm{pot}}^2 \right\rangle_{\mathrm{i}} / \left\langle \boldsymbol{u}_{\mathrm{pot}} \right\rangle_{\mathrm{i}}^2$
β	Relative difference between tortuosities $\alpha_0/\alpha_\infty - 1$
δ	Boundary layer thickness
δ_{s}	Stokes boundary layer thickness $\delta_{\mathrm{s}} = \sqrt{2\nu/\Omega}$
ϵ	Porosity $\epsilon = V_{\mathrm{f}}/V$
ε	Length scale ratio ℓ/L
θ	Polar angle
κ	Wave number
λ	Eigenvalue
λ_{crit}	Critical wavelength
μ	Dynamic viscosity of the fluid
μ_{F}	Floquet multiplier
ν	Kinematic viscosity of the fluid
ρ	Density of the fluid
$\boldsymbol{\tau}_{\mathrm{w}}$	Wall shear stress $\boldsymbol{\tau}_{\mathrm{w}} = \mu \left(\boldsymbol{\nabla} \otimes \boldsymbol{u}\right)^{\mathrm{T}} \cdot \boldsymbol{n}$
τ	Time (integration variable, $\tau \leq t$)
φ	Phase angle $\varphi = \Omega t \mod 2\pi$
$\chi(M)$	Euler characteristic of a manifold (eq. C.2)
χ	Euler characteristic of a polyhedron (eq. C.3)
χ_{f}	Characteristic function of the fluid phase
$\boldsymbol{\omega}$	Vorticity $\boldsymbol{\omega} = \boldsymbol{\nabla} \times \boldsymbol{u}$
ω	Angular frequency (complex variable)
ω_x, ω_y, ω_z	Components of vorticity in Cartesian coordinates

Upper-case Roman Letters

$\boldsymbol{A}$	Tensor of virtual inertia $\boldsymbol{A} = \int_{A_{\mathrm{fs}}} \boldsymbol{\Phi} \otimes \boldsymbol{n} \, \mathrm{d}A / [(1-\epsilon)V]$
A_{fs}	Fluid-solid interface area
B	Coefficient of the quadratic term in the proposed model (eq. 4.7)
$\boldsymbol{C}_{\mathrm{a}}$	Acceleration coefficient tensor (eq. 1.47)
C	Coefficient of the boundary layer drag in the proposed model (eq. 4.10)
C_{w}	Constant of the WALE model
E	Number of edges in a mesh
$\mathcal{F}$	Set of faces of a mesh

F	Number of faces in a mesh
$\boldsymbol{I}$	Identity tensor
$\boldsymbol{K}$	Permeability tensor
K	Permeability
$\hat{K}(\omega)$	Dynamic permeability (eq. B.2)
$\boldsymbol{L}$	Viscous length scale tensor (appendix D.6, eq. 3.3)
L	Field scale
L_x, L_y, L_z	Length of the computational domain in the x-, y and z-directions
N_x, N_y, N_z	Number of cells in the x-, y and z-directions
M	Manifold
P	Pore geometry parameter of dynamic permeability models $P = 4\alpha_\infty K/(\epsilon\Lambda^2)$
Q	Second invariant of the velocity gradient tensor $Q = -\frac{1}{2}(\boldsymbol{\nabla}\otimes\boldsymbol{u})^{\mathrm{T}} : (\boldsymbol{\nabla}\otimes\boldsymbol{u})$
R	Pipe radius
$\boldsymbol{S}$	Strain rate tensor $\boldsymbol{S} = \frac{1}{2}\left[\boldsymbol{\nabla}\otimes\boldsymbol{u} + (\boldsymbol{\nabla}\otimes\boldsymbol{u})^{\mathrm{T}}\right]$
T	Period of oscillation
T_{sim}	Simulated time
U	Velocity at the edge of the boundary layer
U_0	Velocity amplitude
$\mathcal{V}$	Set of vertices of a mesh
V	Number of vertices in a mesh
V	Volume of the unit cell
V_{f}	Fluid volume within the unit cell

Lower-case Roman Letters

$\boldsymbol{a}$, $\boldsymbol{b}$, $\boldsymbol{c}$	Lattice vectors of the hexagonal close-packing (eq. 2.1)
a, b, c	Coefficients of the unsteady Forchheimer equation (eq. 1.48)
d	Sphere diameter / pipe diameter
d_{blocked}	Diameter of the fillet bridges at the contact points (eq. 2.17)
$\boldsymbol{e}_x$, $\boldsymbol{e}_y$, $\boldsymbol{e}_z$	Cartesian unit vectors
$\boldsymbol{f}$	Macroscopic pressure gradient
$\boldsymbol{f}_{\boldsymbol{\tau}_{\mathrm{w}}}$	Friction drag
$\boldsymbol{f}_p^{(a)}$	Accelerative pressure drag
$\boldsymbol{f}_p^{(v)}$	Viscous pressure drag

$\boldsymbol{f}_p^{(c)}$	Convective pressure drag
f	Face of a mesh
f_x	x-component of the macroscopic pressure gradient
$h_n(t-\tau, \lvert\langle\boldsymbol{u}\rangle_s\rvert)$	Integral kernel of the proposed model (eq. 4.12)
k	Kinetic energy density $\frac{1}{2}\rho\boldsymbol{u}^2$
ℓ	Pore scale
$\boldsymbol{n}$	Outward unit normal vector of a fluid volume
$p(\boldsymbol{x}, t)$	Pressure
$p_{i,j,k}$	pressure of the Cartesian grid cell (i, j, k)
r	Radial coordinate
r_0	Representative elementary volume scale
t	Time
$\boldsymbol{u}(\boldsymbol{x}, t)$	Velocity
u, v, w	Components of velocity in Cartesian coordinates
u_r, u_θ, u_φ	Components of velocity in spherical coordinates
u_s	Component of velocity along the pipe axis
$u_{i,j,k}$, $v_{i,j,k}$, $w_{i,j,k}$	Staggered components of velocity of the Cartesian grid cell (i, j, k)
$\boldsymbol{u}_{\text{Stokes}}(\boldsymbol{x}, t)$	Velocity in Stokes flow
$\boldsymbol{u}_{\text{pot}}(\boldsymbol{x}, t)$	Velocity in potential flow
$\boldsymbol{v}$	Generic vector field
v	Vertex of a mesh
$\boldsymbol{x}$	Spatial position
x, y, z	Cartesian coordinates

1. Introduction

1.1. Motivation

Flow through porous structures appears frequently in geological, biological and technical processes. A *porous medium* is composed of a connected solid phase in the form of grains or a matrix and a connected void space filled by a fluid (Bear, 2018, p.7). Porous media formed by geological processes include volcanic rock, stone fractured by weathering and erosion, and sediments. The understanding of fluid flow through these porous media is important to source groundwater for drinking and irrigation, to describe the spread of pollutants in the groundwater or to lower the groundwater table for subsurface construction. Furthermore, flow through such porous media also occurs in the extraction of oil and natural gas, the sequestration of carbon dioxide and in cement injections for underground construction. In biology, a wide variety of porous media can be found that interact with fluid flow, for example coral reefs (Lowe et al., 2008), mosses and lichen (Cazaurang et al., 2023), lungs (Miguel, 2012; DeGroot & Straatman, 2012; Berger et al., 2016; DeGroot & Straatman, 2018) or the filter feeding mechanisms of baleen whales, fish and other animals (Zhu et al., 2020, 2021; Wassenbergh & Sanderson, 2023). Finally, porous media are popular in many technical applications due to the high specific surface that is available for reactions and heat transfer and due to the mixing inherent to porous media flow. For example, structures for coastal protection are made of gravel and rocks; packed beds of (often spherical) particles are employed in chemical reactors (Luévano-Rivas et al., 2023), pebble bed nuclear reactors (Nelson, 2009; Andreades et al., 2014; Shams et al., 2014) or for thermal energy storage (Müller-Trefzer et al., 2022). Porous media can also provide damping in oscillatory systems, for instance, to avoid sloshing in tanks (Tsao et al., 2022), to dissipate surge tank oscillations (Asiaban & Fathi-Moghadam, 2018) or to absorb sound. Also, heat exchangers are frequently described using the theory of flow through porous media (Patankar & Spalding, 1974, 1978; Alshare et al., 2010).

While flow through porous media is often considered to be stationary, there are a number of systems in which unsteady or, in particular, oscillatory flow occurs. Some examples are the propagation of acoustic waves through porous media, the propagation of seismic waves through aquifers and wave-induced water flow through the seabed (Gu & Wang, 1991), through rubble-mound breakwaters (van Gent, 1994; Muttray, 2000; Chanda & Pramanik, 2023) and through coral reefs (Lowe et al., 2005, 2007, 2008). Oscillatory and pulsatile flow through porous media is also used in engineering systems such as heat exchangers (Das et al., 2018, pp.155f) and regenerator-type cryocoolers (Cha, 2007; Pathak, 2013; Perrella, 2017; Harvey, 2023), chemical reactors in unsteady operation (Lauschke & Gilles, 1994; Lau et al., 2004; Crittenden et al., 2005; McGlone et al., 2015; Zagoruiko et al., 2021) or swimming reactors (Iliuta & Larachi, 2016; Gong & Wu, 2021). Transient flow can also occur during the charging and discharging of thermal energy storage (Müller-Trefzer et al., 2022).

In these applications, the objective is usually to enhance mass or heat transfer, for which there are three main mechanisms are available: First, porous media provide an intrinsic mixing mechanism that is caused by the flow repeatedly branching and merging, leading to chaotic advection (Lester et al., 2013). Second, turbulence can lead to a strong mixing of the flow. Third, unsteady flow can lead to increased velocity gradients near the wall and a more uniform flow distribution within the porous medium (Dasgupta & Atta, 2017), thus improving the mixing and heat transfer in the flow (Ni et al., 2003; Saberinejad & Keshavarz, 2016; Bianchi et al., 2020; Choudhari et al., 2022). In contrast, Stokes flow, which is the most ubiquitous flow regime in porous media flow, minimises the dissipation rate for a given flow rate (Batchelor, 2000, pp.227f); consequently, the velocity gradients in the flow are relatively mild and the flow distribution is nonuniform.

Despite the wide range of applications, there are few fundamental studies of oscillatory flow through porous media as will be seen in the following sections. Unsteady flow through porous media has mostly been described by semi-empirical models (Sollitt & Cross, 1972; Gu & Wang, 1991; van Gent, 1993; Hall et al., 1995) whose theoretical basis is somewhat unclear (Burcharth & Andersen, 1995). A thorough understanding of unsteady flow through porous media is important for the analysis and design of many environmental and engineering systems; for example, there is a growing interest in industrial processes with intermittent energy supply due to the increasing use of wind and solar power (Matthischke et al., 2016; Cheema & Krewer, 2018; Chen & Yang, 2021; Bielefeld et al., 2023).

The objectives of the present work are thus to establish an understanding of the microscopic behaviour of nonlinear oscillatory flow through a porous medium, to assess and improve the modelling of unsteady porous media flow on a macroscopic scale, and to provide high-fidelity reference data.

1.2. Description of porous media flow

This section discusses the concept of a porous medium and introduces the main formalisms — the volume-averaging theory and periodic homogenisation — for describing flow in porous media. It is outlined under which conditions these theories lead to the flow problem that is the subject of this thesis. For a comprehensive review and comparison of these approaches the reader is referred to the work of Davit et al. (2013).

1.2.1. Concept of a porous medium

In simple terms, a porous medium may be defined as (Bear, 2013, p.13)

(a) a portion of space occupied by *heterogeneous* or *multiphase* matter. At least one of the phases comprising this matter is not *solid*. They may be gaseous and/or liquid phases. The solid phase is called the *solid matrix*. The space within the porous medium domain that is not part of the solid matrix is referred to as *void space* (or *pore space*).

(b) The solid phase should be distributed throughout the porous medium within the domain occupied by a porous medium [...]

(c) At least some of the pores comprising the void space should be interconnected. [...]

In general, the geometry of a porous medium — for example, the shape, position and orientation of each grain in a pile of sand — is extremely complex and practically impossible to determine precisely. It is therefore necessary to consider porous media in a statistical manner (Bear, 2013, p.13). The basic idea is to treat the porous medium as a *continuum*, i.e. a locally uniform material with certain properties that describe the average microscopic behaviour in the neighbourhood region of any point (Bear, 2013, p.19). This approach coincides with the intuitive perception that sand, flour, sponge or cotton wool are uncountable and apportionable substances like water or butter. An example of a porous medium property is the hydraulic conductivity[1] k, a constant of proportionality between the flow rate $\dot{V}$ through the porous medium and the difference in hydraulic head Δh, which was found by Darcy (1856) in his famous experiment (figure 1.1). In the modern notation, *Darcy's law* is

$$\dot{V} = kA\frac{\Delta h}{\Delta s} \tag{1.1}$$

where A is the cross-sectional area and Δs is the length of the porous medium sample. Another such property is the porosity ϵ that describes the ratio of the void space to the overall volume of a porous medium.

For the continuum description to be valid, the porous medium must have well separated length scales. In particular, the pore scale ℓ, which represents the typical size of the individual pores (e.g. the diameter of a sand grain), must be much smaller than the field scale L, which represents a characteristic distance over which averaged quantities such as porosity or pressure vary (e.g. the thickness of a layer of soil). Then, at any point one may find a *representative elementary volume* (REV) of size r_0 centred around that point, which is large compared to the pore scale and small compared to the field scale, such that the porous medium within the REV is homogeneous in a statistical sense. In particular, the average values of microscopic quantities over the REV volume should be "independent of small variations in the size of the REV" (Bear, 2018, p.20). For example, figure 1.2 shows the porosity of the hexagonal close-packing of spheres, which will be discussed in detail in section 2.2.1, as a function of the REV size for 100 randomly placed spherical averaging volumes. It can be seen that for $d_{\mathrm{avg}}/d \gtrsim 2$ an approximate convergence of the porosity is obtained. Note that field scale inhomogeneities, which are not present in this example, can lead to a divergent behaviour for large averaging volumes.

Various approaches have been developed to derive the governing equations on the field scale from the governing equations on the pore scale, relating the bulk properties of the porous medium to the pore geometry. Two of these approaches — the volume-averaging theory and the homogenisation theory — will be discussed in the following sections.

1.2.2. Volume-averaging theory

The main idea of the volume averaging approach to flow through porous media (Whitaker, 1966, 1967; Anderson & Jackson, 1967; Slattery, 1967) is to apply a moving volume average to flow fields inside the porous medium. Thereby, the pore scale features are blurred until

[1] The hydraulic conductivity is related to the permeability K as $k = \rho g K/\mu$. The permeability depends only on the pore geometry.

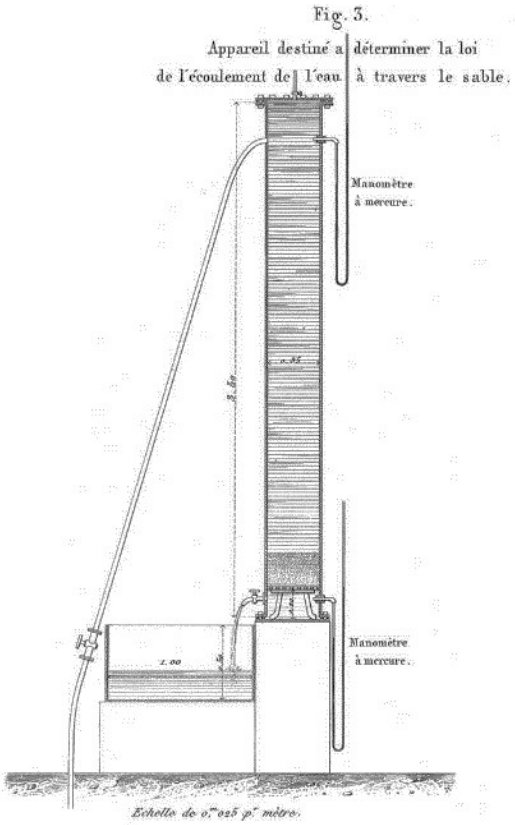

Figure 1.1: Experimental setup of Henry Darcy to determine the law of water flow through sand (Darcy, 1856, planche 24, fig. 3). The setup consists of a sand-filled pipe through which water flows from top to bottom and exits into a reservoir. The hydraulic head is measured by mercury gauges at the top and bottom and the flow rate is measured by the rate of change of the water in the reservoir.

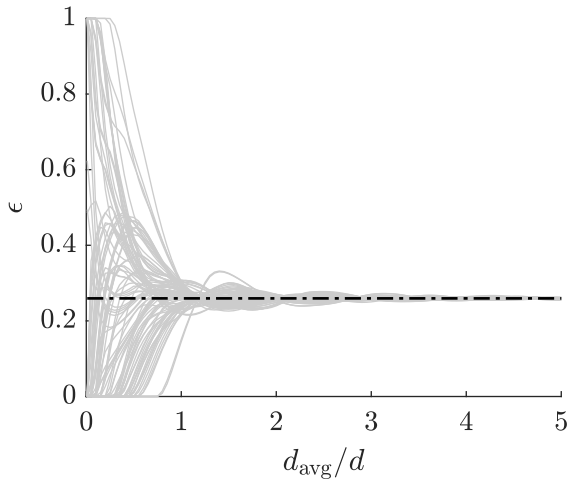

Figure 1.2: Porosity of the hexagonal close-packing arrangement of spheres as a function of the diameter d_{avg} of a spherical averaging volume. The grey curves correspond to 100 random placements of the centre of the averaging volume inside the primitive unit cell; the black line represents the theoretically expected porosity $\epsilon = 1 - \pi/(3\sqrt{2}) = 0.2595$.

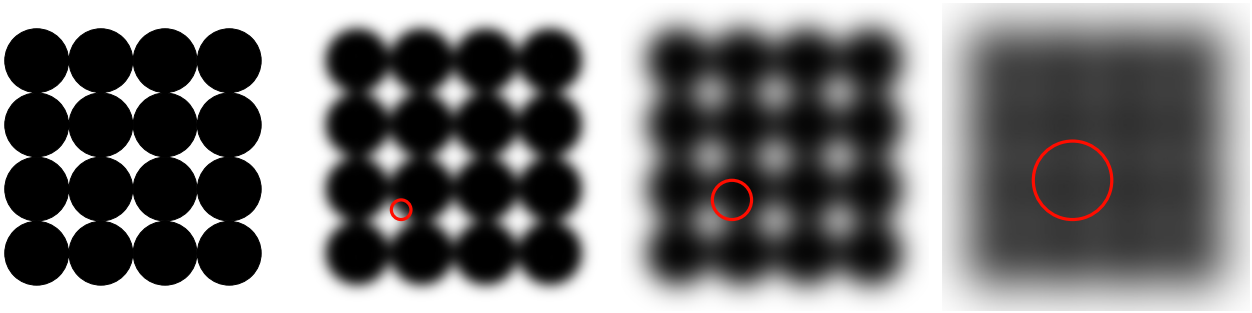

Figure 1.3: Conceptual sketch of the volume-averaging approach. The average over the REV of size d_{avg} (red circle) blurs the void space and the matrix such that a homogeneous medium is obtained.

homogeneous fields are obtained (figure 1.3). The volume-averaging technique can be considered a special case of a spatial filtering operation in which a box filter is employed (Anderson & Jackson, 1967; Davit et al., 2013; Wood et al., 2020). The averaging volume is chosen as the REV with a characteristic size r_0 and — insofar as fluid flow through a stationary matrix is concerned — the integration is performed only over the pore space within the averaging volume. Commonly, one distinguishes the *intrinsic average*

$$\langle \psi \rangle_{\mathrm{i}} = \frac{1}{V_{\mathrm{f}}} \int_{V_{\mathrm{f}}} \psi \, \mathrm{d}V \,, \tag{1.2}$$

which relates the integral of some quantity ψ to the volume V_{f} occupied by the fluid phase, and the *superficial average*

$$\langle \psi \rangle_{\mathrm{s}} = \frac{1}{V} \int_{V_{\mathrm{f}}} \psi \, \mathrm{d}V = \epsilon \, \langle \psi \rangle_{\mathrm{i}} \,, \tag{1.3}$$

which relates the integral to the total volume V comprising fluid and solid phases (Whitaker, 1996). Here, the notation of Zhu & Manhart (2016) has been adopted for the averages. Depending on the research question, one or the other form of the average is favoured. For instance, if one is concerned with the volume flux per unit area, the superficial velocity $\langle \boldsymbol{u} \rangle_{\mathrm{s}}$ is preferable because it satisfies a continuity equation (Whitaker, 1996). On the other hand, if one is interested in dispersion phenomena, the intrinsic velocity $\langle \boldsymbol{u} \rangle_{\mathrm{i}}$ is preferable as it is more representative of the speed at which the fluid particles move in the flow. Following Gray (1975), the velocity and pressure can be decomposed into average and deviation components

$$\boldsymbol{u} = \langle \boldsymbol{u} \rangle_{\mathrm{i}} + \tilde{\boldsymbol{u}} \,, \tag{1.4a}$$

$$p = \langle p \rangle_{\mathrm{i}} + \tilde{p} \,. \tag{1.4b}$$

The volume-averaged quantities vary over distances between the REV scale r_0 and the field scale L, whereas the deviation quantities vary over distances between the pore scale ℓ and the REV scale r_0.

In order to obtain governing equations for the volume-averaged flow quantities, the moving average operation is applied to the incompressible Navier-Stokes equations (Batchelor, 2000,

p.147) describing the flow on the pore scale. The terms are then reformulated using the spatial averaging theorem

$$\langle \boldsymbol{\nabla}\psi \rangle_\mathrm{s} = \boldsymbol{\nabla}\langle \psi \rangle_\mathrm{s} + \frac{1}{V}\int_{A_\mathrm{fs}} \psi\, \boldsymbol{n}\, \mathrm{d}A\,, \tag{1.5}$$

which prescribes how the volume average can be interchanged with spatial differentiation (Whitaker, 1985). Here, A_fs is the fluid-solid interface inside V and $\boldsymbol{n}$ is the normal vector pointing from the fluid into the solid domain.
A straightforward application of the spatial averaging theorem to the incompressible Navier-Stokes equations results in

$$\boldsymbol{\nabla} \cdot \langle \boldsymbol{u} \rangle_\mathrm{s} = 0 \tag{1.6a}$$

and

$$\rho \left[\frac{\partial \langle \boldsymbol{u} \rangle_\mathrm{s}}{\partial t} + \boldsymbol{\nabla} \cdot \langle \boldsymbol{u} \otimes \boldsymbol{u} \rangle_\mathrm{s} \right] = -\boldsymbol{\nabla}\langle p \rangle_\mathrm{s} - \frac{1}{V}\int_{A_\mathrm{fs}} p\, \boldsymbol{n}\, \mathrm{d}A + \mu\, \Delta \langle \boldsymbol{u} \rangle_\mathrm{s} + \frac{1}{V}\int_{A_\mathrm{fs}} \boldsymbol{\tau}_\mathrm{w}\, \mathrm{d}A\,, \tag{1.6b}$$

where $\boldsymbol{\tau}_\mathrm{w} = \mu\, (\boldsymbol{\nabla} \otimes \boldsymbol{u})^\mathrm{T} \cdot \boldsymbol{n}$ is the wall shear stress and no-slip and impermeable wall boundary conditions were assumed on A_fs. The integral terms represent the pressure and friction forces at the fluid-solid interface. The pressure terms may be rewritten in terms of the intrinsic pressure $\langle p \rangle_\mathrm{i}$ and the pressure deviation $\tilde{p}$ provided that $r_0^2 \ll L^2$ (Whitaker, 1986, eq. 2.21)

$$\rho \left[\frac{\partial \langle \boldsymbol{u} \rangle_\mathrm{s}}{\partial t} + \boldsymbol{\nabla} \cdot \langle \boldsymbol{u} \otimes \boldsymbol{u} \rangle_\mathrm{s} \right] = -\epsilon\, \boldsymbol{\nabla}\langle p \rangle_\mathrm{i} \underbrace{- \frac{1}{V}\int_{A_\mathrm{fs}} \tilde{p}\, \boldsymbol{n}\, \mathrm{d}A}_{\text{pressure drag}} + \mu\, \Delta \langle \boldsymbol{u} \rangle_\mathrm{s} + \underbrace{\frac{1}{V}\int_{A_\mathrm{fs}} \boldsymbol{\tau}_\mathrm{w}\, \mathrm{d}A}_{\text{friction drag}}\,. \tag{1.7}$$

In this formulation, it becomes apparent that the pressure drag is caused predominantly by the pressure deviation, while the macroscopic pressure gradient appears as the source term driving the flow.
By imposing the additional length scale constraint $\ell \ll r_0$, neglecting spatial variations in porosity and decomposing the velocity according to equation (1.4), the volume-averaged Navier-Stokes equations can be simplified as (Whitaker, 1996, eqns. 1.24, 1.32)

$$\boldsymbol{\nabla} \cdot \langle \boldsymbol{u} \rangle_\mathrm{s} = 0 \tag{1.8a}$$

$$\begin{aligned} &\rho\, \frac{\partial \langle \boldsymbol{u} \rangle_\mathrm{i}}{\partial t} + \rho\, (\langle \boldsymbol{u} \rangle_\mathrm{i} \cdot \boldsymbol{\nabla})\, \langle \boldsymbol{u} \rangle_\mathrm{i} + \underbrace{\rho\, \epsilon^{-1} \boldsymbol{\nabla} \cdot \langle \tilde{\boldsymbol{u}} \otimes \tilde{\boldsymbol{u}} \rangle_\mathrm{s}}_{\text{volume filter}} \\ &= -\boldsymbol{\nabla}\langle p \rangle_\mathrm{i} + \mu\, \Delta \langle \boldsymbol{u} \rangle_\mathrm{i} + \underbrace{\frac{1}{V_\mathrm{f}}\int_{A_\mathrm{fs}} \left(-\tilde{p}\boldsymbol{I} + \mu\, (\boldsymbol{\nabla} \otimes \tilde{\boldsymbol{u}})^\mathrm{T} \right) \cdot \boldsymbol{n}\, \mathrm{d}A}_{\text{surface filter}}\,. \end{aligned} \tag{1.8b}$$

The *surface filter* and the *volume filter* are unclosed terms arising from the local velocity deviation $\tilde{\boldsymbol{u}}$ and the pressure deviation $\tilde{p}$. In essence, the surface filter represents the resistance force exerted by the matrix onto the flow, while the volume filter represents the convective

transport occurring on the pore scale.
The deviations from the volume-average are governed by a closure problem that is solved on a representative region of the porous medium, which is not necessarily identical to the REV (Whitaker, 1996, eqns. 2.2, 2.5, 2.17):

$$\boldsymbol{\nabla} \cdot \tilde{\boldsymbol{u}} = 0 \tag{1.9a}$$

$$\begin{aligned} &\rho \frac{\partial \tilde{\boldsymbol{u}}}{\partial t} + \rho \left(\boldsymbol{u} \cdot \boldsymbol{\nabla}\right) \tilde{\boldsymbol{u}} + \rho \left(\tilde{\boldsymbol{u}} \cdot \boldsymbol{\nabla}\right) \langle \boldsymbol{u} \rangle_{\mathrm{i}} - \underbrace{\rho\, \epsilon^{-1} \boldsymbol{\nabla} \cdot \langle \tilde{\boldsymbol{u}} \otimes \tilde{\boldsymbol{u}} \rangle_{\mathrm{s}}}_{\text{volume filter}} \\ &= -\boldsymbol{\nabla} \tilde{p} + \mu\, \Delta \tilde{\boldsymbol{u}} - \underbrace{\frac{1}{V_{\mathrm{f}}} \int_{A_{\mathrm{fs}}} \left(-\tilde{p} \boldsymbol{I} + \mu \left(\boldsymbol{\nabla} \otimes \tilde{\boldsymbol{u}}\right)^{\mathrm{T}}\right) \cdot \boldsymbol{n}\, \mathrm{d}A}_{\text{surface filter}}, \end{aligned} \tag{1.9b}$$

with the wall boundary condition

$$\tilde{\boldsymbol{u}} = \underbrace{-\langle \boldsymbol{u} \rangle_{\mathrm{i}}}_{\text{source}} \quad \text{on } A_{\mathrm{fs}} \tag{1.9c}$$

driving the flow. The surface and volume filter terms represent the exchange between the volume-averaged momentum equation (1.8b) and the momentum equation in the closure problem (1.9b). The sum of the two equations recovers the Navier-Stokes equations at the pore scale.
In order for the closure problem to be complete, boundary conditions need to be specified on the open pore walls. Different boundary conditions have been discussed in the literature (Guibert et al., 2016). For example, the domain of the closure problem can be assumed periodic such that triply periodic boundary conditions may be used on the pressure deviation and the velocity (Patankar et al., 1977; Brenner, 1980) or the velocity deviation (Whitaker, 1996). For general porous media, a periodic representative region may be obtained, for example, by a stochastic reconstruction procedure (Gerke et al., 2019). Another possibility is the "effective medium approach" (Bruggeman, 1935; Landauer, 1952; Stroud, 1975; Guibert et al., 2016): The REV is considered to be surrounded by a homogenised medium whose properties are self-consistently defined as those arising from the solution of the closure problem.
The solution of the unit cell problem requires detailed information on the pore space geometry and can generally only be achieved at high computational cost. Therefore, the objective of modelling is to directly parameterise the integrals of the pressure deviation and the wall shear stress in terms of the volume-averaged velocity to bypass the pore scale problem.

1.2.3. Periodic homogenisation

This section sketches the main idea of the periodic homogenisation approach based on the references (Ene & Sanchez-Palencia, 1975; Lévy, 1987; Allaire, 1997; Auriault, 2002; Davit et al., 2013). The homogenisation approach considers porous media occupying a domain of length L and consisting of unit cells of period ℓ. Here, a periodic porous medium is assumed from the outset, whereas in the volume-averaging theory the periodicity of the

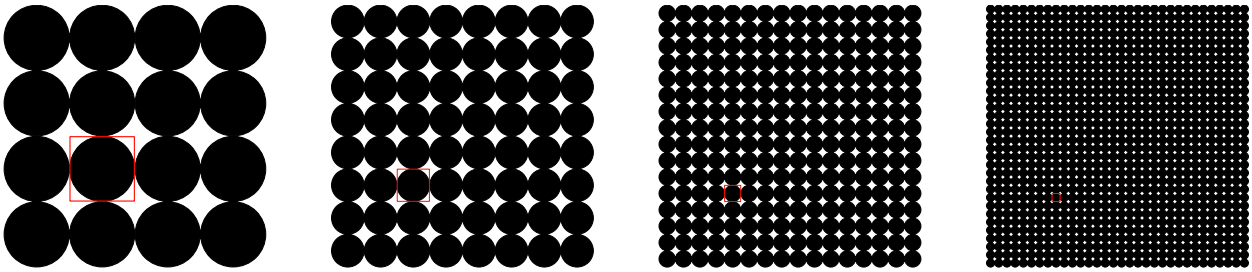

Figure 1.4: Conceptual sketch of the homogenisation approach. The size ℓ of the unit cell is reduced until a homogeneous medium is obtained.

porous medium is assumed only in the development of the closure problem (Davit et al., 2013). The porous medium is characterised by the length scale ratio $\varepsilon = \ell/L$, which is a small parameter. In essence, homogenisation theory aims to find an asymptotic description of the flow problem in the limit $\varepsilon \to 0$ (Lévy, 1987), in which the unit cells become very small and the pore space and matrix are homogeneously distributed throughout the domain (figure 1.4).
The variations of the flow can then be considered "locally periodic", that is the difference in the function values between two points that are one period apart, i.e. $\boldsymbol{x}_1 - \boldsymbol{x}_2 = O(\ell)$, is very small, but the difference in the function values between two points that are many periods apart, i.e. $\boldsymbol{x}_1 - \boldsymbol{x}_2 = O(L)$, can be very large (Ene & Sanchez-Palencia, 1975; Lévy, 1987). Mathematically, this is achieved by introducing a stretched pore scale coordinate $\boldsymbol{y} = \boldsymbol{x}/\varepsilon$ in addition to the field scale coordinate $\boldsymbol{x}$. The velocity and pressure are then expressed in terms of both variables

$$\boldsymbol{u}(\boldsymbol{x}, t) = \boldsymbol{u}(\boldsymbol{x}, \boldsymbol{y}, t)\,, \tag{1.10a}$$
$$p(\boldsymbol{x}, t) = p(\boldsymbol{x}, \boldsymbol{y}, t)\,, \tag{1.10b}$$

where the functions are triply periodic in the $\boldsymbol{y}$-coordinate (Lévy, 1987). The derivatives of these functions can be obtained using the chain rule of differentiation, e.g.

$$\boldsymbol{\nabla} p = \boldsymbol{\nabla}_{\boldsymbol{x}} p + \varepsilon^{-1} \boldsymbol{\nabla}_{\boldsymbol{y}} p\,. \tag{1.11}$$

Notably, the changes with respect to $\boldsymbol{x}$ are by a factor ε smaller than the changes with respect to $\boldsymbol{y}$. Therefore, the dependency on $\boldsymbol{x}$ describes the slowly varying part of the function and the dependency on $\boldsymbol{y}$ describes the rapidly varying part of the function.
The velocity and the pressure are sought for in the form of perturbation series in the length scale ratio ε, which is a small parameter:

$$\boldsymbol{u}(\boldsymbol{x}, \boldsymbol{y}, t) = \boldsymbol{u}_0(\boldsymbol{x}, \boldsymbol{y}, t) + \varepsilon\, \boldsymbol{u}_1(\boldsymbol{x}, \boldsymbol{y}, t) + O\left(\varepsilon^2\right)\,, \tag{1.12a}$$
$$p(\boldsymbol{x}, \boldsymbol{y}, t) = p_0(\boldsymbol{x}, \boldsymbol{y}, t) + \varepsilon\, p_1(\boldsymbol{x}, \boldsymbol{y}, t) + O\left(\varepsilon^2\right)\,. \tag{1.12b}$$

The crucial step of the process is to decide upon the scaling of the velocity and the pressure. Here, the normalised velocity $\hat{\boldsymbol{u}} = \boldsymbol{u}/u_{\mathrm{ref}}$ is defined based on a reference velocity and — in anticipation of Darcy's law (1.42) — the normalised pressure is defined as $\hat{p} = p/\left(\mu\, u_{\mathrm{ref}}\, L/\ell^2\right)$.

In addition, the dimensionless field scale coordinate $\hat{\boldsymbol{x}} = \boldsymbol{x}/L$, the dimensionless pore scale coordinate $\hat{\boldsymbol{y}} = \boldsymbol{y}/L = \boldsymbol{x}/\ell$ and the dimensionless time $\hat{t} = t/t_{\mathrm{ref}}$ are introduced. The Reynolds number and the Womersley number are defined as $Re = u_{\mathrm{ref}}\ell/\nu$ and $Wo^2 = \ell^2/(\nu t_{\mathrm{ref}})$, respectively, and are assumed to be independent of ε in the following. Then, the nondimensional Navier-Stokes equations can be obtained as

$$\varepsilon\, \boldsymbol{\nabla}_{\hat{\boldsymbol{x}}} \cdot \hat{\boldsymbol{u}} + \boldsymbol{\nabla}_{\hat{\boldsymbol{y}}} \cdot \hat{\boldsymbol{u}} = 0\,, \tag{1.13a}$$

and

$$\begin{aligned} &Wo^2 \frac{\partial \hat{\boldsymbol{u}}}{\partial \hat{t}} + \varepsilon Re \boldsymbol{\nabla}_{\hat{\boldsymbol{x}}} \cdot (\hat{\boldsymbol{u}} \otimes \hat{\boldsymbol{u}}) + Re \boldsymbol{\nabla}_{\hat{\boldsymbol{y}}} \cdot (\hat{\boldsymbol{u}} \otimes \hat{\boldsymbol{u}}) \\ &= -\boldsymbol{\nabla}_{\hat{\boldsymbol{x}}} \hat{p} - \varepsilon^{-1} \boldsymbol{\nabla}_{\hat{\boldsymbol{y}}} \hat{p} + \varepsilon^2 \Delta_{\hat{\boldsymbol{x}}\hat{\boldsymbol{x}}} \hat{\boldsymbol{u}} + \varepsilon \Delta_{\hat{\boldsymbol{x}}\hat{\boldsymbol{y}}} \hat{\boldsymbol{u}} + \varepsilon \Delta_{\hat{\boldsymbol{y}}\hat{\boldsymbol{x}}} \hat{\boldsymbol{u}} + \Delta_{\hat{\boldsymbol{y}}\hat{\boldsymbol{y}}} \hat{\boldsymbol{u}}\,. \end{aligned} \tag{1.13b}$$

Note that the choice of normalisation determines the importance of the different terms with respect to ε and leads to different equations that may also include nonlocal interactions (Allaire, 1997; Davit et al., 2013).
After introducing the perturbation series (1.12) into the Navier-Stokes equations (1.13), the terms are grouped based on powers of ε. The balance of order ε^{-1} results in

$$0 = -\boldsymbol{\nabla}_{\hat{y}} \hat{p}_0\,; \tag{1.14}$$

consequently, the leading-order pressure contribution $p_0(\hat{\boldsymbol{x}}, \hat{\boldsymbol{y}}, t)$ is independent of the pore scale coordinate $\hat{\boldsymbol{y}}$ and reduces to $\hat{p}_0(\hat{\boldsymbol{x}}, t)$. The balance of order ε^0 results in the equations

$$\boldsymbol{\nabla}_{\hat{\boldsymbol{y}}} \cdot \hat{\boldsymbol{u}}_0 = 0 \tag{1.15a}$$

$$Wo^2 \frac{\partial \hat{\boldsymbol{u}}_0}{\partial \hat{t}} + Re \boldsymbol{\nabla}_{\hat{\boldsymbol{y}}} \cdot (\hat{\boldsymbol{u}}_0 \otimes \hat{\boldsymbol{u}_0}) = \underbrace{-\boldsymbol{\nabla}_{\hat{\boldsymbol{x}}} \hat{p}_0}_{\text{source}} - \boldsymbol{\nabla}_{\hat{\boldsymbol{y}}} \hat{p}_1 + \Delta_{\hat{\boldsymbol{y}}\hat{\boldsymbol{y}}} \hat{\boldsymbol{u}}_0\,. \tag{1.15b}$$

These equations correspond to the incompressible Navier-Stokes equations on a unit cell with the macroscopic pressure gradient $\boldsymbol{\nabla}_{\hat{\boldsymbol{x}}} \hat{p}_0$ acting as a momentum source term. The velocity $\hat{\boldsymbol{u}}_0$ must satisfy the no-slip and impermeable wall boundary conditions on the pore walls and both the velocity and the pressure $\hat{p}_1$ are triply periodic with respect to $\hat{\boldsymbol{y}}$. The continuity equation of order ε^1 is

$$\boldsymbol{\nabla}_{\hat{\boldsymbol{x}}} \cdot \hat{\boldsymbol{u}}_0 + \boldsymbol{\nabla}_{\hat{\boldsymbol{y}}} \cdot \hat{\boldsymbol{u}}_1 = 0\,. \tag{1.16}$$

Integrating the continuity equation with respect to $\hat{\boldsymbol{y}}$ and using the periodicity and the impermeable wall boundary conditions for $\hat{\boldsymbol{u}}_1$, we obtain

$$\boldsymbol{\nabla}_{\hat{\boldsymbol{x}}} \cdot \langle \hat{\boldsymbol{u}}_0 \rangle_{\mathrm{s}} = 0\,. \tag{1.17}$$

This equation expresses the conservation of mass on the field scale. For $\varepsilon \ll 1$, the higher-order contributions in ε may be neglected and the equations can be transformed back to the

dimensional form:

$$\boldsymbol{\nabla}_{\boldsymbol{x}} \cdot \langle \boldsymbol{u} \rangle_{\mathrm{s}} = 0 \tag{1.18a}$$

$$\boldsymbol{\nabla}_{\boldsymbol{y}} \cdot \boldsymbol{u} = 0 \tag{1.18b}$$

$$\frac{\partial \boldsymbol{u}}{\partial t} + \boldsymbol{\nabla}_{\boldsymbol{y}} \cdot (\boldsymbol{u} \otimes \boldsymbol{u}) = -\frac{1}{\rho} \boldsymbol{\nabla}_{\boldsymbol{y}} \tilde{p} + \nu \Delta_{\boldsymbol{y}\boldsymbol{y}} \boldsymbol{u} - \frac{1}{\rho} \boldsymbol{\nabla}_{\boldsymbol{x}} \langle p \rangle_{\mathrm{i}} \,. \tag{1.18c}$$

Here, the velocity has been identified as $\boldsymbol{u} = \boldsymbol{u}_0$, the macroscopic pressure as $\langle p \rangle_{\mathrm{i}} = p_0$ and the microscopic pressure as $\tilde{p} = \varepsilon\, p_1$. This system of equations is also known as the "two-pressure [Navier-]Stokes system" (Allaire, 1997), since it involves a macroscopic pressure variable $\langle p \rangle_{\mathrm{i}}$ enforcing the continuity equation on the field scale and a microscopic pressure variable $\tilde{p}$ enforcing the continuity equation on the unit cell.

The solution of the homogenised system may proceed in two independent steps (Ene & Sanchez-Palencia, 1975): First, a relationship is established between the macroscopic pressure gradient and the superficial velocity based on the unit cell problem. In steady linear flow, this relationship is given by Darcy's law

$$\langle \boldsymbol{u} \rangle_{\mathrm{s}} = -\frac{K}{\mu} \boldsymbol{\nabla}_{\boldsymbol{x}} \langle p \rangle_{\mathrm{i}} \,, \tag{1.19}$$

while it is given by the Navier-Stokes equations averaged over the unit cell in general

$$\rho \frac{\partial \langle \boldsymbol{u} \rangle_{\mathrm{s}}}{\partial t} = \underbrace{-\frac{1}{V} \int_{A_{\mathrm{fs}}} \tilde{p}\, \boldsymbol{n}\, \mathrm{d}A_{\boldsymbol{y}}}_{\text{pressure drag}} + \underbrace{\frac{1}{V} \int_{A_{\mathrm{fs}}} \boldsymbol{\tau}_{\mathrm{w}}\, \mathrm{d}A_{\boldsymbol{y}}}_{\text{friction drag}} - \epsilon\, \boldsymbol{\nabla}_{\boldsymbol{x}} \langle p \rangle_{\mathrm{i}} \,. \tag{1.20}$$

Second, the continuity equation on the field scale is used to determine the macroscopic pressure field, for instance

$$\boldsymbol{\nabla}_{\boldsymbol{x}} \cdot \left(-\frac{K}{\mu} \boldsymbol{\nabla}_{\boldsymbol{x}} \langle p \rangle_{\mathrm{i}} \right) = 0 \,. \tag{1.21}$$

Note that the above results (1.18) and (1.20) are consistent with the results (1.8a) and (1.9) of the volume-averaging approach, since the macroscopic convective and diffusive terms are asymptotically negligible for $Re\,(\ell/L) \ll 1$ and $\ell \ll L$ (Whitaker, 1986, 1996) and the volume-averaged velocity is nearly constant over the REV.

1.2.4. Other approaches

Based on the volume-averaging theory, Lasseux et al. (2019) developed an upscaling approach for unsteady porous media flow, in which a generalised step response is determined from a closure problem involving the instantaneous pore scale velocity.

The method of Bloch wave homogenisation (Allaire & Conca, 1996, 1998) is based on the quantum mechanical description of crystals. In this approach, the pore scale ℓ is kept fixed while the domain size L tends to infinity, whereas in the theory of periodic homogenisation

the porous medium domain is kept fixed on the field scale L while the pore scale ℓ tends to zero (Allaire & Conca, 1996). The relation between the two approaches was investigated by Wellander (2009).

1.3. Review of prior research

This section contains an overview of prior research relevant to the problem of oscillatory flow through porous media. Before reviewing the literature, some terminology for temporally varying flow must be established (figure 1.5). First, one can distinguish between *steady* flow, which is constant in time, and *unsteady* flow, which varies over time. Second, one can characterise the flow based on the statistical properties of the boundary conditions, of the forcing and of the velocity and pressure over time. A flow is statistically *stationary* in the wide sense if the mean value is independent of time and if the autocorrelation between two instants t_1 and t_2 only depends on the difference $t_1 - t_2$ (Gardner, 1986, pp.105f). Trivially, steady flow is stationary. Furthermore, flow is statistically periodic or *cyclostationary* in the wide sense if the mean value is invariant with respect to a time shift by a period T and if the autocorrelation between two instants t_1 and t_2 is the same as at the instances $t_1 + T$ and $t_2 + T$ (Gardner, 1986, pp.323f). Cyclostationary flow can be further divided into *oscillatory* flow, which has a zero time mean (Akhavan et al., 1991a), and *pulsatile* flow, which has a non-zero time mean. In this work, the definition of oscillatory flow is slightly relaxed to allow for non-zero secondary flow in the time mean, which however must not result in an overall volume flow rate. Finally, a flow is termed *transient* if it tends to a "steady state", which is either stationary or cyclostationary, for large times (Schlichting & Gersten, 2017, p.645).

1.3.1. Investigations of oscillatory flow

In the following, the current knowledge on oscillatory flow is summarised irrespective of the application. In particular, flow in response to an oscillatory forcing such as an oscillating pressure gradient or volume flow rate is considered. On the other hand, flow for which the oscillation is a product of the flow itself, for example the von Kármán vortex street, is not considered. The characteristic features of oscillatory flow are highlighted using simple canonical flow cases (figure 1.6). The focus is placed on the velocity distribution, the drag, and the transition to turbulence.

Stokes boundary layer

The Stokes boundary layer describes flow in a semi-infinite domain bounded by a tangentially oscillating wall. For this case there is an analytical solution to the incompressible Navier-Stokes equations and it serves as a simple example to illustrate some of the properties of oscillatory flow in general.

The x-coordinate is supposed to be aligned with the direction of motion of the wall and the y-coordinate is chosen to describe the distance from the wall ($y = 0$). In the canonical statement of the problem, the wall oscillates with a tangential velocity $U(t) = U_0 \cos(\Omega t)$ and the fluid is assumed to be at rest for $y \to \infty$. In order to facilitate the comparison

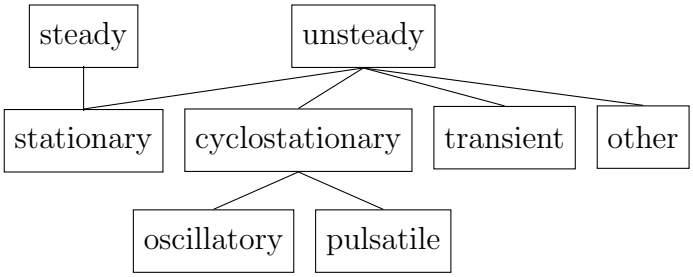

Figure 1.5: Terminology for the temporal variability of fluid flow.

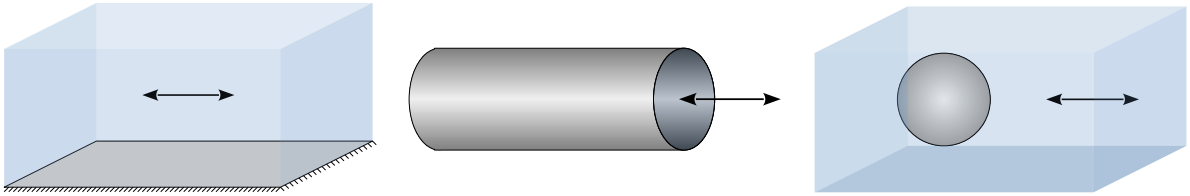

(a) Stokes boundary layer **(b)** oscillatory pipe flow **(c)** oscillatory flow around a sphere

Figure 1.6: Canonical flow cases in the study of oscillatory flow.

to the flow cases discussed in the following, the flow is considered in a coordinate system moving with the wall such that the wall is at rest and the fluid is driven by a body force $f_x = -\rho\Omega U_0 \sin(\Omega t)$. Thus, the following solution is obtained (Schlichting & Gersten, 2017, p.129):

$$u(y,t) = U_0 \left[e^{-y/\delta_\mathrm{s}} \cos\left(\Omega t - y/\delta_\mathrm{s}\right) - \cos\left(\Omega t\right) \right] \tag{1.22}$$

where

$$\delta_\mathrm{s} = \sqrt{\frac{2\,\nu}{\Omega}} \tag{1.23}$$

is the characteristic thickness of the Stokes boundary layer. The wall shear stress

$$\tau_\mathrm{w} = \mu \left.\frac{\partial u}{\partial y}\right|_{y=0} = -\rho\sqrt{\Omega\,\nu}\,U_0 \cos\left(\Omega t + \frac{\pi}{4}\right) \tag{1.24}$$

leads the far-field velocity by a phase angle $\pi/4$, which is characteristic of oscillatory boundary layer flow (Schlichting & Gersten, 2017, p.142).
Figure 1.7 shows the velocity profiles of the Stokes boundary layer at six instants in the first half of the cycle. It is clearly visible that the phase of the oscillation varies with the wall distance and that the deviation from the cosinusoidal oscillation in the outer flow ($y \to \infty$) decreases with the wall distance. Moreover, at certain times the velocity profile exhibits both local maxima and inflection points. Since velocity profiles with inflection points are unstable (Schlichting & Gersten, 2017, p.432), these phases are susceptible to the growth of

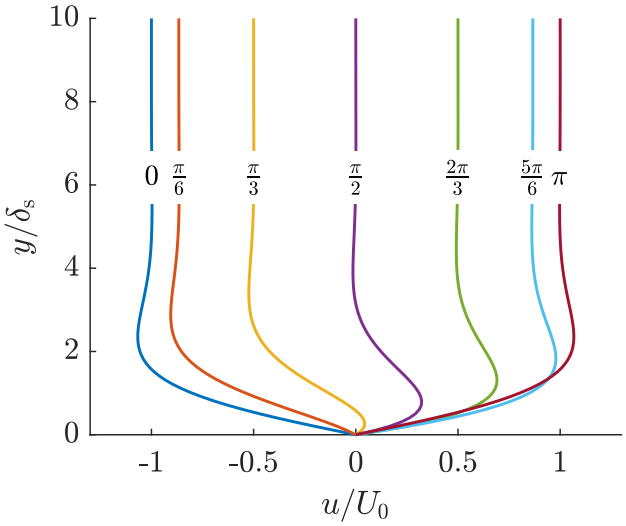

Figure 1.7: Velocity profiles of the Stokes boundary layer over half a cycle. The curves are labelled with the corresponding value Ωt.

perturbations and the onset of turbulence.

Indeed, experimental observations show that the flow becomes unstable for $Re_\delta = U_0\,\delta_s/\nu \approx 500 - 550$ and turbulence "explosively" appears at the beginning of the deceleration phase (Akhavan et al., 1991a,b). Blennerhassett & Bassom (2002) performed a linear stability analysis of the oscillatory Stokes boundary layer and showed that the oscillatory boundary layer is linearly unstable above a critical Reynolds number $Re_{\delta,\mathrm{crit}} = 1416$. However, this result does not explain the above experimental results. Ozdemir et al. (2014) performed direct numerical simulations of the Stokes boundary layer for different initial conditions. They observed "self-sustaining transitional flow" at $Re_\delta = 600$ that is created by a linear modal amplification of the initial disturbance and then sustained by nonlinear self-interaction (whereas the disturbance would decay according to linearised dynamics). They also report intermittently turbulent flow for $Re_\delta = 800$ and 1000. The mechanism described by Ozdemir et al. (2014) was also observed by Biau (2016), who investigated optimal perturbation patterns for $Re_\delta = 564$ that exhibit exponential growth before saturating and evolving into turbulence. These patterns consist of a sequence of flat, strongly inclined spanwise vortices with an alternating direction of rotation. It is observed that "[t]he amplification is fast; the whole transition can be realised within one deceleration phase. Following the transient, the flow is close to the laminar state in the accelerated phase, but turbulent bursts are triggered during the decelerated phase of the cycle".

Oscillatory pipe flow

While the effect of the wall in the Stokes boundary layer extends to infinity, this is obviously not possible in porous media where the flow domain is limited to the pore space. The consequences of this confinement can be understood by considering oscillatory pipe flow.

The analytical solution for laminar oscillatory flow in a circular pipe was first published by Sexl (1930) and rederived by Womersley (1955). For flow in a pipe of radius R driven by a

complex oscillatory body force $f_x\, e^{\mathrm{i}\Omega t}$, the streamwise velocity component reads

$$u_s(r,t) = -\frac{\mathrm{i}}{\rho\,\Omega}\left[1 - \frac{\mathrm{J}_0\left(\sqrt{-\frac{\mathrm{i}\Omega}{\nu}}\,r\right)}{\mathrm{J}_0\left(\sqrt{-\frac{\mathrm{i}\Omega}{\nu}}\,R\right)}\right] f_x\, e^{\mathrm{i}\Omega t}\,, \tag{1.25}$$

where r is the radial coordinate of the pipe cross-section and J_0 is the zero-th order Bessel function of the first kind. Note that the solution is linear in the body force and other solutions can be obtained by superposition. Rewriting the solution in dimensionless form

$$\frac{\mu\, u_s(r,t)}{f_x\, d^2} = -\frac{\mathrm{i}}{Wo^2}\left[1 - \frac{\mathrm{J}_0\left(\sqrt{-\mathrm{i}}\; Wo\, \frac{r}{d}\right)}{\mathrm{J}_0\left(\sqrt{-\mathrm{i}}\; Wo\, \frac{1}{2}\right)}\right] e^{\mathrm{i}\Omega t}\,, \tag{1.26}$$

with the pipe diameter d, it is found to be parametrised by the Womersley number

$$Wo = \sqrt{\frac{\Omega}{\nu}}\, d\,, \tag{1.27}$$

which (up to a factor of $\sqrt{2}$) represents the ratio of the pipe diameter to the Stokes boundary layer thickness δ_s (equation 1.23). It can be shown that for small Womersley numbers (low frequencies), the amplitude of the velocity becomes independent of Wo whereas for large Womersley numbers (high frequencies), the amplitude of the velocity is damped with Wo^{-2}. Furthermore, the phase lag of the velocity behind the exciting force approaches 0 for small Womersley numbers and $\pi/2$ for large Womersley numbers. For the centreline velocity, the low and high frequency asymptotes intersect at $Wo = 4$, indicating the transition between the low and high frequency regimes.
The velocity profiles are plotted in figure 1.8 for the Womersley numbers 0.01 and 100. In the low frequency regime (figure 1.8a), the velocity profiles have a parabolic shape. They are the steady-state profiles corresponding to the instantaneous body force (Schlichting & Gersten, 2017, p.140). In the high frequency regime (figure 1.8b), the velocity profiles have a uniform core velocity profile and a Stokes boundary layer along the wall. An important property of these velocity profiles is the *annular effect* that was first observed by Richardson & Tyler (1929): "[O]wing to inertia, the velocity in annuli remote from the centre of the orifice [is] much greater than at the centre itself [...]".
The net force exerted by the flow onto the pipe is given by the wall shear stress

$$\tau_\mathrm{w} = -\mu\left.\frac{\partial u_s}{\partial r}\right|_{r=R} = \frac{f_x d}{\sqrt{-\mathrm{i}}\, Wo}\,\frac{\mathrm{J}_1\left(\sqrt{-\mathrm{i}}\; Wo\, \frac{1}{2}\right)}{\mathrm{J}_0\left(\sqrt{-\mathrm{i}}\; Wo\, \frac{1}{2}\right)}\, e^{\mathrm{i}\Omega t}\,. \tag{1.28}$$

For small Womersley numbers, the wall shear stress reduces to

$$\tau_\mathrm{w} \approx \frac{f_x d}{4}\, e^{\mathrm{i}\Omega t}\,, \tag{1.29}$$

which simply expresses the steady-state equilibrium between the wall shear stress and the

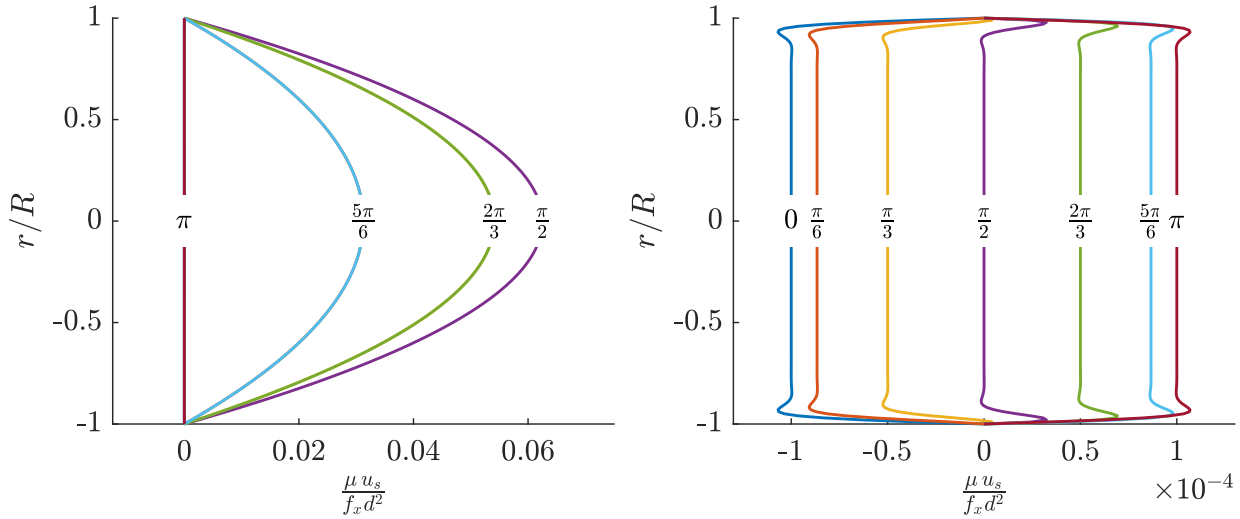

(a) Low frequency regime ($Wo = 0.01$) **(b)** High frequency regime ($Wo = 100$)

Figure 1.8: Velocity profiles of oscillatory pipe flow over half a cycle. The curves are labelled with the corresponding value Ωt.

body force. For high Womersley numbers, the wall shear stress tends to

$$\tau_\mathrm{w} \approx -\mathrm{i}\frac{f_x d}{Wo}\, e^{\mathrm{i}\Omega t + \mathrm{i}\frac{\pi}{4}}\,. \tag{1.30}$$

Hence, like in the Stokes boundary layer, the wall shear stress leads the velocity in the core flow by $\pi/4$.

The transition of the oscillatory pipe flow to turbulence depends on the Reynolds number Re_δ and the Womersley number or, alternatively, on the Hagen number (Martin, 2010)

$$Hg = \frac{f_x d^3}{\rho\nu^2} = \frac{\rho U_0 \Omega d^3}{\rho\nu^2} = \frac{Re_\delta\, Wo^3}{\sqrt{2}} \tag{1.31}$$

and the Womersley number.[2] In their experimental study, Hino et al. (1976) observed four distinct flow regimes and postulated a fifth. In laminar flow (i), the velocity profile is described by the analytical solution (1.25). In distorted laminar flow (ii), the velocity profile near the centreline is a little flatter and wider than the analytical prediction. Furthermore, the phase lag between the boundary layer and the core flow is reduced. In weakly turbulent flow (iii), "small amplitude perturbations are superposed on the distorted laminar flow". In conditionally turbulent flow (iv), "turbulence appears only in the decelerating phase, while in the accelerating phase the flow recovers to laminar-like flow". Finally, they hypothesised

[2]Note that the Hagen number is also referred to as a pressure gradient-based Reynolds number, e.g. (Schlichting & Gersten, 2017, p.416). It is also related to the friction velocity-based Reynolds number Re_τ, which is commonly used to describe stationary turbulent flow, as

$$Re_\tau = \frac{u_\tau\, R}{\nu} = \sqrt{\frac{f_x R}{2\rho}}\frac{R}{\nu} = \sqrt{\frac{Hg}{16}}\,.$$

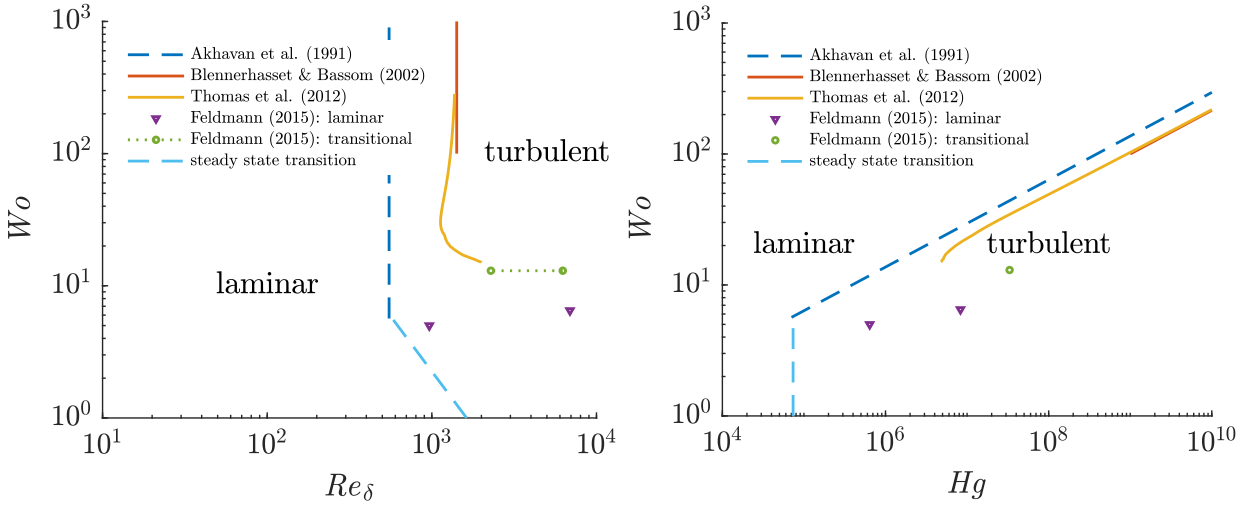

(a) Re_δ–Wo parameter space

(b) Hg–Wo parameter space

Figure 1.9: Transition to turbulence in oscillatory pipe flow. The dashed lines represent the experimentally observed transition, and the continuous lines represent marginal linear stability.

about a fully turbulent flow regime (v), in which turbulence persists over the whole cycle. Note that other authors, e.g. Akhavan et al. (1991a), group the regimes (ii) and (iii) into "disturbed laminar flow".

Figure 1.9 summarises the current knowledge on the transition. The dashed lines represent the experimentally observed transition at $Re_\delta \approx 550$ (Akhavan et al., 1991a) and the transition of stationary flow at $Hg \approx 73600$ corresponding to $Re = \langle u \rangle_\mathrm{i} \, d/\nu = 2300$ (Schlichting & Gersten, 2017, p.117). The solid lines show the critical boundary predicted by a Floquet linear stability analysis of the Stokes boundary layer (Blennerhassett & Bassom, 2002) and of oscillatory pipe flow (Thomas et al., 2012). It can be seen that for high Womersley numbers, the transition only depends on Re_δ and corresponds to the transition of the Stokes boundary layer. Using direct numerical simulations, Xu et al. (2021) demonstrated that oscillatory pipe flow exhibits transient growth of disturbances similar to the Stokes boundary layer (Biau, 2016). Finally, the direct numerical simulations of Feldmann (2015) suggest that at low Womersley numbers the oscillatory flow is more stable than in stationary conditions. Interestingly, Feldmann (2015) reported a flow which alternates between a laminar and a turbulent half-cycle (cf. figure 1.9a).

The transient behaviour of oscillatory pipe flow has been studied by Feldmann (2015, pp.132f, pp.140f). For the laminar cases, the number of cycles for the transient to decay was found to be proportional to Wo^2, suggesting that the transient behaviour is dominated by viscous effects. In contrast, for a turbulent case initialised with a fully developed turbulent pipe flow, Feldmann (2015) observed that most of the transient decays during the first period of the oscillation. The transient has completely decayed after three cycles, whereas in laminar flow at the same Womersley number approximately 45 cycles would be required.

Oscillatory flow around a sphere

The case of oscillatory flow around a sphere illustrates the effect of a geometric blocking of the flow: Part of the sphere is normal to the imposed acceleration, whereas the Stokes boundary layer and the oscillatory pipe flow are only accelerated tangentially to the wall. This leads to a nonzero pressure drag and to the added mass effect. Moreover, the laminar flow around a sphere can become nonlinear, leading to flow separation and streaming patterns in the time-averaged flow. Finally, a different instability mechanism can be observed due to the curved streamlines.
In the canonical setting, the uniform far field velocity oscillates harmonically in time with an amplitude U_0 and a frequency Ω. The flow is characterised by the Reynolds number defined as

$$Re_0 = \frac{U_0\, d}{\nu}\,, \tag{1.32}$$

where d is the sphere diameter, and by the Strouhal number defined as

$$St = \frac{\Omega\, d}{2U_0} \tag{1.33}$$

which represents the ratio of the radius of the sphere to amplitude of fluid displacement (Mei & Adrian, 1992; Chang & Maxey, 1994). Note that a Womersley number based on the sphere diameter can be defined as $Wo = \sqrt{2\, Re_0\, St} = \sqrt{\Omega d^2/\nu}$; such a parameter was used, for example, in Riley (1967).
Neglecting convective effects, Stokes (1851) determined the force on a sphere in oscillatory motion with a velocity $U_0\, e^{\mathrm{i}\Omega t}$. His solution is given in terms of the stream function in spherical coordinates:

$$\tilde{\psi}(r,\theta) = U_0\, e^{\mathrm{i}\Omega t}\, \frac{d^2}{8} \left[\left(1 + \frac{6}{\sqrt{\mathrm{i}}\, Wo} + \frac{12}{\mathrm{i}\, Wo^2} \right) \frac{d}{2r} - \frac{6}{\sqrt{\mathrm{i}}\, Wo} \left(1 + \frac{1}{\sqrt{\mathrm{i}}\, Wo} \frac{d}{r} \right) e^{-\sqrt{\mathrm{i}}\, Wo \left(\frac{r}{d} - \frac{1}{2} \right)} \right] \sin^2\theta\,. \tag{1.34}$$

For a sphere at rest with the fluid in the far field moving with a velocity $-U_0\, e^{\mathrm{i}\Omega t}$, the stream function is

$$\psi(r,\theta) = \tilde{\psi}(r,\theta) - U_0\, e^{\mathrm{i}\Omega t}\, \frac{r^2}{2}\, \sin^2\theta \tag{1.35}$$

where the second term corresponds to a uniform flow (Branlard, 2017). The radial and polar velocity components can be obtained as

$$u_r = \frac{1}{r^2\, \sin\theta} \frac{\partial \psi}{\partial \theta}\,, \tag{1.36a}$$

$$u_\theta = -\frac{1}{r\, \sin\theta} \frac{\partial \psi}{\partial r}\,. \tag{1.36b}$$

Figure 1.10 shows the velocity field and the streamlines for oscillatory flow around a sphere at different Womersley numbers. For low frequencies, the solution consists of a single mode

and the velocity increases monotonically away from the sphere. For high frequencies, the flow consists of two modes, with the real part containing the potential flow and the imaginary part containing only the boundary layer.[3] Notably, the potential flow velocity overshoots the far field value U_0 close to the sphere. The streamlines indicate that the disturbance of the far field flow is significantly weaker for the high frequency than for the low frequency.

From Stokes' solution, the sum of the pressure and friction forces F_p and F_f on the sphere can be obtained as

$$\frac{(F_p + F_\mathrm{f})}{\rho\Omega U_0 \frac{1}{6}\pi d^3} = \underbrace{\left(1+\frac{1}{2}\right) e^{\mathrm{i}\Omega t + \mathrm{i}\frac{\pi}{2}}}_{\text{inviscid flow}} + \underbrace{\frac{9}{Wo}\, e^{\mathrm{i}\Omega t + \mathrm{i}\frac{\pi}{4}}}_{\text{boundary layer}} + \underbrace{\frac{18}{Wo^2}\, e^{\mathrm{i}\Omega t}}_{\text{Stokes' law}} . \tag{1.37}$$

The first term is independent of the viscosity and advances the outer flow velocity by $\pi/2$. It represents the sum of the buoyancy of the sphere in the acceleration field and of the *added mass* force which is caused by the modification of the potential flow field by the presence of the sphere. A review of the added mass effect was given e.g. by Brennen (1982). The second term represents the boundary layer drag and — just as for the Stokes boundary layer — advances the outer flow velocity by $\pi/4$. Finally, the third term is in phase with the outer flow velocity and represents the instantaneous steady-state drag given by the classical Stokes' law (Batchelor, 2000, eq. 4.9.19). Compared to the oscillatory pipe flow discussed in the previous section, there are two main differences: (i) The drag includes an inviscid component determined by the potential flow, and (ii) the pressure contributes to the drag. Note that Stokes' solution (1.37) is inconsistent with the Navier-Stokes equations in that for $Wo^2 \ll Re$ the vorticity far from the sphere should be transported by convection rather than by unsteady diffusion (Mei & Adrian, 1992; Mei, 1994). This inconsistency is associated with the idealised assumption of an unbounded domain and does not occur, for example, in the triple periodic arrays of spheres considered in this work (Happel & Brenner, 1983, pp.44–49).

Using direct numerical simulation, Chang & Maxey (1994) obtained nonlinear solutions for oscillatory flow in the parameter range $0.01 \leq Re_0 \leq 16.7$ and $0.1 \leq St \leq 10$. They found that oscillatory flow may facilitate flow separation: In some cases, a separation bubble forms for Reynolds numbers as low as 5, whereas separation occurs only for $Re_0 \geq 20.7$ in steady flow. The separation bubble appears during the deceleration phase of each cycle (Chang & Maxey, 1994) and "for higher Re the separation occurs earlier [in the cycle]" (Alassar & Badr, 1997). The length of the separation region increases with the Reynolds number and decreases with the Strouhal number (Chang & Maxey, 1994). "[T]he separation bubble creates an asymmetry in the flow; the accelerating and decelerating phases of the oscillation cycle are not direct opposites of each other and create time-independent streaming patterns." (Chang & Maxey, 1994). These streaming patterns were investigated in detail by Satish et al. (2022) and Li et al. (2023). The separation also leads to a "layering effect" in the vorticity caused by the shedding of vorticity of opposite sign in each half-cycle (Chang & Maxey, 1994).

[3] It can be seen from equation (1.22) that the phase of the Stokes boundary layer varies with the wall distance; it is therefore included in both the real and the imaginary part. On the other hand, the potential flow has the same phase everywhere.

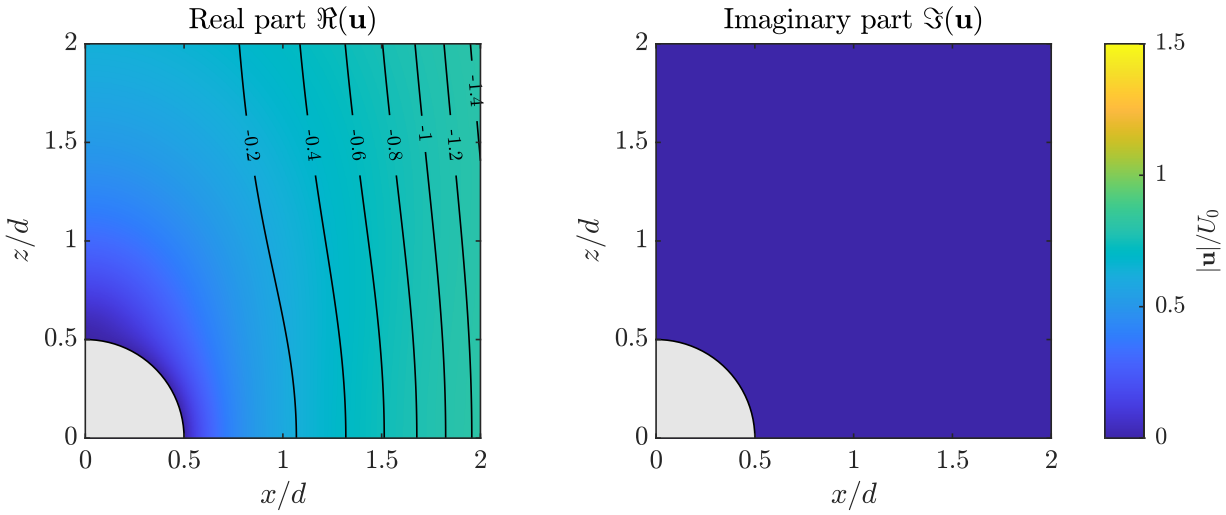

(a) Low frequency regime ($Wo = 10^{-2}$)

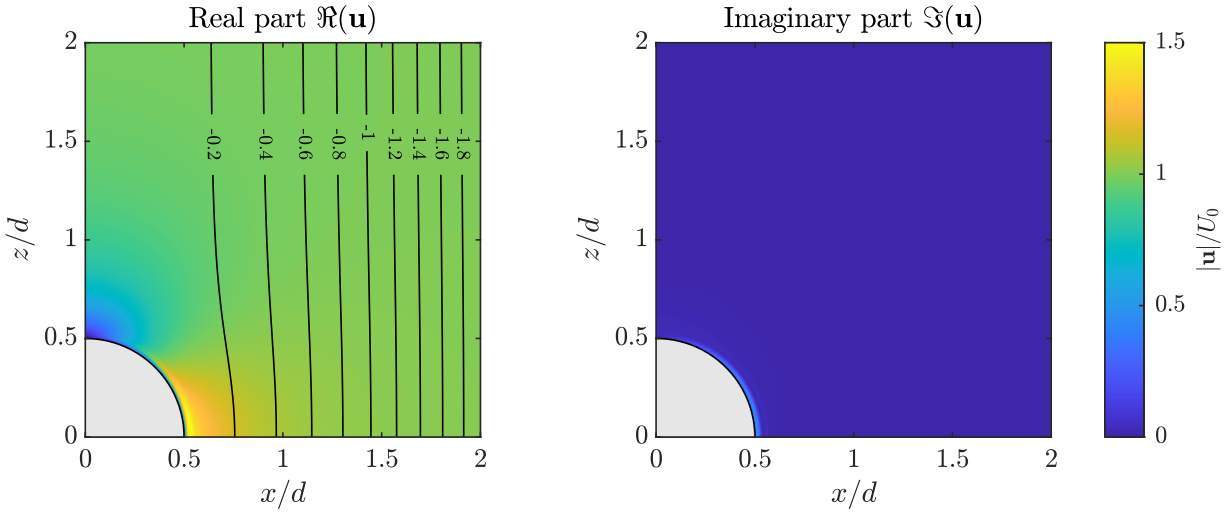

(b) High frequency regime ($Wo = 10^{2}$)

Figure 1.10: Velocity magnitude and isocontours of the streamfunction $\psi/(U_0\, d^2)$ of the Stokes solution for linear oscillatory flow around a sphere evaluated at $t = 0$. The far field velocity oscillates along the z-direction.

In a follow-up study, Chang & Maxey (1995) investigated nonlinear accelerating flow around a sphere. They found that the added-mass effect in response to a sudden acceleration could be linked to a jump in the pressure force that has the same distribution as in irrotational flow.

Otto (1992) investigated the stability of oscillatory flow around a sphere in the high-frequency limit ($Wo \to \infty$). The flow was found to be unstable with respect to Taylor-Görtler vortices at $\theta = \pi/2$, corresponding to $z = 0$, where the outer flow velocity is largest (cf. figure 1.10b). The instability was found to be similar to the case of oscillatory flow around a cylinder (Honji, 1981; Hall, 1984). The wavelength of the most unstable perturbation along

the circumference at $\theta = \pi/2$ resulted as

$$\lambda_{\mathrm{crit}} = \frac{2\pi}{0.51}\sqrt{\frac{2\nu}{\Omega}} = \frac{17.42\,d}{Wo}\,. \tag{1.38}$$

The critical Reynolds number can be expressed in terms of the Womersley number as

$$Re_{0,\mathrm{crit}} = \sqrt{16.956\,Wo^2\left[2^{-3/2}\,Wo + O(Wo^{1/2})\right]} = 2.45\,Wo^{3/2} + O(Wo)\,. \tag{1.39}$$

This value can be compared with the critical Reynolds number for the oscillatory Stokes boundary layer. Since the maximum tangential velocity of the potential flow around the sphere is $3/2\,U_0$, we have

$$Re_{0,\mathrm{crit,Stokes}} = \frac{2}{3\sqrt{2}}\,Re_{\delta,\mathrm{crit}}\;Wo \approx \frac{2}{3\sqrt{2}}\,550\;Wo\,. \tag{1.40}$$

The critical Reynolds number for the transition of the Stokes boundary layer is smaller than the critical Reynolds for the centrifugal instability only for Womersley numbers larger than $1.1 \cdot 10^4$. At smaller Womersley numbers, the centrifugal instability is dominant for as long as the high-frequency approximation of Otto (1992) remains valid. It seems likely that also for oscillatory flow through porous media the transition of the Stokes boundary layer is only significant at very high Womersley numbers.

1.3.2. Investigations of stationary porous media flow

This section gives a brief summary of the main findings on statistically stationary flow through porous media. The literature on flow regimes in porous media can be roughly divided into "pore-scale studies that attempt to resolve the various 'point' terms in the Navier-Stokes equations" and "bulk-scale studies that consider the relationship between volume-averaged components of the Navier-Stokes equations and the bulk hydraulic gradient" (Horton & Pokrajac, 2009). Since the direct numerical simulation approach has been chosen in the present work, an emphasis is placed on the pore scale studies. Furthermore, the scope is limited to sphere packs, since such a porous medium is considered as a model in the present work.

The flow state is determined by the Reynolds number, which is defined here using the superficial velocity and the sphere diameter

$$Re = \frac{|\langle \boldsymbol{u} \rangle_{\mathrm{s}}|\,d}{\nu}\,. \tag{1.41}$$

This definition of the Reynolds number has been used, for example, by Ergun (1952), Jolls & Hanratty (1969), Macdonald et al. (1979) and Dybbs & Edwards (1984); other definitions commonly used for flow through porous media can be found in (Wood et al., 2020). It is common to distinguish four flow regimes (Dybbs & Edwards, 1984; Rode et al., 1994; Montillet, 2004; Horton & Pokrajac, 2009; Wood et al., 2020): (i) The linear or Darcy regime, (ii) the steady nonlinear or inertial regime, (iii) the unsteady nonlinear or transitional

regime, and (iv) the chaotic or turbulent regime. In the following, the definitions and characteristic features of these flow regimes are reviewed. Note that there is no general agreement on the Reynolds number values delimiting these flow regimes (Liu et al., 2021); the values of Wood et al. (2020) for $\epsilon = 0.4$ are reported below to indicate an order of magnitude.

Linear flow ($Re < 10$)

At small Reynolds numbers, the pore scale flow is dominated by molecular diffusion and can be described by the Stokes equations for creeping flow. It is important to recognise that the pore scale flow can exhibit a complex topology despite the apparent simplicity of these equations (Moffatt, 2014). For instance, the flow can locally oppose the direction of the macroscopic pressure gradient (Maier et al., 1998; Johns et al., 2000; Kooshapur, 2016, p.25f) and sequences of corner vortices (*Moffatt eddies*) may occur in narrow gaps (Chaudhary et al., 2011; Maier et al., 1998; Crevacore et al., 2016; Davis et al., 1976; Pasol et al., 2005). Furthermore, the complex topology of the pore space can lead to chaotic advection (Lester et al., 2013).
Due to the linearity of the Stokes equations, there is a linear relationship between the pressure gradient $\boldsymbol{\nabla}\langle p\rangle_{\mathrm{i}}$ and the superficial velocity $\langle \boldsymbol{u}\rangle_{\mathrm{s}}$. For isotropic porous media, this relationship is expressed by Darcy's law (Darcy, 1856; Bear, 2018, p.266)

$$-\boldsymbol{\nabla}\langle p\rangle_{\mathrm{i}} = \frac{\mu}{K}\langle \boldsymbol{u}\rangle_{s}\,, \tag{1.42}$$

where K denotes the *permeability* of the porous medium and μ is the dynamic viscosity of the fluid. For anisotropic porous media, the scalar permeability has to be replaced by a tensor. "The permeability, which has dimensions of (length)^2, depends upon the details of the pore geometry in a complex fashion" (Avellaneda & Torquato, 1991). The permeability is commonly approximated by the semi-empirical Kozeny-Carman equation (Bear, 2013, p.165)

$$K = \frac{d^2}{180}\frac{\epsilon^3}{(1-\epsilon)^2}\,. \tag{1.43}$$

The permeability has also been computed directly from numerical solutions to the Stokes equations for various porous medium geometries, for example by Zick & Homsy (1982).
Note that some experiments have pointed towards a lower limit of applicability for Darcy's law (Kutiĺek, 1972; Bear, 2013, pp.127f): For fluid to flow through the porous medium, a small threshold of pressure gradient must be exceeded. This "pre-Darcy" regime cannot be explained from the Stokes equations with no-slip boundary conditions, but is either a consequence of imperfections in the experiments (Kutiĺek, 1972; Boettcher et al., 2022), e.g. contamination of the fluid with fine particles, entrapped gases or temperature fluctuations, or of other physical processes such as osmotic effects (Bolt & Groenevelt, 1969) or the adherence of fluid layers to the wall (von Engelhardt & Tunn, 1954; Stieß, 2009, pp.78f). Consequently, the occurrence of pre-Darcy flow is likely to be independent of the Reynolds number (Boettcher et al., 2022). In the remainder of this thesis, pre-Darcy behaviour will not be considered.

Steady nonlinear flow ($10 < Re < 150$)

At larger Reynolds numbers the influence of fluid inertia can no longer be neglected. While the pore scale flow remains laminar, the converging-diverging flow pattern transforms into jet-like inertial cores (Dybbs & Edwards, 1984; Hill et al., 2001b; Horton & Pokrajac, 2009; Chukwudozie & Tyagi, 2013; Sakai & Manhart, 2020) and flow separation regions appear (Wegner et al., 1971; Karabelas et al., 1973).
Due to the nonlinear convective term, Darcy's law (1.42) is not valid in this regime. For weakly nonlinear flow through an isotropic porous medium, Mei & Auriault (1991) derived a cubic correction to Darcy's law

$$-\boldsymbol{\nabla}\langle p\rangle_{\mathrm{i}} = \frac{\mu}{K}\langle \boldsymbol{u}\rangle_{\mathrm{s}} + b_{\mathrm{MA}}\langle \boldsymbol{u}\rangle_{\mathrm{s}}\langle \boldsymbol{u}\rangle_{\mathrm{s}}^{2} \,, \tag{1.44}$$

where b_{MA} is a nonnegative coefficient. Firdaouss et al. (1997) presented an alternative derivation from a "reversibility hypothesis" that is satisfied for many ordered porous media. They observed a quadratic correction in a numerical example for which the hypothesis was not satisfied. In contrast, Skjetne & Auriault (1999b) demonstrated that the cubic behaviour is a consequence of the skew-symmetry $\langle[(\boldsymbol{u}\cdot\boldsymbol{\nabla})\boldsymbol{v}]\cdot\boldsymbol{w}\rangle_{\mathrm{i}} = -\langle[(\boldsymbol{u}\cdot\boldsymbol{\nabla})\boldsymbol{w}]\cdot\boldsymbol{v}\rangle_{\mathrm{i}}$ of the convective term in the Navier-Stokes equations and thus should be expected irrespective of the pore geometry. Similarly, Wang (2000) demonstrated that the cubic behaviour is due to the incompressibility of the velocity field, which in turn is a prerequisite for the skew-symmetry. The cubic correction to Darcy's law has been observed in numerical simulations of flow through various ordered and disordered porous media (Koch & Ladd, 1997; Rojas & Koplik, 1998; Hill et al., 2001a). In numerical simulations, a high grid resolution may be necessary to observe the weakly nonlinear behaviour (Lasseux et al., 2011).
For strongly nonlinear flow, the equation (1.44) is no longer valid and the cubic term is overtaken by a quadratic term (Rojas & Koplik, 1998). The relationship between the macroscopic pressure gradient and the superficial velocity is then represented by the empirical Forchheimer equation (Forchheimer, 1901)

$$-\boldsymbol{\nabla}\langle p\rangle_{\mathrm{i}} = a\langle \boldsymbol{u}\rangle_{\mathrm{s}} + b\,|\langle \boldsymbol{u}\rangle_{\mathrm{s}}|\,\langle \boldsymbol{u}\rangle_{\mathrm{s}} \,. \tag{1.45}$$

The coefficients a and b are determined from experiments or numerical simulations; correlations have been given in (Ergun, 1952; Macdonald et al., 1979). Apart from the generally good agreement with experimental results, the Forchheimer equation has some theoretical support. Giorgi (1997) derived the Forchheimer equation from the Oseen equations, in which the convecting velocity was approximated by the intrinsic volume-averaged velocity. It should be noted, however, that this linearisation breaks the aforementioned skew-symmetry of the convective term. Whitaker (1996) developed a form of the closure problem in the volume-averaging theory from which, under certain order-of-magnitude estimates, the "quadratic dependence of the Forchheimer correction seems entirely plausible".

Unsteady nonlinear flow ($150 < Re < 300$)

When the Reynolds number is increased beyond a critical value, the flow starts to exhibit temporal fluctuations whose intensity increases with the Reynolds number. The fluctuation

intensity has been used as an indicator for transition in (Jolls & Hanratty, 1966; Kingston & Nunge, 1973; Seguin et al., 1998a; Bu et al., 2015). Just above the critical Reynolds number the fluctuations are temporally periodic at a single frequency (Koch & Ladd, 1997; Hill & Koch, 2002; Horton & Pokrajac, 2009; Finn et al., 2012; Agnaou et al., 2016; Srikanth et al., 2021); this is the signature of a Hopf bifurcation of the steady flow (Hill & Koch, 2002; Agnaou et al., 2016; Srikanth et al., 2021). These oscillations have been associated with "porescale vortical motion and vortex shedding" (Finn et al., 2012), "pulsations of the inertial core" (Horton & Pokrajac, 2009), "the oscillation of asymmetric vortices" (Agnaou et al., 2016), "laminar wake oscillations" (Dybbs & Edwards, 1984) or with "the development of a vortex [...] whose axis is aligned with the flow and whose direction of rotation alternates with the fundamental frequency." (Hill & Koch, 2002). In the unsteady nonlinear regime, the drag deviates from the Forchheimer equation (1.45) fitted to the steady nonlinear regime; at higher Reynolds numbers, the Forchheimer equation provides a good fit, but with different coefficients (Fand et al., 1987; Burcharth & Andersen, 1995; Hill & Koch, 2002; Sakai & Manhart, 2020).

For flow through a face-centred cubic sphere pack, (Hill & Koch, 2002) observed secondary Hopf bifurcations at higher Reynolds numbers leading to quasi-periodic behaviour (characterised by a discrete frequency spectrum composed of incommensurable frequencies) or chaotic behaviour (characterised by a continuous frequency spectrum). This is consistent with the Ruelle-Takens-Newhouse transition scenario (Ruelle & Takens, 1971; Newhouse et al., 1978): With increasing Reynolds number, the flow undergoes a sequence of Hopf bifurcations that each introduce a new frequency of oscillation into the system — the flow is steady, periodic, quasi-periodic with two incommensurable frequencies, quasi-periodic with three incommensurable frequencies and so on. Once three incommensurable frequencies are present, "[t]he time dependence of the flow [...] becomes chaotic, with sensitive dependence on initial condition, a situation which one may call turbulent" (Newhouse et al., 1978). Such a scenario has been observed for example in converging-diverging channel flow (Guzmán & Amon, 1994), which is somewhat similar to a porous medium. A different route to chaos has been observed by Koch & Ladd (1997): The first Hopf bifurcation "is followed by a sequence of period-doubling transitions leading eventually to chaotic fluctuations in the mean velocity".

Chaotic flow ($Re > 300$)

When the Reynolds number is large enough, a turbulence-like flow state with a wide range of spatial and temporal scales can be observed (Patil & Liburdy, 2013b, 2015; He et al., 2019). According to the definition of Seguin et al. (1998b), the intensity of the wall shear stress fluctuations in the turbulent regime depends only weakly on the Reynolds number. The integral length scale of the flow L_{11} based on the longitudinal two-point velocity correlation has a magnitude between $0.05\,d$ and $0.1\,d$ and decreases with the Reynolds number (Patil & Liburdy, 2015; He et al., 2019). For very high Reynolds numbers ($1360 < Re$), an "asymptotic regime" can be observed in which "the turbulence can be approximated as being locally isotropic over most of the pore space" (Wood et al., 2020) and in which the Kolmogorov microscale estimates apply (Patil & Liburdy, 2015). At these Reynolds numbers, the macroscopic pressure gradient depends on the square of the superficial velocity (Macdonald et al., 1979).

Various models for turbulent flow through porous media have been proposed based on classical Reynolds-averaged turbulence models (Masuoka & Takatsu, 1996; Nakayama & Kuwahara, 1999; Chandesris et al., 2006; Teruel & Rizwan-uddin, 2009a,b; Kuwata et al., 2014) or based on the conceptual similarity of the volume-averaging theory to explicitly filtered large–eddy simulation (Jouybari & Lundström, 2019; Wood et al., 2020). A comprehensive review on the main results on turbulent flow in porous media and its description can be found in (Wood et al., 2020).

1.3.3. Investigations of unsteady porous media flow

This section reviews the main findings on unsteady nonstationary flow through porous media. Flow regimes for nonstationary flow can be defined in analogy to the flow regimes of Dybbs & Edwards (1984) for stationary flow described in the previous section. The pore scale flow can exhibit a linear regime, a laminar nonlinear regime, a transitional regime and a chaotic regime.

Oscillatory flow

Oscillatory flow through porous media is characterised by two independent dimensionless numbers. One usually involves the amplitude of the superficial velocity or of the macroscopic pressure gradient, the other is usually a measure for the frequency of the flow. The Reynolds number based on the maximum velocity over the cycle

$$Re = \limsup_{t\to\infty} \frac{|\langle \boldsymbol{u} \rangle_\mathrm{s}|\, d}{\nu}\,, \tag{1.46}$$

has been frequently employed (Gu & Wang, 1991; van Gent, 1993; Hall et al., 1995; Nakajo et al., 2009), but also the Hagen number $Hg = |\boldsymbol{\nabla}\langle p \rangle_\mathrm{i}|\, d^3/(\rho\nu^2)$ has been used as a "dimensionless body force" (Graham & Higdon, 2002; Iervolino et al., 2010). A dimensionless frequency has been used either in the form of a ratio of the frequency of the flow to a characteristic frequency of the porous medium based on the porosity and the permeability (Johnson et al., 1987; Smeulders et al., 1992; Pride et al., 1993; Zhu & Manhart, 2016) or in the form of the Womersley number $Wo = \sqrt{\Omega\, d^2/\nu}$, which has been used under different names by Simon & Seume (1988), Gu & Wang (1991), Graham & Higdon (2002), Jin & Leong (2006), Iervolino et al. (2010), Pathak & Ghiaasiaan (2011), Bağcı et al. (2016) and Ni et al. (2018), or in the form of the the Keulegan-Carpenter number $KC = 2\pi Re/\,Wo^2$ (van Gent, 1993; Burcharth & Andersen, 1995).
Linear oscillatory flow through porous media is governed by the unsteady Stokes equations and is generally well understood (Landau & Lifshits, 1987, pp.83f; Batchelor, 2000, pp.353f). At low Womersley numbers, the flow is dominated by viscosity and the velocity field tends to a quasi-steady Stokes flow. At high Womersley numbers, the effect of viscosity is confined to the near-wall region, whereas the bulk flow is dominated by the local inertia. The velocity field has a boundary layer structure with oscillatory Stokes boundary layers near the walls and a potential flow in the core. The behaviour of the superficial velocity in linear flow has been the subject of many investigations, especially in the acoustics of porous media. Biot (1956a,b) developed a theory for linear unsteady flow in porous media based on the model

of oscillatory pipe flow. In his theory, the response of the superficial velocity depends on a frequency-dependent dynamic viscosity. The transition between the low- and high-frequency behaviour of the dynamic viscosity is determined by a characteristic frequency of the porous medium that depends on the size and shape of the pores. In a refined approach, Johnson et al. (1987) introduced the frequency-dependent *dynamic permeability* $\hat{K}(\omega)$ in analogy to Darcy's law (1.42). They derived a model expression for $\hat{K}(\omega)$ in the frequency domain by blending the low-frequency asymptotics given by Darcy's law with the high-frequency asymptotics derived from boundary layer theory. The coefficients in this model — the permeability K, the characteristic viscous length Λ and the high-frequency limit of the dynamic tortuosity α_∞ — depend on the Stokes flow and potential flow solutions and are related to the eigenvalues and eigenfunctions of the Stokes operator (Avellaneda & Torquato, 1991). The model has been found to accurately describe oscillatory flow through various sphere packs (Chapman & Higdon, 1992) and multiple extensions have been proposed (Champoux & Allard, 1991; Pride et al., 1993). A comprehensive review of these models can be found, for instance, in (Lafarge, 2009). Motivated by the volume-averaging theory, the unsteady Darcy equation

$$\rho \boldsymbol{C}_\mathrm{a} \cdot \frac{\mathrm{d}\langle \boldsymbol{u} \rangle_\mathrm{s}}{\mathrm{d}t} = -\boldsymbol{\nabla} \langle p \rangle_\mathrm{i} - \frac{\mu}{K} \langle \boldsymbol{u} \rangle_s \tag{1.47}$$

has been used to describe linear unsteady flow through porous media in the time domain (Nield, 1991). Different expressions for the acceleration coefficient tensor $\boldsymbol{C}_\mathrm{a}$ have been proposed (Burcharth & Andersen, 1995; Hill et al., 2001a; Zhu et al., 2014). It has been shown by Zhu & Manhart (2016) that the unsteady Darcy equation can accurately describe oscillatory flow at low and high frequencies if the acceleration coefficient is chosen based on the Stokes flow and the potential flow, respectively.

Nonlinear oscillatory flow through porous media has mostly been studied with a focus on the resistance and overall heat transfer behaviour. For instance, van Gent (1993) and Hall et al. (1995) conducted experiments of oscillatory flow through sediment, rock and sphere packs. The experiments were evaluated in the framework of the unsteady Forchheimer equation (Polubarinova-Kochina, 1962; Sollitt & Cross, 1972)

$$-\boldsymbol{\nabla} \langle p \rangle_\mathrm{i} = a \langle \boldsymbol{u} \rangle_\mathrm{s} + b \left| \langle \boldsymbol{u} \rangle_\mathrm{s} \right| \langle \boldsymbol{u} \rangle_\mathrm{s} + c \frac{\mathrm{d}\langle \boldsymbol{u} \rangle_\mathrm{s}}{\mathrm{d}t} \,. \tag{1.48}$$

The relationship between the amplitude of the superficial velocity and of the macroscopic pressure gradient was investigated, for example, by Hsu et al. (1999), Pamuk & Özdemir (2014), Bağcı et al. (2016) and Perrella (2017), and was shown to follow a similar correlation as in the steady state, although with different coefficients. Based on the unsteady Forchheimer equation (1.48), Gu & Wang (1991) divided the Re–Wo^2 parameter space into regions dominated by the linear term, the nonlinear term and the acceleration term. These estimates are discussed in section 3.5.2.

In nonlinear flow, a phenomenon called "acoustic streaming" can be observed: The interactions in the convective term lead to a time-averaged velocity field whose amplitude is proportional to the square of the velocity and inversely proportional to the frequency (Lighthill, 1978; Manor, 2021).

Indications on the transition behaviour of oscillatory flow through porous media can be found

in the work of Roberts & Mackley (1996) who investigated the route to chaos for oscillatory flow through baffled channels. They observed that the flow undergoes a pitchfork bifurcation from a space-time symmetric state, in which the flow is invariant under a half-period time shift with a reversal of the flow direction, to a space-time asymmetric state. A period-doubling bifurcation then leads into a chaotic flow state.
Using particle tracking velocimetry, Nakajo et al. (2008, 2009) measured turbulent oscillatory flow inside a regular sphere pack at the Reynolds numbers $Re = 212$ and 416 and Keulegan-Carpenter numbers $KC = 2.8$ and 14. This corresponds to the Womersley numbers $Wo = 21.8$ and 30.5 for the lower and $Wo = 9.8$ and 13.8 for the higher value of KC, respectively. At the lower Keulegan-Carpenter number the turbulent kinetic energy (TKE) lags behind the superficial velocity and the TKE does not decrease to zero when the flow direction is reversed. The superficial velocity undergoes a rapid acceleration during which hardly any fluctuations can be detected, while relatively strong fluctuations can be observed during the peak and deceleration phase. At the higher Keulegan-Carpenter number the TKE is mostly in phase with the superficial velocity and only lags behind during the (shorter) acceleration phase. The TKE is close to zero when the flow direction is reversed; this is reminiscent of the turbulent oscillatory pipe flow (Akhavan et al., 1991b). The superficial velocity behaves similarly during the acceleration and the deceleration phase.

Pulsatile flow

A frequently studied case is pulsatile flow driven by a sinusoidal forcing with non-zero mean (Paek et al., 1999; Graham & Higdon, 2002; Iervolino et al., 2010; Pathak & Ghiaasiaan, 2011). An additional dimensionless parameter is necessary to describe the relative strength of the harmonic and the mean component (Graham & Higdon, 2002; Iervolino et al., 2010). Other waveforms were studied by Graham & Higdon (2002). In general, the "oscillatory forcing may act to either increase or decrease the flow rate" (Graham & Higdon, 2002). Dasgupta & Atta (2017) performed numerical simulations of pulsatile flow through different sphere packs. The flow was driven by square wave variations in the flow rate, where the minimum flow rate was set to zero ("on-off") or to half of the maximum flow rate ("min-max"). In both cases, the velocity distributions were found to be more uniform in pulsatile flow than in stationary flow.

Transient flow

Linear transient flow, which is started from rest by a constant macroscopic pressure gradient, was investigated by Hill et al. (2001a) and Zhu et al. (2014). In both works, the temporal evolution of the flow was approximated by the unsteady Darcy equation (1.47). For the acceleration coefficient, Hill et al. (2001a) considered the small time limit, in which the flow is approximately inviscid, and the large time limit, in which the flow is close to the steady state, and they presented explicit expressions for dilute arrays of spheres. Note that these limit cases coincide with those of Zhu & Manhart (2016) for high- and low-frequency oscillatory flow, respectively. At large times, the acceleration coefficient is determined via the kinetic energy equation as $\boldsymbol{C}_\mathrm{a} = \langle \boldsymbol{u}_\mathrm{Stokes}^2 \rangle_\mathrm{s} \,/\, \langle \boldsymbol{u}_\mathrm{Stokes} \rangle_\mathrm{s}^2 \, \boldsymbol{I}$, where $\boldsymbol{u}_\mathrm{Stokes}$ is the velocity field in the Stokes flow (Hill et al., 2001a; Zhu et al., 2014).
Nonlinear transient flow was studied by Zhu (2016) using direct numerical simulations of

flow through different porous media. He found that the occurrence of nonlinear effects does not depend on the instantaneous Reynolds number, but can be approximately described by the Reynolds number $|\langle \boldsymbol{u} \rangle_\mathrm{s}| \, \delta_\mathrm{s}/\nu$ formed with the instantaneous Stokes layer thickness $\delta_\mathrm{s} = \sqrt{2\nu t}$. Sakai & Manhart (2020) performed direct numerical simulations of transient flow through a hexagonal sphere pack for different steady-state Reynolds numbers. Based on the symmetry-breaking behaviour of the flow, the different cases could be assigned to the flow regimes of Dybbs & Edwards (1984). The nonlinearity in the flow is associated with the formation of vortical structures, which develop in a consistent time sequence over a wide range of Reynolds numbers. Notably, for $Re \geq 59$ the superficial velocity overshoots its steady-state value (Sakai & Manhart, 2022); a similar observation was made by Hill & Koch (2002) for the face-centred cubic sphere pack. In Sakai & Manhart (2022), this overshoot was linked to an inter-component transfer of kinetic energy.

1.4. Research questions

The present work is concerned with two main areas of research. The first research area is the description and understanding of the pore scale flow in different flow regimes. The investigation is guided by the following research questions: For a given set of parameters, which flow state can be observed in oscillatory flow through a porous medium, i.e. is the flow laminar, transitional or turbulent? For which parameters are nonlinear effects significant? How can the transition from laminar to turbulent flow be identified? How does turbulence behave in oscillatory flow?
The second research area addresses the modelling of the flow in terms of the superficial velocity and the macroscopic pressure gradient. In particular, the research questions are: How good are the existing models and in which flow regimes can they be applied? How should the model parameters be chosen? How can the behaviour of the drag force and of of the dissipation rate be understood and used to develop improved models?

1.5. Outline of the dissertation

The present work is a publication-based dissertation. Therefore, the main results are presented in the form of peer-reviewed journal articles and conference contributions, which are reprinted in the appendix. The second chapter describes and discusses the methodology used within this thesis. The third chapter focuses on the flow regimes that occur in oscillatory flow through a hexagonal close-packed arrangement of spheres. After a brief overview of the simulation results, the following publications are summarised and the results are discussed in the context of the flow regimes:

- Unglehrt, L. & Manhart, M. 2022a Onset of nonlinearity in oscillatory flow through a hexagonal sphere pack. *Journal of Fluid Mechanics* **944**, A30.
- Unglehrt, L. & Manhart, M. 2022b Symmetry Breaking and Turbulence in Oscillatory Flow Through a Hexagonal Sphere Pack. In *Proceedings of TSFP-12 (2022) Osaka*. Osaka, Japan.

- Unglehrt, L. & Manhart, M. 2023b Direct and Large-Eddy simulation of turbulent oscillatory flow through a hexagonal sphere pack. In Direct and Large Eddy Simulation XIII, 1st edn. (ed. C. Marchioli, M. V. Salvetti, M. Garcia-Villalba & P. Schlatter), ERCOFTAC Series 31, pp. 118–123. Springer Cham.

The fourth chapter is concerned with the modelling of unsteady flow through porous media. After outlining the modelling framework and objectives, a summary of the following publications is provided:

- Unglehrt, L. & Manhart, M. Assessment of models for nonlinear oscillatory flow through a hexagonal sphere pack. *Manuscript submitted for publication.*
- Unglehrt, L. & Manhart, M. 2023c A model for the dissipation rate in linear unsteady flow through porous media. *Journal of Fluid Mechanics* **975**, A42.
- Unglehrt, L. & Manhart, M. 2023a Decomposition of the drag force in steady and oscillatory flow through a hexagonal sphere pack. *Journal of Fluid Mechanics* **974**, A32.

Based on these results, a model is proposed for the friction and the viscous pressure drag, resulting in a new model for unsteady flow through porous media. Finally, the current state of modelling is discussed and possible future modelling strategies are suggested. The conclusion briefly summarises the main findings of this thesis and indicates how the present work can be continued.

2. Methodology

> In our opinion, the greatest strength of DNS is the stringent control it allows over the flow being studied. Exploiting this strength and using it to examine idealized flows [...] is how DNS is likely to be most useful.
>
> (Moin & Mahesh, 1998)

> At best one may observe *a priori* that a porous medium is, or is not, spatially periodic. But this is not the same as saying that the system is random, nor even that a spatially periodic model will result in grossly erroneous predictions of transport properties in disordered systems.
>
> (Brenner, 1980)

2.1. Outline of the approach

The main research tool of the present work is the direct numerical simulation of the incompressible Navier-Stokes equations. Due to the absence of further modelling, direct numerical simulation results have a high fidelity and provide highly resolved information about the flow. However, direct numerical simulations are computationally expensive due to the large number of degrees of freedom required to resolve the flow. The approach of direct numerical simulation originates from turbulence research where "[...] it complements the time-trusted methodology of experimental research" (Moin & Mahesh, 1998). It has also been successfully applied to the study of porous media flow where "[...] direct numerical simulation (DNS) appears to be an important tool in understanding turbulence in porous materials for the foreseeable future" (Wood et al., 2020).
Due to the large computational cost, the focus is limited to a single porous medium geometry — a triply periodic hexagonal close-packed arrangement of spheres — and a sinusoidal time dependence of the macroscopic pressure gradient. Implicitly, the assumption of a sufficiently large scale separation between the pore scale and the macroscale is made such that the volume averaging and homogenisation approaches outlined in section 1.2 are applicable and a spatially constant macroscopic pressure gradient may be assumed on the pore scale. The flow was computed for a wide range of Hagen and Womersley numbers, which determine the amplitude and the frequency of the macroscopic pressure gradient. The simulated cases cover the low, medium and high frequency regime as well as linear, laminar nonlinear, transitional and turbulent flow.

2.2. Problem statement

This section provides a description of the flow problem that is investigated in this work. The selected porous medium geometry is described and the size of the simulation domain is discussed. The governing equations and boundary conditions are given and the dimensionless parameters that determine the flow are derived.

2.2.1. Geometry of the hexagonal sphere pack

Following the preceding studies of Zhu et al. (2014), Zhu & Manhart (2016), Kooshapur (2016) and Sakai & Manhart (2020), a hexagonal close-packed arrangement of uniform spheres was chosen as the porous medium. This geometry has also been investigated in various experiments (Dybbs & Edwards, 1984; Hendricks et al., 1998) and numerical studies (Hendricks et al., 1998; Lee et al., 2009; Finn et al., 2012; Finn, 2013). The hexagonal close-packing (hcp) can be constructed starting from a layer in the x-y-plane in which the spheres are arranged in a hexagonal pattern (Conway & Sloane, 1999, pp.7–8; Borchardt-Ott, 1997, pp.252f). The spheres of the second layer are placed in the gaps of the first layer such that the spheres are again arranged in a hexagonal pattern that is shifted with respect to the first layer. If the third layer of spheres is placed such that the spheres lie directly above the spheres in first layer, the hcp is obtained ($\dots abab \dots$). Conversely, if the third layer of spheres is placed such that the spheres do not lie directly above the spheres in the first layer and the fourth layer is placed such that the spheres lie directly above the spheres in the first layer, the cubic close-packing (ccp, also known as face-centred cubic packing or fcc) is obtained ($\dots abcabc \dots$). Both packings have the minimum porosity $\epsilon = 1 - \pi/(3\sqrt{2}) \approx 0.26$ that can be achieved in a packing of spheres of the same diameter (Hales et al., 2017). However, while the hcp arrangement belongs to the hexagonal crystal system (space group 194), the ccp arrangement belongs to the cubic crystal system (space group 225) (Borchardt-Ott, 1997, p.255; Cockroft, 1999). The ccp arrangement was studied for example by Wegner et al. (1971), Karabelas et al. (1973), Maier et al. (1998), Hill et al. (2001a,b), Hill & Koch (2002), He et al. (2019) and Apte et al. (2022). Figure 2.1 displays the primitive and Cartesian unit cells of the hcp and ccp arrangements.

The primitive unit cell of the hcp is the parallelepiped spanned by the vectors (Conway & Sloane, 1999, p.114)

$$\boldsymbol{a} = d\,\boldsymbol{e}_x\,, \tag{2.1a}$$

$$\boldsymbol{b} = \frac{d}{2}\,\boldsymbol{e}_x + \frac{\sqrt{3}d}{2}\,\boldsymbol{e}_y\,, \tag{2.1b}$$

$$\boldsymbol{c} = \frac{2\sqrt{6}d}{3}\,\boldsymbol{e}_z\,. \tag{2.1c}$$

The spheres are located at the positions

$$\boldsymbol{x}_{\mathrm{c},1} = 0\,\boldsymbol{a} + 0\,\boldsymbol{b} + 0\,\boldsymbol{c}\,, \tag{2.2a}$$

$$\boldsymbol{x}_{\mathrm{c},2} = \frac{1}{3}\,\boldsymbol{a} + \frac{1}{3}\,\boldsymbol{b} + \frac{1}{2}\,\boldsymbol{c}\,, \tag{2.2b}$$

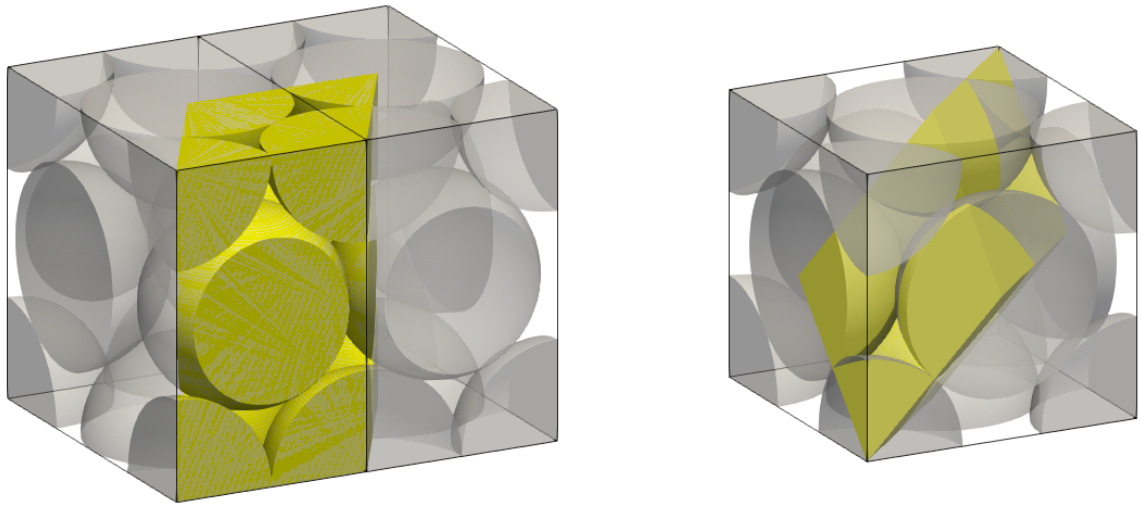

(a) hcp **(b)** ccp

Figure 2.1: Visualisation of the primitive unit cells (yellow) and the Cartesian unit cells (black outline) of the hexagonal and cubic close-packings.

which lie on the corner and in the interior of the primitive unit cell, respectively. The coordinates of the sphere centres in the hcp arrangement can be enumerated by the integers i, j and k as (Sakai & Manhart, 2020)

$$\boldsymbol{x}_\mathrm{c} = \begin{bmatrix} 2\,i + (j+k) \bmod 2 \\ \sqrt{3}\,\left[j + \frac{1}{3}(k \bmod 2)\right] \\ \frac{2\sqrt{6}}{3}\,k \end{bmatrix} \frac{d}{2}\,. \tag{2.3}$$

The Cartesian unit cell has a length d along the x-direction, $\sqrt{3}\,d$ along the y-direction and $2\sqrt{6}/3\,d$ along the z-direction.

Characteristic features

In the following, some characteristics of the hcp geometry are described, which are important for the discussion of the velocity field in chapter 3. The hcp has two kinds of pores: The *tetrahedral pores* are bounded by four spheres arranged on the corners of a regular tetrahedron and the *octahedral pores* are bounded by eight spheres arranged on the corners of a regular octahedron. These are shown in figure 2.2a–b. Note that the ccp consists of the same two kinds of pores in a different spatial arrangement (see figure 2.2c–d).

A particular feature of the hcp is that there exist straight channels along the x-direction and at 60° angles to the x-axis with respect to the z-axis. These channels can be identified in figure 2.3 as unobstructed "white" regions. Due to a contact point in the centre of the channels, these channels branch from an octahedral pore into two tetrahedral pores and merge again in an adjacent octahedral pore (Sakai & Manhart, 2020). Similar channels can be found in the ccp along the $\boldsymbol{e}_x + \boldsymbol{e}_y$, $\boldsymbol{e}_x + \boldsymbol{e}_z$ and $\boldsymbol{e}_y + \boldsymbol{e}_z$ directions. In the hcp, additional

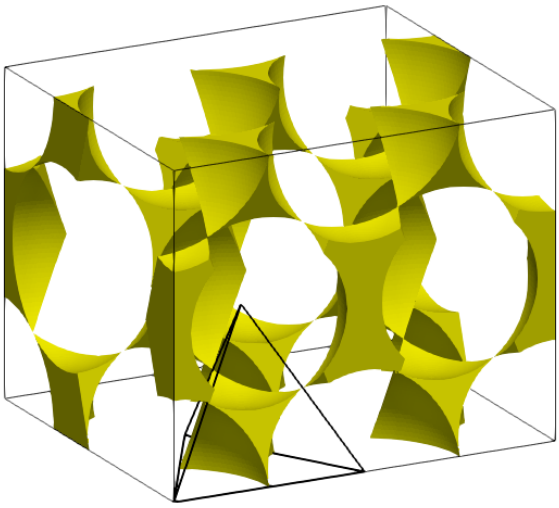

(a) Tetrahedral pores (hcp)

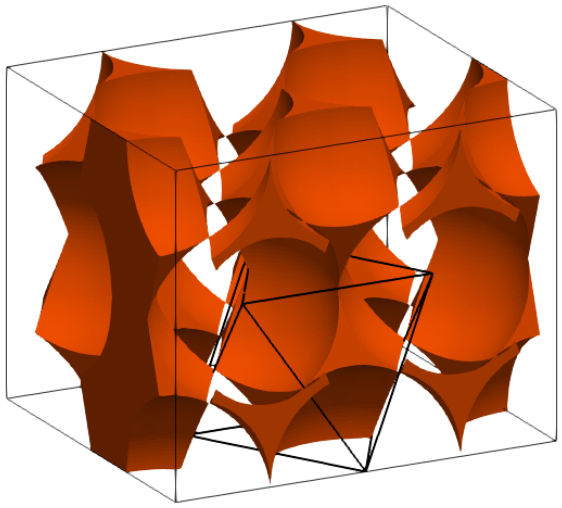

(b) Octahedral pores (hcp)

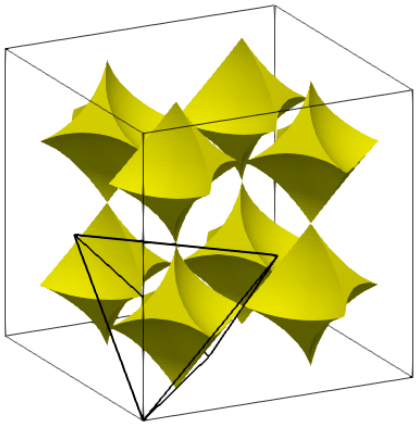

(c) Tetrahedral pores (ccp)

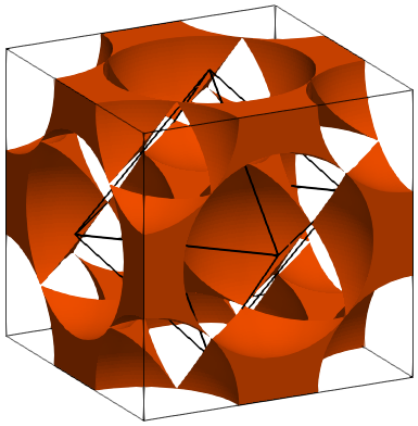

(d) Octahedral pores (ccp)

Figure 2.2: Visualisation of the tetrahedral and octahedral pores in the hexagonal and cubic close-packings. The isolated tetrahedral and octahedral pores are shown in figure A.1.

channels of a different kind can be found along the z-direction, which are not obstructed by contact points; these are however insignificant for the present work, since the macroscopic pressure gradient is applied along the x-direction.

For the analysis of the flow (cf. section 3.1) two particular sections will be used that give a good impression of the flow behaviour (Sakai & Manhart, 2020). These sections are displayed in figure 2.4. On the one hand, the plane $x = d$ (highlighted in orange) is considered, which is perpendicular to the flow and cuts through the midplanes of the octahedral and tetrahedral pores; on the other hand, the plane $\sqrt{3}/3\, y - \sqrt{6}/3\, z = 0$ (highlighted in yellow) is considered, which cuts through the channels along the x-direction.

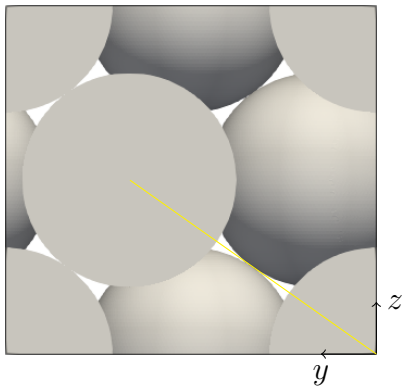

Figure 2.3: View through the hcp along the x-axis from $x = 0$. The yellow line indicates the section in figure 2.4.

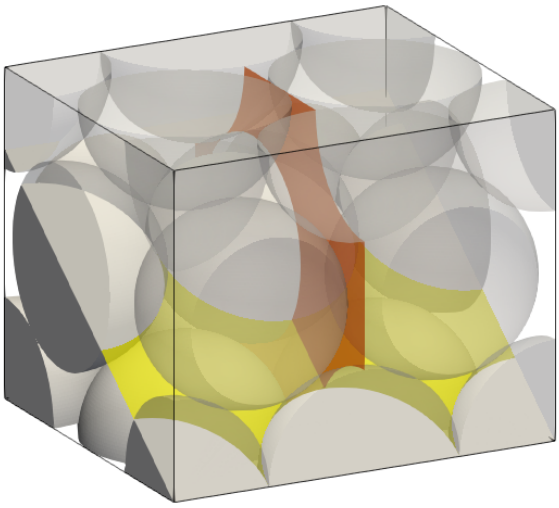

Figure 2.4: Characteristic sections through the hcp used for studying the flow.

2.2.2. Symmetries of the hexagonal sphere pack

The symmetries of the hcp are described by the space group $P6_3/mmc$ (Cockroft, 1999). The letter P indicates a "primitive" Bravais lattice (Hoffmann, 2020, p.175). Since the space group belongs to the hexagonal crystal system, the symbols $6_3/m$, m and c refer to the directions $\boldsymbol{c}$, $\boldsymbol{a}$ and $\boldsymbol{a} + \boldsymbol{b}$ (Hoffmann, 2020, p.175).[1] The sub-symbol 6_3 denotes a six-fold screw axis parallel to the $\boldsymbol{c}$-direction with a half-unit shift $1/2\,\boldsymbol{c}$ (Hoffmann, 2020, pp.165f). The axis is given by the equation $(0, \sqrt{3}/3\,d, z)$. The sub-symbol m denotes a mirror plane with normal vector $\boldsymbol{c}$ that is given by the equation $z = \sqrt{6}d/3$. The second symbol m denotes another mirror plane with normal vector $\boldsymbol{a}$ that is given by the equation $x = 0$. Finally, the symbol c denotes a glide plane (i.e. the combination of a reflection and a shift parallel to the plane) with a half-unit shift along the lattice vector $\boldsymbol{c}$ (Hoffmann, 2020, pp.152f). The glide plane has the equation $\sqrt{3}/2\,(x - d/3) + 1/2\,y = 0$ and a shift vector $1/2\,\boldsymbol{c}$. All other symmetries can be obtained by a combination of these elements and shifts by the lattice vectors (Hoffmann, 2020, p.175). For example, performing two 60° screw rotations and compensating the shift with the negative lattice vector $-\boldsymbol{c}$ corresponds to a pure rotation by 120°. Thus, the six-fold screw axis also implies a three-fold rotation axis. Or, applying the 60° screw symmetry to the glide plane results in the glide plane $y = \sqrt{3}d/3$. Together with the reflectional symmetry about $z = \sqrt{6}d/3$ this implies the two-fold axis of rotation $(x, \sqrt{3}d/3, \sqrt{6}d/6)$. Figure 2.5 shows the generating symmetry elements together with the primitive unit cell of the hcp.

[1] Note that crystallographic convention defines the second axis at a 120° angle to the $\boldsymbol{a}$-direction (Hoffmann, 2020, pp.23f), i.e. $\boldsymbol{b}' = -d/2\,\boldsymbol{e}_x + \sqrt{3}d/2\,\boldsymbol{e}_y$, and to place the origin at the centre of inversion (Hoffmann, 2020, p.198). In the present coordinates, the centre of inversion is located at $(0, \sqrt{3}d/3, \sqrt{6}d/6)$.

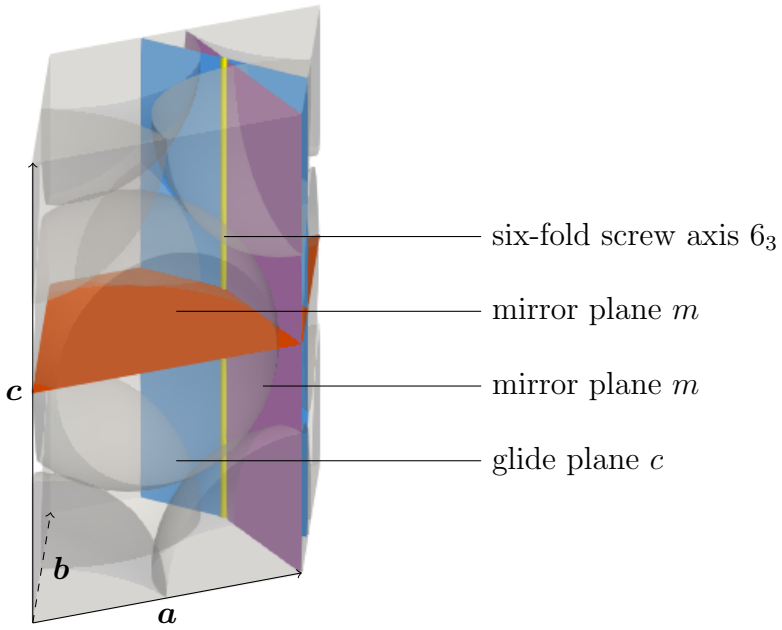

Figure 2.5: Primitive unit cell of the hcp with the generating symmetry elements of the space group $P6_3/mmc$. The yellow line is the six-fold screw axis (6_3), the red and purple planes are the mirror planes normal to the z- and x-axes (mm), and the blue plane is the glide plane (c). Note that for clarity some of the elements were translated on the lattice.

Symmetries of macroscopic quantities

The symmetries of the geometry constrain the shape of the macroscopic tensorial properties of the sphere pack like the permeability tensor $\boldsymbol{K}$, the tensor of virtual inertia $\boldsymbol{A}$ or the viscous length scale tensor $\boldsymbol{L}$. This is known as *Neumann's principle* (Hartmann, 1984; Voigt, 1966, pp.19-20). For the hcp, the 3-fold rotational symmetry about the z-axis and the reflectional symmetries normal to the x- and z-axes require the tensors to have the form (Voigt, 1966, pp.305f, p.312)

$$\boldsymbol{T} = \begin{bmatrix} T_{xx} & 0 & 0 \\ 0 & T_{xx} & 0 \\ 0 & 0 & T_{zz} \end{bmatrix}, \tag{2.4}$$

where the entries T_{xx} and T_{zz} are generally not identical.[2] Therefore, the hcp is an anisotropic porous medium. Note that for tensors involving the velocity field, e.g. the Forchheimer cor-

[2]For example, the reflectional symmetry of the hcp in the z-direction implies that a macroscopic pressure gradient inside the x-y-plane does not lead to a superficial velocity in the z-direction. Thus, the elements K_{zx} and K_{zy} of the permeability tensor are zero.

rection tensor (Whitaker, 1996), the above considerations only hold for as long as the velocity field shares the symmetries imposed by the geometry. Furthermore, some tensorial symmetries may be established independently of the geometry based on physical considerations (Biot, 1962; Lasseux & Valdés-Parada, 2017).

Symmetries of the velocity field

In laminar flow, the geometry of the sphere pack can imprint symmetries onto the velocity field depending on the direction of the macroscopic pressure gradient. In particular, the velocity field contains only those rotational symmetries of the geometry for which the axis of rotation is aligned with the direction of the pressure gradient, and only those mirror symmetries of the geometry for which the normal vector of the mirror plane is orthogonal to the direction of the pressure gradient.
In the present flow configuration, the macroscopic pressure gradient is directed along the x-direction and the simulation domain has an extent $L_x = 2\,d$, $L_y = \sqrt{3}\,d$ and $L_z = 2\sqrt{6}/3\,d$ (see section 2.2.3). The velocity field has four spatial symmetries:

$$\mathcal{S}_z\boldsymbol{u} = \begin{bmatrix} 1 & 0 & 0 \\ 0 & 1 & 0 \\ 0 & 0 & -1 \end{bmatrix} \cdot \boldsymbol{u}\left(x, y, \frac{2\sqrt{6}}{3}d - z, t\right) \tag{2.5a}$$

represents the reflection symmetry with respect to $z = \sqrt{6}d/3$,

$$\mathcal{T}_x\boldsymbol{u} = \boldsymbol{u}(x - d, y, z, t) \tag{2.5b}$$

and

$$\mathcal{T}_{xy}\boldsymbol{u} = \boldsymbol{u}\left(x - \frac{d}{2}, y - \frac{\sqrt{3}}{2}d, z, t\right) \tag{2.5c}$$

represent the translational invariances and

$$\mathcal{R}_x\boldsymbol{u} = \begin{bmatrix} 1 & 0 & 0 \\ 0 & -1 & 0 \\ 0 & 0 & -1 \end{bmatrix} \cdot \boldsymbol{u}\left(x, \frac{2\sqrt{3}}{3}d - y, \frac{\sqrt{6}}{3}d - z, t\right) \tag{2.5d}$$

represents the 180° rotation symmetry around the axis $(x, \sqrt{3}d/3, \sqrt{6}d/6)$. These symmetries are displayed in figure 2.6; each transformation maps the sphere pack onto itself (up to a shift by the lattice vectors of the hcp).

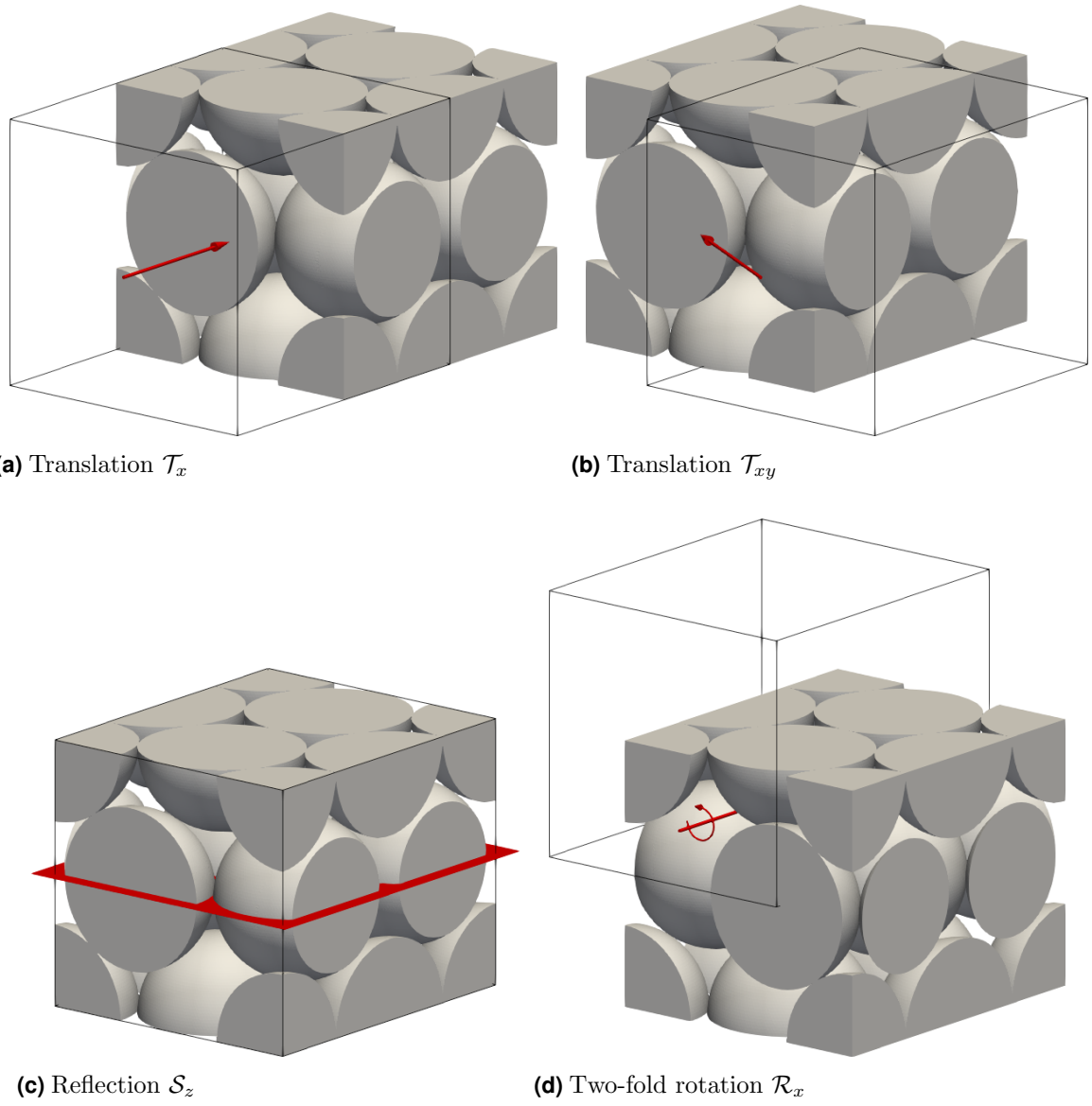

(a) Translation $\mathcal{T}_x$

(b) Translation $\mathcal{T}_{xy}$

(c) Reflection $\mathcal{S}_z$

(d) Two-fold rotation $\mathcal{R}_x$

Figure 2.6: Symmetries of laminar flow in a hexagonal sphere pack due to a macroscopic pressure gradient along the x-direction. The black box represents the position of the sphere pack before the application of the symmetry operation.

2.2.3. Size of the simulation domain

Fully developed laminar flow has the same periodicity as the sphere pack geometry. Therefore, it is possible to simulate the laminar flow regime using a single unit cell (Patankar et al., 1977). If the Reynolds number becomes sufficiently large, the periodicity of the flow may be broken. Thus, a too small domain may constrain the flow to a periodic state that would not be present in a larger domain. Therefore, the size of the simulation domain and the possibility of symmetry breaking are essential for a faithful representation of the transition from laminar to turbulent flow. The influence of the domain size on the transition can be estimated based on the work of Agnaou et al. (2016), who studied the first Hopf bifurcation of steady flow through various two-dimensional porous media. They found that for porosities

$\epsilon \lesssim 0.45$ the critical Reynolds number is essentially independent of the domain size (Agnaou et al., 2016, fig. 10). For turbulent flow, a too small domain may lead to additional correlations between turbulent fluctuations and can thus alter the turbulence statistics. For flow through sphere packs, Hill & Koch (2002) stated that a "[l]ong-range coupling is unlikely, because hydrodynamic interactions in random porous media are rapidly attenuated at separations larger than a few particle diameters." This view was confirmed by He et al. (2019) who simulated turbulent flow through a face-centred cubic sphere pack: "Although a single unit cell is used in the present work, computations were performed in a $3 \times 3 \times 3$ configuration as well to evaluate effects of the periodic boundary condition on the flow structures. As is shown later, the integral scales for all Reynolds numbers studied in this work are much smaller than the particle diameter and thus the unit cell domain showed little variation in statistics compared to a larger domain". For turbulent porous media flow in general, "[...] the sizes of turbulent structures do not exceed far beyond the pore scale, even for high-porosity, low-tortuosity configurations" (Wood et al., 2020).
In the present work, the computational domain was chosen in accordance with Zhu et al. (2014), Zhu & Manhart (2016) and Sakai & Manhart (2020). It consists of two Cartesian unit cells that are stacked along the x-direction, in which the macroscopic pressure gradient is applied. The computational domain therefore has a length of $L_x = 2\,d$, $L_y = \sqrt{3}\,d$ and $L_z = 2\sqrt{6}/3\,d$ in the x-, y- and z-directions, respectively. The domain contains eight octahedral pores, none of which are direct neighbours of themselves across the periodic boundary, and allows the breaking of the periodicities along the direction of the macroscopic pressure gradient as well as the breaking of two other symmetries (see section 2.2.2). In the light of the above considerations, the present choice of computational domain favours the use of a high grid resolution over achieving fully domain size independent results. Nevertheless, the results of He et al. (2019) suggest that only small discrepancies would be obtained for a larger computational domain.

2.2.4. Governing equations

Assuming that the wavelength of macroscopic pressure variations is much larger than the sphere diameter (Johnson & Sen, 1981) or, equivalently, assuming that the frequency of the flow is much smaller than the speed of sound divided by the sphere diameter (Batchelor, 2000, p.169), the pore scale flow is governed by the incompressible Navier-Stokes equations. These can be written in divergence form as

$$\boldsymbol{\nabla} \cdot \boldsymbol{u} = 0\,, \tag{2.6}$$

$$\frac{\partial \boldsymbol{u}}{\partial t} + \boldsymbol{\nabla} \cdot (\boldsymbol{u} \otimes \boldsymbol{u}) = -\frac{1}{\rho}\boldsymbol{\nabla}\tilde{p} + \nu\,\Delta\boldsymbol{u} + \frac{1}{\rho}\boldsymbol{f}\,, \tag{2.7}$$

where ρ is the density and ν is the kinematic viscosity of the fluid. The velocity and the pressure deviation satisfy triply periodic boundary conditions $\boldsymbol{u}(\boldsymbol{x}+\boldsymbol{L},t) = \boldsymbol{u}(\boldsymbol{x},t)$ and $\tilde{p}(\boldsymbol{x}+\boldsymbol{L},t) = \tilde{p}(\boldsymbol{x},t)$, where $\boldsymbol{L} \in \{L_x\,\boldsymbol{e}_x, L_y\,\boldsymbol{e}_y, L_z\,\boldsymbol{e}_z\}$ is a shift by the length of the computational domain. Moreover, the velocity field satisfies no-slip and no-penetration boundary conditions on the spheres. At the starting time $t = 0$, the flow is at rest.
The body force $\boldsymbol{f}$ represents the macroscopic pressure gradient (see section 1.2) and is

constant in space and sinusoidally oscillating in time:

$$\boldsymbol{f} = f_x \sin(\Omega t)\, \boldsymbol{e}_x \,. \tag{2.8}$$

Note that due to the periodic boundary conditions it is not possible to directly specify the volume flow rate. If a volume flow rate was to be imposed, the corresponding body force would have to be determined by a feedback control law. On the other hand, in experiments the flow is usually driven by a moving piston (van Gent, 1993; Hall et al., 1995; Jin & Leong, 2006; Pamuk & Özdemir, 2014). Here, it is more natural to specify a sinuosoidal volume flow rate corresponding to a fixed rotational speed of the wheel driving the piston. In contrast, if the macroscopic pressure gradient was to be specified, a force control would have to be used for the piston.

Dimensionless form of the governing equations

The problem can be nondimensionalised with the sphere diameter d, the density ρ and the kinematic viscosity ν. This results in the dimensionless coordinates $\hat{\boldsymbol{x}} = \boldsymbol{x}/d$ in which the spheres have unit diameter, the dimensionless viscous time $\hat{t} = t\,\nu/d^2$, the dimensionless velocity $\hat{u} = \boldsymbol{u}\,d/\nu$, which takes the form of a Reynolds number, and the dimensionless pressure deviation $\hat{p} = \tilde{p}\,d^2/(\rho\nu^2)$. The incompressible Navier-Stokes equations (2.7) can thus be written as

$$\frac{\partial \hat{\boldsymbol{u}}}{\partial \hat{t}} + \hat{\boldsymbol{\nabla}} \cdot (\hat{\boldsymbol{u}} \otimes \hat{\boldsymbol{u}}) = -\hat{\boldsymbol{\nabla}}\hat{p} + \hat{\Delta}\hat{\boldsymbol{u}} + Hg\, \sin\!\big(Wo^2 \hat{t}\big)\, \boldsymbol{e}_x \,, \tag{2.9}$$

where the Hagen number is defined as

$$Hg = \frac{f_x\, d^3}{\rho\nu^2} \tag{2.10}$$

and the Womersley number is defined as

$$Wo = \sqrt{\frac{\Omega\, d^2}{\nu}} \,. \tag{2.11}$$

It can be seen that these are the only dimensionless parameters appearing in the nondimensionalised flow problem (as the spheres have unit diameter) and thus a two-dimensional parameter space needs to be explored. As discussed in (Unglehrt & Manhart, 2022a, reprinted in appendix D.1), the Reynolds number arises as the cycle-maximum of the volume average of the resulting velocity field $\hat{\boldsymbol{u}}$.

2.3. Choice of simulation parameters

The main objective in the design of the present study was to simulate flow in all accessible regimes, i.e. linear, laminar nonlinear, transitional and turbulent flow at low, medium and high frequencies. In the previous section, it was found that the flow is determined by two independent parameters: the Hagen number and the Womersley number. In linear

flow, the transition between the low and high frequency regime occurs around the frequency $\Omega_0 = \epsilon\,\nu/(\alpha_\infty\,K)$ (Pride et al., 1993), which corresponds to a Womersley number $Wo_0 = 30.5$ for the hexagonal sphere pack. The simulations were carried out at the three Womersley numbers 10, 31.62 ($= 10^{1.5}$) and 100. These belong to the low, medium and high frequency regime in linear flow, respectively. The Hagen numbers were chosen on a grid of integer and rational powers of 10; the grid was extended until all desired flow regimes were observed. The simulation time for the cases LF1–LF4, MF1–MF4 and HF1–HF5 was determined such that the differences in the superficial velocity and kinetic energy between the last two cycles were less than 1% of their respective peak values. For the cases LF5 and LF6 transient effects could be observed only in the first half cycle. For the case MF5 a longer time was simulated in order to observe the growth of an instability (Unglehrt & Manhart, 2022b, reprinted in appendix D.2). For the case MF6 an approximate convergence of the average quantities was obtained. Finally, for the turbulent cases HF6 and HF7 a simulation time of 10 cycles was chosen to evaluate phase-averaged statistics. The simulation parameters are listed in table 2.1 and figure 2.7 shows the distribution of the present simulation cases in the *Hg*–*Wo* parameter space. For reference, the simulations of Zhu & Manhart (2016) and Sakai & Manhart (2020) are included in the figure.

It is interesting to consider under which circumstances the simulated flow conditions would occur in the physical world. Therefore, in figure 2.8 the simulation parameters are compared with the parameter ranges investigated in some more applied studies. The cited studies mainly concern sphere packs, for which the unknown parameters were estimated using the tables in (Chapman & Higdon, 1992). For comparability, the parameter space is spanned with the Reynolds number $Re/(1-\epsilon)$, which has been used frequently to evaluate flow through sphere packs of different porosities (Ergun, 1952; Macdonald et al., 1979; Wood et al., 2020), and the frequency ratio Ω/Ω_0, which characterises the linear frequency response (Pride et al., 1993). Low frequency nonlinear flow can be found in industrial applications such as heat exchangers and chemical reactors whereas high frequency nonlinear flow is typical of water wave induced flow in marine and coastal environments.

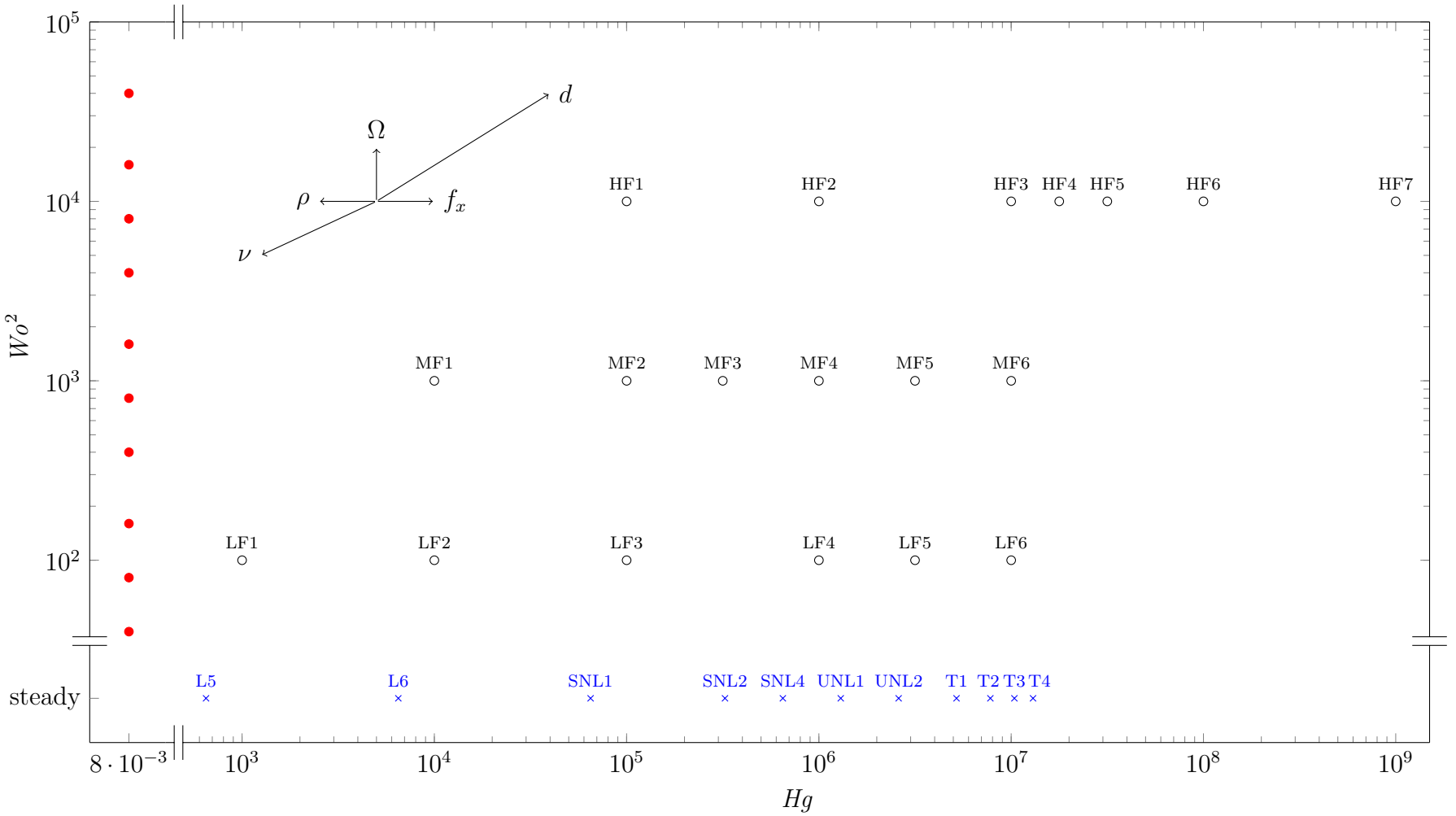

Figure 2.7: Simulations of oscillatory flow through the hexagonal sphere pack in the Hg–Wo^2 parameter space. The open circles indicate the present simulations, the red bullets indicate the simulations of linear flow performed by Zhu & Manhart (2016) and the blue crosses indicate the simulations of stationary flow performed by Sakai & Manhart (2020).

Case	Wo	Hg	Re	$d/\Delta x$	$T/\Delta t$	T_{sim}/T	CPU-h	Remarks
LF1	10	$1.00 \cdot 10^3$	0.171	384	80,000	1.5	20,000	
LF2	10	$1.00 \cdot 10^4$	1.7	384	80,000	2.25	31,000	
LF3	10	$1.00 \cdot 10^5$	14.8	384	80,000	1.4	36,000	
LF4	10	$1.00 \cdot 10^6$	76.7	384	160,000	1.25	35,000	
LF5	10	$3.16 \cdot 10^6$	158	384	160,000	2.27	277,000	
LF6	10	$1.00 \cdot 10^7$	307	384	640,000	1.56	450,000	
MF1	31.6	$1.00 \cdot 10^4$	0.857	384	80,000	3	43,000	
MF2	31.6	$1.00 \cdot 10^5$	8.57	384	80,000	3	43,000	
MF3	31.6	$3.16 \cdot 10^5$	26.9	384	80,000	3	43,000	
MF4	31.6	$1.00 \cdot 10^6$	73.1	384	40,000	3	146,000	
MF5	31.6	$3.16 \cdot 10^6$	157	384	80,000	6.4	214,000	
MF6	31.6	$1.00 \cdot 10^7$	298	384	80,000	2.26	273,000	
HF1	100	$1.00 \cdot 10^5$	1.3	384	40,000	20.4	282,000	
HF2	100	$1.00 \cdot 10^6$	13	384	40,000	19.9	411,000	
HF3	100	$1.00 \cdot 10^7$	132	384	40,000	6.32	158,000	
HF4	100	$1.78 \cdot 10^7$	253	384	40,000	8	71,000	
			252	768	40,000	8	286,000	
HF5	100	$3.16 \cdot 10^7$	464	384	40,000	6	217,000	
			465	768	40,000	6	253,000	
HF6	100	$1.00 \cdot 10^8$	1090	384	40,000	10	138,000	
			1090	768	80,000	4.26	661,000	
HF7	100	$1.00 \cdot 10^9$	3650	384	40,000	2.1	376,000	underresolved DNS
			3620	384	160,000	10.1	699,000	LES with $C_{\mathrm{w}} = 0.316$
			3580	384	160,000	10	698,000	LES with $C_{\mathrm{w}} = 0.5$

Table 2.1: Parameters of the simulations of oscillatory flow through a hexagonal close-packed arrangement of spheres. The overall computation time of these simulations was 5.86 million CPU hours. Additional simulations were conducted for each case at 48, 96 and 192 cpd.

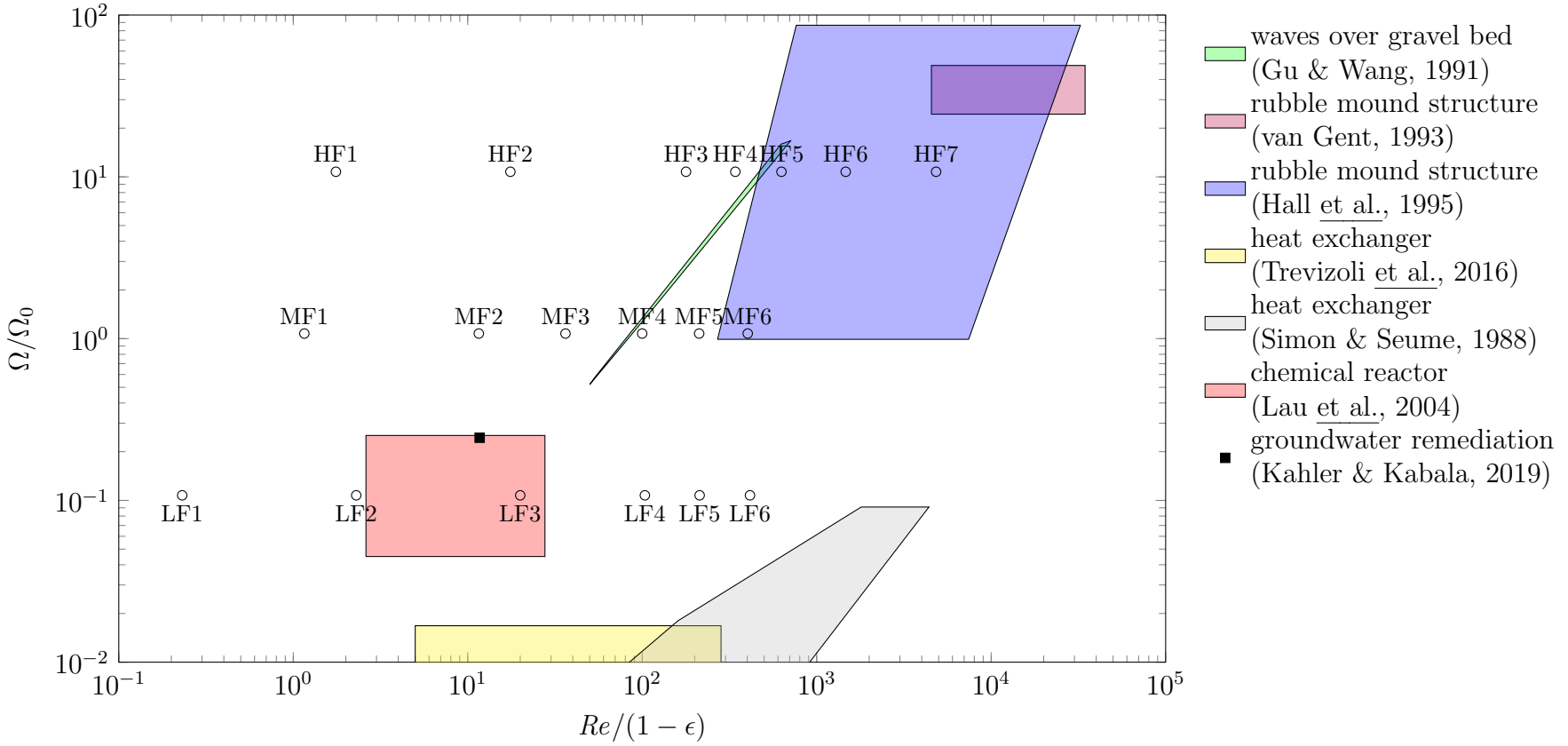

Figure 2.8: Applications of oscillatory porous media flow in the $Re/(1-\epsilon)$–Ω/Ω_0 parameter space. Unknown properties of the porous media were estimated based on the tables in (Chapman & Higdon, 1992).

2.4. Numerical method

This section provides a description and verification of the numerical method that was used to conduct the direct numerical simulations in this work.

2.4.1. Discussion of numerical methods

First, a brief overview is given of the numerical methods that have been applied to the direct numerical simulation of pore scale flow in other studies. The main challenge in the porous media setting is the accurate representation of the pore space and the no-slip and no-penetration boundary conditions on the fluid-solid interface (Wood et al., 2020).
For linear flow through lattice packings of spheres, very efficient and accurate approximations are available: For instance, Zick & Homsy (1982) employed an integral equation method based on the fundamental solution to the Stokes equations and Chapman & Higdon (1992) used a collocation method based on the expansion of the solution to the unsteady Stokes equations in spherical harmonics (Lamb, 1945, article 353).
For the other cases, i.e. nonlinear flow or complex geometries, two main approaches can be distinguished. On the one hand, the pore space can be represented by a body-fitted mesh on which the Navier-Stokes equations are then discretised using a finite volume or finite element method. For example, a finite volume method with body-fitted mesh has been employed in (Shams et al., 2014; Jin et al., 2015; Chu et al., 2018). On the other hand, a Cartesian grid can be used that covers both the fluid and the solid phase. The solid-fluid interface is then represented by an immersed boundary condition. The most common approach in this category is the Lattice Boltzmann method that was used for example in (Maier et al., 1998; Hill et al., 2001a,b; Hill & Koch, 2002; Schure et al., 2004; Jin et al., 2015). Also the finite volume approach with a ghost-cell immersed boundary method, that was used for example in (Zhu et al., 2014; Zhu & Manhart, 2016; Sakai & Manhart, 2020), or with a distributed forcing immersed boundary method, used e.g. in (Finn & Apte, 2013; He et al., 2019), belongs to this category. The immersed boundary methods can be further categorised according to whether the interface tractions are applied at a discrete location or are distributed over a certain band around the interface, and according to their conservation properties with respect to mass and momentum (Mittal & Iaccarino, 2005). A comparison between the body-fitted mesh approach and the Cartesian grid approach can be found in (Finn & Apte, 2013).

2.4.2. Description of the flow solver

The simulations in the present work were performed using the code MGLET (Manhart et al., 2001; Manhart, 2004). The solver employs multi-level block-structured Cartesian grids and the computation is parallelised over the grid blocks ("grids") using the Message Passing Interface (MPI). The incompressible Navier-Stokes equations are solved in the primitive variable formulation given in equation (2.7) with the velocity $\boldsymbol{u}$ and the pressure deviation $\tilde{p}$ as unknowns. The spatial derivatives are approximated by a second order symmetry-preserving finite volume scheme with a staggered arrangement of variables (Harlow & Welch, 1965; Verstappen & Veldman, 2003). Hence, the semi-discretised convective term conserves

the kinetic energy.
The time stepping is performed using an explicit low storage third order Runge–Kutta method that conserves energy within a high accuracy (Williamson, 1980, scheme 7). In every sub-step, a Poisson equation is solved for the pressure to make the stage velocity divergence-free. This can be interpreted either as an extension of the projection method (Chorin, 1968) or as a half-explicit Runge–Kutta method for differential-algebraic equations (Hairer & Wanner, 2010, pp.520f). Overall, the time integration scheme has a third order convergence for the velocity and a first order convergence for the pressure as the time step is refined. It should be noted that "[...] the projection method is stable, but not energy-conserving" despite the symmetry-preserving spatial discretisation (Hokpunna & Manhart, 2010). However, the results in (Unglehrt et al., 2022a) suggest that the energy conservation error decreases at third order with the time step size.
Complex geometries are treated using a ghost cell immersed boundary method (Peller, 2010). In this approach, the cells cut by the geometry do not have their own momentum balance and are thus referred to as ghost cells. Instead, the velocity values in these cells are set depending on the neighbouring values such that the no-slip and no-penetration boundary conditions are satisfied. In each ghost cell, the fluid-solid interface is represented as a plane fitted to the intersection points between the solid geometry and the cell edges, and the velocity profile is approximated with a linear least-squares fit to the velocity values of the neighbouring fluid cells. From this assumed velocity profile, two interpolation stencils can be derived that express the velocity value of the ghost cells in terms of the velocity values of the neighbouring fluid cells. On the one hand, the convected velocities of the ghost cells are approximated by second order accurate point values that are also used to evaluate the diffusive term. On the other hand, the convecting velocities of the ghost cells are approximated by a second-order accurate approximation to the specific volume flux across the open cell area. Thus, a second order convergence behaviour is expected. In order to satisfy the global conservation of mass, the convecting velocity has to be divergence-free also in each ghost cell. This constraint is enforced by an iterative procedure that alternates between the pressure Poisson equation, for which the velocities at the boundary between fluid cells and ghost cells are fixed, and a flux correction procedure which directly modifies the convecting velocities of the ghost cells (Peller, 2010).
In conclusion, the immersed boundary method in MGLET can be considered a hybrid between the ghost cell approach, which is used for the momentum equation, and the cut cell approach, which is used for the continuity equation. The main advantage of this approach in comparison to a complete cut cell method, for example (Unglehrt et al., 2022b), is that there is no additional time step restriction due to small cut cells at the interface. The mass conservation, the sharp and impermeable representation of the fluid-solid interface and the second order accuracy make the method well suited to simulate flow through complex porous media (Peller, 2010, pp.172f). The main drawback of the present method is the unavailability of wall shear stress and wall pressure values, as the momentum equation and the pressure Poisson equation are not solved for the interface cells.

2.4.3. Verification of the flow solver

In this section, the flow solver is verified against analytical and high-fidelity numerical solutions of the Navier-Stokes equations. In particular, the spatial accuracy is investigated for flow cases without and with an immersed boundary. For the triply periodic flow of Antuono (2020), an exact second order convergence is observed; for the linear instability of Poiseuille flow and for transient flow through an oblique pipe, a near second order convergence is observed. Finally, the third order convergence of the time integration scheme is confirmed for transient flow through an oblique pipe. An additional verification case is presented in (Unglehrt & Manhart, 2022a, reprinted in appendix D.1).

Spatial convergence in Antuono's triply periodic vortex flow

First, the correctness of the core flow solver implementation is verified. Antuono (2020) presented a triply periodic analytical solution to the incompressible Navier-Stokes equations

$$u = U_0 \frac{4\sqrt{2}}{3\sqrt{3}} \left[\sin\left(\kappa x - \frac{5}{6}\pi\right) \cos\left(\kappa y - \frac{\pi}{6}\right) \sin(\kappa z) - \cos\left(\kappa z - \frac{5}{6}\pi\right) \sin\left(\kappa x - \frac{\pi}{6}\right) \sin(\kappa y) \right] e^{-3\kappa^2 \nu t} , \tag{2.12a}$$

$$v = U_0 \frac{4\sqrt{2}}{3\sqrt{3}} \left[\sin\left(\kappa y - \frac{5}{6}\pi\right) \cos\left(\kappa z - \frac{\pi}{6}\right) \sin(\kappa x) - \cos\left(\kappa x - \frac{5}{6}\pi\right) \sin\left(\kappa y - \frac{\pi}{6}\right) \sin(\kappa z) \right] e^{-3\kappa^2 \nu t} , \tag{2.12b}$$

$$w = U_0 \frac{4\sqrt{2}}{3\sqrt{3}} \left[\sin\left(\kappa z - \frac{5}{6}\pi\right) \cos\left(\kappa x - \frac{\pi}{6}\right) \sin(\kappa y) - \cos\left(\kappa y - \frac{5}{6}\pi\right) \sin\left(\kappa z - \frac{\pi}{6}\right) \sin(\kappa x) \right] e^{-3\kappa^2 \nu t} , \tag{2.12c}$$

$$p = -\frac{1}{2} \rho \left| \boldsymbol{u} \right|^2 , \tag{2.12d}$$

which represents an exponentially decaying self-similar velocity field.
The flow is discretised in a cubic domain $[0, L]^3$ with periodic boundary conditions, where $L = 2\pi/\kappa$ represents the wavelength of the flow. The four grid resolutions $\Delta x/L = 1/20$, $1/40$, $1/80$ and $1/160$ are compared, where a uniform grid spacing was used for all cases and the domain was decomposed into blocks of 20^3 cells. The simulations were performed for 8000 time steps up to a dimensionless time $\nu T/L^2 = 2 \cdot 10^{-4}$ and the Reynolds number was chosen as $Re = U_0 L/\nu = 100$.
Figure 2.9 shows the error with respect to the analytical solution in the L^∞-norm. Clearly, the velocity components and the pressure exhibit a second-order convergence behaviour. The convergence order can be computed as 1.9995 for the velocity and 2.0081 for the pressure. Notably, the errors do not differ between the velocity components, thus showing the symmetry of the implementation of the discretisation.

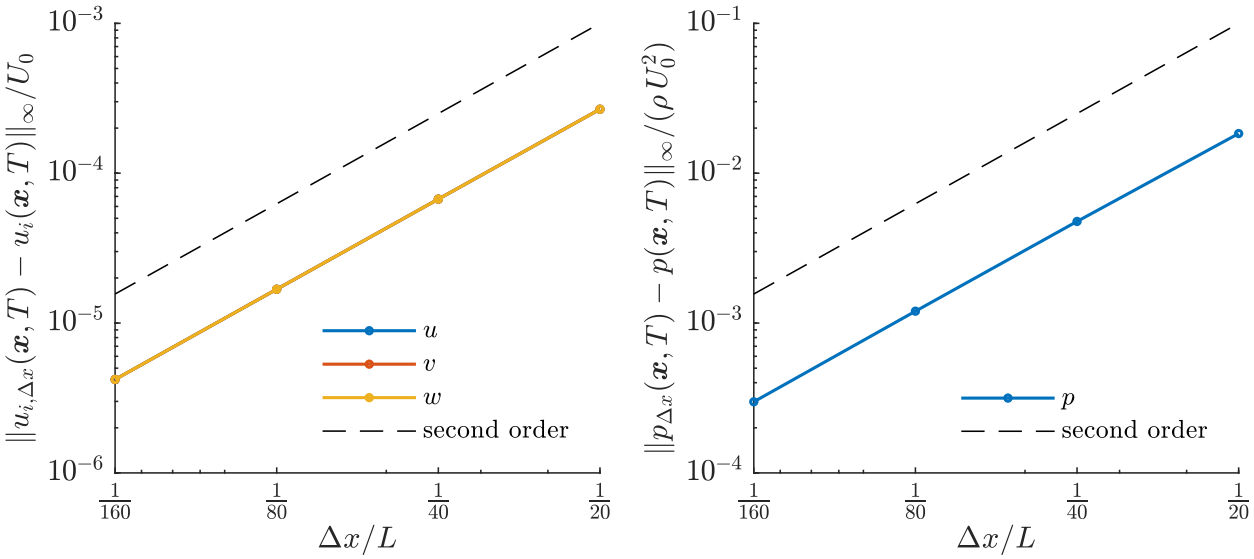

Figure 2.9: Grid convergence of the velocity and pressure fields $\boldsymbol{u}(\boldsymbol{x}, T)$ and $p(\boldsymbol{x}, T)$ to the analytical solution of Antuono (2020) in the L^∞-norm. The dashed lines indicate second order convergence with the grid spacing Δx.

Linear instability in plane channel flow

Second, the accuracy of the flow solver is investigated for the example of a linear instability of Poiseuille flow. The choice of this test case is motivated by the objective of simulating the flow through a hexagonal sphere pack in different flow regimes; it is therefore necessary to faithfully capture the transition from laminar to turbulent flow. The linear instability of Poiseuille flow has been used as a test case for flow solvers by Mohan Rai & Moin (1991), Das & Mathew (2001) and Schwertfirm et al. (2008).
Following these references, Poisseuille flow is considered at the supercritical Reynolds number $Re = u_{\max} h/\nu = 7500$ where h is the channel half-width; the critical Reynolds number is $Re_{\text{crit}} = 5772$ (Orszag, 1971). The initial velocity field is a superposition of the parabolic profile

$$u(y) = u_{\max}\left(1 - \frac{y^2}{h^2}\right) \tag{2.13}$$

of the Poiseuille solution and a two-dimensional perturbation $u''(x, y), v''(x, y)$ with a relative amplitude of 10^{-4}. The perturbation was selected as the most unstable eigenmode of the Orr-Sommerfeld equation for a streamwise wavenumber $\kappa = 1/h$. The Orr-Sommerfeld equation was solved numerically on the same grid as the wall-normal velocity component using the finite difference method of Pozrikidis (2017, pp.722f). Furthermore, a pressure gradient was specified according to the Poiseuille solution. The domain size was chosen as $2\pi h$ in the streamwise, $2h$ in the wall-normal, and h in the spanwise direction. The flow was simulated at three grid resolutions: $128 \times 256 \times 10$, $256 \times 512 \times 10$, and $512 \times 1024 \times 10$. No refinement was applied in the spanwise direction since both the flow and the initial evolution of the perturbation are two-dimensional. The simulated time was $u_{\max} T/h = 40$ and the dimensionless time step size $u_{\max}\,\Delta t/\Delta y = 0.032$ was constant for all cases.

N_x	N_y	$\Im(\omega)\ h/u_{\max}$	relative error
128	256	0.00220086	1.53×10^{-2}
256	512	0.00222753	3.33×10^{-3}
512	1024	0.00223321	7.66×10^{-4}

Table 2.2: Grid convergence of growth rate of Orr-Sommerfeld test case. A second order convergence of the growth rate to the result of (Das & Mathew, 2001) can be observed.

For the linear instability, the perturbation energy

$$E(t) = \int_V \frac{1}{2} \left[(u'')^2 + (v'')^2 \right] \mathrm{d}V \tag{2.14}$$

must grow exponentially as

$$E(t) = E(0)\, e^{2\Im(\omega)t}\,, \tag{2.15}$$

where $\Im(\omega)$ is the imaginary part of the largest eigenvalue of the Orr-Sommerfeld equation. The growth rate was determined from the perturbation energy using a least squares fit. In table 2.2, the growth rate is compared to the result of Das & Mathew (2001) obtained with a spectral code, $\omega\, h/u_{\max} = 0.24989154 + 0.0022349\mathrm{i}$. The growth rate converges to the reference value at approximately second order with the grid spacing (the apparent order of convergence is 2.14).

Spatial convergence in transient oblique pipe flow

Third, the spatial convergence of the ghost cell immersed boundary method is demonstrated. Following Unglehrt et al. (2022b), transient flow through an oblique pipe oriented in $(1, 1, 1)$-direction is considered. The flow is impulsively started from rest with a pressure gradient applied along the x-direction. The flow configuration is shown in figure 2.10. The design of the test case is inspired by Dröge & Verstappen (2005), Meyer et al. (2010) and Peller (2010) who considered steady or transient flow through an oblique channel. The streamwise velocity in transient laminar pipe flow is given by the analytical solution (Pozrikidis, 2017, pp.509f):

$$u_s(r,t) = -\frac{1}{4\mu}\frac{1}{\sqrt{3}}\frac{\mathrm{d}p}{\mathrm{d}x}\left[R^2 - r^2 - 8R^2 \sum_{n=1}^{\infty} \frac{1}{\alpha_n^3} \frac{\mathrm{J}_0(\alpha_n r/a)}{\mathrm{J}_1(\alpha_n)} \exp\left(-\alpha_n^2 \frac{\nu t}{R^2} \right) \right], \tag{2.16}$$

where R is the radius of the pipe, $\mathrm{J}_0(z)$ and $\mathrm{J}_1(z)$ are the Bessel functions of the first kind and α_n is the n-th zero of the Bessel function $\mathrm{J}_0(z)$.
The oblique pipe test case is well suited for the verification of the immersed boundary method for several reasons. Firstly, there is an analytical solution which allows to show the convergence of the numerical solution to the solution of the Navier-Stokes equations. Secondly,

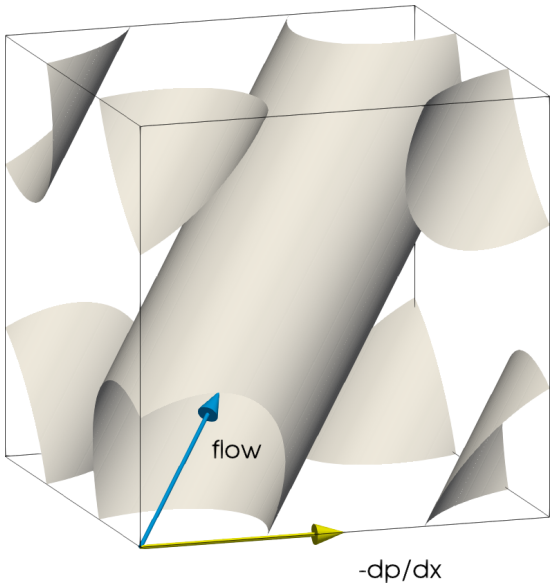

Figure 2.10: Configuration of the oblique pipe test case (Unglehrt et al., 2022b, Creative Commons BY 4.0 license (`http://creativecommons.org/licenses/by/4.0/`), unchanged).

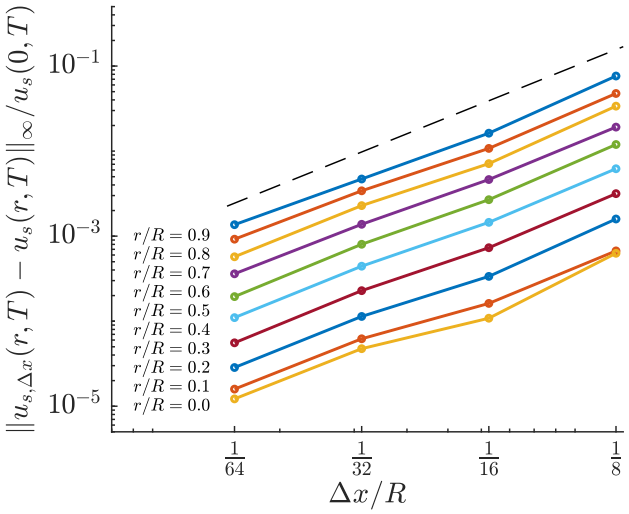

Figure 2.11: Grid convergence of the streamwise velocity $u_s(r,T)$ at probe points with $r/a = 0, 0.1, \ldots, 0.9$ in the L^∞-norm for transient flow through an oblique pipe. The dashed line indicates second order convergence with the grid spacing Δx.

the flow can be computed in a finite domain with periodic boundary conditions (unlike, for example, the Stokes flow around a sphere for which an infinite domain is assumed). Thirdly, the oblique placement of the pipe within the Cartesian grid leads to many different intersections of the pipe geometry with the Cartesian grid. Finally, the case allows to check the interaction between the pressure correction and the immersed boundary, since the momentum that is introduced into the u-component of velocity needs to be redistributed to the other components by the pressure.

A cubic domain of length $4R$ was selected such that the pipe segments that are folded back into the domain by the triple periodic boundary conditions do not collide with the segment along the diagonal. The domain is discretised by cubic cells of four sizes: $\Delta x = R/4$, $R/8$, $R/16$, $R/32$, and $R/64$. The flow was simulated for 4000 time steps until the time $\nu T/R^2 = 0.04$. The velocity field was sampled at concentrically arranged probe points with a radial distance $r/R = 0, 0.1, \ldots, 0.9$ from the centre line and 36 points along the circumference. Figure 2.11 shows the maximum error with respect to the analytical solution for each radial distance as a function of the normalised grid spacing $\Delta x/R$. The decrease of the error is not perfectly uniform with the grid spacing; an average order of convergence based on the coarsest and the finest grid between 1.8 and 1.98 is observed. This may be attributed to the use of the first order approximation $\boldsymbol{u} = 0$ in interface cells that do not have enough neighbours to construct an interpolation stencil. Apart from these sacrifices for the sake of robustness, the convergence behaviour of the ghost cell immersed boundary method is fully satisfactory.

Temporal convergence in transient oblique pipe flow

Finally, the convergence of the time integration scheme is investigated. Again, the case of transient flow through an oblique pipe is considered, but the grid resolution is kept constant at $\Delta x = R/16$ while the time step is varied. This test case was found to be sensitive to the coupling between the pressure correction in the fluid cells and the flux correction in the interface cells. It is therefore necessary to set a strict tolerance for the velocity divergence. Due to the coarse grid resolution, the spatial discretisation error dominates over the temporal discretisation error and the analytical solution cannot be used as a reference. Hence, the order of convergence can only be determined *assuming* that the scheme converges to the correct solution. For this, numerical solutions were computed at four different time steps $\nu\Delta t/R^2 = 8 \cdot 10^{-5}$, $1.6 \cdot 10^{-4}$, $3.2 \cdot 10^{-4}$, and $6.4 \cdot 10^{-4}$ and the apparent order of convergence of the centreline velocity for the two successive triples of values was determined (see e.g. Celik et al. (2008)). This resulted in the values 2.990 and 2.994 for the coarse and the fine triple, respectively, confirming the third order accuracy of the Runge–Kutta method.

2.5. Grid design

This section describes the computational grids employed for the simulations. The selection of the cell size is discussed in terms of the resolution of the geometry and the resolution of the flow.

2.5.1. Description of the grid configuration

In the present work, a block-structured Cartesian grid with uniformly sized cells is used. The flow is computed on different grids that are successively refined by a factor of 2. The nominal grid resolution based on the cell size in the x-direction is 48, 96, 192, 384 and 768 cells per diameter (cpd), respectively. The incommensurable periodicities in the x-, y- and z-directions lead to a slightly different grid resolution in each coordinate direction.[3] The cells therefore have an aspect ratio of $1 : 0.99 : 0.98$. The number of cells and the grid spacings are given in table 2.3. For the resolutions 384 cpd and 768 cpd, the grid blocks situated completely inside the spheres have been eliminated, thus reducing the number of cells in the grid by 40% and 60%, respectively.

2.5.2. Resolution of the geometry

This section examines the quality of the representation of the sphere pack geometry on the Cartesian grid for the different grid resolutions. The table 2.4 shows the number of fluid and interface cells as well as the porosity $\epsilon_{\Delta x}$ and the relative error in the porosity. It can be seen that the number of interface cells increases by about a factor of 4 with each refinement step; this is to be expected as the spheres are a smooth surface and thus have a box-counting

[3] The number of cells in the y- and the z- direction was determined with the constraint that the total number of cells is divisible by 28, which is the number of cores per compute node on the Linux Cluster of the Leibniz Supercomputing Centre, thus allowing a balanced distribution of the computational load.

nominal res.	N_x	N_y	N_z	$\Delta x/d$	$\Delta y/d$	$\Delta z/d$	no. of cells
48 cpd	96	84	80	0.02083	0.02062	0.02041	645,120
96 cpd	192	168	160	0.01042	0.01031	0.01021	5,160,960
192 cpd	384	336	320	0.00521	0.00515	0.00510	41,287,680
384 cpd	768	672	640	0.00260	0.00258	0.00255	198,696,960
768 cpd	1536	1344	1280	0.00130	0.00129	0.00128	1,070,596,096

Table 2.3: Grids for the grid convergence study.

nominal res.	no. of fluid cells	no. of interface cells	porosity $\epsilon_{\Delta x}$	porosity error $\frac{\epsilon_{\Delta x}-\epsilon}{\epsilon}$
48 cpd	152,480	46,272	0.245284	−5.5%
96 cpd	1,268,352	198,016	0.255954	−1.4%
192 cpd	10,508,439	844,073	0.259716	0.76%
384 cpd	84,713,980	3,501,806	0.259104	−0.16%
768 cpd	682,003,524	14,758,976	0.259477	−0.017%

Table 2.4: Grid convergence of the pore volume. The porosity $\epsilon_{\Delta x}$ at resolution Δx was calculated from the fluid cells and the open volumes of the interface cells.

dimension of 2. Also, the porosity converges to the true value $\epsilon = 0.2595195....$ In the relative porosity error, there is an outlier from the trend at a resolution of 192 cpd. A possible reason for this nonmonotonic convergence is that the pore space is concave at the spheres and thus the pore volume is overestimated by the piecewise linear representation of the wall, while the spheres are "sintered" at the contact points by the immersed boundary method (as discussed below), and the pore volume is underestimated. The outlier could therefore be caused by a momentary overtaking of the error at the concave walls.

Blocking of the contact point regions

The contact points between the spheres pose a problem for the Cartesian grid approach used in MGLET. The immersed boundary method approximates the wall in each cell by a single plane. Therefore, regions where the distance between the spheres is less than the grid spacing cannot be resolved because the cells are intersected by both spheres. These cells are considered to be solid. Since it is not possible to define a single plane representing the wall, no interpolation is used for these cells.

The affected regions can be estimated as a cylinder around the contact point, containing all points of both spheres that have a distance of less than $2\,\Delta x$ to the other sphere. The

diameter of this cylinder is

$$\frac{d_{\text{blocked}}}{d} = 2\sqrt{\frac{2\,\Delta x}{d} - \frac{\Delta x^2}{d^2}}\,, \tag{2.17}$$

which decreases asymptotically as $O(\sqrt{\Delta x})$. Figure 2.12 shows the smallest and largest diameters of the blocked regions in the discretised geometry as a function of the grid resolution. The theoretical prediction for d_{blocked} at a gap width of $2\,\Delta x$ agrees well with the upper limit found from the simulations. Assuming that the blocked region is a perfect cylinder of diameter d_{blocked} around the contact point, the missing pore volume and missing surface area can be calculated as

$$V_{\text{missing}} = 3\pi d\Delta x^2 - \frac{4}{3}\pi\Delta x^3 \tag{2.18}$$

$$A_{\text{missing}} = -4\pi d\,\Delta x + 4\pi d\,\Delta x\sqrt{\frac{2\,\Delta x}{d} - \frac{\Delta x^2}{d^2}} + 2\pi\Delta x^2 \tag{2.19}$$

using geometric formulae for a spherical cap. Therefore, the volume converges at second order, the surface area converges at first order and the wall position converges at half order when refining the grid. Consequently, the contact points between the spheres reduce the order of accuracy of the immersed boundary method.

In some studies the geometry of the sphere pack was modified by introducing bridges connecting the spheres, thereby avoiding small cells in body-fitted meshes close to the contact points (Kuroki et al., 2009; Nelson, 2009; Finn et al., 2012). A dedicated study was carried out by Finn & Apte (2013) who found that "for moderate Reynolds numbers the region of fluid very close to the contact point has little effect on the bulk flow, and may be safely removed as is deliberately done in the bridge meshing technique.". For oscillatory flow, however, this conclusion needs to be revisited (this will be discussed in detail in the following section). In this work, the bridges are automatically introduced by the simulation code depending on the grid spacing. Since it was unknown how the flow would behave in the vicinity of the contact points and what grid resolution would ultimately be used, no grid-independent bridges were introduced.

2.5.3. Resolution of the flow

The finite volume discretisation of MGLET uses the midpoint rule and linear interpolation to compute the values of the convective and diffusive fluxes. The leading error term of the midpoint rule and of the interpolated convective fluxes contains the second derivatives of the velocity field (Lomax et al., 2011, pp.70f; Ferziger & Perić, 2002, p.77) and the leading error term of the Laplacian depends on the fourth derivatives (Lomax et al., 2011, p.31). The grid resolution requirements are thus determined by the regions of high curvatures and fourth derivatives in the velocity field.

For the general case of unsteady nonlinear or possibly turbulent flow, the grid resolution requirements are difficult to estimate. Hence, the determination of the final resolution mainly rests on a grid study conducted for each flow case (Unglehrt & Manhart, 2022a, 2023b,a, reprinted in appendices D.1, D.3 and D.6). However, some estimates for the required grid

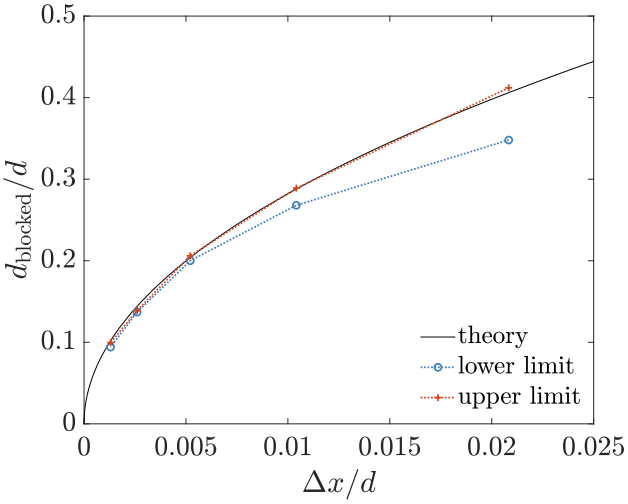

Figure 2.12: Diameter of blocked region around contact points. The smallest and largest diameters of the blocked regions in the discrete geometry are compared to equation (2.17), which assumes that the gap between the spheres is closed where its height is less than $2\,\Delta x$.

resolution can be derived for oscillatory flow at high Womersley numbers and for turbulent stationary flow. These will be discussed in the following.

High frequency oscillatory boundary layer

In the high frequency limit $Wo \to \infty$, oscillatory flow can be decomposed into an approximately inviscid core flow and a boundary layer near solid walls. For small convective accelerations, one can expand the solution to the boundary layer equation in the Keulegan-Carpenter number $KC = 2\pi\, Re/\, Wo^2$ and the leading order contribution u_0 is governed by the local equation

$$\frac{\partial u_0}{\partial t} - \nu\, \frac{\partial^2 u_0}{\partial y^2} = \frac{\partial U}{\partial t}\,, \tag{2.20}$$

where U is the velocity at the edge of the boundary layer (Schlichting & Gersten, 2017, pp.352f). It can be shown that this boundary value problem is identical to the Stokes problem with wall velocity $-U$ when viewed in a coordinate frame moving with the wall (Batchelor, 2000, p.354). Hence, in oscillatory flow the 99 % boundary layer thickness of the envelope of the velocity profiles is

$$\delta_{99} = 4.6\, \sqrt{\frac{2\,\nu}{\Omega}}\,, \tag{2.21}$$

which is the value from the second Stokes problem (Schlichting & Gersten, 2017, p.129). The boundary layer contains an extremum of the second derivative of the tangential velocity in wall normal direction. The accuracy of the approximation in the boundary layer depends on the grid Womersley number $Wo_{\Delta y} = \sqrt{\Omega/\nu}\,\Delta y$ as can be seen from discretising the second

Stokes problem.[4] In order to achieve 1 % relative accuracy in the velocity, a grid Womersley number $Wo_{\Delta y} < 0.3464$ is required. This is equivalent to 19 cells distributed over δ_{99}. The required resolution of the spheres can be expressed in terms of the Womersley number as

$$\frac{d}{\Delta y} = \frac{Wo}{Wo_{\Delta y}} \,. \tag{2.22}$$

For the high frequency cases at $Wo = 100$, this compiles to a required grid resolution of 289 cells per sphere diameter.

Flow near the contact points

As discussed previously (see section 2.5.2), the Cartesian grid method introduces bridges at the contact points of the spheres. Insofar as the simulations should represent the flow through a packing of exact spheres, the grid resolution must be chosen such that these bridges have a negligible effect on the flow. In Stokes flow the highest velocities appear away from the boundaries (see figure 2.13a) and thus the modification of the contact point geometry has only a minor effect. In contrast, for high frequencies ($Wo \to \infty$), the flow field tends to the potential flow field in which the highest velocities are concentrated near the contact points (see figure 2.13b and the discussion in (Unglehrt & Manhart, 2022a, reprinted in appendix D.1)). In other words, the small viscosity allows the flow to penetrate into the gaps near the contact points. In order to obtain reliable results, the blocked contact point regions should be "hidden" in the viscous boundary layers of the flow. The oscillatory boundary layer locally resembles the Stokes boundary layer for $Wo \to \infty$ (see the preceding section), and it thus has a constant characteristic thickness $\delta_\mathrm{s} = \sqrt{2\nu/\Omega}$ everywhere. Near the contact points,

[4] The differential equation for the second Stokes problem reads in the frame moving with the wall:

$$\frac{\partial u}{\partial t} = \nu \, \frac{\partial^2 u}{\partial y^2} - U_0 \, \Omega \, \sin(\Omega \, t) \,.$$

A finite volume discretisation in y-direction yields:

$$\frac{\mathrm{d}\bar{u}_j}{\mathrm{d}t} = \nu \, \frac{\bar{u}_{j-1} - 2\,\bar{u}_j + \bar{u}_{j+1}}{\Delta y^2} - U_0 \, \Omega \, \sin(\Omega \, t) \,.$$

The modified differential equation for this discretisation is

$$\left.\frac{\partial u}{\partial t}\right|_j = \nu \, \left.\frac{\partial^2 u}{\partial y^2}\right|_j - U_0 \, \Omega \, \sin(\Omega \, t) - \nu \, \frac{\Delta y^2}{12} \, \left.\frac{\partial^4 u}{\partial y^4}\right|_j + O\left(\Delta y^4\right) \,.$$

Plugging in the exact solution (Schlichting & Gersten, 2017, p.129), the error e of the discretisation results in

$$e = -\frac{1}{12} \, Wo_{\Delta y}^2 \; u|_j + O\left(Wo_{\Delta y}^4\right) \,.$$

and hence, the accuracy of the finite volume scheme is uniquely determined by $Wo_{\Delta y}$.

(a) Stokes flow **(b)** Potential flow

Figure 2.13: Velocity magnitude $|\boldsymbol{u}|$ in the plane $x = d$ in Stokes flow (Sakai & Manhart, 2020; Unglehrt & Manhart, 2023a, case L4) and potential flow (Unglehrt & Manhart, 2023a) through the hexagonal sphere pack. The main flow direction is perpendicular to the section.

the boundary layers of adjacent spheres meet at a distance

$$\frac{r_\delta}{d} = \sqrt{\frac{\sqrt{2}}{Wo} + \frac{2}{Wo^2}} \tag{2.23}$$

from the contact point, which is approximately $0.12\,d$ for $Wo = 100$. The blocked region around the contact points ("bridges") should be contained in this boundary layer (i.e. $d_{\text{blocked}} < 2\,r_\delta$); from figure 2.12 one can find that the grid resolution at $Wo = 100$ should be at least 192 cpd.

For nonlinear flow, a similar problem can be observed: As the Reynolds number is increased, the high velocity regions move into the gaps near the contact points (see figure 3.2 which shows the velocity field for the low frequency cases). Consequently, the grid resolution of the contact points is also important for flow at higher Reynolds numbers. The effect of the contact point resolution can be seen at the example of the case HF6 ($Re = 1086$, $Wo = 100$). Figure 2.14 shows the instantaneous velocity magnitude at the time $\Omega t = 6.64\pi$ for the grid resolutions 192 cpd, 384 cpd and 768 cpd. While the peak values of the velocity magnitude are quite similar for the different resolutions, the region of high velocity magnitude approaches the contact point as the grid is refined. There are also significant variations in the shape of the separation region. Since the figure 2.14 shows an instantaneous state of the flow, the shape of the separation region is affected by turbulent fluctuations and wake oscillations. However, some trends can be observed: The opening angle and the width of the separation region behind the contact points increase with increasing grid resolution, while the length of the separation region decreases with increasing resolution. In conclusion, the grid resolution near the contact points becomes important when the flow is dominated by inertial or convective effects.

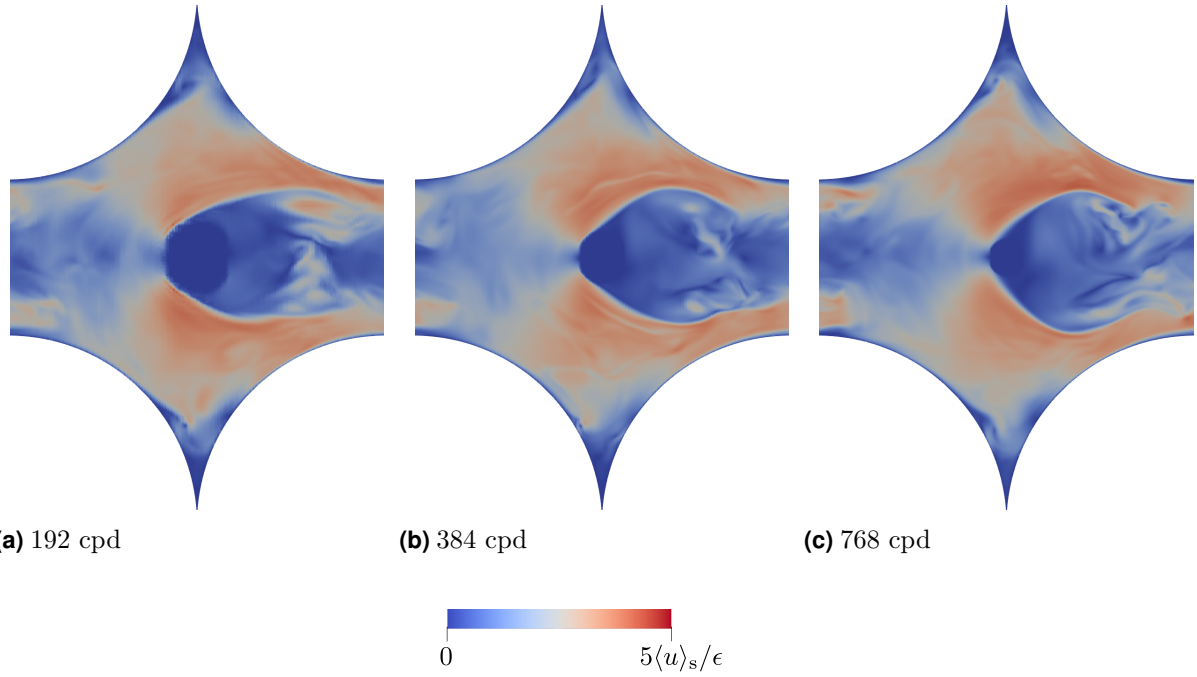

(a) 192 cpd **(b)** 384 cpd **(c)** 768 cpd

Figure 2.14: Effect of the grid resolution on the instantaneous velocity magnitude $|\boldsymbol{u}|$ near the contact points for the case HF6 after 3.32 periods. The figure shows the section $\sqrt{3}/3\,y - \sqrt{6}/3\,z = 0$. The main flow direction goes from left to right.

Turbulent flow

The required grid resolution in a turbulent flow can be assessed by comparing the grid spacing with the Kolmogorov scale (Moin & Mahesh, 1998), which expresses the smallest scales of motion in a turbulent flow. It is defined as (Pope, 2000, p.185)

$$\eta = \left(\frac{\nu^3}{2\nu\, \overline{\boldsymbol{S}' : \boldsymbol{S}'}} \right)^{1/4} \tag{2.24}$$

where $2\nu\, \overline{\boldsymbol{S}' : \boldsymbol{S}'}$ is the mean dissipation rate of the TKE. Such an estimate is only valid in the asymptotic turbulent regime, i.e. $Re > 1679$ for statistically steady turbulent flow (Wood et al., 2020, from Re_H). Based on time resolved particle image velocimetry in a sphere pack with $\epsilon = 0.45$, (Patil & Liburdy, 2015) reported the following estimate for the Kolmogorov scale:

$$\eta \approx 1.32\, Re_\mathrm{pore}^{-3/4}\, D_\mathrm{H} \quad \text{where } Re_\mathrm{pore} = \frac{\langle u\rangle_\mathrm{s}\, D_\mathrm{H}}{\epsilon\,\nu} > 2800 \quad \text{and } D_\mathrm{H} = \frac{2}{3}\frac{\epsilon}{1-\epsilon} d\,. \tag{2.25}$$

For the hcp, this relation can be rewritten as

$$\eta \approx 0.33\, Re^{-3/4}\, d \quad \text{for } Re > 3110\,. \tag{2.26}$$

In the present dataset, this estimate is reasonably applicable only for the cases HF6 ($Re = 1086$) and HF7 ($Re = 3580$), which have an amplitude close to what would be expected for

a stationary flow (Unglehrt & Manhart, 2023b, reprinted in appendix D.3). For the case HF6, the estimate would suggest $d/\eta \approx 573$. Thus, a fully resolved DNS has probably been reached at the highest resolution (768 cpd), and the second highest resolution (384 cpd) is still reasonably well resolved. For the case HF7, the Kolmogorov length scale is about $d/\eta \approx 1402$. This does not seem to be achievable with the computational resources available for the present work.[5]. Consequently, a large-eddy simulation approach was chosen for this case (see section 2.6).
The required grid resolution for the turbulence-like cases LF6 and MF6 was estimated in (Unglehrt & Manhart, 2023a, reprinted in appendix D.6) according to (Finn, 2013; He et al., 2019) as 342 cpd. The resolution of 384 cpd that was determined by the grid study can therefore be judged sufficient.

2.6. Large-eddy simulation of the case HF7

In this section, the case HF7, which has by far the largest Reynolds number in the present study, will be discussed in detail. For this case, the results at a resolution of 384 cpd indicated that the next grid resolution of 768 cpd would likely not be sufficient to fully resolve all scales of turbulent motion. Therefore a wall-resolved large-eddy simulation (LES) was performed at a resolution of 384 cpd.

2.6.1. Discussion of the sub-grid scale model

Due to the high Womersley number, thin boundary layers appear at the pore walls and the core flow is almost laminar during the acceleration phase. Therefore, the choice of the sub-grid scale (SGS) model deserves special attention. The sub-grid stresses were represented using the WALE model (Nicoud & Ducros, 1999). This particular model has the property that the sub-grid stresses are exactly zero for a simple shear flow. Furthermore, the sub-grid stresses of the WALE model decrease with the cube of the wall distance. Hence, the simulation of the near wall flow should be only mildly affected by the WALE model. The influence of the SGS model is assessed based on an instantaneous velocity field at time $\Omega t = 0.32\pi$ just after the transition to turbulence has occurred. Figure 2.15 shows the ratio ν_{SGS}/ν for the WALE model computed a priori from the underresolved DNS and a posteriori from the LES (both at a grid resolution of 384 cpd). Both fields have a relatively similar magnitude and spatial distribution. In the turbulent regions, the SGS viscosity is approximately 2 to 3 times larger than the molecular viscosity. Consequently, the LES is well resolved. In the boundary layers and irrotational regions of the flow, it can be seen that the SGS viscosity is significantly smaller than the fluid viscosity. This suggests that the SGS model has a small influence on the flow in these regions. Also, the distribution of the regions of high SGS viscosity is relatively similar between the two fields, indicating that the transition to turbulence takes place in a rather similar manner with and without the SGS

[5]The required computing time can be estimated from the large-eddy simulation of the case HF7, which consumed about 669,000 CPU-h for 10 oscillation periods. To reach the Kolmogorov scale, both the grid resolution and the number of time steps would have to be quadrupled (for a constant Courant-Friedrichs-Lewy number), resulting in an increase by a factor of 4^4. The computational cost would thus be in the order of 170 million CPU-h.

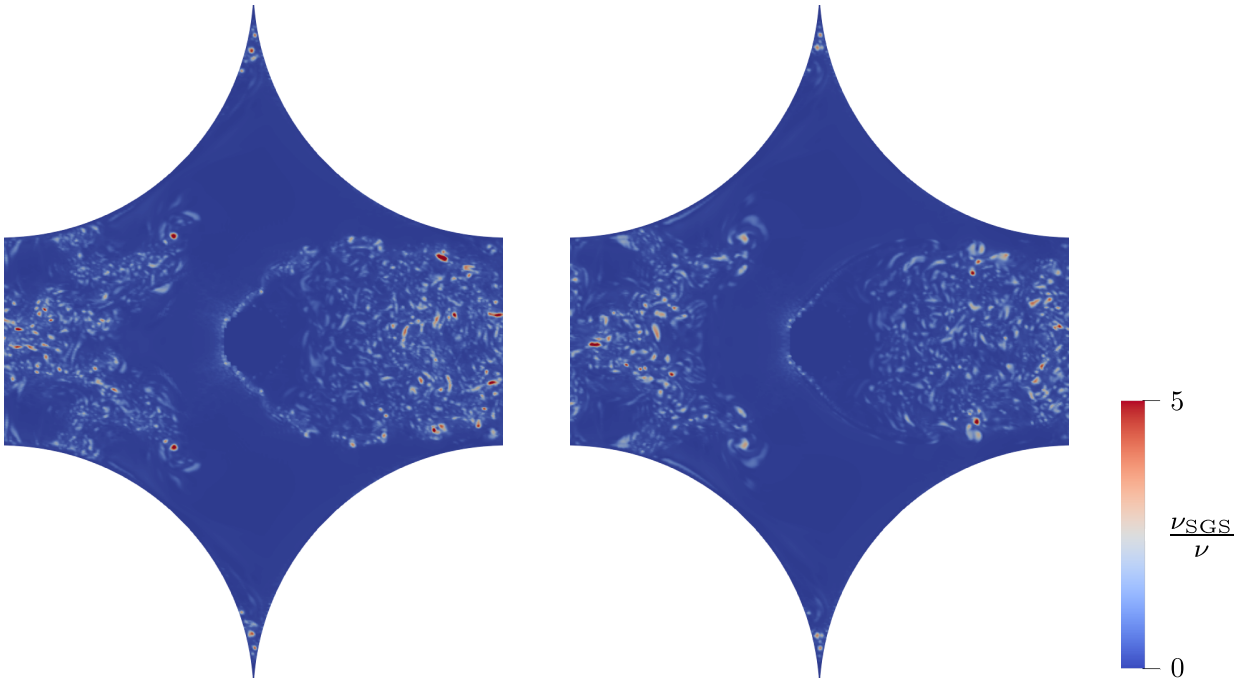

(a) a priori evaluation (underresolved DNS) **(b)** a posteriori evaluation (LES)

Figure 2.15: Ratio of the SGS viscosity ν_{SGS} to the kinematic viscosity ν of ν_{SGS}/ν for the case HF7 at a resolution of 384 cpd just after the transition to turbulence ($\Omega t = 0.32\pi$).

model. Notably, the SGS viscosity determined from the underresolved DNS shows a high intensity in the shear layers emanating from the touching point in the centre of the plot, while this is absent in the SGS viscosity determined from the LES. A possible explanation is that a shear layer instability occurs in the underresolved DNS, which is suppressed in the LES. A comparison of the superficial velocity between the underresolved DNS and the LES (figure 2.16 shows that the laminar starting flow remains unaffected by the SGS model. When the turbulence sets in, it can be observed that the LES results in a smaller superficial velocity than the underresolved DNS; this is expected due to the increased effective viscosity. In conclusion, these results indicate that the WALE model exhibits a very desirable behaviour in that it hardly affects the boundary layers and irrotational flow regions, but increases the viscosity in the small turbulent structures.

2.6.2. Verification of the sub-grid scale model implementation

A sanity check of the implementation of the WALE model in MGLET can be based on the property of the WALE model that no SGS viscosity is produced in a pure shear flow (Nicoud & Ducros, 1999). An example for such a flow is the transient laminar flow through an oblique pipe (see section 2.4.3). Here, the same setup is used as for the investigation of the spatial convergence with the modification that when the grid is refined by a factor of 2, the pressure gradient and the molecular viscosity are divided by 4. Thus, the reduction in the filtering length $\Delta := \Delta x$ of the WALE viscosity is compensated. It can be expected that the eddy viscosity is small already at coarse grids since the flow is unidirectional and constant along the streamwise direction. As the grid is refined, the WALE viscosity

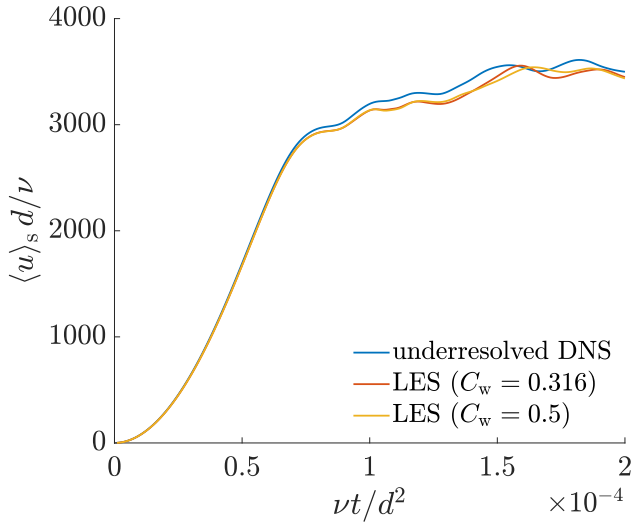

Figure 2.16: Comparison of the superficial velocity in the starting flow resulting from the underresolved DNS at 384 cpd and the LES at 384 cpd for the case HF7.

should converge to zero as the simulation approximates the exact velocity field (see section 2.4.3).
For the coarsest grid spacing of $R/\Delta x = 8$, the ratio of the intrinsic volume-averaged SGS viscosity $\langle \nu_{\mathrm{SGS}} \rangle_s$ to the molecular viscosity ν has the value $3.7 \cdot 10^{-6}$. As the grid is refined to $R/\Delta x = 16$ and 32, the ratio has the values $6.2 \cdot 10^{-8}$ and $6.4 \cdot 10^{-10}$, respectively. Finally, at $R/\Delta x = 128$ the SGS viscosity is zero to machine precision. It can thus be concluded that the present implementation complies with the absence of SGS viscosity in a pure shear flow. A further verification and validation of the WALE model implementation in MGLET for a turbulent channel flow at $Re_\tau = 180$ can be found in (Peller, 2010, pp.118–119). The SGS viscosity was observed to decrease with the cube of the wall distance which is in line with the theoretical expectations.

2.7. Temporal resolution

In this section, the simulation time step is discussed in terms of stability and accuracy. The explicit Runge–Kutta scheme used in MGLET is conditionally stable, i.e. there is a limit for the time step size below which numerical errors are damped. For a system of ordinary differential equations $\mathrm{d}\boldsymbol{x}/\mathrm{d}t = \boldsymbol{F}(\boldsymbol{x})$, the scheme is stable if the condition $|R(\lambda_{\boldsymbol{J}} \Delta t)| \leq 1$ holds for all eigenvalues $\lambda_{\boldsymbol{J}}$ of the Jacobian $\boldsymbol{J} = (\boldsymbol{\nabla} \otimes \boldsymbol{F})^{\mathsf{T}}$ of the right-hand side (Hairer & Wanner, 2010, p.15). The stability function $R(z)$ for the three-stage third order explicit Runge–Kutta method has the form (Hairer & Wanner, 2010, p.17):

$$R(z) = 1 + z + \frac{z^2}{2} + \frac{z^3}{6} \,. \tag{2.27}$$

The spatial discretisation of the incompressible Navier-Stokes equations results in a large nonlinear system of ordinary differential equations for which the Jacobian eigenvalues are not available in closed form. Following Dröge (2006), the eigenvalues are estimated for the cases

where diffusion dominates over convection or vice versa using Gershgorin's circle theorem (appendix A.2). The diffusive operator imposes the constraint

$$4\,\nu\,\Delta t\left(\frac{1}{\Delta x^2}+\frac{1}{\Delta y^2}+\frac{1}{\Delta z^2}\right)\leq 2.5127\,, \tag{2.28}$$

where $|R(-2.5127)|=1$. The ratio $\nu\,\Delta t\left(1/\Delta x^2+1/\Delta y^2+1/\Delta z^2\right)$ is sometimes referred to as numerical diffusion number (Pozrikidis, 2017). The convective operator leads to the constraint

$$CFL_u\leq\sqrt{3}\,, \tag{2.29}$$

where $\left|R(\pm\mathrm{i}\sqrt{3})\right|=1$ and CFL_u is the Courant-Friedrichs-Lewy number of the u-momentum equation. It is defined as

$$\begin{aligned}CFL_u=\Delta t\,\max_{i,j,k}\Bigg(&\frac{|u_{i,j,k}+u_{i+1,j,k}|+|u_{i-1,j,k}+u_{i,j,k}|}{4\Delta x}\\&+\frac{|v_{i,j,k}+v_{i+1,j,k}|+|v_{i,j-1,k}+v_{i+1,j-1,k}|}{4\Delta y}\\&+\frac{|w_{i,j,k}+w_{i+1,j,k}|+|w_{i,j,k-1}+w_{i+1,j,k-1}|}{4\Delta z}\Bigg)\,.\end{aligned} \tag{2.30}$$

The corresponding constraints for the v- and w-components of the momentum equations can be obtained by exchanging u with v or w, i with j or k and Δx with Δy or Δz, respectively. Generally, the diffusion number constraint is dominant for low Reynolds numbers and fine grids whereas the Courant-Friedrichs-Lewy number constraint is dominant for high Reynolds numbers and coarse grids.
The basic error characteristics of the time stepping scheme can be understood by looking at the linear system

$$\frac{\mathrm{d}\boldsymbol{x}}{\mathrm{d}t}=\boldsymbol{J}\cdot\boldsymbol{x}\,, \tag{2.31}$$

where $\boldsymbol{J}$ is assumed to be constant in time. Multiplying this equation with an eigenvector $\boldsymbol{v}$ such that $\boldsymbol{v}\cdot\boldsymbol{J}=\lambda_{\boldsymbol{J}}\,\boldsymbol{v}$, the modal equation is obtained as

$$\frac{\mathrm{d}(\boldsymbol{v}\cdot\boldsymbol{x})}{\mathrm{d}t}=\lambda_{\boldsymbol{J}}\,(\boldsymbol{v}\cdot\boldsymbol{x})\;. \tag{2.32}$$

At time $t=n\Delta t$, the analytical and numerical solutions are (Hairer & Wanner, 2010, pp.15–16)

$$\boldsymbol{v}\cdot\boldsymbol{x}(n\Delta t)=\left(e^{\lambda_{\boldsymbol{J}}\Delta t}\right)^n\boldsymbol{v}\cdot\boldsymbol{x}(0)\,, \tag{2.33}$$

$$\boldsymbol{v}\cdot\boldsymbol{x}_n=R(\lambda_{\boldsymbol{J}}\Delta t)^n\,\boldsymbol{v}\cdot\boldsymbol{x}(0)\,. \tag{2.34}$$

The error can therefore be assessed by comparing the numerical amplification factor $R(z)$ to the exact amplification factor e^z (Hirsch, 2007, pp.434f). The relative amplitude and the relative phase are defined as $|R(z)/e^z|$ and $\arg\left[R(z)/e^z\right]$, respectively.

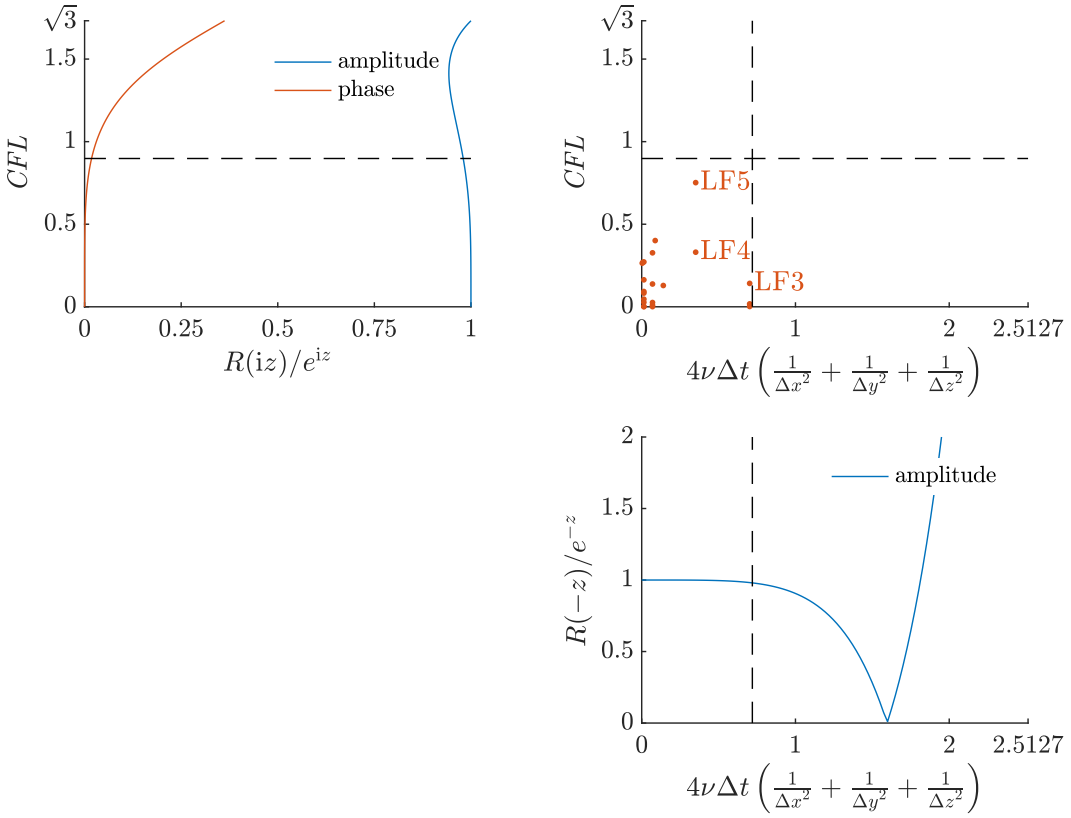

Figure 2.17: Courant-Friedrichs-Lewy number and numerical diffusion number of the simulations at 384 cpd and 768 cpd (top right), relative amplitude and relative phase of the explicit Runge–Kutta scheme along the imaginary axis as a function of the Courant-Friedrichs-Lewy number (top left) and along the negative real axis as a function of the numerical diffusion number (bottom right). The dashed lines indicate a 2% error in amplitude.

Figure 2.17 shows the dimensionless time step size of the simulations at the resolutions 384 cpd and 768 cpd together with the error characteristics of the explicit Runge–Kutta scheme. It can be seen that in all cases the amplitude and phase errors associated with the fastest time scales (eigenvalues) in the numerical solution are less than 2%. The highest errors are expected for the simulations at $Wo = 10$ for which the oscillation was very slow compared to the convective and diffusive time scale.

2.8. Sampling strategy

Three types of data were sampled from the simulations. First, time series of the volume-averaged velocity and kinetic energy and of the pressure drag were sampled at each time step. The high temporal resolution was chosen to accurately determine time derivatives and frequency spectra. Since the pressure is not available in the interface cells, the pressure drag was determined by evaluating the pressure force onto the boundary between the fluid cells and the interface cells which forms a stair-step approximation of the pore geometry. Second, instantaneous fields of the velocity and the pressure were extracted, which contain a restartable snapshot of the simulation. This was facilitated by the performant parallel

Case	$d/\Delta x$	$T/\Delta t_{\mathrm{bulk}}$	$T/\Delta t_{\mathrm{snapshot}}$	$T/\Delta t_{\mathrm{probes}}$	Remarks
LF1	384	$80,000$	12.5	200	
LF2	384	$80,000$	12.5	200	
LF3	384	$80,000$	100	800	
LF4	384	$160,000$	100	400	
LF5	384	$160,000$	100	800	
LF6	384	$640,000$	100	1600	
MF1	384	$80,000$	50	400	
MF2	384	$80,000$	50	–	
MF3	384	$80,000$	50	–	
MF4	384	$40,000$	25	200	
MF5	384	$80,000$	50	400	
MF6	384	$80,000$	50	400	
HF1	384	$40,000$	25	200	
HF2	384	$40,000$	25	200	
HF3	384	$40,000$	25	200	
HF4	384	$40,000$	50	200	
	768	$40,000$	50	200	
HF5	384	$40,000$	25	200	
	768	$40,000$	25	–	
HF6	384	$40,000$	25	200	
	768	$80,000$	25	800	
HF7	384	$40,000$	25	–	underresolved DNS
	384	$160,000$	25	200	LES with $C_{\mathrm{w}} = 0.316$
	384	$160,000$	25	200	LES with $C_{\mathrm{w}} = 0.5$

Table 2.5: Sampling frequencies for time series ($T/\Delta t_{\mathrm{bulk}}$), instantaneous fields ($T/\Delta t_{\mathrm{snapshot}}$) and probe points ($T/\Delta t_{\mathrm{probes}}$).

I/O implementation in MGLET (Sakai et al., 2019). A relatively low sampling rate (table 2.5) had to be chosen due to the large file size of the snapshots (3.3–4.2 GB at 384 cpd and 28 GB at 768 cpd using gzip compression). Third, probe point data of the velocity and the pressure was sampled at an intermediate temporal resolution (table 2.5). The probe points were placed in the planes $x/d = 1/192$, $x/d = 47/192$, $x/d = 49/192$, $x/d = 95/192$, $x/d = 97/192$ and $x/d = 383/192$ at a spatial resolution corresponding to 96 cpd. This allows to estimate the full velocity gradient in the planes $x/d = 0$, $x/d = 1/4$ and $x/d = 1/2$. Further probe points were located in the centres of the pores determined by the centroids of a Delaunay tesselation of the sphere positions.

3. Flow regimes

This chapter investigates the flow regimes in oscillatory flow through a hexagonal close-packing of spheres. The main questions are which flow regime is obtained for a given amplitude and frequency of the forcing (determined by the Hagen and the Womersley number), and how the flow regimes can be identified. First, a brief overview of the simulation results is given. Then, a summary of the following publications is provided:

- Unglehrt, L. & Manhart, M. 2022a Onset of nonlinearity in oscillatory flow through a hexagonal sphere pack. *Journal of Fluid Mechanics* **944**, A30.
- Unglehrt, L. & Manhart, M. 2022b Symmetry Breaking and Turbulence in Oscillatory Flow Through a Hexagonal Sphere Pack. In *Proceedings of TSFP-12 (2022) Osaka*. Osaka, Japan.
- Unglehrt, L. & Manhart, M. 2023b Direct and Large-Eddy simulation of turbulent oscillatory flow through a hexagonal sphere pack. In Direct and Large Eddy Simulation XIII, 1st edn. (ed. C. Marchioli, M. V. Salvetti, M. Garcia-Villalba & P. Schlatter), ERCOFTAC Series 31, pp. 118–123. Springer Cham.

Finally, the findings are brought together to form an approximate overall picture, and the results are discussed in terms of their implications for the transition process.

3.1. Description of the simulation dataset

This section aims to give an overview of the simulation dataset. In particular, the amplitude and phase behaviour of the superficial velocity as well as instantaneous velocity and vorticity fields at the maximum superficial velocity are qualitatively discussed. A detailed analysis of the simulations can be found in the respective articles.

3.1.1. Amplitude and phase behaviour

This section briefly discusses the amplitude and phase behaviour of the superficial velocity with respect to the Hagen and Womersley number. The data are taken from the last cycle of the simulation; a Gaussian low-pass filter with standard deviation $10\,\Omega$ was applied for the cases LF5, LF6, MF6, HF6 and HF7 in order to filter out high-frequency fluctuations in the superficial velocity. While this procedure lowers the amplitudes by about 1%, the time at which the maximum occurs can be identified more robustly. Figure 3.1a shows the amplitude of the superficial velocity as a function of the Hagen and the Womersley numbers. The relative amplitude of the superficial velocity with respect to Darcy flow is constant for small Hagen numbers and only depends on the Womersley number; the flow is linear in this

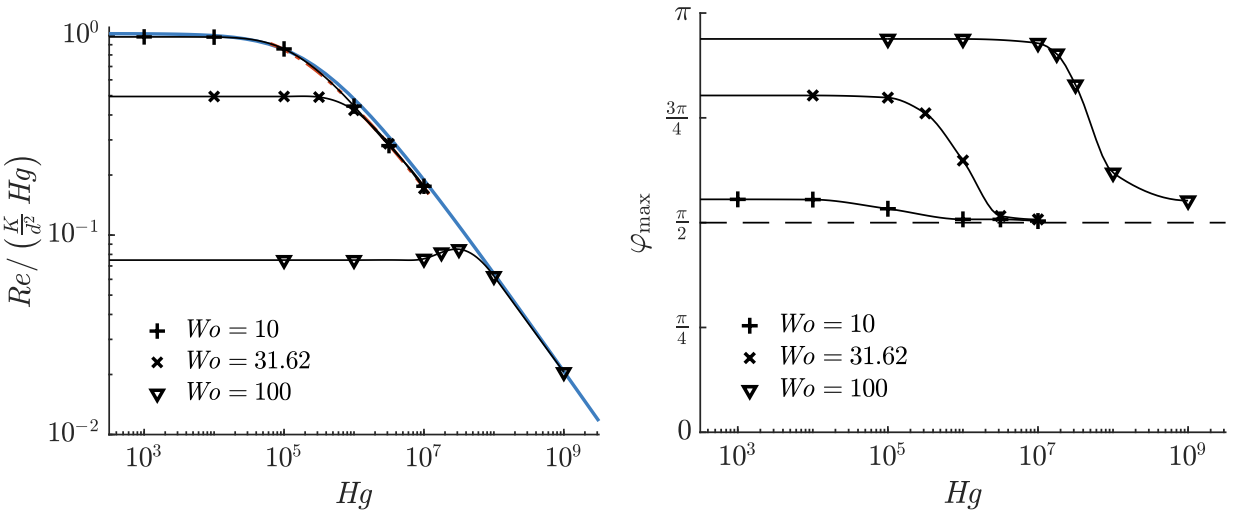

(a) Amplitude of the superficial velocity

(b) Phase of the maximum superficial velocity

Figure 3.1: (a) Amplitude of the superficial velocity relative to the velocity predicted by Darcy's law. The blue line represents the Ergun equation (Macdonald et al., 1979); the red dash-dotted line represents the correlation of Sakai & Manhart (2020). (b) Phase angle at which the maximum superficial velocity occurs in the last simulated cycle. The dashed line indicates the maximum of the macroscopic pressure gradient.

region. On the other hand, for large Hagen numbers the amplitude of the superficial velocity only depends on the Hagen number and the amplitude agrees with the empirical correlations of Macdonald et al. (1979) for stationary flow. As the Womersley number increases, the range of Hagen numbers for which the flow is linear increases and the transition between the linear and the inertial behaviour is shifted towards higher Hagen numbers. Interestingly, the amplitude of the superficial velocity never exceeds the corresponding value for stationary flow at the same Hagen number.

Figure 3.1b shows the phase angle at which the superficial velocity attains its maximum in the last simulated cycle. For low Hagen numbers, the phase angle varies strongly with the Womersley number. While the maximum of the superficial velocity occurs shortly after the maximum of the macroscopic pressure gradient for $Wo = 10$, the maximum of the superficial velocity lags behind the excitation by almost a quarter period for $Wo = 100$. The phase lag of the superficial velocity with respect to the macroscopic pressure gradient decreases as the Hagen number is increased. For $Wo = 10$ and $Wo = 31.62$ and $Hg \geq 3.16 \cdot 10^6$, the superficial velocity is almost perfectly in phase with the excitation.

3.1.2. Velocity and vorticity field at the maximum superficial velocity

An impression of the pore scale flow can be obtained by examining instantaneous velocity and vorticity fields close to the time of the maximum superficial velocity. According to Sakai & Manhart (2020), the flow is visualised in the section $x = d$, which is normal to the applied macroscopic pressure gradient, and in the section $\sqrt{3}/3\,y - \sqrt{6}/3\,z = 0$, which is oriented along the macroscopic pressure gradient. The position of these planes within the sphere pack is shown in the figure 2.4.

The figures 3.2, 3.3 and 3.4 show the spatial distribution of the velocity magnitude $|\boldsymbol{u}|$ and of the streamwise vorticity ω_x in the section $x = d$ at $Wo = 10$, 31.62 and 100, respectively. Note that ω_x in the plane $x = d$ is nonzero only in nonlinear flow, since the fore-aft symmetry of linear flow implies $v = w = 0$ in this plane (Unglehrt & Manhart, 2022a, reprinted in appendix D.1). At the lowest Womersley number, the results are in close agreement with the observations of Sakai & Manhart (2020); in particular, the streamwise vorticity in the octahedral pores clearly shows the four- and eight-vortex structures and the appearance of chaotic motion. A similar trend can be observed at the intermediate Womersley number; however, the structures seem to develop at higher Reynolds numbers than at $Wo = 10$. At the highest Womersley number the picture is different: here the flow structures in the octahedral pores appear only at very high Reynolds numbers.
The distribution of the velocity magnitude in the plane $\sqrt{3}/3\, y - \sqrt{6}/3\, z = 0$ is shown in the figure 3.5. The contours of $u = 0$ indicate regions of reverse flow. As the Reynolds number increases, the high velocity regions concentrate into inertial cores and a separation region forms behind the contact point located in the centre of the section. The inertial cores have a "C" shaped cross section (see figures 3.2, 3.3 and 3.4). The length of the inertial cores and of the separation region increases with the Reynolds number and tends to decrease with the Womersley number. This suggests a dependence on the displacement of the fluid particles. Finally, the high velocity regions move closer to the contact point with increasing Reynolds and Womersley numbers.

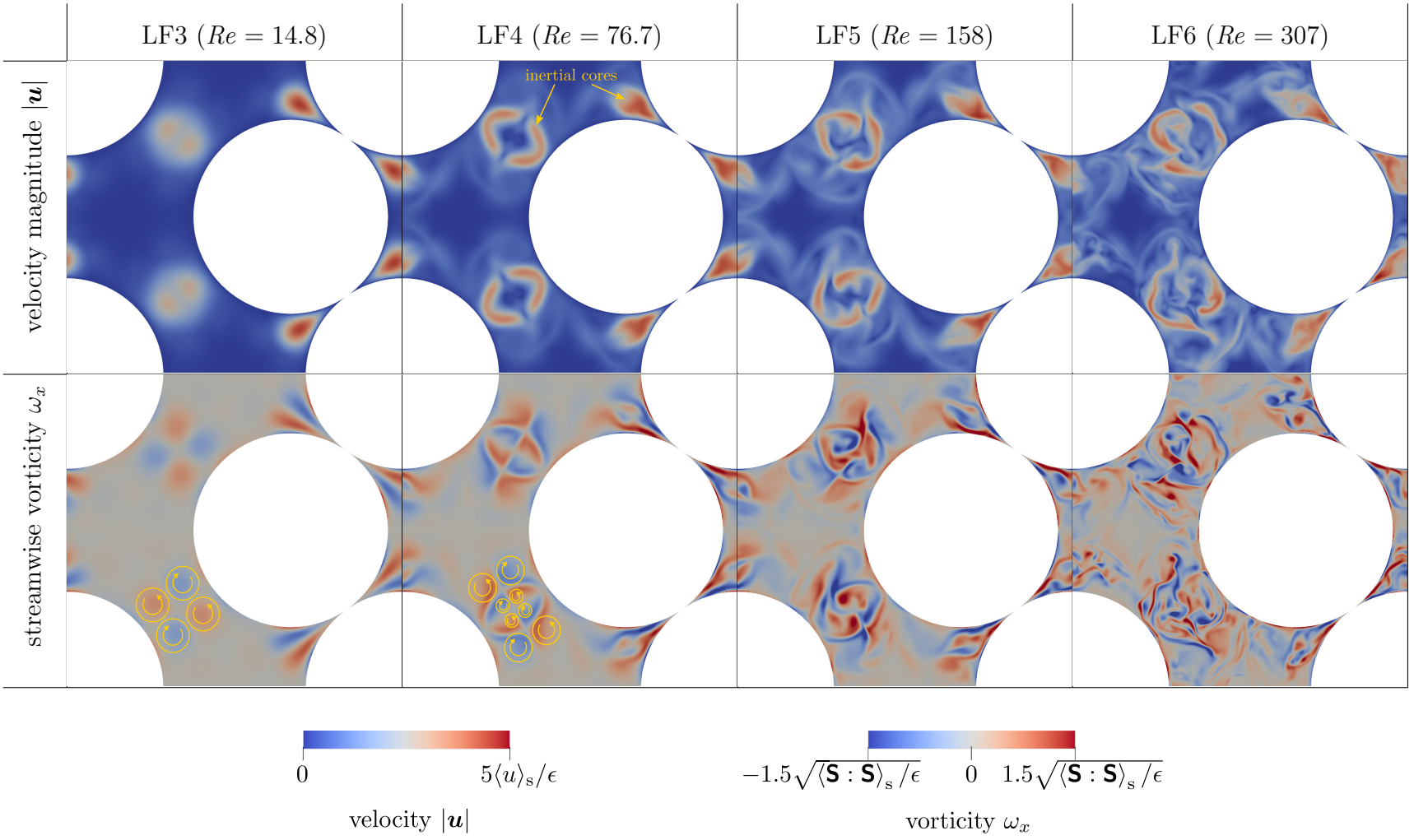

Figure 3.2: Velocity magnitude $|\boldsymbol{u}|$ and streamwise vorticity ω_x in the plane $x = d$ at the maximum superficial velocity for $Wo = 10$. The flow is perpendicular to the plane. The colours are chosen based on the superficial velocity and strain rate.

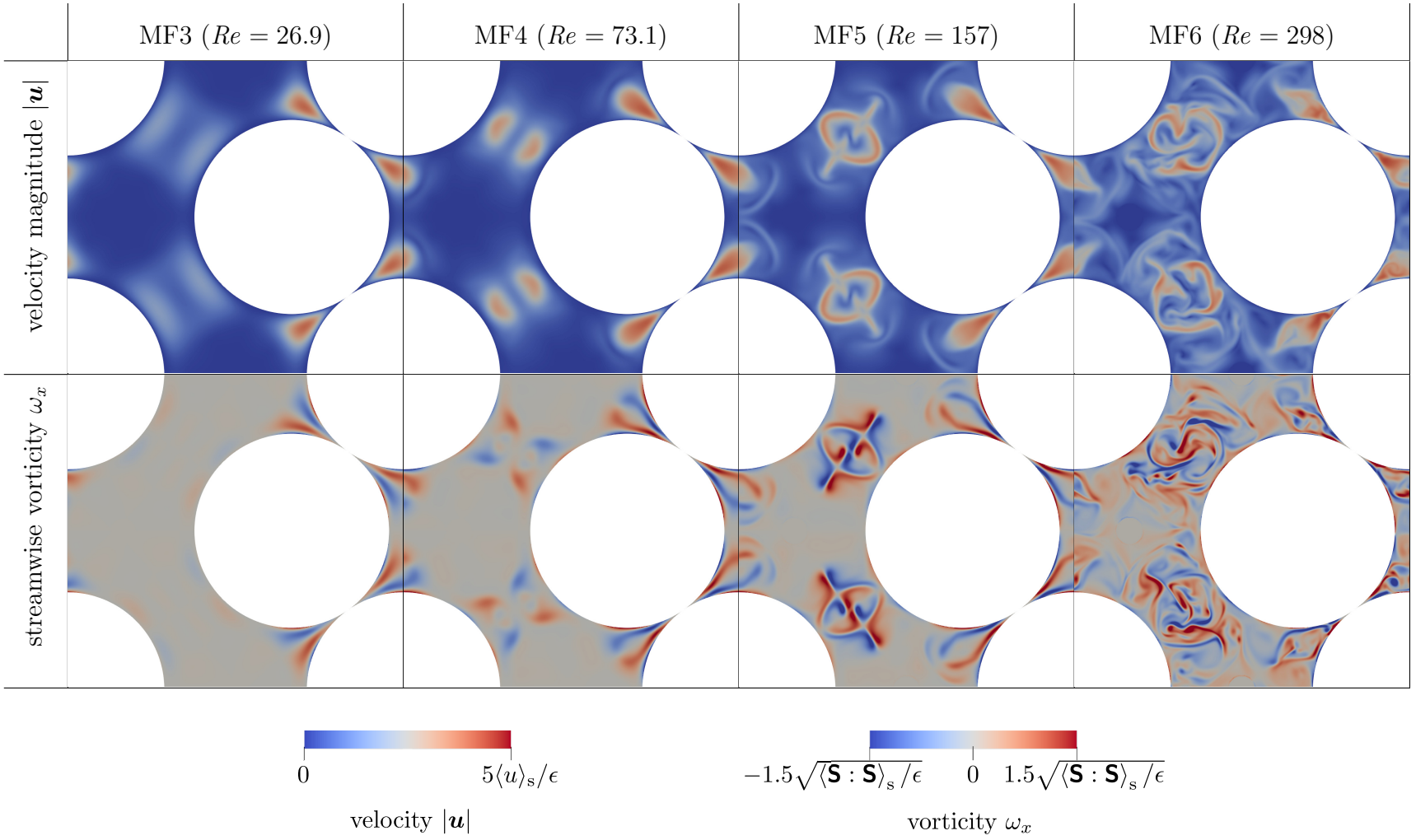

Figure 3.3: Velocity magnitude $|\boldsymbol{u}|$ and streamwise vorticity ω_x in the plane $x = d$ at the maximum superficial velocity for $Wo = 31.62$. The flow is perpendicular to the plane. The colours are chosen based on the superficial velocity and strain rate.

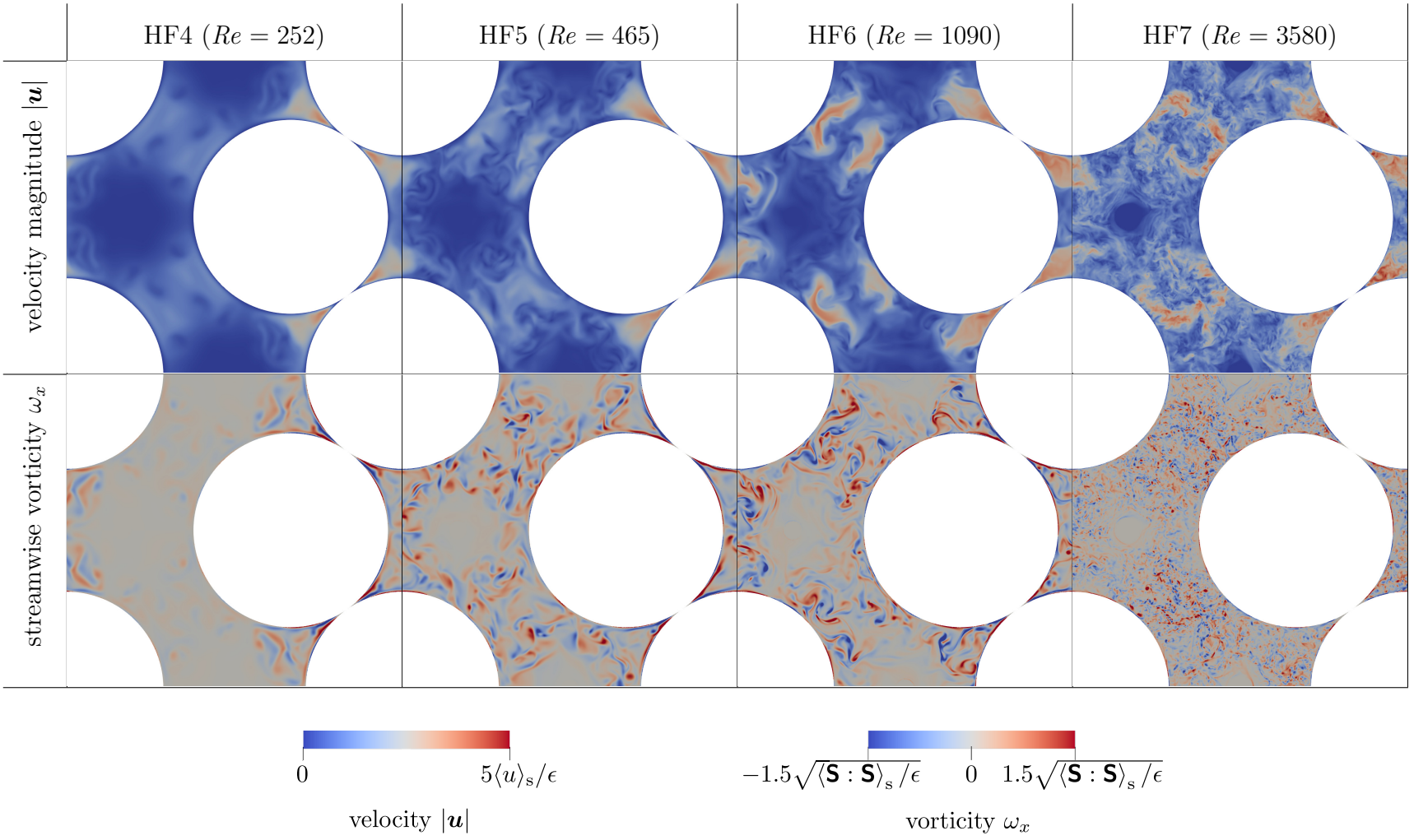

Figure 3.4: Velocity magnitude $|\boldsymbol{u}|$ and streamwise vorticity ω_x in the plane $x = d$ at the maximum superficial velocity for $Wo = 100$. The flow is perpendicular to the plane. The colours are chosen based on the superficial velocity and strain rate.

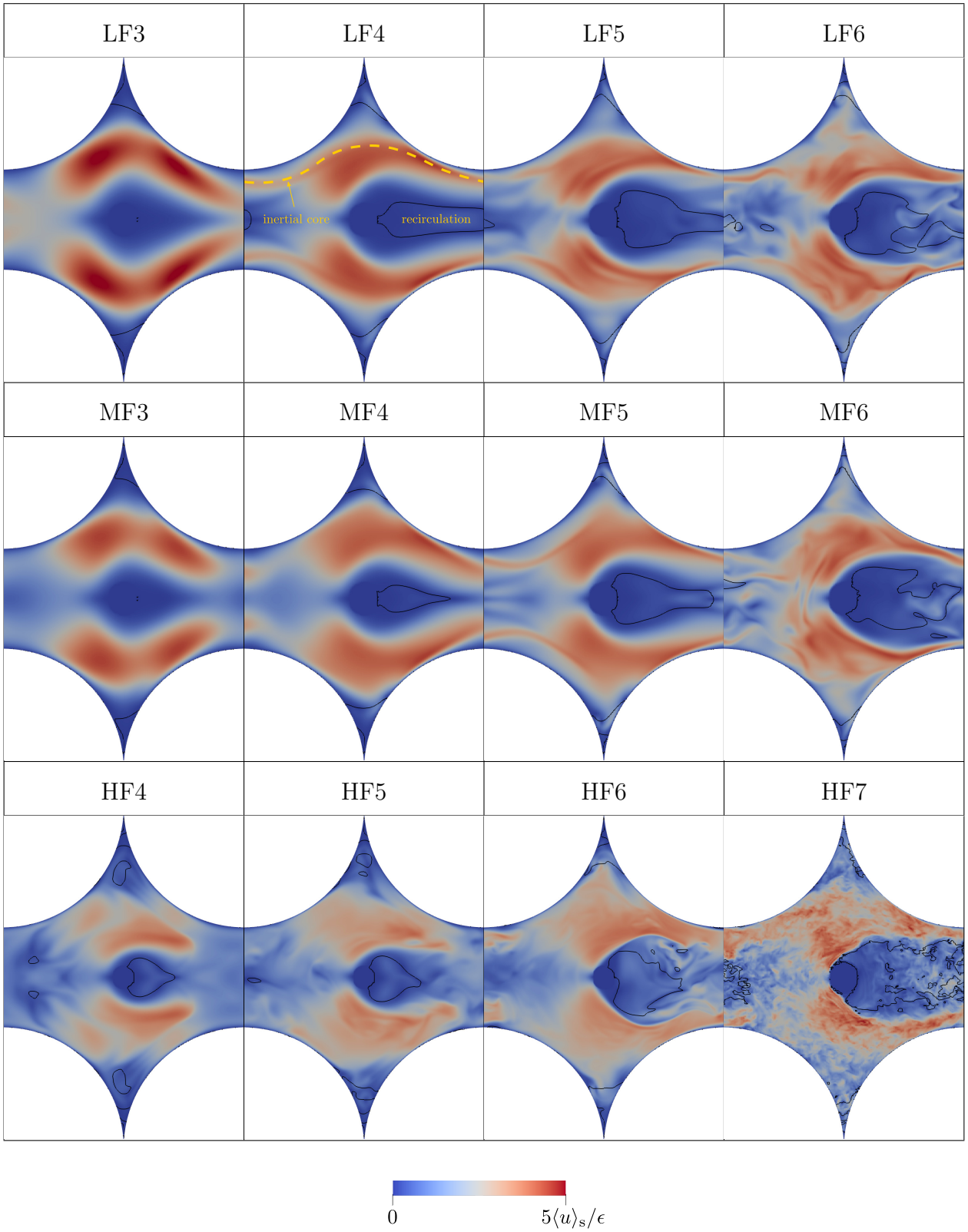

Figure 3.5: Velocity magnitude $|\boldsymbol{u}|$ in the plane $\sqrt{3}/3\,y - \sqrt{6}/3\,z = 0$ with contours $u = 0$. The flow goes from left to right and the colours are chosen based on the superficial velocity.

3.2. Summary: Onset of nonlinearity in oscillatory flow through a hexagonal sphere pack

This contribution concerns the identification and characterisation of weakly nonlinear flow as opposed to linear flow. We address the research questions of how to quantify the strength of nonlinear effects, for which values of the Hagen and the Womersley number linear (nonlinear) flow can be found, and how the nonlinearity affects the flow. The study is based on direct numerical simulations of oscillatory flow through a hexagonal sphere pack for the three Womersley numbers 10, 31.62 and 100 and different Hagen numbers.

First, we show that linear flow is obtained for the simulations at the lowest Hagen numbers by comparing the time series of the superficial velocity and the kinetic energy for the same Womersley number in the appropriate normalisations. The nonlinearity is investigated using a temporal Fourier analysis of the velocity field. If the flow is linear, only the Fourier coefficients at the excitation frequency are nonzero, whereas in nonlinear flow there are also other harmonics due to interactions between the Fourier modes in the convective term of the Navier-Stokes equations. The zeroth and second harmonics, which are the first signs of nonlinearity, are not present in the superficial velocity, which contains only odd harmonics. The strength of the nonlinear effects in the flow is quantified using the ratios of the volume-averaged energy of the Fourier coefficient fields to the total signal energy of the velocity field. The flow state of the different cases is thus characterised as linear, weakly nonlinear or strongly nonlinear. The Hagen number (or the Reynolds number) determines the onset of nonlinearity at low frequencies, while the ratio $Hg/\,Wo^4$ (or $Re/\,Wo^2$) determines the onset of nonlinearity at high frequencies. The Reynolds number range for linear behaviour is larger at $Wo = 100$ than at $Wo = 10$ and 31.62.

We then examine the nonlinear effects on the pore scale velocity field. While the linear flow cases show a fore-aft symmetric velocity field, this symmetry disappears in the nonlinear cases. For sufficiently large Hagen numbers, a separation region appears behind the contact points. At $Wo = 10$ the highest velocities are found near the centres of the tetrahedral pores. As the Womersley number is increased, the high velocity regions move closer to the contact points and the length of the separation region decreases. The instantaneous strength of nonlinear effects is investigated based on the deviation from the fore-aft symmetry. The velocity field is decomposed into a symmetric and an antisymmetric part, and the kinetic energy of the antisymmetric part $\langle k_{\mathrm{anti}} \rangle_{\mathrm{s}}$ is used as an indicator for the nonlinearity. As expected, the amplitude of $\langle k_{\mathrm{anti}} \rangle_{\mathrm{s}}$ increases with the Hagen number. While the kinetic energy of the antisymmetric part is nearly in phase with the superficial velocity at $Wo = 10$, there is a significant phase lag of $\langle k_{\mathrm{anti}} \rangle_{\mathrm{s}}$ with respect to the superficial velocity at the higher Womersley numbers. Hence, the nonlinear effects cannot be easily parametrised in terms of the superficial velocity.

Finally, the weakly nonlinear flow is discussed in terms of the Fourier modes. It is shown that the breaking of the fore-aft symmetry leads to a nonzero time-averaged velocity field, i.e. a zeroth harmonic. To leading order, the time-averaged level of $\langle k_{\mathrm{anti}} \rangle_{\mathrm{s}}$ depends on the magnitude of the zeroth and second harmonics, and the variation of $\langle k_{\mathrm{anti}} \rangle_{\mathrm{s}}$ over the cycle is determined by the interference of the zeroth and second harmonics. A space-time symmetry composed of a half-period shift in time and of the fore-aft symmetry is found to be the reason why the even harmonics do not contribute to the superficial velocity.

3.3. Summary: Symmetry breaking and turbulence in oscillatory flow through a hexagonal sphere pack

This contribution addresses the question of how the transition of oscillatory flow from the laminar to the turbulence-like flow state can be identified based on objective measures. Inspired by Hill & Koch (2002) and Sakai & Manhart (2020), who described a sequence of symmetry-breaking bifurcations for stationary flow through a face-centred cubic and hexagonal sphere pack, respectively, symmetry breaking is used to investigate the flow state in oscillatory flow through a hexagonal sphere pack based on the four simulation cases MF3–MF6 at $Wo = 31.62$ with Reynolds numbers 27, 74, 157 and 297.

First, we consider the instantaneous velocity field in the y-z-plane (perpendicular to the macroscopic pressure gradient) at the maximum superficial velocity. At the three lower Reynolds numbers, the velocity field is smooth and the flow structures are arranged in a symmetrical pattern. At $Re = 297$ the flow structures are disordered and the velocity field gives the impression of mixing and vortical motion. The former cases thus appear to be laminar whereas the latter case appears to be in a turbulence-like state.

The streamwise component of the superficial velocity gradually develops nonsinusoidal behaviour with increasing Reynolds number. However, we do not observe any salient features that would clearly distinguish the laminar and the turbulence-like cases. The transverse components of the superficial velocity are close to zero for the two lower Reynolds numbers (27 and 74), which is a consequence of the symmetries of the sphere pack. On the other hand, for the two higher Reynolds numbers (157 and 297) a phase plot of $\langle v \rangle_\mathrm{s}$ and $\langle w \rangle_\mathrm{s}$ shows an irregular, apparently chaotic behaviour of the transverse components.

We then analyse the symmetry breaking process of the velocity field, which in the hexagonal close-packing can have four independent symmetries. For each symmetry, the velocity field is decomposed into a symmetric and an antisymmetric part; a nonzero kinetic energy of the antisymmetric part indicates the breaking of the corresponding symmetry. While the two lower Reynolds number cases show no signs of symmetry breaking, at $Re = 157$ the kinetic energy of all antisymmetric parts grows approximately exponentially over several cycles and saturates at 0.3% of the maximum total kinetic energy. As this growth is modulated by the oscillation, the process resembles a Floquet instability. At the highest Reynolds number, the kinetic energy of the antisymmetric parts grows much faster and reaches a level of 10% of the maximum total kinetic energy after about 1.5 cycles.

To investigate the flow structures responsible for the symmetry breaking, we decompose the velocity field into a part that is symmetric with respect to all symmetries ('symmetry-group average') and a residual. Since the ensemble mean of the velocity field must respect the symmetries imposed by the geometry, this residual has an ensemble mean of zero. It is therefore a subset of the fluctuations around the ensemble mean of the velocity field and can be used to obtain an impression of the geometric features of the fluctuations. At $Re = 157$ the residual velocity is about 30 times weaker than the symmetry-group-averaged velocity and its highest magnitudes are found close to the dominant average flow features, suggesting that the case MF5 is in a transitional flow state. At $Re = 297$ the residual velocity shows flow structures that are quite uniformly distributed throughout the large pores. These show little resemblance to the average flow structures and have a significantly smaller scale, which is consistent with a turbulence-like flow state.

3.4. Summary: Direct and Large–Eddy simulation of turbulent oscillatory flow through a hexagonal sphere pack

In this contribution turbulent oscillatory flow at $Wo = 100$, corresponding to the high frequency regime in linear flow, is investigated. A direct numerical simulation was performed for $Hg = 10^8$ (case HF6), resulting in a Reynolds number of 1086, and a wall-resolved large–eddy simulation was conducted for $Hg = 10^9$ (case HF7) using the WALE model (Nicoud & Ducros, 1999), resulting in a Reynolds number of 3580.
The amplitude of the superficial velocity agrees well with the Ergun equation (Macdonald et al., 1979) evaluated for the maximum macroscopic pressure gradient. The superficial velocity has a temporal lag with respect to the macroscopic pressure gradient which decreases with increasing Reynolds number. At the higher Reynolds number a short period of strong acceleration is observed in the superficial velocity. At the end of this phase a separation region appears in the instantaneous velocity field. Subsequently, the superficial velocity exhibits a plateau-like period of weak acceleration before deceleration.
We investigate the behaviour of the volume-averaged mean and turbulent kinetic energy (MKE and TKE, respectively) and of their dissipation rates for the case HF6 ($Re = 1086$). The one-point statistics were calculated using a phase average based on 9 simulated cycles. The 4 spatial symmetries were used to increase the number of samples, resulting in a total of 144 samples. The TKE is not in phase with the MKE. Rather, the TKE is small during the acceleration phase and large during the deceleration phase. The TKE is nonzero throughout the entire cycle, indicating that the flow does not fully relaminarise. The total volume-averaged dissipation rate exhibits a hysteresis over the volume-averaged kinetic energy. This can be explained using the Reynolds decomposition: The direct dissipation rate shows a weakly hysteretic behaviour over the MKE and the turbulent dissipation rate shows a weakly hysteretic behaviour over the TKE. The turbulent dissipation rate can be well approximated by a power law of the form

$$2\nu \left\langle \overline{\boldsymbol{S}'} : \boldsymbol{S}' \right\rangle_{\mathrm{s}} \approx \frac{22.7}{d} \left\langle \frac{1}{2} \overline{\boldsymbol{u}' \cdot \boldsymbol{u}'} \right\rangle_{\mathrm{s}}^{3/2} , \tag{3.1}$$

indicating that the TKE production occurs on an essentially fixed length scale. The case HF7 departs from this power law during deceleration. A possible reason for this discrepancy may lie in the sub-grid scale model of the large–eddy simulation.

3.5. Discussion

3.5.1. Flow regimes in the parameter space

In this section, the results of the different investigations are combined to give a fuller picture of the flow regimes in parameter space. The regimes refer to flow in response to a sinusoidal forcing after the transient has decayed. Figure 3.6 presents a partitioning of the Hg–Wo parameter space into linear flow, weakly nonlinear flow, strongly nonlinear flow, separated flow and transitional and turbulence-like flow.
The extent of the linear region as well as the subdivision of the nonlinear region into weakly

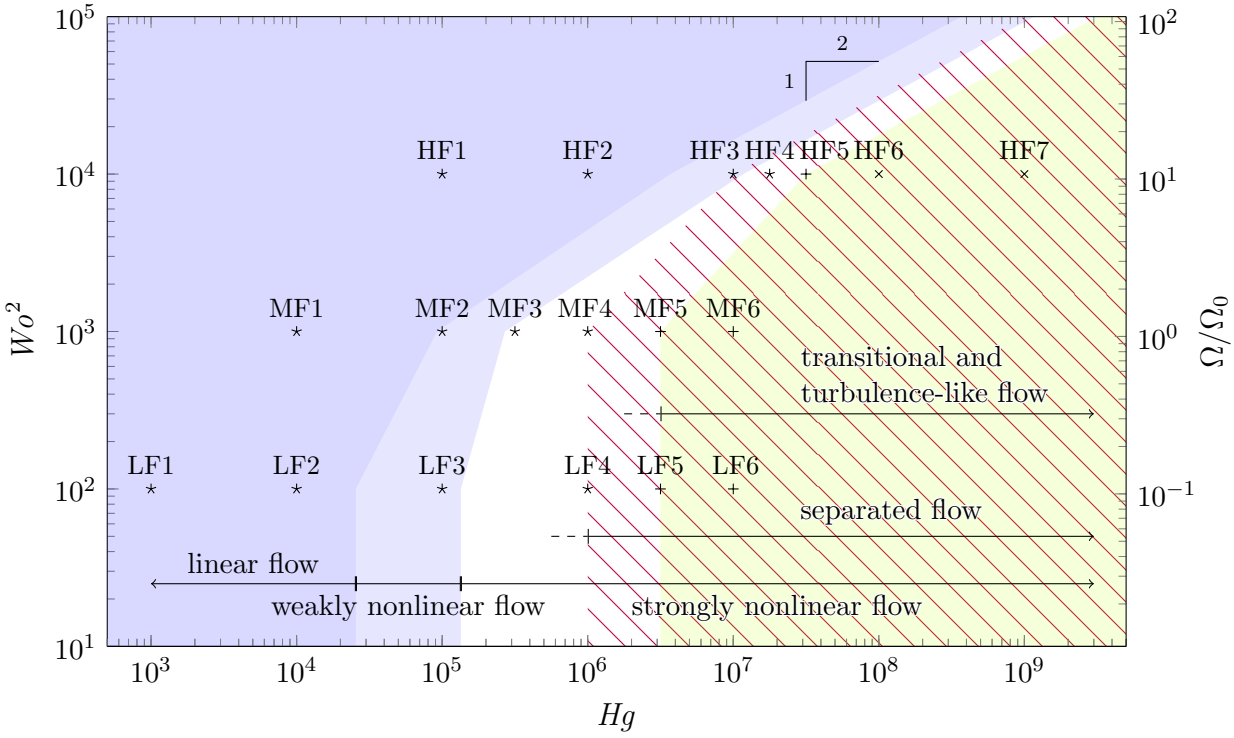

Figure 3.6: Flow regimes in oscillatory flow through a hexagonal close-packed arrangement of spheres. Dark blue: linear flow (> 99 % of the energy in first harmonic), light blue: weakly nonlinear flow (> 95 % of the energy in first harmonic), purple shaded: separated flow ($u < 0$ behind the contact points), green: transitional and turbulence-like flow (symmetry breaking).

and strongly nonlinear flow was determined in (Unglehrt & Manhart, 2022a, reprinted in appendix D.1). The linear regime was extrapolated to high Womersley numbers by assuming a dependency of the onset of nonlinearity on the ratio Hg/Wo^4, which measures the relative importance of the convective term compared to the linear terms in the Navier-Stokes equations. This scaling for the onset of nonlinearity at high Womersley numbers is consistent with the simulation results of Ren et al. (2021) for two- and three-dimensional oscillatory flow around a cylinder. However, this extrapolation is not valid if the linear oscillatory flow undergoes an instability. The different instabilities and estimates for their occurrence are discussed in section 3.5.4.

The criterion for separated flow was the occurrence of a region behind the contact point in the plane $\sqrt{3}/3\,y - \sqrt{6}/3\,z = 0$, where u-velocities are opposite to $\langle u \rangle_s$ (see figure 3.5). Due to the highly three-dimensional nature of the flow, the surface $u = 0$ cannot capture the exact shape of the separation region. The calculation of the actual streamsurface bounding the separation region would require knowledge of the separation line at the wall, which is difficult to obtain (see appendix C).

The regime boundary for transitional and turbulence-like flow was determined by applying the analysis of symmetry breaking from (Unglehrt & Manhart, 2022b, reprinted in appendix D.2) to the other simulation cases. It can be seen in the figures 3.2, 3.3 and 3.4 that the

cases LF6, MF6, HF5, HF6 and HF7, for which the symmetries are broken, have disordered velocity and vorticity fields and give the visual impression of mixing and vortical motion.
A comparison with the study by He et al. (2019), who performed direct numerical simulations of flow through a face-centred cubic sphere pack at Reynolds numbers 222–740, suggests that the cases LF6 and MF6 contain only a limited range of spatial scales. In particular, for the simulations of He et al. (2019), the decay of the energy spectrum essentially takes place within one decade of the wave number. On the other hand, the instantaneous fields in figure 3.4 show that the cases HF5, HF6 and HF7 have significantly finer spatial scales. Hence, the cases LF6 and MF6 should be considered as turbulence-like, whereas especially the case HF7 is well in line with the common understanding of turbulence.

3.5.2. Comparison with macroscopic flow regimes

The flow regimes discussed above were defined using the full flow fields obtained from direct numerical simulations. For practical purposes, it is interesting to compare these results to the flow regime estimation of Gu & Wang (1991) based on the behaviour of the superficial velocity. They partitioned the Re–Wo^2 parameter space into regions dominated by one or two terms of the unsteady Forchheimer equation (Polubarinova-Kochina, 1962; Sollitt & Cross, 1972)

$$\underbrace{\rho \frac{\alpha_\infty}{\epsilon} \frac{\mathrm{d}\langle \boldsymbol{u} \rangle_\mathrm{s}}{\mathrm{d}t}}_{=:f_\mathrm{i}} = -\boldsymbol{\nabla} \langle p \rangle_\mathrm{i} - \underbrace{\frac{\mu}{K} \langle \boldsymbol{u} \rangle_\mathrm{s}}_{=:f_\mathrm{l}} \underbrace{- b \, |\langle \boldsymbol{u} \rangle_\mathrm{s}| \, \langle \boldsymbol{u} \rangle_\mathrm{s}}_{=:f_\mathrm{n}} , \tag{3.2}$$

which is given here in the parametrisation investigated in appendix D.4. The ratios between the different terms defined by Gu & Wang (1991) can be evaluated using the parameter values for the hexagonal sphere pack (cf. appendix D.4) as

$$\left| \frac{\text{“inertial resistance”}\ f_\mathrm{i}}{\text{“laminar resistance”}\ f_\mathrm{l}} \right| = 1.08 \cdot 10^{-3} \, Wo^2 \tag{3.3a}$$

$$\left| \frac{\text{“turbulent resistance”}\ f_\mathrm{n}}{\text{“laminar resistance”}\ f_\mathrm{l}} \right| = 1.54 \cdot 10^{-2} \, Re \tag{3.3b}$$

$$\left| \frac{\text{“turbulent resistance”}\ f_\mathrm{n}}{\text{“inertial resistance”}\ f_\mathrm{i}} \right| = 14.2 \, \frac{Re}{Wo^2} \, . \tag{3.3c}$$

The “L Region” is dominated by the linear term ($f_\mathrm{l} > 10\, f_\mathrm{i}$ and $f_\mathrm{l} > 10\, f_\mathrm{n}$), the “N Region” is dominated by the nonlinear term ($f_\mathrm{n} > 10\, f_\mathrm{l}$ and $f_\mathrm{n} > 10\, f_\mathrm{i}$) and the “I Region” is dominated by the inertial term ($f_\mathrm{i} > 10\, f_\mathrm{l}$ and $f_\mathrm{i} > 10\, f_\mathrm{n}$). Moreover, there are regions determined by the interaction of two and three of the forces. Figure 3.7 shows the flow regimes based on the pore scale flow and the regions of Gu & Wang (1991). The linear regime approximately coincides with the L and I regions and their interaction region. The L and I regions are arranged symmetrically with respect to the characteristic frequency Ω_0 of the sphere pack and their boundary towards high Reynolds numbers lies in the weakly nonlinear flow regime. However, the interaction region misses a part of the linear regime between the cases LF2 and MF2.

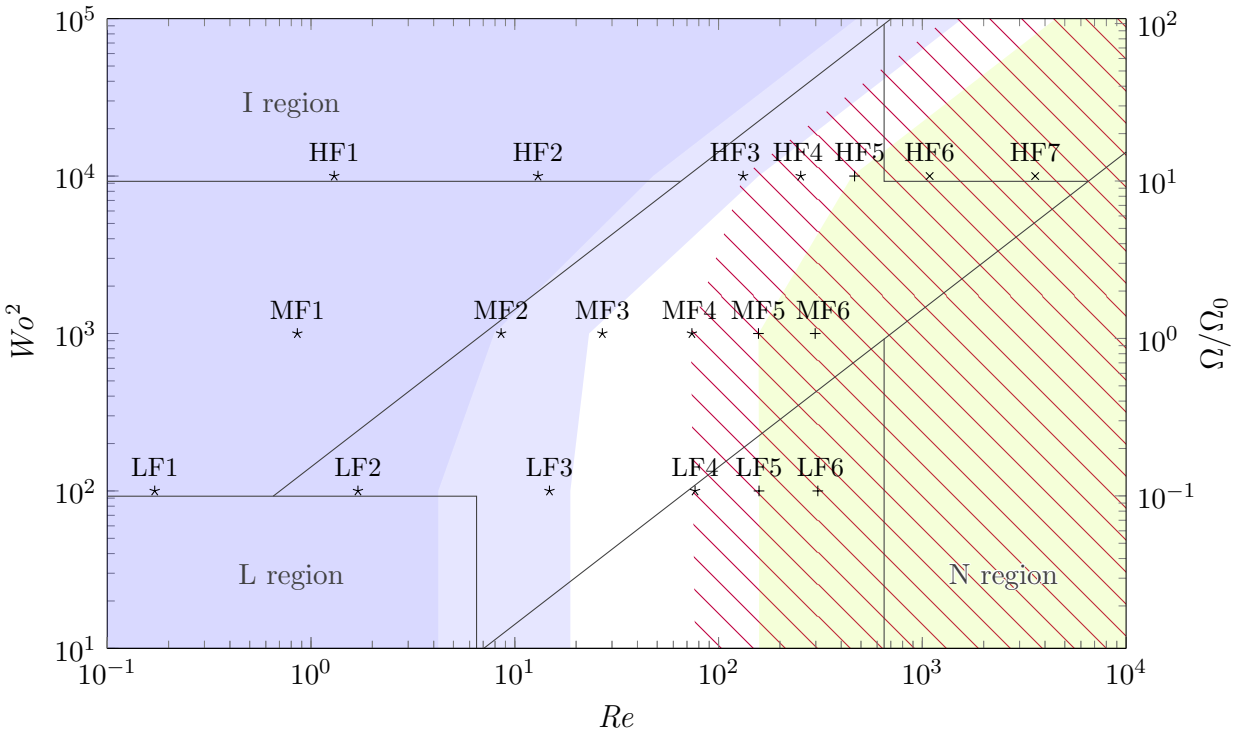

Figure 3.7: Comparison of flow regimes with the estimation of Gu & Wang (1991). The L region is dominated by the linear term of the unsteady Forchheimer equation, the N region is dominated by the nonlinear term and the I region by the inertial term. The colours and shadings are defined as in figure 3.6.

The N region is completely contained within the transitional and turbulence-like flow regime, but does not capture its full extent. Thus, the N region rather corresponds to the state of asymptotic turbulence (Patil & Liburdy, 2015; Wood et al., 2020) than to a merely chaotic, turbulence-like state. The interaction region between the L and N regions misses some part of the low frequency regime close to the case LF3, which can be considered quasi-steady. In conclusion, the estimation of flow regimes using the unsteady Forchheimer equation is consistent with the present results if appropriate values are used for the model parameters. However, transitional and turbulence-like flow can be found outside the region dominated by the nonlinear term of the unsteady Forchheimer equation.

3.5.3. Conceptual view of flow instabilities

In this section, the possibilities for hydrodynamic instability in the present flow case are discussed from the mathematical perspectives of linear stability theory and bifurcation theory. The relevance of different physical instability mechanisms is assessed in the following section. These discussions provide a starting point for future systematic study of the transition to turbulence in oscillatory flow through porous media.

Linear stability theory

Linear stability theory is concerned with the question of whether a given base flow $\boldsymbol{u}$, p is unstable with respect to certain infinitesimal perturbations. The evolution of the perturbations $\boldsymbol{u}''$, p'' is governed by the linearised Navier-Stokes equations

$$\boldsymbol{\nabla} \cdot \boldsymbol{u}'' = 0 \tag{3.4a}$$

$$\frac{\partial \boldsymbol{u}''}{\partial t} + (\boldsymbol{u} \cdot \boldsymbol{\nabla})\boldsymbol{u}'' + \underbrace{(\boldsymbol{u}'' \cdot \boldsymbol{\nabla})\boldsymbol{u}}_{\text{source}} = -\frac{1}{\rho}\boldsymbol{\nabla} p'' + \nu \, \Delta \boldsymbol{u}'' \,. \tag{3.4b}$$

The perturbations lose energy through viscous dissipation and, depending on their shape, receive energy from or lose energy to the base flow. The *modal approach* investigates perturbations that are eigenmodes of the linearised Navier-Stokes equations (Schmid, 2007). In general, the modal approach can only make statements about the asymptotic behaviour of a perturbation for large times (Schmid, 2007). For a steady base flow, one looks for modes undergoing an exponential growth in time, i.e.

$$\boldsymbol{u}''(\boldsymbol{x}, t) = e^{\lambda t} \, \boldsymbol{u}''(\boldsymbol{x}, 0) \,, \tag{3.5}$$

where eigenvalues with positive real part ($\Re(\lambda) > 0$) indicate instability. For an oscillatory base flow, one looks for modes exhibiting a net amplification over one cycle while coming back to the same spatial distribution, i.e.

$$\boldsymbol{u}''(\boldsymbol{x}, t + T) = \mu_{\mathrm{F}} \, \boldsymbol{u}''(\boldsymbol{x}, t) = e^{\lambda T} \, \boldsymbol{u}''(\boldsymbol{x}, t) \,, \tag{3.6}$$

where Floquet multipliers outside the unit circle ($|\mu_{\mathrm{F}}| > 1$) indicate instability (Schmid & Henningson, 2001, pp.223f). This type of instability is also known as "parametric resonance" (Drazin & Reid, 2004, pp.354f) and is investigated using Floquet theory. On the other hand, the *nonmodal approach* aims to maximise the growth of an initial condition over a finite time horizon while allowing the perturbation to change its spatial shape. Due to the nonorthogonality of the eigenmodes of the linearised Navier-Stokes equations, initial conditions composed of two or more stable modes can experience a *transient growth* caused by differences in the decay rates of the modes (Schmid, 2007; Theofilis, 2011; Schmid & Henningson, 2001, p.100). While such a perturbation has to decay in the long run, its temporary amplification may be strong enough to result in a nonlinear evolution of the perturbation. Notably, transient growth phenomena can occur both for combinations of eigenmodes and combinations of Floquet modes (Schmid, 2007, fig 2. and fig. 8).

In the present case of oscillatory flow through a hexagonal sphere pack, a first complication arises from the nonlinearity of the base flow. The base flow varies with the Reynolds number and it is not possible to determine the critical Reynolds number directly from the stability problem. Rather, the stability analysis has to start from the known stable region and the Reynolds number of the base flow has to be incrementally increased until a neutrally stable state is reached. When investigating the primary instability of the flow, one has to ensure that the base flow satisfies all known symmetries, because if the symmetries are broken, an instability must have occurred. A second complication is that it is unclear which type of stability analysis is most appropriate for the present case. On the one hand, the results at

$Wo = 10$ are in general agreement with the findings of Hill & Koch (2002) and Sakai & Manhart (2020) for stationary flow, suggesting that a quasi-static approach can be applied. Such an approach considers only the stability of the instantaneous velocity fields and can be justified by a Wentzel-Kramers-Brillouin (WKB) approximation in which the base flow is assumed to vary little during the growth of instabilities (Hall & Parker, 1976; Davis, 1976; Hall et al., 1994). Due to the long oscillation period, a Floquet instability analysis at low Womersley numbers would be computationally expensive and probably not relevant, since the transient amplification of a perturbation may be more important than the net amplification over a cycle. On the other hand, the symmetry breaking behaviour of the case MF5 at $Wo = 31.62$ suggests the presence of a modal Floquet instability. Similarly, in the case HF5 at $Wo = 100$, symmetry breaking and turbulence develop only after several cycles, which is consistent with a Floquet instability. However, the results of (Ozdemir et al., 2014; Biau, 2016) show that the oscillatory Stokes boundary layer undergoes a nonmodal instability at a subcritical Reynolds number, indicating that a Floquet stability analysis may be insufficient at high Womersley numbers. In conclusion, a unified study of stability is likely to require a nonmodal stability analysis. A Floquet stability analysis can be a useful first step in understanding the instability behaviour at intermediate and high Womersley numbers.

Bifurcation theory

Bifurcation theory is concerned with the behaviour of equilibria and limit cycles of a dynamical system as a function of a slowly varied parameter (Drazin & Reid, 2004, p.402). In the present case, this parameter can be the Reynolds number or the Hagen number. Nonlinear dynamical systems can have multiple equilibria or limit cycles that may be stable or unstable. A bifurcation occurs if the system undergoes a qualitative change in response to a parameter variation (Nayfeh & Balachandran, 2008, p.70), such as a change in stability or the appearance or disappearance of an equilibrium or limit cycle. Depending on these changes, bifurcations can be classified as "safe", "explosive" or "dangerous" (Thompson et al., 1994). One further distinguishes between local bifurcations, for which the changes are confined to the state space neighbourhood of the equilibrium (Nayfeh & Balachandran, 2008, pp.69f), and global bifurcations (Nayfeh & Balachandran, 2008, p.121). Local bifurcations can be identified using modal stability theory.

When the base flow is neutrally stable with respect to a perturbation, different cases can be distinguished based on the eigenvalues of the linear stability problem. These cases are known as codimension-1 bifurcations, since they occur in response to the variation of a single parameter (Nayfeh & Balachandran, 2008, p.70). If a single eigenvalue is zero, a static bifurcation occurs; if a pair of complex-conjugate eigenvalues has zero real part, a dynamic bifurcation occurs (Nayfeh & Balachandran, 2008, p.70). The static bifurcations of a steady state are the saddle-node bifurcation and the subcritical pitchfork bifurcation, in which the steady state disappears or becomes unstable, the transcritical bifurcation, in which the system switches onto another solution branch, and the supercritical pitchfork bifurcation, in which the steady state bifurcates into a pair of steady states (Nayfeh & Balachandran, 2008, pp.70f). Note that the pitchfork bifurcation is associated with symmetry breaking and is changed in the presence of imperfections (Crawford & Knobloch, 1991; Drazin & Reid, 2004, pp.407f). The simplest dynamic bifurcation of a steady state is the supercritical Hopf

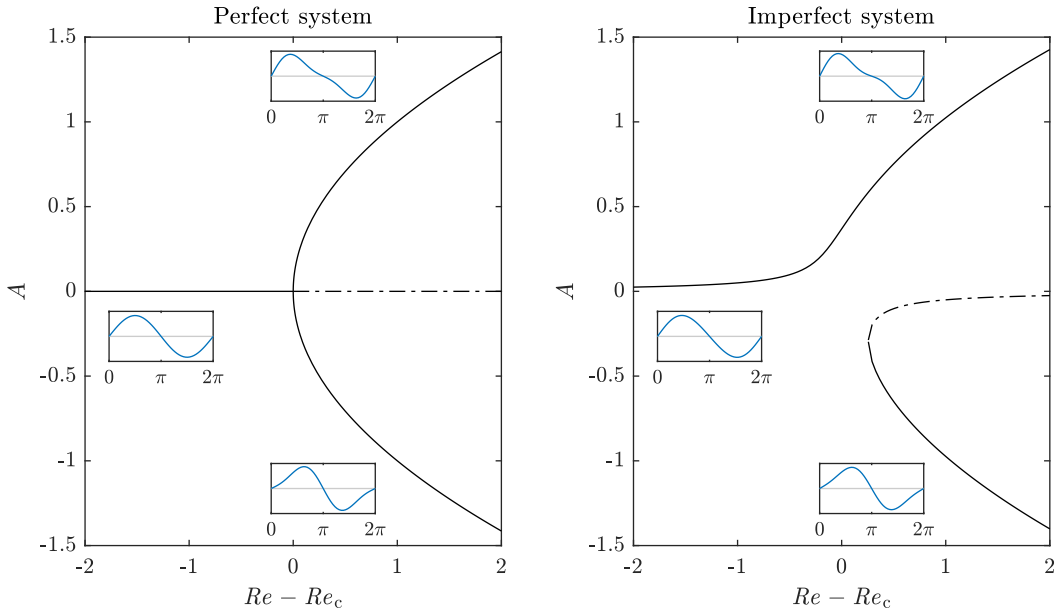

Figure 3.8: Bifurcation diagrams of a pitchfork bifurcation in a perfect and an imperfect system according to (Drazin & Reid, 2004, pp.411f), where A represents the amplitude of a symmetry-breaking mode. The insets exemplify the breaking of the space-time symmetry observed by Roberts & Mackley (1996). The curves on the lower branch can be obtained from the curves on the upper branch by a half-period shift and a mirroring.

bifurcation, in which the steady state becomes unstable and a limit cycle appears, i.e. the system begins to oscillate (Nayfeh & Balachandran, 2008, pp.77f). According to Ruelle & Takens (1971), the Hopf bifurcation may be essential for the transition to turbulence. For a limit cycle, a period doubling bifurcation ($\mu_F = -1$), a pitchfork bifurcation ($\mu_F = 1$) or a secondary Hopf bifurcation ($\mu_F = e^{\pm\theta}$) occurs depending on where the Floquet multipliers μ_F leave the unit circle (Nayfeh & Balachandran, 2008, pp.187f).

Using bifurcation theory, some results obtained for symmetric systems can be extrapolated to systems with small imperfections. For example, consider the supercritical pitchfork bifurcation observed by Roberts & Mackley (1996), which breaks the space-time symmetry of the forward and the backward half-cycles. If the system is perfectly symmetric, there is an equal probability for the system to select either one of the two limit cycles with broken symmetry. If the system has an imperfection, the forward and backward half-cycles are never identical. Close to the bifurcation point, a strong amplification of the difference between the half-cycles would be observed. Beyond the bifurcation point, a large enough perturbation could lead to a switch to the other solution branch. Figure 3.8 qualitatively illustrates the expected behaviour. Notably, the critical Reynolds number for the bifurcation increases with the size of the imperfection (Drazin & Reid, 2004, pp.411f).

In the present case, the bifurcation theory of equilibria applies for $Wo \to 0$, i.e. when the macroscopic pressure gradient is varied quasi-statically. The stationary flow undergoes several Hopf bifurcations that lead to periodic, quasi-periodic and chaotic flow (Hill & Koch, 2002; Sakai & Manhart, 2020). The behaviour of the Hopf bifurcation in response to an oscillatory forcing depends on the ratio between the eigenfrequency ω_H of the bifurcation

and the forcing frequency Ω. If $\omega_\mathrm{H}/\Omega \gg 1$, the flow can be expected to behave similarly to the stationary case. In particular, high frequency fluctuations due to the Hopf bifurcation appear when the instantaneous Reynolds number exceeds the critical value for the bifurcation and disappear when the Reynolds number falls below the critical value. This is known as "periodic bursting" (Golubitsky et al., 2001). Due to the "slow passage" effect, the Hopf bifurcation appears slightly delayed compared to the stationary case (Golubitsky et al., 2001). The behaviour of the Hopf bifurcation in response to a harmonic forcing near the eigenfrequency ω_H has been studied by Lingnau et al. (2020). As the "detuning" ratio ω_H/Ω approaches 1 from above, the Hopf bifurcation oscillates with the frequency Ω; for detuning ratios less than about 0.8, phase locking occurs, i.e. the detuning ratio snaps to certain fixed values given by the "devil's staircase" function, and for ω_H/Ω less than about 0.2, the Hopf bifurcation is no longer excited. Note that phase locking has also been observed in the transition of thermal convection to turbulence (Gollub & Benson, 1980, route I).
Another scenario of bifurcations has been observed by Roberts & Mackley (1996) for oscillatory flow through a baffled channel. After the aforementioned pitchfork bifurcation, a sequence of period doubling bifurcations leads to a chaotic flow state. Similar to the case of Roberts & Mackley (1996), oscillatory flow through the hexagonal sphere pack has a space-time symmetry composed of a half-period shift in time and a subsequent reflection (Unglehrt & Manhart, 2022a, reprinted in appendix D.1). To investigate the possibility of a supercritical pitchfork bifurcation similar to Roberts & Mackley (1996), an indicator function for the space-time symmetry at the probe point positions near $x = 0$ is constructed analogously to (Roberts & Mackley, 1996) as

$$\chi_{0.5}(t) = \frac{\int_A \left| u\left(\frac{d}{192}, y, z, t\right) + u\left(-\frac{d}{192}, y, z, t - T/2\right) \right| \,\mathrm{d}y\,\mathrm{d}z}{\int_A \left| u\left(\frac{d}{192}, y, z, t\right) \right| \,\mathrm{d}y\,\mathrm{d}z} \,. \tag{3.7}$$

If $\chi_{0.5} = 0$, the space-time symmetry holds exactly. Figure 3.9 shows the temporal evolution of the indicator function for the different simulations. For the cases LF1–4, MF1 and MF4, and HF1–HF3, the indicator function decays in time to small values. The other cases show relatively large values of $\chi_{0.5}$, suggesting that the space-time symmetry is broken. These observations are consistent with the hypothesised supercritical pitchfork bifurcation in that all cases with small or decaying $\chi_{0.5}$ have intact spatial symmetries, ruling out other symmetry-breaking bifurcations. However, a dedicated study is required to clarify which bifurcation is responsible for the breaking of the space-time symmetry.

3.5.4. Physical instability mechanisms

This section discusses various physical instability mechanisms and assesses their relevance in the light of the present simulation results.

Vortex instability

For stationary flow through a face-centred sphere pack, Hill & Koch (2002) described a symmetry-breaking instability of the vortex system in the octahedral pores, which transitions from a steady state with eight vortices to an oscillatory state with nine vortices. The centre vortex of the system was found to periodically change its sense of rotation. The dynamics

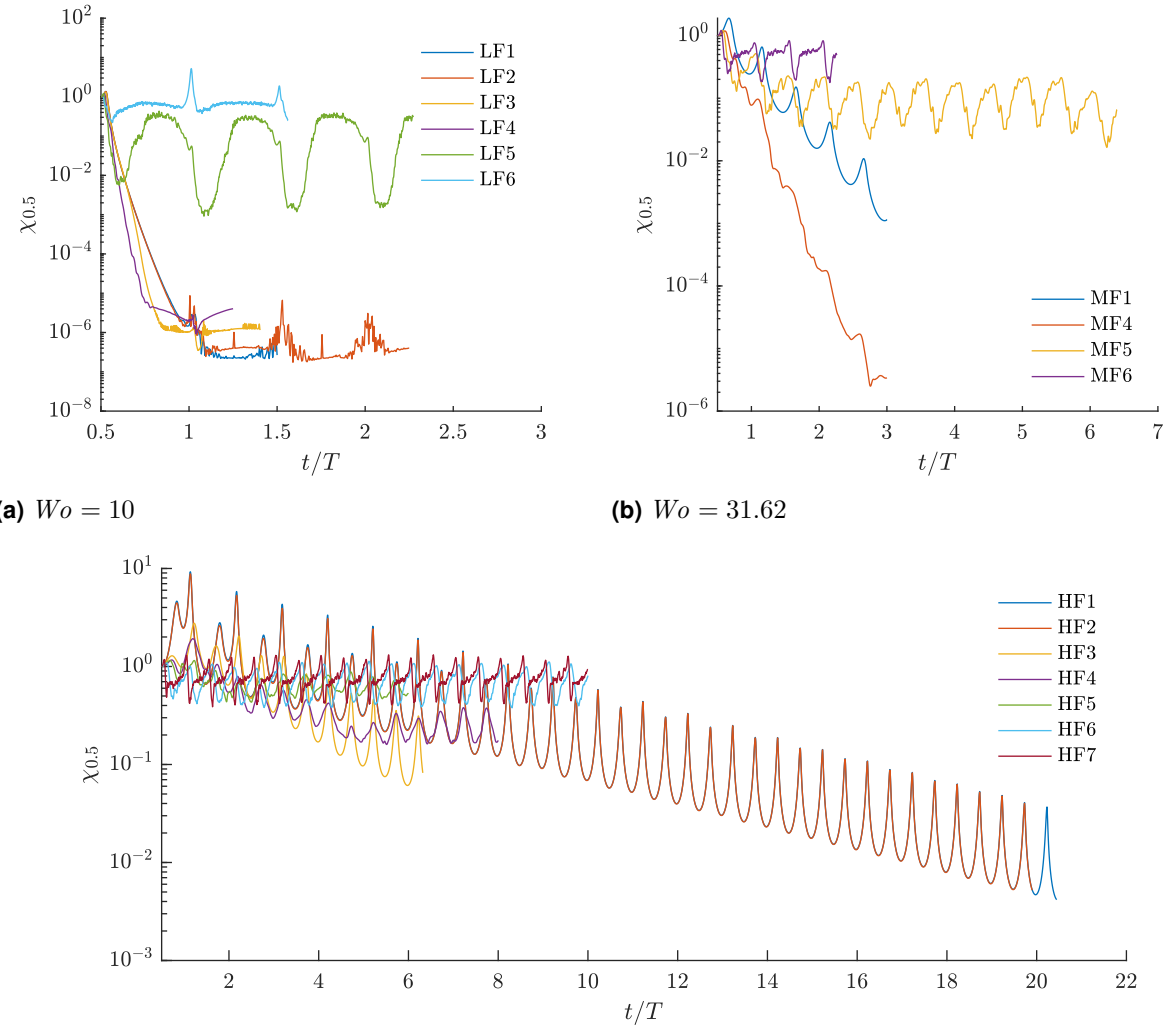

(a) $Wo = 10$

(b) $Wo = 31.62$

(c) $Wo = 100$

Figure 3.9: Indicator function $\chi_{0.5}$ for the space-time symmetry of a half-period time shift with a subsequent mirroring.

of this instability have been explained with an induced inward motion of those vortices that have an opposite sense of rotation with respect to the centre vortex. Similarly, Sakai & Manhart (2020) reported the change from an eight-vortex pattern in the octahedral pore to a six- and then five-vortex pattern. Note that the number of vortices is $2 \cdot 4 + 1 = 9$ for the face-centred sphere pack, which has a 4-fold rotational symmetry and for which four jets enter the octahedral pore, and $2 \cdot 2 + 1 = 5$ for the the hexagonal close-packing, which has a 2-fold rotational symmetry and for which two jets enter the octahedral pore. Hill & Koch (2002) observed the first Hopf bifurcation, which breaks a reflectional symmetry of the flow, at a critical Reynolds number of $Re \approx 60$ and the second Hopf bifurcation, which breaks the 4-fold rotational symmetry of the flow, at $Re \approx 100$. On the other hand, Sakai & Manhart (2020) reported steady flow at $Re = 59$, unsteady nonlinear flow at $Re = 91$, and a breaking of the 2-fold rotational symmetry between $Re = 138$ and 209. When the simulation at $Re = 91$ was continued, a decaying harmonic oscillation was observed in the

superficial velocity (Unglehrt & Manhart, 2023a, reprinted in appendix D.6), indicating that this case is below the critical Reynolds number of the Hopf bifurcation. An explanation for this significant difference in the critical Reynolds numbers of the bifurcations between these closely related geometries could be that the vortex system created by four jets is more easily destabilised than the vortex system created by two jets. Further investigation is required to clarify the relationship between the two cases.
In oscillatory flow through the hexagonal sphere pack, similar vortex instabilities can be observed at $Wo = 10$ and $Wo = 31.62$. At $Wo = 100$ a vortex system in the octahedral pore appears only for the cases HF5, HF6 and HF7. While this system also features periodic reorganisations, it is significantly more complex and eventually goes to a chaotic state. This difference could be related to an incomplete development of the inertial cores indicated by the longitudinal sections through the velocity field in figure 3.5. It seems that the vortices only occur if the inertial cores extend into the octahedral pore.

Centrifugal instability

Linear oscillatory flow around a sphere exhibits a centrifugal instability at high Womersley numbers (cf. section 1.3.1). Therefore, the relevance of centrifugal instability mechanisms to oscillatory flow through a hexagonal sphere pack is assessed in the following. Centrifugal instability can arise due to streamline curvature (or rotation) and is caused by "[...] an imbalance between the centrifugal force acting on fluid elements and the pressure" (Schmid & Henningson, 2001, p.207). The centrifugal instability therefore has an inviscid mechanism which was first investigated by Rayleigh (Drazin & Reid, 2004, p.69). For viscous flow, the instability is known as Görtler instability for laminar boundary layers along curved walls and as Dean instability for flow through curved channels (Drazin & Reid, 2004, pp.108f, pp.115f). In both situations, the flow is unstable to streamwise vortices. The theoretical treatment of these cases assumes that the boundary layer thickness or the channel height is small compared to the radius of curvature, respectively. Since the size of the pores in the sphere pack is comparable to the radius of curvature ($R = d/2$), the Dean instability is not applicable here. On the other hand, the Görtler instability could occur in boundary layers along the spheres as well as at the stagnation points (Schlichting & Gersten, 2017, p.484). The instability is governed by the Görtler number

$$G\ddot{o} = \frac{U\,\delta}{\nu}\left(\frac{\delta}{R}\right)^{\frac{1}{2}}\,, \tag{3.8}$$

where U is a characteristic velocity, δ is the boundary layer thickness and $R = d/2$ is the radius of curvature. For a steady laminar boundary layer with $\delta/d \sim 1/\sqrt{Re}$, the Görtler number depends on the Reynolds number as

$$G\ddot{o} \sim Re\left(\frac{1}{\sqrt{Re}}\right)^{\frac{3}{2}} \sim Re^{\frac{1}{4}}\,. \tag{3.9}$$

For an oscillatory boundary layer with $\delta/d \sim Wo^{-1}$, the Görtler number scales as

$$G\ddot{o} \sim Re\; Wo^{-3/2}\,, \tag{3.10}$$

which is consistent with the relation (1.39) for the critical Reynolds number in linear oscillatory flow around a sphere (cf. section 1.3.1).
The relevance of the Görtler instability to the present setting is first investigated based on a velocity field of the low-frequency case LF5. The tangential velocity profiles shown in figure 3.10 lie inside the plane $\sqrt{3}/3\,y - \sqrt{6}/3\,z = 0$, which is a longitudinal section through the inertial cores (cf. figures 2.4 and 3.5). The inviscid stability of the profiles can be assessed by making the crude assumption that the flow in this plane is two-dimensional. The profile is potentially unstable in regions where the magnitude of the tangential velocity decreases in the radial direction (Floryan, 1986). The viscous stability of the profiles can be assessed using the Görtler number. For a wall jet along a convex wall, Floryan (1986) defined the velocity scale as the velocity maximum $u_{t,,\max}$ and the length scale $\delta = \sqrt{\nu x^*/u_{t,,\max}}$ based on the distance x^* from the virtual origin of the wall jet. The virtual origin can be estimated from the wall distance of the maximum using the wall jet similarity solution (Schlichting & Gersten, 2017, p.181) as

$$x^* = 0.192\,\frac{u_{t,,\max}\,\delta_{u_{t,,\max}}^2}{\nu}\,, \tag{3.11}$$

resulting in $\delta = 0.44\,\delta_{u_{t,,\max}}$. The Görtler number can then be expressed as

$$G\ddot{o} = \frac{u_{t,,\max}\,(0.44\,\delta_{u_{t,,\max}})}{\nu}\left(\frac{0.44\,\delta_{u_{t,,\max}}}{d/2}\right)^{\frac{1}{2}}\,. \tag{3.12}$$

A centrifugal instability is possible if $G\ddot{o} \gtrsim 3.2$ (Floryan, 1986). The tangential velocity profiles F–H shown in figure 3.10 resemble a wall jet with an inviscidly unstable velocity distribution. The profile G has a value $G\ddot{o} = 4.05$ of the Görtler number, which is above the minimum critical value of 3.2 given by Floryan (1986). This suggests that the flow in the case LF5 might be susceptible to a centrifugal instability. However, visualisations of the flow at the maximum superficial velocity using the Q-criterion (Hunt et al., 1988) and the rortex criterion (Liu et al., 2018) did not show Taylor-Görtler vortices. This difference may be reconciled by noting that in the analyses of Floryan (1986) the spanwise direction is treated as a homogeneous direction allowing arbitrary wavenumbers. For the kinematically admissible perturbations in the sphere pack, which are composed of many wavenumbers, the critical Görtler number would be larger than 3.2.
For oscillatory flow at high Womersley numbers, the steady flow analysis of Floryan (1986) is clearly not applicable; the occurrence of a centrifugal instability is estimated based on the results of Otto (1992) instead. Like the potential flow around a sphere, the potential flow through the hexagonal close-packing contains inviscidly unstable profiles (figure 3.11). For the sphere, the most unstable profile is located at the equator and has a tangential velocity $3/2\,U_0$ at the wall; for the hexagonal sphere pack, the most unstable profiles F and N have a tangential velocity $3.6\,\langle u\rangle_{\mathrm{i}}$ at the wall. Assuming these tangential velocities to be equal, the critical Reynolds number can be estimated from the criterion (1.39) of Otto (1992) for linear oscillatory flow around a sphere as

$$Re_{\mathrm{crit}} \approx \frac{\epsilon}{3.6}\,\frac{2}{3}\,2.45\;Wo^{3/2} = 0.12\;Wo^{3/2}\,, \tag{3.13}$$

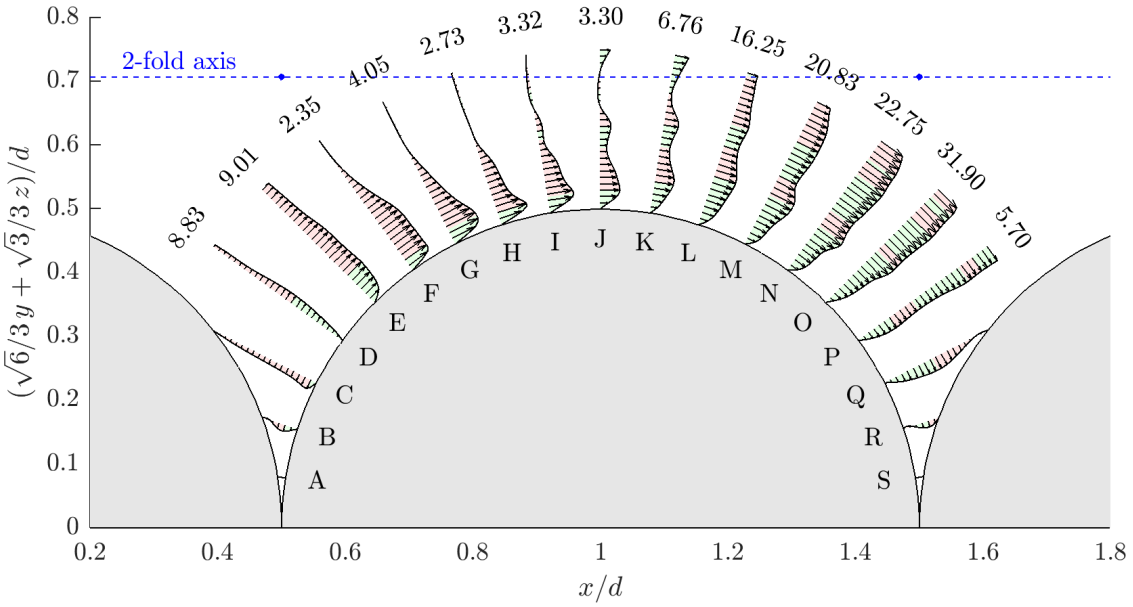

Figure 3.10: Tangential profiles in the plane $\sqrt{3}/3\,y - \sqrt{6}/3\,z = 0$ at the maximum superficial velocity for the case LF5 ($Re = 158$, $Wo = 10$). The colours indicate the inviscid stability, which is assessed based on the radial derivative of the squared tangential velocity (Floryan, 1986): The stable parts of the profile with $\partial u_t^2/\partial r > 0$ are shaded in green and the unstable parts of the profile with $\partial u_t^2/\partial r < 0$ are shaded in red. The value of the Görtler number $Gö$ is indicated for each profile.

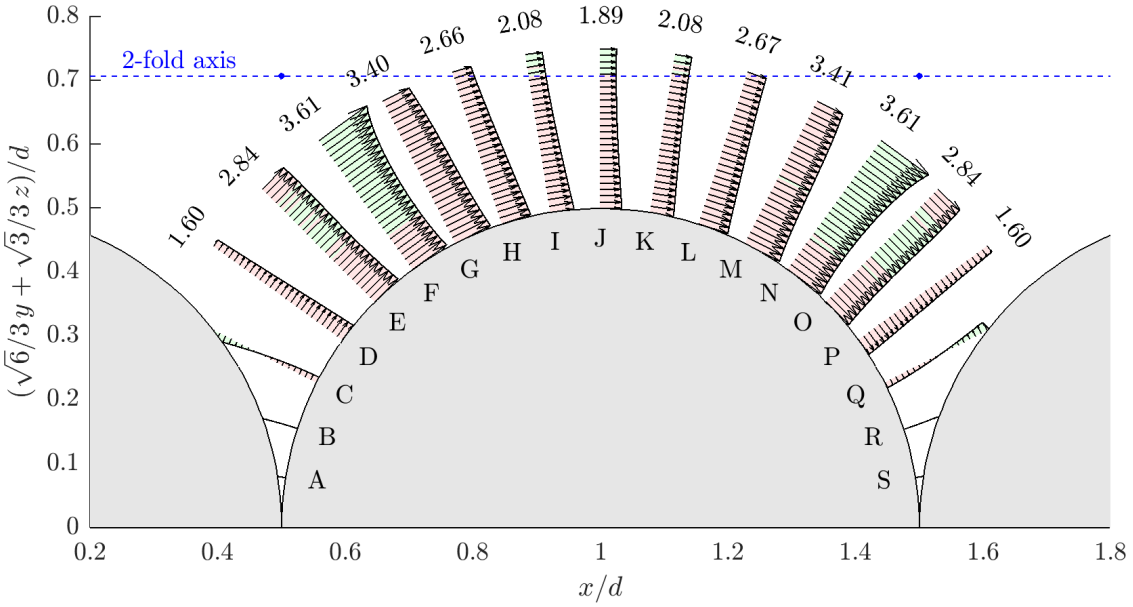

Figure 3.11: Tangential velocity profiles in the plane $\sqrt{3}/3\,y - \sqrt{6}/3\,z = 0$ of the potential flow through the hexagonal close-packing. The colours indicate the inviscid stability, which is assessed based on the radial derivative of the squared tangential velocity (Floryan, 1986): The stable parts of the profile with $\partial u_t^2/\partial r > 0$ are shaded in green and the unstable parts of the profile with $\partial u_t^2/\partial r < 0$ are shaded in red. The ratio of the wall velocity to the intrinsic velocity $\langle u \rangle_i$ is indicated for each profile.

which compiles to $Re_{\mathrm{crit}} \approx 120$ at $Wo = 100$. Using equation (1.38), the wavelength of the instability can be estimated as $\lambda_{\mathrm{crit}} \approx 0.17\,d$, which would fit into the pores. Consequently, a centrifugal instability appears plausible for the cases HF3–HF7. However, visualisations of instantaneous flow fields for the cases HF3 and HF4 using the Q-criterion (Hunt et al., 1988) and the rortex criterion (Liu et al., 2018) did not show Taylor-Görtler vortices. At the lower Womersley numbers, the wavelength of the instability and the oscillatory boundary thickness would probably be too large to justify a comparison with the calculations of Otto (1992).
In conclusion, although no direct evidence for a centrifugal instability was found in the simulations, the above analysis of the velocity profiles suggests that such an instability is plausible in the range of Reynolds and Womersley numbers where symmetry breaking was observed. It should be noted that the Görtler instability of a steady flow is generally considered to obey the principle of exchange of stabilities, i.e. it corresponds to a static bifurcation (Drazin & Reid, 2004, p.12, p.118). This means that it would not directly increase the temporal complexity of the flow. However, it could pave the way for vortex instabilities (Schlichting & Gersten, 2017, pp.484f). The appearance of a centrifugal instability in the oscillatory boundary layer would also affect the flow regimes described in section 3.5.1. So far, the onset of nonlinear flow at high Womersley numbers has been assumed to scale as $Re \sim Wo^2$ based on the nondimensional Navier-Stokes equations. On the other hand, the onset of the centrifugal instability scales as $Re \sim Wo^{3/2}$. Thus, for large Womersley numbers the centrifugal instability could already occur in linear flow, causing the flow to become nonlinear earlier than expected. Confirmation of this hypothesis will probably require a Floquet stability analysis similar to (Otto, 1992), for which the linear base flow could be obtained in semi-analytical form using the method of Chapman & Higdon (1992).

Kelvin-Helmholtz instability

The Kelvin-Helmholtz instability (Drazin & Reid, 2004, pp.14f, pp.237f) describes the rolling up of a shear layer into a train of vortices. In the present dataset, structures that are characteristic of a Kelvin-Helmholtz were observed only for the case HF7 ($Re = 3580$, $Wo = 100$), which has the highest Reynolds number in the present study. Figure 3.12 shows that the pressure field in the section $\sqrt{3}/3\,y - \sqrt{6}/3\,z = 0$ contains a series of local minima in the shear layers around the separation region, suggesting a train of vortices emanating from each shear layer. The velocity field shows waves in the shear layer, whose amplitude increases with the distance from the contact point. As would be expected for a Kelvin-Helmholtz instability, the streamwise component of the vorticity ω_x has small values in the region of the shear layer, while the transverse component of the vorticity $\omega_\perp = \sqrt{6}/3\,\omega_y + \sqrt{3}/3\,\omega_z$ shows the shear layer breaking up into isolated vortices.

Wake instability

Separated flow around bluff bodies has an instability that leads to the formation of the von Kármán vortex street, which is a staggered arrangement of vortices with an alternating sense of rotation (Batchelor, 2000, pp.255f). “Unlike in a classical flow around a cylinder, a von Kármán vortex street cannot be formed in porous media” due the strongly confined pore space (Srikanth et al., 2021). However, other wake instabilities have been observed which

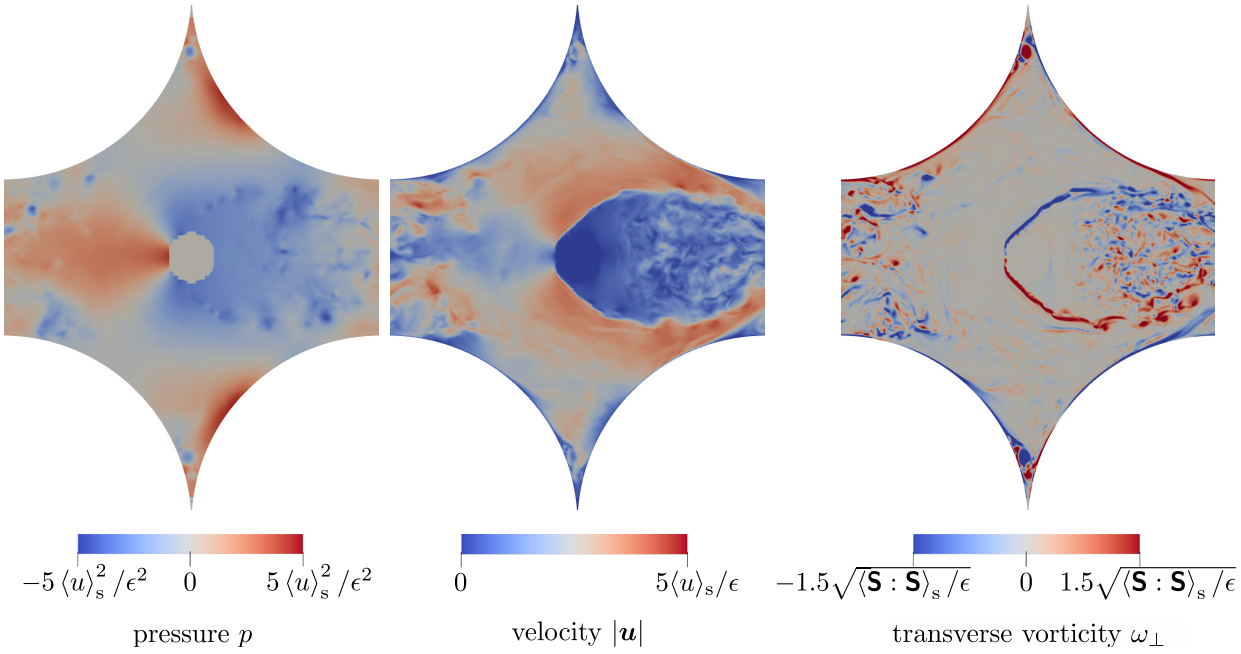

Figure 3.12: Instantaneous pressure p, velocity magnitude $|\boldsymbol{u}|$ and out-of-plane vorticity $\omega_\perp$ in the plane $\sqrt{3}/3\,y - \sqrt{6}/3\,z = 0$ for the case HF7 at $\Omega t = 16.32\pi$, indicating a Kelvin-Helmholtz instability of the separated shear layer.

lead to a symmetry breaking of the flow. For instance, diagonal flow through a staggered array of square cylinders undergoes a pitchfork bifurcation (Yang & Wang, 2000) and inline flow through a cubic array of cylinders undergoes a Hopf bifurcation (Agnaou et al., 2016; Srikanth et al., 2021).

In the present case of the hexagonal sphere pack, lateral oscillations of the inertial cores around the separation region are observed; these correspond to a breaking of the rotational symmetry. It should be noted that the vortex systems investigated by Sakai & Manhart (2020) are cross-sections of the inertial cores and the separation region. Since the flow still maintains its rotational symmetry after the occurrence of the vortex instability (Sakai & Manhart, 2020), the lateral oscillations are only a secondary instability. Still, it would be interesting to investigate the relationship between these oscillations and the vortex instability mechanism described by Hill & Koch (2002).

Boundary layer instability

Another possible source of instabilities is the boundary layer along the spheres. Since velocity profiles with inflection points are inviscidly unstable, this instability might be relevant close to the separation lines, where the flow detaches from the spheres (Drazin & Reid, 2004, p.131, pp.229f). Velocity profiles without inflection point are significantly more stable (Drazin & Reid, 2004, p.232) and an instability for these profiles seems to be rather unlikely given that various inviscid instability mechanisms are present in the flow.

At high Womersley numbers, the velocity field approaches a potential flow with Stokes boundary layers. As discussed in section 1.3.1, the oscillatory Stokes boundary layer exhibits a subcritical instability for $Re_\delta \gtrsim 564$ (Biau, 2016). As for oscillatory flow around

a sphere, this instability would dominate over the centrifugal instability for large Womersley numbers. Furthermore, the instability of the oscillatory Stokes boundary layer leads to a departure from the laminar onset of nonlinearity, which is estimated to take place for $Re \gtrsim 37000$ and $Wo \gtrsim 1700$ (Unglehrt & Manhart, 2022a, reprinted in appendix D.1).

4. Modelling

This chapter is concerned with the modelling of unsteady flow through porous media. First, the modelling framework is introduced and the choice of state variables is discussed. Then, a summary of the following publications is given

- Unglehrt, L. & Manhart, M. Assessment of models for nonlinear oscillatory flow through a hexagonal sphere pack. *Manuscript submitted for publication.*
- Unglehrt, L. & Manhart, M. 2023c A model for the dissipation rate in linear unsteady flow through porous media. *Journal of Fluid Mechanics* **975**, A42.
- Unglehrt, L. & Manhart, M. 2023a Decomposition of the drag force in steady and oscillatory flow through a hexagonal sphere pack. *Journal of Fluid Mechanics* **974**, A32.

Based on these results a new model for unsteady flow through porous media is proposed, which is based on a novel parametrisation of the friction and the viscous pressure drag. Finally, the key findings with respect to modelling are summarised and suggestions are given for the development of improved models.

4.1. Modelling framework and objectives

When the pore scale and the field scale are sufficiently well separated ($\ell \ll L$), the flow through a porous medium can be described by the macroscopic continuity equation and a local relationship between the macroscopic pressure gradient and the superficial velocity (Ene & Sanchez-Palencia, 1975). The modelling problem is to express this relationship solely in terms of macroscopic quantities. In particular, the time series of the superficial velocity $\langle \boldsymbol{u} \rangle_{\mathrm{s}}(t)$ shall be predicted for any given time series $\boldsymbol{f}(t)$ of the macroscopic pressure gradient. Such a relationship can be expressed in a number of ways. The simplest possibilities are algebraic equations like the Forchheimer equation (1.45) and ordinary differential equations like the unsteady Forchheimer equation (1.48). More complicated representations are systems of ordinary differential equations, fractional differential equations, delay-differential equations and Volterra series. Besides modelling the relationship in the time domain, it is also possible to formulate the model in the image domain of an integral transform like the Fourier or Laplace transform. Other possibilities include statistical and probabilistic models and various machine-learning methods. It is desirable for the model to have the following properties:

1. The model should be formulated continuously with respect to time, i.e. independently of a time step size.
2. The model should be invariant with respect to a time shift.

3. The coefficients ("model constants") appearing in the model parametrisation should only depend on the geometry of the porous medium, but not on the flow state or on the forcing. This would — at least in theory — make it possible to tabulate these coefficients for different geometries or to develop correlations like the Kozeny-Carman equation for the permeability.

In the following, models are explored in the framework of the volume-averaged momentum equation and of the volume-averaged kinetic energy equation. For general porous media, these equations can be obtained using volume-averaging (cf. section 1.2.2) or periodic homogenisation (cf. section 1.2.3) for a sufficiently large separation between the pore scale and the field scale ($\ell \ll L$). The equations thus have the implicit assumption that the gradients of the superficial velocity are negligibly small. The volume-averaged momentum equation

$$\rho \frac{\mathrm{d}\langle \boldsymbol{u} \rangle_\mathrm{s}}{\mathrm{d}t} = \underbrace{-\frac{1}{V}\int_{A_\mathrm{fs}} \tilde{p}\,\boldsymbol{n}\,\mathrm{d}A}_{\text{pressure drag}} + \underbrace{\frac{1}{V}\int_{A_\mathrm{fs}} \boldsymbol{\tau}_\mathrm{w}\,\mathrm{d}A}_{\text{friction drag}} + \epsilon\,\boldsymbol{f} \tag{4.1}$$

can be obtained directly from the superficial average of the incompressible Navier-Stokes equations (2.7) over a triply periodic porous domain using Gauss' theorem. The fluxes over the periodic boundaries cancel due to the periodicity of $\boldsymbol{u}$ and $\tilde{p}$ and the convective flux across the fluid-solid interface vanishes due to the impermeable wall boundary condition $\boldsymbol{u} \cdot \boldsymbol{n} = 0$. The pressure drag and the friction drag depend on the pore scale flow and are thus unclosed with respect to the superficial velocity. Note that the total force exerted by the fluid onto the spheres also contains a contribution from the macroscopic pressure gradient in addition to the pressure drag and the friction drag. The volume-averaged kinetic energy equation is given as (Zhu et al., 2014; Paéz-García et al., 2017)

$$\frac{\mathrm{d}\langle k \rangle_\mathrm{s}}{\mathrm{d}t} = \underbrace{\langle \boldsymbol{u} \rangle_\mathrm{s} \cdot \boldsymbol{f}}_{\text{power input}} - \underbrace{2\mu \langle \boldsymbol{S} : \boldsymbol{S} \rangle_\mathrm{s}}_{\text{dissipation rate}}, \tag{4.2}$$

where $k = \frac{1}{2}\rho \boldsymbol{u}^2$ is the kinetic energy density and $\boldsymbol{S} = \frac{1}{2}\left[\boldsymbol{\nabla} \otimes \boldsymbol{u} + (\boldsymbol{\nabla} \otimes \boldsymbol{u})^\mathrm{T}\right]$ is the strain rate tensor. In this equation, the relationships between the volume-averaged kinetic energy, the volume-averaged dissipation rate and the superficial velocity are generally unknown.

4.2. State variables

The first design decision in the development of a model is the selection of state variables used to express the unclosed terms in the volume-averaged momentum equation (4.1). In the incompressible Navier-Stokes equations (2.7), the flow state at time t is given by the velocity $\boldsymbol{u}(\boldsymbol{x}, t)$ and the pressure $p(\boldsymbol{x}, t)$ in the sense that these fields determine the flow in the near future. The choice of state variables in a model determines which flow states can be distinguished from each other. In the present configuration, it is only necessary to distinguish between flow states that can be reached by the action of a spatially constant

macroscopic pressure gradient.

There are different possible choices for the state variables. On the one hand, the state variables can be defined as explicit functions of the pore scale fields. Simple examples are the superficial velocity, the volume-averaged kinetic energy or the volume-averaged dissipation rate, which arise naturally in the volume averaging theory. It is also possible to define the state variables by projecting the pore scale flow onto a set of spatial modes, which could be obtained from the proper orthogonal decomposition (POD). Such an approach has been occasionally employed in the computational homogenisation of multi-scale structures to model the response of the microstructure (Xia et al., 2013; Goury et al., 2016; Redeker & Haasdonk, 2016; Soldner et al., 2016). These projected variables would be governed by their own evolution equations and are hidden variables in the model.

On the other hand, the state variables can be constructed from a single variable. For example, one may use the value of the variable and its time derivatives, e.g. $\langle \boldsymbol{u} \rangle_\mathrm{s}$, $\mathrm{d}\langle \boldsymbol{u} \rangle_\mathrm{s}/\mathrm{d}t$ and $\mathrm{d}^2\langle \boldsymbol{u} \rangle_\mathrm{s}/\mathrm{d}t^2$ (Kantz & Schreiber, 2003, pp.152f). Alternatively, the history of the variable may be used, e.g. $\langle \boldsymbol{u} \rangle_\mathrm{s}(t-\tau)$ for all $\tau < t$. The theoretical basis for this approach is Taken's embedding theorem (Takens, 1981; Stark, 1999). It states that for a deterministic and finite-dimensional dynamical system it is typically possible to determine the state of the system by considering a collection of n time-lagged values of a scalar variable, e.g. $\langle u \rangle_\mathrm{s}(t)$, $\langle u \rangle_\mathrm{s}(t-\Delta t)$, $\langle u \rangle_\mathrm{s}(t-2\Delta t)$, $\ldots$, $\langle u \rangle_\mathrm{s}(t-(n-1)\Delta t)$. In general, the number of time-lagged values (*embedding dimension*) must be at least $n > 2D_\mathrm{F}$ where D_F is the box-counting dimension of the attractor of the dynamical system.[1] Notably, generalisations of Taken's theorem admit the simultaneous use of multiple variables (Deyle & Sugihara, 2011). The representation of the state of the system by the history of a variable can also be motivated by the Volterra-Wiener theory of dynamical systems (Rugh, 1981). A nonlinear time-invariant system with input $u(t)$ and output $y(t)$ is represented by a Volterra series

$$y(t) = h_0 + \int_0^t h_1(\tau_1) u(t-\tau_1)\,\mathrm{d}\tau_1 + \int_0^t \int_0^t h_2(\tau_1,\tau_2) u(t-\tau_1) u(t-\tau_2)\,\mathrm{d}\tau_1\,\mathrm{d}\tau_2 + \ldots \quad (4.3)$$

with kernel functions h_0, $h_1(t_1)$, $h_2(t_1,t_2)$, $\ldots$, $h_n(t_1,\ldots,t_n)$. The convergence of this series has been discussed, for example, by Boyd & Chua (1985). A relatively recent review of the Volterra series can be found in (Cheng et al., 2017).

In the present work, the state is represented by the superficial velocity and its history like in the dynamic permeability models of Johnson et al. (1987) and Pride et al. (1993) for linear flow. The use of the kinetic energy as an additional state variable would require a model for the dissipation rate in nonlinear flow, which is currently not available.

[1] "[T]he main result of the embedding theorems is that it is not the dimension D of the underlying true state space that is important for the minimal dimension of the embedding space, but only the fractal dimension D_F of the invariant measure generated by the dynamics in the true state space. In dissipative systems, D_F can be much smaller than D" (Kantz & Schreiber, 2003, p.147).

4.3. Summary: Assessment of models in nonlinear oscillatory flow through a hexagonal sphere pack

This contribution presents a review and comparative evaluation of different models for unsteady flow through porous media. The models can be categorised into unsteady extensions of the Darcy and Forchheimer equations (Darcy, 1856; Forchheimer, 1901) and into dynamic permeability models (Johnson et al., 1987) which have a convolution structure in the time domain. The unsteady Darcy equation (Hill et al., 2001a; Zhu et al., 2014) can be seen as a low frequency approximation to the dynamic permeability model of Pride et al. (1993). Also, the dynamic permeability model of Johnson et al. (1987) is a special case of the model of Pride et al. (1993) in which the static viscous tortuosity α_0 is expressed as a function of the other porous medium parameters. By considering the implied kinetic energy equation of the unsteady Forchheimer equation, realisability constraints for the coefficients in the unsteady Forchheimer equation are derived from Helmholtz's minimum dissipation theorem and Kelvin's minimum energy theorem[2].

The linear models are compared with respect to the dynamic permeability computed from the results of Zhu & Manhart (2016) for linear oscillatory flow through a hexagonal sphere pack; the nonlinear models are compared with respect to the superficial velocity time series from the present direct numerical simulation database. The coefficients of the dynamic permeability models are determined based on their definitions in terms of the Stokes flow and the potential flow. For the unsteady Darcy equation, we consider two different values of the acceleration coefficient based on the static viscous tortuosity α_0 and the high-frequency limit of the dynamic tortuosity α_∞ (Zhu & Manhart, 2016). For the unsteady Forchheimer equation, the coefficients of the acceleration term and the linear term are chosen such that the equation reduces to the unsteady Darcy equation for linear flow; the coefficient of the nonlinear term is determined by a best fit to the direct numerical simulations of steady flow by Sakai & Manhart (2020).

In the evaluation for linear flow, the models of Johnson et al. (1987) and of Pride et al. (1993) show an excellent accuracy over the whole frequency range. We reproduce the observations of Zhu & Manhart (2016) that the unsteady Darcy equation with the acceleration coefficient chosen based on α_0 is accurate at low frequencies, but the predictions deteriorate towards higher frequencies; when the acceleration coefficient is chosen based on α_∞, the predictions are worst at medium frequencies, but approach the correct low and high frequency limits. Finally, the model of Turo & Umnova (2013) has excessive damping at low and medium frequencies. This is a consequence of the additive superposition of the steady state and the high frequency drag compared to a frequency-domain blending in the models of Johnson et al. (1987) and Pride et al. (1993). This motivates us to propose a nonlinear extension of the model of Pride et al. (1993) in the spirit of Turo & Umnova (2013).

In the evaluation for nonlinear flow, the unsteady Forchheimer equation is accurate at low frequencies, but has large errors for linear flow at high frequencies. For nonlinear flow at high frequencies, it shows an acceptable accuracy for the acceleration coefficient based on α_∞ and a low accuracy for the acceleration coefficient based on α_0. This behaviour can be explained

[2]Derivations of these theorems for periodic porous media are provided in the appendix B.

in that the quadratic term of the unsteady Forchheimer equation overpredicts the nonlinear drag at high frequencies, while the acceleration term provides insufficient damping for α_∞ and excessive damping for α_0. The better accuracy of the unsteady Forchheimer equation with α_∞ for high frequency nonlinear flow is thus the result of an error compensation. The nonlinear extension of the model of Pride et al. (1993) is accurate for linear flow and for low frequency nonlinear flow. The predictions gradually deteriorate for high frequency nonlinear flow. The model of Turo & Umnova (2013) is inaccurate at low frequencies due to the excessive damping in the linear part of the model; its high frequency behaviour is the same as for the extended Pride et al. (1993) model.

4.4. Summary: A model for the dissipation rate in linear unsteady flow through porous media

In this contribution, a model for the volume-averaged dissipation rate in linear unsteady flow is proposed. Inspired by the theory of Johnson et al. (1987), we derive an asymptotic expression for the dissipation rate for small times from boundary layer theory. For this, the velocity field is approximated as a potential flow with unsteady Stokes boundary layers. The resulting expression for the volume-averaged dissipation rate

$$2\mu \left\langle \boldsymbol{S} : \boldsymbol{S} \right\rangle_\mathrm{s} = \frac{2\,\mu\,\alpha_\infty}{\epsilon\,\Lambda} \int_0^t \int_0^t \frac{\mathrm{d}\langle \boldsymbol{u} \rangle_\mathrm{s}}{\mathrm{d}\tau_1} \cdot \frac{\mathrm{d}\langle \boldsymbol{u} \rangle_\mathrm{s}}{\mathrm{d}\tau_2} \frac{1}{\sqrt{\pi\nu[(t-\tau_1)+(t-\tau_2)]}}\,\mathrm{d}\tau_1\,\mathrm{d}\tau_2 \tag{4.4}$$

has the form of a second-order Volterra system. In the steady state, the volume-averaged dissipation rate is given as (Murthy & Singh, 1997; Zhu et al., 2014)

$$2\mu \left\langle \boldsymbol{S} : \boldsymbol{S} \right\rangle_\mathrm{s} = \frac{\mu}{K} \left\langle \boldsymbol{u} \right\rangle_\mathrm{s}^2 \,. \tag{4.5}$$

Formally, this can be rewritten as a second-order Volterra system by expressing the velocity as the integral of the acceleration. The model for the dissipation rate is constructed as a second-order Volterra system with a kernel blending the small time asymptotic and the steady state expression. The blending is performed following Churchill & Usagi (1972) by taking the n-th root of the sum of the n-th powers of the asymptotic kernel expressions and results in a one-parameter family of models with the family parameter n.
First, the model is validated for transient flow through a porous medium composed of circular tubes for which an analytical solution exists (Johnson et al., 1987; Pozrikidis, 2017, pp.509f.). The small time asymptotic expression (4.4) is demonstrated to approach the exact solution for the volume-averaged dissipation rate at small times. Moreover, the most accurate model predictions are obtained for a blending parameter $n = 2$, resulting in an instantaneous error of 7% in the volume-averaged dissipation rate. Second, the model is validated against numerical simulations of transient and oscillatory flow through a hexagonal sphere pack (Unglehrt & Manhart, 2022a, reprinted in appendix D.1) and through a cylinder array. The model is found to significantly improve predictions with respect to the steady state expression 4.5 for small times and high frequencies. The most accurate results are obtained for values of the blending parameter n between 2 and 3.

4.5. Summary: Decomposition of the drag force in steady oscillatory flow through a hexagonal sphere pack

The objective of this article is to understand the behaviour of the drag force in stationary and oscillatory porous media flow in terms of its various sources. We address the question of how the pressure drag can be separated according to its sources and assess the relative importance of the different contributions depending on the Reynolds number and the Womersley number.

The pressure decomposition of Graham (2019) is adapted to the setting of a periodic porous medium. The pressure is decomposed into three components according to its source terms in the pressure Poisson equation: The accelerative pressure $p^{(a)}$ is a reaction force that is directly proportional to the macroscopic pressure gradient; it ensures that the macroscopic pressure gradient does not accelerate the fluid normal to the wall. The viscous pressure $p^{(v)}$ arises from the normal component of the viscous force at the wall, and the convective pressure $p^{(c)}$ arises from imbalances in the convective acceleration. For incompressible flow, the source of the convective pressure is proportional to the Q-invariant of the velocity gradient tensor.

Using an auxiliary potential $\boldsymbol{\Phi}$ (Batchelor, 2000, eq. 6.4.11) and Green's second identity, a new form of the volume-averaged momentum equation is obtained for periodic porous media:

$$\rho \frac{\mathrm{d}\langle \boldsymbol{u} \rangle_\mathrm{s}}{\mathrm{d}t} = \underbrace{-\frac{1}{V}\int_{A_\mathrm{fs}} \left(\boldsymbol{I} - \boldsymbol{\nabla} \otimes \boldsymbol{\Phi}\right)^\mathrm{T} \cdot \boldsymbol{\tau}_\mathrm{w} \,\mathrm{d}A}_{\text{friction and viscous pressure drag}} + \underbrace{\frac{1}{V}\int_{V_\mathrm{f}} \boldsymbol{\Phi}\, 2\,\rho\, Q \,\mathrm{d}V}_{\text{convective pressure drag}} + \underbrace{\left[\epsilon \boldsymbol{I} - (1-\epsilon)\,\boldsymbol{A}\right] \cdot \boldsymbol{f}}_{\text{effective forcing}} . \quad (4.6)$$

Here, the viscous and convective contribution to the pressure drag are separated into different terms. Interestingly, the macroscopic pressure gradient $\boldsymbol{f}$ is partially compensated by the accelerative pressure drag. This has a similar effect to the "acceleration coefficient tensor" (Nield, 1991) or "virtual mass coefficient" (Sollitt & Cross, 1972; Burcharth & Andersen, 1995).

Then, we evaluate the contributions of the different terms in the volume-averaged momentum equation for the direct numerical simulations of stationary flow by Sakai & Manhart (2020) and the present simulations of oscillatory flow. In particular, the scaling of the drag components with the Reynolds number is investigated. For steady flow at low Reynolds numbers, the theory of (Mei & Auriault, 1991) is confirmed: The friction drag and the viscous pressure drag scale with Re, while the convective pressure drag and the next order terms of the friction drag and viscous pressure drag scale with Re^3. A quadratic term in the Reynolds number is absent. At high Reynolds numbers (Re = 200–350), the friction drag and the viscous pressure drag scale as $Re^{1.4}$ which is close to the steady laminar boundary scaling; the convective pressure drag due to the time-averaged velocity field scales with Re^2. This suggests that the flow has a boundary layer structure with an outer flow that is only weakly affected by the Reynolds number. This picture is consistent with experimental observations in the literature (Jolls & Hanratty, 1969; Karabelas et al., 1973; Dybbs & Edwards, 1984). The convective pressure drag due to the temporal fluctuations of the velocity increases with the Reynolds number, but does not show a clear scaling yet.

For low and medium frequency oscillatory flow ($Wo = 10$, 31.62), the behaviour of the drag forces is similar to the stationary case. At low Reynolds numbers, the friction and viscous pressure drag depend linearly on the Reynolds number whereas the convective pressure drag is proportional to Re^3. At high Reynolds numbers, the friction and viscous pressure drag are consistent with a steady laminar boundary layer scaling, but the convective pressure drag does not scale with Re^2. This is likely because in contrast to the stationary case, the convective pressure drag is not decomposed into the contributions of the time-averaged and fluctuating velocity. For high frequency oscillatory flow ($Wo = 100$), the low Reynolds number scaling is again similar to the stationary case. However, no steady laminar boundary layer scaling of the friction and viscous pressure drag could be observed at high Reynolds numbers. This could be explained by the boundary layer growth which is limited by convection at low and medium Womersley numbers, but is limited by the period of oscillation at high Womersley numbers. In other words, the boundary layer does not become quasi-steady. For the convective pressure drag, no quadratic scaling could be observed. This might be because the period of oscillation is too short for the drag producing structures (e.g. the flow separations) to form.

4.6. A new model for unsteady flow through porous media

This section presents an improved model for unsteady flow through porous media. The model is based on the volume-averaged momentum equation with the pressure decomposition (4.6). The parametrisation of the combined friction and viscous pressure drag is a blending of the model of Pride et al. (1993) for linear unsteady flow and a steady laminar boundary layer scaling at large Reynolds numbers; the convective pressure drag is approximated by a quadratic Forchheimer-type nonlinearity

$$\boldsymbol{f}_p^{(c)} = -\frac{\epsilon}{\alpha_\infty}\frac{B\rho}{d}\left|\langle\boldsymbol{u}\rangle_\mathrm{s}\right|\langle\boldsymbol{u}\rangle_\mathrm{s}\,, \tag{4.7}$$

as no other suitable parametrisation was found. The challenges in developing an improved model for the convective pressure drag are discussed in section 4.7.2. In the above parametrisation, B is a dimensionless parameter that is still to be determined (cf. section 4.6.2). In the following, the parametrisation for the friction and the viscous pressure drag is derived and validated a priori against the present simulations. The predictions of the complete model are then evaluated a posteriori and compared with other models.

4.6.1. Parametrisation of the friction and the viscous pressure drag

In this section, a model for the friction and viscous pressure drag is derived. Similar to the model for the dissipation rate (section 4.4), the model is constructed by blending two asymptotic expressions for an integral kernel. This approach is similar in spirit to the work of Muzychka & Yovanovich (2006), who used the method of Churchill & Usagi (1972) to interpolate between the Stokes and Blasius boundary layer solutions.

On the one hand, flow at small Reynolds numbers is accurately represented by the dynamic permeability model of Pride et al. (1993). This model implies the following linear parame-

trisation for the sum of the friction drag and the viscous pressure drag (cf. appendix B.1)

$$\boldsymbol{f}_{\mathrm{lin}} = -\left(\frac{\epsilon}{\alpha_\infty}\frac{\mu}{K} - \frac{2\mu}{\Lambda^2\beta}\right)\langle\boldsymbol{u}\rangle_{\mathrm{s}} - \rho\sqrt{\nu}\frac{2}{\Lambda}\int_{-\infty}^{t}\left(\frac{\nu\,\langle\boldsymbol{u}\rangle_{\mathrm{s}}}{\Lambda^2\beta^2} + \frac{\mathrm{d}\langle\boldsymbol{u}\rangle_{\mathrm{s}}}{\mathrm{d}\tau}\right)\frac{e^{-\frac{\nu(t-\tau)}{\Lambda^2\beta^2}}}{\sqrt{\pi(t-\tau)}}\,\mathrm{d}\tau\,. \quad (4.8)$$

Here, $\beta = \alpha_0/\alpha_\infty - 1$ is the relative difference between the static viscous tortuosity α_0 and the high-frequency limit of the dynamic tortuosity α_∞ and Λ is the viscous length of Johnson et al. (1987). Using integration by parts and the initial condition $\langle\boldsymbol{u}\rangle_{\mathrm{s}}(-\infty) = 0$, this expression can be rewritten as the convolution of the acceleration with a kernel

$$\boldsymbol{f}_{\mathrm{lin}} = -\mu\int_{-\infty}^{t}\frac{\mathrm{d}\langle\boldsymbol{u}\rangle_{\mathrm{s}}}{\mathrm{d}\tau}\underbrace{\left[\frac{\epsilon}{\alpha_\infty K} + \frac{2}{\Lambda}\frac{e^{-\frac{\nu(t-\tau)}{\Lambda^2\beta^2}}}{\sqrt{\pi\nu(t-\tau)}} - \frac{2}{\Lambda^2\beta}\,\mathrm{erfc}\left(\sqrt{\frac{\nu(t-\tau)}{\Lambda^2\beta^2}}\right)\right]}_{\text{convolution kernel } [(\text{length})^{-2}]}\mathrm{d}\tau\,. \quad (4.9)$$

On the other hand, the friction drag and the viscous pressure drag are assumed to approach a steady laminar boundary layer scaling

$$\boldsymbol{f}_{\mathrm{b.l.}} = C\,\rho\sqrt{\nu}\,\frac{|\langle\boldsymbol{u}\rangle_{\mathrm{s}}|^{1/2}\,\langle\boldsymbol{u}\rangle_{\mathrm{s}}}{d^{3/2}} \quad (4.10)$$

at large Reynolds numbers, where C is a dimensionless constant. Note that this expression is consistent with the drag law of Skjetne & Auriault (1999a). The boundary layer drag (4.10) is brought to a similar form as equation (4.9) by taking the integral of the derivative

$$\boldsymbol{f}_{\mathrm{b.l.}} = \int_{-\infty}^{t}\frac{\mathrm{d}}{\mathrm{d}\tau}\left(C\,\rho\sqrt{\nu}\,\frac{|\langle\boldsymbol{u}\rangle_{\mathrm{s}}|^{1/2}\,\langle\boldsymbol{u}\rangle_{\mathrm{s}}}{d^{3/2}}\right)\mathrm{d}\tau = \mu\int_{-\infty}^{t}\frac{\mathrm{d}\langle\boldsymbol{u}\rangle_{\mathrm{s}}}{\mathrm{d}\tau}\underbrace{\left[\frac{3}{2}\,C\sqrt{\frac{|\langle\boldsymbol{u}\rangle_{\mathrm{s}}|}{\nu d^3}}\right]}_{[(\text{length})^{-2}]}\mathrm{d}\tau\,, \quad (4.11)$$

where it was again assumed that $\langle\boldsymbol{u}\rangle_{\mathrm{s}}(-\infty) = 0$. The model for the friction and the viscous pressure drag is chosen as the integral

$$\boldsymbol{f}_{\tau_{\mathrm{w}}} + \boldsymbol{f}_p^{(v)} = -\mu\int_{-\infty}^{t}\frac{\mathrm{d}\langle\boldsymbol{u}\rangle_{\mathrm{s}}}{\mathrm{d}\tau}\,h_n(t-\tau, |\langle\boldsymbol{u}\rangle_{\mathrm{s}}(\tau)|)\,\mathrm{d}\tau\,, \quad (4.12a)$$

where the kernel is obtained by blending the linear drag and the boundary layer drag using the method of Churchill & Usagi (1972):

$$h_n(t-\tau, |\langle\boldsymbol{u}\rangle_{\mathrm{s}}(\tau)|) = \left[\left(\frac{\epsilon}{\alpha_\infty K} + \frac{2}{\Lambda}\frac{e^{-\frac{\nu(t-\tau)}{\Lambda^2\beta^2}}}{\sqrt{\pi\nu(t-\tau)}} - \frac{2}{\Lambda^2\beta}\,\mathrm{erfc}\left(\sqrt{\frac{\nu(t-\tau)}{\Lambda^2\beta^2}}\right)\right)^n + \left(\frac{3}{2}\,C\sqrt{\frac{|\langle\boldsymbol{u}\rangle_{\mathrm{s}}|}{\nu d^3}}\right)^n\right]^{1/n}. \quad (4.12b)$$

The parameter C is unknown and has to be determined along with the parameter B in the parametrisation of the convective pressure drag (cf. section 4.6.2). Note that the other parameters have explicit definitions in terms of the Stokes flow (K, α_0) and the potential flow (Λ, α_∞) and could in principle be taken from the literature (Chapman & Higdon, 1992; Lee et al., 2009).

From a physical point of view, the model describes a competition of length scales for diffusion. At small times, diffusion is unlimited and the characteristic distance of diffusion is of the order $\delta \sim \sqrt{\nu t}$. At large times, diffusion is either limited by the pore size, giving a characteristic distance of the order $\sqrt{K}$, or by convection, giving a characteristic distance of the order of the boundary layer thickness $\delta \sim \sqrt{\nu d / |\langle \boldsymbol{u} \rangle_\mathrm{s}|}$. Recognising that $\sqrt{K}$, $2/\Lambda$ and $1/d$ can represent different forms of specific surface area[3], the model can be interpreted as the sum of wall shear stress increments that are determined with a time- and velocity-dependent length scale and specific surface area:

$$\boldsymbol{f}_{\tau_\mathrm{w}} + \boldsymbol{f}_p^{(v)} \approx -\int_0^{\langle \boldsymbol{u} \rangle_\mathrm{s}} \frac{\text{surface}}{\text{volume}} \underbrace{\left(\mu \frac{\mathrm{d}\langle \boldsymbol{u} \rangle_\mathrm{s}}{\text{diffusive length scale}} \right)}_{\text{wall shear stress increment}} . \tag{4.14}$$

A particular feature of the model is that the temporal boundary layer can either fill the entire pore space or develop into a steady convective boundary layer.

The blending parameter n is determined such that the drag at small Reynolds numbers is composed of a linear and a cubic contribution in the superficial velocity; this limiting behaviour has been derived for steady flow by Mei & Auriault (1991), Firdaouss et al. (1997) and Skjetne & Auriault (1999b) and is satisfied by the present simulation dataset (Unglehrt & Manhart, 2023a, reprinted in appendix D.6). This limiting behaviour can only be achieved when $n = 4$, in which case the kernel has the Taylor expansion

$$\begin{aligned} h_n(t-\tau, |\langle \boldsymbol{u} \rangle_\mathrm{s}(\tau)|) = {} & \frac{\epsilon}{\alpha_\infty K} + \frac{2}{\Lambda} \frac{e^{-\frac{\nu(t-\tau)}{\Lambda^2\beta^2}}}{\sqrt{\pi\nu(t-\tau)}} - \frac{2}{\Lambda^2\beta} \operatorname{erfc}\left(\sqrt{\frac{\nu(t-\tau)}{\Lambda^2\beta^2}} \right) \\ & + \frac{81 C^4 |\langle \boldsymbol{u} \rangle_\mathrm{s}|^2}{64\nu^2 d^6} \left(\frac{\epsilon}{\alpha_\infty K} + \frac{2}{\Lambda} \frac{e^{-\frac{\nu(t-\tau)}{\Lambda^2\beta^2}}}{\sqrt{\pi\nu(t-\tau)}} - \frac{2}{\Lambda^2\beta} \operatorname{erfc}\left(\sqrt{\frac{\nu(t-\tau)}{\Lambda^2\beta^2}} \right) \right)^{-3} \\ & + O\left(|\langle \boldsymbol{u} \rangle_\mathrm{s}|^4 \right) \end{aligned} \tag{4.15}$$

in the superficial velocity. Multiplying the kernel by the acceleration gives the desired limit-

[3] The specific surface area of the sphere pack is proportional to $1/d$ and is given by

$$S = \frac{1}{V} \cdot \underbrace{\frac{(1-\epsilon)V}{\pi d^3/6}}_{\text{number of spheres}} \cdot \underbrace{\pi d^2}_{\text{sphere surface}} = \frac{6(1-\epsilon)}{d} . \tag{4.13}$$

Also, according to the Kozeny-Carman equation, the square root of the permeability is inversely proportional to the specific surface area (Bear, 2018, pp.260f) and the ratio $2/\Lambda$ describes a specific surface weighted by the potential flow field (Johnson et al., 1987).

ing behaviour that does not contain a quadratic contribution in the superficial velocity.

4.6.2. Determination of the model parameters

Following the comparison approach of the contribution *Assessment of models for nonlinear oscillatory flow through a hexagonal sphere pack* (appendix D.4), the unknown model parameters B and C are determined based on the resistance behaviour in stationary flow. Therefore, the parametrisation of the friction and the viscous pressure drag (4.12) is simplified to a time-independent resistance law. In the limit of stationary flow ($\nu \to \infty$ for fixed Re), the model can be simplified to

$$\boldsymbol{f}_{\tau_\mathrm{w}} + \boldsymbol{f}_p^{(v)} = -\mu \int_{-\infty}^{t} \frac{\mathrm{d}\langle \boldsymbol{u} \rangle_\mathrm{s}}{\mathrm{d}\tau} \left[\left(\frac{\epsilon}{\alpha_\infty K} \right)^4 + \left(\frac{3}{2} C \sqrt{\frac{|\langle \boldsymbol{u} \rangle_\mathrm{s}(\tau)|}{\nu d^3}} \right)^4 \right]^{1/4} \mathrm{d}\tau \,. \tag{4.16}$$

It is further assumed that the flow is unidirectional along the x-direction and that $\langle u \rangle_\mathrm{s}(t) = 0$ for $t \to -\infty$. With the substitution $\eta = 9C^2\alpha_\infty^2 K^2/(4\epsilon^2 \nu d^3)\, \langle u \rangle_\mathrm{s}(\tau)$, the friction and viscous pressure drag in stationary flow is rewritten as

$$\left[f_{\tau_\mathrm{w} x} + f_{px}^{(v)} \right] \frac{d^3}{\rho \nu^2} = -\frac{4\epsilon^3}{9C^2\alpha_\infty^3 (K/d^2)^3} \int_0^{9C^2\alpha_\infty^2 K^2/(4\epsilon^2\nu d^3)\, \langle u \rangle_\mathrm{s}(t)} \left[1 + \eta^2 \right]^{1/4} \mathrm{d}\eta \,. \tag{4.17}$$

The integral can be evaluated in terms of the Gaussian hypergeometric function ${}_2F_1(a, b; c; x)$, resulting in [4]

$$\left[f_{\tau_\mathrm{w} x} + f_{px}^{(v)} \right] \frac{d^3}{\rho \nu^2} = -\frac{\epsilon d^2}{\alpha_\infty K}\, Re\; {}_2F_1\left(-\frac{1}{4}, \frac{1}{2}; \frac{3}{2}; -\left[\left(\frac{3}{2} \frac{C\alpha_\infty K}{\epsilon d^2} \right)^2 Re \right]^2 \right) . \tag{4.21}$$

For the present arguments, the hypergeometric function tends to 1 as $Re \to 0$ and it tends to $C\alpha_\infty K/(\epsilon d^2)\sqrt{Re}$ as $Re \to \infty$. Consequently, the Darcy drag and the steady laminar boundary layer drag are recovered in the limits.

[4] The integral was obtained with the Wolfram Alpha computer algebra system (Wolfram Alpha LLC, 2023) as

$$\int_0^u \left(1 + s^2\right)^{1/4} \mathrm{d}s = u\; {}_2F_1\left(-\frac{1}{4}, \frac{1}{2}; \frac{3}{2}; -u^2 \right) . \tag{4.18}$$

The result can be checked using the integral representation for the hypergeometric function

$${}_2F_1(a, b; c; z) = \frac{\Gamma(c)}{\Gamma(b)\,\Gamma(c-b)} \int_0^1 t^{b-1}(1-t)^{c-b-1}(1-tz)^{-a}\, \mathrm{d}t \,. \tag{4.19}$$

given by Abramowitz & Stegun (1972, eq. 15.3.1). Inserting the arguments, the identity simplifies to

$$u\; {}_2F_1\left(-\frac{1}{4}, \frac{1}{2}; \frac{3}{2}; -u^2 \right) = \frac{u}{2} \int_0^1 t^{-1/2} \left(1 + tu^2\right)^{1/4} \mathrm{d}t \,. \tag{4.20}$$

The integral is obtained with the substitution $s = u\, t^{1/2}$, where $\mathrm{d}s = u/2\, t^{-1/2}\, \mathrm{d}t$.

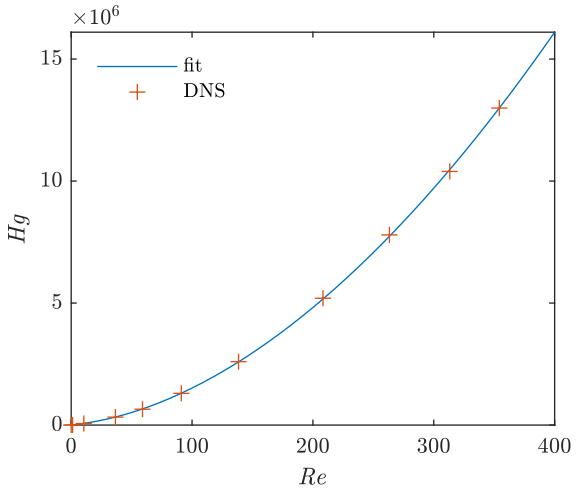

Figure 4.1: Fit of the model equation (4.22) to the DNS of stationary flow by Sakai & Manhart (2020) and Unglehrt & Manhart (2023a, reprinted in appendix D.6).

With the volume-averaged momentum equation (4.1) and the parametrisation of the convective pressure drag (4.7), the complete resistance law is obtained

$$Hg = B\,|Re|\,Re + \frac{d^2}{K}\,Re\;{}_2F_1\left(-\frac{1}{4},\frac{1}{2};\frac{3}{2};-\left[\left(\frac{3}{2}\frac{C\alpha_\infty K}{\epsilon d^2}\right)^2 Re\right]^2\right) . \tag{4.22}$$

The dimensionless model parameters B and C are determined by a nonlinear least-squares fit to the simulation results for stationary flow through the hexagonal close-packing given by Sakai & Manhart (2022) and Unglehrt & Manhart (2023a, reprinted in appendix D.6). The parameters result as

$$B = 55.8 \tag{4.23a}$$
$$C = 141.9 \tag{4.23b}$$

and the corresponding fit is shown in figure 4.1. Notably, the normalised modelled convective pressure drag $f_{px}^{(c)} / \left(\frac{1}{2}\rho \langle u \rangle_s^2 / d\right) = 2\epsilon B/\alpha_\infty = 17.9$ is relatively close to the asymptotic value of 16.0 exhibited by the direct convective pressure drag in stationary flow (Unglehrt & Manhart, 2023a, reprinted in appendix D.6).

4.6.3. A priori validation

In this section, the proposed parametrisation for the friction and viscous pressure drag is validated in an a priori sense: the parametrisation is evaluated for the superficial velocity from the simulations and compared to the friction and viscous pressure drag determined from the simulation data (Unglehrt & Manhart, 2023a, reprinted in appendix D.6).
The figures 4.2,4.3 and 4.4 show the simulated friction and viscous pressure drag and the predictions of the new model (4.12) for the last simulated period. The predictions of the linear parametrisation of Pride et al. (1993) given by the equation (4.9) are also plotted

to indicate the switching of the new model between the small and large Reynolds number asymptotes. At $Wo = 10$ and 31.62, the model predictions are in good agreement with the simulation results. For the cases LF4–LF6, the switch of the model between the linear and the nonlinear parametrisation is clearly visible. At $Wo = 100$ the proposed model overestimates the friction and the viscous pressure drag. Since this is also the case for the linear parametrisation in the simulation HF2, for which the model of Pride et al. (1993) accurately predicts the superficial velocity (appendix D.4), it could be suspected that the drag evaluation from the simulations is slightly inaccurate at high frequencies. For the cases HF5–HF7, the model significantly overpredicts the drag. A possible reason for this is the absence of the steady laminar boundary layer scaling at $Wo = 100$, which is discussed in appendix B.5. Overall, the proposed model is able to represent the drag curves from the simulations with a satisfactory degree of accuracy; in particular, the waveform of the drag is predicted very well.

4.6.4. A posteriori validation

In this section, the model results are compared to the present DNS dataset. The comparison is conducted according to appendix D.4. The complete model is given by the volume-averaged momentum equation (4.6) with the parametrisations (4.7) and (4.12) as

$$\rho \frac{\mathrm{d}\langle \boldsymbol{u} \rangle_\mathrm{s}}{\mathrm{d}t} = \underbrace{-\mu \int_{-\infty}^{t} \frac{\mathrm{d}\langle \boldsymbol{u} \rangle_\mathrm{s}}{\mathrm{d}\tau} h_4(t-\tau, |\langle \boldsymbol{u} \rangle_\mathrm{s}(\tau)|)\, \mathrm{d}\tau}_{\text{friction and viscous pressure drag}} \underbrace{- \frac{\epsilon}{\alpha_\infty} \frac{B\rho}{d} |\langle \boldsymbol{u} \rangle_\mathrm{s}| \langle \boldsymbol{u} \rangle_\mathrm{s}}_{\text{convective pressure drag}} \underbrace{- \frac{\epsilon}{\alpha_\infty} \boldsymbol{\nabla} \langle p \rangle_\mathrm{i}}_{\text{effective forcing}}, \quad (4.24)$$

where the kernel is given by equation (4.12). Note that an isotropic porous medium has been assumed such that the tensor of virtual inertia is given as $\boldsymbol{A} = \epsilon \left(1 - \alpha_\infty^{-1}\right) / (1 - \epsilon)\, \boldsymbol{I}$. For the comparison with the DNS, a sinusoidal macroscopic pressure gradient was applied and the superficial velocity was set to zero for $t \leq 0$. The model was integrated until the end of the DNS time series. The predicted superficial velocity is compared to the DNS during the last simulated cycle (see appendix D.4 for a detailed discussion of the comparison metrics).
The time derivative was discretised using the backward Euler method and the history term was approximated using the midpoint rule with equidistant time steps, resulting in the discrete model

$$\begin{aligned} \frac{\langle \boldsymbol{u} \rangle_\mathrm{s}^{n+1} - \langle \boldsymbol{u} \rangle_\mathrm{s}^{n}}{\Delta t} = &-\nu \sum_{j=0}^{n} \frac{\langle \boldsymbol{u} \rangle_\mathrm{s}^{j+1} - \langle \boldsymbol{u} \rangle_\mathrm{s}^{j}}{\Delta t} h_4\left(\left(n - j + \frac{1}{2}\right)\Delta t, \left|\frac{\langle \boldsymbol{u} \rangle_\mathrm{s}^{j} + \langle \boldsymbol{u} \rangle_\mathrm{s}^{j+1}}{2}\right|\right) \Delta t \\ &- \frac{\epsilon}{\alpha_\infty} \frac{B}{d} \left|\langle \boldsymbol{u} \rangle_\mathrm{s}^{n+1}\right| \langle \boldsymbol{u} \rangle_\mathrm{s}^{n+1} - \frac{\epsilon}{\rho \alpha_\infty} \boldsymbol{\nabla} \langle p \rangle_\mathrm{i}^{n+1} \,. \end{aligned} \quad (4.25)$$

In every time step, a nonlinear equation was solved using the routine `fsolve` in MATLAB, where the value of $\langle \boldsymbol{u} \rangle_\mathrm{s}$ from the previous time step was used as an initial guess. As the kernel $h_4(t - \tau, |\langle \boldsymbol{u} \rangle_\mathrm{s}(\tau))$ approaches the fractional derivative kernel of order 1/2 for $\tau \to t$, the above discretisation is of order 1/2 (Jacobs et al., 2023). The time step size was successively halved until the root-mean square value of the predicted superficial velocity differed by less than 0.25% between two refinements.

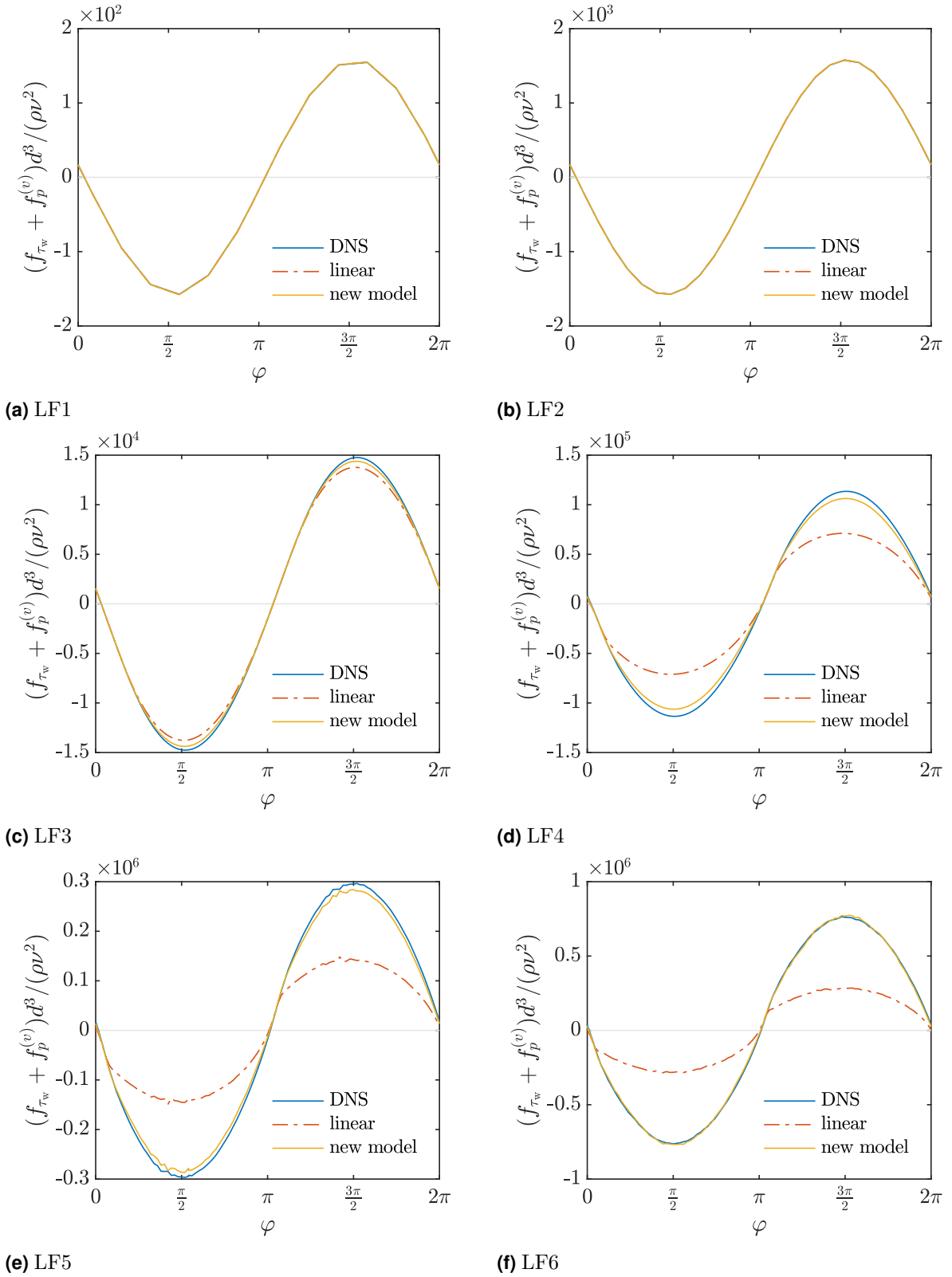

(a) LF1 **(b)** LF2

(c) LF3 **(d)** LF4

(e) LF5 **(f)** LF6

Figure 4.2: Comparison of the sum of the friction and viscous pressure drag from the DNS at $Wo = 10$ with the predictions of the linear model (4.9) of Pride et al. (1993) and of the new model (4.12) given the simulated superficial velocity.

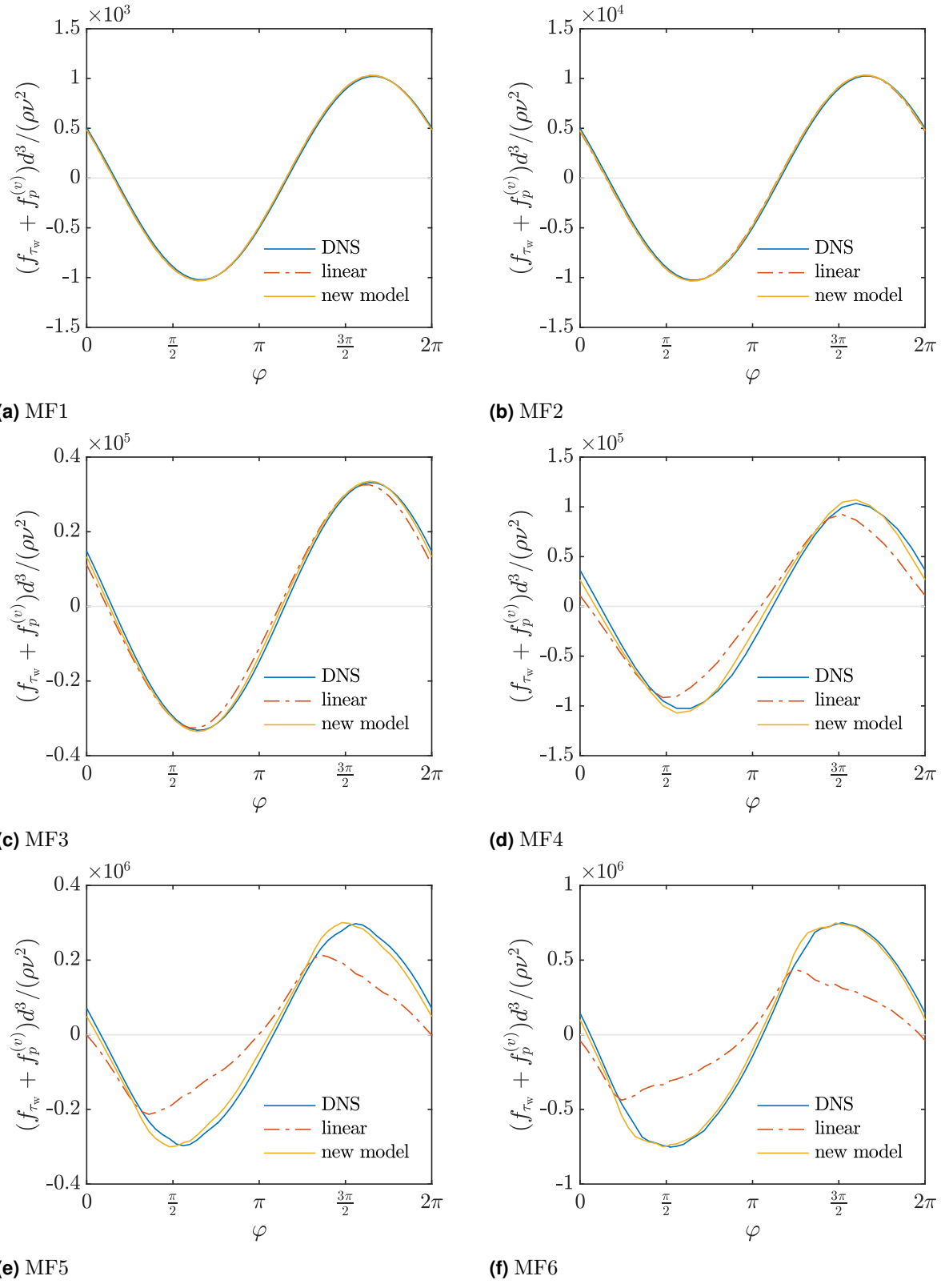

(a) MF1 **(b)** MF2

(c) MF3 **(d)** MF4

(e) MF5 **(f)** MF6

Figure 4.3: Comparison of the sum of the friction and viscous pressure drag from the DNS at $Wo = 31.62$ with the predictions of the linear model (4.9) of Pride et al. (1993) and of the new model (4.12) given the simulated superficial velocity.

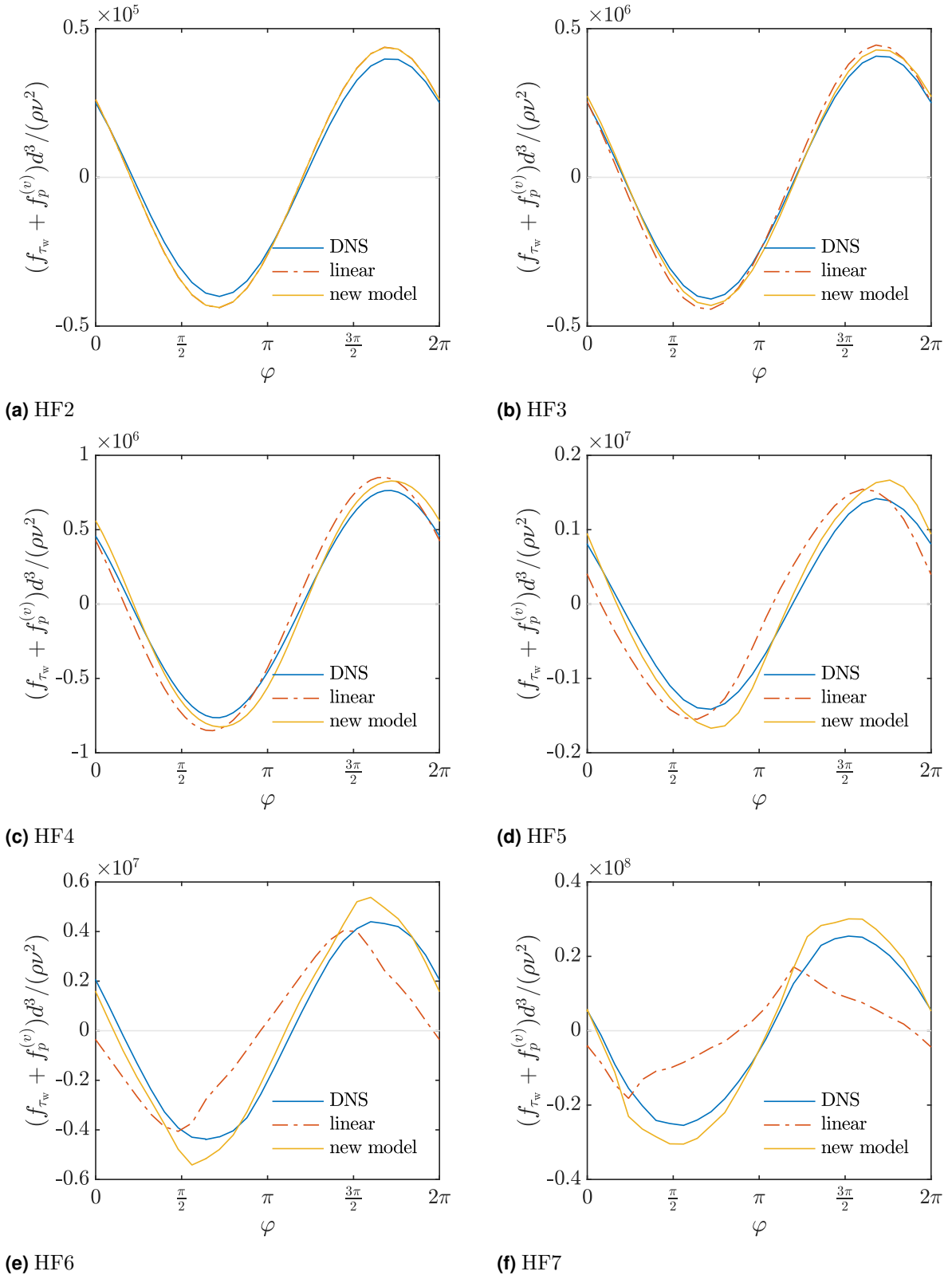

(a) HF2 **(b)** HF3

(c) HF4 **(d)** HF5

(e) HF6 **(f)** HF7

Figure 4.4: Comparison of the sum of the friction and viscous pressure drag from the DNS at $Wo = 100$ with the predictions of the linear model (4.9) of Pride et al. (1993) and of the new model (4.12) given the simulated superficial velocity.

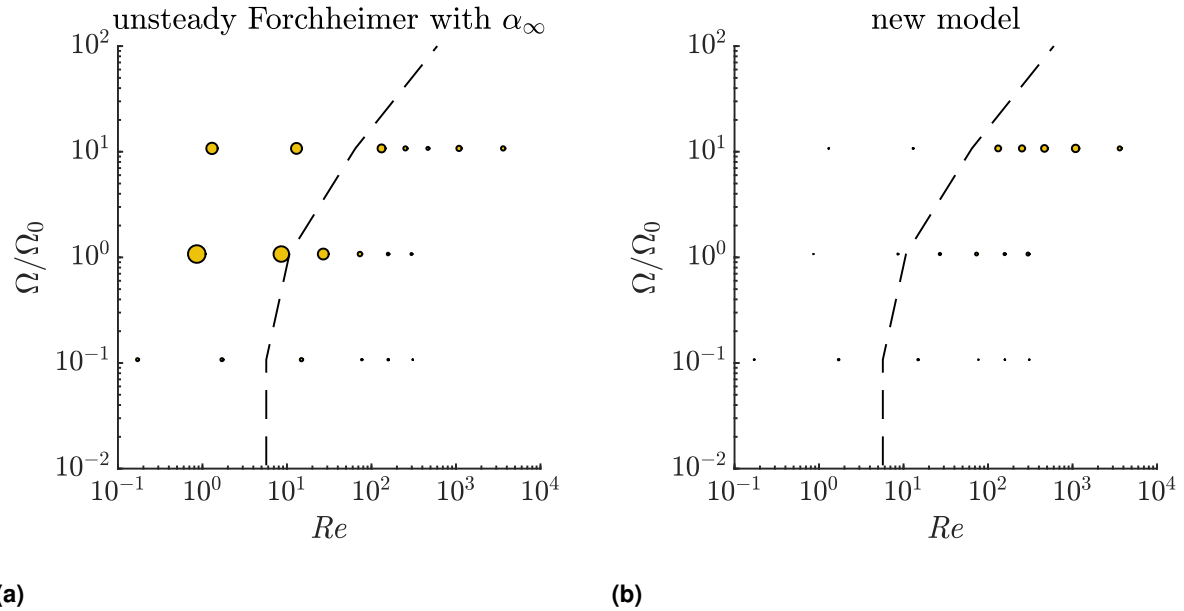

(a) **(b)**

Figure 4.5: Distribution of the L^2 model error in the Re–Ω/Ω_0 parameter space. The diameter of the circles is proportional to the L^2 error. The dashed line indicates the approximate boundary between linear and nonlinear flow.

Figure 4.5 shows the L^2 error with respect to the simulations for the new model as well as for the unsteady Forchheimer equation with the acceleration coefficient based on the high-frequency limit of the dynamic tortuosity α_∞. The new model has consistently small errors at low and intermediate frequencies and for linear flow. The errors for nonlinear flow at high frequencies are however modestly larger than for the unsteady Forchheimer equation. Table 4.1 shows the L^2 amplitude and phase errors of the new model together with the other models considered in the model comparison (appendix D.4). The new model outperforms the extended Pride et al. (1993) model in the nonlinear regime and has slightly higher errors in the linear regime. The still considerable errors at high frequencies can be attributed to the parametrisation of the convective pressure drag, for which it was assumed that the convective pressure drag is in phase with the superficial velocity. However, this is not true for the high frequency cases (Unglehrt & Manhart, 2023a, reprinted in appendix D.6). In conclusion, the proposed model is able to predict the flow with a very satisfactory level of accuracy over the considered region of the parameter space. When the parameters for the model are available, the proposed model should be preferred to the unsteady Forchheimer equation due to its more robust predictions.

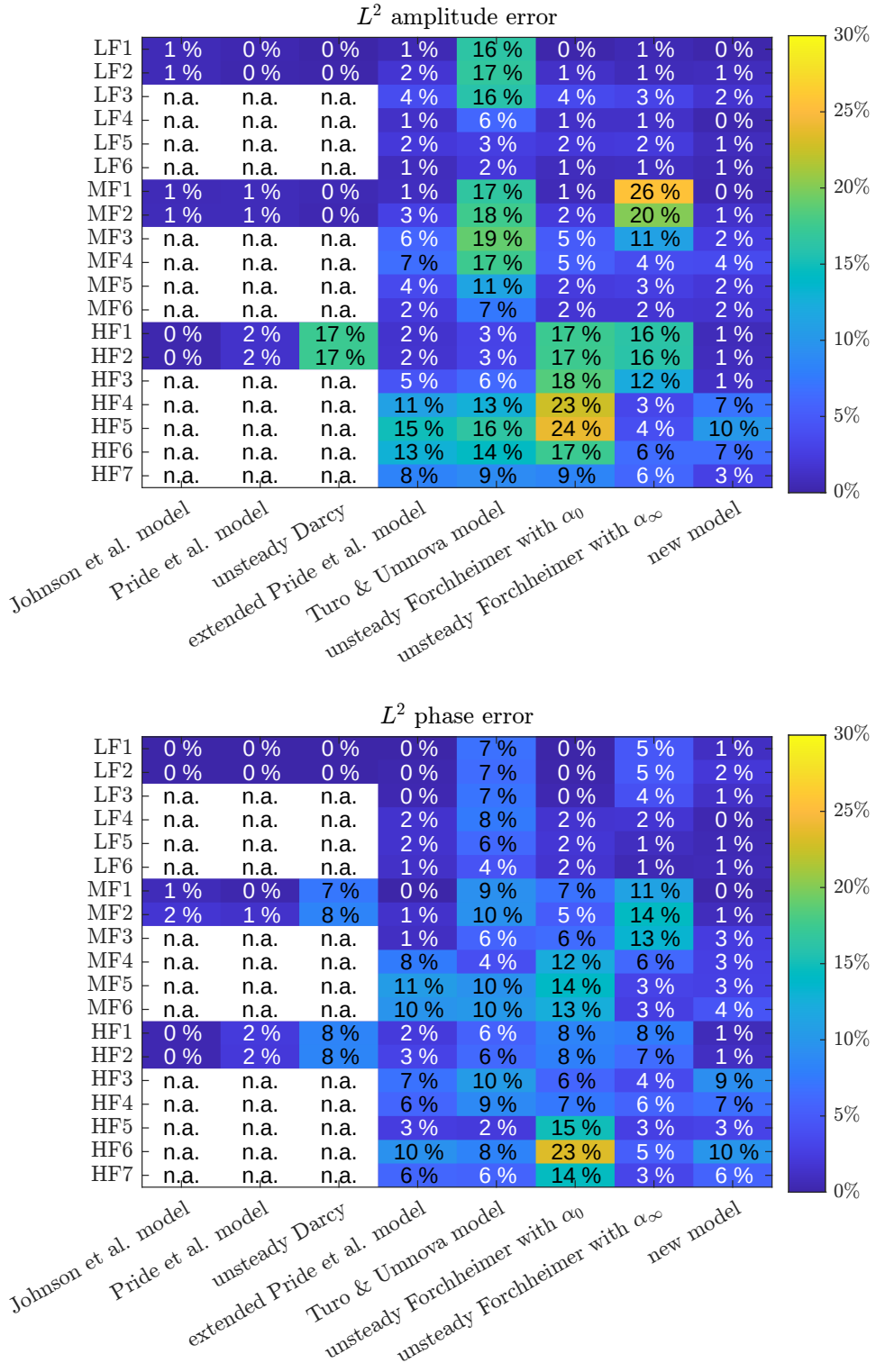

Table 4.1: Amplitude and phase contribution to the L^2 error normalised with $\max \langle u \rangle_s$ of the respective flow case. The entries where a linear model would be applied to a nonlinear flow case are marked as n.a. (not applicable).

4.7. Discussion

This section summarises the present findings concerning the modelling of unsteady flow through porous media. Then, the challenges in developing a parametrisation of the convective pressure drag are discussed. Finally, a brief review is given on machine-learning methods that could complement the classical modelling efforts.

4.7.1. Summary

For linear unsteady flow, the dynamic permeability models of Johnson et al. (1987) and Pride et al. (1993) provide a very accurate description of the superficial velocity over the entire frequency range. This is demonstrated in figure 4.6, where the amplitude and phase of the direct numerical simulations of Zhu & Manhart (2016) are plotted together with the dynamic permeability models and the unsteady Darcy equation (Zhu et al., 2014; Zhu & Manhart, 2016). The formulation of Pride et al. (1993) contains the correct limiting time scales at low and high frequencies discussed by Zhu & Manhart (2016). For flow at medium and high frequencies, the history term in the dynamic permeability models becomes important; for these frequencies, the unsteady Darcy equation cannot accurately capture the amplitude and phase behaviour. The proposed model for the dissipation rate complements the dynamic permeability models in that it allows to obtain the dissipation rate and the kinetic energy from a given time series of the superficial velocity without requiring additional material parameters. Hence, a larger set of flow quantities is available for modelling other physical processes, for example dispersion.

For unsteady nonlinear flow, the main models in the literature — the unsteady Forchheimer equation (Polubarinova-Kochina, 1962; Sollitt & Cross, 1972) and the model of Turo & Umnova (2013) — are able to predict the flow in some regions of the parameter space, but have large errors in the other regions. For example, the unsteady Forchheimer equation gives good results at low frequencies, but it cannot simultaneously match the linear medium- and high-frequency regime and the nonlinear high-frequency regime. The large errors for medium- and high-frequency linear flow are particularly undesirable, because they limit the applicability of the model for complicated waveforms containing higher harmonics. An extension of the dynamic permeability model of Pride et al. (1993) using the approach of Turo & Umnova (2013) shows a more benign behaviour, with small errors for linear flow and for low-frequency nonlinear flow, and gradually increasing errors towards high-frequency nonlinear flow.

To inform the development of improved models, the drag in stationary and oscillatory flow was investigated in detail. While the contributions of the friction and the pressure drag had already been analysed by Fourar et al. (2004) and (Srikanth et al., 2021), the aim was to understand the role of the pressure drag. Based on the pressure decomposition of Graham (2019), the pressure drag could be decomposed into three components according to their source terms. The accelerative pressure drag is a reaction force to the macroscopic pressure gradient that compensates the wall-normal component of the macroscopic pressure gradient. Since the accelerative pressure drag has a closed form representation in terms of the potential flow, it could be removed from the modelling problem. The viscous pressure drag results from the divergence of the wall shear stress; its scaling behaviour is therefore similar to that

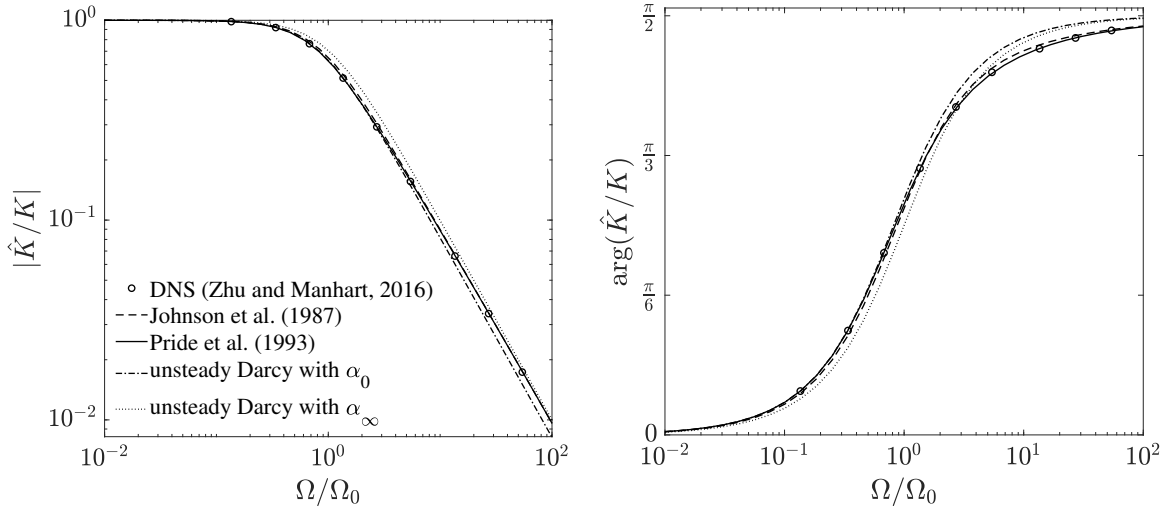

(a) Amplitude (cylinder array)

(b) Phase (cylinder array)

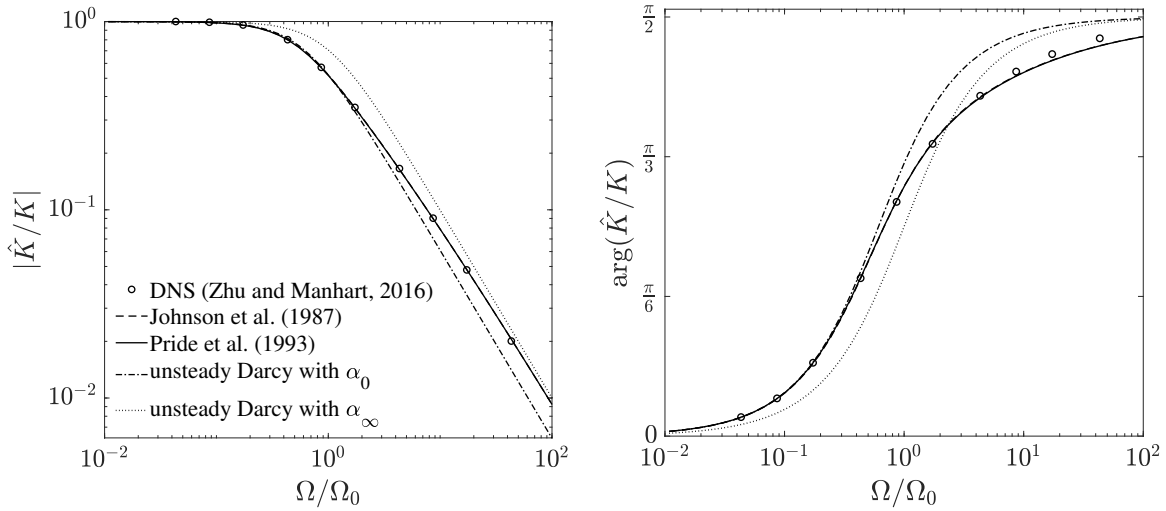

(c) Amplitude (hexagonal sphere pack)

(d) Phase (hexagonal sphere pack)

Figure 4.6: Dynamic permeability for linear oscillatory flow through a cylinder array and a hexagonal sphere pack. Comparison of DNS data of Zhu & Manhart (2016) and models of Johnson et al. (1987), Pride et al. (1993) and Zhu et al. (2014).

of the friction drag. In particular, at high Reynolds numbers a steady laminar boundary layer scaling was observed for both the friction and the viscous pressure drag; this scaling has occasionally been considered for the friction drag within a porous medium (Jolls & Hanratty, 1969; Skjetne & Auriault, 1999a; Hsu et al., 1999). Finally, the convective pressure drag is caused by imbalances in the convective acceleration and represents the drag due to nonlinear effects such as vortices, shear layers or separation regions.

Based on this investigation, a new model is proposed, in which the parametrisation of the friction and the viscous pressure drag combines the model of Pride et al. (1993) at small Reynolds numbers with the steady laminar boundary layer scaling at large Reynolds numbers. The convective pressure drag is parametrised with a Forchheimer-type nonlinearity, as no suitable mathematical representation of the complex behaviour of the convective pres-

sure drag could be found. Compared to the linear model of Pride et al. (1993), the resulting model contains two additional coefficients representing the behaviour of stationary nonlinear flow. The proposed model accurately represents linear flow as well as low- and medium-frequency nonlinear flow; high-frequency nonlinear flow is represented with modest errors due to the simplistic parametrisation of the convective pressure drag. Consequently, the model represents a notable improvement over existing models in the literature, both in terms of prediction accuracy and physical interpretability. In particular, the separate parametrisation of the friction and viscous pressure drag on the one hand and the convective pressure drag on the other hand could facilitate the development of improved models for scalar transport: The friction and the viscous pressure drag represent the velocity gradient near the fluid-solid interface, which is important to determine heat or mass transfer across the fluid-solid interface; the convective pressure drag represents nonlinear processes in the bulk flow and could possibly be related to scalar mixing. Future research could aim at improving the convective pressure drag parametrisation and at investigating the applicability of the proposed model to general unsteady flow and different porous medium geometries.

4.7.2. Modelling the convective pressure drag

In this section, the problems inherent to modelling the convective pressure drag are discussed. Unlike for the friction and the viscous pressure drag, the results on the functional form of the convective pressure drag are very scarce. The convective pressure drag scales with Re^3 at small Reynolds numbers and probably scales with Re^2 at large Reynolds numbers. Moreover, the convective pressure drag is in phase with the superficial velocity at low Womersley numbers, while it lags behind the superficial velocity at high Womersley numbers. In the following, the modelling of the convective pressure drag is approached from different sides based on the simulation results.

Weakly nonlinear flow

For weakly nonlinear flow, the convective pressure drag exhibits a cubic dependency on the Reynolds number (Unglehrt & Manhart, 2023a, reprinted in appendix D.6). Figure 4.7 shows the convective pressure drag normalised by $\rho(\max \langle u \rangle_\mathrm{s})^3/\nu$ as a function of the superficial velocity $\langle u \rangle_\mathrm{s} / (\max \langle u \rangle_\mathrm{s})$. This normalisation leads to a collapse of the results for LF1 and LF2, MF1 and MF2 and HF1 and HF2, but the convective pressure drag does not follow the curve

$$f_{px}^{(c)} \frac{\nu}{\rho \left(\max \langle u \rangle_\mathrm{s}\right)^3} = -c \left(\frac{\langle u \rangle_\mathrm{s}}{\max \langle u \rangle_\mathrm{s}} \right)^3 \tag{4.26}$$

which is the only possible function $\langle u \rangle_\mathrm{s}(t) \mapsto f_{px}^{(c)}(t)$ consistent with the cubic scaling. This suggests that the superficial velocity and the convective pressure drag are related by a functional. It is reasonable to suppose that the relationship can be represented by a causal

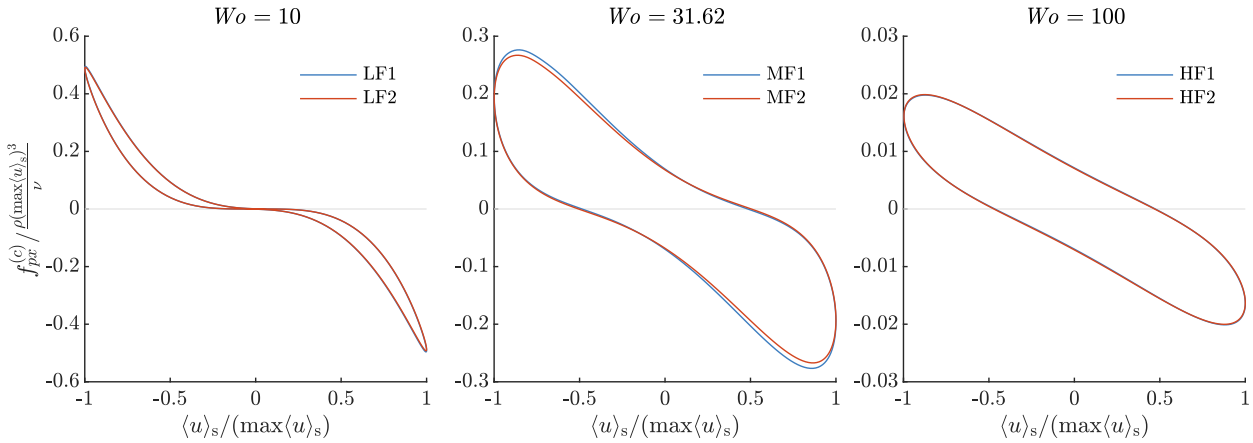

Figure 4.7: Convective pressure drag in the cubic normalisation as a function of the superficial velocity for the weakly nonlinear cases LF1, LF2, MF1, MF2, HF1 and HF2.

degree-3 homogeneous system (Rugh, 1981, pp.3f)

$$f_{px}^{(c)}(t) = -\int_{-\infty}^{t}\int_{-\infty}^{t}\int_{-\infty}^{t} h(t-\tau_1, t-\tau_2, t-\tau_3)\,\langle u\rangle_s(\tau_1)\,\langle u\rangle_s(\tau_2)\,\langle u\rangle_s(\tau_3)\,\mathrm{d}\tau_1\,\mathrm{d}\tau_2\,\mathrm{d}\tau_3\,, \quad (4.27)$$

wherein the Volterra kernel $h(t_1, t_2, t_3)$ has units of $\rho d^6/\nu^4$. Without loss of generality the kernel can be assumed symmetric with respect to permutations of its arguments (Rugh, 1981, pp.11f)

$$h(t_1,t_2,t_3) = h(t_1,t_3,t_2) = h(t_2,t_1,t_3) = h(t_2,t_3,t_1) = h(t_3,t_1,t_2) = h(t_3,t_2,t_1)\,. \quad (4.28)$$

For steady flow, the convective pressure drag should be proportional to $\langle u\rangle_s^3$ which means that the integral

$$c = \int_0^\infty\int_0^\infty\int_0^\infty h(t_1,t_2,t_3)\,\mathrm{d}t_1\,\mathrm{d}t_2\,\mathrm{d}t_3 \quad (4.29)$$

has to converge to a positive constant value. The relationship (4.27) also implies that the convective pressure drag is periodic if the superficial velocity is periodic. The kernel acts as a low-pass filter, which can be seen from the normalised amplitudes 0.5, 0.28 and 0.02 in figure 4.7 for $Wo = 10$, 31.62 and 100, respectively. However, the asymptotic decay behaviour of the kernel for high Womersley numbers is unknown.

In the following, it will be investigated whether the Volterra system (4.27) is able to represent the behaviour of the convective pressure drag. To make the system amenable to a fitting procedure, the kernel is expanded in the Laguerre functions $l_n(x)$, which form a basis of $L^2([0,\infty])$, as

$$h(t_1,t_2,t_3) = \sum_{i=0}^{N}\sum_{j=0}^{N}\sum_{k=0}^{N} c_{ijk}\,l_i(at_1)\,l_j(at_2)\,l_k(at_3)\,, \quad (4.30)$$

where a^{-1} is a time scale and c_{ijk} are the expansion coefficients (Wiener, 1958, p.92; Schetzen,

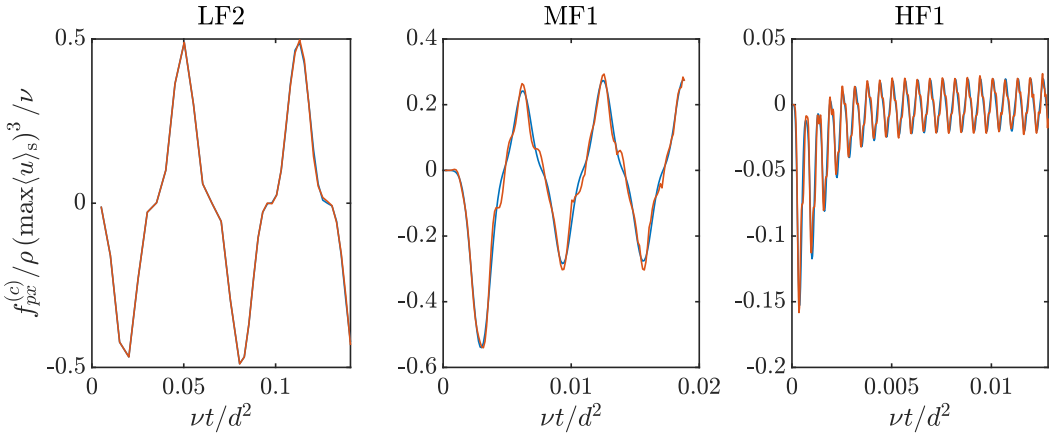

Figure 4.8: Best fit of the Volterra system (4.27) for the convective pressure drag in weakly nonlinear flow. The kernel is parametrised by a Laguerre function expansion with $N = 10$ and $ad^2/\nu = 487$. The blue curve represents the convective pressure drag of the simulations; the red curve represents the fit.

1980, ch.16). Due to the symmetry of the kernel, there are $(N + 1)(N + 2)(N + 3)/6$ independent coefficients. For a given value of a, the coefficients c_{ijk} can be determined by a linear least-squares fit to the superficial velocity and the convective pressure drag time series; the optimal value of a is found by a parameter search. As shown in figure 4.8, the Volterra representation is able to fit the entire temporal evolution with acceptable accuracy. The robustness of the approach was assessed by using the Legendre and the Chebychev rational functions instead of the Laguerre functions. While a similar quality of fit was achieved, the identified kernels differed considerably. Apart from the decay for large times imposed by the choice of basis, the only common feature of the kernels is a singularity at $h(0, 0, 0)$ and a weaker singularity for $h(t_1, 0, 0)$. It is hoped that the identification of the kernel will improve with a larger database, allowing more terms to be used in the expansion of the kernel. A future study could also attempt to directly identify the kernel $h(t_1, t_2, t_3)$ using the approach outlined by Schetzen (1980, pp.81f, pp.87f), in which the kernel can be determined from derivatives of the convective pressure drag response to various superimposed step changes of the superficial velocity.

Strongly nonlinear flow

A major challenge in modelling the convective pressure drag in strongly nonlinear flow is the hysteretic behaviour exhibited by the convective pressure drag with respect to the superficial velocity. During acceleration, the convective pressure drag is smaller than in stationary flow for the same value of $\langle u\rangle_s$, whereas during deceleration, the convective pressure drag is larger than in stationary flow for the same value of $\langle u\rangle_s$ (Unglehrt & Manhart, 2023a, reprinted in appendix D.6). Furthermore, the convective pressure drag approaches a clear scaling behaviour only for large Reynolds numbers. In stationary flow, the direct convective pressure drag due to the mean velocity field scales with Re^2 for Reynolds numbers above 91, but the turbulent convective pressure drag due to the Reynolds stresses shows no clear scaling with the Reynolds number in the investigated Reynolds number range (Unglehrt & Manhart, 2023a, reprinted in appendix D.6). For very large Reynolds numbers, a Re^2 scaling of the

total drag has been observed experimentally (Macdonald et al., 1979), and thus the total convective pressure drag should approach the same scaling.
Unfortunately, the above findings do not suggest a suitable model structure for the convective pressure drag. Various correlations in terms of the superficial velocity and the acceleration have been attempted, however without success. For the cases LF4–LF6, MF5 and MF6 a good correlation of the convective pressure drag with the volume-averaged kinetic energy could be observed. However, a hysteretic behaviour of the convective pressure drag over the kinetic energy was observed for the other cases.
It may be promising to model the convective pressure drag in the framework of the Reynolds decomposition, as the direct convective pressure drag could be expected to follow a quadratic scaling with the Reynolds number like for the stationary cases. The turbulent convective pressure drag could be parametrised in terms of the volume-averaged TKE, for which an auxiliary evolution equation would have to be formulated. However, this approach was not applied to the present dataset since for most of the cases the simulated time was too short to determine the Reynolds decomposition.

4.7.3. Machine-learning approaches

In this section, the potential applications of machine-learning methods to the modelling of unsteady porous media flow are discussed.

Model formulation

Due to the great attention given to the development of machine learning methods in the recent years, a large number of different model architectures are available. For an overview of machine learning methods in fluid mechanics, the reader is referred to the reviews by Brunton et al. (2020) and Sharma et al. (2023). In the following, some approaches are highlighted that seem promising in view of the present modelling problem (section 4.1).
First, the functional relationships between the superficial velocity and the macroscopic pressure gradient could be represented by a Volterra series (Rugh, 1981). This would allow existing models for linear flow, e.g. the model of Pride et al. (1993), to be reused as the linear term of the series. However, the estimation of the higher order Volterra kernels quickly becomes expensive in terms of the amount of training data and the computational effort. This problem can be alleviated by expanding the kernels in terms of the Laguerre functions (Israelsen & Smith, 2014; Wiener, 1958, p.92). Considering the conceptual similarity of the Volterra series to the Taylor series, the Volterra series approach seems to be appropriate only for weakly nonlinear flow.
A second approach could use the neural ordinary differential equation framework (Chen et al., 2019). In this model architecture, the right hand side of an ordinary differential equation is represented by a neural network. Here, the drag terms in the volume-averaged momentum equation (4.1) would be parametrised by a neural network. The inputs of the neural networks are the state variables of the model (section 4.2). When the state variables are chosen as weighted integrals over the history of the superficial velocity

$$\boldsymbol{v}_n(t) = \int_{-\infty}^{t} \langle \boldsymbol{u} \rangle_{\mathrm{s}}(\tau)\, l_n(t-\tau)\, \mathrm{d}\tau\,, \tag{4.31}$$

a continuous form of convolutional neural networks is obtained. The so-called Laguerre-Volterra networks (Marmarelis & Zhao, 1997; Geng & Marmarelis, 2017) are obtained if the weights are the Laguerre functions $l_n(t)$ (Schetzen, 1980, p.349).
Third, in the "physics guided" approach of Pawar et al. (2021) and Bock et al. (2021) a machine-learning model is developed to correct the predictions of a simple potential flow model. In the present setting, the predictor model could be, for example, the unsteady Forchheimer equation, while the corrector could be a neural ordinary differential equation.
A fourth possibility would be to determine the right hand side of a system of ordinary differential equations by selecting suitable terms from a large collection of candidates (Brunton et al., 2016). In the present case, the biggest challenge is to develop a comprehensive set of candidate terms.
Finally, when pore scale flow data is included in the modelling, a reduced-order model can be determined from a Galerkin projection of the Navier-Stokes equations onto a set of modes. A machine-learning model represents the effects of the discarded modes onto the retained modes (Ahmed et al., 2021); this can be achieved through the use of the Mori-Zwanzig formalism which introduces history terms for the retained modes (Menier et al., 2023a). A related approach uses neural auto-encoders to map the full flow state onto a reduced state; the dynamics for the reduced state are again described using the Mori-Zwanzig formalism (Menier et al., 2023b; Gupta et al., 2023).

Physical constraints

Neural networks are "fundamentally interpolative" and overfitting can occur due to their large number of parameters (Brunton et al., 2020). These problems must be considered here, since the present dataset contains only 19 scalar time series for the superficial velocity and the limit cases for high Reynolds and Womersley numbers are not included in the dataset. Therefore, "it is important to explicitly incorporate partially known physics, such as symmetries, constraints, and conserved quantities" (Brunton et al., 2020).
For unsteady porous media flow, the first requirement is that the model must be stable due to the dissipative nature of the flow. Second, the model should satisfy several realisability constraints: Kelvin's minimum energy theorem provides a lower bound for the kinetic energy in terms of the superficial velocity, Helmholtz' minimum dissipation theorem (section B.4) provides a lower bound for the dissipation rate in terms of the superficial velocity, and there exists an upper bound for the kinetic energy similar to the inequality of Doering & Foias (2002, eq. 16), which by Kelvin's minimum energy theorem (section B.3) implies an upper bound for the superficial velocity. Third, the resistance behaviour of the flow is known in several limit cases: Steady flow at low Reynolds numbers satisfies Darcy's law with a cubic correction term (Mei & Auriault, 1991; Skjetne & Auriault, 1999b) and steady flow at high Reynolds numbers approaches a quadratic scaling of the drag (Macdonald et al., 1979). Slowly varying linear flow is described by the unsteady Darcy equation (Zhu et al., 2014; Zhu, 2016) and rapidly varying flow is described by the boundary layer asymptotics for the superficial velocity (Johnson et al., 1987) and the dissipation rate (equation 4.4). Finally, as discussed in section 2.2.2, the symmetries of the pore space constrain the macroscopic behaviour and lead to special forms of macroscopic tensorial properties like the permeability.

There are many different possibilities to enforce physical constraints in machine learning models (Karniadakis et al., 2021; Sharma et al., 2023). Generally, one can distinguish between methods that enforce physical constraints only during the training stage and methods for which the constraint is incorporated into the model architecture. The former kind penalise the violation of the physical constraint with an additional loss term or use other methods of constrained optimisation like the augmented Lagrange method (Fioretto et al., 2021). When the training data is subjected to noise, physical constraints can be incorporated in a probabilistic sense using virtual observables (Kaltenbach & Koutsourelakis, 2020). The methods of the latter kind depend on the nature of the constraint. For example, a shift invariance of the model can be enforced by choosing a convolution structure for the model input. Other constraints can be realised by projecting the model predictions onto the constraint manifold (Yang et al., 2020; Shankar et al., 2022) or by inverting the constraints to determine parts of the output (Beucler et al., 2021). One can also map the data to the constraint manifold, perform a prediction of latent variables and map them back to the original data space (Li et al., 2020; Wang & Song, 2023). For example, reduced-order models constructed using POD modes automatically satisfy the divergence-free constraint if the modes are divergence-free. Note that it is possible to enforce stability of such a model by choosing particular forms of the latent variable dynamics (Kaltenbach & Koutsourelakis, 2021; Kaptanoglu et al., 2021; Omichi et al., 2023).

5. Conclusion and outlook

5.1. Conclusion

This section aims to give an overview of the current understanding of oscillatory flow through porous media.

5.1.1. Pore scale flow

Linear flow can be described in terms of two limit cases. In the first case, the velocity field approaches the Stokes flow for low Womersley numbers; in the second case, the velocity field approaches a potential flow with Stokes boundary layers for high Womersley numbers. The appearance of nonlinear effects is found to depend on the instantaneous Reynolds number for small Wo and on the ratio Re/Wo^2 for large Wo. Note that the onset of nonlinearity for high Womersley numbers could occur earlier if the linear flow undergoes an instability. The nonlinear regime is characterised by inertial cores, complex vortex systems, laminar boundary layer flow and separation regions. For medium and large Wo, the intensity of nonlinear effects is found to lag behind the superficial velocity. The transition of the flow from the laminar to a turbulence-like state was initially expected to behave similarly to oscillatory pipe flow (Hino et al., 1976; Akhavan et al., 1991a), i.e. to depend on the Reynolds number Re_δ based on the Stokes boundary layer thickness. However, Stokes boundary layers are formed only at high Womersley numbers and their transition would require very large Reynolds numbers. Instead, the transition appears to be linked to the instability of the vortex system in the octahedral pore. At low Womersley numbers, turbulent flow is only observed over parts of the cycle and a relaminarisation occurs when the flow changes direction. Conversely, flow at high Womersley numbers can sustain turbulence if the period of oscillation is sufficiently close to the turbulent time scales. The largest turbulent length scales are limited to the pore scale (He et al., 2019; Rao & Jin, 2022), while the smallest scales depend on the Reynolds number and approach the Kolmogorov theory for large Reynolds numbers (He et al., 2019; Patil & Liburdy, 2015). Consequently, the flow is in a turbulence-like state at low Reynolds numbers, and approaches a fully turbulent state at high Reynolds numbers. The appearance of a turbulence-like state leads to a quasi-stationary flow, as the turbulent momentum transport can quickly equilibrate the flow.

5.1.2. Drag processes

In the literature, the drag in flow through porous media has been analysed either in terms of the friction drag and the pressure drag (Fourar et al., 2004; Srikanth et al., 2021) or in terms of the unsteady Forchheimer equation (van Gent, 1993; Hall et al., 1995). In the present work, a more detailed view of the drag process in oscillatory flow through porous media has

been developed based on the pressure decomposition of Graham (2019). The drag is found to consist of four contributions:

- The friction drag is the integral of the wall shear stress at the fluid-solid interface. It is linearly dependent on the superficial velocity for small Reynolds numbers and approaches a steady laminar boundary layer scaling for large Reynolds numbers. For medium and high Womersley numbers, the friction drag is characterised by the interaction between time-limited Stokes boundary layers and convection-limited boundary layers that behave in a quasi-equilibrium fashion.
- The viscous pressure drag is caused by the wall shear stress divergence and therefore has a similar scaling as the friction drag. The wall-normal component of the gradient of the viscous pressure balances the wall-normal component of the viscous force. As discussed by Graham (2019), the viscous pressure is responsible, for example, for the pressure drop in steady laminar channel flow and for the excess pressure in stagnation point flow. For the hexagonal sphere pack considered in the present work, the viscous pressure drag accounts for approximately half of the friction drag and shows a similar scaling behaviour.
- The accelerative pressure drag arises as a reaction force to the macroscopic pressure gradient, ensuring that the fluid is not accelerated in wall-normal direction at the fluid-solid interface. The accelerative pressure drag is therefore directly proportional to the macroscopic pressure gradient. It is similar to the added-mass effect, in which the fluid is accelerated in the vicinity of an accelerating body, thus preventing the body from moving into regions occupied by the fluid and causing a resistance proportional to the acceleration of the body. The accelerative pressure drag is independent of the velocity and the fluid properties and its value can be determined from a potential flow problem.
- The convective pressure drag arises from the divergence of the convective accelerations and represents the drag due to features like separation, inertial cores, shear layers and vortices. It is also known as "Q-induced force" (Aghaei-Jouybari et al., 2022) and is related to the vorticity-induced force of Howe (1995), Li & Wu (2018) and Menon & Mittal (2021). In stationary flow, the convective pressure drag due to the mean velocity field is found to scale quadratically with the Reynolds number for $Re \gtrsim 90$; the convective pressure drag due to the Reynolds stresses is found to be significantly smaller than the convective pressure drag due to the mean velocity field. The convective pressure drag in oscillatory flow is not well understood and its modelling is difficult, since it is not in phase with the superficial velocity.

5.1.3. Modelling

The classical approaches to modelling unsteady flow through porous media are based on the unsteady Forchheimer equation (Polubarinova-Kochina, 1962; Sollitt & Cross, 1972) and the dynamic permeability models (Johnson et al., 1987; Lafarge, 2009). In the present work, the findings of Chapman & Higdon (1992) could be confirmed that the superficial velocity in the linear regime is described by the models of Johnson et al. (1987) and Pride et al. (1993) with excellent accuracy. The unsteady Forchheimer equation is appropriate at low Womersley numbers and for strongly nonlinear flow, but has large errors for linear flow at medium or high Womersley numbers depending on the choice of the acceleration coefficient.

This deficiency could be alleviated by combining a time-domain formulation of the dynamic permeability model of Pride et al. (1993) and a Forchheimer-type nonlinearity. However, the Forchheimer term with a coefficient determined from stationary flow data overestimates the nonlinear drag at high Womersley numbers.
A new model has been proposed based on the aforementioned decompoosition of the drag: The friction and the viscous pressure drag are parameterised by a history term that combines the linear model of Pride et al. (1993) with a steady laminar boundary scaling, and the convective pressure drag is simply represented by a Forchheimer-type nonlinearity, which however has a smaller coefficient than in the unsteady Forchheimer equation. The proposed model is able to accurately represent linear flow and nonlinear flow at low and medium Womersley numbers and the error increases modestly towards nonlinear flow at high Womersley numbers. The model coefficients of the linear part have a clear theoretical definition in terms of the Stokes flow and the potential flow and depend only on the geometry of the porous medium. Also, a new model for the dissipation rate in linear unsteady flow has been proposed, which may be used to construct models for dispersion in unsteady flow through porous media. Both proposed models have been constructed by blending two asymptotic limits within a convolution integral using the method of Churchill & Usagi (1972).
Finally, the present study has contributed a publicly available dataset for modelling the relationship between the superficial velocity and the macroscopic pressure gradient, which may facilitate the construction of improved, possibly machine-learned models.

5.2. Outlook

In the following, several topics are highlighted that could deserve further attention. Notably, some of the investigations could be conducted using the present simulation dataset.

5.2.1. Velocity distribution and dispersion modelling

Vasheghani Farahani & Mousavi Nezhad (2022) investigated the changes of the velocity probability density function (PDF) $f(\boldsymbol{u})$ in simple cubic and irregular sphere packs with the Reynolds number. With the present dataset, such an analysis could be extended to oscillatory flow.
One motivation for studying the velocity PDF is the modelling of tracer dispersion in a porous medium with Markov velocity processes (Meyer & Tchelepi, 2010, 2011; Kooshapur, 2016). In particular, this modelling approach aims to represent the conditional PDF $f(\mathrm{d}\boldsymbol{u}|\boldsymbol{u})$ of the velocity change $\mathrm{d}\boldsymbol{u}$ incurred by a Lagrangian particle over a time interval $\mathrm{d}t$ given a velocity $\boldsymbol{u}$. This conditional PDF can be readily evaluated from the snapshot velocity fields from the present simulations, which could therefore contribute to the development of dispersion models for unsteady flow.

5.2.2. Wall shear stress

It would also be worthwhile to investigate the wall shear stress in stationary and oscillatory flow. From the wall shear stress field, it is possible to identify separation lines on the spheres,

which can be used as seed points to integrate the streamsurfaces delimiting regions of separated flow (Hui, 1988; Tobak, 1997; Wu et al., 2000; Wiebel et al., 2009). The extent of these regions may be helpful for a more detailed analysis of the convective pressure drag. Some considerations on the analysis of the wall shear stress field topology are summarised in appendix C.
For high Schmidt numbers, the wall shear stress also determines the rate of heat or mass transfer near the wall (Ogawa et al., 1991; Rode et al., 1994), which is of interest in the design of packed bed reactors (Eigenberger, 2000). The present dataset could thus help to assess the efficacy of heat or mass transfer in oscillatory flow at different parameters.

5.2.3. Transient behaviour

The transient towards oscillatory pipe flow was investigated by (Feldmann, 2015) and the transient towards stationary flow through a hexagonal sphere pack was investigated by Zhu et al. (2014), Zhu (2016) and Sakai & Manhart (2020). Similarly, the present dataset could be analysed with a focus on the duration of the transient and the overshooting of the transient response compared to the amplitude in the cyclostationary state.

5.2.4. Turbulent oscillatory flow

The turbulence structure in stationary flow through packed beds was studied, for example, by He et al. (2019), Patil & Liburdy (2013a), Patil & Liburdy (2013b) and Patil & Liburdy (2015), and it would be interesting to investigate in which respects turbulent oscillatory flow agrees with their findings. Also, the study of turbulent oscillatory flow by Nakajo et al. (2008, 2009) could be an interesting reference for comparison.
Further, the interaction between the acceleration and the spatial scales of the turbulent motion are an interesting subject. The spatial scales could be defined, for example, using an orthogonal expansion or a scale space approach (Lindeberg, 1994). In the former approach, the Stokes eigenfunctions could be employed, which satisfy the eigenvalue problem (Avellaneda & Torquato, 1991)

$$\boldsymbol{\nabla} \cdot \boldsymbol{\Psi}_n = 0\,, \tag{5.1a}$$

$$\Delta \boldsymbol{\Psi}_n + \boldsymbol{\nabla} Q_n = -\epsilon_n \boldsymbol{\Psi}_n\,. \tag{5.1b}$$

The velocity eigenfunctions $\boldsymbol{\Psi}_n$ generalise the Fourier series to three-dimensional divergence-free vector fields and satisfy the no-slip and impermeable wall boundary conditions at the spheres. The inverse square root of the eigenvalue ϵ_n defines the "wavelength" of the mode $\boldsymbol{\Psi}_n$. The pressure eigenfunctions Q_n ensure the divergence-free constraint. In the latter approach, the filtering method of Johnson (2022) could be promising.
Finally, the budget of TKE could be evaluated and compared to turbulence models from the literature (Masuoka & Takatsu, 1996; Nakayama & Kuwahara, 1999; Chandesris et al., 2006; Teruel & Rizwan-uddin, 2009a,b; Kuwata et al., 2014; Jouybari & Lundström, 2019).

5.2.5. Transition to turbulence

As discussed in section 3.5.4, the transition mechanisms in oscillatory flow through a hexagonal close-packing are unclear. The instability of linear oscillatory flow at high frequencies is of particular importance, as it could potentially lead to an earlier onset of nonlinearity. The results of a linear stability analysis would be very helpful in extending the understanding of the flow regimes in oscillatory flow. A computationally feasible starting point could be the Floquet stability analysis of linear flow at large Womersley numbers, for which the base flow in the sphere pack can be obtained using the method of Chapman & Higdon (1992).

5.2.6. Extension of the known parameter space

An interesting subject of future research would be to investigate flow outside the present parameter range, in particular towards higher Reynolds and Womersley numbers. In these regions, the grid resolution is dictated by increasingly small turbulent structures, the thickness of the oscillatory boundary layers, and the resolution requirements near the contact points if exactly touching spheres are to be considered (cf. section 2.5.3).
For the present Cartesian grid approach, DNS would likely become uneconomical under these conditions and thus the following approximations could be considered. First, the resolution requirements due to turbulent structures can be relaxed by a large-eddy simulation approach (cf. section 2.6). Second, the resolution near the wall may be improved by modelling the near-wall boundary layer flow (Unglehrt et al., 2022b). Third, a permeability tensor could be assigned to the fillet bridges at the contact points. In a simple approximation, the parabolic velocity profile of Poiseuille flow could be used to model the flow in the gap. In a more sophisticated approach, one could attempt to derive the asymptotic solution near the contact point from the Stokes equations in tangent-sphere coordinates (Moon & Spencer, 1988, p.104f.), which is similar in spirit to the Moffatt solution for flow in an acute corner (Moffatt, 2021).
An alternative to the Cartesian grid approach is presented by the use of higher order methods. For example, the spectral element method with tetrahedral elements (Sherwin & Karniadakis, 1996) facilitates the use of higher order discretisations on a body-conforming mesh, which can be generated at a reasonable effort. Finally, pseudo-spectral methods based on vector spherical harmonics (Chapman & Higdon, 1992; Dumas & Leonard, 1994) could be considered in which the boundary conditions on the spheres are represented exactly and collocation conditions are imposed on the faces of the Voronoi cells of the spheres. However, the competitiveness of these approaches compared to the Cartesian grid method is unknown.

5.2.7. Generalised settings

As the present study has focused mainly on a single porous medium geometry, an obvious next step would be to consider sphere packs with a different, possibly irregular arrangement of spheres and a different porosity or even multidisperse granular media and foams. Also, flow in response to different forcings with nonsinusoidal waveforms could be investigated (Graham & Higdon, 2002). In such settings, it would be especially valuable to validate the proposed

model for the relationship between the superficial velocity and the macroscopic pressure gradient, and to develop correlations for the model parameters.

5.2.8. Experimental validation

Finally, it would be very valuable to conduct an experimental investigation to validate and complement the present results. In particular, an experiment would be well-suited to analyse turbulent oscillatory flow with a phase-averaging approach, as it is comparatively easy to achieve statistically converged results. Among current measurement techniques, particle image velocimetry or particle tracking velocimetry with refractive index matching[1] (Nakajo et al., 2009; Patil & Liburdy, 2013a; Häfeli et al., 2014; Souzy et al., 2020) and magnetic resonance velocimetry (Johns et al., 2000; Suekane et al., 2003; Yang et al., 2013; Ricke et al., 2023) appear to be a suitable choice. A comparison between figure 3.7 and (van Gent, 1993, figure 2) and (Losada et al., 1995, figure 9) shows that the simulations HF6 and HF7 lie in a similar region of the parameter space as the experiments of (van Gent, 1993; Smith, 1991; Hall et al., 1995; Losada et al., 1995) and are thus accessible to experimental validation.

[1] While is common practice to adjust the refractive index of the fluid to the one of the solid, Fort & Bardet (2021) suggested a polymer which matches the refractive index of water and can be cast in thick units.

References

Abgrall, R. 1996 Numerical discretization of the first-order Hamilton-Jacobi equation on triangular meshes. *Communications on Pure and Applied Mathematics* **49** (12), 1339–1373.

Abramowitz, M. & Stegun, I. A. 1972 Handbook of Mathematical Functions with Formulas, Graphs, and Mathematical Tables, 10th edn. Applied Mathematics Series (Washington, D.C.) 55. Washington, D.C.: U.S. Department of Commerce.

Aghaei-Jouybari, M., Seo, J.-H., Yuan, J., Mittal, R. & Meneveau, C. 2022 Contributions to pressure drag in rough-wall turbulent flows: Insights from force partitioning. *Physical Review Fluids* **7** (8), 084602.

Agnaou, M., Lasseux, D. & Ahmadi, A. 2016 From steady to unsteady laminar flow in model porous structures: An investigation of the first Hopf bifurcation. *Computers & Fluids* **136**, 67–82.

Ahmed, S. E., Pawar, S., San, O., Rasheed, A., Iliescu, T. & Noack, B. R. 2021 On closures for reduced order models – A spectrum of first-principle to machine-learned avenues. *Physics of Fluids* **33** (9), 091301.

Akhavan, R., Kamm, R. D. & Shapiro, A. H. 1991a An investigation of transition to turbulence in bounded oscillatory Stokes flows Part 1. Experiments. *Journal of Fluid Mechanics* **225**, 395–422.

Akhavan, R., Kamm, R. D. & Shapiro, A. H. 1991b An investigation of transition to turbulence in bounded oscillatory Stokes flows Part 2. Numerical simulations. *Journal of Fluid Mechanics* **225**, 423–444.

Alassar, R. S. & Badr, H. M. 1997 Oscillating viscous flow over a sphere. *Computers & Fluids* **26** (7), 661–682.

Allaire, G. 1997 One-Phase Newtonian Flow. In Homogenization and Porous Media (ed. Ulrich Hornung), Interdisciplinary Applied Mathematics , pp. 45–76. New York: Springer.

Allaire, G. & Conca, C. 1996 Bloch-wave homogenization for a spectral problem in fluid-solid structures. *Archive for Rational Mechanics and Analysis* **135** (3), 197–257.

Allaire, G. & Conca, C. 1998 Bloch wave homogenization and spectral asymptotic analysis. *Journal de Mathématiques Pures et Appliquées* **77** (2), 153–208.

Alshare, A. A., Simon, T. W. & Strykowski, P. J. 2010 Simulations of flow and heat transfer in a serpentine heat exchanger having dispersed resistance with porous-continuum and continuum models. *International Journal of Heat and Mass Transfer* **53** (5), 1088–1099.

Anderson, T. B. & Jackson, R. 1967 Fluid Mechanical Description of Fluidized Beds. Equations of Motion. *Industrial & Engineering Chemistry Fundamentals* **6** (4), 527–539.

Andreades, C., Cisneros, A. T., Choi, J. K., Chong, A. Y. K., Fratoni, M., Hong, S., Huddar, L. R., Huff, K. D., Krumwiede, D. L., Laufer, M. R., Munk, M., Scarlat, R. O., Zweibaum, N., Greenspan, E. & Peterson, P. F. 2014 Technical Description of the "Mark 1" Pebble-Bed Fluoride-Salt-Cooled High-Temperature Reactor (PB-FHR) Power Plant. Tech. Rep. UCBTH- 14- 002. Department of Nuclear Engineering University of California, Berkeley, CA.

Antuono, M. 2020 Tri-periodic fully three-dimensional analytic solutions for the Navier–Stokes equations. *Journal of Fluid Mechanics* **890**, A23.

Apte, S. V., Oujia, T., Matsuda, K., Kadoch, B., He, X. & Schneider, K. 2022 Clustering of inertial particles in turbulent flow through a porous unit cell. *Journal of Fluid Mechanics* **937**, A9.

Armstrong, M. A. 1983 Basic Topology. Undergraduate Texts in Mathematics . New York: Springer New York.

Asiaban, P. & Fathi-Moghadam, M. 2018 Flow throttling in surge tanks using porous structures. *International Journal of Pressure Vessels and Piping* **168**, 301–309.

Auriault, J.-L. 2002 Upscaling Heterogeneous Media by Asymptotic Expansions. *Journal of Engineering Mechanics* **128** (8), 817–822.

Avellaneda, M. & Torquato, S. 1991 Rigorous link between fluid permeability, electrical conductivity, and relaxation times for transport in porous media. *Physics of Fluids A: Fluid Dynamics* **3** (11), 2529–2540.

Bağci, Ö., Arbak, A., De Paepe, M. & Dukhan, N. 2016 Experimental results for oscillatory water flow in 10-ppi metal foam at low-frequencies. *Journal of Physics: Conference Series* **745**, 032040.

Barth, T. J. & Sethian, J. A. 1998 Numerical Schemes for the Hamilton–Jacobi and Level Set Equations on Triangulated Domains. *Journal of Computational Physics* **145** (1), 1–40.

Batchelor, G. K. 2000 An Introduction to Fluid Dynamics. Cambridge Mathematical Library . Cambridge: Cambridge University Press.

Bear, J. 2013 Dynamics of Fluids in Porous Media. New York: Dover Publications.

Bear, J. 2018 Modeling Phenomena of Flow and Transport in Porous Media. Theory and Applications of Transport in Porous Media 31. Cham: Springer International Publishing.

Berger, L., Bordas, R., Burrowes, K., Grau, V., Tavener, S. & Kay, D. 2016 A poroelastic model coupled to a fluid network with applications in lung modelling. *International Journal for Numerical Methods in Biomedical Engineering* **32** (1), e02731.

Beucler, T., Pritchard, M., Rasp, S., Ott, J., Baldi, P. & Gentine, P. 2021 Enforcing Analytic Constraints in Neural Networks Emulating Physical Systems. *Physical Review Letters* **126** (9), 098302.

Bhatia, H., Jadhav, S., Bremer, P.-T., Chen, G., Levine, J. A., Nonato, L. G. & Pascucci, V. 2011 Edge maps: Representing flow with bounded error. In 2011 IEEE Pacific Visualization Symposium, pp. 75–82. Hong Kong: IEEE.

Bianchi, P., Williams, J. D. & Kappe, C. O. 2020 Oscillatory flow reactors for synthetic chemistry applications. *Journal of Flow Chemistry* **10** (3), 475–490.

Biau, D. 2016 Transient growth of perturbations in Stokes oscillatory flows. *Journal of Fluid Mechanics* **794**, R4.

Bielefeld, S., Cvetković, M. & Ramírez, A. 2023 Should we exploit flexibility of chemical processes for demand response? Differing perspectives on potential benefits and limitations. *Frontiers in Energy Research* **11**, 1190174.

Biot, M. A. 1956a Theory of Propagation of Elastic Waves in a Fluid-Saturated Porous Solid. I. Low-Frequency Range. *The Journal of the Acoustical Society of America* **28** (2), 168–178.

Biot, M. A. 1956b Theory of Propagation of Elastic Waves in a Fluid-Saturated Porous Solid. II. Higher Frequency Range. *The Journal of the Acoustical Society of America* **28** (2), 179–191.

Biot, M. A. 1962 Mechanics of Deformation and Acoustic Propagation in Porous Media. *Journal of Applied Physics* **33** (4), 1482–1498.

Blennerhassett, P. J. & Bassom, Andrew P. 2002 The linear stability of flat Stokes layers. *Journal of Fluid Mechanics* **464**, 393–410.

Bock, F. E., Keller, S., Huber, N. & Klusemann, B. 2021 Hybrid Modelling by Machine Learning Corrections of Analytical Model Predictions towards High-Fidelity Simulation Solutions. *Materials* **14** (8), 1883.

Boettcher, K. E. R., Fischer, M.-D., Neumann, T. & Ehrhard, P. 2022 Experimental investigation of the pre–Darcy regime. *Experiments in Fluids* **63** (2), 42.

Bolt, G. H. & Groenevelt, P. H. 1969 Coupling Phenomena as a Possible Cause of "Non-Darcian" Behaviour of Water in Soil. *International Association of Scientific Hydrology. Bulletin* **14** (2), 17–28.

Borchardt-Ott, W. 1997 Kristallographie. Berlin, Heidelberg: Springer Berlin Heidelberg.

Boyd, S. & Chua, L. 1985 Fading memory and the problem of approximating nonlinear operators with Volterra series. *IEEE Transactions on Circuits and Systems* **32** (11), 1150–1161.

Branlard, E. 2017 Spherical Geometry Models: Flow About a Sphere and Hill's Vortex. In Wind Turbine Aerodynamics and Vorticity-Based Methods: Fundamentals and Recent Applications (ed. E. Branlard), Research Topics in Wind Energy , pp. 407–417. Cham: Springer International Publishing.

Brennen, C. E. 1982 A Review of Added Mass and Fluid Inertial Forces. Tech. Rep. CR 82.010. Naval Civil Engineering Laboratory, Port Hueneme, CA.

Brenner, H. 1980 Dispersion resulting from flow through spatially periodic porous media. *Philosophical Transactions of the Royal Society of London. Series A, Mathematical and Physical Sciences* **297** (1430), 81–133.

Bronštejn, I. N. & Semendjaev, K. A. 1981 Taschenbuch Der Mathematik, Ergänzende Kapitel, 2nd edn. Frankfurt am Main: Deutsch.

Bruggeman, D. a. G. 1935 Berechnung verschiedener physikalischer Konstanten von heterogenen Substanzen. I. Dielektrizitätskonstanten und Leitfähigkeiten der Mischkörper aus isotropen Substanzen. *Annalen der Physik* **416** (7), 636–664.

Brunton, S. L., Noack, B. R. & Koumoutsakos, P. 2020 Machine Learning for Fluid Mechanics. *Annual Review of Fluid Mechanics* **52** (1), 477–508.

Brunton, S. L., Proctor, J. L. & Kutz, J. N. 2016 Discovering governing equations from data by sparse identification of nonlinear dynamical systems. *Proceedings of the National Academy of Sciences of the United States of America* **113** (15), 3932–3937.

Bu, S., Yang, J., Dong, Q. & Wang, Q. 2015 Experimental study of flow transitions in structured packed beds of spheres with electrochemical technique. *Experimental Thermal and Fluid Science* **60**, 106–114.

Burcharth, H. F. & Andersen, O. K. 1995 On the one-dimensional steady and unsteady porous flow equations. *Coastal Engineering* **24** (3-4), 233–257.

Cabral, B. & Leedom, L. C. 1993 Imaging vector fields using line integral convolution. In Proceedings of the 20th Annual Conference on Computer Graphics and Interactive Techniques - SIGGRAPH '93, pp. 263–270. Anaheim, CA: ACM Press.

Cazaurang, S., Marcoux, M., Pokrovsky, O. S., Loiko, S. V., Lim, A. G., Audry, S., Shirokova, L. S. & Orgogozo, L. 2023 Numerical assessment of morphological and hydraulic properties of moss, lichen and peat from a permafrost peatland. *Hydrology and Earth System Sciences* **27** (2), 431–451.

Celik, I. B., Urmila, G., Roache, P-J., Freitas, C. J., Coleman, H. & Raad, P. E. 2008 Procedure for Estimation and Reporting of Uncertainty Due to Discretization in CFD Applications. *Journal of Fluids Engineering* **130** (7), 078001.

Cha, J. J. 2007 Hydrodynamic Parameters of Micro Porous Media for Steady and Oscillatory Flow: Application to Cryocooler Regenerators. PhD thesis, Georgia Institute of Technology, Atlanta, Georgia.

Champoux, Y. & Allard, J.-F. 1991 Dynamic tortuosity and bulk modulus in air-saturated porous media. *Journal of Applied Physics* **70** (4), 1975–1979.

Chanda, A. & Pramanik, S. 2023 Effects of a thin vertical porous barrier on the water wave scattering by a porous breakwater. *Physics of Fluids* **35** (6), 062120.

Chandesris, M., Serre, G. & Sagaut, P. 2006 A macroscopic turbulence model for flow in porous media suited for channel, pipe and rod bundle flows. *International Journal of Heat and Mass Transfer* **49** (15-16), 2739–2750.

Chang, E. J. & Maxey, M. R. 1994 Unsteady flow about a sphere at low to moderate Reynolds number. Part 1. Oscillatory motion. *Journal of Fluid Mechanics* **277**, 347–379.

Chang, E. J. & Maxey, M. R. 1995 Unsteady flow about a sphere at low to moderate Reynolds number. Part 2. Accelerated motion. *Journal of Fluid Mechanics* **303**, 133–153.

Chapman, A. M. & Higdon, J. J. L. 1992 Oscillatory Stokes flow in periodic porous media. *Physics of Fluids A: Fluid Dynamics* **4** (10), 2099–2116.

Chaudhary, K., Cardenas, M. B., Deng, W. & Bennett, P. C. 2011 The role of eddies inside pores in the transition from Darcy to Forchheimer flows. *Geophysical Research Letters* **38** (24), L24405.

Cheema, I. I. & Krewer, U. 2018 Operating envelope of Haber–Bosch process design for power-to-ammonia. *RSC Advances* **8** (61), 34926–34936.

Chen, C. & Yang, A. 2021 Power-to-methanol: The role of process flexibility in the integration of variable renewable energy into chemical production. *Energy Conversion and Management* **228**, 113673.

Chen, R. T. Q., Rubanova, Y., Bettencourt, J. & Duvenaud, D. 2019 Neural Ordinary Differential Equations. In Advances in Neural Information Processing Systems (ed. S. Bengio, H. Wallach, H. Larochelle, N. Cesa-Bianchi & R. Garnett), , vol. 31, pp. 6571–6583. Curran Associates, Inc.

Cheng, C. M., Peng, Z. K., Zhang, W. M. & Meng, G. 2017 Volterra-series-based nonlinear system modeling and its engineering applications: A state-of-the-art review. *Mechanical Systems and Signal Processing* **87**, 340–364.

Cheny, Y. & Botella, O. 2010 The LS-STAG method: A new immersed boundary/level-set method for the computation of incompressible viscous flows in complex moving geometries with good conservation properties. *Journal of Computational Physics* **229** (4), 1043–1076.

Chorin, A. J. 1968 Numerical solution of the Navier-Stokes equations. *Mathematics of Computation* **22** (104), 745–762.

Choudhari, M., Gawali, B. S. & Patil, J. D. 2022 Oscillating flow heat transfer: A comprehensive review. *Energy Sources, Part A: Recovery, Utilization, and Environmental Effects* **44** (3), 7598–7619.

Chu, X., Weigand, B. & Vaikuntanathan, V. 2018 Flow turbulence topology in regular porous media: From macroscopic to microscopic scale with direct numerical simulation. *Physics of Fluids* **30** (6), 065102.

Chukwudozie, C. & Tyagi, M. 2013 Pore scale inertial flow simulations in 3-D smooth and rough sphere packs using lattice Boltzmann method. *AIChE Journal* **59** (12), 4858–4870.

Churchill, S. W. & Usagi, R. 1972 A general expression for the correlation of rates of transfer and other phenomena. *AIChE Journal* **18** (6), 1121–1128.

Cockroft, J. K. 1999 A Hypertext Book of Crystallographic Space Group Diagrams and Tables. London: Birkbeck College.

Conway, J. H. & Sloane, N. J. A. 1999 Sphere Packings, Lattices and Groups. Grundlehren der Mathematischen Wissenschaften 290. New York: Springer New York.

Crawford, J. D. & Knobloch, E. 1991 Symmetry and Symmetry-Breaking Bifurcations in Fluid Dynamics. *Annual Review of Fluid Mechanics* **23** (1), 341–387.

Crevacore, E., Tosco, T., Sethi, R., Boccardo, G. & Marchisio, D. L. 2016 Recirculation zones induce non-Fickian transport in three-dimensional periodic porous media. *Physical Review E* **94** (5), 053118.

Crittenden, B. D., Lau, A., Brinkmann, T. & Field, R. W. 2005 Oscillatory flow and axial dispersion in packed beds of spheres. *Chemical Engineering Science* **60** (1), 111–122.

Darcy, H. 1856 Les fontaines publiques de la ville de Dijon. Paris: Victor Dalmont.

Das, A. & Mathew, J. 2001 Direct numerical simulation of turbulent spots. *Computers & Fluids* **30** (5), 533–541.

Das, M. K., Mukherjee, P. P. & Muralidhar, K. 2018 Modeling Transport Phenomena in Porous Media with Applications. Mechanical Engineering Series . Cham: Springer International Publishing.

Dasgupta, S. & Atta, A. 2017 Computational studies on flow maldistribution of Newtonian liquids in periodic packed beds. In 27th European Symposium on Computer Aided Process Engineering, Pt A (ed. A. Espuna, M. Graells & L. Puigjaner), , vol. 40A, pp. 1057–1062. Amsterdam: Elsevier Science Bv.

Davis, A. M. J., O'Neill, M. E., Dorrepaal, J. M. & Ranger, K. B. 1976 Separation from the surface of two equal spheres in Stokes flow. *Journal of Fluid Mechanics* **77** (4), 625–644.

Davis, H. T. 1962 Introduction to Nonlinear Differential and Integral Equations. New York: Dover.

Davis, S. H. 1976 The Stability of Time-Periodic Flows. *Annual Review of Fluid Mechanics* **8** (1), 57–74.

Davit, Y., Bell, C. G., Byrne, H. M., Chapman, L. A.C., Kimpton, L. S., Lang, G. E., Leonard, K. H. L., Oliver, J. M., Pearson, N. C., Shipley, R. J., Waters, S. L., Whiteley, J. P., Wood, B. D. & Quintard, M. 2013 Homogenization via formal multiscale asymptotics and volume averaging: How do the two techniques compare? *Advances in Water Resources* **62**, 178–206.

DeGroot, C. & Straatman, A. 2018 A porous media model of alveolar duct flow in the human lung. *Journal of Porous Media* **21**, 405–422.

DeGroot, C. T. & Straatman, A. G. 2012 Towards a porous media model of the human lung. *AIP Conference Proceedings* **1453** (1), 69–74.

Deyle, E. R. & Sugihara, G. 2011 Generalized Theorems for Nonlinear State Space Reconstruction. *PLoS ONE* **6** (3), e18295.

do Goes, F., Desbrun, M. & Tong, Y. 2015 Vector field processing on triangle meshes. In SIGGRAPH Asia 2015 Courses, SA '15 . New York: Association for Computing Machinery.

Doering, C. R. & Foias, C. 2002 Energy dissipation in body-forced turbulence. *Journal of Fluid Mechanics* **467**, 289–306.

Drazin, P. G. & Reid, W. H. 2004 Hydrodynamic Stability, 2nd edn. Cambridge Mathematical Library . Cambridge: Cambridge University Press.

Dröge, M. 2006 Cartesian grid methods for turbulent flow simulation in complex geometries. PhD thesis, University of Groningen, Groningen.

Dröge, M. & Verstappen, R. 2005 A new symmetry-preserving Cartesian-grid method for computing flow past arbitrarily shaped objects. *International Journal for Numerical Methods in Fluids* **47** (8-9), 979–985.

Dumas, G. & Leonard, A. 1994 A Divergence-Free Spectral Expansions Method for 3-Dimensional Flows in Spherical-Gap Geometries. *Journal of Computational Physics* **111** (2), 205–219.

Dybbs, A. & Edwards, R. V. 1984 A New Look at Porous Media Fluid Mechanics — Darcy to Turbulent. In Fundamentals of Transport Phenomena in Porous Media (ed. J. Bear & M. Y. Corapcioglu), NATO ASI Series 82, pp. 199–256. Dordrecht: Springer Netherlands.

Eigenberger, G. 2000 Fixed-Bed Reactors. In Ullmann's Encyclopedia of Industrial Chemistry, 6th edn. (ed. M. Bohnet), , vol. 15, pp. 14–52. Weinheim: Wiley-VCH.

Ene, H. & Sanchez-Palencia, E. 1975 Equations et phénomènes de surface pour l'écoulement dans un milieu poreux. *Journal de Mécanique* **14** (1), 73–108.

Ergun, S. 1952 Fluid Flow Through Packed Columns. *Chemical Engineering Progress* **48** (2), 89–94.

Fand, R. M., Kim, B. Y. K., Lam, A. C. C. & Phan, R. T. 1987 Resistance to the Flow of Fluids Through Simple and Complex Porous Media Whose Matrices Are Composed of Randomly Packed Spheres. *Journal of Fluids Engineering* **109** (3), 268–273.

Feldmann, D. 2015 Eine numerische Studie zur turbulenten Bewegungsform in der oszillierenden Rohrströmung. PhD thesis, Technische Universität Ilmenau, Ilmenau.

Ferziger, J. H. & Perić, M. 2002 Computational Methods for Fluid Dynamics, 3rd edn. Berlin, New York: Springer.

Finn, J. R. 2013 A numerical study of inertial flow features in moderate Reynolds number flow through packed beds of spheres. PhD thesis, Oregon State University, Corvallis, OR.

Finn, J. R. & Apte, S. V. 2013 Relative performance of body fitted and fictitious domain simulations of flow through fixed packed beds of spheres. *International Journal of Multiphase Flow* **56**, 54–71.

Finn, J. R., Apte, S. V. & Wood, B. D. 2012 Characteristics of Porescale Vortical Structures in Random and Arranged Packed Beds of Spheres. In Volume 2: Fora, pp. 129–138. Rio Grande, PR: American Society of Mechanical Engineers.

Fioretto, F., van Hentenryck, P., Mak, T. W. K., Tran, C., Baldo, F. & Lombardi, M. 2021 Lagrangian Duality for Constrained Deep Learning. In Machine Learning and Knowledge Discovery in Databases. Applied Data Science and Demo Track (ed. Y. Dong, G. Ifrim, D. Mladenić, C. Saunders & S. van Hoecke), Lecture Notes in Computer Science , pp. 118–135. Cham: Springer International Publishing.

Firdaouss, M., Guermond, J.-L. & Le Quéré, P. 1997 Nonlinear corrections to Darcy's law at low Reynolds numbers. *Journal of Fluid Mechanics* **343**, 331–350.

Floryan, J. M. 1986 Görtler instability of boundary layers over concave and convex walls. *The Physics of Fluids* **29** (8), 2380–2387.

Forchheimer, P. 1901 Wasserbewegung durch Boden. *Zeitschrift des Vereins deutscher Ingenieure* **45**, 1782–1788.

Fort, C. & Bardet, P. M. 2021 Refractive-index-matched polymer for experimental fluid dynamics in water. *Experiments in Fluids* **62** (12), 249.

Foss, J. F. 2007 Topological Considerations in Fluid Mechanics Measurements. In Springer Handbook of Experimental Fluid Mechanics (ed. C. Tropea, A. L. Yarin & J. F. Foss), Springer Handbooks , pp. 909–918. Berlin, Heidelberg: Springer.

Foss, J. F., Hedden, M., Barros, J. M. & Christensen, K. T. 2016 A topological evaluation procedure to assess the integrity of a PIV vector field. *Measurement Science and Technology* **27** (9), 094007.

Fourar, M., Radilla, G., Lenormand, R. & Moyne, C. 2004 On the non-linear behavior of a laminar single-phase flow through two and three-dimensional porous media. *Advances in Water Resources* **27** (6), 669–677.

Gardner, W. A. 1986 Introduction to Random Processes: With Applications to Signals and Systems. New York: Macmillan Pub. Co.

Geng, K. & Marmarelis, V. Z. 2017 Methodology of Recurrent Laguerre-Volterra Network for Modeling Nonlinear Dynamic Systems. *IEEE transactions on neural networks and learning systems* **28** (9), 2196–2208.

Gerke, K. M., Karsanina, M. V. & Katsman, R. 2019 Calculation of tensorial flow properties on pore level: Exploring the influence of boundary conditions on the permeability of three-dimensional stochastic reconstructions. *Physical Review E* **100** (5), 053312.

Giorgi, T. 1997 Derivation of the Forchheimer Law Via Matched Asymptotic Expansions. *Transport in Porous Media* **29** (2), 191–206.

Gollub, J. P. & Benson, S. V. 1980 Many routes to turbulent convection. *Journal of Fluid Mechanics* **100** (03), 449–470.

Golubitsky, M., Josic, K. & Kaper, T. J. 2001 An unfolding theory approach to bursting in fast–slow systems. In Global Analysis of Dynamical Systems. CRC Press.

Gong, H. & Wu, M. 2021 Numerical Simulation of Full-Scale Three-Dimensional Fluid Flow in an Oscillating Reactor. *Frontiers in Energy Research* **9**, 674615.

Gortler, S. J., Gotsman, C. & Thurston, D. 2006 Discrete one-forms on meshes and applications to 3D mesh parameterization. *Computer Aided Geometric Design* **23** (2), 83–112.

Goury, O., Kerfriden, P. & Bordas, S. 2016 Automatised selection of load paths to construct reduced-order models in computational damage micromechanics: From dissipation-driven random selection to Bayesian optimization. *Computational Mechanics* **58** (2), 213–234.

Gradštejn, I. S. & Ryžik, J. M. 2009 Table of Integrals, Series and Products, 7th edn. Amsterdam: Elsevier Acad. Press.

Graham, D. R. & Higdon, J. J. L. 2002 Oscillatory forcing of flow through porous media. Part 2. Unsteady flow. *Journal of Fluid Mechanics* **465**, 237–260.

Graham, W. R. 2019 Decomposition of the forces on a body moving in an incompressible fluid. *Journal of Fluid Mechanics* **881**, 1097–1122.

Gray, William G. 1975 A derivation of the equations for multi-phase transport. *Chemical Engineering Science* **30** (2), 229–233.

Gu, Z. & Wang, H. 1991 Gravity waves over porous bottoms. *Coastal Engineering* **15** (5-6), 497–524.

Guibert, R., Horgue, P., Debenest, G. & Quintard, M. 2016 A Comparison of Various Methods for the Numerical Evaluation of Porous Media Permeability Tensors from Pore-Scale Geometry. *Mathematical Geosciences* **48** (3), 329–347.

Günther, T. & Baeza Rojo, I. 2021 Introduction to Vector Field Topology. In Topological Methods in Data Analysis and Visualization VI (ed. I. Hotz, T. Bin Masood, F. Sadlo & J. Tierny), Mathematics and Visualization , pp. 289–326. Cham: Springer International Publishing.

Gupta, P., Schmid, P. J., Sipp, D., Sayadi, T. & Rigas, G. 2023 Mori-Zwanzig latent space Koopman closure for nonlinear autoencoder, arXiv: 2310.10745.

Guzmán, A. M. & Amon, C. H. 1994 Transition to chaos in converging–diverging channel flows: Ruelle–Takens–Newhouse scenario. *Physics of Fluids* **6** (6), 1994–2002.

Häfeli, R., Altheimer, M., Butscher, D. & von Rohr, P. R. 2014 PIV study of flow through porous structure using refractive index matching. *Experiments in Fluids* **55** (5), 1717.

Hairer, E. & Wanner, G. 2010 Solving Ordinary Differential Equations II: Stiff and Differential-Algebraic Problems, 2nd edn. Springer Series in Computational Mathematics 14. Berlin: Springer.

Hales, T., Adams, M., Bauer, G., Dang, T. D., Harrison, J., Hoang, L. T., Kaliszyk, C., Magron, V., Mclaughlin, S., Nguyen, T. T., Nguyen, Q. T., Nipkow, T., Obua, S., Pleso, J., Rute, J., Solovyev, A., Ta, T. H. A., Tran, N. T., Trieu, T. D., Urban, J., Vu, K. & Zumkeller, R. 2017 A Formal Proof of the Kepler Conjecture. *Forum of Mathematics, Pi* **5**, e2.

Hall, K. R., Smith, G. M. & Turcke, D. J. 1994 Development of a Non-Linear Porous Media Flow Relationship for Oscillatory Unsteady Flow. *Journal of Coastal Research* **10** (1), 158–169.

Hall, K. R., Smith, G. M. & Turcke, D. J. 1995 Comparison of oscillatory and stationary flow through porous media. *Coastal Engineering* **24** (3-4), 217–232.

Hall, P. 1984 On the stability of the unsteady boundary layer on a cylinder oscillating transversely in a viscous fluid. *Journal of Fluid Mechanics* **146**, 347–367.

Hall, P. & Parker, K. H. 1976 The stability of the decaying flow in a suddenly blocked channel. *Journal of Fluid Mechanics* **75** (2), 305–314.

Haller, G. 2004 Exact theory of unsteady separation for two-dimensional flows. *Journal of Fluid Mechanics* **512**, 257–311.

Happel, J. & Brenner, H. 1983 Low Reynolds Number Hydrodynamics: With Special Applications to Particulate Media. Mechanics of Fluids and Transport Processes 1. Dordrecht: Springer Netherlands.

Harlow, F. H. & Welch, J. E. 1965 Numerical Calculation of Time-Dependent Viscous Incompressible Flow of Fluid with Free Surface. *The Physics of Fluids* **8** (12), 2182–2189.

Hartmann, E. 1984 An Introduction to Crystal Physics. Cardiff, Wales: University College Cardiff Press.

Harvey, J. 2023 Oscillatory compressible flow and heat transfer in porous media : Application to cryocooler regenerators. PhD thesis, Georgia Institute of Technology, Atlanta, Georgia.

He, X., Apte, S. V., Finn, J. R. & Wood, B. D. 2019 Characteristics of turbulence in a face-centred cubic porous unit cell. *Journal of Fluid Mechanics* **873**, 608–645.

Helman, J. & Hesselink, L. 1989 Representation and Display of Vector Field Topology in Fluid Flow Data Sets. *Computer* **22**, 27–36.

Hendricks, R. C., Athavale, M. M., Lattime, S. B. & Braun, M. J. 1998 Virtual and Experimental Visualization of Flows in Packed Beds of Spheres Simulating Porous Media Flows. In Eigth International Symposium on Flow Visualization. Sorrento, Italy.

Hill, R. J. & Koch, D. L. 2002 The transition from steady to weakly turbulent flow in a close-packed ordered array of spheres. *Journal of Fluid Mechanics* **465**, 59–97.

Hill, R. J., Koch, D. L. & Ladd, A. J. C. 2001a The first effects of fluid inertia on flows in ordered and random arrays of spheres. *Journal of Fluid Mechanics* **448**, 213–241.

Hill, R. J., Koch, D. L. & Ladd, A. J. C. 2001b Moderate-Reynolds-number flows in ordered and random arrays of spheres. *Journal of Fluid Mechanics* **448**, 243–278.

Hino, M., Sawamoto, M. & Takasu, S. 1976 Experiments on transition to turbulence in an oscillatory pipe flow. *Journal of Fluid Mechanics* **75** (2), 193–207.

Hirsch, C. 2007 Numerical Computation of Internal and External Flows: Fundamentals of Computational Fluid Dynamics, 2nd edn. Oxford; Burlington, MA: Elsevier/Butterworth-Heinemann.

Hoffmann, F. 2020 Introduction to Crystallography. Cham: Springer International Publishing.

Hokpunna, A. & Manhart, M. 2010 Compact fourth-order finite volume method for numerical solutions of Navier–Stokes equations on staggered grids. *Journal of Computational Physics* **229** (20), 7545–7570.

Honji, H. 1981 Streaked flow around an oscillating circular cylinder. *Journal of Fluid Mechanics* **107**, 509–520.

Horton, N. A. & Pokrajac, D. 2009 Onset of turbulence in a regular porous medium: An experimental study. *Physics of Fluids* **21** (4), 045104.

Howe, M. S. 1995 On the Force and Moment on a Body in an Incompressible Fluid, with Application to Rigid Bodies and Bubbles at High and Low Reynolds Numbers. *The Quarterly Journal of Mechanics and Applied Mathematics* **48** (3), 401–426.

Hsu, C.-T., Fu, H. & Cheng, P. 1999 On Pressure-Velocity Correlation of Steady and Oscillating Flows in Regenerators Made of Wire Screens. *Journal of Fluids Engineering* **121** (1), 52–56.

Hui, W. H. 1988 Unsteady three-dimensional flow separation. Contractor Report 19880006379. NASA.

Hunt, J. C. R., Abell, C. J., Peterka, J. A. & Woo, H. 1978 Kinematical studies of the flows around free or surface-mounted obstacles; applying topology to flow visualization. *Journal of Fluid Mechanics* **86** (1), 179–200.

Hunt, J. C. R., Wray, A. A. & Moin, P. 1988 Eddies, streams, and convergence zones in turbulent flows. In Studying Turbulence Using Numerical Simulation Databases, 2. Proceedings of the 1988 Summer Program (ed. P. Moin, W. C. Reynolds & J. Kim), pp. 193–208. Center for Turbulence Research, Stanford.

Iervolino, M., Manna, M. & Vacca, A. 2010 Pulsating Flow through Porous Media. In Turbulence and Interactions (ed. E. H. Hirschel, W. Schröder, K. Fujii, W. Haase, B. van Leer, M. A. Leschziner, M. Pandolfi, J. Periaux, A. Rizzi, B. Roux, Y. I. Shokin, M. Deville, T.-H. Lê & P. Sagaut), , vol. 110, pp. 167–173. Berlin, Heidelberg: Springer Berlin Heidelberg.

Iliuta, I. & Larachi, F. 2016 Three-dimensional simulations of gas-liquid cocurrent downflow in vertical, inclined, and oscillating packed beds. *AIChE Journal* **62** (3), 916–927.

Israelsen, B. W. & Smith, D. A. 2014 Generalized Laguerre Reduction of the Volterra Kernel for Practical Identification of Nonlinear Dynamic Systems. In 2014 Spring Meeting & 10th Global Congress on Process Safety. New Orleans, LA: American Institute of Chemical Engineers.

Jacobs, B. A., Laurén, F. & Nordström, J. 2023 On the order reduction of approximations of fractional derivatives: An explanation and a cure. *BIT Numerical Mathematics* **63** (1), 17.

Jin, L. & Leong, K. C. 2006 Heat Transfer Performance of Metal Foam Heat Sinks Subjected to Oscillating Flow. *IEEE Transactions on Components and Packaging Technologies* **29** (4), 856–863.

Jin, Y., Uth, M.-F., Kuznetsov, A. V. & Herwig, H. 2015 Numerical investigation of the possibility of macroscopic turbulence in porous media: A direct numerical simulation study. *Journal of Fluid Mechanics* **766**, 76–103.

Johns, M. L., Sederman, A. J., Bramley, A. S., Gladden, L. F. & Alexander, P. 2000 Local transitions in flow phenomena through packed beds identified by MRI. *AIChE Journal* **46** (11), 2151–2161.

Johnson, D. L., Koplik, J. & Dashen, R. 1987 Theory of dynamic permeability and tortuosity in fluid-saturated porous media. *Journal of Fluid Mechanics* **176**, 379–402.

Johnson, D. L. & Sen, P. N. 1981 Multiple scattering of acoustic waves with application to the index of refraction of fourth sound. *Physical Review B* **24** (5), 2486–2496.

Johnson, P. L. 2022 A physics-inspired alternative to spatial filtering for large-eddy simulations of turbulent flows. *Journal of Fluid Mechanics* **934**, A30.

Jolls, K. R. & Hanratty, T. J. 1966 Transition to turbulence for flow through a dumped bed of spheres. *Chemical Engineering Science* **21** (12), 1185–1190.

Jolls, K. R. & Hanratty, T. J. 1969 Use of electrochemical techniques to study mass transfer rates and local skin friction to a sphere in a dumped bed. *AIChE Journal* **15** (2), 199–205.

Jouybari, N. F. & Lundström, T. S. 2019 A Subgrid-Scale Model for Turbulent Flow in Porous Media. *Transport in Porous Media* **129** (3), 619–632.

Jubin, B. 2009 A generalized Poincaré-Hopf index theorem , arXiv: 0903.0697.

Kahler, D. M. & Kabala, Z. J. 2019 Acceleration of Groundwater Remediation by Rapidly Pulsed Pumping: Laboratory Column Tests. *Journal of Environmental Engineering* **145** (1), 06018009.

Kaltenbach, S. & Koutsourelakis, P.-S. 2020 Incorporating physical constraints in a deep probabilistic machine learning framework for coarse-graining dynamical systems. *Journal of Computational Physics* **419**, 109673.

Kaltenbach, S. & Koutsourelakis, P.-S. 2021 Physics-Aware, Probabilistic Model Order Reduction with Guaranteed Stability. In International Conference on Learning Representations. Vienna.

Kantz, H. & Schreiber, T. 2003 Nonlinear Time Series Analysis, 2nd edn. Cambridge: Cambridge University Press.

Kaptanoglu, A. A., Callaham, J. L., Aravkin, A., Hansen, C. J. & Brunton, S. L. 2021 Promoting global stability in data-driven models of quadratic nonlinear dynamics. *Physical Review Fluids* **6** (9), 094401.

Karabelas, A. J., Wegner, T. H. & Hanratty, T. J. 1973 Flow pattern in a close packed cubic array of spheres near the critical Reynolds number. *Chemical Engineering Science* **28** (3), 673–682.

Karniadakis, G. E., Kevrekidis, I. G., Lu, L., Perdikaris, P., Wang, S. & Yang, L. 2021 Physics-informed machine learning. *Nature Reviews Physics* **3** (6), 422–440.

Kenwright, D. N. 1998 Automatic detection of open and closed separation and attachment lines. In Proceedings Visualization '98 (Cat. No.98CB36276), pp. 151–158. Research Triangle Park, NC: IEEE.

Kingston, G. & Nunge, R. J. 1973 Transition to unsteady flow and intensity of velocity fluctuations in a porous medium. *The Canadian Journal of Chemical Engineering* **51** (2), 246–248.

Koch, D. L. & Ladd, A. J. C. 1997 Moderate Reynolds number flows through periodic and random arrays of aligned cylinders. *Journal of Fluid Mechanics* **349**, 31–66.

Kooshapur, S. 2016 Modelling dispersion on the pore scale based on the velocity distribution function. PhD thesis, Technische Universität München, München.

Kress, W. & Lötstedt, P. 2006 Time step restrictions using semi-explicit methods for the incompressible Navier–Stokes equations. *Computer Methods in Applied Mechanics and Engineering* **195** (33), 4433–4447.

Kuroki, M., Ookawara, S. & Ogawa, K. 2009 A High-Fidelity CFD Model of Methane Steam Reforming in a Packed Bed Reactor. *Journal of Chemical Engineering of Japan* **42** (Supplement 1), S73–S78.

Kutiĺek, M. 1972 Non-Darcian Flow of Water in Soils — Laminar Region. In Fundamentals of Transport Phenomena in Porous Media (ed. IAHR International Association for Hydraulic Research), Developments in Soil Science 2, pp. 327–340. Amsterdam; London; New York: Elsevier.

Kuwata, Y., Suga, K. & Sakurai, Y. 2014 Development and application of a multi-scale k–ϵ model for turbulent porous medium flows. *International Journal of Heat and Fluid Flow* **49**, 135–150.

Kwok, Y.-K. & Tam, K.-K. 1993 Linearized stability analysis of staggered-grid difference schemes for multidimensional viscous incompressible flows. *Numerical Methods for Partial Differential Equations* **9** (3), 313–322.

Lafarge, D. 1993 Propagation du son dans les matériaux poreux á structure rigide saturés par un fluide viscothermique: Définition de paramètres géométriques, analogie electromagnétique, temps de relaxation. PhD thesis, Université du Maine, Le Mans.

Lafarge, D. 2009 The Equivalent Fluid Model. In Materials and Acoustics Handbook (ed. M. Bruneau & C. Potel), pp. 153–204. London: ISTE.

Lamb, H. 1945 Hydrodynamics, 6th edn. New York: Dover publications.

Landau, L. D. & Lifshits, E. M. 1987 Fluid Mechanics, 2nd edn., *Course of Theoretical Physics*, vol. 6. Oxford, England ; New York: Pergamon Press.

Landauer, R. 1952 The Electrical Resistance of Binary Metallic Mixtures. *Journal of Applied Physics* **23** (7), 779–784.

Lasseux, D., Abbasian Arani, A. A. & Ahmadi, A. 2011 On the stationary macroscopic inertial effects for one phase flow in ordered and disordered porous media. *Physics of Fluids* **23** (7), 073103.

Lasseux, D. & Valdés-Parada, F. J. 2017 Symmetry properties of macroscopic transport coefficients in porous media. *Physics of Fluids* **29** (4), 043303.

Lasseux, D., Valdés-Parada, F. J. & Bellet, F. 2019 Macroscopic model for unsteady flow in porous media. *Journal of Fluid Mechanics* **862**, 283–311.

Lau, A., Crittenden, B. D. & Field, R. W. 2004 Enhancement of liquid phase adsorption column performance by means of oscillatory flow: An experimental study. *Separation and Purification Technology* **35** (2), 113–124.

Lauschke, G. & Gilles, E. 1994 Circulating reaction zones in a packed-bed loop reactor. *Chemical Engineering Science* **49** (24, Part 2), 5359–5375.

Lee, C.-Y., Leamy, M. J. & Nadler, J. H. 2009 Acoustic absorption calculation in irreducible porous media: A unified computational approach. *The Journal of the Acoustical Society of America* **126** (4), 1862–1870.

Lester, D. R., Metcalfe, G. & Trefry, M. G. 2013 Is Chaotic Advection Inherent to Porous Media Flow? *Physical Review Letters* **111** (17), 174101.

Lévy, T. 1987 Introduction to homogenization theory. In Homogenization Techniques for Composite Media (ed. Enrique Sanchez-Palencia & André Zaoui), Lecture Notes in Physics 272, pp. 63–74. Berlin, Heidelberg: Springer Berlin Heidelberg.

Li, J. & Wu, Z.-N. 2018 Vortex force map method for viscous flows of general airfoils. *Journal of Fluid Mechanics* **836**, 145–166.

Li, P., Collis, J. F., Brumley, D. R., Schneiders, L. & Sader, J. E. 2023 Structure of the streaming flow generated by a sphere in a fluid undergoing rectilinear oscillation. *Journal of Fluid Mechanics* **974**, A37.

Li, S.-H., Dong, C.-X., Zhang, L. & Wang, L. 2020 Neural Canonical Transformation with Symplectic Flows. *Physical Review X* **10** (2), 021020.

Lighthill, J. 1978 Acoustic streaming. *Journal of Sound and Vibration* **61** (3), 391–418.

Lighthill, M. J. 1963 Attachment and separation in three-dimensional flow. In Laminar Boundary Layers (ed. L. Rosenhead), The Fluid Motion Memoirs , pp. 72–82. Oxford: Oxford University Press.

Lindeberg, T. 1994 Scale-space theory: A basic tool for analyzing structures at different scales. *Journal of Applied Statistics* **21** (1-2), 225–270.

Lingnau, B., Shortiss, K., Dubois, F., Peters, F. H. & Kelleher, B. 2020 Universal generation of devil's staircases near Hopf bifurcations via modulated forcing of nonlinear systems. *Physical Review E* **102** (3), 030201.

Liu, C., Gao, Y., Tian, S. & Dong, X. 2018 Rortex—A new vortex vector definition and vorticity tensor and vector decompositions. *Physics of Fluids* **30** (3), 035103.

Liu, L., Deng, J., Zhang, D. & Gu, H. 2021 Review of the experimental research on the thermal-hydraulic characteristics in the pebble bed nuclear reactor core and fusion breeder blankets. *International Journal of Energy Research* **45** (8), 11352–11383.

Liu, T., Woodiga, S. & Ma, T. 2011 Skin friction topology in a region enclosed by penetrable boundary. *Experiments in Fluids* **51** (6), 1549–1562.

Lomax, H., Pulliam, T. H & Zingg, D. W 2011 Fundamentals of Computational Fluid Dynamics. Scientific Computation . Berlin; London: Springer.

Losada, I. J., Losada, M. A. & Martín, F. L. 1995 Experimental study of wave-induced flow in a porous structure. *Coastal Engineering* **26** (1-2), 77–98.

Lowe, R. J., Falter, J. L., Koseff, J. R., Monismith, S. G. & Atkinson, M. J. 2007 Spectral wave flow attenuation within submerged canopies: Implications for wave energy dissipation. *Journal of Geophysical Research* **112**, C05018.

Lowe, R. J., Koseff, J. R., Monismith, S. G. & Falter, J. L. 2005 Oscillatory flow through submerged canopies: 2. Canopy mass transfer. *Journal of Geophysical Research* **110**, C10017.

Lowe, R. J., Shavit, U., Falter, J. L., Koseff, J. R. & Monismith, S. G. 2008 Modeling flow in coral communities with and without waves: A synthesis of porous media and canopy flow approaches. *Limnology and Oceanography* **53** (6), 2668–2680.

Luévano-Rivas, O. A., Quiroz-Ramirez, J. J., Suarez-Toriello, V. A., Huerta-Rosas, B., Sánchez-Ramirez, E. & Segovia-Hernández, J. G. 2023 Upscaling of mass and heat transport applied to reactive packing catalytic porous media. *Chemical Engineering Science* **265**, 118206.

Macdonald, I. F., El-Sayed, M. S., Mow, K. & Dullien, F. A. L. 1979 Flow through Porous Media-the Ergun Equation Revisited. *Industrial & Engineering Chemistry Fundamentals* **18** (3), 199–208.

Maier, R. S., Kroll, D. M., Kutsovsky, Y. E., Davis, H. T. & Bernard, R. S. 1998 Simulation of flow through bead packs using the lattice Boltzmann method. *Physics of Fluids* **10** (1), 60–74.

Manhart, M. 2004 A zonal grid algorithm for DNS of turbulent boundary layers. *Computers & Fluids* **33** (3), 435–461.

Manhart, M., Tremblay, F. & Friedrich, R. 2001 MGLET: A parallel code for efficient DNS and LES of complex geometries. In Parallel Computational Fluid Dynamics 2000 (ed. C. B. Jenssen, T. Kvamsdal, H. I. Andersson, B. Pettersen, A. Ecer, J. Periaux, N. Satofuka & P. Fox), pp. 449–456. Amsterdam: North-Holland.

Manor, O. 2021 Acoustic flow in porous media. *Journal of Fluid Mechanics* **920**, A11.

Marmarelis, V. Z. & Zhao, X. 1997 Volterra models and three-layer perceptrons. *IEEE Transactions on Neural Networks* **8** (6), 1421–1433.

Martin, H. 2010 Dimensionless Numbers. In VDI Heat Atlas, 2nd edn. (ed. VDI e. V.), pp. 11–13. Berlin, Heidelberg: Springer Berlin Heidelberg.

Masuoka, T. & Takatsu, Y. 1996 Turbulence model for flow through porous media. *International Journal of Heat and Mass Transfer* **39** (13), 2803–2809.

Matthischke, S., Krüger, R., Rönsch, S. & Güttel, R. 2016 Unsteady-state methanation of carbon dioxide in a fixed-bed recycle reactor — Experimental results for transient flow rate ramps. *Fuel Processing Technology* **153**, 87–93.

Mazzi, V., Gallo, D., Calò, K., Najafi, M., Khan, M. O., De Nisco, G., Steinman, D. A. & Morbiducci, U. 2019 A Eulerian method to analyze wall shear stress fixed points and manifolds in cardiovascular flows. *Biomechanics and Modeling in Mechanobiology* **19**, 1403–1423.

McGlone, T., Briggs, N. E. B., Clark, C. A., Brown, C. J., Sefcik, J. & Florence, A. J. 2015 Oscillatory Flow Reactors (OFRs) for Continuous Manufacturing and Crystallization. *Organic Process Research & Development* **19** (9), 1186–1202.

Mei, C. C. & Auriault, J.-L. 1991 The effect of weak inertia on flow through a porous medium. *Journal of Fluid Mechanics* **222**, 647–663.

Mei, R. 1994 Flow due to an oscillating sphere and an expression for unsteady drag on the sphere at finite Reynolds number. *Journal of Fluid Mechanics* **270**, 133–174.

Mei, R. & Adrian, R. J. 1992 Flow past a sphere with an oscillation in the free-stream velocity and unsteady drag at finite Reynolds number. *Journal of Fluid Mechanics* **237**, 323–341.

Menier, E., Bucci, M. A., Yagoubi, M., Mathelin, L. & Schoenauer, M. 2023a CD-ROM: Complemented Deep-Reduced Order Model. *Computer Methods in Applied Mechanics and Engineering* **410**, 115985.

Menier, E., Kaltenbach, S., Yagoubi, M., Schoenauer, M. & Koumoutsakos, P. 2023b Interpretable learning of effective dynamics for multiscale systems , arXiv: 2309.05812.

Menon, K. & Mittal, R. 2021 On the initiation and sustenance of flow-induced vibration of cylinders: Insights from force partitioning. *Journal of Fluid Mechanics* **907**, A37.

Meyer, D. W. & Tchelepi, H. A. 2010 Particle-based transport model with Markovian velocity processes for tracer dispersion in highly heterogeneous porous media. *Water Resources Research* **46** (11).

Meyer, D. W. & Tchelepi, H. A. 2011 Correction to "Particle-based transport model with Markovian velocity processes for tracer dispersion in highly heterogeneous porous media". *Water Resources Research* **47** (11).

Meyer, M., Devesa, A., Hickel, S., Hu, X. Y. & Adams, N. A. 2010 A conservative immersed interface method for Large-Eddy Simulation of incompressible flows. *Journal of Computational Physics* **229** (18), 6300–6317.

Miguel, A. F. 2012 Lungs as a Natural Porous Media: Architecture, Airflow Characteristics and Transport of Suspended Particles. In Heat and Mass Transfer in Porous Media (ed. J. M. P. Q. Delgado), Advanced Structured Materials 13, pp. 115–137. Berlin, Heidelberg: Springer Berlin Heidelberg.

Mittal, R. & Iaccarino, G. 2005 Immersed Boundary Methods. *Annual Review of Fluid Mechanics* **37** (1), 239–261.

Moffatt, H. K. 2014 Helicity and singular structures in fluid dynamics. *Proceedings of the National Academy of Sciences* **111** (10), 3663–3670.

Moffatt, H. K. 2021 Some topological aspects of fluid dynamics. *Journal of Fluid Mechanics* **914**, P1.

Mohan Rai, M. & Moin, P. 1991 Direct simulations of turbulent flow using finite-difference schemes. *Journal of Computational Physics* **96** (1), 15–53.

Moin, P. & Mahesh, K. 1998 Direct Numerical Simulation: A Tool in Turbulence Research. *Annual Review of Fluid Mechanics* **30** (1), 539–578.

Montillet, A. 2004 Flow Through a Finite Packed Bed of Spheres: A Note on the Limit of Applicability of the Forchheimer-Type Equation. *Journal of Fluids Engineering* **126** (1), 139–143.

Moon, P. H. & Spencer, D. E. 1988 Field Theory Handbook: Incl. Coordinate Systems, Differential Equations and Their Solutions, 2nd edn. Berlin: Springer.

Müller-Trefzer, F., Niedermeier, K., Daubner, M. & Wetzel, T. 2022 Experimental investigations on the design of a dual-media thermal energy storage with liquid metal. *Applied Thermal Engineering* **213**, 118619.

Murthy, P. V. S. N. & Singh, P. 1997 Effect of viscous dissipation on a non-Darcy natural convection regime. *International Journal of Heat and Mass Transfer* **40** (6), 1251–1260.

Muttray, M. 2000 Wellenbewegung an und in einem geschütteten Wellenbrecher - Laborexperimente im Großmaßstab und theoretische Untersuchungen. PhD thesis, Technische Universität Braunschweig, Braunschweig.

Muzychka, Y. S. & Yovanovich, M. M. 2006 Unsteady Viscous Flows and Stokes's First Problem. In Fluids Engineering, ASME International Mechanical Engineering Congress and Exposition , pp. 89–99. Chicago, IL: ASMEDC.

Nakajo, S., Shigematsu, T., Sakashita, N., Tsujimoto, G. & Takehara, K. 2008 An Experimental Study on the Effect of Oscillatory Flow on Turbulence Propertiesinduced by Porous Media. In Proceedings of Coastal Engineering, JSCE, , vol. 55, pp. 841–845.

Nakajo, S., Shigematsu, T., Sakashita, N., Tsujimoto, G. & Takehara, K. 2009 120. oscillatory turbulent flow inside and around porous media. In Proceedings of Coastal Dynamics 2009, pp. 1–14. World Scientific.

Nakayama, A. & Kuwahara, F. 1999 A Macroscopic Turbulence Model for Flow in a Porous Medium. *Journal of Fluids Engineering* **121** (2), 427–433.

Nave, G. K., Nolan, P. J. & Ross, S. D. 2019 Trajectory-free approximation of phase space structures using the trajectory divergence rate. *Nonlinear Dynamics* **96** (1), 685–702.

Nayfeh, A. H. & Balachandran, B. 2008 Applied Nonlinear Dynamics: Analytical, Computational, and Experimental Methods, 1st edn. Wiley Series in Nonlinear Science . Weinheim: Wiley-VCH.

Nelson, B. L. 2009 Scaling Analysis for the Pebble Bed of the Very High Temperature Gas-cooled Reactor Thermal Hydraulic Test Facility. M.Sc. thesis, Oregon State University, Corvallis, OR.

Newhouse, S., Ruelle, D. & Takens, F. 1978 Occurrence of strange AxiomA attractors near quasi periodic flows on T^m, $m \geqq 3$. *Communications in Mathematical Physics* **64** (1), 35–40.

Ni, M., Peng, H., Sultan, U., Luo, K. & Xiao, G. 2018 A quantitative method to describe the flow characteristics of an oscillating flow including porous media. *International Journal of Heat and Mass Transfer* **119**, 860–866.

Ni, X., Mackley, M. R., Harvey, A. P., Stonestreet, P., Baird, M. H. I. & Rama Rao, N. V. 2003 Mixing Through Oscillations and Pulsations—A Guide to Achieving Process Enhancements in the Chemical and Process Industries. *Chemical Engineering Research and Design* **81** (3), 373–383.

Nicoud, F. & Ducros, F. 1999 Subgrid-Scale Stress Modelling Based on the Square of the Velocity Gradient Tensor. *Flow, Turbulence and Combustion* **62** (3), 183–200.

Nield, D. A. 1991 The limitations of the Brinkman-Forchheimer equation in modeling flow in a saturated porous medium and at an interface. *International Journal of Heat and Fluid Flow* **12** (3), 269–272.

Ogawa, K., Yoshikawa, S. & Lee, J. S. 1991 Effect of packing arrangement on flow characteristics and mass transfer on the surface of a packing sphere. *Journal of Chemical Engineering of Japan* **24** (6), 788–793.

Omichi, H., Ishize, T. & Fukagata, K. 2023 Machine learning based dimension reduction for a stable modeling of periodic flow phenomena, arXiv: 2311.08765.

Orszag, S. A. 1971 Accurate solution of the Orr–Sommerfeld stability equation. *Journal of Fluid Mechanics* **50** (4), 689–703.

Otto, S. R. 1992 On stability of the flow around an oscillating sphere. *Journal of Fluid Mechanics* **239**, 47–63.

Ozdemir, C. E., Hsu, T.-J. & Balachandar, S. 2014 Direct numerical simulations of transition and turbulence in smooth-walled Stokes boundary layer. *Physics of Fluids* **26** (4), 045108.

Paek, J. W., Kang, B. H. & Hyun, J. M. 1999 Transient cool-down of a porous medium in pulsating flow. *International Journal of Heat and Mass Transfer* **42** (18), 3523–3527.

Paéz-García, C. T., Valdés-Parada, F. J. & Lasseux, D. 2017 Macroscopic momentum and mechanical energy equations for incompressible single-phase flow in porous media. *Physical Review E* **95** (2), 023101.

Pamuk, M. T. & Özdemir, M. 2014 Hydrodynamic Aspects of Oscillating Flow Through Porous Media Consisting of Steel Spheres. In Progress in Exergy, Energy, and the Environment (ed. I. Dincer, A. Midilli & H. Kucuk), pp. 633–640. Cham: Springer International Publishing.

Pasol, L., Chaoui, M., Yahiaoui, S. & Feuillebois, F. 2005 Analytical solutions for a spherical particle near a wall in axisymmetrical polynomial creeping flows. *Physics of Fluids* **17** (7), 073602.

Patankar, S. V., Liu, C. H. & Sparrow, E. M. 1977 Fully Developed Flow and Heat Transfer in Ducts Having Streamwise-Periodic Variations of Cross-Sectional Area. *Journal of Heat Transfer* **99** (2), 180–186.

Patankar, S. V. & Spalding, D. B. 1974 A calculation procedure for the transient and steady-state behavior of shell-and-tube heat exchangers. In Heat exchangers: Design and Theory Sourcebook (ed. N. Afgan & E. U. Schlünder), , vol. 1. Washington, D.C.: Scripta Book Company.

Patankar, S. V. & Spalding, D. B. 1978 Computer analysis of the three-dimensional flow and heat transfer in a steam generator. *Forschung im Ingenieurwesen* **44** (2), 47–52.

Pathak, M. G. 2013 Periodic flow physics in porous media of regenerative cryocoolers. PhD thesis, Georgia Institute of Technology, Atlanta, Georgia.

Pathak, M. G. & Ghiaasiaan, S. M. 2011 Convective heat transfer and thermal dispersion during laminar pulsating flow in porous media. *International Journal of Thermal Sciences* **50** (4), 440–448.

Patil, V. A. & Liburdy, J. A. 2013a Flow structures and their contribution to turbulent dispersion in a randomly packed porous bed based on particle image velocimetry measurements. *Physics of Fluids* **25** (11), 113303.

Patil, V. A. & Liburdy, J. A. 2013b Turbulent flow characteristics in a randomly packed porous bed based on particle image velocimetry measurements. *Physics of Fluids* **25** (4), 043304.

Patil, V. A. & Liburdy, J. A. 2015 Scale estimation for turbulent flows in porous media. *Chemical Engineering Science* **123**, 231–235.

Pawar, S., San, O., Aksoylu, B., Rasheed, A. & Kvamsdal, T. 2021 Physics guided machine learning using simplified theories. *Physics of Fluids* **33** (1), 011701.

Peller, N. 2010 Numerische Simulation turbulenter Strömungen mit Immersed Boundaries. PhD thesis, Technische Universität München, München.

Perrella, M. D. 2017 Periodic Flow Hydrodynamic Resistance Parameters for Various Regenerator Filler Materials at Cryogenic Temperatures. PhD thesis, Georgia Institute of Technology, Atlanta, Georgia.

Polubarinova-Kochina, P. I. 1962 Theory of Ground Water Movement. Princeton, NJ: Princeton University Press.

Pope, S. B. 2000 Turbulent Flows. Cambridge ; New York: Cambridge University Press.

Pozrikidis, C. 2017 Fluid Dynamics: Theory, Computation, and Numerical Simulation, 3rd edn. Springer US.

Pride, S. R., Morgan, F. D. & Gangi, A. F. 1993 Drag forces of porous-medium acoustics. *Physical Review B* **47** (9), 4964–4978.

Rao, F. & Jin, Y. 2022 Possibility for survival of macroscopic turbulence in porous media with high porosity. *Journal of Fluid Mechanics* **937**, A17.

Redeker, M. & Haasdonk, B. 2016 A POD–EIM reduced two-scale model for precipitation in porous media. *Mathematical and Computer Modelling of Dynamical Systems* **22** (4), 323–344.

Ren, J., Mao, X. & Fu, S. 2021 Image-based flow decomposition using empirical wavelet transform. *Journal of Fluid Mechanics* **906**, A36.

Richardson, E. G. & Tyler, E. 1929 The transverse velocity gradient near the mouths of pipes in which an alternating or continuous flow of air is established. *Proceedings of the Physical Society* **42** (1), 1–15.

Ricke, A., Sadeghi, M. & Dreher, W. 2023 Magnetic Resonance Velocimetry for porous media: Sources and reduction of measurement errors for improved accuracy. *Experiments in Fluids* **64** (7), 132.

Riley, N. 1967 Oscillatory Viscous Flows. Review and Extension. *IMA Journal of Applied Mathematics* **3** (4), 419–434.

Roberts, E. P. L. & Mackley, M. R. 1996 The development of asymmetry and period doubling for oscillatory flow in baffled channels. *Journal of Fluid Mechanics* **328**, 19–48.

Rode, S., Midoux, N., Latifi, M. A., Storck, A. & Saatdjian, E. 1994 Hydrodynamics of liquid flow in packed beds: An experimental study using electrochemical shear rate sensors. *Chemical Engineering Science* **49** (6), 889–900.

Rojas, S. & Koplik, J. 1998 Nonlinear flow in porous media. *Physical Review E* **58** (4), 4776–4782.

Rubinstein, J. & Torquato, S. 1989 Flow in random porous media: Mathematical formulation, variational principles, and rigorous bounds. *Journal of Fluid Mechanics* **206**, 25–46.

Ruelle, D. & Takens, F. 1971 On the nature of turbulence. *Communications in Mathematical Physics* **20** (3), 167–192.

Rugh, W. J. 1981 Nonlinear System Theory: The Volterra/Wiener Approach. Johns Hopkins Series in Information Sciences and Systems . Baltimore: Johns Hopkins University Press.

Saberinejad, H. & Keshavarz, A. 2016 Reciprocating turbulent flow heat transfer enhancement within a porous medium embedded in a circular tube. *Applied Thermal Engineering* **102**, 1355–1365.

Sakai, Y. & Manhart, M. 2020 Consistent Flow Structure Evolution in Accelerating Flow Through Hexagonal Sphere Pack. *Flow, Turbulence and Combustion* **105** (2), 581–606.

Sakai, Y. & Manhart, M. 2022 Why Velocity Overshoots in Accelerating Porous Media. In Proceedings of TSFP-12 (2022) Osaka. Osaka.

Sakai, Y., Mendez, S., Strandenes, H., Ohlerich, M., Pasichnyk, I., Allalen, M. & Manhart, M. 2019 Performance Optimisation of the Parallel CFD Code MGLET across Different HPC Platforms. In Proceedings of the Platform for Advanced Scientific Computing Conference, PASC '19 . Zurich: ACM Press.

Santhosh, S., Qin, H., Klose, B. F., Jacobs, G. B., Vétel, J. & Serra, M. 2023 Spike formation theory in three-dimensional flow separation. *Journal of Fluid Mechanics* **969**, A25.

Satish, S., Leontini, J. S., Manasseh, R., Sannasiraj, S. A. & Sundar, V. 2022 Numerical Investigation on the Mean Flow Fields Generated by an Oscillating Sphere. In OCEANS 2022 - Chennai, pp. 1–5. Chennai: IEEE.

Schetzen, M. 1980 The Volterra and Wiener Theories of Nonlinear Systems. New York: Wiley.

Schlichting, H. & Gersten, K. 2017 Boundary-Layer Theory. Berlin, Heidelberg: Springer Berlin Heidelberg.

Schmid, P. J. 2007 Nonmodal Stability Theory. *Annual Review of Fluid Mechanics* **39** (1), 129–162.

Schmid, P. J. & Henningson, D. S. 2001 Stability and Transition in Shear Flows. Applied Mathematical Sciences 142. New York: Springer New York.

Schroeder, W., K., Martin. & Lorensen, B. 2006 The Visualization Toolkit (4th ed.). Kitware.

Schure, M. R., Maier, R. S., Kroll, D. M. & Davis, H. T. 2004 Simulation of ordered packed beds in chromatography. *Journal of Chromatography A* **1031** (1-2), 79–86.

Schwertfirm, F., Mathew, J. & Manhart, M. 2008 Improving spatial resolution characteristics of finite difference and finite volume schemes by approximate deconvolution pre-processing. *Computers & Fluids* **37** (9), 1092–1102.

Seguin, D., Montillet, A. & Comiti, J. 1998a Experimental characterisation of flow regimes in various porous media—I: Limit of laminar flow regime. *Chemical Engineering Science* **53** (21), 3751–3761.

Seguin, D., Montillet, A., Comiti, J. & Huet, F. 1998b Experimental characterization of flow regimes in various porous media—II: Transition to turbulent regime. *Chemical Engineering Science* **53** (22), 3897–3909.

Serra, M., Crouzat, S., Simon, G., Vétel, J. & Haller, G. 2020 Material spike formation in highly unsteady separated flows. *Journal of Fluid Mechanics* **883**, A30.

Serra, M., Vétel, J. & Haller, G. 2018 Exact theory of material spike formation in flow separation. *Journal of Fluid Mechanics* **845**, 51–92.

Sexl, T. 1930 Über den von E. G. Richardson entdeckten "Annulareffekt". *Zeitschrift für Physik* **61** (5-6), 349–362.

Shams, A., Roelofs, F., Komen, E.M.J. & Baglietto, E. 2014 Large eddy simulation of a randomly stacked nuclear pebble bed. *Computers & Fluids* **96**, 302–321.

Shankar, V., Portwood, G. D., Mohan, A. T., Mitra, P. P., Krishnamurthy, D., Rackauckas, C., Wilson, L. A., Schmidt, D. P. & Viswanathan, V. 2022 Validation and parameterization of a novel physics-constrained neural dynamics model applied to turbulent fluid flow. *Physics of Fluids* **34** (11), 115110.

Sharma, P., Chung, W. T., Akoush, B. & Ihme, M. 2023 A Review of Physics-Informed Machine Learning in Fluid Mechanics. *Energies* **16** (5), 2343.

Sherwin, S.J. & Karniadakis, G. E. 1996 Tetrahedral hp Finite Elements: Algorithms and Flow Simulations. *Journal of Computational Physics* **124** (1), 14–45.

Simon, T. W. & Seume, J. R. 1988 A Survey of Oscillating Engine Heat Exchangers. Tech. Rep. NASA-CR-182108. University of Minnesota, Minneapolis, MN.

Skjetne, E. & Auriault, J.-L. 1999a High-Velocity Laminar and Turbulent Flow in Porous Media. *Transport in Porous Media* **36** (2), 131–147.

Skjetne, E. & Auriault, J.-L. 1999b New insights on steady, non-linear flow in porous media. *European Journal of Mechanics - B/Fluids* **18** (1), 131–145.

Skraba, P., Wang, B., Chen, G. & Rosen, P. 2014 2D Vector Field Simplification Based on Robustness. In 2014 IEEE Pacific Visualization Symposium, pp. 49–56.

Slattery, J. C. 1967 Flow of viscoelastic fluids through porous media. *AIChE Journal* **13** (6), 1066–1071.

Smeulders, D. M. J., Eggels, R. L. G. M. & Van Dongen, M. E. H. 1992 Dynamic permeability: Reformulation of theory and new experimental and numerical data. *Journal of Fluid Mechanics* **245**, 211–227.

Smith, G. M 1991 Comparison of stationary and oscillatory flow through porous media. M.Sc. thesis, Queen's University, Kingston, ON.

Soldner, D., Brands, B., Zabihyan, R., Steinmann, P. & Mergheim, J. 2016 Computational Homogenisation using Reduced-Order Modelling applied to Hyperelasticity. *PAMM* **16** (1), 551–552.

Sollitt, C. K. & Cross, R. H. 1972 Wave Transmission through Permeable Breakwaters. In Coastal Engineering 1972, pp. 1827–1846. Vancouver, British Columbia: American Society of Civil Engineers.

Souzy, M., Lhuissier, H., Méheust, Y., Le Borgne, T. & Metzger, B. 2020 Velocity distributions, dispersion and stretching in three-dimensional porous media. *Journal of Fluid Mechanics* **891**, A16.

Srikanth, V., Huang, C.-W., Su, T. S. & Kuznetsov, A. V. 2021 Symmetry breaking of turbulent flow in porous media composed of periodically arranged solid obstacles. *Journal of Fluid Mechanics* **929**, A2.

Stark, J. 1999 Delay Embeddings for Forced Systems. I. Deterministic Forcing. *Journal of Nonlinear Science* **9** (3), 255–332.

Stiess, M. 2009 Mechanische Verfahrenstechnik - Partikeltechnologie 1, 3rd edn. Springer-Lehrbuch . Berlin: Springer.

Stokes, G. G. 1851 On the Effect of the Internal Friction of Fluids on the Motion of Pendulums. *Transactions of the Cambridge Philosophical Society* **9** (2).

Straub, A., Karch, G. K., Sadlo, F. & Ertl, T. 2021 Implicit Visualization of 2D Vector Field Topology for Periodic Orbit Detection. In Topological Methods in Data Analysis and Visualization VI (ed. I. Hotz, T. Bin Masood, F. Sadlo & J. Tierny), Mathematics and Visualization , pp. 159–180. Cham: Springer International Publishing.

Stroud, D. 1975 Generalized effective-medium approach to the conductivity of an inhomogeneous material. *Physical Review B* **12** (8), 3368–3373.

Suekane, T., Yokouchi, Y. & Hirai, S. 2003 Inertial flow structures in a simple-packed bed of spheres. *AIChE Journal* **49** (1), 10–17.

Takens, F. 1981 Detecting strange attractors in turbulence. In Dynamical Systems and Turbulence, Warwick 1980 (ed. D. Rand & L.-S. Young), Lecture Notes in Mathematics , pp. 366–381. Berlin, Heidelberg: Springer.

Teruel, F. E. & Rizwan-uddin 2009a A new turbulence model for porous media flows. Part I: Constitutive equations and model closure. *International Journal of Heat and Mass Transfer* **52** (19-20), 4264–4272.

Teruel, F. E. & Rizwan-uddin 2009b A new turbulence model for porous media flows. Part II: Analysis and validation using microscopic simulations. *International Journal of Heat and Mass Transfer* **52** (21), 5193–5203.

Theisel, H., Weinkauf, T., Hege, H.-C. & Seidel, H.-P. 2003 Saddle connectors - an approach to visualizing the topological skeleton of complex 3D vector fields. In IEEE Transactions on Ultrasonics, Ferroelectrics and Frequency Control, pp. 225–232. Seattle, WA: IEEE.

Theofilis, V. 2011 Global Linear Instability. *Annual Review of Fluid Mechanics* **43** (1), 319–352.

Thomas, C., Bassom, A. P. & Blennerhassett, P. J. 2012 The linear stability of oscillating pipe flow. *Physics of Fluids* **24** (1), 014106.

Thompson, J., Stewart, H. & Ueda, Y. 1994 Safe, explosive, and dangerous bifurcations in dissipative dynamical systems. *Physical review. E, Statistical physics, plasmas, fluids, and related interdisciplinary topics* **49**, 1019–1027.

Tobak, M. 1997 Topologically derived separation onset conditions for two- and three-dimensional laminar flows. In 35th Aerospace Sciences Meeting and Exhibit. Reno,NV,U.S.A.: American Institute of Aeronautics and Astronautics.

Trevizoli, P. V., Peixer, G. F. & Barbosa, J. R. 2016 Thermal–hydraulic evaluation of oscillating-flow regenerators using water: Experimental analysis of packed beds of spheres. *International Journal of Heat and Mass Transfer* **99**, 918–930.

Tsao, W.-H., Chen, Y.-C., Kees, C. E. & Manuel, L. 2022 The Effect of Porous Media on Wave-Induced Sloshing in a Floating Tank. *Applied Sciences* **12** (11), 5587.

Turo, D. & Umnova, O. 2013 Influence of Forchheimer's nonlinearity and transient effects on pulse propagation in air saturated rigid granular materials. *The Journal of the Acoustical Society of America* **134** (6), 4763–4774.

Unglehrt, L., Jenssen, U., Kurz, F., Schanderl, W., Kreuzinger, J., Schwertfirm, F. & Manhart, M. 2022a Large–Eddy Simulation of the Flow Inside a Scour Hole Around a Circular Cylinder Using a Cut Cell Immersed Boundary Method. *Flow, Turbulence and Combustion* .

Unglehrt, L., Kreuzinger, J. & Manhart, M. 2022b A wall model for high-fidelity large-eddy simulation. In Proc. Conference on Modelling Fluid Flow (CMFF'22), p. 117. Budapest.

Unglehrt, L. & Manhart, M. 2022a Onset of nonlinearity in oscillatory flow through a hexagonal sphere pack. *Journal of Fluid Mechanics* **944**, A30.

Unglehrt, L. & Manhart, M. 2022b Symmetry Breaking and Turbulence in Oscillatory Flow Through a Hexagonal Sphere Pack. In Proceedings of TSFP-12 (2022) Osaka. Osaka.

Unglehrt, L. & Manhart, M. 2023a Decomposition of the drag force in steady and oscillatory flow through a hexagonal sphere pack. *Journal of Fluid Mechanics* **974**, A32.

Unglehrt, L. & Manhart, M. 2023b Direct and Large–Eddy simulation of turbulent oscillatory flow through a hexagonal sphere pack. In Direct and Large Eddy Simulation XIII: Proceedings of DLES13, 1st edn. (ed. C. Marchioli, M. V. Salvetti, M. Garcia-Villalba & P. Schlatter), ERCOFTAC Series 31, pp. 118–123. Cham: Springer Cham.

van Gent, M. R. A. 1993 Stationary and oscillatory flow through coarse porous media. *Communications on hydraulic and geotechnical engineering* **No. 1993-09**.

van Gent, M. R. A. 1994 The modelling of wave action on and in coastal structures. *Coastal Engineering* **22** (3-4), 311–339.

van Hinsberg, M. A. T., ten Thije Boonkkamp, J. H. M. & Clercx, H. J. H. 2011 An efficient, second order method for the approximation of the Basset history force. *Journal of Computational Physics* **230** (4), 1465–1478.

Varga, R. S. 2004 Geršgorin and His Circles. Springer Series in Computational Mathematics 36. Berlin, New York: Springer.

Vasheghani Farahani, M. & Mousavi Nezhad, M. 2022 On the effect of flow regime and pore structure on the flow signatures in porous media. *Physics of Fluids* **34** (11), 115139.

Verstappen, R. W. C. P. & Veldman, A. E. P. 2003 Symmetry-preserving discretization of turbulent flow. *Journal of Computational Physics* **187** (1), 343–368.

Voigt, W. 1966 Lehrbuch der Kristallphysik. Wiesbaden: Vieweg+Teubner Verlag.

von Engelhardt, W. & Tunn, W. 1954 Über das Strömen von Flüssigkeiten durch Sandsteine. *Heidelberger Beiträge zur Mineralogie und Petrographie* **4** (1), 12–25.

Wang, G. & Song, M. 2023 Temporal Constrained Feasible Subspace Learning for Human Pose Forecasting. In Proceedings of the Thirty-Second International Joint Conference on Artificial Intelligence, pp. 1451–1459. Macau: International Joint Conferences on Artificial Intelligence Organization.

Wang, L. 2000 Flows Through Porous Media: A Theoretical Development at Macroscale. *Transport in Porous Media* **39** (1), 1–24.

Wang, W., Wang, W. & Li, S. 2018 Detection and classification of critical points in piecewise linear vector fields. *Journal of Visualization* **21** (1), 147–161.

Wassenbergh, S. & Sanderson, S. 2023 Hydrodynamic analysis of bioinspired vortical cross-step filtration by computational modelling. *Royal Society Open Science* **10**, 230315.

Wegner, T. H., Karabelas, A. J. & Hanratty, T. J. 1971 Visual studies of flow in a regular array of spheres. *Chemical Engineering Science* **26** (1), 59–63.

Weinkauf, T. 2008 Extraction of Topological Structures in 2D and 3D Vector Fields. PhD thesis, Otto-von-Guericke-Universität, Magdeburg.

Wellander, N. 2009 The two-scale Fourier transform approach to homogenization; periodic homogenization in Fourier space. *Asymptotic Analysis* **62** (1-2), 1–40.

Whitaker, S. 1966 The Equations of Motion in Porous Media. *Chemical Engineering Science* **21**, 291–300.

Whitaker, S. 1967 Diffusion and dispersion in porous media. *AIChE Journal* **13** (3), 420–427.

Whitaker, S. 1985 A Simple Geometrical Derivation of the Spatial Averaging Theorem. *Chemical Engineering Education* **19** (1), 18–21 and 50–52.

Whitaker, S. 1986 Flow in porous media I: A theoretical derivation of Darcy's law. *Transport in Porous Media* **1** (1), 3–25.

Whitaker, S. 1996 The Forchheimer equation: A theoretical development. *Transport in Porous Media* **25** (1), 27–61.

Wiebel, A., Tricoche, X. & Scheuermann, G. 2009 Extraction of Separation Manifolds using Topological Structures in Flow Cross Sections. In Topology-Based Methods in Visualization II (ed. H.-C. Hege, K. Polthier & G. Scheuermann), Mathematics and Visualization (MATHVISUAL) , pp. 31–43. Berlin, Heidelberg: Springer Berlin, Heidelberg.

Wiener, N. 1958 Nonlinear Problems in Random Theory. Cambridge, MA: MIT Press.

Williamson, J. H 1980 Low-storage Runge-Kutta schemes. *Journal of Computational Physics* **35** (1), 48–56.

Wolfram Alpha LLC 2023 Wolfram|Alpha.

Womersley, J. R. 1955 Method for the calculation of velocity, rate of flow and viscous drag in arteries when the pressure gradient is known. *The Journal of Physiology* **127** (3), 553–563.

Wood, B. D., He, X. & Apte, S. V. 2020 Modeling Turbulent Flows in Porous Media. *Annual Review of Fluid Mechanics* **52** (1), 171–203.

Wu, J. Z., Tramel, R. W., Zhu, F. L. & Yin, X. Y. 2000 A vorticity dynamics theory of three-dimensional flow separation. *Physics of Fluids* **12** (8), 1932–1954.

Xia, L., Raghavan, B., Breitkopf, P. & Zhang, W. 2013 Numerical material representation using proper orthogonal decomposition and diffuse approximation. *Applied Mathematics and Computation* **224**, 450–462.

Xu, D., Song, B. & Avila, M. 2021 Non-modal transient growth of disturbances in pulsatile and oscillatory pipe flows. *Journal of Fluid Mechanics* **907**, R5.

Yang, S., He, X. & Zhu, B. 2020 Learning Physical Constraints with Neural Projections. In Advances in Neural Information Processing Systems (ed. H. Larochelle, M. Ranzato, R. Hadsell, M. F. Balcan & H. Lin), , vol. 33, pp. 5178–5189. Curran Associates, Inc.

Yang, T. & Wang, L. 2000 Microscale flow bifurcation and its macroscale implications in periodic porous media. *Computational Mechanics* **26** (6), 520–527.

Yang, X., Scheibe, T. D., Richmond, M. C., Perkins, W. A., Vogt, S. J., Codd, S. L., Seymour, J. D. & McKinley, M. I. 2013 Direct numerical simulation of pore-scale flow in a bead pack: Comparison with magnetic resonance imaging observations. *Advances in Water Resources* **54**, 228–241.

Yuan, G. & Li, Y. 2019 Estimation of the regions of attraction for autonomous nonlinear systems. *Transactions of the Institute of Measurement and Control* **41** (1), 97–106.

Zagoruiko, A. N., Bobrova, L., Vernikovskaya, N. & Zazhigalov, S. 2021 Unsteady-state operation of reactors with fixed catalyst beds. *Reviews in Chemical Engineering* **37** (1), 193–225.

Zhu, T. 2016 Unsteady porous-media flows. PhD thesis, Technische Universität München, München.

Zhu, T. & Manhart, M. 2016 Oscillatory Darcy Flow in Porous Media. *Transport in Porous Media* **111** (2), 521–539.

Zhu, T., Waluga, C., Wohlmuth, B. & Manhart, M. 2014 A Study of the Time Constant in Unsteady Porous Media Flow Using Direct Numerical Simulation. *Transport in Porous Media* **104** (1), 161–179.

Zhu, Y., Hu, D., Li, C., Zhuang, C. & Yang, G. 2021 CFD-DEM simulation of the hydrodynamic filtration performance in balaenid whale filter feeding. *Science of The Total Environment* **787**, 147696.

Zhu, Y., Yang, G., Zhuang, C., Li, C. & Hu, D. 2020 Oral cavity flow distribution and pressure drop in balaenid whales feeding: A theoretical analysis. *Bioinspiration & Biomimetics* **15** (3), 036004.

Zick, A. A. & Homsy, G. M. 1982 Stokes flow through periodic arrays of spheres. *Journal of Fluid Mechanics* **115**, 13–26.

A. Appendix: Methodology

A.1. Tetrahedral and octahedral pores

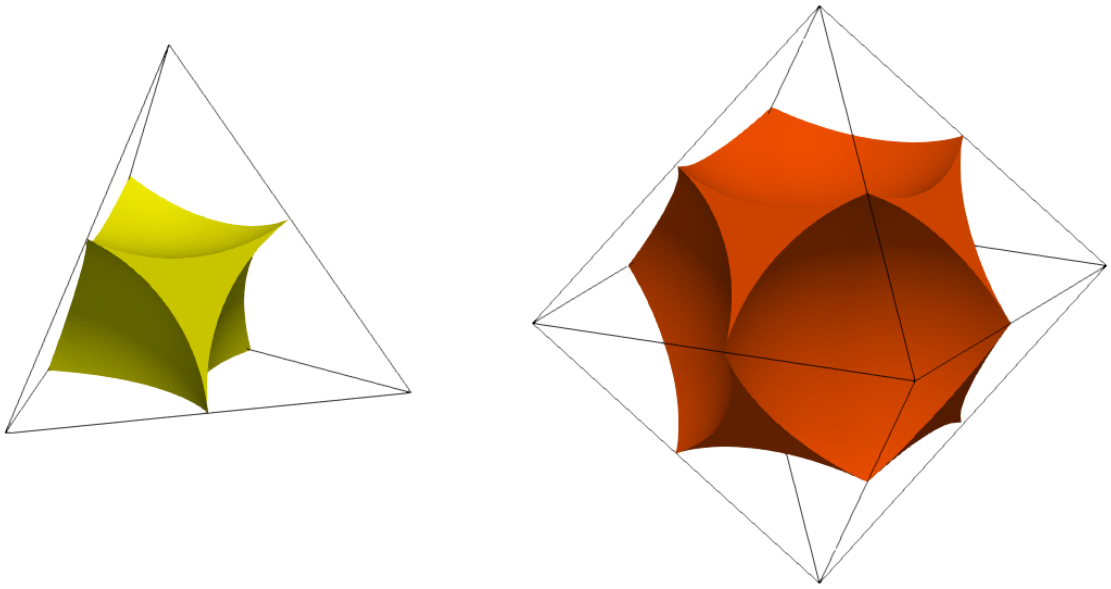

(a) Tetrahedral pore **(b)** Octahedral pore

Figure A.1: Visualisation of the isolated tetrahedral and octahedral pores. The pore geometries are obtained from the regular tetrahedron or octahedron of side length d, respectively, by subtracting spheres of diameter d located on the corners. The volume of the tetrahedral pore is $V_{\mathrm{tet}}/d^3 = \frac{1}{6\sqrt{2}} - \frac{1}{6}\arccos\left(\frac{23}{27}\right) \approx 0.026$ and the volume of the octahedral pore is $V_{\mathrm{oct}}/d^3 = \frac{\sqrt{2}}{3} + \frac{\pi}{2} - 2\arccos\left(\frac{1}{\sqrt{3}}\right) \approx 0.132$.

A.2. Eigenvalues of the spatial discretisation

In this section, the eigenvalues of the semi-discretised convective and diffusive operators are estimated using Gershgorin's circle theorem following Dröge (2006). In MGLET, the incompressible Navier-Stokes equations are discretised on a uniform Cartesian grid indexed by i, j, k with cells of size Δx, Δy, Δz as

$$0 = \frac{u_{i,j,k} - u_{i-1,j,k}}{\Delta x} + \frac{v_{i,j,k} - v_{i,j-1,k}}{\Delta y} + \frac{w_{i,j,k} - w_{i,j,k-1}}{\Delta z} \tag{A.1a}$$

$$\begin{aligned}
\frac{\mathrm{d}u_{i,j,k}}{\mathrm{d}t} = &- \frac{\frac{1}{4}(u_{i,j,k} + u_{i+1,j,k})(u_{i,j,k} + u_{i+1,j,k}) - \frac{1}{4}(u_{i-1,j,k} + u_{i,j,k})(u_{i-1,j,k} + u_{i,j,k})}{\Delta x} \\
&- \frac{\frac{1}{4}(v_{i,j,k} + v_{i+1,j,k})(u_{i,j,k} + u_{i,j+1,k}) - \frac{1}{4}(v_{i,j-1,k} + v_{i+1,j-1,k})(u_{i,j-1,k} + u_{i,j,k})}{\Delta y} \\
&- \frac{\frac{1}{4}(w_{i,j,k} + w_{i+1,j,k})(u_{i,j,k} + u_{i,j,k+1}) - \frac{1}{4}(w_{i,j,k-1} + w_{i+1,j,k-1})(u_{i,j,k-1} + u_{i,j,k})}{\Delta z} \\
&+ \nu \frac{u_{i-1,j,k} - 2u_{i,j,k} + u_{i+1,j,k}}{\Delta x^2} + \nu \frac{u_{i,j-1,k} - 2u_{i,j,k} + u_{i,j+1,k}}{\Delta y^2} \\
&+ \nu \frac{u_{i,j,k-1} - 2u_{i,j,k} + u_{i,j,k+1}}{\Delta z^2} - \frac{1}{\rho} \frac{p_{i+1,j,k} - p_{i,j,k}}{\Delta x}
\end{aligned} \tag{A.1b}$$

and the momentum equations in the y- and z-directions follow from exchanging u with v or w, i with j or k and Δx with Δy and Δz, respectively. Using the continuity equation, the momentum equation can be rearranged to the form

$$\begin{aligned}
\frac{\mathrm{d}u_{i,j,k}}{\mathrm{d}t} = &\left[-2\nu \left(\frac{1}{\Delta x^2} + \frac{1}{\Delta y^2} + \frac{1}{\Delta z^2} \right) \right] u_{i,j,k} + \left[\frac{\nu}{\Delta x^2} - \frac{\frac{1}{4}(u_{i,j,k} + u_{i+1,j,k})}{\Delta x} \right] u_{i+1,j,k} \\
&+ \left[\frac{\nu}{\Delta x^2} + \frac{\frac{1}{4}(u_{i-1,j,k} + u_{i,j,k})}{\Delta x} \right] u_{i-1,j,k} + \left[\frac{\nu}{\Delta y^2} - \frac{\frac{1}{4}(v_{i,j,k} + v_{i+1,j,k})}{\Delta y} \right] u_{i,j+1,k} \\
&+ \left[\frac{\nu}{\Delta y^2} + \frac{\frac{1}{4}(v_{i,j-1,k} + v_{i+1,j-1,k})}{\Delta y} \right] u_{i,j-1,k} + \left[\frac{\nu}{\Delta z^2} - \frac{\frac{1}{4}(w_{i,j,k} + w_{i+1,j,k})}{\Delta z} \right] u_{i,j,k+1} \\
&+ \left[\frac{\nu}{\Delta z^2} + \frac{\frac{1}{4}(w_{i,j,k-1} + w_{i+1,j,k-1})}{\Delta z} \right] u_{i,j,k-1} - \frac{1}{\rho} \frac{p_{i+1,j,k} - p_{i,j,k}}{\Delta x} \,.
\end{aligned} \tag{A.2}$$

The terms in brackets correspond to the entries of the convective and diffusive operator matrices $\boldsymbol{C}(\boldsymbol{u})$ and $\boldsymbol{D}$ (Verstappen & Veldman, 2003). In order to determine the eigenvalues of the Navier-Stokes operator, the right hand side of the equation needs to be linearised.

In a simplified analysis, the convecting velocities contained in the convective operator matrix $\boldsymbol{C}(\boldsymbol{u})$ can be assumed independent of the convected velocities (Kwok & Tam, 1993; Dröge, 2006; Kress & Lötstedt, 2006). Moreover, the effects of the pressure and the boundary conditions are ignored. The momentum equations then reduce to independent convection-diffusion equations and the terms in brackets represent the constant coefficients of the convective and

diffusive operator matrices. It is important to keep in mind that these simplifications result in a linear system that is not identical to the result of a formal linearisation using the Jacobian matrix of the right hand side of equation (A.1).
Following (Dröge, 2006), we estimate their eigenvalues using Gershgorin's circle theorem: For each row of a matrix, a circle in the complex plane can be defined whose centre is the diagonal entry and whose radius is the sum of the absolute values of the off-diagonal entries. The eigenvalues of the matrix are contained in the union of these circles (Varga, 2004, pp.1f). Here, the centre of the circle is given by the coefficient of $u_{i,j,k}$ and the radius is given by the sum of the absolute values of the off-diagonal entries. For the diffusive operator matrix, the Gershgorin circle thus results as

$$\left| z + 2\nu \left(\frac{1}{\Delta x^2} + \frac{1}{\Delta y^2} + \frac{1}{\Delta z^2} \right) \right| \leq 2\nu \left(\frac{1}{\Delta x^2} + \frac{1}{\Delta y^2} + \frac{1}{\Delta z^2} \right) \tag{A.3}$$

where $z \in \mathbb{C}$. Since the diffusion operator is a real symmetric matrix whose eigenvalues lie on the real axis (Verstappen & Veldman, 2003), the inequality can be simplified to

$$-4\nu \left(\frac{1}{\Delta x^2} + \frac{1}{\Delta y^2} + \frac{1}{\Delta z^2} \right) \leq \lambda_{\boldsymbol{D}} \leq 0\,. \tag{A.4}$$

For the convective operator, we obtain the Gershgorin circles

$$\begin{aligned} |z| \leq \frac{1}{4} & \frac{|u_{i,j,k} + u_{i+1,j,k}| + |u_{i-1,j,k} + u_{i,j,k}|}{\Delta x} \\ + \frac{1}{4} & \frac{|v_{i,j,k} + v_{i+1,j,k}| + |v_{i,j-1,k} + v_{i+1,j-1,k}|}{\Delta y} \\ + \frac{1}{4} & \frac{|w_{i,j,k} + w_{i+1,j,k}| + |w_{i,j,k-1} + w_{i+1,j,k-1}|}{\Delta z}\,. \end{aligned} \tag{A.5}$$

The union of these concentric circles is easily determined by taking the maximum over the right hand side. Since the convective operator matrix is skew-symmetric (Verstappen & Veldman, 2003), its eigenvalues lie on the imaginary axis. We thus obtain

$$-\frac{CFL_u}{\Delta t} \leq \mathrm{i}\lambda_{\boldsymbol{C}(\boldsymbol{u})} \leq \frac{CFL_u}{\Delta t} \tag{A.6}$$

where we define the Courant-Friedrichs-Lewy number as

$$\begin{aligned} CFL_u = \Delta t \max_{i,j,k} \Bigg(& \frac{|u_{i,j,k} + u_{i+1,j,k}| + |u_{i-1,j,k} + u_{i,j,k}|}{4\Delta x} \\ & + \frac{|v_{i,j,k} + v_{i+1,j,k}| + |v_{i,j-1,k} + v_{i+1,j-1,k}|}{4\Delta y} \\ & + \frac{|w_{i,j,k} + w_{i+1,j,k}| + |w_{i,j,k-1} + w_{i+1,j,k-1}|}{4\Delta z} \Bigg)\,. \end{aligned} \tag{A.7}$$

Note that there are also other definitions of the Courant-Friedrichs-Lewy number that were derived using different approximations (Cheny & Botella, 2010).

B. Appendix: Modelling

This appendix contains some derivations that were omitted from the manuscript *Assessment of models for nonlinear oscillatory flow through a hexagonal sphere pack* (appendix D.4) for the sake of brevity, in particular the derivation of the time domain formulation of the model of Pride et al. (1993) and the derivations of the discretisations for the models of Pride et al. (1993) and Turo & Umnova (2013). Also, proofs are given for Kelvin's minimum energy theorem and Helmholtz's minimum dissipation theorem in the setting of triply periodic porous media. Finally, the scaling of the friction and the viscous pressure drag is investigated for the cases HF6 and HF7, which were not considered in (Unglehrt & Manhart, 2023a, reprinted in appendix D.6).

B.1. Time domain formulation of the model of Pride et al. (1993)

In this section, a time domain formulation is derived for the model of Pride et al. (1993), which can be expressed in terms of the dynamic permeability as

$$\hat{K}(\omega) = \frac{K}{\mu} \frac{1}{\left(1 - \frac{P}{2\beta} + \sqrt{\frac{P^2}{4\beta^2} + \mathrm{i}P\frac{\omega}{\Omega_0}}\right) + \mathrm{i}\frac{\omega}{\Omega_0}} \,. \tag{B.1}$$

The dynamic permeability relates the Fourier transforms of the superficial velocity and of the macroscopic pressure gradient by a generalisation of Darcy's law

$$\mathcal{F}\left\{\langle \boldsymbol{u} \rangle_\mathrm{s}\right\}(\omega) = -\frac{\hat{K}(\omega)}{\mu} \mathcal{F}\left\{\boldsymbol{\nabla} \langle p \rangle_\mathrm{i}\right\}(\omega) \,. \tag{B.2}$$

Multiplying with the denominator of the dynamic permeability and taking the inverse Fourier transform, the following equation is obtained

$$\mathcal{F}^{-1}\left\{\left[\left(1 - \frac{P}{2\beta} + \sqrt{\frac{P^2}{4\beta^2} + \mathrm{i}P\frac{\omega}{\Omega_0}}\right) + \mathrm{i}\frac{\omega}{\Omega_0}\right] \mathcal{F}\left\{\langle \boldsymbol{u} \rangle_\mathrm{s}\right\}(\omega)\right\}(t) = -\frac{K}{\mu} \boldsymbol{\nabla} \langle p \rangle_\mathrm{i} \,. \tag{B.3}$$

The aim of this derivation is to resolve the inverse Fourier transform into an expression in the time domain. Expanding the brackets and using the linearity and the derivative property $\mathrm{i}\omega = \mathcal{F}\left\{\mathrm{d}/\mathrm{d}t\right\}(\omega)$ of the Fourier transform, the left hand side can be rewritten as

$$\left(1 - \frac{P}{2\beta}\right) \langle \boldsymbol{u} \rangle_\mathrm{s} + \frac{1}{\Omega_0} \frac{\mathrm{d}\langle \boldsymbol{u} \rangle_\mathrm{s}}{\mathrm{d}t} + \sqrt{\frac{P}{\Omega_0}}\, \mathcal{F}^{-1}\left\{\sqrt{\mathrm{i}\omega + \frac{P\,\Omega_0}{4\beta^2}}\, \mathcal{F}\left\{\langle \boldsymbol{u} \rangle_\mathrm{s}\right\}(\omega)\right\}(t) = -\frac{K}{\mu} \boldsymbol{\nabla} \langle p \rangle_\mathrm{i} \,. \tag{B.4}$$

The remaining term is expanded as

$$\begin{aligned}\mathcal{F}^{-1}\left\{\sqrt{\mathrm{i}\omega+\frac{P\,\Omega_0}{4\beta^2}}\,\mathcal{F}\left\{\langle\boldsymbol{u}\rangle_{\mathrm{s}}\right\}(\omega)\right\}(t) =& \mathcal{F}^{-1}\left\{\frac{1}{\sqrt{\mathrm{i}\omega+\frac{P\,\Omega_0}{4\beta^2}}}\left[\mathrm{i}\omega\mathcal{F}\left\{\langle\boldsymbol{u}\rangle_{\mathrm{s}}\right\}(\omega)\right]\right\}(t)\\ &+\frac{P\,\Omega_0}{4\beta^2}\mathcal{F}^{-1}\left\{\frac{1}{\sqrt{\mathrm{i}\omega+\frac{P\,\Omega_0}{4\beta^2}}}\mathcal{F}\left\{\langle\boldsymbol{u}\rangle_{\mathrm{s}}\right\}(\omega)\right\}(t)\end{aligned} \tag{B.5}$$

such that the following Fourier transform pair can be applied

$$\mathcal{F}\left\{\frac{e^{-\frac{P\,\Omega_0}{4\beta^2}t}}{\sqrt{\pi t}}\theta(t)\right\}(\omega)=\frac{1}{\sqrt{\mathrm{i}\omega+\frac{P\,\Omega_0}{4\beta^2}}}\,. \tag{B.6}$$

Here, $\theta(t)$ denotes the Heaviside function. The pair follows from a Laplace transform pair given by Gradštejn & Ryžik (2009, p.1110, pair 26 for $\nu=\frac{1}{2}$ and $s=\mathrm{i}\omega$). Using the convolution property of the Fourier transform, the remaining term can be finally evaluated as

$$\mathcal{F}^{-1}\left\{\sqrt{i\left(\omega-\frac{\mathrm{i}\,P\,\Omega_0}{4\beta^2}\right)}\mathcal{F}\left\{\langle\boldsymbol{u}\rangle_{\mathrm{s}}\right\}(\omega)\right\}(t)=\int_{-\infty}^{t}\left(\frac{\Omega_0\,P}{4\beta^2}\,\langle\boldsymbol{u}\rangle_{\mathrm{s}}+\frac{\mathrm{d}\langle\boldsymbol{u}\rangle_{\mathrm{s}}}{\mathrm{d}\tau}\right)\frac{e^{-\frac{\Omega_0\,P}{4\beta^2}(t-\tau)}}{\sqrt{\pi(t-\tau)}}\,\mathrm{d}\tau\,. \tag{B.7}$$

Thus, the complete time domain representation of the model of Pride et al. (1993) results as

$$\frac{1}{\Omega_0}\frac{\mathrm{d}\langle\boldsymbol{u}\rangle_{\mathrm{s}}}{\mathrm{d}t}+\left(1-\frac{P}{2\beta}\right)\langle\boldsymbol{u}\rangle_{\mathrm{s}}+\sqrt{\frac{P}{\Omega_0}}\int_{-\infty}^{t}\left(\frac{\Omega_0\,P}{4\beta^2}\,\langle\boldsymbol{u}\rangle_{\mathrm{s}}+\frac{\mathrm{d}\langle\boldsymbol{u}\rangle_{\mathrm{s}}}{\mathrm{d}\tau}\right)\frac{e^{-\frac{\Omega_0\,P}{4\beta^2}(t-\tau)}}{\sqrt{\pi(t-\tau)}}\,\mathrm{d}\tau=-\frac{K}{\mu}\boldsymbol{\nabla}\langle p\rangle_{\mathrm{i}}\,. \tag{B.8}$$

With the parameter definitions $P=4\alpha_\infty K/(\epsilon\Lambda^2)$ and $\Omega_0=\epsilon\nu/(\alpha_\infty K)$, the model can also be written as

$$\begin{aligned}\rho\,\frac{\mathrm{d}\langle\boldsymbol{u}\rangle_{\mathrm{s}}}{\mathrm{d}t}=&-\frac{\epsilon}{\alpha_\infty}\boldsymbol{\nabla}\langle p\rangle_{\mathrm{i}}-\left(\frac{\epsilon}{\alpha_\infty}\frac{\mu}{K}-\frac{2\mu}{\Lambda^2\,\beta}\right)\langle\boldsymbol{u}\rangle_{\mathrm{s}}\\ &-\rho\,\sqrt{\nu}\,\frac{2}{\Lambda}\int_{-\infty}^{t}\left(\frac{\nu}{\Lambda^2\,\beta^2}\,\langle\boldsymbol{u}\rangle_{\mathrm{s}}+\frac{\mathrm{d}\langle\boldsymbol{u}\rangle_{\mathrm{s}}}{\mathrm{d}\tau}\right)\frac{e^{-\frac{\nu(t-\tau)}{\Lambda^2\,\beta^2}}}{\sqrt{\pi(t-\tau)}}\,\mathrm{d}\tau\,.\end{aligned} \tag{B.9}$$

Note that the time domain representation of the model of Johnson et al. (1987) can be obtained by setting $\beta=P/2=2\alpha_\infty K/(\epsilon\Lambda^2)$:

$$\rho\,\frac{\mathrm{d}\langle\boldsymbol{u}\rangle_{\mathrm{s}}}{\mathrm{d}t}=-\frac{\epsilon}{\alpha_\infty}\boldsymbol{\nabla}\langle p\rangle_{\mathrm{i}}-\rho\,\sqrt{\nu}\,\frac{2}{\Lambda}\int_{-\infty}^{t}\left(\frac{\nu\epsilon^2\Lambda^2}{4\alpha_\infty^2K^2}\,\langle\boldsymbol{u}\rangle_{\mathrm{s}}+\frac{\mathrm{d}\langle\boldsymbol{u}\rangle_{\mathrm{s}}}{\mathrm{d}\tau}\right)\frac{e^{-\frac{\nu(t-\tau)\epsilon^2\Lambda^2}{4\alpha_\infty^2K^2}}}{\sqrt{\pi(t-\tau)}}\,\mathrm{d}\tau\,. \tag{B.10}$$

B.2. Derivation of the discretisations of the dynamic permeability models

This section presents the derivation of the time discretisations of the models of Pride et al. (1993) and Turo & Umnova (2013) used in the manuscript *Assessment of models for nonlinear oscillatory flow through a hexagonal sphere pack* (appendix D.4).

B.2.1. Derivation of the discretisation of the model of Pride et al. (1993)

The time domain formulation of the model of Pride et al. (1993) is given by equation (B.9). First, the equation is divided by the density and the time derivative is discretised using the implicit Euler method

$$\langle \boldsymbol{u} \rangle_{\mathrm{s}}^{n+1} = \langle \boldsymbol{u} \rangle_{\mathrm{s}}^{n} + \Delta t \, \boldsymbol{F}^{n+1} \,, \tag{B.11a}$$

where the right hand side is given as

$$\begin{aligned} \boldsymbol{F}^{n+1} = &- \frac{\epsilon}{\rho \, \alpha_\infty} \boldsymbol{\nabla} \langle p \rangle_{\mathrm{i}}^{n+1} - \left(\frac{\epsilon}{\alpha_\infty} \frac{\nu}{K} - \frac{2\nu}{\Lambda^2 \, \beta} \right) \langle \boldsymbol{u} \rangle_{\mathrm{s}}^{n+1} \\ &- \frac{2\sqrt{\nu}}{\Lambda} \int_{-\infty}^{t^{n+1}} \left(\frac{\nu}{\Lambda^2 \, \beta^2} \langle \boldsymbol{u} \rangle_{\mathrm{s}} + \frac{\mathrm{d} \langle \boldsymbol{u} \rangle_{\mathrm{s}}}{\mathrm{d}\tau} \right) \frac{e^{-\frac{\nu(t^{n+1}-\tau)}{\Lambda^2 \, \beta^2}}}{\sqrt{\pi (t^{n+1}-\tau)}} \, \mathrm{d}\tau \,. \end{aligned} \tag{B.11b}$$

The integration domain is decomposed into the time steps $[t^j, t^{j+1}]$ such that a sum of integrals is obtained

$$\begin{aligned} \boldsymbol{F}^{n+1} = &- \frac{\epsilon}{\rho \, \alpha_\infty} \boldsymbol{\nabla} \langle p \rangle_{\mathrm{i}}^{n+1} - \left(\frac{\epsilon}{\alpha_\infty} \frac{\nu}{K} - \frac{2\nu}{\Lambda^2 \, \beta} \right) \langle \boldsymbol{u} \rangle_{\mathrm{s}}^{n+1} \\ &- \frac{2\sqrt{\nu}}{\Lambda} \sum_{j=-\infty}^{n} \underbrace{\int_{t^j}^{t^{j+1}} \left(\frac{\nu}{\Lambda^2 \, \beta^2} \langle \boldsymbol{u} \rangle_{\mathrm{s}} + \frac{\mathrm{d} \langle \boldsymbol{u} \rangle_{\mathrm{s}}}{\mathrm{d}\tau} \right) \frac{e^{-\frac{\nu(t^{n+1}-\tau)}{\Lambda^2 \, \beta^2}}}{\sqrt{\pi (t^{n+1}-\tau)}} \, \mathrm{d}\tau}_{=: I_j} \,. \end{aligned} \tag{B.12}$$

The velocity is approximated by a piecewise linear interpolant in every interval; this results in the equation

$$I_j = \int_{t^j}^{t^{j+1}} \left[\frac{\nu}{\Lambda^2 \, \beta^2} \langle \boldsymbol{u} \rangle_{\mathrm{s}}^{j} + \left(1 + \frac{\nu(\tau - t^j)}{\Lambda^2 \, \beta^2} \right) \frac{\langle \boldsymbol{u} \rangle_{\mathrm{s}}^{j+1} - \langle \boldsymbol{u} \rangle_{\mathrm{s}}^{j}}{\Delta t} \right] \frac{e^{-\frac{\nu(t^{n+1}-\tau)}{\Lambda^2 \, \beta^2}}}{\sqrt{\pi (t^{n+1}-\tau)}} \, \mathrm{d}\tau \,. \tag{B.13}$$

Using the substitution $\xi = \nu(t^{n+1} - \tau)/(\Lambda^2 \, \beta^2)$, the integral is rewritten as

$$\frac{2\sqrt{\nu}}{\Lambda} I_j = 2\beta \int_{\frac{\nu(t^{n+1}-t^{j+1})}{\Lambda^2 \, \beta^2}}^{\frac{\nu(t^{n+1}-t^{j})}{\Lambda^2 \, \beta^2}} \left[\frac{\nu}{\Lambda^2 \, \beta^2} \langle \boldsymbol{u} \rangle_{\mathrm{s}}^{j} + \left(1 - \xi + \frac{\nu(t^{n+1} - t^j)}{\Lambda^2 \, \beta^2} \right) \frac{\langle \boldsymbol{u} \rangle_{\mathrm{s}}^{j+1} - \langle \boldsymbol{u} \rangle_{\mathrm{s}}^{j}}{\Delta t} \right] \frac{e^{-\xi}}{\sqrt{\pi \xi}} \, \mathrm{d}\xi \,, \tag{B.14}$$

which can be evaluated as

$$\frac{2\sqrt{\nu}}{\Lambda} I_j = 2\beta \left[\operatorname{erf}\left(\sqrt{\xi}\right)\right]_{\frac{\nu(t^{n+1}-t^{j+1})}{\Lambda^2\,\beta^2}}^{\frac{\nu(t^{n+1}-t^{j})}{\Lambda^2\,\beta^2}} \left[\frac{\nu}{\Lambda^2\,\beta^2}\,\langle \boldsymbol{u}\rangle_{\mathrm{s}}^{j} + \left(1+\frac{\nu(t^{n+1}-t^{j})}{\Lambda^2\,\beta^2}\right)\frac{\langle \boldsymbol{u}\rangle_{\mathrm{s}}^{j+1}-\langle \boldsymbol{u}\rangle_{\mathrm{s}}^{j}}{\Delta t}\right] + 2\beta \left[-\frac{1}{2}\operatorname{erf}\left(\sqrt{\xi}\right)+\sqrt{\frac{\xi}{\pi}}e^{-\xi}\right]_{\frac{\nu(t^{n+1}-t^{j+1})}{\Lambda^2\,\beta^2}}^{\frac{\nu(t^{n+1}-t^{j})}{\Lambda^2\,\beta^2}} \frac{\langle \boldsymbol{u}\rangle_{\mathrm{s}}^{j+1}-\langle \boldsymbol{u}\rangle_{\mathrm{s}}^{j}}{\Delta t}\,.$$

Assuming equidistant time steps and defining $h = \frac{\nu\Delta t}{\Lambda^2\beta^2}$, the expression can be further simplified to

$$\begin{aligned}\frac{2\sqrt{\nu}}{\Lambda} I_j = &-\frac{2\beta}{\Delta t}\left\{\left[\operatorname{erf}\left(\sqrt{\xi}\right)\right]_{(n-j)h}^{(n-j+1)h}\left(\frac{1}{2}+(n-j)h\right)+\left[\sqrt{\frac{\xi}{\pi}}e^{-\xi}\right]_{(n-j)h}^{(n-j+1)h}\right\}\langle \boldsymbol{u}\rangle_{\mathrm{s}}^{j}\\ &+\frac{2\beta}{\Delta t}\left\{\left[\operatorname{erf}\left(\sqrt{\xi}\right)\right]_{(n-j)h}^{(n-j+1)h}\left(\frac{1}{2}+(n-j+1)h\right)+\left[\sqrt{\frac{\xi}{\pi}}e^{-\xi}\right]_{(n-j)h}^{(n-j+1)h}\right\}\langle \boldsymbol{u}\rangle_{\mathrm{s}}^{j+1}\,.\end{aligned} \tag{B.15}$$

Finally, the following scheme is obtained

$$a\,\langle \boldsymbol{u}\rangle_{\mathrm{s}}^{n+1} = \langle \boldsymbol{u}\rangle_{\mathrm{s}}^{n} - \Delta t\,\frac{\epsilon}{\rho\,\alpha_\infty}\boldsymbol{\nabla}\langle p\rangle_{\mathrm{i}}^{n+1} - \sum_{k=1}^{\infty} c_k\,\langle \boldsymbol{u}\rangle_{\mathrm{s}}^{n-k+1} \tag{B.16a}$$

with precomputable coefficients

$$a = 1 + h\left(\frac{4\beta^2}{P}-2\beta\right)+2\beta\left[\left(\frac{1}{2}+h\right)\operatorname{erf}\left(\sqrt{h}\right)+\sqrt{\frac{h}{\pi}}e^{-h}\right] \tag{B.16b}$$

$$\begin{aligned}c_k = &-2\beta\left\{\left[\operatorname{erf}\left(\sqrt{\xi}\right)\right]_{(k-1)h}^{kh}\left(\frac{1}{2}+(k-1)h\right)+\left[\sqrt{\frac{\xi}{\pi}}e^{-\xi}\right]_{(k-1)h}^{kh}\right\}\\ &+2\beta\left\{\left[\operatorname{erf}\left(\sqrt{\xi}\right)\right]_{kh}^{(k+1)h}\left(\frac{1}{2}+(k+1)h\right)+\left[\sqrt{\frac{\xi}{\pi}}e^{-\xi}\right]_{kh}^{(k+1)h}\right\}.\end{aligned} \tag{B.16c}$$

Note that in the n-th time step a convolution of length $n+1$ has to be computed. This leads to an algorithmic complexity $O(n^2)$ for the total scheme. Improved schemes could be devised using, for example, the method of van Hinsberg et al. (2011).

B.2.2. Derivation of the discretisation of the model of Turo & Umnova (2013)

In the following, a temporal discretisation of the model of Turo & Umnova (2013) is derived. The model is given by the equation

$$\rho\frac{\mathrm{d}\langle\boldsymbol{u}\rangle_\mathrm{s}}{\mathrm{d}t} = -\frac{\epsilon}{\alpha_\infty}\boldsymbol{\nabla}\langle p\rangle_\mathrm{i} - \frac{\epsilon}{\alpha_\infty}\frac{\mu}{K}\left(1+\xi|\langle\boldsymbol{u}\rangle_\mathrm{s}|\right)\langle\boldsymbol{u}\rangle_\mathrm{s} - \frac{2\rho\sqrt{\nu}}{\Lambda}\int_{-\infty}^{t}\frac{\mathrm{d}\langle\boldsymbol{u}\rangle_\mathrm{s}}{\mathrm{d}\tau}\frac{1}{\sqrt{\pi(t-\tau)}}\,\mathrm{d}\tau\,. \tag{B.17}$$

Again, the equation is divided by the density and the time derivative is discretised using the implicit Euler method

$$\langle\boldsymbol{u}\rangle_\mathrm{s}^{n+1} = \langle\boldsymbol{u}\rangle_\mathrm{s}^{n} + \Delta t\,\boldsymbol{F}^{n+1}\,, \tag{B.18a}$$

where the right hand side is given as

$$\begin{aligned}\boldsymbol{F}^{n+1} = &-\frac{\epsilon}{\rho\,\alpha_\infty}\boldsymbol{\nabla}\langle p\rangle_\mathrm{i}^{n+1} - \frac{\epsilon}{\alpha_\infty}\frac{\nu}{K}\left(1+\xi\left|\langle\boldsymbol{u}\rangle_\mathrm{s}^{n+1}\right|\right)\langle\boldsymbol{u}\rangle_\mathrm{s}^{n+1}\\ &-\frac{2\sqrt{\nu}}{\Lambda}\int_{-\infty}^{t^{n+1}}\frac{\mathrm{d}\langle\boldsymbol{u}\rangle_\mathrm{s}}{\mathrm{d}\tau}\frac{1}{\sqrt{\pi(t^{n+1}-\tau)}}\,\mathrm{d}\tau\,.\end{aligned} \tag{B.18b}$$

The integration domain is decomposed into the time steps $[t^j, t^{j+1}]$ and a sum of integrals is obtained

$$\begin{aligned}\boldsymbol{F}^{n+1} = &-\frac{\epsilon}{\rho\,\alpha_\infty}\boldsymbol{\nabla}\langle p\rangle_\mathrm{i}^{n+1} - \frac{\epsilon}{\alpha_\infty}\frac{\nu}{K}\left(1+\xi\left|\langle\boldsymbol{u}\rangle_\mathrm{s}^{n+1}\right|\right)\langle\boldsymbol{u}\rangle_\mathrm{s}^{n+1}\\ &-\frac{2\sqrt{\nu}}{\Lambda}\sum_{j=-\infty}^{n}\underbrace{\int_{t^j}^{t^{j+1}}\frac{\mathrm{d}\langle\boldsymbol{u}\rangle_\mathrm{s}}{\mathrm{d}\tau}\frac{1}{\sqrt{\pi(t^{n+1}-\tau)}}\,\mathrm{d}\tau}_{=:I_j}\,.\end{aligned} \tag{B.19}$$

After approximating the velocity by a piecewise linear interpolant, the integrals can be evaluated as

$$\begin{aligned}I_j &= \int_{t^j}^{t^{j+1}}\frac{\langle\boldsymbol{u}\rangle_\mathrm{s}^{j+1}-\langle\boldsymbol{u}\rangle_\mathrm{s}^{j}}{\Delta t}\frac{1}{\sqrt{\pi(t^{n+1}-\tau)}}\,\mathrm{d}\tau\\ &= \frac{\langle\boldsymbol{u}\rangle_\mathrm{s}^{j+1}-\langle\boldsymbol{u}\rangle_\mathrm{s}^{j}}{\Delta t}\frac{2}{\sqrt{\pi}}\left(\sqrt{t^{n+1}-t^j}-\sqrt{t^{n+1}-t^{j+1}}\right)\,,\end{aligned} \tag{B.20}$$

and, assuming equidistant time steps, the result can be further simplified to

$$I_j = \frac{\langle\boldsymbol{u}\rangle_\mathrm{s}^{j+1}-\langle\boldsymbol{u}\rangle_\mathrm{s}^{j}}{\sqrt{\Delta t}}\frac{2}{\sqrt{\pi}}\left(\sqrt{n-j+1}-\sqrt{n-j}\right)\,. \tag{B.21}$$

Finally, the following scheme is obtained

$$a\,\langle\boldsymbol{u}\rangle_\mathrm{s}^{n+1} + b\left|\langle\boldsymbol{u}\rangle_\mathrm{s}^{n+1}\right|\langle\boldsymbol{u}\rangle_\mathrm{s}^{n+1} = \langle\boldsymbol{u}\rangle_\mathrm{s}^{n} - \Delta t\,\frac{\epsilon}{\rho\,\alpha_\infty}\boldsymbol{\nabla}\langle p\rangle_\mathrm{i}^{n+1} - \sum_{k=1}^{\infty}c_k\,\langle\boldsymbol{u}\rangle_\mathrm{s}^{n-k+1} \tag{B.22a}$$

with precomputable coefficients

$$a = 1 + \frac{\epsilon}{\alpha_\infty}\frac{\nu\Delta t}{K} + \frac{2\sqrt{\nu\Delta t}}{\Lambda}\frac{2}{\sqrt{\pi}} \tag{B.22b}$$

$$b = \frac{\epsilon}{\alpha_\infty}\frac{\nu\Delta t}{K}\xi \tag{B.22c}$$

$$c_k = \frac{2\sqrt{\nu\Delta t}}{\Lambda}\frac{2}{\sqrt{\pi}}\left(\sqrt{k+1} - 2\sqrt{k} + \sqrt{k-1}\right) . \tag{B.22d}$$

Note that a nonlinear equation needs to be solved in every time step.

B.3. Kelvin's minimum energy theorem

Kelvin's minimum energy theorem states that the potential flow has the smallest kinetic energy of all possible incompressible velocity fields satisfying the same boundary conditions (Batchelor, 2000, p.384). In this section, an inequality is derived for triply periodic porous media expressing this statement in terms of the volume-averaged kinetic energy and the volume-averaged velocity. The investigation of a minimum energy theorem is motivated by the inequality $\langle \boldsymbol{u}^2 \rangle_\mathrm{i} \geq \langle \boldsymbol{u} \rangle_\mathrm{i}^2$ (Zhu et al., 2014), which however does not take into account that a constant velocity field is not kinematically admissible in a general porous domain. Therefore, the lower bound can be improved using the divergence-free constraint and the geometry of the porous domain.
The derivation starts out from Schwarz's inequality (Bronštejn & Semendjaev, 1981, p.12)

$$\left\langle \boldsymbol{u}^2 \right\rangle_\mathrm{i} \left\langle \boldsymbol{v}^2 \right\rangle_\mathrm{i} \geq \left| \frac{1}{V_\mathrm{f}} \int_{V_\mathrm{f}} \boldsymbol{u} \cdot \boldsymbol{v} \, \mathrm{d}V \right|^2 \tag{B.23}$$

for two vector fields $\boldsymbol{u}$ and $\boldsymbol{v}$. The velocity $\boldsymbol{v}$ is chosen as the gradient of a potential ϕ such that

$$\left\langle \boldsymbol{u}^2 \right\rangle_\mathrm{i} \left\langle (\boldsymbol{\nabla}\phi)^2 \right\rangle_\mathrm{i} \geq \left| \frac{1}{V_\mathrm{f}} \int_{V_\mathrm{f}} \boldsymbol{u} \cdot \boldsymbol{\nabla}\phi \, \mathrm{d}V \right|^2 . \tag{B.24}$$

The potential ϕ is chosen as the potential flow satisfying $\boldsymbol{\nabla}\phi \cdot \boldsymbol{n}$ on the fluid-solid interface. Following (Batchelor, 2000, p.402), the potential can be written as

$$\phi = (\boldsymbol{\Phi} - \boldsymbol{x}) \cdot \boldsymbol{w} , \tag{B.25}$$

where $\boldsymbol{w}$ is a constant velocity and $\boldsymbol{\Phi}$ is an auxiliary potential satisfying

$$\Delta\boldsymbol{\Phi} = 0 \tag{B.26a}$$

with the boundary condition

$$(\boldsymbol{\nabla} \otimes \boldsymbol{\Phi})^\mathrm{T} \cdot \boldsymbol{n} = \boldsymbol{n} \tag{B.26b}$$

on the fluid-solid interface and triply periodic boundary conditions. First, the term on the left hand side of the inequality (B.24) is considered. With the velocity potential (B.25), the term can be written as

$$\begin{aligned}\frac{1}{V_\mathrm{f}}\int_{V_\mathrm{f}}\left(\frac{\partial\phi}{\partial x_j}\right)^2\mathrm{d}V &= \frac{1}{V_\mathrm{f}}\int_{V_\mathrm{f}} w_k\left(\frac{\partial\Phi_k}{\partial x_j}-\delta_{kj}\right)\left(\frac{\partial\Phi_l}{\partial x_j}-\delta_{lj}\right)w_l\,\mathrm{d}V \\ &= w_k\Bigg[\underbrace{\frac{1}{V_\mathrm{f}}\int_{V_\mathrm{f}}\frac{\partial\Phi_k}{\partial x_j}\frac{\partial\Phi_l}{\partial x_j}\,\mathrm{d}V}_{=:I_1}-\underbrace{\frac{1}{V_\mathrm{f}}\int_{V_\mathrm{f}}\left(\frac{\partial\Phi_k}{\partial x_l}+\frac{\partial\Phi_l}{\partial x_k}\right)\mathrm{d}V}_{=:I_2}+\delta_{kl}\Bigg]w_l\,.\end{aligned} \tag{B.27}$$

The integral I_1 can be reformulated using Green's first identity

$$\frac{1}{V_\mathrm{f}}\int_{V_\mathrm{f}}\frac{\partial\Phi_k}{\partial x_j}\frac{\partial\Phi_l}{\partial x_j}\,\mathrm{d}V=-\frac{1}{V_\mathrm{f}}\int_{V_\mathrm{f}}\Phi_k\frac{\partial^2\Phi_l}{\partial x_j^2}\,\mathrm{d}V+\frac{1}{V_\mathrm{f}}\int_{\partial V_\mathrm{f}}\Phi_k\frac{\partial\Phi_l}{\partial x_j}\,n_j\,\mathrm{d}A\,, \tag{B.28}$$

where the first integral vanishes because the components Φ_l are solutions to the Laplace equation. Using the periodic boundary conditions and the Neumann boundary condition (B.26b), the second integral can be rewritten as

$$\begin{aligned}\frac{1}{V_\mathrm{f}}\int_{\partial V_\mathrm{f}}\Phi_k\frac{\partial\Phi_l}{\partial x_j}\,n_j\,\mathrm{d}A &= \frac{1}{V_\mathrm{f}}\int_{A_\mathrm{fe}}\Phi_k\frac{\partial\Phi_l}{\partial x_j}\,n_j\,\mathrm{d}A+\frac{1}{V_\mathrm{f}}\int_{A_\mathrm{fs}}\Phi_k\frac{\partial\Phi_l}{\partial x_j}\,n_j\,\mathrm{d}A \\ &= \frac{1}{V_\mathrm{f}}\int_{A_\mathrm{fs}}\Phi_k\,n_l\,\mathrm{d}A=\frac{1-\epsilon}{\epsilon}\,\alpha_{kl}\,,\end{aligned} \tag{B.29}$$

where α_{kl} are the entries of the tensor of virtual inertia $\boldsymbol{A}$ (Batchelor, 2000, p.403). The integral I_2 can be simplified using Gauss' theorem

$$\frac{1}{V_\mathrm{f}}\int_{V_\mathrm{f}}\left(\frac{\partial\Phi_k}{\partial x_l}+\frac{\partial\Phi_l}{\partial x_k}\right)\mathrm{d}V=\frac{1}{V_\mathrm{f}}\int_{\partial V_\mathrm{f}}\left(\Phi_k\,n_l+\Phi_l\,n_k\right)\mathrm{d}A=\frac{1-\epsilon}{\epsilon}\,\left(\alpha_{kl}+\alpha_{lk}\right)\,, \tag{B.30}$$

also resulting in an expression involving the tensor of virtual inertia. With the results for I_1 and I_2 and with the symmetry $\alpha_{kl}=\alpha_{lk}$ (Batchelor, 2000, p.403), equation (B.27) results as

$$\frac{1}{V_\mathrm{f}}\int_{V_\mathrm{f}}\left(\frac{\partial\phi}{\partial x_j}\right)^2\mathrm{d}V=w_k\left(\delta_{kl}-\frac{1-\epsilon}{\epsilon}\,\alpha_{kl}\right)w_l\,. \tag{B.31}$$

The integral on the right hand side of the inequality (B.24) can be simplified to

$$\begin{aligned}\frac{1}{V_\mathrm{f}}\int_{V_\mathrm{f}}u_j\frac{\partial\phi}{\partial x_j}\,\mathrm{d}V &= \frac{1}{V_\mathrm{f}}\int_{V_\mathrm{f}}u_j\left(\frac{\partial\Phi_k}{\partial x_j}-\delta_{kj}\right)w_k\,\mathrm{d}V \\ &= \left(\frac{1}{V_\mathrm{f}}\int_{\partial V_\mathrm{f}}\Phi_k\,u_j\,n_j\,\mathrm{d}A-\langle u_k\rangle_\mathrm{i}\right)w_k=-\langle u_k\rangle_\mathrm{i}\,w_k\,,\end{aligned} \tag{B.32}$$

where the surface integral vanishes due to the no-penetration boundary condition for the velocity $\boldsymbol{u}$ and due to the periodicity of $\boldsymbol{\Phi}$ and $\boldsymbol{u}$. The complete inequality now reads

$$\left\langle \boldsymbol{u}^2 \right\rangle_{\mathrm{i}} \geq \frac{\left| - \left\langle \boldsymbol{u} \right\rangle_{\mathrm{i}} \cdot \boldsymbol{w} \right|^2}{\boldsymbol{w} \cdot \left(\boldsymbol{I} - \frac{1-\epsilon}{\epsilon} \boldsymbol{A} \right) \cdot \boldsymbol{w}} \,, \tag{B.33}$$

with the unknown velocity vector $\boldsymbol{w}$ still to be determined. The right hand side of the inequality is maximised with respect to $\boldsymbol{w}$ to obtain the strongest possible lower bound for the kinetic energy. The stationarity condition

$$\frac{\partial}{\partial \boldsymbol{w}} \left(\frac{\left(\left\langle \boldsymbol{u} \right\rangle_{\mathrm{i}} \cdot \boldsymbol{w} \right)^2}{\boldsymbol{w} \cdot \left(\boldsymbol{I} - \frac{1-\epsilon}{\epsilon} \boldsymbol{A} \right) \cdot \boldsymbol{w}} \right) = 0 \tag{B.34}$$

can be explicitly written as

$$\frac{2 \left(\left\langle \boldsymbol{u} \right\rangle_{\mathrm{i}} \cdot \boldsymbol{w} \right) \left\langle \boldsymbol{u} \right\rangle_{\mathrm{i}} \left[\boldsymbol{w} \cdot \left(\boldsymbol{I} - \frac{1-\epsilon}{\epsilon} \boldsymbol{A} \right) \cdot \boldsymbol{w} \right] - \left(\left\langle \boldsymbol{u} \right\rangle_{\mathrm{i}} \cdot \boldsymbol{w} \right)^2 2 \left(\boldsymbol{I} - \frac{1-\epsilon}{\epsilon} \boldsymbol{A} \right) \cdot \boldsymbol{w}}{\left[\boldsymbol{w} \cdot \left(\boldsymbol{I} - \frac{1-\epsilon}{\epsilon} \boldsymbol{A} \right) \cdot \boldsymbol{w} \right]^2} = 0 \,, \tag{B.35}$$

where the symmetry of $\boldsymbol{A}$ was used. This equation can be factored as

$$\frac{2 \left\langle \boldsymbol{u} \right\rangle_{\mathrm{i}} \cdot \boldsymbol{w}}{\boldsymbol{w} \cdot \left(\boldsymbol{I} - \frac{1-\epsilon}{\epsilon} \boldsymbol{A} \right) \cdot \boldsymbol{w}} \left[\left\langle \boldsymbol{u} \right\rangle_{\mathrm{i}} - \frac{\left\langle \boldsymbol{u} \right\rangle_{\mathrm{i}} \cdot \boldsymbol{w}}{\boldsymbol{w} \cdot \left(\boldsymbol{I} - \frac{1-\epsilon}{\epsilon} \boldsymbol{A} \right) \cdot \boldsymbol{w}} \left(\boldsymbol{I} - \frac{1-\epsilon}{\epsilon} \boldsymbol{A} \right) \cdot \boldsymbol{w} \right] = 0 \,. \tag{B.36}$$

The first factor results in the solution $\left\langle \boldsymbol{u} \right\rangle_{\mathrm{i}} \cdot \boldsymbol{w} = 0$, which implies the trivial inequality $\left\langle \boldsymbol{u}^2 \right\rangle_{\mathrm{i}} \geq 0$. The second factor results in the equation

$$\left\langle \boldsymbol{u} \right\rangle_{\mathrm{i}} - \frac{\left\langle \boldsymbol{u} \right\rangle_{\mathrm{i}} \cdot \boldsymbol{w}}{\boldsymbol{w} \cdot \left(\boldsymbol{I} - \frac{1-\epsilon}{\epsilon} \boldsymbol{A} \right) \cdot \boldsymbol{w}} \left(\boldsymbol{I} - \frac{1-\epsilon}{\epsilon} \boldsymbol{A} \right) \cdot \boldsymbol{w} = 0 \,, \tag{B.37}$$

which means that $\left\langle \boldsymbol{u} \right\rangle_{\mathrm{i}}$ and $\left(\boldsymbol{I} - \frac{1-\epsilon}{\epsilon} \boldsymbol{A} \right) \cdot \boldsymbol{w}$ must be collinear. Since the tensor is invertible, the unknown vector can be written as

$$\boldsymbol{w}_\gamma = \gamma \left(\boldsymbol{I} - \frac{1-\epsilon}{\epsilon} \boldsymbol{A} \right)^{-1} \cdot \left\langle \boldsymbol{u} \right\rangle_{\mathrm{i}} \tag{B.38}$$

with some constant γ. It can be seen that $\boldsymbol{w}_\gamma$ is a solution to equation (B.37) for all nonzero values of γ. Consequently, the inequality results as

$$\boxed{\left\langle \boldsymbol{u}^2 \right\rangle_{\mathrm{i}} \geq \left\langle \boldsymbol{u} \right\rangle_{\mathrm{i}} \cdot \left(\boldsymbol{I} - \frac{1-\epsilon}{\epsilon} \boldsymbol{A} \right)^{-1} \cdot \left\langle \boldsymbol{u} \right\rangle_{\mathrm{i}}} \tag{B.39}$$

and equality holds if $\boldsymbol{u}$ is a potential flow. Note that for an isotropic porous medium, the inequality may be simplified to

$$\left\langle \boldsymbol{u}^2 \right\rangle_{\mathrm{i}} \geq \alpha_\infty \left\langle \boldsymbol{u} \right\rangle_{\mathrm{i}}^2 \,, \tag{B.40}$$

where α_∞ is the high-frequency limit of the dynamic tortuosity. This inequality was stated by Lafarge (1993, p.123).

B.4. Helmholtz's minimum dissipation theorem

In this section, Helmholtz's minimum dissipation theorem (Batchelor, 2000, pp.227f) is rederived for periodic porous media. As a prerequisite, it is shown that the superficial volume-averaged velocity and the filter velocity are identical for a periodic porous medium.

B.4.1. Identity of filter velocity and superficial velocity average

The superficial velocity is defined as

$$\langle \boldsymbol{u} \rangle_{\mathrm{s}} = \frac{1}{V} \int_{V_{\mathrm{f}}} \boldsymbol{u} \, \mathrm{d}V = \frac{1}{V} \int_0^{L_x} \int_0^{L_y} \int_0^{L_z} \boldsymbol{u} \, \chi_{\mathrm{f}} \, \mathrm{d}z \, \mathrm{d}y \, \mathrm{d}x \tag{B.41}$$

for a Cartesian unit cell of the porous medium with an extent L_x, L_y and L_z in the x-, y- and z-direction, respectively. The characteristic function χ_{f} is 1 within the fluid and 0 within the solid. The filter velocity q_x in the x-direction is defined as

$$q_x = \frac{1}{A} \int_0^{L_y} \int_0^{L_z} u \, \chi_{\mathrm{f}} \, \mathrm{d}z \, \mathrm{d}y \tag{B.42}$$

and the superficial velocity average can thus be expressed as the average of the filter velocity

$$\langle u \rangle_{\mathrm{s}} = \frac{1}{L_x} \int_0^{L_x} q_x \, \mathrm{d}x \, . \tag{B.43}$$

Using integration by parts, the superficial velocity can be expressed in terms of the derivative of the filter velocity

$$\langle u \rangle_{\mathrm{s}} = \frac{1}{L_x} \left[q_x \, x \right]_{x=0}^{x=L_x} - \frac{1}{L_x} \int_0^{L_x} x \, \frac{\mathrm{d}q_x}{\mathrm{d}x} \, \mathrm{d}x = q_x|_{x=L_x} - \frac{1}{L_x} \int_0^{L_x} x \, \frac{\mathrm{d}q_x}{\mathrm{d}x} \, \mathrm{d}x \, . \tag{B.44}$$

The integral mass balance at a slice of the unit cell is

$$A \, \frac{\mathrm{d}q_x}{\mathrm{d}x} + \int_0^{L_z} \left[v \, \chi_{\mathrm{f}} \right]_{y=0}^{y=L_y} \, \mathrm{d}z + \int_0^{L_y} \left[w \, \chi_{\mathrm{f}} \right]_{z=0}^{z=L_z} \, \mathrm{d}y = 0 \tag{B.45}$$

and the periodic boundary conditions for v, w and χ_{f} imply that

$$\frac{\mathrm{d}q_x}{\mathrm{d}x} = 0 \, . \tag{B.46}$$

Therefore, the filter velocity q_x is constant and equal to $\langle u \rangle_{\mathrm{s}}$. The same arguments with the y- and z-directions in the place of the x-direction lead to the identity

$$\boxed{\langle \boldsymbol{u} \rangle_{\mathrm{s}} = \boldsymbol{q}} \tag{B.47}$$

of the filter velocity and the superficial velocity on a unit cell with periodic boundary conditions.

B.4.2. Derivation of Helmholtz's minimum dissipation theorem

Helmholtz's minimum dissipation theorem states that "[...] the rate of dissipation in the flow in a given region with negligible inertia forces is less than that in any other solenoidal velocity distribution in the same region (including one which satisfies the complete equation of motion) with the same values of the velocity at all points of the boundary region" (Batchelor, 2000, p.228). The objective of this section is to show that for periodic porous media it is sufficient to require both velocity fields to have the same superficial velocity.
In the following, the velocity $\boldsymbol{u}$ is a solution of the Stokes equations

$$\boldsymbol{\nabla} \cdot \boldsymbol{u} = 0 \tag{B.48a}$$

$$0 = -\boldsymbol{\nabla} p + \mu \Delta \boldsymbol{u} \tag{B.48b}$$

and the velocity $\boldsymbol{u}^*$ is an arbitrary divergence-free velocity field. Both fields are assumed to be triply periodic and to satisfy the no-slip and no-penetration boundary conditions at the fluid-solid interface A_{fs}. The strain rate tensors associated with the velocities $\boldsymbol{u}$ and $\boldsymbol{u}^*$ are $\boldsymbol{S}$ and $\boldsymbol{S}^*$, respectively. Following Batchelor (2000, p.228), the volume-averaged dissipation rate of $\boldsymbol{u}^*$ is decomposed with respect to the dissipation rate of the Stokes flow

$$2\mu \left\langle \boldsymbol{S}^* : \boldsymbol{S}^* \right\rangle_{\mathrm{s}} = 2\mu \left\langle \boldsymbol{S} : \boldsymbol{S} \right\rangle_{\mathrm{s}} + \underbrace{2\mu \left\langle (\boldsymbol{S}^* - \boldsymbol{S}) : (\boldsymbol{S}^* - \boldsymbol{S}) \right\rangle_{\mathrm{s}}}_{\geq 0} + 4\mu \left\langle (\boldsymbol{S}^* - \boldsymbol{S}) : \boldsymbol{S} \right\rangle_{\mathrm{s}} . \tag{B.49}$$

When the squared difference of the strain rate is neglected, the inequality

$$2\mu \left\langle \boldsymbol{S}^* : \boldsymbol{S}^* \right\rangle_{\mathrm{s}} \geq 2\mu \left\langle \boldsymbol{S} : \boldsymbol{S} \right\rangle_{\mathrm{s}} + 4\mu \left\langle (\boldsymbol{S}^* - \boldsymbol{S}) : \boldsymbol{S} \right\rangle_{\mathrm{s}} \tag{B.50}$$

is obtained. Due to the symmetry of $\boldsymbol{S}$, the last term can be rewritten as

$$\frac{2\mu}{V} \int_{V_{\mathrm{f}}} \left(S_{ij}^* - S_{ij} \right) S_{ij} \, \mathrm{d}V = \frac{2\mu}{V} \int_{V_{\mathrm{f}}} \frac{\partial \left(u_i^* - u_i \right)}{\partial x_j} \, S_{ij} \, \mathrm{d}V \, , \tag{B.51}$$

which can be integrated by parts using Gauss' theorem

$$\frac{2\mu}{V} \int_{V_{\mathrm{f}}} \left(S_{ij}^* - S_{ij} \right) S_{ij} \, \mathrm{d}V = \frac{2\mu}{V} \int_{\partial V_{\mathrm{f}}} \left(u_i^* - u_i \right) \, S_{ij} \, n_j \, \mathrm{d}A - \frac{\mu}{V} \int_{V_{\mathrm{f}}} \left(u_i^* - u_i \right) \frac{\partial^2 u_i}{\partial x_j^2} \, \mathrm{d}V \, . \tag{B.52}$$

Since the velocity $\boldsymbol{u}$ satisfies the Stokes equations, the Laplacian of the velocity can be replaced with the pressure gradient

$$\frac{2\mu}{V} \int_{V_{\mathrm{f}}} \left(S_{ij}^* - S_{ij} \right) S_{ij} \, \mathrm{d}V = \frac{2\mu}{V} \int_{\partial V_{\mathrm{f}}} \left(u_i^* - u_i \right) \, S_{ij} \, n_i \, \mathrm{d}A - \frac{1}{V} \int_{V_{\mathrm{f}}} \left(u_i^* - u_i \right) \frac{\partial p}{\partial x_i} \, \mathrm{d}V \, . \tag{B.53}$$

Integrating by parts and splitting the surface integrals into the contributions of the fluid-solid

interface A_{fs} and the open pore areas A_{fe}, the equation canb e rewritten as

$$\begin{aligned}\frac{2\mu}{V}\int_{V_\mathrm{f}}\left(S_{ij}^{*}-S_{ij}\right)S_{ij}\,\mathrm{d}V = &\frac{1}{V}\int_{A_\mathrm{fs}}\left(u_i^{*}-u_i\right)\left[2\,\mu\,S_{ij}-p\,\delta_{ij}\right]\,n_j\,\mathrm{d}A\\ &+\frac{1}{V}\int_{A_\mathrm{fe}}\left(u_i^{*}-u_i\right)\left[2\,\mu\,S_{ij}-p\,\delta_{ij}\right]\,n_j\,\mathrm{d}A\\ &-\frac{1}{V}\int_{V_\mathrm{f}}p\,\frac{\partial\left(u_i^{*}-u_i\right)}{\partial x_i}\,\mathrm{d}V\,.\end{aligned}\tag{B.54}$$

The first integral vanishes due to the no-slip condition on A_{fs} and the last term is zero because both velocity fields are divergence-free. Using the characteristic function χ_f of the fluid domain, the remaining term can be rewritten as

$$\begin{aligned}\frac{2\mu}{V}\int_{V_\mathrm{f}}\left(S_{ij}^{*}-S_{ij}\right)S_{ij}\,\mathrm{d}V = &\frac{1}{V}\left[\int_0^{L_y}\int_0^{L_z}\left(u_i^{*}-u_i\right)\left[2\,\mu\,s_{i1}-p\,\delta_{i1}\right]\chi_\mathrm{f}\,\mathrm{d}z\,\mathrm{d}y\right]_0^{L_x}\\ &+\frac{1}{V}\left[\int_0^{L_x}\int_0^{L_z}\left(u_i^{*}-u_i\right)\left[2\,\mu\,s_{i2}-p\,\delta_{i2}\right]\chi_\mathrm{f}\,\mathrm{d}z\,\mathrm{d}x\right]_0^{L_y}\\ &+\frac{1}{V}\left[\int_0^{L_x}\int_0^{L_y}\left(u_i^{*}-u_i\right)\left[2\,\mu\,s_{i3}-p\,\delta_{i3}\right]\chi_\mathrm{f}\,\mathrm{d}y\,\mathrm{d}x\right]_0^{L_z}\,.\end{aligned}\tag{B.55}$$

Since he velocities $\boldsymbol{u}$ and $\boldsymbol{u}^*$ — and hence also the strain rate $\boldsymbol{S}$ — satisfy periodic boundary conditions at opposite faces of the unit cell, the respective contributions vanish. Furthermore, as the velocity $\boldsymbol{u}$ satisfies the Stokes equations, the pressure gradient is also triply periodic. Hence, the values of p on two opposite faces can only differ by a constant. The equation may thus be further simplified to

$$\begin{aligned}\frac{2\mu}{V}\int_{V_\mathrm{f}}\left(S_{ij}^{*}-S_{ij}\right)S_{ij}\,\mathrm{d}V = &-\frac{[p]_{x=0}^{x=L_x}}{L_x}\left[\frac{1}{L_y\,L_z}\int_0^{L_y}\int_0^{L_z}\left(u^{*}-u\right)\chi_\mathrm{f}\,\mathrm{d}z\,\mathrm{d}y\right]_{x=0}\\ &-\frac{[p]_{y=0}^{y=L_y}}{L_y}\left[\frac{1}{L_x\,L_z}\int_0^{L_x}\int_0^{L_z}\left(v^{*}-v\right)\chi_\mathrm{f}\,\mathrm{d}z\,\mathrm{d}x\right]_{y=0}\\ &-\frac{[p]_{z=0}^{z=L_z}}{L_z}\left[\frac{1}{L_x\,L_y}\int_0^{L_x}\int_0^{L_y}\left(w^{*}-w\right)\chi_\mathrm{f}\,\mathrm{d}y\,\mathrm{d}x\right]_{z=0}\,.\end{aligned}\tag{B.56}$$

In the brackets, the difference between the filter velocities q_x and q_x^*, q_y and q_y^* and q_z and q_z^* can be recognised. Consequently, the integral is zero if the filter velocities $\boldsymbol{q}$ and $\boldsymbol{q}^*$ or, by equation (B.47), the superficial velocities $\langle\boldsymbol{u}\rangle_\mathrm{s}$ and $\langle\boldsymbol{u}^*\rangle_\mathrm{s}$ are equal. This concludes the proof of the minimum dissipation theorem.
The dissipation rate in Stokes flow through a porous medium can be expressed as (Zhu et al., 2014; Paéz-García et al., 2017)

$$2\mu\,\langle\boldsymbol{S}:\boldsymbol{S}\rangle_\mathrm{s} = \mu\,\langle\boldsymbol{u}\rangle_\mathrm{s}\cdot\boldsymbol{K}^{-1}\cdot\langle\boldsymbol{u}\rangle_\mathrm{s}\,.\tag{B.57}$$

For a velocity field $\boldsymbol{u}^*$ with $\langle\boldsymbol{u}\rangle_\mathrm{s} = \langle\boldsymbol{u}^*\rangle_\mathrm{s}$, periodic boundary conditions and no-slip and no-

penetration boundary conditions at the wall, one thus obtains the inequality

$$\boxed{2\mu \left\langle \boldsymbol{S}^* : \boldsymbol{S}^* \right\rangle_\mathrm{s} \geq \mu \left\langle \boldsymbol{u}^* \right\rangle_\mathrm{s} \cdot \boldsymbol{K}^{-1} \cdot \left\langle \boldsymbol{u}^* \right\rangle_\mathrm{s}} \,. \tag{B.58}$$

This inequality has also been derived by Rubinstein & Torquato (1989, eq. 3.9) as a lower bound for the permeability.

B.5. Scaling of the friction drag and the viscous pressure drag at high frequencies

In Unglehrt & Manhart (2023a, reprinted in appendix D.6), it was found that the friction drag and the viscous pressure drag at $Wo = 10$ and $Wo = 31.62$ approach a laminar boundary layer scaling for large Reynolds numbers. However, no scaling could be found at $Wo = 100$. Here, the scaling of the friction drag is briefly re-investigated including the cases HF6 and HF7.

Figure B.1 shows the friction drag and the viscous pressure drag in the steady laminar boundary layer normalisation. In contrast to the lower Womersley numbers, the curves at $Wo = 100$ do not collapse for large Reynolds numbers. Rather, the normalised friction drag for the case HF7 breaks the decreasing trend and the viscous pressure drag for the case HF7 shows a qualitatively different behaviour compared to the other cases; this behaviour is robust to the use of the SGS model. The different behaviour of the case HF7, which has the highest Reynolds number in the present work, could be attributed to strong interactions between the turbulent fluctuations in the bulk and the near-wall flow. Further high Reynolds number cases should be investigated to clarify the scaling of the drag components.

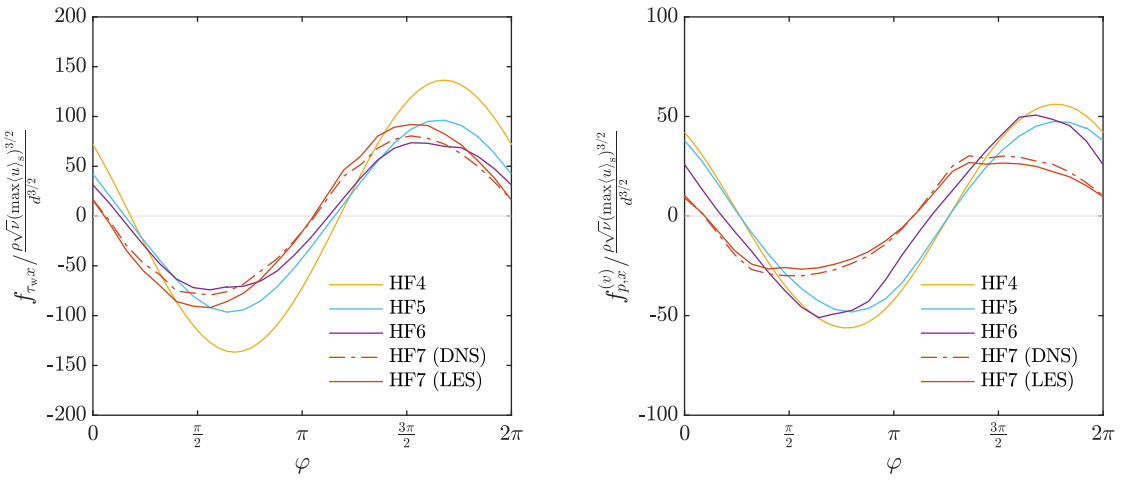

(a) Friction drag

(b) Viscous pressure drag

Figure B.1: Friction drag and viscous pressure drag normalised with $\rho\sqrt{\nu}(\max \langle u \rangle_\mathrm{s})^{3/2}/d^{3/2}$ corresponding to a steady laminar boundary layer scaling for the simulations at $Wo = 100$.

C. Appendix: Wall shear stress

In this section, a robust procedure for the identification of critical points in the wall shear stress field is described. This method is based on a discrete variant of the Poincaré-Hopf theorem. Then, several instantaneous wall shear stress fields are discussed for the case MF4. Finally, the definition of separation lines is reviewed and different possible approaches for their identification are discussed.

C.1. Calculation of the wall shear stress field

The wall shear stress is not explicitly available in the ghost-cell immersed boundary method (cf. sec. 2.4.2) and needs to be computed in a post-processing step. For every sphere of the simulation domain, a triangle mesh is defined on a sphere of diameter $d+2h$, where $h = \Delta x$, and the velocity field is interpolated to this mesh. The wall shear stress is then obtained as

$$\boldsymbol{\tau}_{\mathrm{w}}(\varphi, \theta) = \frac{\mu}{h}\, \boldsymbol{u}(r = d/2 + h, \varphi, \theta)\,. \tag{C.1}$$

As this procedure is inaccurate close to the contact points, a circular region around each contact point is excluded from further analysis.

C.2. Detection and classification of critical points

The first step in analysing the wall shear stress topology is the identification of the critical points $\boldsymbol{p}$, where $\boldsymbol{\tau}_{\mathrm{w}}(\boldsymbol{p}) = 0$. Based on the Poincaré index (section C.2.2), the critical points can be distinguished as saddles (-1) and nodes ($+1$). The nodes are further classified according to the eigenvalues of the Jacobian matrix at the critical point (Helman & Hesselink, 1989; Günther & Baeza Rojo, 2021) as sources, sinks, attracting or repelling foci or centres.

An important consistency check for the identified critical points is provided by the Poincaré-Hopf theorem. It establishes a connection between the Euler characteristic of a surface and the number of critical points of a vector field on that surface.

C.2.1. Euler characteristic

The Euler characteristic $\chi(M)$ is a topological invariant of a manifold M. For surfaces, the Euler characteristic is defined as (Foss, 2007)

$$\chi(M) = 2 - 2\sum \text{handles} - \sum \text{holes}\,. \tag{C.2}$$

For polyhedra, the Euler characteristic can also be computed as (Armstrong, 1983, p.158)

$$\chi = V - E + F\,, \tag{C.3}$$

where V, E and F are the number of vertices, edges and faces in the mesh, respectively. In the hexagonal close-packed arrangement, each sphere has exactly 12 contact points. At these contact points, the numerical algorithm (cf. section 2.5.2) sinters the spheres into one body. When a single sphere is considered, 12 cuts are have to be introduced at the contact points. Thus, the Euler characteristic (C.2) results as

$$\chi(M) = 2 - 2\sum \text{handles} - \sum \text{holes} = 2 - 0 - 12 = -10\,. \tag{C.4}$$

This value has been confirmed numerically using equation (C.3) by considering various triangulations of the surface.

C.2.2. Poincaré index

The behaviour of a vector field $\boldsymbol{v}$ in the neighbourhood of an isolated zero at point $\boldsymbol{p}$ can be characterised by the Poincaré index $\text{index}_{\boldsymbol{p}}(\boldsymbol{v})$. Here, the definition of Davis (1962, pp.351-355) for plane vector fields is reproduced. When a closed curve is traversed in counterclockwise directions, the local vector $\boldsymbol{v}(\boldsymbol{x})/\left|\boldsymbol{v}(\boldsymbol{x})\right|$ performs $2\pi I$ rotations, where I must be an integer. The index of the critical point $\boldsymbol{p}$ is equal to the index I of the closed curve that contains only this critical point. On the other hand, the index of a closed curve enclosing multiple critical points is equal to the sum of the indices of these critical points; else it is zero. For non-degenerate critical points, the index is either -1 for saddle points or $+1$ for sources, sinks, foci and centres.

C.2.3. Poincaré-Hopf theorem

The Poincaré-Hopf theorem is usually formulated for closed manifolds. For manifolds without boundary like the sphere with 12 holes, two different statements are available.

Statement with boundary switch points

Theorem 1 (Poincaré-Hopf theorem (Foss et al., 2016))**.** *"Let [M] be a smooth surface with boundary, and let* $\boldsymbol{v}$ *by a continuously differentiable vector field on [M] which doesn't vanish on [∂M]. Then, the Euler characteristic is equal to"*

$$\chi(M) = \sum_{\boldsymbol{p}\in\{\textit{zeros of }\boldsymbol{v}\}} \text{index}_{\boldsymbol{p}}(\boldsymbol{v}) + \text{wind}_{\partial M}(\boldsymbol{v})\,. \tag{C.5}$$

Here, $\text{wind}_{\partial M}(\boldsymbol{v})$ is the "winding number of $\boldsymbol{v}$ around the boundary". The winding number can also be expressed in terms of the number of points on the boundary at which the normal

component of $\boldsymbol{v}$ vanishes (Liu et al., 2011; Foss et al., 2016):

$$\mathrm{wind}_{\partial M}(\boldsymbol{v}) = \frac{Z^+ - Z^-}{2} \tag{C.6}$$

When following the direction of the vector $\boldsymbol{v}$ along the boundary, the number Z^- counts all zero points of the normal component of $\boldsymbol{v}$ where the vector field changes from an inward to an outward orientation ("negative switch point"). Viceversa, the number Z^+ counts all zero points of the tangent component of $\boldsymbol{v}$ where the vector field changes from an outward to an inward orientation ("positive switch point"). A detailed discussion of switch points in the context of flow visualisation has been given by Weinkauf (2008).
For the present application, the above statement of the Poincaré-Hopf theorem poses a problem when a critical point is located within a contact point region that is cut out of the manifold. Then, the switch points on the cut will not be on the streamlines that connected the removed critical point to the critical points on the remaining manifold. In particular, this could affect separation lines, which connect saddles and sinks (cf. section C.3.1). Therefore, a different formulation of the theorem based on the tangential component of $\boldsymbol{v}$ is considered.

Statement with half-integer indices

The formulation of Jubin (2009) applies to a "smooth manifold with (possibly) boundary" M of arbitrary dimension. The vector field $\boldsymbol{v}$ is assumed to have "no zero on ∂M, and its tangential component [...] restricted to ∂M has isolated zeros". "The index of $[v]$ on $[M]$ at a zero of its tangential component on the boundary is defined to be half the index of its tangential component restricted to the boundary if the vector field points inwards, and minus half it if the vector field points outwards". Since the boundary ∂M of a manifold M is always a manifold without boundary of dimension $\dim M - 1$, the index of the tangential component on the boundary is be integer-valued. Consequently, the index of v can take half-integer values on the boundary.
"[T]he index of a vector field with isolated zeros on a [smooth manifold with (possibly) boundary] is defined to be the sum of its indices on the interior and on the boundary"

$$\mathrm{ind}(\boldsymbol{v}) = \mathrm{ind}_\circ(\boldsymbol{v}) + \mathrm{ind}_\partial(\boldsymbol{v})\,, \tag{C.7}$$

where

$$\mathrm{ind}_\circ(\boldsymbol{v}) = \sum_{\boldsymbol{p}\in\{\text{zeros of } \boldsymbol{v}\}} \mathrm{index}_{\boldsymbol{p}}(\boldsymbol{v}) \tag{C.8}$$

is the index sum in the interior of the manifold and

$$\mathrm{ind}_\partial(\boldsymbol{v}) = \sum_{\boldsymbol{q}\in\{\text{zeros of } \boldsymbol{v}_\parallel\}} -\frac{1}{2}\,\mathrm{sgn}\,(\boldsymbol{v}\cdot\boldsymbol{n})\,\mathrm{index}_{\boldsymbol{q}}(\boldsymbol{v}_\parallel) \tag{C.9}$$

is the index sum on the boundary of the manifold. The outward normal vector of ∂M is de-

noted as $\boldsymbol{n}$ and $\boldsymbol{v}_{\parallel} = \boldsymbol{v} - (\boldsymbol{v} \cdot \boldsymbol{n})\boldsymbol{n}$ is the tangential component of the vector field on the boundary. The Poincaré-Hopf theorem can then be stated as follows.

Theorem 2 (Poincaré-Hopf theorem (Jubin, 2009))**.** *Let $\boldsymbol{v}$ be a vector field with isolated zeros on the compact oriented [smooth manifold with (possibly) boundary] M. Then*

$$\operatorname{ind}(\boldsymbol{v}) = \begin{cases} \chi(M) & \text{if } \dim M \text{ is even,} \\ 0 & \text{if } \dim M \text{ is odd} \end{cases} \tag{C.10}$$

Here, the manifold M represents a surface and $\dim M = 2$.

C.2.4. Discrete Poincaré-Hopf theorem

Gortler et al. (2006) proved a discrete version of the Poincaré-Hopf theorem for discrete 1-forms on polygonal meshes without boundary. A discrete 1-form assigns a real value to each edge of the mesh. In particular, the following 1-form samples a vector field $\boldsymbol{v}$ onto an edge $\overline{\boldsymbol{P}_i\boldsymbol{P}_j}$ of a mesh (do Goes et al., 2015)

$$c_{ij}(\boldsymbol{v}) = \int_{\boldsymbol{P}_i}^{\boldsymbol{P}_j} \boldsymbol{v} \cdot \boldsymbol{t}_{ij} \, \mathrm{d}s \,, \tag{C.11}$$

where $\boldsymbol{t}_{ij}$ is the unit vector along the edge. The values c_{ij} together with the edge orientations thus form a discrete representation of the vector field. For a piecewise linear vector field, the line integral can be evaluated as

$$c_{ij} = \frac{\boldsymbol{v}_i + \boldsymbol{v}_j}{2} \cdot (\boldsymbol{P}_j - \boldsymbol{P}_i) \,, \tag{C.12}$$

where $\boldsymbol{v}_i$, $\boldsymbol{v}_j$ are the values of the vector field at the vertices of the mesh (do Goes et al., 2015). Gortler et al. (2006) defined the index of a vertex v and a face f in terms of the sign changes $\operatorname{sc}(v)$ and $\operatorname{sc}(f)$ in the values of the 1-form as the adjacent sectors are traversed in order as

$$\operatorname{ind}(v) = \frac{2 - \operatorname{sc}(v)}{2} \tag{C.13}$$

$$\operatorname{ind}(f) = \frac{2 - \operatorname{sc}(f)}{2} \tag{C.14}$$

As can be seen from figure C.1, the index is non-zero for singular vertices and faces, i.e. nodes, saddles and foci, and is zero for non-singular vertices and faces.

Theorem 3 (Discrete Poincaré-Hopf theorem (Gortler et al., 2006))**.** *For a non-zero 1-form on a closed oriented manifold mesh with vertices $\mathcal{V}$ and faces $\mathcal{F}$, the sum of the indices*

$$\sum_{v \in \mathcal{V}} \operatorname{ind}(v) + \sum_{f \in \mathcal{F}} \operatorname{ind}(f) = \chi \tag{C.15}$$

is equal to the Euler characteristic of the mesh.

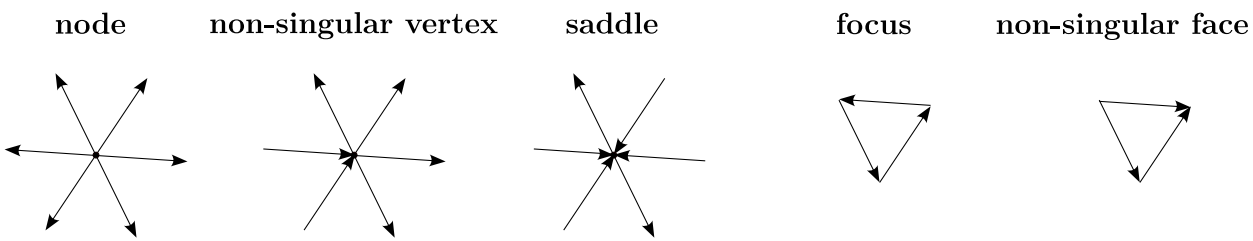

Figure C.1: Different configurations of the sign change sc and index ind in a triangular mesh following Gortler et al. (2006). The arrows indicate the direction of the 1-form c_{ij}.

For meshes with boundary, the index formula for vertices needs to be modified in the following manner

$$\operatorname{ind}(v) = \begin{cases} \frac{2-\operatorname{sc}(v)}{2} & \text{if } v \in \operatorname{int} \mathcal{V}\,, \\ \frac{1-\operatorname{sc}(v)}{2} & \text{if } v \in \partial \mathcal{V}\,, \end{cases} \tag{C.16}$$

where sign changes outside the mesh are not counted.

Proof. Now the discrete Poincaré-Hopf theorem is proved for a mesh with boundary. First, the number of vertices V and the number of faces F are identified within the sum of the indices of all vertices and faces in the mesh

$$\begin{aligned} &\sum_{v \in \mathcal{V}} \operatorname{ind}(v) + \sum_{f \in \mathcal{F}} \operatorname{ind}(f) \\ &= \sum_{v \in \operatorname{int} \mathcal{V}} \frac{2 - \operatorname{sc}(v)}{2} + \sum_{v \in \partial \mathcal{V}} \frac{1 - \operatorname{sc}(v)}{2} + \sum_{f \in \mathcal{F}} \frac{2 - \operatorname{sc}(f)}{2} \\ &= V - \frac{1}{2} \left[\sum_{v \in \operatorname{int} \mathcal{V}} \operatorname{sc}(v) + \sum_{v \in \partial \mathcal{V}} (1 + \operatorname{sc}(v)) + \sum_{f \in \mathcal{F}} \operatorname{sc}(f) \right] + F\,. \end{aligned} \tag{C.17}$$

Then, a sector at a vertex bounded by two edges is considered (cf. figure C.2). There exist four configurations: (i) both vectors point towards the vertex, (ii) both vectors point away from the vertex, (iii) and (iv) one vector points towards and the other points away from the vertex. In the cases (i) and (ii) no sign change occurs for the vertex and a sign change occurs for the face, whereas in the cases (iii) and (iv) a sign change occurs for the vertex and no sign change occurs for the face. Therefore, the number of total sign changes in the mesh is equal to the number of sectors

$$\sum_{v \in \operatorname{int} \mathcal{V}} \operatorname{sc}(v) + \sum_{v \in \partial \mathcal{V}} \operatorname{sc}(v) + \sum_{f \in \mathcal{F}} \operatorname{sc}(f) = \text{number of sectors}\,. \tag{C.18}$$

For an interior vertex, the number of sectors is equal to the number of adjacent edges. For a boundary vertex, the number of sectors is equal to the number of adjacent edges minus one.

When counting all sectors, every edge is counted exactly twice and we obtain

$$\sum_{v\in\operatorname{int}\mathcal{V}} \operatorname{sc}(v) + \sum_{v\in\partial\mathcal{V}} \operatorname{sc}(v) + \sum_{f\in\mathcal{F}} \operatorname{sc}(f) = 2E - \sum_{v\in\partial\mathcal{V}} 1\,, \tag{C.19}$$

where E is the number of edges. In the final step of the proof, equation (C.19) is inserted into equation (C.17) and the definition of the Euler characteristic (C.3) is used to obtain the desired result

$$\sum_{v\in\mathcal{V}} \operatorname{ind}(v) + \sum_{f\in\mathcal{F}} \operatorname{ind}(f) = V - \frac{1}{2}\,[2E] + F = V - E + F = \chi\,. \tag{C.20}$$

□

Similar to the continuous case (Jubin, 2009), the discrete Poincaré index (C.16) can result in half-integer values on the boundary. These points correspond to zeros of the vector component tangential to the boundary. In analogy to the definition of Hunt et al. (1978), the vertices with index $+\frac{1}{2}$ are referred to as "half-nodes" and the vertices with index $-\frac{1}{2}$ are referred to as "half-saddles". The exact nature of the relation between the critical vertices and faces of the discrete 1-form on the one hand and the critical points of the vector field on the other hand remains to be explored.

C.2.5. Detection of critical points using the discrete Poincaré-Hopf theorem

In a first attempt, the method of Wang et al. (2018) was used, which can determine the triangles containing the critical points and the corresponding Poincaré index for piecewise linear wall shear stress fields. However, the approach of Wang et al. (2018) is not easily generalised to manifolds with boundaries and the resulting critical points did not always satisfy the Poincaré-Hopf theorem.

Therefore, the critical points of the wall shear stress field are determined based on the discrete Poincaré index for edge-based discrete vector fields (cf. section C.2.4). This approach can naturally handle manifolds with boundary and guarantees under weak assumptions that the critical points satisfy the discrete Poincaré-Hopf theorem. Due to the discrete nature, the vertices and faces with a nonzero index do not exactly satisfy $\boldsymbol{\tau}_{\mathrm{w}}(\boldsymbol{x}_i^*) = 0$. However, a close agreement with the critical points identified by the method of Wang et al. (2018) could be observed. The identified nodes can be easily classified into sources and sinks using the wall shear stress divergence (Mazzi et al., 2019).

Note that there exists a degenerate case in which the wall shear stress value is zero for some edge. Then, no clear index can be determined for the adjacent vertices and faces. However, adding a perturbation to the zero value leads to a definite orientation of the vector field. In some configurations, the perturbation can locally create or annihilate pairs of critical points. Here, the perturbation of the degenerate case is chosen based on a global numbering of the vertices, where the vector points from the lower to the higher index. Based on the topological simplification concept of Skraba et al. (2014), one could also set the orientation of all edges with $|c_{ij}|$ below a given tolerance such that the total number of critical points is minimal.

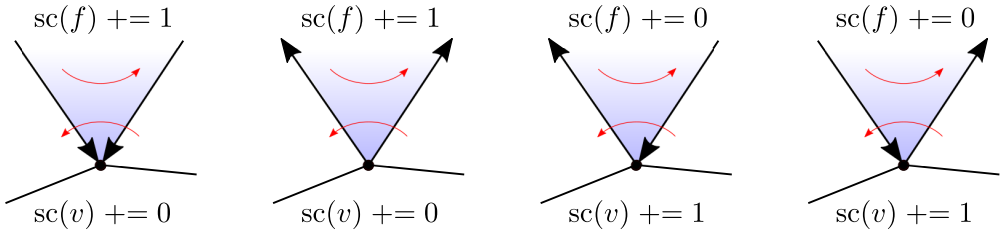

Figure C.2: Sign changes at the traversal of a sector: (i) both vectors point towards the vertex, (ii) both vectors point away from the vertex, (iii) and (iv) one vector points towards and the other points away from the vertex. The red arrows indicate the counting direction of the vertex and the face.

C.2.6. Results

The wall shear stress fields have been investigated for the case MF4 and is displayed in the figures C.3, C.4, C.5 and C.6 at different times. The critical points determined with the discrete Poincaré index show excellent agreement with the line-integral convolution (Cabral & Leedom, 1993) of the wall shear stress field at all times.

Figure C.3 shows a wall shear stress field shortly after the flow has been started from rest. The hexagonal sphere pack is viewed from the section $x = 0$, which is indicated by white dash-dotted lines, along the positive x-direction (cf. figures 2.3 and 2.4). The front spheres are thus seen from the inside. The characteristic boundary layer thickness can be estimated as $\sqrt{2\nu t} = 0.022\,d$, so the flow is still close to the potential flow. The wall shear stress field has an approximate fore-aft symmetry, indicating that the flow is still linear. At most of the contact points there is a pair of half-saddles dividing the flow around the contact point. These half-saddles are a consequence of the hole in the sphere and would disappear if the spheres were moved slightly apart.[1] Finally, the circular regions of transverse flow around some contact points could represent a separation at the rear end of the sphere.

Figure C.4 shows some reorganisations of the wall shear stress field. At the contact points in the mirror plane $z = \sqrt{6}/3\,d$ two half-saddles appear, which are each connected with an attracting focus; as a consequence of the Poincaré-Hopf theorem, a saddle appears to balance the indices $(2 \cdot (-\frac{1}{2}+1)-1 = 0)$. Note that if the spheres were moved slightly apart, the two lateral half-saddles would merge into a regular saddle point on each sphere. This is consistent with (Wegner et al., 1971), who have argued that a saddle is the only possible type of critical point of the wall shear stress field at the contact points.

Figure C.5 shows the wall shear stress field close to the maximum of the superficial velocity ($Re = 73$). The spatial distribution of the wall shear stress is concentrated at the entrance of the tetrahedral pores, where the flow branches and is squeezed from the touching spheres, and inside the tetrahedral pores, where the inertial cores impinge on the wall and are redirected towards the octahedral pores. Behind the contact points inside the channels along the x-direction, the pattern of critical points is similar to those observed by Wegner et al. (1971) for the face-centred cubic sphere pack at $Re = 82$.

Figure C.5 shows the wall shear stress field at a slightly later time, when the magnitude

[1] This is consistent with the Poincaré-Hopf theorem, since a hole contributes -1 to the Euler characteristic of the surface and each of the two half-saddles has an index of $-\frac{1}{2}$.

of the wall shear stress is at its maximum. While the spatial distribution of the wall shear stress does not change significantly, the topology of the wall shear stress field becomes more complex as several saddle-node pairs are born.

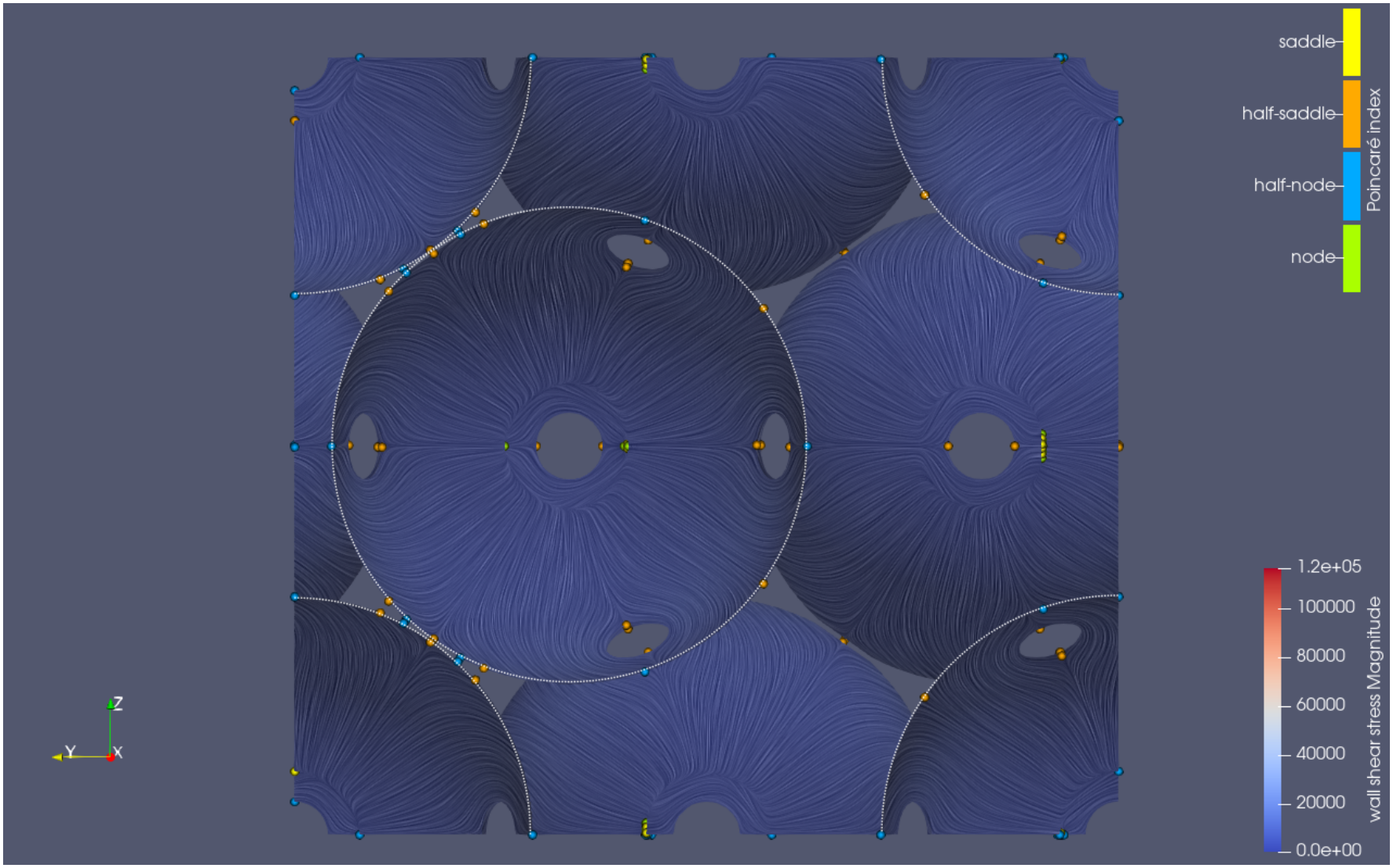

Figure C.3: Line-integral convolution of the wall shear stress field of the case MF4 at $\Omega t = 0.08\pi$ coloured by the wall shear stress magnitude $|\boldsymbol{\tau}_\mathrm{w}|\, d^2/(\rho\nu^2)$. The flow goes into the plane (positive x-direction). The critical points are coloured according to their discrete Poincaré index (C.16).

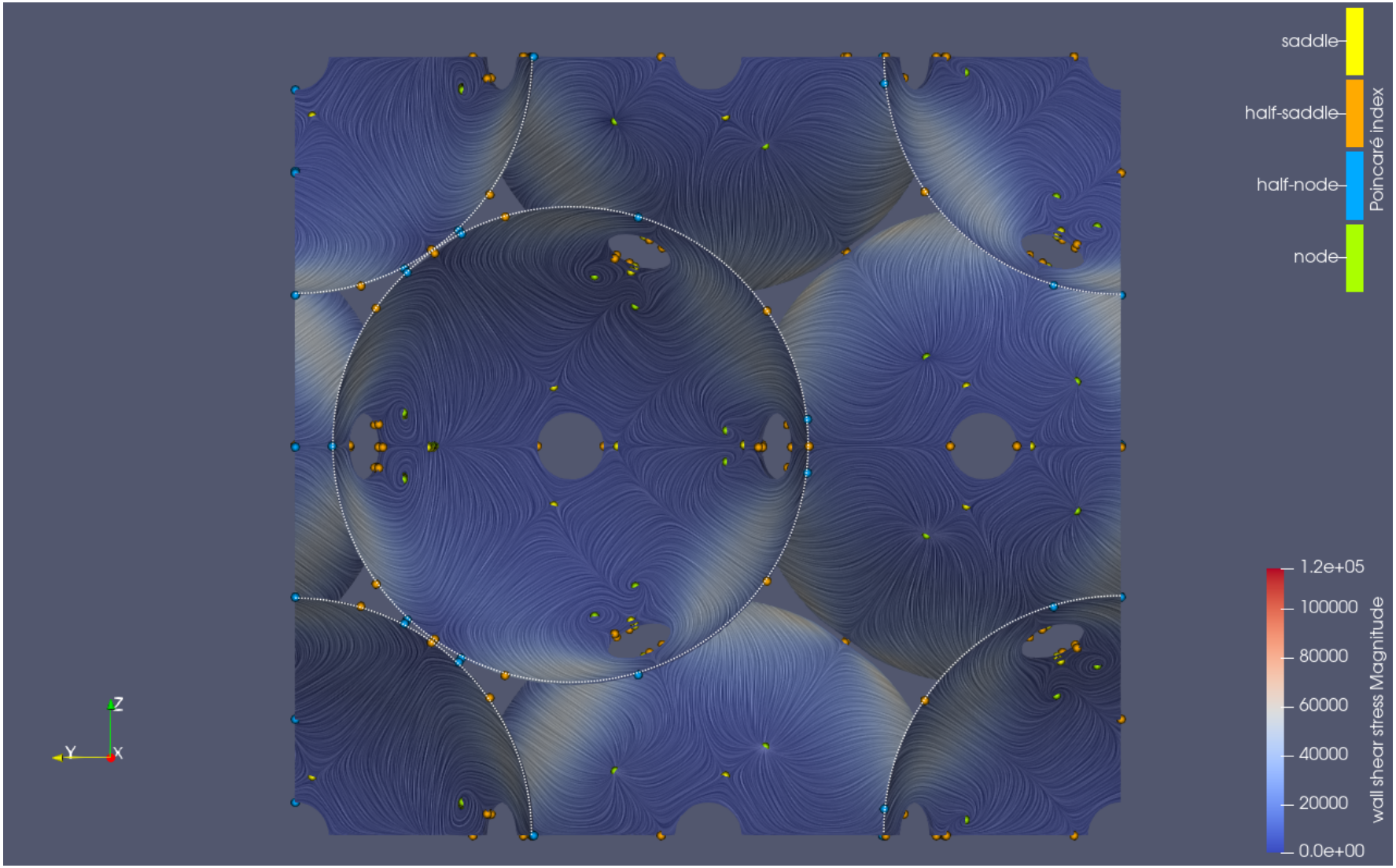

Figure C.4: Line-integral convolution of the wall shear stress field of the case MF4 at $\Omega t = 0.4\pi$ coloured by the wall shear stress magnitude $|\boldsymbol{\tau}_\mathrm{w}|\, d^2/(\rho\nu^2)$. The flow goes into the plane (positive x-direction). The critical points are coloured according to their discrete Poincaré index (C.16).

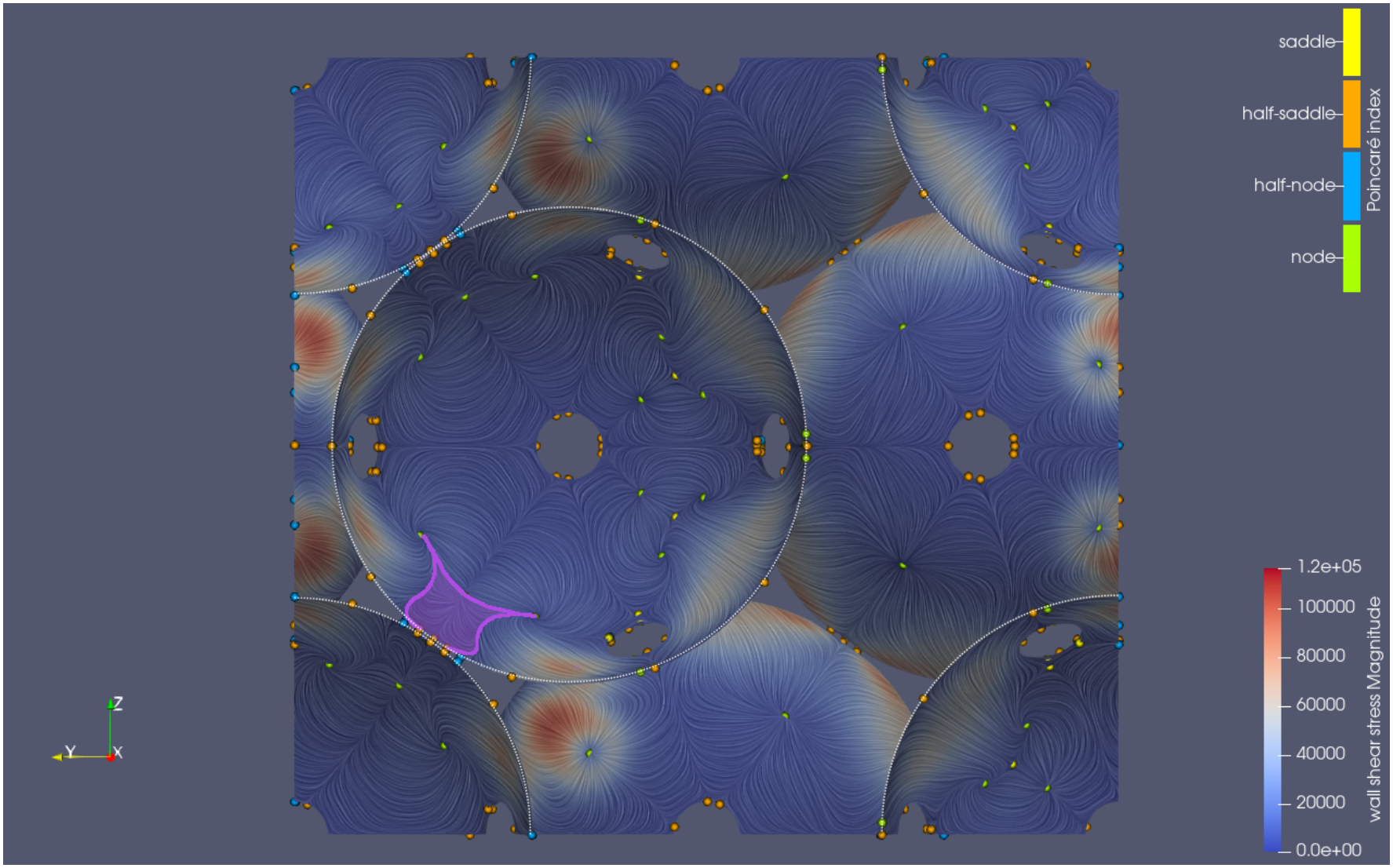

Figure C.5: Line-integral convolution of the wall shear stress field of the case MF4 at $\Omega t = 4.64\pi$ coloured by the wall shear stress magnitude $|\boldsymbol{\tau}_\mathrm{w}|\, d^2/(\rho\nu^2)$. The flow goes into the plane (positive x-direction). The critical points are coloured according to their discrete Poincaré index (C.16). The highlighted region indicates a separation region similar to those reported by Wegner et al. (1971).

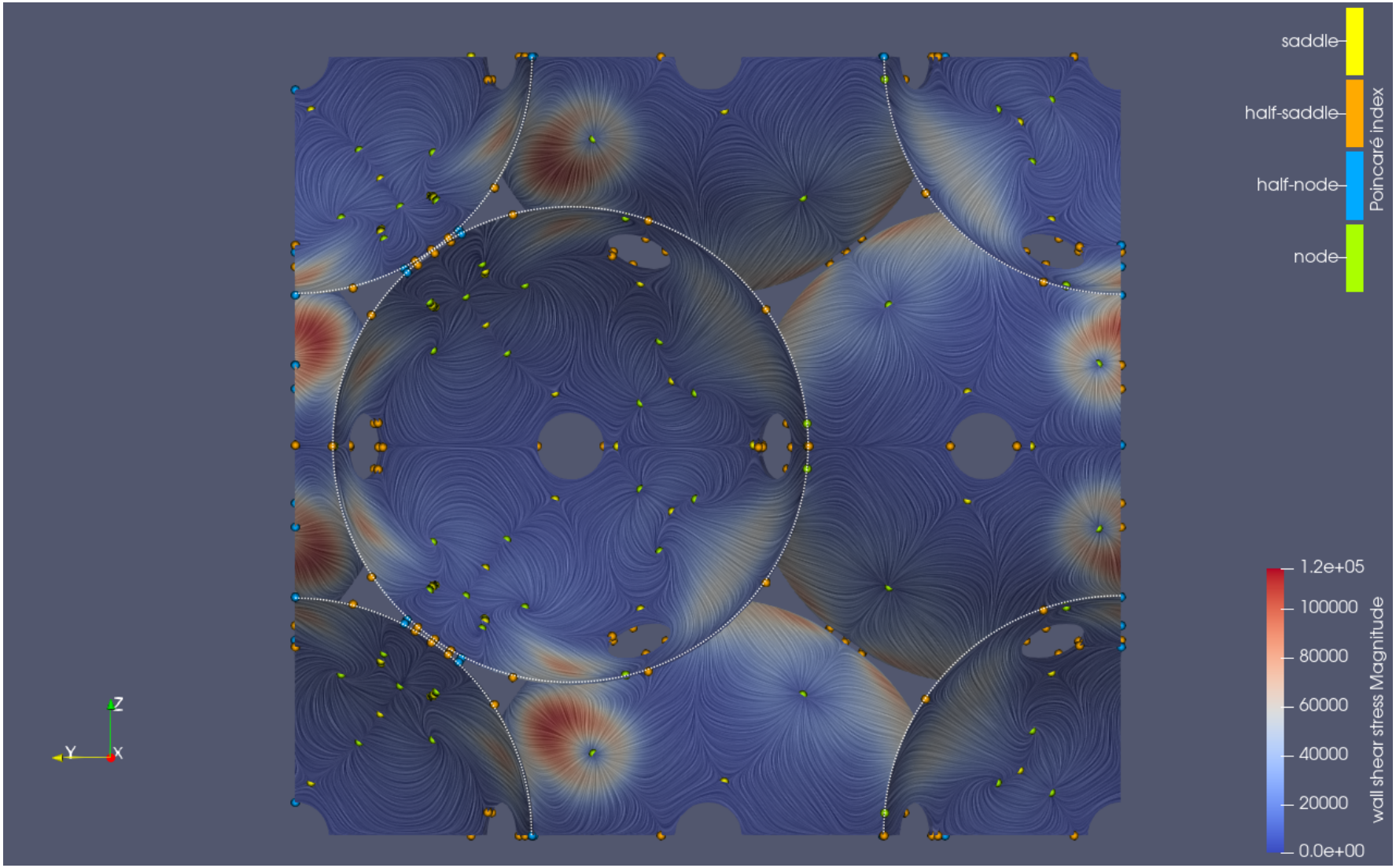

Figure C.6: Line-integral convolution of the wall shear stress field of the case MF4 at $\Omega t = 4.72\pi$ coloured by the wall shear stress magnitude $|\boldsymbol{\tau}_\mathrm{w}|\, d^2/(\rho\nu^2)$. The flow goes into the plane (positive x-direction). The critical points are coloured according to their discrete Poincaré index (C.16).

C.3. Detection of separation lines

The next step in the analysis of the wall shear stress topology is the identification of the separatrices and, in particular, the separation lines. Using the separation lines as seeds, it is also possible to visualise the streamsurfaces bounding the three-dimensional separation region. In the following, the definition of the separation line is reviewed and different approaches for its identification are discussed.

C.3.1. Definition of the separation line

In the classical picture, two-dimensional steady flow separation occurs where the wall shear stress is zero (Schlichting & Gersten, 2017, p.150). However, this simple definition of the separation is not valid for unsteady and three-dimensional flow (Schlichting & Gersten, 2017, p.340, p.353). Based on the work of Lighthill (1963), Hui (1988) proposed a theory for unsteady three-dimensional flow separation, in which the separation emanates from a wall shear stress line "to which all adjacent skin-friction lines converge asymptotically". Furthermore, Hui (1988) concluded "[...] that separation of an unsteady incompressible viscous flow at time t, when viewed from a frame of reference fixed to the body surface, is topologically the same as that of the fictitious steady flow obtained by freezing the unsteady flow at the instant t". A related more general theory of three-dimensional flow separation has been put forward by Wu et al. (2000).
In contrast, Haller (2004) and Serra et al. (2018, 2020) proposed a Lagrangian definition of flow separation in terms of "material spikes". These represent curvature peaks developing in initially wall parallel material line segments. The separation region is delineated by the "backbone", a curve connecting the peaks of the material lines. Also, a Eulerian counterpart has been proposed as the instantaneous limit of the Lagrangian definition Serra et al. (2018, 2020). A fully three-dimensional theory of material spike formation in unsteady flow was presented by Santhosh et al. (2023). Notably, they demonstrated that the backbone of the material spike is "invisible" to the wall shear stress field.
In the present study, we only have a collection of instantaneous flow fields available and thus a Lagrangian definition of flow separation cannot be evaluated using the present dataset. Also, the Eulerian definition of Santhosh et al. (2023) requires time derivatives of the Weingarten map, which describes the curvature of material surfaces, and is therefore challenging to implement. The definition of Hui (1988) thus appears to be a logical first step in the analysis of separation in the present flow.
In the following, a brief summary of the theory of Hui (1988) is given. "An unsteady flow is said to separate from the body surface B at time t if there exists a stream surface S at t that intersects B on the line Γ and if the streamlines on S at time t in the vicinity of Γ all originate from Γ and are directed away from it. The stream surface S is called the instantaneous separation stream surface at the instant t and Γ the instantaneous line of separation" (Hui, 1988). It follows from this definition that the separation line is a wall shear stress line which "[...] must originate from a saddle point of the skin-friction field. It must end at a nodal point of separation if it is a closed curve or at a pair of nodal points if it is an open curve". Furthermore, the wall shear stress component orthogonal to the separation line points towards the separation line. Here, this condition is rewritten in Eulerian form. First,

the separation line $\boldsymbol{X}(s)$ is a wall shear stress line satisfying

$$\frac{\mathrm{d}\boldsymbol{X}}{\mathrm{d}s} = \boldsymbol{\tau}_\mathrm{w}(\boldsymbol{X}(s))\,. \tag{C.21}$$

The normal vector $\boldsymbol{N}(s)$ of the separation line in the plane tangent to the wall is given as the cross product of the wall normal unit vector $\boldsymbol{n}$ (pointing from the fluid to the solid) and the tangent vector of the separation line

$$\boldsymbol{N}(s) = \frac{\mathrm{d}\boldsymbol{X}}{\mathrm{d}s} \times \boldsymbol{n}(\boldsymbol{X}(s)) = \boldsymbol{\tau}_\mathrm{w}(\boldsymbol{X}(s)) \times \boldsymbol{n}(\boldsymbol{X}(s))\,. \tag{C.22}$$

Note that Hui's condition (32), which states that the wall shear stress component normal to the separation line must be zero, is satisfied automatically. Hui's condition (33a) can be written as

$$\boldsymbol{N}(s) \cdot \left(\boldsymbol{\nabla} \otimes \boldsymbol{\tau}_\mathrm{w}(\boldsymbol{X}(s))\right)^\mathrm{T} \cdot \boldsymbol{N}(s) < 0\,, \tag{C.23}$$

which expresses that the normal component of the wall shear stress points towards the separation line. Recognising that the normal vector $\boldsymbol{N}(s)$ in the tangent plane to the wall is proportional to the vorticity vector at the wall, this condition can be rewritten as

$$\boldsymbol{\omega}_\mathrm{w} \cdot \boldsymbol{\nabla}\boldsymbol{\tau}_\mathrm{w} \cdot \boldsymbol{\omega}_\mathrm{w} < 0\,, \tag{C.24}$$

where $\boldsymbol{\omega}_\mathrm{w} = (\boldsymbol{\tau}_\mathrm{w} \times \boldsymbol{n})/\mu$. Note that this quantity is closely related to the trajectory divergence rate defined by Nave et al. (2019) and therefore implies converging trajectories of the wall shear stress.[2] The task of identifying the separation line therefore amounts to finding the wall shear stress line that starts at a saddle, ends at a sink and satisfies the condition (C.24) everywhere.

[2]For a two-dimensional velocity field $\boldsymbol{v}(\boldsymbol{x})$, Nave et al. (2019) define the trajectory divergence rate as

$$\dot{\rho} = \boldsymbol{n} \cdot \boldsymbol{S} \cdot \boldsymbol{n}$$

where $\boldsymbol{S} = \frac{1}{2}\left(\boldsymbol{\nabla}\boldsymbol{v} + (\boldsymbol{\nabla}\boldsymbol{v})^T\right)$ is the strain rate tensor and $\boldsymbol{n} = \boldsymbol{R} \cdot \boldsymbol{v}/|\boldsymbol{v}|$ is the unit velocity field rotated by 90°. Due to the symmetry of the vector-matrix-vector product, the trajectory divergence rate can also be written as

$$\dot{\rho} = \boldsymbol{n} \cdot \boldsymbol{\nabla}\boldsymbol{v} \cdot \boldsymbol{n}$$

Setting $\boldsymbol{v} = \boldsymbol{\tau}_\mathrm{w}/\mu$ and recognising that a 90° rotation of the wall shear stress results in the wall vorticity $\boldsymbol{\omega}_\mathrm{w}$, we obtain

$$\dot{\rho} = \frac{\boldsymbol{\omega}_\mathrm{w} \cdot \boldsymbol{\nabla}(\boldsymbol{\tau}_\mathrm{w}/\mu) \cdot \boldsymbol{\omega}_\mathrm{w}}{|\boldsymbol{\tau}_\mathrm{w}/\mu|^2} = \frac{\boldsymbol{\omega}_\mathrm{w} \cdot \boldsymbol{\nabla}(\boldsymbol{\tau}_\mathrm{w}/\mu) \cdot \boldsymbol{\omega}_\mathrm{w}}{\boldsymbol{\omega}_\mathrm{w} \cdot \boldsymbol{\omega}_\mathrm{w}}\,.$$

C.3.2. Calculation of separation lines

At first glance, having identified the critical points using the procedure outlined in the previous section, it seems straightforward to integrate the separation lines. In particular, the condition (C.24) ensures that small inaccuracies in the location of the (half-)saddle point, where the integration begins, are inconsequential. However, due to the spherical geometry adjacent triangles of the mesh do not lie in the same plane. This leads to discontinuities in the tangential component of the three-dimensional wall shear stress vector field, causing the projection-based streamline integration (Schroeder et al., 2006) to get stuck.

Several alternative methods have been applied to determine the separation line with limited success. First, the method of Kenwright (1998) is based on the phase plane behaviour of the piecewise linear vector field within each triangle. While the line segments identified by this method mostly lie in the correct regions, the line segments are disconnected and significant parts of the separation lines are missing. Second, recognising that the wall shear stress lines on either side of the separation line originate from different attachment points, the method of Yuan & Li (2019) was applied to determine the region in which all wall shear stress lines originate from the same source. Yuan & Li (2019) implicitly represent the region using a level set function ϕ_{LS}, which is the solution of a Hamilton-Jacobi equation

$$\frac{\partial \phi_{\mathrm{LS}}}{\partial t} = -\max(0, \boldsymbol{\tau}_{\mathrm{w}} \cdot \boldsymbol{\nabla} \phi_{\mathrm{LS}}) \ . \tag{C.25}$$

Different discretisations (Abgrall, 1996; Barth & Sethian, 1998) were employed, but the identified region was either significantly too small or encompassed the domains of other sources. Third, the method of Straub et al. (2021) segments the field into regions belonging to different critical points based on streamline integrations. However, this method is computationally expensive and does not result in line features.

An approach that could be considered in the future is the integration of "time ribbons", in which the integration proceeds from the start and the end points simultaneously (Theisel et al., 2003). Also, the edge-map approach of Bhatia et al. (2011) appears to be an interesting alternative to the traditional streamline integration.

D. Publications

D.1. Onset of nonlinearity in oscillatory flow through a hexagonal sphere pack

Division of work between the authors

Lukas Unglehrt performed the simulations and data analysis. Both authors contributed equally to reaching conclusions and writing the paper

Reference

Unglehrt, L. & Manhart, M. 2022 Onset of nonlinearity in oscillatory flow through a hexagonal sphere pack. *Journal of Fluid Mechanics* **944**, A30.

Copyright

J. Fluid Mech. (2022), *vol*. 944, A30, doi:10.1017/jfm.2022.496

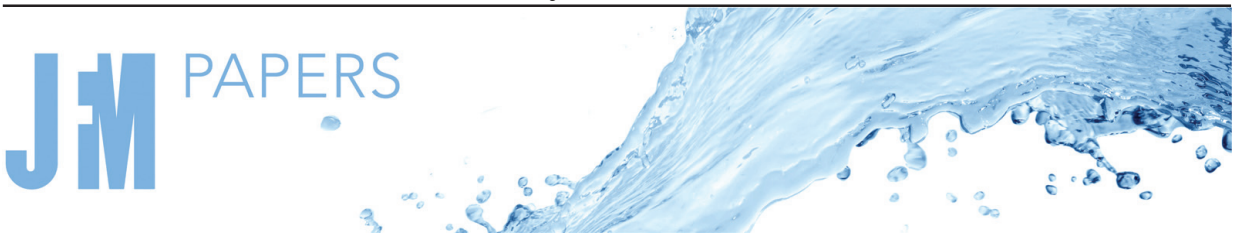

Onset of nonlinearity in oscillatory flow through a hexagonal sphere pack

Lukas Unglehrt[1] **and Michael Manhart**[1],†

[1]Professorship of Hydromechanics, Technical University of Munich, Arcisstr. 21, 80333 Munich, Germany

(Received 11 October 2021; revised 14 March 2022; accepted 13 May 2022)

We simulated laminar flow through a hexagonal sphere pack driven by a sinusoidal volume force using direct numerical simulation. We vary two independent parameters, the Hagen and Womersley numbers, representing the amplitude and frequency of the forcing. First, we determine for which regions in the parameter space nonlinear effects have to be considered. We judge the presence of nonlinear effects from the departure of the superficial velocity and kinetic energy from a linear behaviour as well as from the presence of higher harmonics in the discrete Fourier transform of the velocity field. We discuss the asymptotic behaviour of the onset of nonlinearity in the limits of low and high Womersley number, and we delineate approximately the parameter region that can be described using the linear theory. Second, we document the changes of instantaneous velocity fields with Hagen and Womersley numbers. We show that the onset of nonlinearity is accompanied by a loss of fore–aft symmetry of the flow, and subsequently, we employ the deviation from this symmetry to quantify the strength of nonlinear effects in the instantaneous velocity fields. Based on this analysis, we demonstrate that for higher Womersley numbers, the strongest nonlinear effects occur during the deceleration of the superficial velocity; consequently, the development of the nonlinearity is not in phase with the superficial velocity. Finally, we describe the leading-order nonlinear effects in the frequency domain and the interaction among the nonlinear Fourier modes that leads to a temporal variation in the strength of nonlinear effects.

Key words: porous media

1. Introduction

The study of oscillatory flow in porous media has applications in acoustics, seismology, coastal engineering and marine sciences, and possibly in the engineering of thermal and

† Email address for correspondence: michael.manhart@tum.de

chemical processes. When a pressure wave with a wavelength significantly larger than the pore scale propagates through a porous medium, the pore fluid can be considered to be driven by an oscillatory pressure gradient (Johnson, Koplik & Dashen 1987). The propagation of sound through porous materials as well as of seismic waves through the Earth's crust can be described using the theory of Biot (1956*a*,*b* 1962). The coefficients of this theory can be determined from the solution of the flow problem on the pore scale (Burridge & Keller 1981). In coastal engineering, oscillatory porous media flow is of interest in describing the interaction of water waves with rubble-mound breakwaters. To this end, several experimental investigations of oscillatory flow through sphere packs and rock samples have been undertaken by van Gent (1993) and Hall, Smith & Turcke (1995). Further applications of oscillatory porous media flow in the context of marine sciences include the water wave interaction with porous seabeds (Gu & Wang 1991) or modelling flow in coral communities (Lowe *et al.* 2008). For technical applications, oscillatory porous media flow can be of interest due to the increased heat transfer (Jin & Leong 2006) or dispersion (Crittenden *et al.* 2005) when compared to steady flow. Graham & Higdon (2002) performed a broad investigation of oscillatory flow through two-dimensional porous media. They explored the effect of various types of oscillatory forcing, and demonstrated that a mean flow can be induced opposed to the mean pressure gradient. Moreover, they suggested that oscillatory flow could be applied as a filter to separate fluids of different viscosities. Thereby, an appropriately designed temporal waveform of the pressure gradient induces a mean flow in each fluid that points in opposite directions. Finally, the study of oscillatory flow is also a good starting point for the understanding and modelling of general unsteady flow.

Porous media are characterised by the presence of a macroscale L that is of the order of magnitude of the extent of the porous medium, and a microscale l that is of the order of magnitude of the pore size. When $l \ll L$, the flow through porous media is described commonly in terms of aggregated quantities on the macroscale, for example, the filter velocity that represents the volume flow rate per cross-sectional unit area of the porous medium, and pressure differences over distances of the order $O(L)$. In the simplest case, Darcy's law relates these macroscopic quantities by the permeability K; however, it is applicable only to steady linear flow. For more general configurations, methods have been proposed to derive governing equations for the macroscale flow from first principles, i.e. the conservation laws for mass and momentum. Examples are the volume-averaging approach (Whitaker 1986) or the homogenisation method (Ene & Sanchez-Palencia 1975; Bensoussan, Lions & Papanicolaou 1978; Lévy 1987; Hornung *et al.* 1997). In the volume-averaging approach, the differential equations are averaged locally over a so-called representative elementary volume of the porous medium. Different weighting functions can be used in the definition of the volume average, e.g. a top-hat or Gaussian kernel. The resulting volume-averaged Navier–Stokes equations are unclosed, as they contain microscale quantities describing the flow resistance and dispersion in the pore space. Formally, the equations can be closed by solving a boundary value problem on the representative elementary volume (Whitaker 1986 1996; Lasseux, Valdés-Parada & Bellet 2019). For periodic porous media, the theory of homogenisation presents an alternative to the volume-averaging approach. An artificial spatial coordinate $\boldsymbol{y} = (L/l)\boldsymbol{x}$ is introduced in addition to the spatial coordinate $\boldsymbol{x}$. Using a perturbation series approach with the small variable l/L, the flow problem can be separated into a $\boldsymbol{y}$-dependent boundary problem on the unit cell for which the $\boldsymbol{x}$-dependent terms act as source terms, and a macroscale problem dependent on $\boldsymbol{x}$ and $\boldsymbol{y}$. In conclusion, both the volume-averaging and the homogenisation approach lead to the question of how the flow on a representative elementary volume or unit cell of the porous medium and its integral properties are related

to the macroscopic pressure gradient. In the present work, we investigate this dependency for laminar oscillatory flow in the linear and weakly nonlinear regime.

In the following, we review models that have been used to relate the macroscopic velocity to the macroscopic pressure gradient. The macroscale quantities are expressed in terms of the superficial volume average

$$\langle \psi \rangle_{\mathrm{s}} = \frac{1}{V} \int_{V_f} \psi \, \mathrm{d}V, \tag{1.1}$$

and the intrinsic volume average

$$\langle \psi \rangle_{\mathrm{i}} = \frac{1}{V_f} \int_{V_f} \psi \, \mathrm{d}V, \tag{1.2}$$

where V_f is the fluid volume, and V is the combined fluid and solid volume of the unit cell. The averages are linked by the porosity $\epsilon = V_f/V$ as $\langle \psi \rangle_{\mathrm{s}} = \epsilon \, \langle \psi \rangle_{\mathrm{i}}$.

For steady flow, a widely accepted description of the resistance behaviour is given through the Forchheimer equation (Forchheimer 1901)

$$f_x = a \, \langle u \rangle_{\mathrm{s}} + b \, \langle u \rangle_{\mathrm{s}}^2 \, , \tag{1.3}$$

where f_x represents the macroscopic pressure gradient $-\boldsymbol{\nabla} \langle p \rangle_{\mathrm{i}}$, and $\langle u \rangle_{\mathrm{s}}$ is the superficial velocity. The coefficients a and b are usually determined experimentally. Ergun (1952) proposed porosity-dependent correlations for these coefficients, resulting in the Ergun equation, which have been confirmed in later studies (Macdonald *et al.* 1979). Whitaker (1996) presented a theoretical derivation of the Forchheimer equation from the volume-averaged Navier–Stokes equations. A comprehensive review of the resistance behaviour in stationary porous media flow was given by Wood, He & Apte (2020). One can assume that in oscillatory flow at very low frequencies, there exists a quasi-steady regime in which the resistance behaviour can be described appropriately by the Forchheimer equation and its steady-state coefficients.

Oscillatory flow at small amplitudes is well understood theoretically and can be described accurately by the so-called equivalent fluid model based on the work of Johnson *et al.* (1987) and Champoux & Allard (1991). A comprehensive review of the theory was given by Lafarge (2009). Chapman & Higdon (1992) verified the model of Johnson *et al.* (1987) with highly accurate numerical solutions of the unsteady Stokes equations for oscillatory flow through sphere packs. Turo & Umnova (2013) proposed a model similar to the model of Johnson *et al.* (1987) that is formulated in the time domain and features a Forchheimer-type nonlinearity. They compared their model to data from a shock tube experiment, and obtained 'satisfactory agreement'.

Sollitt & Cross (1972) extended the Forchheimer equation (1.3) with an acceleration term to describe unsteady nonlinear flow in porous media. The unsteady Forchheimer equation possesses a sensible low-frequency limit – the steady Forchheimer equation – but it does not comply with the theoretical high-frequency limit derived by Johnson *et al.* (1987). Furthermore, there does not seem to be a general agreement in the literature on the choice of coefficients; based on an extensive experimental investigation of oscillatory porous media flow, van Gent (1993) suggested correlations for the coefficients in the unsteady Forchheimer equation. Notably, both the coefficient of the acceleration term and of the nonlinear term depend on the frequency of oscillation. Burcharth & Andersen (1995) noted that the coefficients of the unsteady Forchheimer equations are in principle time-dependent. This can be seen in the study of Hall *et al.* (1995), who applied a least

squares fit to determine average values for the coefficients of the linear and nonlinear terms, and obtained a temporally varying and sometimes even negative acceleration coefficient. For strongly accelerated flow, a further arguable point is that the nonlinearity in the unsteady Forchheimer equation depends only on the instantaneous superficial velocity $\langle u \rangle_s$. To the best of our knowledge, this assumption has yet to be examined. Hence, in the absence of a generally valid model, it would be interesting to know under which circumstances oscillatory flow can be considered as linear and thus be described reliably by the equivalent fluid model, and when by contrast we have to resort to nonlinear models.

In this work, we consider laminar oscillatory flow through a periodic sphere pack. First, we seek to address the question of for which values of amplitude and frequency of the oscillatory forcing (represented by the Hagen number Hg and the Womersley number Wo) nonlinear effects have to be considered. We establish a boundary between linear and nonlinear flow in the Hg–Wo^2 parameter space based on the scaling of the volume-averaged velocity and kinetic energy with the Hagen number, and we use the magnitude of the Fourier series coefficients of the velocity field to assess the importance of nonlinear effects.

Second, we investigate how the nonlinearity affects the instantaneous velocity fields at maximum superficial velocity. We find that a key effect is the loss of fore–aft symmetry of the flow. We look into the temporal evolution of this loss of symmetry in order to determine when nonlinear effects occur during the cycle. We observe a phase shift between the superficial velocity and the nonlinear effects at higher frequencies that raises doubts as to whether the modelling of the nonlinearity with a Forchheimer-type closure is appropriate in unsteady flow.

Third, we provide a consistent description of the flow in the frequency domain. We explain the emergence of a time-averaged velocity field, and we discuss the interaction among the Fourier modes that results in a variation of the strength of nonlinear effects throughout the cycle.

2. Problem statement

2.1. *Geometry of the sphere pack*

We consider a hexagonal close-packed arrangement of spheres as a porous medium. The centre coordinates of the spheres (i, j, k) in hexagonal close-packed arrangement are

$$\begin{bmatrix} x_c \\ y_c \\ z_c \end{bmatrix} = \begin{bmatrix} 2i + (j + k) \bmod 2 \\ \sqrt{3}\left[j + \frac{1}{3}(k \bmod 2)\right] \\ \frac{2\sqrt{6}}{3} k \end{bmatrix} \frac{d}{2}, \tag{2.1}$$

and the sphere pack has the periodicities d, $\sqrt{3}\,d$ and $\frac{2\sqrt{6}}{3}\,d$ in the x-, y- and z-directions, respectively. The hexagonal sphere pack has a 60° rotational symmetry in the x–y plane, and a reflection symmetry in the z-direction. The porosity of the sphere pack is $\epsilon = 1 - \frac{\pi}{3\sqrt{2}} = 0.26$. Figure 1($a$) shows the part of the sphere pack that is contained in the simulation domain. A peculiarity of the hexagonal sphere pack geometry is that there exist straight channels along the x-direction with contact points in the centres of the channels. This can be seen in figure 1(b), which shows a section through the sphere pack along the plane $\frac{\sqrt{3}}{3}y - \frac{\sqrt{6}}{3}z = 0$. This plane is parallel to the cut plane used in the analysis of Sakai & Manhart (2020) and results in shifted, but otherwise equivalent, flow fields.

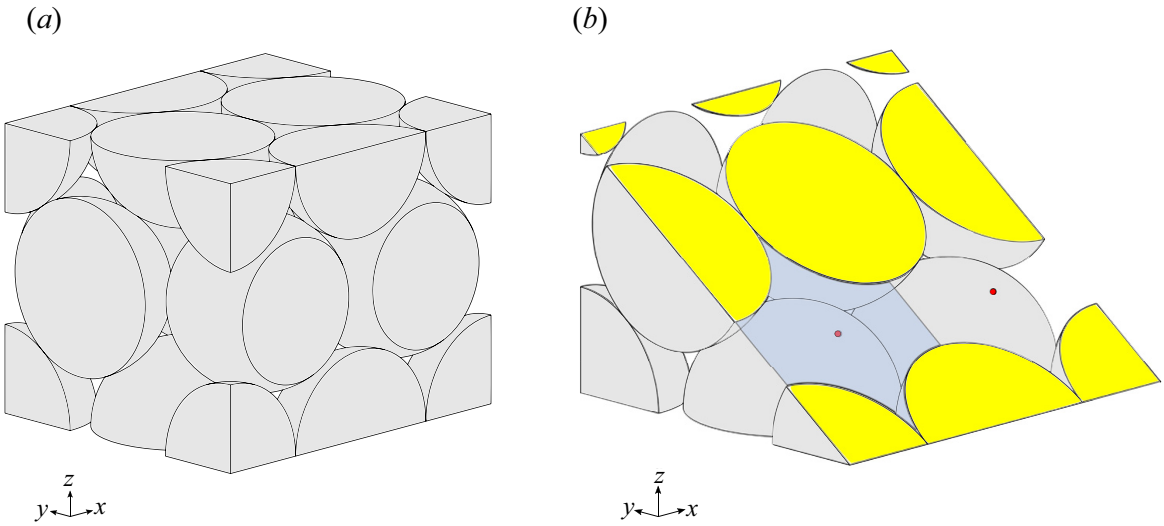

Figure 1. (*a*) Hexagonal sphere pack in the simulation domain. (*b*) Section through the hexagonal sphere pack along the plane $\frac{\sqrt{3}}{3}y - \frac{\sqrt{6}}{3}z = 0$. The contact points are marked by red dots. The area highlighted in blue is the region for which velocity fields are shown in figures 10–15.

2.2. *Governing equations*

The flow in the pore space is governed by the incompressible Navier–Stokes equations

$$\boldsymbol{\nabla} \cdot \boldsymbol{u} = 0, \tag{2.2a}$$

$$\frac{\partial \boldsymbol{u}}{\partial t} + \boldsymbol{\nabla} \cdot (\boldsymbol{u} \otimes \boldsymbol{u}) = -\frac{1}{\rho}\boldsymbol{\nabla} p + \nu\, \Delta \boldsymbol{u} + \frac{1}{\rho}\boldsymbol{f}, \quad \text{with } \boldsymbol{f} = f_x \sin(\Omega t)\, \boldsymbol{e}_x, \tag{2.2b}$$

satisfies no-slip and triple periodic boundary conditions, and is at rest at $t = 0$:

$$\boldsymbol{u}(\boldsymbol{x}, t) = 0 \qquad \text{for } \boldsymbol{x} \text{ on the surface of the spheres,} \tag{2.3a}$$

$$\boldsymbol{u}(\boldsymbol{x}, t) = \boldsymbol{u}(\boldsymbol{x} + \boldsymbol{L}, t) \quad \text{for } \boldsymbol{L} \in \left\{L_x\, \boldsymbol{e}_x, L_y\, \boldsymbol{e}_y, L_z\, \boldsymbol{e}_z\right\}, \tag{2.3b}$$

$$p(\boldsymbol{x}, t) = p(\boldsymbol{x} + \boldsymbol{L}, t) \quad \text{for } \boldsymbol{L} \in \left\{L_x\, \boldsymbol{e}_x, L_y\, \boldsymbol{e}_y, L_z\, \boldsymbol{e}_z\right\}, \tag{2.3c}$$

$$\boldsymbol{u}(\boldsymbol{x}, 0) = 0. \tag{2.3d}$$

The periods L_x, L_y and L_z denote the size of the simulation domain in the x-, y- and z-directions, respectively.

The sinusoidally oscillating force $\boldsymbol{f}$ is constant in space and represents a macroscopic pressure gradient. In inviscid flow, this configuration would lead to a potential flow proportional to $1 - \cos(\Omega t)$ and therefore an oscillation with non-zero mean; however, in viscous flow, the influence of the initial condition decays with time, and the flow reaches a steady oscillation with zero mean. We did not investigate a cosinusoidal forcing, as the starting flow would resemble closely the flow of a fluid at rest subject to a constant force, which was studied by Sakai & Manhart (2020), and the flow after the decay of the transient would be the same as with the sinusoidal force (albeit shifted in time).

2.3. *Dimensional analysis*

In this subsection, we derive and discuss the independent parameters that determine the flow uniquely. The problem as stated in §§ 2.1 and 2.2 is to determine the velocity field $\boldsymbol{u}$

as a function of the position $\boldsymbol{x}$, the time t, the fluid density ρ, the kinematic viscosity ν, and the amplitude and frequency of the forcing f_x and Ω. We deliberately do not consider the porosity ϵ and the permeability K in the dimensional analysis as they depend solely on the geometry and the sphere diameter d. A systematic study of the effects of the pore geometry is beyond the scope of our present work because adding additional parameters would increase significantly the cost of this study.

We now perform a dimensional analysis (Buckingham 1914). Choosing the density ρ, the kinematic viscosity ν and the sphere diameter d as reference variables, we obtain the dimensionless ratios

$$\Pi_1 = \frac{\boldsymbol{x}}{d}, \quad \Pi_2 = \frac{\nu t}{d^2}, \quad \Pi_3 = \frac{f_x d^3}{\rho \nu^2} \quad \text{and} \quad \Pi_4 = \frac{\Omega d^2}{\nu}. \tag{2.4a–d}$$

We can identify Π_3 as the Hagen number $Hg = f_x d^3/(\rho\nu^2)$ (Martin 2010; Awad 2013), which represents a dimensionless pressure gradient in viscous units, and $\sqrt{\Pi_4}$ as the Womersley number $Wo = \sqrt{\Omega d^2/\nu}$ (Womersley 1955), which represents the ratio of the sphere diameter d to the thickness of Stokes' oscillatory boundary layer. Alternatively, Wo^2 can be interpreted (up to a constant) as the ratio of the viscous time scale d^2/ν to the period of excitation $T = 2\pi/\Omega$.

From the Π theorem (Buckingham 1914), we infer that the velocity field can be represented as a function

$$\frac{\boldsymbol{u} d}{\nu} = \boldsymbol{\Phi}\left(\frac{\boldsymbol{x}}{d}, \frac{\nu t}{d^2}; Hg, Wo\right), \tag{2.5}$$

with Hg and Wo as two independent parameters. A dimensionless form of the Navier–Stokes equations follows as

$$\frac{\partial \hat{\boldsymbol{u}}}{\partial \hat{t}} + \hat{\nabla} \cdot \left(\hat{\boldsymbol{u}} \otimes \hat{\boldsymbol{u}}\right) = -\hat{\nabla}\hat{p} + \hat{\Delta}\hat{\boldsymbol{u}} + Hg \sin(Wo^2 \hat{t})\, \boldsymbol{e}_x, \tag{2.6}$$

where $\hat{\boldsymbol{u}} = \boldsymbol{u} d/\nu$, $\hat{\boldsymbol{x}} = \boldsymbol{x}/d$, $\hat{t} = \nu t/d^2$ and $\hat{p} = p d^2/(\rho\nu^2)$. While this is not the only possible way to non-dimensionalise the equations, the present form illustrates the meanings of the Hagen and Womersley numbers. Generally, different dimensionless forms are appropriate for different flow regimes.

A Reynolds number can be obtained by taking a suitable point value or average of the dimensionless velocity field (2.5). Here, we define the Reynolds number based on the sphere diameter and the maximum superficial volume-averaged velocity after the transient has decayed:

$$Re = \limsup_{t\to\infty} \frac{\langle \boldsymbol{u} \rangle_{\mathrm{s}}\, d}{\nu}. \tag{2.7}$$

Since the volume-averaging and the maximum suppress the spatial and temporal dependencies, the Reynolds number can then be expressed as a function of two independent parameters Wo and Hg. Note that this Reynolds number is related to the pore Reynolds number defined, for example, by Wood *et al.* (2020) via the porosity as $Re = \epsilon\, Re_p$. The Hagen number has been employed occasionally in other works in the guise of a pressure-gradient-based Reynolds number (Ene & Sanchez-Palencia 1975; Firdaouss, Guermond & Le Quéré 1997; Iervolino, Manna & Vacca 2010; Lasseux *et al.* 2019) or a dimensionless body force (Graham & Higdon 2002). As the Reynolds number expresses the ratio of the characteristic magnitude of the convective and viscous terms in the Navier–Stokes equations, whereas the dimensionless group $\Pi_3 = f_x d^3/(\rho\nu^2)$ represents the ratio of the body force to the viscous term, we refrained from calling this a Reynolds number and used the definition of Martin (2010) and Awad (2013) instead.

3. Methodology

3.1. *Description of numerical methods*

We performed direct numerical simulation of the incompressible Navier–Stokes equations (2.2) with our in-house code MGLET (Manhart, Tremblay & Friedrich 2001; Manhart 2004; Peller *et al.* 2006; Peller 2010; Sakai *et al.* 2019). For spatial discretisation, MGLET uses an energy-conserving central second-order finite volume method based on a Cartesian grid with a staggered arrangement of variables (Harlow & Welsh 1965; Patankar 1980). For time integration, we employ an explicit three-stage third-order low-storage Runge–Kutta method (Williamson 1980). We employ a variant of the fractional-step method (Chorin 1968) in which in every substep of the Runge–Kutta scheme the stage velocities are made divergence-free by a pressure update. The pressure update is obtained by solving a Poisson equation that is constructed by applying the discrete divergence operator to the stage velocity and the gradient of the pressure update; see e.g. Ferziger & Perić (2002).

Complex geometries are treated using an embedded boundary approach (Peller *et al.* 2006). We now give a brief overview of the employed algorithm. The simulation geometry is determined as a piecewise planar description based on the intersection points of the Cartesian grid with the specified body geometry. The momentum equation is solved only on cells that lie completely within the fluid domain. The interface cells are used to enforce the no-slip boundary condition using a ghost-cell approach (Peller *et al.* 2006). The velocities in the interface cells are computed using two kinds of interpolation (Peller 2010). To evaluate velocity gradients and the convected velocities, we set a second-order accurate point value computed by linear least squares interpolation (extrapolation). To compute the convecting velocities and the divergence, we set an approximation to the mass fluxes through the respective pressure cell face. An iterative flux correction procedure that is coupled to the pressure correction ensures conservation of mass for the interface cells (Peller 2010). In this scheme, no boundary conditions are needed for the pressure at the embedded boundary.

3.2. *Verification of the numerical method*

In order to verify the convergence of our code with spatial grid refinement, we simulated steady flow in a simple cubic lattice of spheres at porosity $\epsilon = 0.875$ driven by a constant-volume force with $Hg = 10^{-4}$. This configuration was investigated previously by Chapman & Higdon (1992), who obtained permeability $K = 0.10355d^2$ by solving the Stokes equations with a solid harmonics collocation method. Since their method is based on a harmonic expansion that satisfies exactly the no-slip boundary condition on the spheres, we consider their method as very accurate and we use their results to verify our scheme.

We computed the flow around a sphere centred in a cubic domain of side length $1.612d$ with periodic boundary conditions at grid resolutions 12.4, 24.8, 49.6, 99.3, 198.5 and 397 cells per sphere diameter (cpd). On the finest grid, we obtained permeability $K_{397} = 0.10358d^2$. For this value, we estimated the relative error with the grid convergence index (Roache 1994; Celik *et al.* 2008), which resulted in a value $GCI_{fine} = 2.8 \times 10^{-5}$ at apparent order $p = 1.8$. Our value differs from the result of Chapman & Higdon (1992) only in the last reported digit, when their value is renormalised to the sphere diameter instead of the domain length. At 24.8 cpd, the computed permeability error is well below 1 %. Furthermore, we evaluated the superficial average of the kinetic energy $\langle k \rangle_s = \left\langle \frac{1}{2}\rho \boldsymbol{u}^2 \right\rangle_s$ and the u-velocity at the point $\boldsymbol{P} = (0.8d, 0.8d, 0.8d)$ relative to the centre

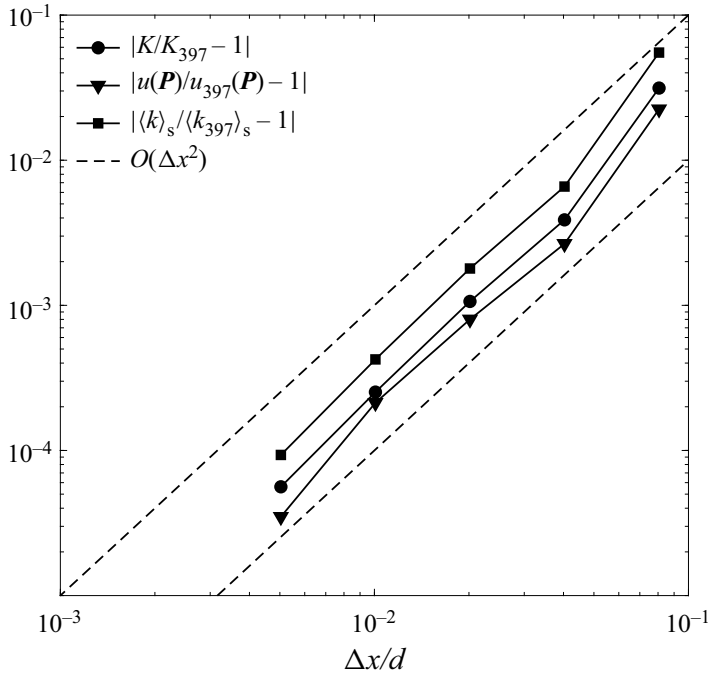

Figure 2. Grid convergence for steady Stokes flow in a simple cubic lattice of spheres at porosity $\epsilon = 0.875$. The permeability K, the velocity at the probe point $\boldsymbol{P} = (0.8d, 0.8d, 0.8d)$ and the kinetic energy $\langle k\rangle_s$ of the flow field are compared to their respective values at the finest grid resolution $d/\Delta x = 397$.

of the sphere. These values are plotted as a function of the grid spacing in figure 2. It can be seen that the relative error decreases at approximately second order with the grid spacing Δx over three orders of magnitude.

Thus we have demonstrated that for the given test case, the embedded boundary method achieves the theoretical second-order convergence and converges to a result close to the reference value.

3.3. *Simulation set-up*

The objective of this study is to investigate the boundary between the linear and nonlinear regimes in the *Hg–Wo* parameter space for oscillating flow in a hexagonal sphere pack. Therefore, we tried to cover unknown and computationally affordable regions in this parameter space beyond the linear regime, which for this particular geometry had already been investigated by Zhu & Manhart (2016).

In a first step, we could assume that nonlinear effects appear if the maximum Reynolds number within a cycle exceeds a certain threshold. Based on the results of Sakai & Manhart (2020), who observed linear behaviour for $Re \leqslant 1$ in steady flow through a hexagonal sphere pack, we chose a threshold value $Re = 1$. For linear flow, two asymptotes exist for the maximum velocity in a cycle as a function of the Womersley number. At the low-frequency limit, the oscillation amplitude reaches the values of the steady state – this is the quasi-steady regime. Here, the end of the linear regime could be estimated at $Hg = d^2/K \approx 5776$ using Darcy's law (which reads $Re = (K/d^2)\,Hg$ in non-dimensional form) and permeability value $K = 1.731 \times 10^{-4}\,d^2$ (Sakai & Manhart 2020). In the high-frequency limit, the amplitude decays with Wo^{-2} for constant Hg. The transition between the low- and high-frequency regimes occurs close to Womersley number $Wo_0 = \sqrt{\epsilon d^2/(\alpha_\infty K)} = 30.5$; this value marks the intersection

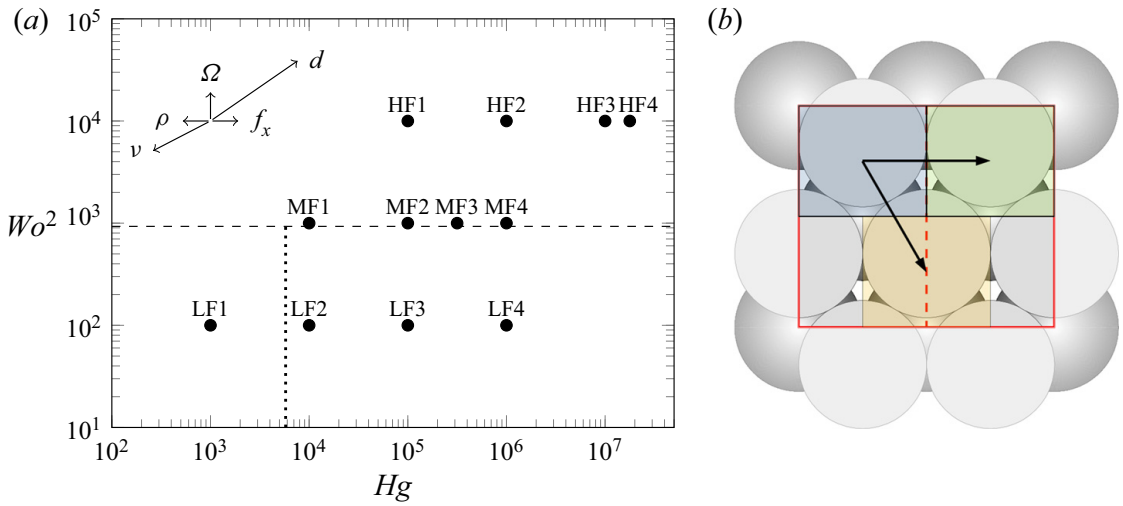

Figure 3. Study design. (*a*) Simulations at low (LF), medium (MF) and high frequency (HF) in the Hg–Wo^2 parameter space. The dotted line indicates the condition $Re = 1$ in quasi-steady Darcy flow. The dashed line indicates the Womersley number Wo_0 that represents the intersection of the low- and high-frequency asymptotes in the linear regime. The arrows indicate the changes in the dimensionless numbers if the respective parameters are doubled. (*b*) Top view of the sphere pack cut in the symmetry plane $z = \frac{\sqrt{6}}{3}\,d$. The red frame represents the simulation domain that consists of two unit cells (indicated by the dashed red line). The coloured areas and arrows represent shift invariances of the geometry in the x-direction and at a 60° angle to the x-direction. Consequently, the simulation domain contains eight repetitions of the minimum box represented by the coloured areas.

of the low- and high-frequency asymptotes of linear flow (Pride, Morgan & Gangi 1993). To cover the range departing from the quasi-steady behaviour, we therefore performed simulations at three different Womersley numbers, $Wo = 10$, 31.62 and 100. The simulation parameters were chosen to lie on a logarithmic grid, leading to equispaced points in the log-log plot and thus a uniform point density over the orders of magnitudes. For each of the three Womersley numbers, we selected various Hagen numbers lying above the linear limit in the quasi-steady regime $Hg \approx 5776$. Figure 3(*a*) shows the simulations in the Hg–Wo^2 parameter space.

We chose a domain size $L_x = 2d$, $L_y = \sqrt{3}\,d$ and $L_z = \frac{2\sqrt{6}}{3}\,d$ with periodic boundary conditions for $\boldsymbol{u}$ and p in the x-, y- and z-directions. This domain represents one unit cell in the y- and z-directions, but includes two periodic repetitions of the unit cell in the x-direction. In the following, we motivate this particular choice for the size of the simulation domain. On the one hand, linear flow has the same symmetries and periodicity as the sphere pack and it can be fully represented with a domain consisting of one unit cell. On the other hand, nonlinear flow does not have to adhere to the symmetries of the sphere pack and also admits solutions that are not periodic on the unit cell. Then the periodic boundary conditions prevent the formation of structures larger than the simulation domain. The selected simulation domain contains two spheres in every lattice direction and possesses multiple symmetries: the sphere pack has a reflection symmetry about the midplane in the z-direction, and two shift invariances in the x-direction and at a 60° angle to the x-direction (see figure 3*b*). For all simulations presented in this work, we have verified numerically that the velocity field satisfies these symmetries. We expect that the above symmetries of the flow in directly adjacent pores would have to be broken before a breaking of the periodicity in the y- and z-direction – symmetries between second-order neighbours – could be observed. Therefore, we limit the domain size to one period in the

y- and z-directions. The relatively compact simulation domain allows us to employ high grid resolutions in order to obtain accurate solutions.

For all cases, we employed a uniform Cartesian grid of nearly cubical cells with aspect ratio $1.00:0.99:0.98$ due to the incommensurate periodicities of the domain. The simulations were performed at grid resolutions 48, 96, 192 and 384 cpd. For the simulation HF4, an additional simulation was performed at grid resolution 768 cpd. These resolutions were chosen based on the convergence of the volume-averaged velocity $\langle \boldsymbol{u} \rangle_s$ and the volume-averaged kinetic energy $\langle k \rangle_s$ (see § 3.4). For comparison, Sakai & Manhart (2020) used grid resolution 320 cpd to simulate transient nonlinear and turbulent flow in a hexagonal sphere pack using the same code, and He *et al.* (2019) used resolution 250 cpd to simulate turbulent flow at $Re = 750$ in a face-centred cubic sphere pack of the same porosity.

The time step was chosen to meet the stability limits for the explicit Runge–Kutta scheme; the Courant–Friedrich–Lewy number was always below 0.33, and the diffusion number was always below 0.35. This resulted in at least 40 000 time steps per cycle of oscillation. We applied a uniform body force $\boldsymbol{f} = f_x \sin(\Omega t)\, \boldsymbol{e}_x$ in the x-direction to drive the flow. As the flow starts from rest, this forcing causes a transient oscillation. The transient establishes a net superficial velocity within a cycle, and leads to differences in the peak values of $\langle \boldsymbol{u} \rangle_s$ and $\langle k \rangle_s$ within one cycle as well as from one cycle to the next. We ran our simulations until these differences were below 1 % of the peak values. Thus the transient has decayed sufficiently to show a periodic solution in time.

For post-processing the simulations, we collected the following data: time-resolved data were obtained for volume-averaged quantities $\langle \boldsymbol{u} \rangle_s$, $\langle u^2 \rangle_s$, $\langle v^2 \rangle_s$ and $\langle w^2 \rangle_s$. Complete three-dimensional fields of $\boldsymbol{u}$ and p have been collected at a sampling rate between 25 and 100 snapshots per cycle, depending on the simulation.

3.4. *Grid convergence*

In this subsection, we discuss the dependency of our simulation results on the grid resolution. We choose two quantities for assessing the quality of the simulations: first, the Reynolds number Re based on the maximum of $\langle u \rangle_s$ in steady oscillatory flow as defined in (2.7); and second, the space–time L^2-norm of the velocity field over the last period of each simulation, as

$$\|\boldsymbol{u}\|_{L^2}^2 = \int_{V_f} \int_T |\boldsymbol{u}|^2 \, \mathrm{d}t \, \mathrm{d}V. \tag{3.1}$$

This quantity can be interpreted as the signal energy of the velocity field. It was calculated as the sum of the quantities $\langle u^2 \rangle_s$, $\langle v^2 \rangle_s$ and $\langle w^2 \rangle_s$, which were collected in every time step. Therefore, the square of every velocity value in every time step of the last period contributes to $\|\boldsymbol{u}\|_{L^2}^2$. Due to reasons explained below, we observe non-monotonic convergence of these quantities. Thus the grid convergence index (Roache 1994) does not give meaningful results, and we report explicitly the errors observed at the various grid resolutions.

Table 1 contains the relative differences of $\|\boldsymbol{u}\|_{L^2}^2$ with respect to their solutions at 384 cpd and the Reynolds number Re within the last cycle for the different resolutions. Generally, the errors increase with Womersley and Hagen numbers. For a Womersley number of 10, an error in $\|\boldsymbol{u}\|_{L^2}^2$ below 0.2 % has been achieved with 192 cpd, and at $Wo = 31.62$, the maximum error is below 1.65 %. At $Wo = 100$, the differences between 192 and 384 cpd remain larger. The maximum error is -4.60 % for simulation HF4 at

Case	Sim. periods	e_{48}	e_{96}	e_{192}	e_{384}	Re_{48}	Re_{96}	Re_{192}	Re_{384}	Re_{768}
LF1	1.5	−4.00 %	1.87 %	−0.13 %	—	0.1628	0.1719	0.1703	0.1705	—
LF2	2.25	−4.00 %	1.86 %	−0.13 %	—	1.624	1.715	1.699	1.701	—
LF3	1.404	−3.89 %	1.68 %	−0.10 %	—	14.13	14.94	14.82	14.84	—
LF4	1.25	−5.37 %	2.43 %	0.14 %	—	70.87	77.49	76.77	76.71	—
MF1	3	−6.59 %	0.03 %	−0.23 %	—	0.8031	0.8559	0.8554	0.857	—
MF2	3	−6.75 %	0.04 %	−0.24 %	—	8.022	8.561	8.556	8.571	—
MF3	3	−7.11 %	0.22 %	−0.22 %	—	25.05	26.9	26.87	26.92	—
MF4	3	−9.32 %	0.81 %	−0.09 %	—	66.37	73.17	73	73.07	—
HF1	20.45	−17.09 %	−4.16 %	−0.87 %	—	1.11	1.255	1.289	1.297	—
HF2	19.9	−17.00 %	−4.16 %	−0.87 %	—	11.1	12.55	12.89	12.97	—
HF3	6.32	−12.64 %	−4.89 %	−1.22 %	—	111.6	126.9	130.9	131.7	—
HF4	8	−11.08 %	−10.15 %	−4.60 %	0.17 %	213	239.4	248.6	251.1	251.8

Table 1. Grid convergence of the velocity field $\boldsymbol{u}(\boldsymbol{x}, t)$ in steady oscillation. The relative error in $\|\boldsymbol{u}\|^2_{L^2}$ is defined as $e_{res} = (\|\boldsymbol{u}_{res}\|^2_{L^2} - \|\boldsymbol{u}_{384}\|^2_{L^2})/\|\boldsymbol{u}_{384}\|^2_{L^2}$, and as $e_{res} = (\|\boldsymbol{u}_{res}\|^2_{L^2} - \|\boldsymbol{u}_{768}\|^2_{L^2})/\|\boldsymbol{u}_{768}\|^2_{L^2}$ for HF4. The Reynolds number Re is defined according to (2.7).

$Wo = 100$ and $Hg = 10^{7.25}$. To assess the error of the simulation at 384 cpd for this case, we performed an additional grid refinement to 768 cpd. The error at the resolution 384 cpd with respect to the more finely resolved simulation is 0.17 %.

The Reynolds number computed according to (2.7) ranges from values below 1.0 to values around 73 at the lower Womersley numbers, and $Re = 251.8$ at $Wo = 100$. From table 1, we see that the simulations have relative errors in Re below 0.5 % at $Wo = 10$, below 0.2 % at $Wo = 31.62$, and below 0.7 % at $Wo = 100$.

In contrast to the test case of § 3.2, we do not achieve the theoretical order of accuracy of our code. We explain this decrease of accuracy order by the presence of contact points between the spheres. These degrade the convergence of the pore volume represented in the Cartesian grid by the embedded boundary method. The representation of the spheres by a plane segment in each Cartesian cell intersecting the sphere surface leads to an overestimation of the pore volume, so the local pore volume decreases with grid refinement. The blocking of the thin gap between spheres in contact, however, leads to a local underestimation of the pore volume, so the pore volume around the contact points increases with grid refinement. These two effects taken together lead to a non-monotonic convergence of the porosity. At the finest grid resolution, 384 cpd, the relative error in the pore volume is −0.16 %.

The influence of blocked pore space around the contact points increases with the Womersley number and could explain the increase in error with Wo. At higher frequencies, the flow has a boundary structure (Schlichting & Gersten 2006). With increasing Wo, the boundary layer thickness along the surface of the spheres decreases, and the velocity field approaches the potential flow solution. Cox & Cooker (2000) showed for the case of potential flow around a sphere touching an infinite plate that the velocity potential behaves as $r^{\sqrt{2}-1}$ close to the contact point, leading to a singularity in the velocity. As the boundary condition on the plate is identical to a symmetry boundary condition, we expect the same behaviour at the contact point of two spheres. Hence for increasing Womersley number, the velocity magnitude and gradients in the immediate vicinity of the contact points increase

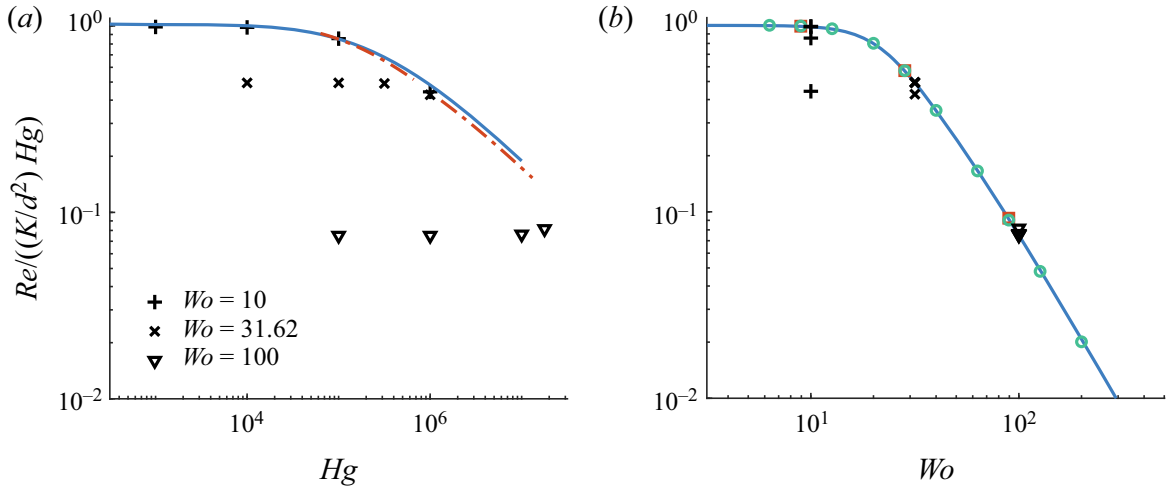

Figure 4. Comparison of the amplitude of the superficial velocity in our simulations (black symbols) with Re observed in (a) steady and (b) linear flow. The values are normalised with the amplitude predicted by Darcy's law. (a) Blue line, Ergun equation (Macdonald *et al.* 1979); red dashed line, Sakai & Manhart (2020). (b) Blue line, model of Pride *et al.* (1993); red squares, Chapman & Higdon (1992); green circles, Zhu & Manhart (2016).

and become asymptotically singular. For high Womersley numbers, this behaviour leads to prohibitive resolution requirements.

In summary, all simulations possess a relative difference below 1.2 % in the Reynolds number as well as in the L^2-norm of the velocity field between the second-finest and finest grids. However, due to the presence of contact points, we do not observe the theoretical order of accuracy of our code. We observed an increase in error with the Hagen and Womersley numbers that we explain by the reduction of the boundary layer thickness on the spheres and the consequently increasing importance of the area close to the contact points.

3.5. *Validation for quasi-steady flow and for linear flow*

In this subsection, we validate our simulation results against data from the literature for the steady and linear flow regimes. In the low-frequency limit ($Wo \to 0$), the flow can be considered as a steady flow at every instant. The amplitude in steady flow can be described by the Ergun equation (Ergun 1952) made dimensionless with ρ, d and ν:

$$Hg = A\,\frac{(1-\epsilon)^2}{\epsilon^3}\,Re + B\,\frac{1-\epsilon}{\epsilon^3}\,Re^2. \tag{3.2}$$

Based on ample experimental data, the coefficients have the values $A = 180$ and $B = 1.8$ for porous media consisting of smooth particles (Macdonald *et al.* 1979). For the hexagonal sphere pack, Sakai & Manhart (2020) have given a similar correlation based on direct numerical simulation results. In figure 4(a), the Reynolds number based on the amplitude of the superficial velocity in our simulations is compared with the Reynolds number observed in steady flow at the same Hagen number. For small Hg, the amplitude is proportional to the Hagen number, as indicated by the horizontal asymptote. For larger Hg, the amplitude increases sublinearly with Hg due to additional nonlinear drag. As expected, the simulations LF1–LF4 at $Wo = 10$ (+ symbols) show good agreement with the steady flow, whereas the amplitudes of the simulations at $Wo = 31.62$ and $Wo = 100$ are significantly smaller than in the steady flow.

In the linear regime, the flow is described accurately by the dynamic permeability model of Pride *et al.* (1993). We determined the model parameters from the potential flow calculations by Chapman & Higdon (1992) for the face-centred cubic sphere pack at the same porosity and from the low-frequency behaviour described by Zhu & Manhart (2016). We would expect that at low Hg, our simulation cases remain linear and therefore follow this behaviour. Figure 4(*b*) compares the Reynolds number based on amplitude of the superficial velocity in all our simulations with the predictions of the model of Pride *et al.* (1993) depending on the Womersley number and the simulation datasets of Chapman & Higdon (1992) and Zhu & Manhart (2016) for linear flow through the face-centred cubic and the hexagonal sphere pack, respectively. The simulations LF1, LF2, MF1, MF2, HF1 and HF2 show excellent agreement with the model predictions as well as with the reference data. The amplitudes of simulations LF3 and LF4 (+ symbols) are significantly lower than the reference data; this can be explained with the nonlinear drag (figure 4*a*). At higher Womersley numbers, the deviation from the linear flow data decreases.

4. Onset of nonlinearity in volume-averaged quantities

In this section, we investigate the onset of nonlinearity in the volume-averaged velocity, kinetic energy and Fourier series coefficients. Our goal is to establish an approximate boundary between linear and nonlinear flow in the Hg–Wo parameter space. Our hypothesis is that the nonlinearity does not occur suddenly when a parameter is changed, but that nonlinear effects change gradually with the Hagen and Womersley numbers. Nevertheless, we try to differentiate between regions that show effectively linear behaviour and regions, in which nonlinear effects are significant. In a first step, we identify nonlinear behaviour in the volume-averaged velocity and kinetic energy. Then we apply a discrete Fourier transform (DFT) to instantaneous velocity fields to characterise the frequency spectrum in response to a sinusoidal excitation. On this basis, we quantify the level of nonlinearity for each simulation conducted, and extrapolate the nonlinear behaviour to larger Womersley and Hagen numbers.

4.1. *Volume-averaged velocity and kinetic energy*

From the definition of linear flow, the velocity is directly proportional to the amplitude of the excitation. The non-dimensional relation (2.5) takes the form

$$\frac{\boldsymbol{u}d}{\nu} = Hg\,\boldsymbol{\Psi}\left(\frac{\boldsymbol{x}}{d}, \frac{\nu t}{d^2}, Wo\right), \quad \text{where } \boldsymbol{\Psi} = \left.\frac{\partial \boldsymbol{\Phi}}{\partial (Hg)}\right|_{Hg=0}. \tag{4.1}$$

Therefore, the volume-averaged velocity $\langle u\rangle_\mathrm{s}$ and the volume-averaged kinetic energy $\langle k\rangle_\mathrm{s} = \left\langle \frac{1}{2}\rho \boldsymbol{u}^2 \right\rangle_\mathrm{s}$ are proportional to Hg and Hg^2, respectively. After the decay of the transient, the average of the function $\boldsymbol{\Psi}$ determines the small-amplitude behaviour displayed in figure 4(*b*). We use this scaling to assess the importance of nonlinear effects in the flow. In figures 5, 6 and 7, we compare the superficial volume-averaged velocity $\langle u\rangle_\mathrm{s}$ and kinetic energy $\langle k\rangle_\mathrm{s}$ in this normalisation for different Womersley numbers. The start of the period is chosen as an integer multiple of 2π, and the excitation is therefore proportional to $\sin\varphi$, with $\varphi \in [0, 2\pi]$. For $Wo = 10$ (figure 5), the curves for the simulations at $Hg = 10^3$ (LF1) and $Hg = 10^4$ (LF2) collapse, indicating that both belong to the linear regime. On the other hand, the simulations at $Hg = 10^5$ (LF3) and $Hg = 10^6$ (LF4) are clearly nonlinear. For $Wo = 31.62$ (figure 6), the simulations at $Hg = 10^4$

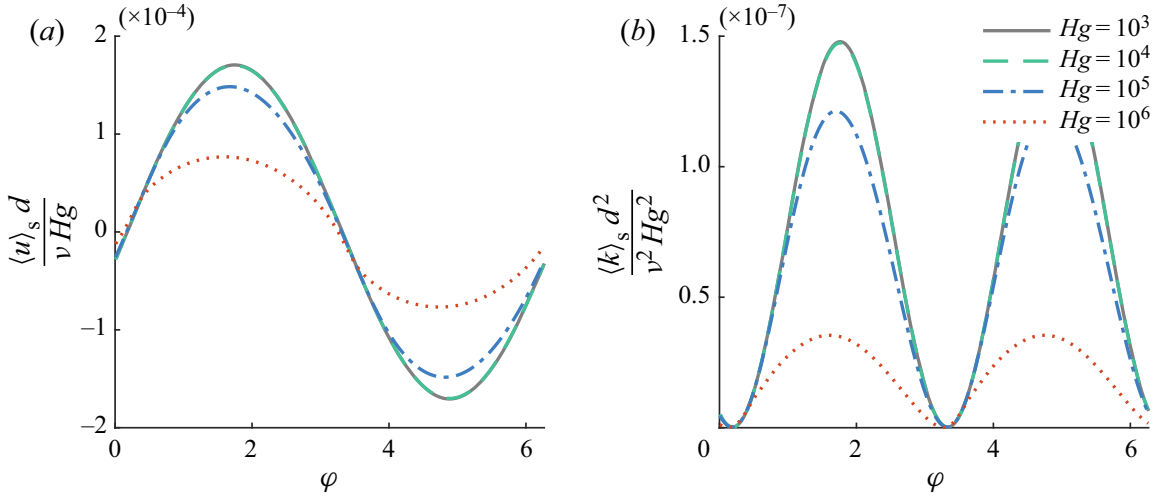

Figure 5. Superficial volume-averaged velocity and kinetic energy at $Wo = 10$ (LF1– LF4), normalised with the Hagen number in steady oscillation. The Reynolds numbers are in the range $Re = 0.17$–77.

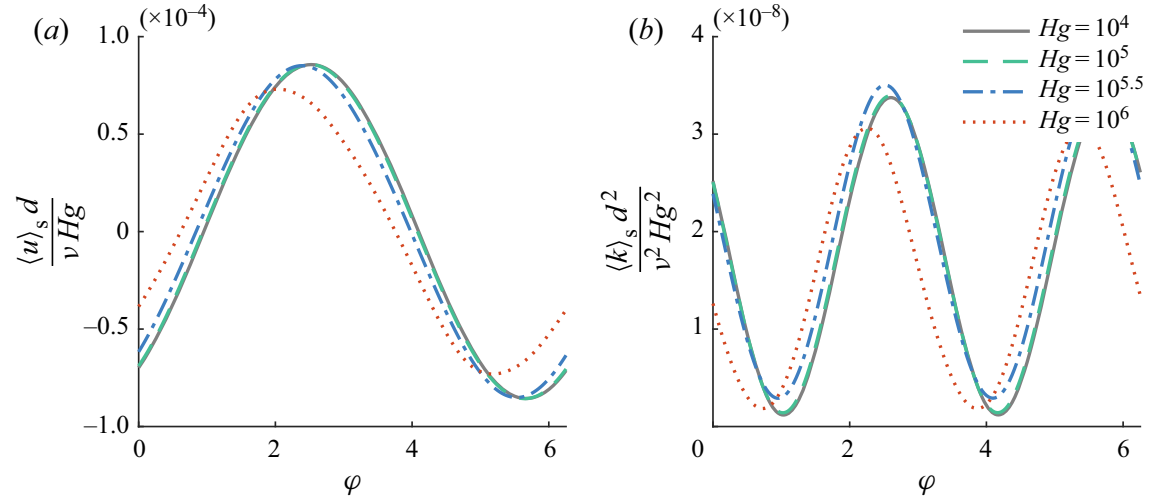

Figure 6. Superficial volume-averaged velocity and kinetic energy at $Wo = 31.62$ (MF1– MF4), normalised with the Hagen number in steady oscillation. The Reynolds numbers are in the range $Re = 0.86$–73.

(MF1) and $Hg = 10^5$ (MF2) are linear, whereas the simulations at $Hg = 10^{5.5}$ (MF3) and $Hg = 10^6$ (MF4) show nonlinear effects. Finally, for $Wo = 100$ (figure 7), the simulations at $Hg = 10^5$ (HF1) and $Hg = 10^6$ (HF2) are linear, whereas the simulations at $Hg = 10^7$ (HF3) and $Hg = 10^{7.25}$ (HF4) are not.

It is important to note that the curves of the volume-averaged velocity $\langle u \rangle_s$ are antisymmetric, and the curves of the volume-averaged kinetic energy $\langle k \rangle_s$ are symmetric, with respect to a half-period shift in time. This indicates that forward and backward flow are the same, regardless of whether the flow is linear or nonlinear.

We observe a phase delay between excitation and $\langle u \rangle_s$ that increases with Womersley number. This behaviour is in line with numerical solutions of the unsteady Stokes and Navier–Stokes equations (Chapman & Higdon 1992; Zhu & Manhart 2016) as well as the theory of Johnson *et al.* (1987) and the unsteady Darcy equation (Zhu & Manhart 2016).

The nonlinearity leads to a reduction in the peak amplitudes of $\langle u \rangle_s$ and $\langle k \rangle_s$ as well as to a reduction of the phase delay to the excitation. However, for the cases MF3 and HF4, we observe a notable increase in the normalised kinetic energy. The reason for this effect is

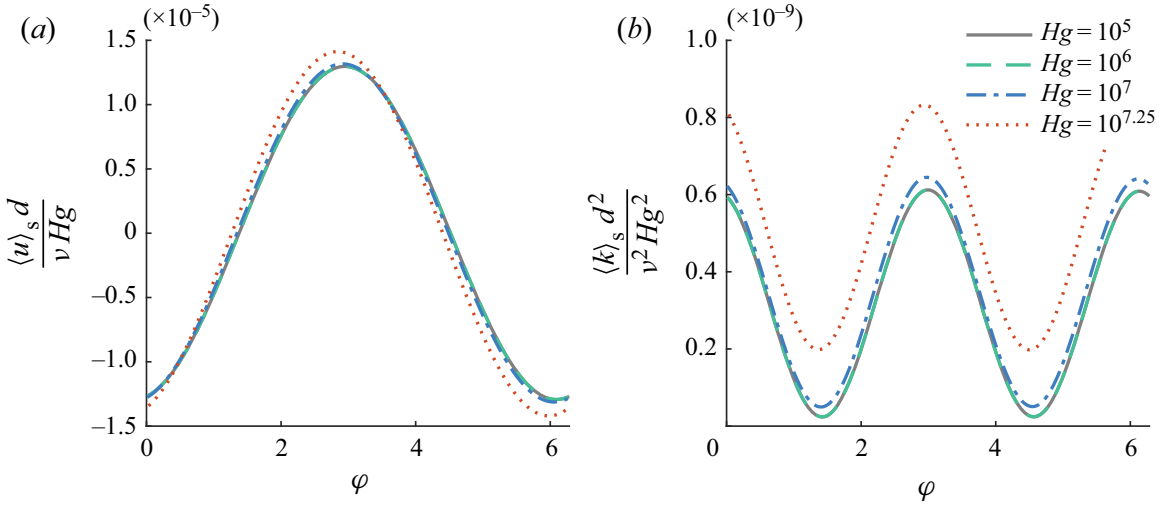

Figure 7. Superficial volume-averaged velocity and kinetic energy at $Wo = 100$ (HF1– HF4), normalised with the Hagen number in steady oscillation. The Reynolds numbers are in the range $Re = 0.13$–252.

that the reduction of the phase lag between the excitation and the volume-averaged velocity increases the power $\boldsymbol{f} \cdot \langle \boldsymbol{u} \rangle_s$ that is fed into the flow.

Based on the deviation of the superficial velocity and kinetic energy from the linear behaviour, we can now find the approximate boundary between linear and nonlinear behaviour. The maximum Reynolds numbers that exhibit linear behaviour are $Re = 1.7$, 8.6 and 13 for $Wo = 10$, 31.62 and 100, respectively. The minimum Reynolds numbers that exhibit apparent nonlinear behaviour are $Re = 14.8$, 26.9 and 132, respectively. We conclude that the onset of nonlinear effects cannot be described solely in terms of the Reynolds number.

4.2. *Fourier series coefficients*

All our cases became periodic in time once the transient had decayed. This is an indicator that the simulated flows are not yet turbulent. Consequently, we can expand the velocity in the last computed cycle in a Fourier series

$$\boldsymbol{u}(\boldsymbol{x}, t) = \sum_{k=-\infty}^{\infty} \boldsymbol{c}_k(\boldsymbol{x})\, \mathrm{e}^{\mathrm{i}k\Omega t} \tag{4.2}$$

using the complex-valued Fourier coefficients $\boldsymbol{c}_k(\boldsymbol{x}) = \boldsymbol{c}^*_{-k}(\boldsymbol{x})$ that represent the modes of oscillation of the flow.

As the excitation is monochromatic, in linear flow there are only two non-zero modes that correspond to a sinusoidal and a cosinusoidal oscillation at the frequency of excitation Ω (the fundamental frequency), and only $\boldsymbol{c}_{\pm 1}$ are non-zero. In nonlinear flow, the convective term in the Navier–Stokes equations leads to interactions between the modes (see Appendix A for the differential equations of the modes $\boldsymbol{c}_k$). First, the (self-)interactions of the modes at the fundamental frequency excite the frequencies $k = 0$ and $|k| = 2$. Further integer frequencies are excited by secondary interactions.

We computed the Fourier series coefficients of the velocity field with a DFT of our snapshot data. Due to the large file size of the instantaneous three-dimensional fields, we have only a low sampling rate between 25 and 100 snapshots per cycle. Aliasing leads to mirroring of high-frequency content into the sampled frequency range, thereby also polluting the low frequencies. However, as we are investigating weakly nonlinear flow,

Case	$\frac{\langle\lvert c_0\rvert^2\rangle_s}{\sum_{k=-N}^{N}\langle\lvert c_k\rvert^2\rangle_s}$	$\frac{2\langle\lvert c_1\rvert^2\rangle_s}{\sum_{k=-N}^{N}\langle\lvert c_k\rvert^2\rangle_s}$	$\frac{2\langle\lvert c_2\rvert^2\rangle_s}{\sum_{k=-N}^{N}\langle\lvert c_k\rvert^2\rangle_s}$	$\frac{2\langle\lvert c_3\rvert^2\rangle_s}{\sum_{k=-N}^{N}\langle\lvert c_k\rvert^2\rangle_s}$
LF2	0.06 %	99.91 %	0.03 %	0.00 %
LF3	2.82 %	95.84 %	1.15 %	0.16 %
LF4 (100 samples)	10.06 %	85.61 %	2.45 %	1.21 %
LF4 (50 samples)	10.07 %	85.61 %	2.45 %	1.21 %
LF4 (25 samples)	10.07 %	85.61 %	2.45 %	1.21 %
MF1	0.01 %	99.99 %	0.00 %	0.00 %
MF2	0.89 %	98.93 %	0.18 %	0.00 %
MF3	4.30 %	94.15 %	1.31 %	0.21 %
MF4	8.99 %	85.64 %	3.28 %	1.17 %
HF1	0.00 %	100.00 %	0.00 %	0.00 %
HF2	0.03 %	99.97 %	0.00 %	0.00 %
HF3	2.78 %	96.64 %	0.52 %	0.05 %
HF4	8.59 %	85.47 %	3.50 %	1.22 %

Table 2. Contribution of the Fourier coefficients at the frequencies $k = 0$, $|k| = 1$, $|k| = 2$ and $|k| = 3$ to the L^2-norm of velocity.

most of the energy is concentrated at and near the fundamental frequency. The energy content near and beyond the Nyquist frequency is therefore several orders of magnitude below the fundamental frequency, and we do not expect significant aliasing effects in the dominant modes $k = 0$, $|k| = 1$ and $|k| = 2$ that are the focus of our analysis. In order to assess quantitatively the effect of aliasing on our results, we computed the DFT of the nonlinear case LF4 using 25, 50 and 100 samples, and we documented the coefficients in table 2. The dominant coefficients as well as the total energy (not shown) are robust with respect to the sample size, and we see only a marginal effect of aliasing.

By Plancherel's theorem, the sum of the squared moduli of the Fourier coefficients corresponds to the L^2-norm of the velocity field over one period of oscillation T. Hence we have

$$\|\boldsymbol{u}\|_{L^2}^2 = TV \sum_{k=-\infty}^{\infty} \left\langle |\boldsymbol{c}_k|^2 \right\rangle_s = TV \sum_{k=-\infty}^{\infty} \langle \boldsymbol{c}_k \cdot \boldsymbol{c}_k^* \rangle_s \,, \tag{4.3}$$

where $\|\boldsymbol{u}\|_{L^2}^2$ is defined in (3.1), and $V = 4\sqrt{2}\,d^3$ denotes the volume of the simulation domain. The values $\langle|\boldsymbol{c}_k|^2\rangle_s$ correspond to a volume-averaged power spectral density of the velocity field. As $\boldsymbol{c}_0$ and $\boldsymbol{c}_{\pm 2}$ are excited directly by the (self-)interaction of the fundamental frequency, they can be regarded as key indicators for the appearance of a nonlinear effect. We can thus quantify the importance of nonlinear effects from the contributions of the Fourier coefficients to the L^2-norm of the velocity.

Figure 8 shows the volume average of the squared modulus of the Fourier series coefficients $\langle|\boldsymbol{c}_k|^2\rangle_s$ (marked with blue circles) as a function of the frequency k. This volume average represents the cycle-integrated energy at the specific frequency. We can see that most of the energy is concentrated at the fundamental frequency ($|k| = 1$). In a linear flow, all the energy would be concentrated at this frequency. The contributions of the first four frequencies to the cycle-integrated energy are given in table 2. For every Womersley number, there is at least one simulation (LF2, MF1 and HF2) for which the fundamental frequency contains more than 99.9 % of the energy, and the energies at $k = 0$ and $|k| = 2$ are smaller than at $|k| = 1$ by at least three orders of magnitude. These cases

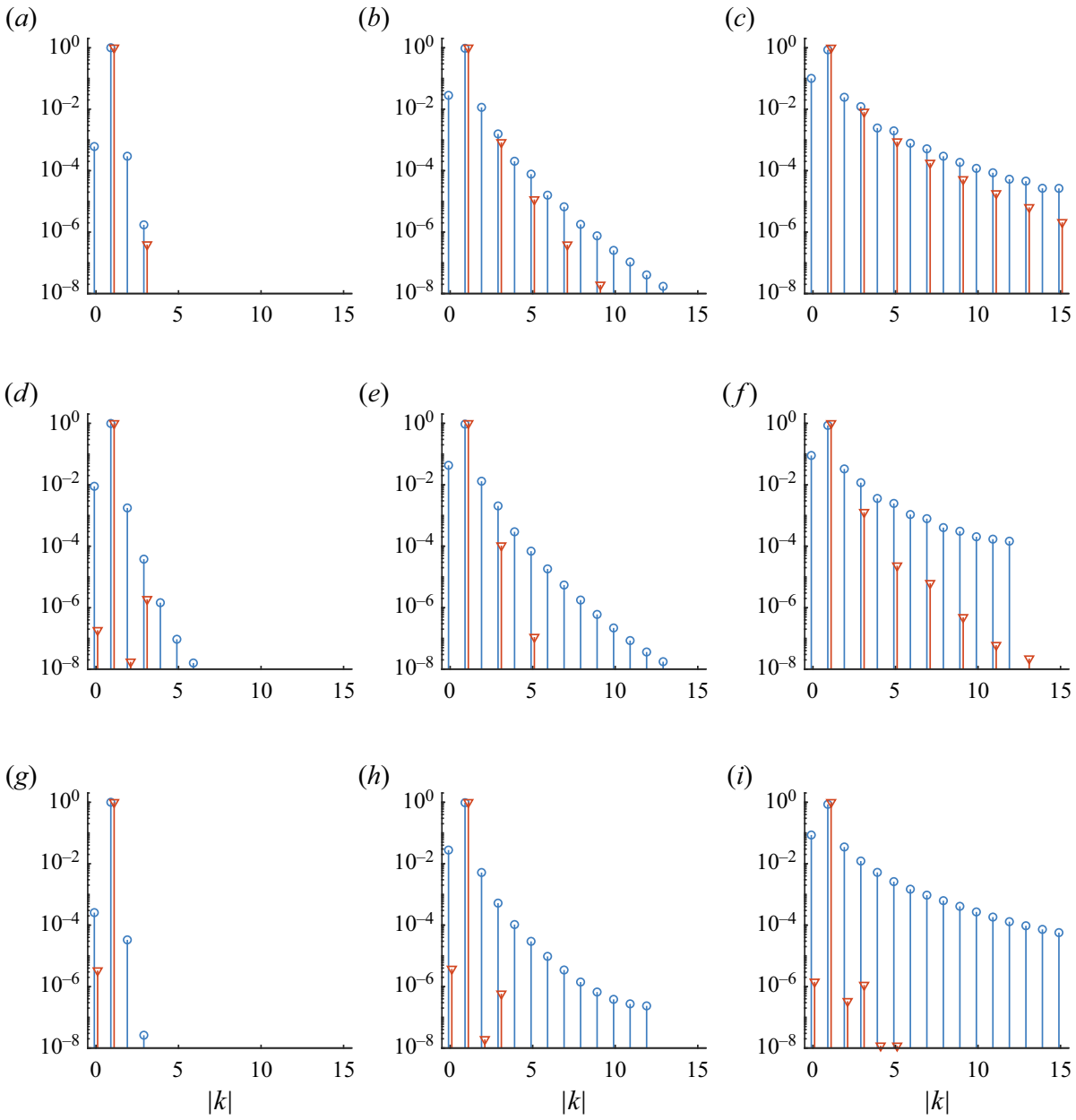

Figure 8. Volume average of the squared modulus of Fourier series coefficients $\langle |c_k|^2 \rangle_s$ (blue circles) and squared modulus of volume-averaged Fourier coefficients $\langle |c_k|^2 \rangle_s$ (red triangles). The contributions of $\langle |c_k|^2 \rangle_s$ and $\langle |c_{-k}|^2 \rangle_s$ for $k \neq 0$, as well as of $|\langle c_k \rangle_s|^2$ and $|\langle c_{-k} \rangle_s|^2$, are added together. The values are normalised by the sum of all coefficients. (*a*) LF2 (25 samples). (*b*) LF3 (100 samples). (*c*) LF4 (100 samples). (*d*) MF2 (50 samples). (*e*) MF3 (50 samples). (*f*) MF4 (25 samples). (*g*) HF2 (25 samples). (*h*) HF3 (25 samples). (*i*) HF4 (50 samples).

are effectively linear. With increasing Hg, the energy contributions of the constant mode ($k = 0$) and the overtones ($|k| > 1$) increase. This is clear evidence of nonlinear behaviour because the frequencies $|k| \neq 1$ can be excited only by frequency interactions within the nonlinear term.

The simulations LF3, MF3 and HF3 have a comparable distribution of energy among the modes. Therefore, we consider these simulations to have a similar degree of nonlinearity. The same is apparent for the simulations LF4, MF4 and HF4, which have a higher degree of nonlinearity than the former ones.

Figure 8 also shows the squared modulus of the volume average of the Fourier series coefficients $|\langle c_k \rangle_s|^2$ (marked by red triangles). These correspond to the Fourier series

coefficients of the superficial velocity $\langle \boldsymbol{u} \rangle_\mathrm{s}$:

$$\langle \boldsymbol{u} \rangle_\mathrm{s}(t) = \sum_{k=-\infty}^{\infty} \langle \boldsymbol{c}_k \rangle_\mathrm{s} \, \mathrm{e}^{\mathrm{i}k\Omega t}. \tag{4.4}$$

This equation can be derived by volume-averaging the decomposition (4.2). We observe that in general, only the Fourier coefficients of the odd frequency components are non-zero. The reason for this is that the superficial velocity is antisymmetric with respect to a half-period shift in time. This will be discussed in detail in § 5.3. In some cases, small non-zero values occur for even frequency components, too. We consider these values to be the footprint of a transient that has not completely decayed. Interestingly, the modes at $k = 0$ and $|k| = 2$ that seem to be the dominant nonlinear effect in the coefficients $\langle |\boldsymbol{c}_k|^2 \rangle_\mathrm{s}$ do not contribute to the coefficients $|\langle \boldsymbol{c}_k \rangle_\mathrm{s}|^2$ (hence these modes have zero volume-averaged velocity). Furthermore, we see that in all cases, the relative importance of the higher harmonics for the volume-averaged velocity is lower than for the complete velocity field. This is particularly visible for the simulation HF4: while the volume-averaged square moduli of the Fourier coefficients indicate strong nonlinear effects, the volume-averaged velocity is perfectly sinusoidal. Consequently, a virtually sinusoidal superficial velocity in response to a sinusoidal forcing does not necessarily imply a linear flow.

4.3. *Boundary in parameter space*

In the preceding subsections, we have established approximate regions of linearity and nonlinearity for $Wo = 10$, $Wo = 31.62$ and $Wo = 100$. Assuming a smooth dependency of the nonlinearity onset on the frequency, we can determine approximate boundaries in the range of Womersley numbers from 10 to 100 using interpolation. However, this raises the question of how the onset of nonlinearity behaves for Womersley numbers outside this interval.

For low frequencies ($Wo \to 0$), the flow becomes quasi-stationary, and as for the steady regime, the onset of nonlinearity depends only on the Reynolds number, or equivalently, the Hagen number, and is independent of the Womersley number.

On the other hand, for the high-frequency limit, we can derive the scaling of the onset of nonlinearity from the Navier–Stokes equations. We introduce the non-dimensional variables $\tilde{\boldsymbol{x}} = \boldsymbol{x}/d$, $\tilde{t} = \Omega t$, $\tilde{\boldsymbol{u}} = \boldsymbol{u}\rho\Omega/f_x$ and $\tilde{p} = p/(f_x d)$ into the Navier–Stokes equations (2.2):

$$\frac{\partial \tilde{\boldsymbol{u}}}{\partial \tilde{t}} + \frac{Hg}{Wo^4} \tilde{\boldsymbol{\nabla}} \cdot (\tilde{\boldsymbol{u}} \otimes \tilde{\boldsymbol{u}}) = -\tilde{\boldsymbol{\nabla}}\tilde{p} + \frac{1}{Wo^2} \tilde{\Delta}\tilde{\boldsymbol{u}} + \sin\tilde{t}\, \boldsymbol{e}_x. \tag{4.5}$$

In this normalisation, the unsteady term, the pressure gradient and the forcing are all $O(1)$. At the limit $Wo \to \infty$, the solution exhibits a boundary layer structure with an inviscid core flow and a viscous boundary layer. The importance of the convective term is determined by the ratio $Hg/Wo^4 = f_x/(\rho\Omega^2 d)$ – the larger the frequency, the higher the force that needs to be applied to create nonlinear effects. Therefore, we expect that the ratio Hg/Wo^4 governs the onset of nonlinearity at the high-frequency limit. Recognising that $Re \propto Hg/Wo^2$ at the high-frequency limit where the flow is linear, the ratio Re/Wo^2 can also be used to quantify the strength of nonlinear effects.

Our proposed scaling is consistent with the results of Gu & Wang (1991): they discussed the relative importance of drag components in a porous medium in the Re–Wo^2 parameter

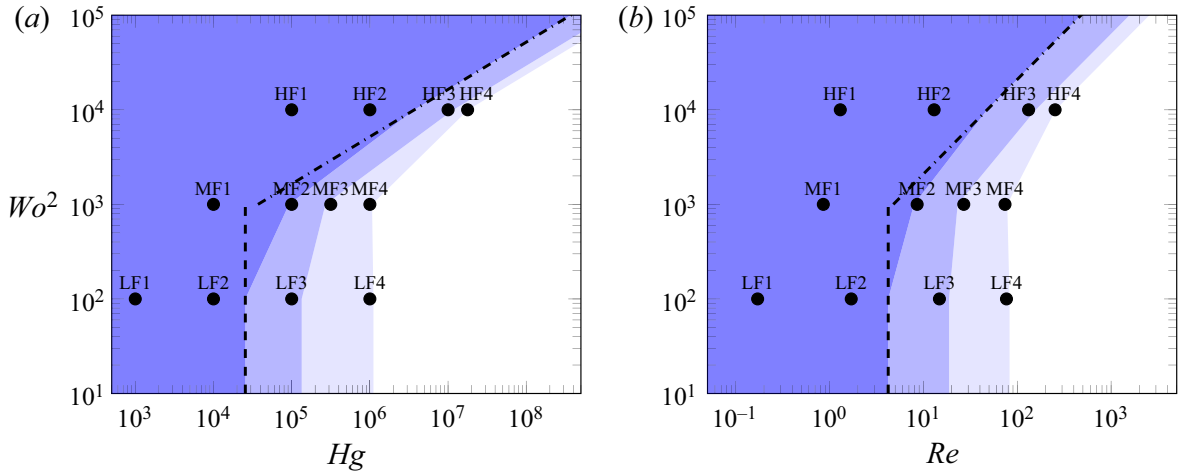

Figure 9. Levels of nonlinearity in the hexagonal sphere pack, where • indicates a simulation performed in this study. Dark blue: linear (>99 % of the energy in the first harmonic). Medium blue: weakly nonlinear (>95 % of the energy in the first harmonic). Light blue and white: strongly nonlinear (>85 % and <85 % of the energy in the first harmonic, respectively). The dashed and dash-dotted lines represent the low- and high-frequency asymptotes that were used to extrapolate the behaviour of the flow, respectively.

space based on the unsteady Forchheimer equation (Sollitt & Cross 1972). They predicted that for low frequencies, the nonlinear drag force would be negligible below a certain Reynolds number, and for high frequencies, the nonlinear drag force would be negligible below a certain value of the ratio Re/Wo^2.

As the simulations at $Wo = 100$ already exhibit thin boundary layers, we expect that we can extrapolate the onset of nonlinearity to higher Womersley numbers by keeping Hg/Wo^4 constant. A different development of the onset of nonlinearity would be expected if the boundary layers become turbulent. However the following estimation demonstrates that this transition does not become relevant for another two orders of magnitude in Re and Wo^2 beyond the range covered in this study. For low values of Hg/Wo^4 and high Womersley numbers, the boundary layers are locally identical to the Stokes boundary layer; see e.g. Schlichting & Gersten (2006, p. 354f)). It has been shown that the Stokes boundary layer becomes turbulent at $Re_{\delta,crit} = U_0/\nu\sqrt{2\nu/\Omega} \approx 600$, where U_0 is the velocity of the outer potential flow (Carstensen, Sumer & Fredsøe 2010). We approximate U_0 as equal to $5\,\langle u\rangle_{\mathrm{i}}$, which is a characteristic velocity in the high-frequency regime (see figure 12); hence we can express $Re_\delta \approx (5\sqrt{2}/\epsilon)\,Re/Wo \approx 27Re/Wo$. The transition of the boundary layer thus defines the line $27Re/Wo = 600$. Intersecting this with $Re/Wo^2 = 0.013$ for simulation HF3, we obtain $Re \approx 37\,000$ and $Wo \approx 1700$ ($Wo^2 = 2.9 \times 10^6$).

Based on the asymptotic behaviour, we extrapolate our results approximately from the previous subsection. Figure 9 shows the simulations and the 99 %, 95 % and 85 % contours of the relative magnitude of the fundamental harmonic, $2\left\langle|\boldsymbol{c}_1|^2\right\rangle_{\mathrm{s}} / \sum_{k=-N}^{N}\left\langle|\boldsymbol{c}_k|^2\right\rangle_{\mathrm{s}}$, in the Hg–Wo^2 and Re–Wo^2 parameter spaces. The interpolation was performed over $\log Hg$ and $\log Re$ for each Womersley number with the piecewise cubic Hermite interpolating polynomial method in MATLAB (Fritsch & Carlson 1980). We extrapolated the contours with lines $Hg = \text{const.}$ for low Womersley numbers, and lines $Hg/Wo^4 = \text{const.}$ for high Womersley numbers.

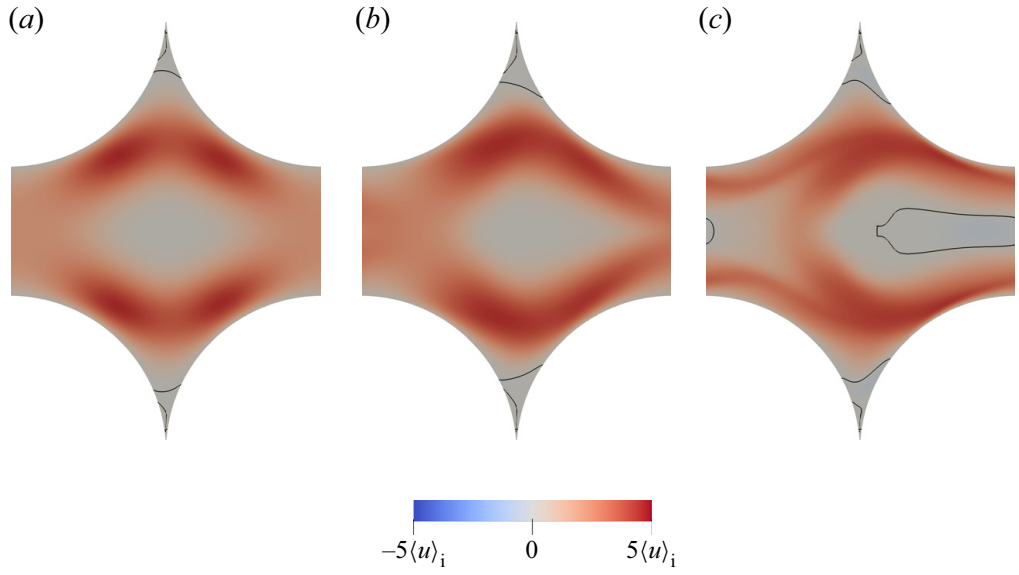

Figure 10. Velocity u in the x-direction in the plane $\frac{\sqrt{3}}{3}y - \frac{\sqrt{6}}{3}z = 0$ at the maximum superficial velocity for $Wo = 10$. The range of colours is set depending on the intrinsically volume-averaged velocity, and the lines indicate the contour $u = 0$: (*a*) $Hg = 10^4$, $Re = 1.7$ (LF2); (*b*) $Hg = 10^5$, $Re = 15$ (LF3); (*c*) $Hg = 10^6$, $Re = 77$ (LF4).

In conclusion, figure 9 summarises the results of the preceding sections and shows for which values of the parameters Hg, Re and Wo the flow can be considered effectively linear, weakly nonlinear or strongly nonlinear.

5. Manifestations of nonlinearity in the velocity field

In this section, we investigate how the velocity field in the pore is modified by the nonlinearity. We observe that the nonlinearity leads to a breaking of a fore–aft symmetry in the flow, and we employ the violation of this symmetry to quantify the strength of nonlinearity in the instantaneous velocity fields. On this basis, we investigate the question of whether the nonlinearity occurs in phase with the instantaneous superficial velocity. Finally, we combine our previous findings in a comprehensive and consistent description of nonlinear effects in the frequency domain.

5.1. *Velocity field at maximum superficial velocity*

In order to understand which changes in the flow accompany the appearance of nonlinearity, we investigate how representative instantaneous velocity fields vary with respect to the Hagen and Womersley numbers. As the nonlinearity depends strongly on the velocity magnitude, we consider instantaneous fields close to the maximum superficial velocity. We visualise the local symmetry plane $\frac{\sqrt{3}}{3}y - \frac{\sqrt{6}}{3}z = 0$, which is highlighted in figure 1(*b*). This plane contains open channels in the x-direction that are constricted by spheres touching the plane from above and below. Consequently, high velocities are found near the contact points in this plane. Figures 10, 11 and 12 show the spatial distribution of the velocity component in the x-direction in this section for $Wo = 10$, 31.62 and 100, respectively.

The flow enters the simulation domain on the left through the maximum flow cross-section. The flow is divided by the contact point in the centre of the section and

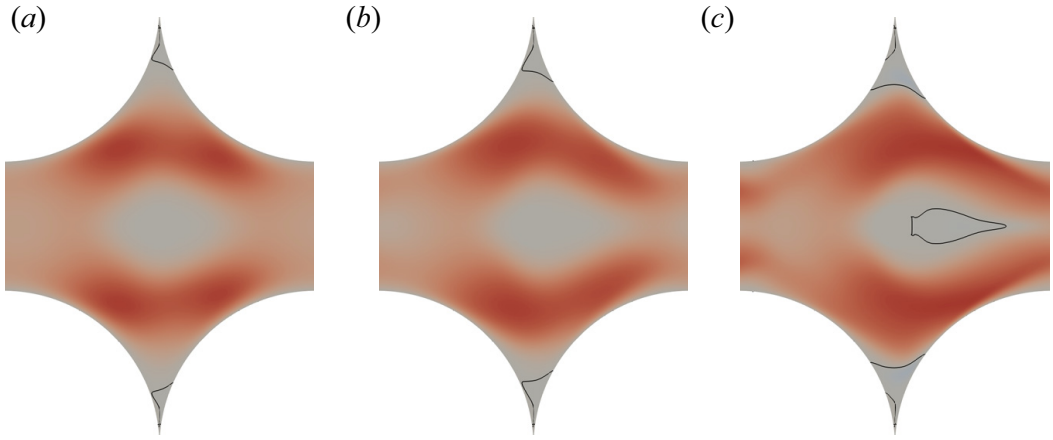

Figure 11. Velocity u in the x-direction in the plane $\frac{\sqrt{3}}{3}y - \frac{\sqrt{6}}{3}z = 0$ at the maximum superficial velocity for $Wo = 31.62$. The range of colours is set depending on the intrinsically volume-averaged velocity, and the lines indicate the contour $u = 0$: (*a*) $Hg = 10^5$, $Re = 8.6$ (MF2); (*b*) $Hg = 10^{5.5}$, $Re = 27$ (MF3); (*c*) $Hg = 10^6$, $Re = 73$ (MF4).

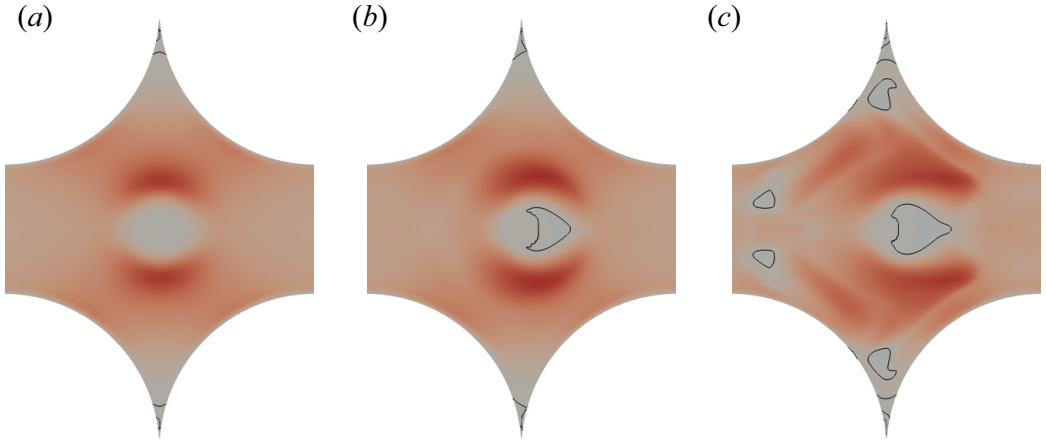

Figure 12. Velocity u in the x-direction in the plane $\frac{\sqrt{3}}{3}y - \frac{\sqrt{6}}{3}z = 0$ at the maximum superficial velocity for $Wo = 100$. The range of colours is set depending on the intrinsically volume-averaged velocity, and the lines indicate the contour $u = 0$: (*a*) $Hg = 10^5$, $Re = 13$ (HF2); (*b*) $Hg = 10^7$, $Re = 132$ (HF3); (*c*) $Hg = 10^{7.25}$, $Re = 252$ (HF4).

diverted through two adjacent smaller pores. Then the flow merges as it enters the next repetition of the domain.

For small Hagen numbers, the velocity field exhibits a fore–aft symmetry (see figures 10*a*, 11*a* and 12*a*):

$$\boldsymbol{u}(\boldsymbol{x}, t) = \begin{bmatrix} u(x, y, z, t) \\ v(x, y, z, t) \\ w(x, y, z, t) \end{bmatrix} = \begin{bmatrix} u(2d - x, y, z, t) \\ -v(2d - x, y, z, t) \\ -w(2d - x, y, z, t) \end{bmatrix} =: \mathcal{S}\boldsymbol{u}(\boldsymbol{x}, t). \tag{5.1}$$

With increasing Hagen number, the distribution becomes asymmetric, and flow separation appears behind the contact points and along the spheres on the side of the pores. This is consistent with the observations of Sakai & Manhart (2020). The fore–aft symmetry is characteristic of the (unsteady) Stokes flow regime (Batchelor 2000); the deviation from this symmetry indicates the presence of nonlinear effects in the flow. We can see that at $Wo = 10$, the velocity field is still symmetric at $Hg = 10^4$ (LF2) while it is asymmetric at $Hg = 10^5$ (LF2). At $Wo = 31.62$, the velocity field at $Hg = 10^5$ (MF2) is almost

symmetric, whereas a more pronounced asymmetry can be observed at $Hg = 10^{5.5}$ (MF3). Finally, at $Wo = 100$, the symmetry remains up to $Hg = 10^6$ (HF2) while the velocity field at $Hg = 10^7$ (HF3) is asymmetric. Notably, the symmetric cases were classified as linear and the asymmetric cases were classified as nonlinear in the analyses of the previous section.

For the simulations LF4, MF4, HF3 and HF4, we observe a region of negative velocity in the x-direction behind the contact point, indicating a local backflow and a flow separation at the contact point. These recirculation regions have already been observed in steady flow by Maier *et al.* (1998). The length of the recirculation region decreases from $Wo = 10$ to $Wo = 100$. Additional regions of negative velocity can also be observed in simulation HF4 (figure 12*c*). Consideration of the temporal evolution of the flow suggests that these regions are the residuals of velocity minima in the previous half-cycle.

We observe that with increasing Womersley numbers, the high velocity regions move closer to the contact point. The reason for this is that the region affected by diffusion becomes smaller as Wo increases and recedes into the contact point region. A more detailed discussion of this behaviour can be found at the end of § 3.4.

In summary, the onset of nonlinearity leads to a fore–aft asymmetry in the velocity field. The parameters for which such an asymmetry is noticeable are in good agreement with the previous analyses based on global quantities. For larger Hagen numbers, a flow separation develops at the contact points in the centre of the plane $\frac{\sqrt{3}}{3}y - \frac{\sqrt{6}}{3}z = 0$, which becomes less pronounced with increasing Womersley number. It is conceivable that the asymmetry and flow separation lead to a higher concentration of the flow into a smaller cross-section, which could result in a higher instantaneous drag. This could explain the decline of the superficial velocity with increasing Hg observed in the LF and MF cases.

5.2. *Temporal evolution of the strength of nonlinearity*

In this subsection, we seek to answer the question of how the asymmetry of the velocity field, and consequently the nonlinearity, evolves over the course of the cycle. In particular, we aim to investigate whether the nonlinear effects develop in phase with the volume-averaged velocity, as this has important implications for the modelling of nonlinear oscillatory flow.

In order to quantify the asymmetry of the instantaneous velocity fields, we decompose the fields into a component that satisfies the fore–aft symmetry (5.1) and a component that satisfies the corresponding antisymmetry:

$$\boldsymbol{u}_{sym}(\boldsymbol{x}, t) = \tfrac{1}{2}\left(\boldsymbol{u}(\boldsymbol{x}, t) + \mathcal{S}\boldsymbol{u}(\boldsymbol{x}, t)\right), \tag{5.2a}$$

$$\boldsymbol{u}_{anti}(\boldsymbol{x}, t) = \tfrac{1}{2}\left(\boldsymbol{u}(\boldsymbol{x}, t) - \mathcal{S}\boldsymbol{u}(\boldsymbol{x}, t)\right). \tag{5.2b}$$

This additive decomposition of the velocity is also a decomposition of kinetic energy: the total kinetic energy can be written as

$$\langle k\rangle_\mathrm{s} = \tfrac{1}{2}\rho\left\langle\left(\boldsymbol{u}_{sym} + \boldsymbol{u}_{anti}\right)^2\right\rangle_\mathrm{s} = \tfrac{1}{2}\rho\left[\left\langle\boldsymbol{u}_{sym}^2\right\rangle_\mathrm{s} + 2\left\langle\boldsymbol{u}_{sym}\cdot\boldsymbol{u}_{anti}\right\rangle_\mathrm{s} + \left\langle\boldsymbol{u}_{anti}^2\right\rangle_\mathrm{s}\right], \tag{5.3}$$

where we have dropped the arguments of the velocity field for notational simplicity. The cross-term can be written further as

$$2\left\langle\boldsymbol{u}_{sym}\cdot\boldsymbol{u}_{anti}\right\rangle_\mathrm{s} = \tfrac{1}{2}\left\langle(\boldsymbol{u} + \mathcal{S}\boldsymbol{u})\cdot(\boldsymbol{u} - \mathcal{S}\boldsymbol{u})\right\rangle_\mathrm{s} = \tfrac{1}{2}\left[\langle\boldsymbol{u}^2\rangle_\mathrm{s} - \langle(\mathcal{S}\boldsymbol{u})^2\rangle_\mathrm{s}\right] = 0, \tag{5.4}$$

which is equal to zero since the symmetry operation does not change the kinetic energy of

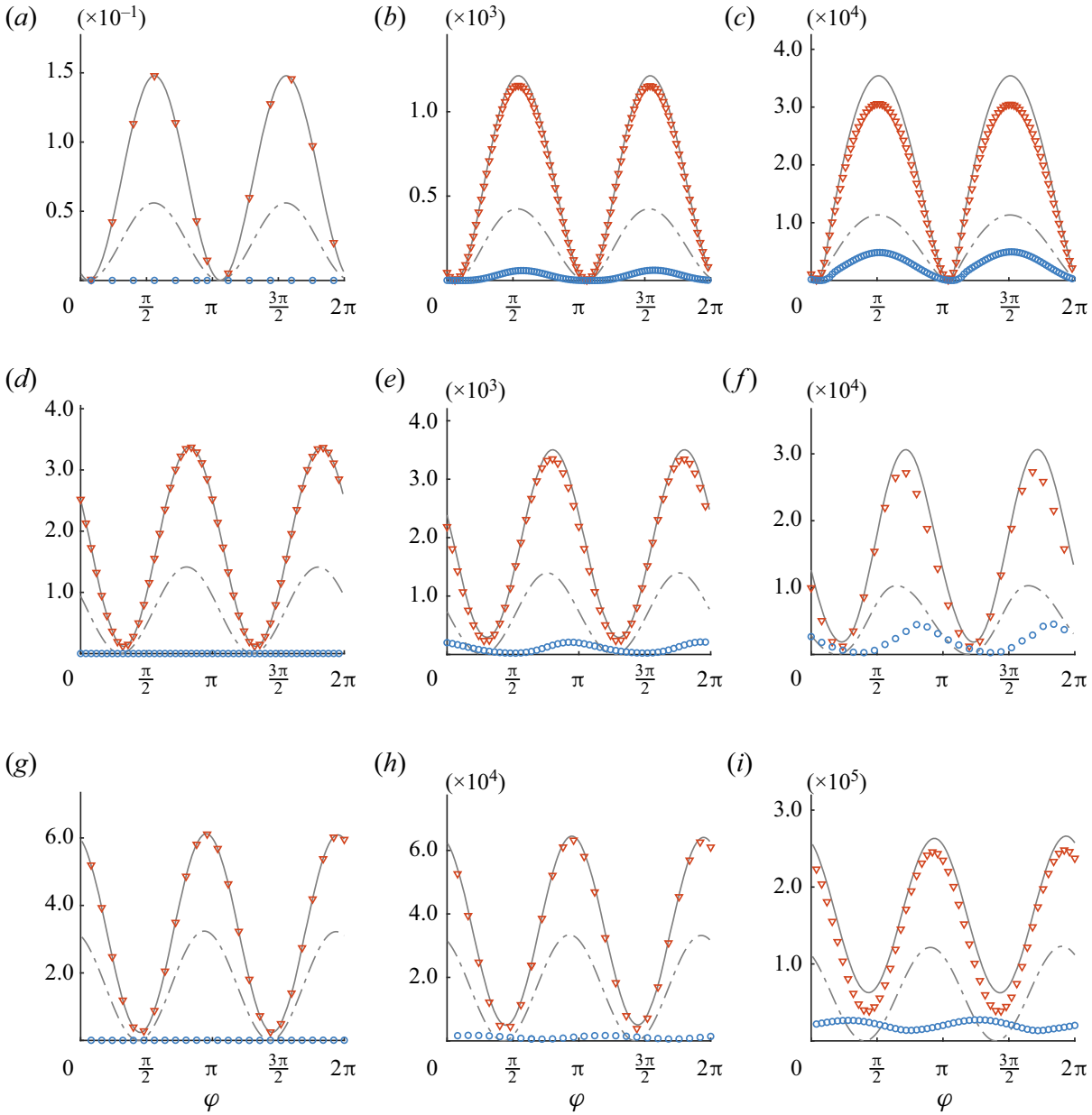

Figure 13. Kinetic energy of symmetric and antisymmetric parts of the velocity field. Red triangles, $\langle k_{sym}\rangle_s$. Blue circles, $\langle k_{anti}\rangle_s$. Grey solid line, $\langle k\rangle_s$. Grey dash-dotted line, $\frac{1}{2}(\rho/\epsilon)\,\langle \boldsymbol{u}\rangle_s^2$. (*a*) LF1, (*b*) LF3, (*c*), LF4, (*d*) MF1, (*e*) MF3, (*f*) MF4, (*g*) HF1, (*h*) HF3, (*i*) HF4.

the flow. Hence we have the decomposition of the kinetic energy:

$$\langle k\rangle_s = \langle k_{sym}\rangle_s + \langle k_{anti}\rangle_s\,. \tag{5.5}$$

Figure 13 shows the temporal evolution of the kinetic energy of the symmetric and antisymmetric components over the course of one period. The quantities $\langle k_{sym}\rangle_s$ and $\langle k_{anti}\rangle_s$ (symbols) are computed from instantaneous velocity fields; the total kinetic energy $\langle k\rangle_s$ as well as the energy of the volume-averaged velocity $\frac{1}{2}(\rho/\epsilon)\,\langle \boldsymbol{u}\rangle_s^2$ (lines) are known in every time step. We can see in figures 13(*a*,*d*,*g*) that for simulations LF1, MF1 and HF1, which we have identified as linear cases, no kinetic energy is present in the antisymmetric component. With increasing Hagen number, the relative importance of the antisymmetric component increases. This is consistent with our expectation that the kinetic energy of the antisymmetric part $\langle k_{anti}\rangle_s$ can be used as measure of the intensity of nonlinear effects.

Figure 13 also shows the squared superficial velocity (dash-dotted line). At $Wo = 10$, the peaks of $\frac{1}{2}(\rho/\epsilon)\,\langle \boldsymbol{u}\rangle_{\mathrm{s}}^2$, $\langle k_{sym}\rangle_{\mathrm{s}}$ and $\langle k_{anti}\rangle_{\mathrm{s}}$ occur almost at the same time. On the other hand, for $Wo = 31.62$ and 100, the peak of the kinetic energy of the symmetric component is slightly delayed and the peak of the kinetic energy of the antisymmetric component is significantly delayed with respect to the peak of the squared superficial velocity. At higher Womersley numbers, the maximum strength of nonlinear effects is thus attained during the deceleration phase of the cycle. The delay between $\langle k_{sym}\rangle_{\mathrm{s}}$ and $\frac{1}{2}(\rho/\epsilon)\,\langle \boldsymbol{u}\rangle_{\mathrm{s}}^2$ occurs for both linear and nonlinear cases. We explain this with the phase difference between the bulk flow and the boundary layers that is a well-known feature of oscillatory flow at high Womersley numbers (Schlichting & Gersten 2006). On the other hand, the additional delay between the symmetric and the antisymmetric components can be seen as the time that is required for the nonlinear flow structures to form by inertia.

In summary, we found that for $Wo = 31.62$ and 100, the maximum intensity of nonlinear effects can be found during deceleration of the bulk flow, while for $Wo = 10$, the nonlinear effects are almost in phase with the bulk flow. Interestingly, the kinetic energy of the antisymmetric part of the velocity field is delayed with respect to the squared superficial velocity. This observation is important for the modelling of nonlinear unsteady porous media flow because current models based on the unsteady Forchheimer equation (Sollitt & Cross 1972) assume that the nonlinear drag is proportional to $|\langle u\rangle_{\mathrm{s}}|\,\langle u\rangle_{\mathrm{s}}$ and thus in phase with the squared superficial velocity. Our data suggest that this assumption does not hold for higher Womersley numbers.

5.3. *Analysis of the nonlinear Fourier modes*

In the analysis of the Fourier coefficients presented in § 4.2, we demonstrated that the modes $\boldsymbol{c}_0$, $\boldsymbol{c}_{-2}$ and $\boldsymbol{c}_2$ are the leading-order nonlinear effects in weakly nonlinear flow. In this subsection, we investigate the properties of these modes in detail, and we establish a link to the time domain analysis in the preceding subsection.

A surprising result of the Fourier decomposition of the flow is a non-zero constant contribution $\boldsymbol{c}_0$. This implies the existence of a non-zero time-averaged velocity field. At the onset of nonlinear effects, this mode is the most dominant mode other than the fundamental frequency. As illustrated in figure 14, the time-averaged velocity field is a consequence of the antisymmetry of forward and backward flow during the cycle. By averaging the velocity fields from the forward and backward phase, an antisymmetric time-averaged velocity field with zero superficial velocity is obtained. In linear flow, velocity fields that are half a period apart are completely symmetric, therefore no time-averaged flow occurs. Thus the presence of a time-averaged velocity field is indeed a nonlinear effect.

A different interpretation can be obtained from the Fourier approach: for weakly nonlinear flow, the flow is dominated by the modes $\boldsymbol{c}_{-1}$ and $\boldsymbol{c}_1$, and their interaction in the convective term is the principal source of the time-averaged velocity field $\boldsymbol{c}_0$. This effect is known commonly as acoustic streaming (Schlichting & Gersten 2006, pp. 363–366). Lighthill (1978) discussed this phenomenon comprehensively, and Manor (2021) has investigated recently acoustic streaming in porous media.

Figure 15 shows the time-averaged velocity field in the sectioned plane for the simulations LF3, MF3 and HF3 (all of which have approximately 95 % of their signal energy concentrated at the fundamental frequency). We can see that all fields have an antisymmetric distribution of velocity. As the frequency increases, the regions of large

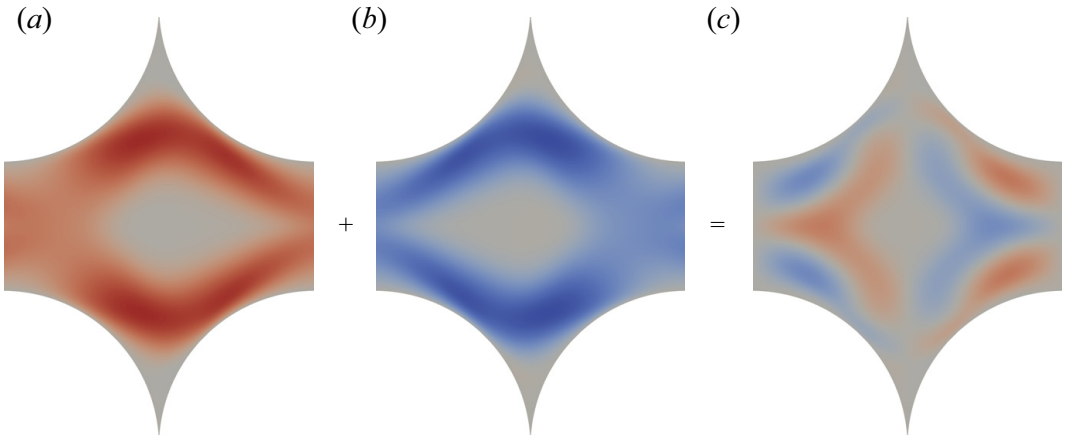

Figure 14. Velocity in the x-direction for LF3. The fields (a,b) are taken at the cycle maximum and minimum of the volume-averaged velocity $\langle u\rangle_s$. The colours range from $-5\,\langle u\rangle_i$ (blue) to $5\,\langle u\rangle_i$ (red) in (a,b), and from $-\langle u\rangle_i$ to $\langle u\rangle_i$ in (c). (a) Forward flow ($\langle u\rangle_s > 0$). (b) Backward flow ($\langle u\rangle_s < 0$). (c) Time-averaged flow ($\langle u\rangle_s = 0$).

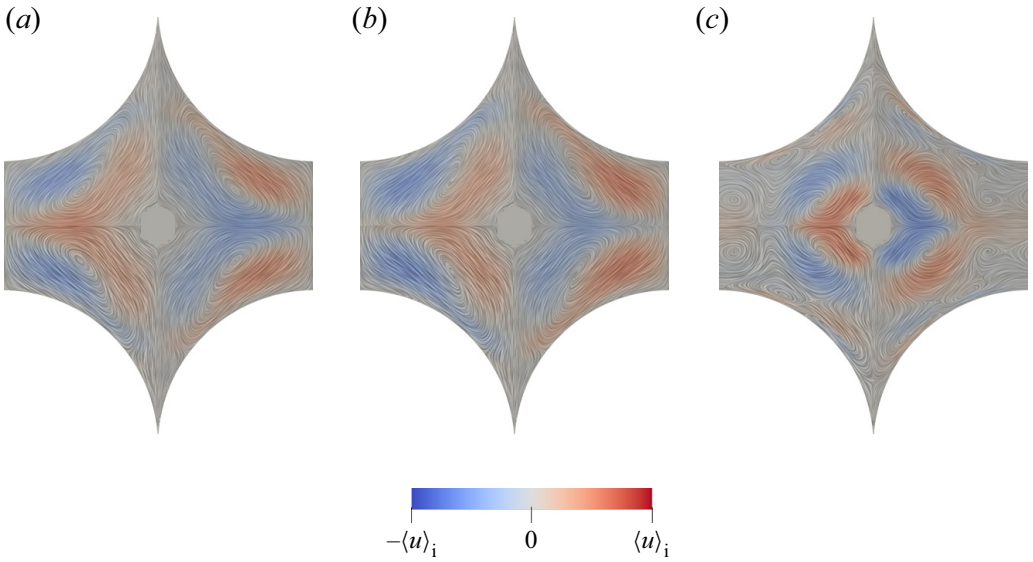

Figure 15. Time-averaged velocity in the x-direction and LIC visualisation of the velocity field for $Wo = 10$, 31.62 and 100 in weakly nonlinear flow. The colours range from $-\langle u\rangle_i$ (blue) to $\langle u\rangle_i$ (red). (a) LF3, (b) MF3, (c) HF3.

velocity magnitude of the time-averaged flow move closer to the contact point, and the velocity magnitude in the bulk flow goes to zero. In the line integral convolution (LIC) visualisation (Cabral & Leedom 1993; Laramee, Jobard & Hauser 2003) of the time-averaged velocity field, we can observe two pairs of counter-rotating vortices in the plane $\frac{\sqrt{3}}{3}y - \frac{\sqrt{6}}{3}z = 0$. Note that the LIC for the case HF3 does not result in a symmetric pattern; deviations occur in regions of small velocity magnitude. We ascribe this to the low number of samples (25 samples) that were used to perform the time average.

The time-averaged vortices have several effects. On the one hand, it can be shown that they contribute to the asymmetry of the forward and reverse flows. On the other hand, it is evident that they cause additional mixing in the streamwise and cross-streamwise directions, which obviously has to be taken into account when volume-averaged scalar transport models are designed. This additional scalar transport can be effective even in

cases in which the change in the superficial velocity was marginal (as in the cases HF3 and HF4).

We now direct our attention to the other nonlinear modes, $|k| \geqslant 2$. First, we show that these modes also possess a defined symmetry; second, we investigate the interaction of these modes with the constant mode $\boldsymbol{c}_0$. We notice that in laminar flow, the velocity field satisfies a spatiotemporal symmetry (half-period symmetry): due to the sinusoidal excitation, in steady oscillation the velocity fields at two instants with a time difference of half a period are mirrored with the symmetry $\mathcal{S}$ (defined in (5.1)):

$$\boldsymbol{u}(\boldsymbol{x}, t + T/2) = -\mathcal{S}\boldsymbol{u}(\boldsymbol{x}, t). \tag{5.6}$$

This means that the velocity fields in forward and backward flow are mirror images of each other (reflections in the x-direction). Direct consequences of this symmetry are the half-period symmetries of the superficial velocity and kinetic energy:

$$\langle u \rangle_\mathrm{s}(t + T/2) = -\langle u \rangle_\mathrm{s}(t), \tag{5.7a}$$

$$\langle k \rangle_\mathrm{s}(t + T/2) = \langle k \rangle_\mathrm{s}(t). \tag{5.7b}$$

This behaviour can be observed in figures 5, 6 and 7. Another consequence of the half-period symmetry is that the Fourier coefficients can be written as

$$\boldsymbol{c}_k = \frac{1}{T}\int_0^T \frac{1}{2}\Big(\boldsymbol{u}(\boldsymbol{x}, t) - (-1)^k \mathcal{S}\boldsymbol{u}(\boldsymbol{x}, t)\Big)\,\mathrm{e}^{\mathrm{i}k\Omega t}\,\mathrm{d}t \tag{5.8}$$

(see Appendix B for the derivation). The even-k Fourier coefficients satisfy $\boldsymbol{c}_k = -\mathcal{S}\boldsymbol{c}_k$ and therefore possess a fore–aft antisymmetry, whereas the odd-k Fourier coefficients satisfy $\boldsymbol{c}_k = \mathcal{S}\boldsymbol{c}_k$ and have a fore–aft symmetry. The antisymmetric fields have a zero superficial volume-averaged velocity in the x-direction. This is consistent with the spectra of $\langle u \rangle_\mathrm{s}$ presented in figure 8, which contain only odd-frequency components. Consequently, the modes $\boldsymbol{c}_0$, $\boldsymbol{c}_{-2}$ and $\boldsymbol{c}_2$, which are dominant at the onset of nonlinearity, cannot be observed directly with the superficial velocity $\langle u \rangle_\mathrm{s}$.

In the following, we aim to understand how the time-averaged velocity field $\boldsymbol{c}_0$ interacts with the modes $\boldsymbol{c}_{-2}$ and $\boldsymbol{c}_2$ to produce the oscillating strength of nonlinear effects that we observed in § 5.2. In a first step, we recognise that the antisymmetric part of the velocity field can be expressed solely in terms of even Fourier components as

$$\boldsymbol{u}_{anti}(\boldsymbol{x}, t) = \sum_{k\ \mathrm{even}} \boldsymbol{c}_k(\boldsymbol{x})\,\mathrm{e}^{\mathrm{i}k\Omega t} = \boldsymbol{c}_0(\boldsymbol{x}) + \boldsymbol{c}_{-2}(\boldsymbol{x})\,\mathrm{e}^{-\mathrm{i}2\Omega t} + \boldsymbol{c}_2(\boldsymbol{x})\,\mathrm{e}^{\mathrm{i}2\Omega t} + \cdots, \tag{5.9}$$

where we have omitted the coefficients $\boldsymbol{c}_{\pm 4}$, $\boldsymbol{c}_{\pm 6}$, and so on, which, as we have seen in § 4.2, are small at the onset of nonlinearity. As we have discussed previously in § 4.2, all Fourier coefficients in this series are generated by the nonlinear term in the Navier–Stokes equations. From this series, we obtain the volume-averaged kinetic energy of the antisymmetric component as

$$\begin{aligned}\langle k_{anti} \rangle_\mathrm{s} = \tfrac{1}{2}\rho\Big[&\left\langle \boldsymbol{c}_0^2 \right\rangle_\mathrm{s} + \langle \boldsymbol{c}_{-2} \cdot \boldsymbol{c}_2 \rangle_\mathrm{s} + \langle \boldsymbol{c}_0 \cdot \boldsymbol{c}_{-2} \rangle_\mathrm{s}\,\mathrm{e}^{-\mathrm{i}2\Omega t} + \langle \boldsymbol{c}_0 \cdot \boldsymbol{c}_2 \rangle_\mathrm{s}\,\mathrm{e}^{\mathrm{i}2\Omega t} \\ &+ \left\langle \boldsymbol{c}_{-2}^2 \right\rangle_\mathrm{s}\,\mathrm{e}^{-\mathrm{i}4\Omega t} + \left\langle \boldsymbol{c}_2^2 \right\rangle_\mathrm{s}\,\mathrm{e}^{\mathrm{i}4\Omega t} + \cdots\Big],\end{aligned} \tag{5.10}$$

which we can reformulate using $\boldsymbol{c}_0^* = \boldsymbol{c}_0$ and $\boldsymbol{c}_2^* = \boldsymbol{c}_{-2}$ as

$$\langle k_{anti}\rangle_s = \tfrac{1}{2}\rho\Big[\Big\langle|\boldsymbol{c}_0|^2\Big\rangle_s + \Big\langle|\boldsymbol{c}_2|^2\Big\rangle_s + \langle \boldsymbol{c}_0\cdot\boldsymbol{c}_{-2}\rangle_s\, \mathrm{e}^{-\mathrm{i}2\Omega t} + \langle \boldsymbol{c}_0\cdot\boldsymbol{c}_2\rangle_s\, \mathrm{e}^{\mathrm{i}2\Omega t} + \Big\langle \boldsymbol{c}_{-2}^2\Big\rangle_s \mathrm{e}^{-\mathrm{i}4\Omega t} + \Big\langle \boldsymbol{c}_2^2\Big\rangle_s \mathrm{e}^{\mathrm{i}4\Omega t} + \cdots\Big]. \tag{5.11}$$

We first consider just the first line of this equation. These terms make up a harmonic oscillation at frequency 2Ω. The terms $\big\langle|\boldsymbol{c}_0|^2\big\rangle_s + \big\langle|\boldsymbol{c}_2|^2\big\rangle_s$ represent the constant mean value of the oscillation; their value can be read from table 2. The terms oscillating at frequency 2Ω represent interference between the modes $\boldsymbol{c}_0$, $\boldsymbol{c}_{-2}$ and $\boldsymbol{c}_2$. They depend on the spatial correlations $\langle \boldsymbol{c}_0\cdot\boldsymbol{c}_{-2}\rangle_s$ and $\langle \boldsymbol{c}_0\cdot\boldsymbol{c}_2\rangle_s$. Hence if the spatial distributions of $\boldsymbol{c}_0$, $\boldsymbol{c}_{-2}$ and $\boldsymbol{c}_2$ are very similar, then the oscillation extends from zero to twice the mean value. For example, this is the case for simulation LF3 (see figure 13*b*). On the other hand, if the spatial distribution of the modes differs substantially, the extrema of the oscillation approach the base level (see, for example, figure 13*i*). Consequently, these interference terms represent the variation of the nonlinearity throughout the cycle. Finally, we consider the terms at the higher frequency 4Ω. These terms modify the harmonic oscillation described above by changing the steepness of the rising and falling parts of the curve. This can be interpreted as different formation and destruction times for the asymmetry. The effect of these terms is visible in figures 13(*c*) and 13(*f*), where the curve of $\langle k_{anti}\rangle_s$ is no longer sinusoidal.

In conclusion, we arrive at the following picture of the flow in terms of the Fourier modes. The linear flow is represented by the modes $\boldsymbol{c}_{-1}$ and $\boldsymbol{c}_1$, and satisfies the fore–aft symmetry (5.1). Interactions of these modes via the convective term of the Navier–Stokes equations result in the antisymmetric modes $\boldsymbol{c}_0$, $\boldsymbol{c}_{-2}$ and $\boldsymbol{c}_2$. As a consequence of the antisymmetry, these modes do not contribute directly to the superficial velocity $\langle u\rangle_s$. However, these modes represent secondary flow structures (see figure 15) which cause additional mixing and dissipation. The kinetic energy stored in these modes seems to be related to a phase shift of the bulk flow (see § 4.1), therefore these effects should be taken into account in the modelling of such flow.

6. Conclusion

6.1. *Summary*

We performed direct numerical simulations of laminar oscillatory flow through a hexagonal sphere pack driven by a sinusoidal force. We varied the Hagen number and the Womersley number, which represent the amplitude and frequency of the forcing, respectively.

We verified our solver with a highly accurate numerical solution of Stokes flow in a simple cubic sphere pack taken from the literature (Chapman & Higdon 1992). We checked the discretisation error of our hexagonal sphere pack simulations by comparing numerical solutions at grid resolutions of 48, 96, 192 and 384 cells per sphere diameter for each case. This resulted in errors below 1.2 % in the Reynolds number as well as in the space–time L^2-norm of the velocity.

Our first objective was to analyse for which regions in the Hg–Wo^2 or Re–Wo^2 parameter spaces the flow can be considered as linear. As a first indicator of linearity, we selected the scaling of the superficial volume-averaged velocity with the Hagen number and of the superficial volume-averaged kinetic energy with the square of the Hagen number. As a second indicator of linearity, we chose the magnitude of the Fourier series coefficients

of the velocity field other than the fundamental harmonic. For low Womersley numbers, the onset of nonlinear effects depends solely on the Reynolds number based on the cycle-maximum of the superficial velocity. For high Womersley numbers, it depends on the ratio of the Reynolds number to the square of the Womersley number. Other than quantifying the amount of nonlinearity in the flow, the Fourier analysis showed that for weakly nonlinear flow, the zeroth and second harmonics are the dominant nonlinear effects. Interestingly, these harmonics are not contained in the spectrum of the superficial velocity; the superficial velocity is therefore not a suitable indicator of nonlinearity.

Our second objective was to investigate how the onset of nonlinearity affects the instantaneous velocity fields. We showed that nonlinearity leads to a loss of fore–aft symmetry in the instantaneous velocity field, and that the loss of symmetry agrees with our previous definitions of nonlinearity. We use the departure from this symmetry to quantify the instantaneous strength of nonlinear effects. We found that at $Wo = 10$, the nonlinear effects are almost in phase with the bulk flow. On the other hand, for $Wo = 31.62$ and 100, the nonlinear effects are strongest during the deceleration phase of the bulk flow; we therefore observe a phase delay of between the superficial velocity and the kinetic energy of the antisymmetric part of the velocity field. This delay raises doubts about the general applicability of the unsteady Forchheimer equation, which is based on the assumption that the nonlinear drag is proportional to $|\langle u\rangle_s|\,\langle u\rangle_s$ and therefore is in phase with the superficial velocity.

Finally, we investigated flow in the frequency domain. The onset of nonlinearity manifests through the appearance of Fourier modes at zero and two times the frequency of excitation. The zero frequency mode represents a time-averaged velocity field that is caused by the asymmetry of the velocity fields. This time-averaged velocity field causes a secondary flow that increases mixing in cross-streamwise direction. A closer look at the symmetry properties of the Fourier modes revealed that the modes $\boldsymbol{c}_0$, $\boldsymbol{c}_{-2}$ and $\boldsymbol{c}_2$, which represent the most dominant nonlinear effects, possess a fore–aft antisymmetry. Therefore, these modes have zero superficial velocity, raising further doubts about whether the superficial velocity provides sufficient information to model nonlinear effects. Finally, we discussed the interaction among the nonlinear Fourier modes that leads to a harmonic oscillation of the magnitude of nonlinearity over the cycle.

6.2. *Future issues*

Further research should be conducted to confirm the high-frequency asymptote $Hg/Wo^4 =$ const. for the onset of nonlinearity that was postulated based on the non-dimensional Navier–Stokes equations in the high-frequency limit. An outstanding question in the present study is how the delay time between the maximum superficial velocity and the maximum kinetic energy of the antisymmetric part of the velocity field scales with Hg, Wo and Re. Moreover, it would be interesting to study the behaviour of the drag force at the onset of nonlinearity, and to determine the instigating processes. Finally, an attempt to understand the relation of the present results to the flow structure development reported by Sakai & Manhart (2020) for nonlinear transient flow would be worthwhile.

As a generalisation of this study, it would be interesting to apply the forcing in different directions and thus break the symmetry between forward and backward flow. Furthermore, one could investigate different, possibly random, arrangements of spheres or other porous media. For steady flow, Firdaouss *et al.* (1997) showed that the resistance law in weakly nonlinear flow has the same form for both isotropic and a large class of periodic porous media with certain reflectional symmetries of the unit cell. Therefore, it might be expected

that the observations made in our present study about the Fourier coefficients of the velocity field and the superficial velocity would generalise to isotropic porous media.

Finally, it has been observed that oscillation can enhance the scalar transport in linear and nonlinear porous media flow (Crittenden *et al.* 2005). It would thus be of great interest to look more closely at how the nonlinear secondary motion in oscillatory flow modifies the scalar transport properties. This would have implications for the design of chemical reactors and the understanding of mass and heat transfer in environmental flows, for example in coral reefs.

Supplementary material. Time-resolved data of the superficial volume-averaged velocity and kinetic energy are available at https://doi.org/10.1017/jfm.2022.496.

Acknowledgements. We would like to express our thanks to Y. Sakai for helpful discussions during the writing of this paper.

Funding. The authors gratefully acknowledge the financial support of the Deutsche Forschungsgemeinschaft (DFG, German Research Foundation) under grant no. MA2062/13-1. Computing time was granted by the Leibniz Supercomputing Centre on its Linux-Cluster.

Declaration of interests. The authors report no conflict of interest.

Author ORCIDs.
Lukas Unglehrt https://orcid.org/0000-0002-1299-0430;
Michael Manhart https://orcid.org/0000-0001-7809-6282.

Author contributions. L.U. performed the simulations and data analysis. Both authors contributed equally to reaching conclusions and writing the paper.

Appendix A. Governing equation for Fourier series coefficients

We insert the Fourier series representations

$$\boldsymbol{u}(\boldsymbol{x}, t) = \sum_{k=-\infty}^{\infty} \boldsymbol{c}_k(\boldsymbol{x})\, \mathrm{e}^{\mathrm{i}k\Omega t}, \tag{A1a}$$

$$p(\boldsymbol{x}, t) = \sum_{k=-\infty}^{\infty} d_k(\boldsymbol{x})\, \mathrm{e}^{\mathrm{i}k\Omega t} \tag{A1b}$$

of velocity and pressure into the Navier–Stokes equations (2.2) and thus obtain the governing equations for the Fourier modes $\boldsymbol{c}_k(\boldsymbol{x})$, $k \in \mathbb{Z}$:

$$\nabla \cdot \boldsymbol{c}_k = 0, \tag{A2a}$$

$$\mathrm{i}k\Omega \boldsymbol{c}_k + \sum_{m=-\infty}^{\infty} \nabla \cdot (\boldsymbol{c}_m \otimes \boldsymbol{c}_{k-m}) = -\frac{1}{\rho} \nabla d_k + \nu\, \Delta \boldsymbol{c}_k + \frac{1}{\rho} \boldsymbol{f}_k, \tag{A2b}$$

where $\boldsymbol{f}_k$ are the Fourier coefficients of the excitation. For the sinusoidal excitation, only the coefficients of the fundamental frequency are non-zero: $\boldsymbol{f}_{-1} = \mathrm{i}f_x/2\, \boldsymbol{e}_x$ and $\boldsymbol{f}_1 = -\mathrm{i}f_x/2\, \boldsymbol{e}_x$.

Hence energy is fed into the system at $k = \pm 1$ and redistributed to the other modes via the convective term. For small Hg, the fundamental harmonics are dominant with $\boldsymbol{c}_{\pm 1} \propto Hg$. The Fourier modes $\boldsymbol{c}_0$, $\boldsymbol{c}_{-2}$ and $\boldsymbol{c}_2$ are then created from an interaction of the Fourier modes $\boldsymbol{c}_{-1}$ and $\boldsymbol{c}_1$, resulting in $\boldsymbol{c}_0 \propto Hg^2$, $\boldsymbol{c}_{-2} \propto Hg^2$ and $\boldsymbol{c}_2 \propto Hg^2$.

Appendix B. Symmetries of the Fourier coefficients

The Fourier modes are defined as

$$\boldsymbol{c}_k = \frac{1}{T}\int_0^T \boldsymbol{u}(\boldsymbol{x}, t)\exp(\mathrm{i}k\Omega t)\,\mathrm{d}t. \tag{B1}$$

Dividing the period into halves, we can write, with the substitution $\tau = t - T/2$,

$$\boldsymbol{c}_k = \frac{1}{T}\left[\int_0^{T/2} \boldsymbol{u}(\boldsymbol{x}, t)\exp(\mathrm{i}k\Omega t)\,\mathrm{d}t + \exp(\mathrm{i}k\Omega T/2)\int_0^{T/2} \boldsymbol{u}(\boldsymbol{x}, \tau + T/2)\exp(\mathrm{i}k\Omega \tau)\,\mathrm{d}\tau\right], \tag{B2}$$

and using the half-period symmetry (5.6), we obtain

$$\boldsymbol{c}_k = \frac{1}{T}\left[\int_0^{T/2} \boldsymbol{u}(\boldsymbol{x}, t)\exp(\mathrm{i}k\Omega t)\,\mathrm{d}t - \exp(\mathrm{i}k\Omega T/2)\int_0^{T/2} \mathcal{S}\boldsymbol{u}(\boldsymbol{x}, t)\exp(\mathrm{i}k\Omega t)\,\mathrm{d}t\right]. \tag{B3}$$

On the other hand, we can use the substitution $\tau = t + T/2$ instead:

$$\boldsymbol{c}_k = \frac{1}{T}\left[\exp(-\mathrm{i}k\Omega T/2)\int_{T/2}^{T} \boldsymbol{u}(\boldsymbol{x}, \tau - T/2)\exp(\mathrm{i}k\Omega \tau)\,\mathrm{d}\tau + \int_{T/2}^{T} \boldsymbol{u}(\boldsymbol{x}, t)\exp(\mathrm{i}k\Omega t)\,\mathrm{d}t\right]. \tag{B4}$$

Using the periodicity of the flow, $\boldsymbol{u}(\boldsymbol{x}, \tau - T/2) = \boldsymbol{u}(\boldsymbol{x}, \tau + T/2)$, and the symmetry (5.6), we arrive at

$$\boldsymbol{c}_k = \frac{1}{T}\left[-\exp(-\mathrm{i}k\Omega T/2)\int_{T/2}^{T} \mathcal{S}\boldsymbol{u}(\boldsymbol{x}, t)\exp(\mathrm{i}k\Omega t)\,\mathrm{d}t + \int_{T/2}^{T} \boldsymbol{u}(\boldsymbol{x}, t)\exp(\mathrm{i}k\Omega t)\,\mathrm{d}t\right]. \tag{B5}$$

Adding (B3) and (B5) with weights $\frac{1}{2}$, and noting that $\exp(\mathrm{i}k\Omega T/2) = \exp(-\mathrm{i}k\Omega T/2) = (-1)^k$, we obtain

$$\boldsymbol{c}_k = \frac{1}{T}\int_0^T \frac{1}{2}\Big(\boldsymbol{u}(\boldsymbol{x}, t) - (-1)^k \mathcal{S}\boldsymbol{u}(\boldsymbol{x}, t)\Big)\exp(\mathrm{i}k\Omega t)\,\mathrm{d}t. \tag{B6}$$

Comparing this with the decomposition (5.2), we see that for even k, the coefficients $\boldsymbol{c}_k$ depend only on the antisymmetric part of the velocity and are thus antisymmetric, whereas for odd k, the coefficients $\boldsymbol{c}_k$ depend only on the symmetric part of the velocity and are thus symmetric.

References

Awad, M. 2013 Hagen number versus Bejan number. *Therm. Sci.* **17** (4), 1245–1250.

Batchelor, G.K. 2000 *An Introduction to Fluid Dynamics*. Cambridge University Press.

Bensoussan, A., Lions, J.-L. & Papanicolaou, G. 1978 *Asymptotic Analysis for Periodic Structures*. Studies in Mathematics and its Applications, vol. 5. North-Holland Pub. Co.

Biot, M.A. 1956*a* Theory of propagation of elastic waves in a fluid-saturated porous solid. I. Low-frequency range. *J. Acoust. Soc. Am.* **28** (2), 168–178.

Biot, M.A. 1956*b* Theory of propagation of elastic waves in a fluid-saturated porous solid. II. Higher frequency range. *J. Acoust. Soc. Am.* **28** (2), 179–191.

Biot, M.A. 1962 Mechanics of deformation and acoustic propagation in porous media. *J. Appl. Phys.* **33** (4), 1482–1498.

BUCKINGHAM, E. 1914 On physically similar systems; illustrations of the use of dimensional equations. *Phys. Rev.* **4** (4), 345–376.

BURCHARTH, H. & ANDERSEN, O. 1995 On the one-dimensional steady and unsteady porous flow equations. *Coast. Engng* **24** (3–4), 233–257.

BURRIDGE, R. & KELLER, J.B. 1981 Poroelasticity equations derived from microstructure. *J. Acoust. Soc. Am.* **70** (4), 1140–1146.

CABRAL, B. & LEEDOM, L.C. 1993 Imaging vector fields using line integral convolution. In *Proceedings of the 20th Annual Conference on Computer Graphics and Interactive Techniques – SIGGRAPH '93*, pp. 263–270. ACM.

CARSTENSEN, S., SUMER, B.M. & FREDSØE, J. 2010 Coherent structures in wave boundary layers. Part 1. Oscillatory motion. *J. Fluid Mech.* **646**, 169–206.

CELIK, I.B., URMILA, G., ROACHE, P.J., FREITAS, C.J., COLEMAN, H. & RAAD, P.E. 2008 Procedure for estimation and reporting of uncertainty due to discretization in CFD applications. *Trans. ASME J. Fluids Engng* **130** (7), 078001.

CHAMPOUX, Y. & ALLARD, J.-F. 1991 Dynamic tortuosity and bulk modulus in air-saturated porous media. *J. Appl. Phys.* **70** (4), 1975–1979.

CHAPMAN, A.M. & HIGDON, J.J.L. 1992 Oscillatory Stokes flow in periodic porous media. *Phys. Fluids* A*: Fluid Dyn.* **4** (10), 2099–2116.

CHORIN, A.J. 1968 Numerical solution of the Navier–Stokes equations. *Maths Comput.* **22** (104), 745–762.

COX, S.J. & COOKER, M.J. 2000 Potential flow past a sphere touching a tangent plane. *J. Engng Maths* **38** (3), 355–370.

CRITTENDEN, B., LAU, A., BRINKMANN, T. & FIELD, R. 2005 Oscillatory flow and axial dispersion in packed beds of spheres. *Chem. Engng Sci.* **60** (1), 111–122.

ENE, H. & SANCHEZ-PALENCIA, E. 1975 Equations et phénomènes de surface pour l'écoulement dans un milieu poreux. *J. Méc.* **14**, 73–108.

ERGUN, S. 1952 Fluid flow through packed columns. *Chem. Engng Prog.* **48** (2), 89–94.

FERZIGER, J.H. & PERIĆ, M. 2002 *Computational Methods for Fluid Dynamics*, 3rd edn. Springer.

FIRDAOUSS, M., GUERMOND, J.-L. & LE QUÉRÉ, P. 1997 Nonlinear corrections to Darcy's law at low Reynolds numbers. *J. Fluid Mech.* **343**, 331–350.

FORCHHEIMER, P. 1901 Wasserbewegung durch Boden. *Z. Verein. Deutsch. Ing.* **45**, 1782–1788.

FRITSCH, F.N. & CARLSON, R.E. 1980 Monotone piecewise cubic interpolation. *SIAM J. Numer. Anal.* **17** (2), 238–246.

VAN GENT, M.R.A. 1993 Stationary and oscillatory flow through coarse porous media. *Communications on Hydraulic and Geotechnical Engineering* 1993-09.

GRAHAM, D.R. & HIGDON, J.J.L. 2002 Oscillatory forcing of flow through porous media. Part 2. Unsteady flow. *J. Fluid Mech.* **465**, 237–260.

GU, Z. & WANG, H. 1991 Gravity waves over porous bottoms. *Coast. Engng* **15** (5–6), 497–524.

HALL, K.R., SMITH, G.M. & TURCKE, D.J. 1995 Comparison of oscillatory and stationary flow through porous media. *Coast. Engng* **24** (3–4), 217–232.

HARLOW, F.H. & WELSH, J.E. 1965 Numerical calculation of time-dependent viscous incompressible flow with free surface. *Phys. Fluids* **8**, 2182–2189.

HE, X., APTE, S.V., FINN, J.R. & WOOD, B.D. 2019 Characteristics of turbulence in a face-centred cubic porous unit cell. *J. Fluid Mech.* **873**, 608–645.

HORNUNG, U., KADANOFF, L., MARSDEN, J.E., SIROVICH, L., WIGGINS, S., JOHN, F. (Eds) 1997 *Homogenization and Porous Media*. Interdisciplinary Applied Mathematics, vol. 6. Springer.

IERVOLINO, M., MANNA, M. & VACCA, A. 2010 Pulsating flow through porous media. In *Turbulence and Interactions* (ed. E.H. Hirschel, W. Schröder, K. Fujii, W. Haase, B. Leer, M.A. Leschziner, M. Pandolfi, J. Periaux, A. Rizzi, B. Roux, Y.I. Shokin, M. Deville, T.-H. Lê & P. Sagaut), vol. 110, pp. 167–173. Springer.

JIN, L. & LEONG, K.C. 2006 Heat transfer performance of metal foam heat sinks subjected to oscillating flow. *IEEE Trans. Compon. Packag. Technol.* **29** (4), 856–863.

JOHNSON, D.L., KOPLIK, J. & DASHEN, R. 1987 Theory of dynamic permeability and tortuosity in fluid-saturated porous media. *J. Fluid Mech.* **176**, 379–402.

LAFARGE, D. 2009 The equivalent fluid model. In *Materials and Acoustics Handbook* (ed. M. Bruneau & C. Potel), pp. 153–204. ISTE.

LARAMEE, R., JOBARD, B. & HAUSER, H. 2003 Image space based visualization of unsteady flow on surfaces. In *IEEE Transactions on Ultrasonics, Ferroelectrics and Frequency Control*, pp. 131–138. IEEE.

LASSEUX, D., VALDÉS-PARADA, F.J. & BELLET, F. 2019 Macroscopic model for unsteady flow in porous media. *J. Fluid Mech.* **862**, 283–311.

LÉVY, T. 1987 Introduction to homogenization theory. In *Homogenization Techniques for Composite Media* (ed. E. Sanchez-Palencia & A. Zaoui), Lecture Notes in Physics, vol. 272, pp. 63–74. Springer.

LIGHTHILL, S.J. 1978 Acoustic streaming. *J. Sound Vib.* **61** (3), 391–418.

LOWE, R.J., SHAVIT, U., FALTER, J.L., KOSEFF, J.R. & MONISMITH, S.G. 2008 Modeling flow in coral communities with and without waves: a synthesis of porous media and canopy flow approaches. *Limnol. Oceanogr.* **53** (6), 2668–2680.

MACDONALD, I.F., EL-SAYED, M.S., MOW, K. & DULLIEN, F.A.L. 1979 Flow through porous media – the Ergun equation revisited. *Ind. Engng Chem. Fundam.* **18** (3), 199–208.

MAIER, R.S., KROLL, D.M., KUTSOVSKY, Y.E., DAVIS, H.T. & BERNARD, R.S. 1998 Simulation of flow through bead packs using the lattice Boltzmann method. *Phys. Fluids* **10** (1), 60–74.

MANHART, M. 2004 A zonal grid algorithm for DNS of turbulent boundary layers. *Comput. Fluids* **33** (3), 435–461.

MANHART, M., TREMBLAY, F. & FRIEDRICH, R. 2001 MGLET: a parallel code for efficient DNS and LES of complex geometries. In *Parallel Computational Fluid Dynamics 2000* (ed. C.B. Jenssen *et al.*), pp. 449–456. North-Holland.

MANOR, O. 2021 Acoustic flow in porous media. *J. Fluid Mech.* **920**, A11.

MARTIN, H. 2010 Dimensionless numbers. In *VDI Heat Atlas*, 2nd edn. (ed. VDI e. V.), pp. 11–13. Springer.

PATANKAR, S. 1980 *Numerical Heat Transfer and Fluid Flow*. Series in Computational Methods in Mechanics and Thermal Sciences. McGraw–Hill.

PELLER, N. 2010 Numerische simulation turbulenter Strömungen mit immersed boundaries. PhD thesis, Technische Universität München, München.

PELLER, N., DUC, A.L., TREMBLAY, F. & MANHART, M. 2006 High-order stable interpolations for immersed boundary methods. *Intl J. Numer. Meth. Fluids* **52** (11), 1175–1193.

PRIDE, S.R., MORGAN, F.D. & GANGI, A.F. 1993 Drag forces of porous-medium acoustics. *Phys. Rev.* B **47** (9), 4964–4978.

ROACHE, P.J. 1994 Perspective: a method for uniform reporting of grid refinement studies. *Trans. ASME J. Fluids Engng* **116** (3), 405–413.

SAKAI, Y. & MANHART, M. 2020 Consistent flow structure evolution in accelerating flow through hexagonal sphere pack. *Flow Turbul. Combust.* **105** (2), 581–606.

SAKAI, Y., MENDEZ, S., STRANDENES, H., OHLERICH, M., PASICHNYK, I., ALLALEN, M. & MANHART, M. 2019 Performance optimisation of the parallel CFD code MGLET across different HPC platforms. In *Proceedings of the Platform for Advanced Scientific Computing Conference – PASC '19*, pp. 1–13. ACM.

SCHLICHTING, H. & GERSTEN, K. 2006 *Grenzschicht-Theorie*, 10th edn. Springer.

SOLLITT, C.K. & CROSS, R.H. 1972 Wave transmission through permeable breakwaters. *Coastal Engineering 1972*. 1827–1846.

TURO, D. & UMNOVA, O. 2013 Influence of Forchheimer's nonlinearity and transient effects on pulse propagation in air saturated rigid granular materials. *J. Acoust. Soc. Am.* **134** (6), 4763–4774.

WHITAKER, S. 1986 Flow in porous media I: a theoretical derivation of Darcy's law. *Transp. Porous Media* **1** (1), 3–25.

WHITAKER, S. 1996 The Forchheimer equation: a theoretical development. *Transp. Porous Media* **25** (1), 27–61.

WILLIAMSON, J. 1980 Low-storage Runge–Kutta schemes. *J. Comput. Phys.* **35** (1), 48–56.

WOMERSLEY, J.R. 1955 Method for the calculation of velocity, rate of flow and viscous drag in arteries when the pressure gradient is known. *J. Physiol.* **127** (3), 553–563.

WOOD, B.D., HE, X. & APTE, S.V. 2020 Modeling turbulent flows in porous media. *Annu. Rev. Fluid Mech.* **52** (1), 171–203.

ZHU, T. & MANHART, M. 2016 Oscillatory Darcy flow in porous media. *Transp. Porous Media* **111** (2), 521–539.

D.2. Symmetry breaking and turbulence in oscillatory flow through a hexagonal sphere pack

Division of work between the authors

Lukas Unglehrt conducted the simulations and devised the analysis of the data. Both authors contributed to writing the manuscript and reaching conclusions.

Reference

Unglehrt, L. & Manhart, M. 2022 Symmetry Breaking and Turbulence in Oscillatory Flow Through a Hexagonal Sphere Pack. In *Proceedings of TSFP-12 (2022) Osaka*. Osaka, Japan.

Copyright

12th International Symposium on Turbulence and Shear Flow Phenomena (TSFP12)
Osaka, Japan, July 19–22, 2022

SYMMETRY BREAKING AND TURBULENCE IN OSCILLATORY FLOW THROUGH A HEXAGONAL SPHERE PACK

Lukas Unglehrt
Professorship of Hydromechanics
Technical University of Munich
Arcisstr. 21, 80335 Munich, Germany
lukas.unglehrt@tum.de

Michael Manhart
Professorship of Hydromechanics
Technical University of Munich
Arcisstr. 21, 80335 Munich, Germany
michael.manhart@tum.de

ABSTRACT

The appearance of turbulence in oscillatory flow through a hexagonal sphere pack was investigated by means of direct numerical simulation. The Reynolds numbers lie between 26.9 and 297 and the Womersley number is 31.62. We characterised the flow state based on instantaneous velocity fields and the time series of the superficial velocity. The velocity fields were decomposed into symmetric and antisymmetric components with respect to the symmetries of the sphere pack. Based on the temporal evolution of the kinetic energy of the antisymmetric components, it is possible to distinguish between laminar, transitional and turbulent flow. Finally, the velocity fields were decomposed with respect to the average over the realisations that can be obtained by applying the symmetries of the hexagonal sphere pack. For the turbulent flow case, a significant scale separation between the average and fluctuating velocity fields is observed.

INTRODUCTION

Oscillatory porous media flow occurs in wave-induced transport processes in coral reefs (Lowe *et al.*, 2008) or in the sediment bed; moreover, it could be of interest to enhance solute transport in chemical reactors (Crittenden *et al.*, 2005). Other applications include for example wave-induced flow through rubble-mound breakwaters (van Gent, 1993; Hall *et al.*, 1995). In order to describe these transport processes, it is essential to know whether the pore scale flow is turbulent, as turbulence is associated with strong mixing.

Starting with Dybbs & Edwards (1984), the microscale behaviour of stationary turbulent flow through regular and random sphere packs has been studied numerically (e.g. Hill & Koch, 2002; He *et al.*, 2019; Sakai & Manhart, 2020) and experimentally (e.g. Patil & Liburdy, 2012, 2013). Four flow regimes are commonly distinguished (Dybbs & Edwards, 1984) depending on the Reynolds number: i) linear flow, ii) steady nonlinear flow, iii) unsteady nonlinear flow and iv) chaotic / turbulent flow. The transition to turbulent flow generally occurs for Reynolds numbers around 120 (Fand *et al.*, 1987). In regular sphere packs, the emergence of chaotic and turbulent flow can be related to symmetry breaking bifurcations that occur around a Reynolds number of 100 (Hill & Koch, 2002) or for $138 < Re < 209$ (Sakai & Manhart, 2020).

Experimental studies of turbulent oscillatory porous media flow have been performed with a focus on the behaviour of bulk flow quantities (van Gent, 1993; Hall *et al.*, 1995; Losada *et al.*, 1995; Pamuk & Özdemir, 2014; Bağcı *et al.*, 2016) or on the processes at the interface between the porous medium and a free flow (Shigematsu *et al.*, 2018). On the other hand, numerical simulations of oscillatory flow through two-dimensional porous media configurations were performed by Graham & Higdon (2002), Iervolino *et al.* (2010) and Kardgar & Jafarian (2021). In our upcoming work (Unglehrt & Manhart, 2022), the onset of nonlinear effects was investigated in laminar oscillatory flow through a hexagonal sphere pack by numerical simulation.

The flow state in oscillatory flow depends on two dimensionless parameters: the Hagen number Hg representing the amplitude and the Womersley number Wo representing the frequency of the forcing. The Reynolds number Re is a unique function of the Hagen and Womersley number. Therefore, either of Hagen or Reynolds number can be used to characterise the flow state. Based on a model equation, Gu & Wang (1991) estimated which flow regime might be expected for a given combination of Re and Wo.

In the present contribution, we investigate the onset of turbulence in oscillatory flow through an idealised porous medium geometry by means of direct numerical simulation. A visual inspection of the instantaneous velocity fields suggests that the simulation database includes both laminar and turbulent simulations. However, it is unclear how to objectively quantify the flow state. Commonly, turbulence is characterised by temporal and spatial properties of the velocity fluctuations about the mean, e.g. the frequency or wavenumber spectra or the spatial two-point correlations. In the present case, the definition of a fluctuation is not trivial since the flow is unsteady and inhomogeneous in all spatial directions. One could perform a phase-dependent time average, but this comes at a large computational expense since the flow needs to be integrated over many cycles. As our objective is to merely differentiate between laminar and turbulent flow, we consider this cost to be disproportionate. On the other hand, especially at higher Womersley numbers analyses of the full velocity have the problem that the mean flow does not vary slowly compared to the turbulence and that the boundary and shear layers are not large compared to the turbulent scales. Therefore, the objective of the present work is to find quantitative evidence that allows to discern the laminar and the turbulent flow state.

First, we investigate the behaviour of the streamwise and cross-streamwise components of the superficial volume-averaged velocity. Second, we analyse the breaking of the symmetries that are imposed onto the flow by the sphere pack geometry. Third, we propose to average the flow over an ensemble of realisations that is generated using the symmetries

of the sphere pack geometry. This allows us to separate the velocity fields into an average and fluctuating part based on which we can distinguish laminar, transitional and turbulent cases.

METHODOLOGY

Numerical method

We performed direct numerical simulation of the incompressible Navier-Stokes equations with our in-house code MGLET that is based on Cartesian block-structured grids. The spatial discretisation in MGLET uses a second-order central finite volume scheme with a staggered arrangement of variables and the temporal discretisation employs a third-order explicit Runge-Kutta method. The no-slip boundary conditions on the spheres is enforced by a discrete-forcing immersed boundary method that is described in Peller *et al.* (2006); Peller (2010). The momentum fluxes near the immersed boundary are evaluated using a linear least-squares ghost-cell interpolation/extrapolation approach. The conservation of mass is enforced in every substep of the time integration scheme using a flux correction procedure in the interface cells and by solving a Poisson equation for a correction pressure in the field.

Study design

As a porous medium, we choose a hexagonal close-packed arrangement of spheres of diameter d. It has a porosity of 0.259 which is the lower limit for packings of equal spheres. The flow is described by the incompressible Navier-Stokes equations with an an oscillatory volume force $f_x \sin \Omega t$ in the x–direction. Initially, the flow is at rest.

The problem is governed by two independent parameters: the Hagen number $Hg = f_x d^3/(\rho \nu^2)$ represents the ratio of the amplitude of the applied volume force to the viscous forces and the Womersley number $Wo = \sqrt{\Omega d^2/\nu}$ represents the ratio of the sphere diameter to the thickness of the oscillatory Stokes boundary layer. The Reynolds number Re is based on the sphere diameter d and the amplitude of the superficial volume-averaged velocity after the decay of the transient. The superficial velocity is defined as

$$\langle u \rangle_\mathrm{s} := \frac{1}{V} \int_{V_\mathrm{f}} u \, \mathrm{d}V$$

with the fluid volume V_f and the total volume V.

We consider flow at a Womersley number of 31.62 and four values of the Hagen number. In linear flow, the selected value of the Womersley number lies at the transition between the low and the high frequency regime that are governed by Stokes flow and potential flow, respectively. Consequently, our simulations belong to the mid frequency (MF) regime. The simulation parameters are reported in table 1.

Domain size and grid spacing

The simulation domain consists of two unit cells in the x–direction and one unit cell in the y- and z–direction. It thus has an extent $2d \times \sqrt{3}d \times 2\sqrt{6}/3d$. For this size, the domain contains two spheres in every lattice direction. He *et al.* (2019) used a domain of the same volume for their direct numerical simulations of turbulent flow in a face-centred cubic sphere pack. They state that "the unit cell domain showed little variation in statistics compared to a larger domain".

Table 1: Simulation parameters.

case	Hg	Wo	Re	number of cycles
MF3	$10^{5.5}$	31.62	26.9	3[†]
MF4	10^{6}	31.62	74.0	4[†] / 1.32[‡]
MF5	$10^{6.5}$	31.62	157	6.3975
MF6	10^{7}	31.62	297	1.63

[†] These simulations are presented in (Unglehrt & Manhart, 2022).

[‡] This simulation was recomputed with a more finely resolved triangle representation of the sphere pack geometry to match the other simulations.

The flow was computed with grid resolutions of 48, 96, 192 and 384 cells per diameter (cpd), resulting in a total number of 88 million fluid cells at 384 cpd. The error of the numerical solution was estimated based on the space-time L^2-norm of the velocity and on the oscillation amplitude of the superficial velocity $\langle u \rangle_\mathrm{s}$ which is used to form the Reynolds number. For all simulations the relative difference between the finest and the second finest resolution is less than 1.3%.

The resolution requirements come from the wall boundary layers and possibly the turbulence in the bulk. The characteristic thickness of the oscillatory boundary layer can be estimated as $\delta = \sqrt{2\nu/\Omega}$ which we resolve with 17 cells. On the other hand, He *et al.* (2019) employed a grid resolution of 250 (cpd) to simulate stationary turbulent flow up to $Re = 741$.

RESULTS

Instantaneous velocity fields

Figure 1a–d displays a section through the velocity field perpendicular to the main flow direction for our simulations. As the Hagen number is increased by powers of $\sqrt{10}$, the velocity field develops pronounced flow structures in the large pores, resembling those in transient flow described by Sakai & Manhart (2020). Due to the regular layout of the structures, we would consider the cases MF3–MF5 as laminar. At the highest Reynolds number, the velocity field is asymmetrical and irregular vortical structures can be made out. Intuitively, we would consider the case MF6 (figure 1d) as turbulent. In the following, we discuss quantitative evidence that allows us to objectively decide on the flow state.

Superficial velocity

In this section, we discuss the behaviour of the superficial velocity as the flow state changes from laminar to (presumably) turbulent. The time series of the streamwise superficial velocity (figure 1e–h) remains relatively smooth throughout the changes in the velocity field. This is in contrast to the stationary case for which Hill & Koch (2002) and Sakai & Manhart (2020) reported (quasi-) periodic or chaotic oscillations of the streamwise superficial velocity. At the lowest Reynolds number, $\langle u \rangle_\mathrm{s}$ has a time lag with respect to the forcing and the amplitude is 25% below the steady state amplitude. As the Reynolds number is increased, the phase lag reduces and the peak amplitude approaches the steady state value that would be attained for the same Hagen number. At the highest Reynolds number, we observe a plateau rather than a pronounced peak.

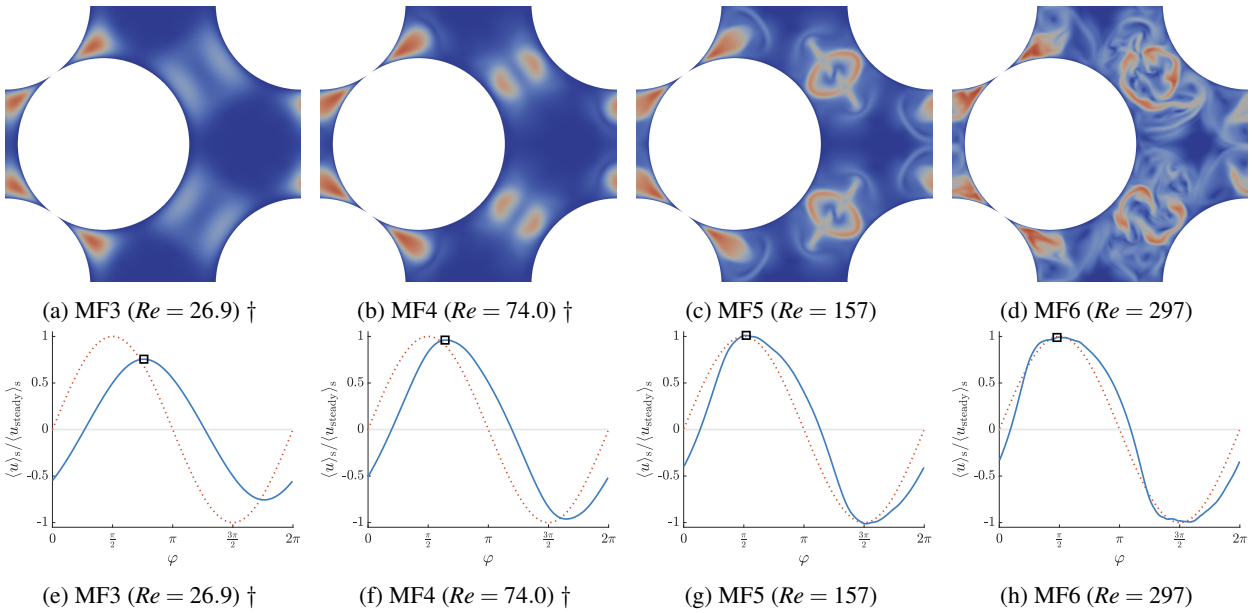

(a) MF3 ($Re = 26.9$) † (b) MF4 ($Re = 74.0$) † (c) MF5 ($Re = 157$) (d) MF6 ($Re = 297$)

(e) MF3 ($Re = 26.9$) † (f) MF4 ($Re = 74.0$) † (g) MF5 ($Re = 157$) (h) MF6 ($Re = 297$)

† simulations from (Unglehrt & Manhart, 2022)

Figure 1: (a)–(d) Velocity magnitude in the y-z-plane perpendicular to the flow direction. The velocity fields correspond to the time of the maximum superficial velocity. (e)–(f) Forcing (dotted red line) and superficial velocity (blue line) over one period. The superficial velocity is normalised with the steady state value (i.e. for a constant pressure gradient) obtained from the amplitude of the forcing via the relations given by Sakai & Manhart (2020). The black symbol marks the time of the snapshot presented in (a)–(d).

The cross-streamwise components of the superficial velocity, $\langle v \rangle_s$ and $\langle w \rangle_s$, are orthogonal to the imposed volume force. For the cases MF3 and MF4, these components are very small as a consequence of the symmetries of the sphere pack imprinted on the flow. On the other hand, for the cases MF5 and MF6 significant nonzero values of the cross-streamwise components can be observed. Figure 2 shows a plot of $\langle v \rangle_s$ and $\langle w \rangle_s$ for the latter simulations. The curves start out at the origin and spread out into the plane. For the case MF5, the amplitude of $\langle v \rangle_s$ is approximately 30 times larger than the amplitude of $\langle w \rangle_s$ and approximately 400 times smaller than the amplitude of $\langle u \rangle_s$. A clustering of points at the origin indicates that the cross-streamwise components grow in time. For the case MF6, the amplitude of $\langle v \rangle_s$ and $\langle w \rangle_s$ is approximately 60 times smaller than the amplitude of $\langle u \rangle_s$. Both cases shown in figure 2 exhibit irregular orbits, indicating chaotic behaviour. Moreover, the cross-streamwise components of the superficial velocity are only weakly correlated with the streamwise superficial velocity (represented by the colour of the curves).

While for MF6 the observed chaotic behaviour of the cross-streamwise components is in line with irregular structure of the velocity field shown in figure 1d, the visual impression of the velocity field of the case MF5 (figure 1c) does not suggest any chaotic behaviour in this case. This could be explained with the relatively low magnitude of the cross-streamwise components.

In conclusion, the streamwise superficial velocity changes gradually with Reynolds number and we could not identify features in the time series that could be used to clearly discern laminar and turbulent flow. Suprisingly, for higher Reynolds numbers the time and value of the maximum $\langle u \rangle_s$ coincide with the results of a quasi-steady approximation. On the other hand, the cross-streamwise components are very small for the cases MF3 and MF4 whereas they are nonzero and exhibit chaotic behaviour for MF5 and MF6.

Quantification of symmetry breaking

In this section, we investigate the symmetry breaking of the flow which was already indicated by the cross-streamwise components of the superficial velocity.[1] Based on the works of Hill & Koch (2002) and Sakai & Manhart (2020), the symmetry breaking can be considered a prerequisite of turbulent flow in the sphere pack.

When a forcing is applied along the x–direction, laminar flow through the hexagonal sphere pack exhibits four symmetries: the flow is invariant with respect to

1. a translation by d in the x–direction ($\mathscr{T}_x$)
2. a translation by d at a 60° angle to the x–direction ($\mathscr{T}_{xy}$)
3. a reflection around $z = \sqrt{6}/3\,d$ ($\mathscr{S}_z$)
4. a rotation by π about the axis $y = \sqrt{3}/3$, $z = \sqrt{6}/6$ ($\mathscr{R}_x$)

Figure 3 displays the result of these transformations applied to the sphere pack inside the simulation domain. Considering the periodic boundary conditions of the domain, the original and the transformed configurations of the spheres are congruent.

In order to investigate the possible breaking of these symmetries, we decompose the instantaneous velocity fields into a component $\mathbf{u}_{\mathrm{sym}}$ that is symmetric with respect to one of the symmetries, and a corresponding antisymmetric component $\mathbf{u}_{\mathrm{anti}}$. The kinetic energy of the antisymmetric component, $\langle k_{\mathrm{anti}} \rangle_s = \left\langle \frac{1}{2} \rho \mathbf{u}_{\mathrm{anti}}^2 \right\rangle_s$, measures the violation of the symmetry under consideration. Figure 4 displays the temporal evolution of $\langle k_{\mathrm{anti}} \rangle_s$ for the various symmetries. For the cases MF3 and MF4 we observe that all symmetries are satisfied to an accuracy of more than 10^{-7}. The amplitude of the antisymmetric components remains stationary. This indicates that the flow

[1] Please note the following connection between the symmetries and the cross-streamwise components of the superficial velocity: If the flow is symmetric under the rotation $\mathscr{R}_x$, then $\langle v \rangle_s = \langle w \rangle_s = 0$ and if the flow is symmetric under the reflection $\mathscr{S}_z$, then $\langle w \rangle_s = 0$.

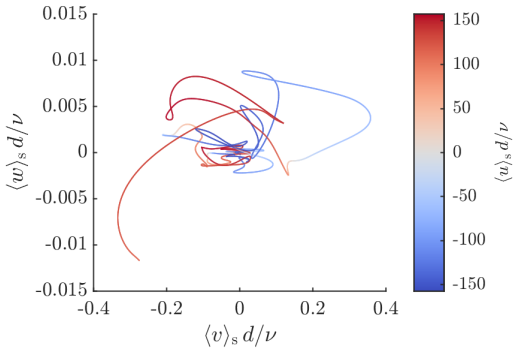

(a) MF5 ($Re = 157$)

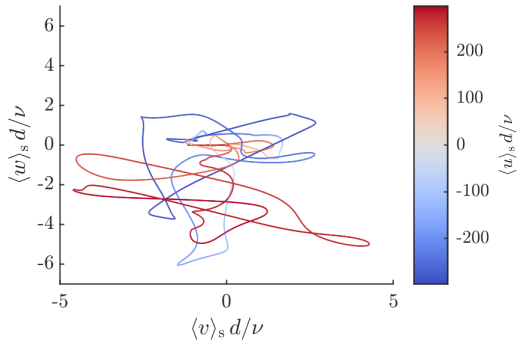

(b) MF6 ($Re = 297$)

Figure 2: Cross-streamwise components of the superficial velocity; the curves are coloured by the streamwise component of the superficial velocity. The irregular orbits indicate chaotic flow.

is stable with respect to the symmetry breaking and supports the hypothesis that the flow is laminar in these cases. For the case MF5 a simultaneous exponential growth of the energy of all antisymmetric components can be observed. After approximately 5 cycles, the kinetic energy of the $\mathscr{R}_x$-antisymmetric part saturates at 0.3% of the maximum total kinetic energy (cf. figure 4d). This suggests that (i) there exists a linear instability mechanism that facilitates the growth of the antisymmetric part and (ii) a nonlinear self-interaction of the instability occurs which limits its growth. However, this does not necessarily imply that the flow becomes turbulent. Finally, for the case MF6 a fast growth of the antisymmetric components can be observed. The kinetic energy of the antisymmetric components with respect to $\mathscr{R}_x$, $\mathscr{S}_z$ and $\mathscr{T}_{xy}$ peaks between 9 and 10% of the cycle maximum of the total kinetic energy.

The initial values of $\langle k_{\text{anti}} \rangle_s$ turned out to depend on the accuracy of the triangle representation of the spheres, from which the interpolation stencils and coefficients in the immersed boundary method are generated. There exist two sources of the initial symmetry breaking perturbations in our code: asymmetric interpolants at the immersed boundary and the residual of the pressure correction. A visual inspection of the antisymmetric parts of the velocity field shows that only the physically meaningful parts of these perturbations are amplified.

Symmetry group averaging

In the preceding sections, it was demonstrated that the antisymmetric components of the velocity field show unsta-

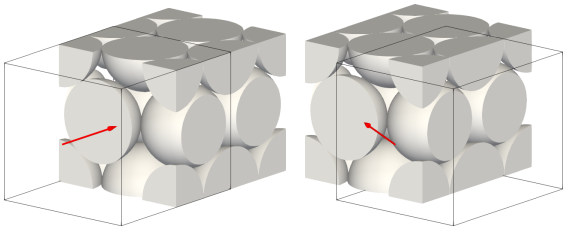

(a) Translation $\mathscr{T}_x$ (b) Translation $\mathscr{T}_{xy}$

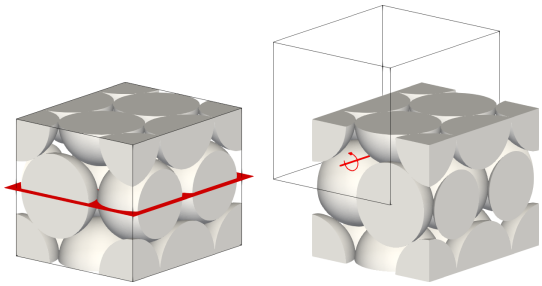

(c) Reflection $\mathscr{S}_z$ (d) Two-fold rotation $\mathscr{R}_x$

Figure 3: Symmetries of laminar flow in a hexagonal sphere pack due to a volume force along the x–direction. The black box represents the position of the sphere pack before the application of the symmetry operation.

ble or chaotic dynamics at $Re = 157$ and $Re = 297$. A direct inspection of the spatial distribution of the antisymmetric components is however not informative as in general, turbulent motion is neither symmetric nor antisymmetric. On the other hand, the mean velocity field of a turbulent flow is usually symmetric. Therefore, we decompose the velocity field into a part that satisfies all of the symmetries

$$\overline{\mathbf{u}} = \frac{1}{16} (\mathscr{I} + \mathscr{R}_x)(\mathscr{I} + \mathscr{T}_x)(\mathscr{I} + \mathscr{T}_{xy})(\mathscr{I} + \mathscr{S}_z)\mathbf{u} \qquad (1)$$

where $\mathscr{I}$ is the identity, and a residual component $\mathbf{u}' = \mathbf{u} - \overline{\mathbf{u}}$ which is in general neither symmetric nor antisymmetric with respect to any symmetry.

Alternatively, this decomposition can be interpreted as an average over the ensemble of 16 velocity fields that is generated by the action of the symmetry group. Such a symmetry average was used by Sirovich (1987); Sirovich & Park (1990) to enlarge the sample size for a proper orthogonal decomposition. Please note that while equation (1) can be understood as an ensemble average, it may not converge to the same result as a time or phase average. For example, Srikanth *et al.* (2021) investigated a persistent symmetry breaking phenomenon in a porous medium for which the time-averaged flow is asymmetrical. As there is an equal probability for the flow to deviate to either side, the ensemble mean flow would be symmetrical.

The symmetry group average (1) underestimates the energy of the turbulent fluctuations compared to the ensemble mean. This can be demonstrated as follows. As the flow problem is symmetric, the ensemble mean $E[\mathbf{u}]$ is symmetric and invariant with respect to $\mathscr{R}_x$, $\mathscr{T}_x$, $\mathscr{T}_{xy}$ and $\mathscr{S}_z$. For example, $\mathscr{R}_x E[\mathbf{u}] = E[\mathbf{u}]$ and $E[\mathscr{R}_x \mathbf{u}] = E[\mathbf{u}]$. Hence, the ensemble mean does not change under the symmetry group average, i.e. $\overline{E[\mathbf{u}]} = E[\mathbf{u}]$ and $E[\overline{\mathbf{u}}] = E[\mathbf{u}]$, and the expectation of the fluctuation about the symmetry group average is zero, i.e. $E[\mathbf{u}'] = E[\mathbf{u} - \overline{\mathbf{u}}] = 0$. Therefore $\mathbf{u}'$ is a part of the fluctuation about the ensemble mean.

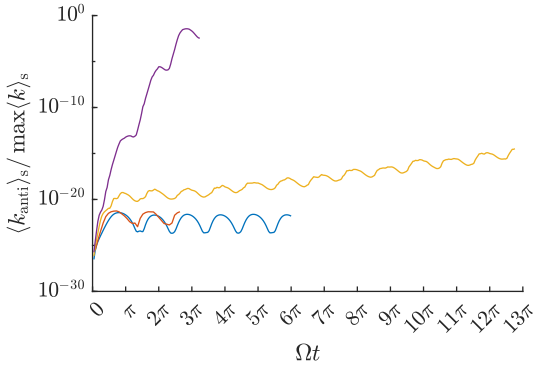

(a) Translation $\mathscr{T}_x$

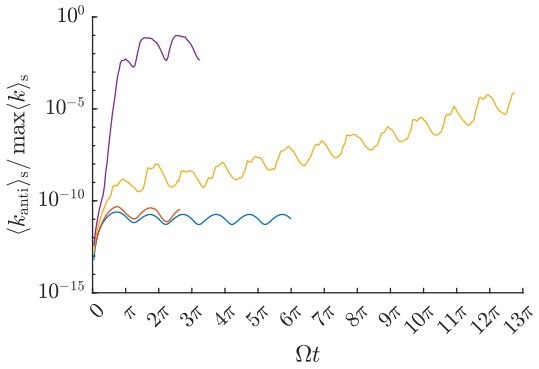

(b) Translation $\mathscr{T}_{xy}$

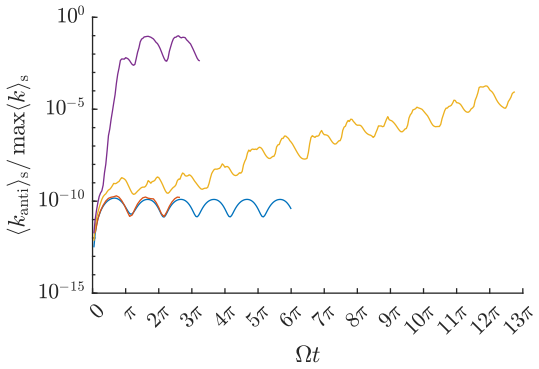

(c) Reflection $\mathscr{S}_z$

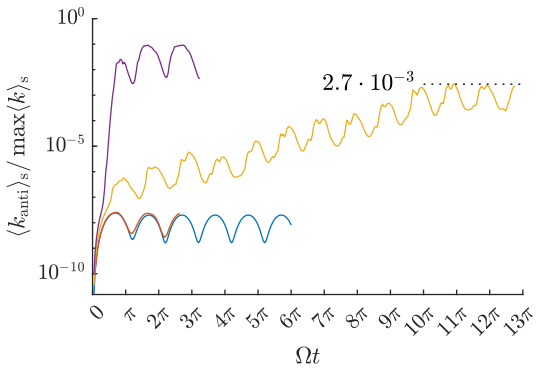

(d) Two-fold rotation $\mathscr{R}_x$

Figure 4: Volume-averaged kinetic energy of the antisymmetric components. — MF3 ($Re = 26.9$), — MF4 ($Re = 74.0$), — MF5 ($Re = 157$), and — MF6 ($Re = 297$). The kinetic energy $\langle k_{\mathrm{anti}}\rangle_{\mathrm{s}}$ is normalised with the maximum total kinetic energy of the last cycle.

Figure 5 displays the spatial distribution of the magnitude of $\overline{\mathbf{u}}$ and $\mathbf{u}'$. For the case MF5 the symmetry group averaged velocity field $\overline{\mathbf{u}}$ looks identical to the instantaneous field in figure 1c. This is due to the low energy of the antisymmetric components (cf. figure 4). The residual component $\mathbf{u}'$ features symmetric patterns that are arranged near the high-velocity features in $\overline{\mathbf{u}}$. For the case MF6, the symmetry group averaged velocity field contains symmetric versions of the high-intensity regions near the contact points and inside the large pores that can be identified in figure 1d. The residual velocity field $\mathbf{u}'$ does not contain these features; instead many irregular and small scale vortices can be identified.

CONCLUSION

We performed direct numerical simulation of oscillatory flow through a hexagonal sphere pack at $Wo = 31.62$ and four Reynolds numbers. We investigated instantaneous velocity fields, the time series of the streamwise and cross-streamwise superficial velocity and the breaking of the symmetries of the flow. Moreover, the velocity field was averaged over the ensemble of realisations generated from the instantaneous velocity fields by applying the symmetries of the sphere pack, and the spatial distributions of the average and fluctuation field were discussed. The resulting average field approximates the ensemble mean of the flow and the resulting fluctuations are a subset of the fluctuations about the ensemble mean.

At $Re = 26.9$ and $Re = 74.0$ the cross-streamwise components of the superficial velocity are nearly zero and the flow shares all symmetries of the sphere pack. Consequently, these cases can be considered as laminar. On the other hand, the symmetries of the flow are broken for $Re = 157$ and $Re = 297$ and the cross-streamwise superficial velocity show nonzero values and chaotic behaviour. At $Re = 157$ the antisymmetric parts of the velocity field with respect to the symmetries of the sphere pack grow exponentially in time, indicating that a linear instability is present in the flow. Eventually, the antisymmetric part with respect to the rotation symmetry (cf. figure 3d) saturates at 0.3% of the total kinetic energy and a similar behaviour could be expected for the other symmetries. The fluctuations with respect to the symmetry group average have an ordered appearance, corroborating that this flow case is not yet turbulent. Consequently, we categorise it as a transitional flow. Finally, at $Re = 297$ the symmetries are broken rapidly and the antisymmetric parts of the velocity field peak at approximately 10% of the total kinetic energy. The fluctuations about the symmetry group average consist of disorderd vortical structures and a scale separation can be observed between the fluctuating and the average field. Together with the chaotic behaviour of the cross-streamwise superficial velocity, this strongly supports the view that this case exhibits turbulent flow.

Further investigations may be necessary to assess the effect of the domain size and the dependency of the results on the Womersley number. Moreover, our findings for the case at $Re = 157$ suggest that a Floquet-type linear instability analysis of the flow could be interesting.

ACKNOWLEDGEMENTS

The authors gratefully acknowledge the financial support of the DFG under grant no. MA2062/13-1. Computing time was granted by the Leibniz Supercomputing Centre on its Linux-Cluster.

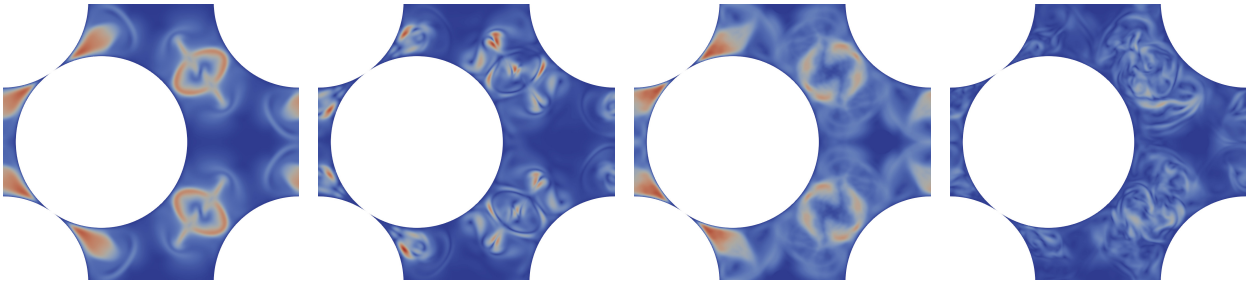

(a) $|\overline{\mathbf{u}}|$ for MF5 ($Re = 157$) (b) $30\,|\mathbf{u}'|$ for MF5 ($Re = 157$) (c) $|\overline{\mathbf{u}}|$ for MF6 ($Re = 297$) (d) $|\mathbf{u}'|$ for MF6 ($Re = 297$)

Figure 5: Magnitude of the symmetry group average velocity $\overline{\mathbf{u}}$ and the corresponding fluctuation $\mathbf{u}'$ in the y-z-plane perpendicular to the flow direction. The velocity fields correspond to figure 1c–d.

REFERENCES

Bağcı, Ö., Arbak, A., De Paepe, M. & Dukhan, N. 2016 Experimental results for oscillatory water flow in 10-ppi metal foam at low-frequencies. *Journal of Physics: Conference Series* **745**, 032040.

Crittenden, B. D., Lau, A., Brinkmann, T. & Field, R. W. 2005 Oscillatory flow and axial dispersion in packed beds of spheres. *Chemical Engineering Science* **60** (1), 111–122.

Dybbs, A. & Edwards, R. V. 1984 A New Look at Porous Media Fluid Mechanics — Darcy to Turbulent. In *Fundamentals of Transport Phenomena in Porous Media* (ed. J. Bear & M. Y. Corapcioglu), *NATO ASI Series*, vol. 82, pp. 199–256. Dordrecht: Springer Netherlands.

Fand, R. M., Kim, B. Y. K., Lam, A. C. C. & Phan, R. T. 1987 Resistance to the Flow of Fluids Through Simple and Complex Porous Media Whose Matrices Are Composed of Randomly Packed Spheres. *Journal of Fluids Engineering* **109** (3), 268–273.

Graham, D. R. & Higdon, J. J. L. 2002 Oscillatory forcing of flow through porous media. Part 2. Unsteady flow. *Journal of Fluid Mechanics* **465**.

Gu, Z. & Wang, H. 1991 Gravity waves over porous bottoms. *Coastal Engineering* **15** (5-6), 497–524.

Hall, K. R., Smith, G. M. & Turcke, D. J. 1995 Comparison of oscillatory and stationary flow through porous media. *Coastal Engineering* **24** (3-4), 217–232.

He, X., Apte, S. V., Finn, J. R. & Wood, B. D. 2019 Characteristics of turbulence in a face-centred cubic porous unit cell. *Journal of Fluid Mechanics* **873**, 608–645.

Hill, R. J. & Koch, D. L. 2002 The transition from steady to weakly turbulent flow in a close-packed ordered array of spheres. *Journal of Fluid Mechanics* **465**, 59–97.

Iervolino, M., Manna, M. & Vacca, A. 2010 Pulsating Flow through Porous Media. In *Turbulence and Interactions* (ed. E. H. Hirschel, W. Schröder, K. Fujii, W. Haase, B. Leer, M. A. Leschziner, M. Pandolfi, J. Periaux, A. Rizzi, B. Roux, Y. I. Shokin, M. Deville, T.-H. Lê & P. Sagaut), , vol. 110, pp. 167–173. Berlin, Heidelberg: Springer Berlin Heidelberg.

Kardgar, A. & Jafarian, A. 2021 Numerical simulation of turbulent oscillating flow in porous media. *Scientia Iranica* **28** (2), 743–756.

Losada, I. J., Losada, M. A. & Martín, F. L. 1995 Experimental study of wave-induced flow in a porous structure. *Coastal Engineering* **26** (1-2), 77–98.

Lowe, R. J., Shavit, U., Falter, James L., Koseff, J. R. & Monismith, S. G. 2008 Modeling flow in coral communities with and without waves: A synthesis of porous media and canopy flow approaches. *Limnology and Oceanography* **53** (6), 2668–2680.

Pamuk, M. T. & Özdemir, M. 2014 Hydrodynamic Aspects of Oscillating Flow Through Porous Media Consisting of Steel Spheres. In *Progress in Exergy, Energy, and the Environment* (ed. I. Dincer, A. Midilli & H. Kucuk), pp. 633–640. Cham: Springer International Publishing.

Patil, V. A. & Liburdy, J. A. 2012 Flow Structure Identification in Unsteady Flow in Porous Media. In *Proceedings of the Asme Fluids Engineering Division Summer Meeting, 2012, Vol 1, Pts a and B, Symposia*, pp. 775–781. New York: Amer Soc Mechanical Engineers.

Patil, V. A. & Liburdy, J. A. 2013 Flow structures and their contribution to turbulent dispersion in a randomly packed porous bed based on particle image velocimetry measurements. *Physics of Fluids* **25** (11), 113303.

Peller, N. 2010 Numerische Simulation turbulenter Strömungen mit Immersed Boundaries. PhD thesis, Technische Universität München, München.

Peller, N., Le Duc, A., Tremblay, F. & Manhart, M. 2006 High-order stable interpolations for immersed boundary methods. *International Journal for Numerical Methods in Fluids* **52** (11), 1175–1193.

Sakai, Y. & Manhart, M. 2020 Consistent Flow Structure Evolution in Accelerating Flow Through Hexagonal Sphere Pack. *Flow, Turbulence and Combustion* **105** (2), 581–606.

Shigematsu, T., Nakajo, S. & Okada, Y. 2018 An experimental study on the interaction between oscillatory flow and idealized porous bed. *Journal of Coastal Research* pp. 981–985.

Sirovich, L. 1987 Turbulence and the Dynamics of Coherent Structures Part II: Symmetries and Transformations. *Quarterly of Applied Mathematics* **XLV**, 573–82.

Sirovich, L. & Park, H. 1990 Turbulent thermal convection in a finite domain: Part I. Theory. *Physics of Fluids A: Fluid Dynamics* **2** (9), 1649–1658.

Srikanth, V., Huang, C.-W., Su, Timothy S. & Kuznetsov, A. V. 2021 Symmetry breaking of turbulent flow in porous media composed of periodically arranged solid obstacles. *Journal of Fluid Mechanics* **929**.

Unglehrt, L. & Manhart, M. 2022 Onset of nonlinearity in oscillatory flow through a hexagonal sphere pack. *Submitted to Journal of Fluid Mechanics*.

van Gent, M. R. A. 1993 Stationary and oscillatory flow through coarse porous media. *Communications on hydraulic and geotechnical engineering, No. 1993-09* .

D.3. Direct and Large–Eddy simulation of turbulent oscillatory flow through a hexagonal sphere pack

Division of work between the authors

Lukas Unglehrt performed the simulations and the analysis of the data. Both authors contributed to writing the manuscript and to reaching conclusions.

Reference

Unglehrt, L. & Manhart, M. 2023 Direct and Large-Eddy simulation of turbulent oscillatory flow through a hexagonal sphere pack. In Direct and Large Eddy Simulation XIII, 1st edn. (ed. C. Marchioli, M. V. Salvetti, M. Garcia-Villalba & P. Schlatter), ERCOFTAC Series 31, pp. 118–123. Springer Cham.

Copyright

Direct and Large–Eddy Simulation of Turbulent Oscillatory Flow Through a Hexagonal Sphere Pack

L. Unglehrt and M. Manhart(✉)

Professorship of Hydromechanics, Technical University of Munich, Munich, Germany
michael.manhart@tum.de

1 Introduction

In coastal engineering, the description of wave transmission and attenuation through rubble-mound breakwaters requires a model for the wave-induced flow inside the pore space of the breakwater [10,16]. Extensive experimental investigations of oscillatory porous media flow were performed [3,7,15] in order to determine the coefficients of the unsteady Forchheimer equation [5] which relates the superficial velocity and the pressure gradient. These coefficients do not solely depend on the geometry, but they vary with time or frequency [2,3,15], raising doubts about the validity of this equation.

In order to gain insight into the flow physics and to obtain a high-fidelity data base for modelling, we simulated the flow through a hexagonal close-packed arrangement of spheres with uniform diameter d driven by a sinusoidal pressure gradient $f_x \sin(\Omega t)\,\mathbf{e}_x$. The flow problem is governed by two independent parameters: the Hagen number $Hg = f_x d^3/(\rho\nu^2)$ and the Womersley number $Wo = \sqrt{\Omega d^2/\nu}$. We define the Reynolds number as $Re = \max\langle u\rangle_\mathrm{s}\, d/\nu$ with the superficial velocity

$$\langle u\rangle_\mathrm{s} = \frac{1}{L_x L_y L_z}\int_{V_\mathrm{f}} u\,\mathrm{d}V \tag{1}$$

where L_x, L_y, L_z are the domain sizes, $V_\mathrm{f} = \varepsilon L_x L_y L_z$ is the fluid volume and $\varepsilon = 0.259$ is the porosity. We performed a direct numerical simulation (DNS) at $Hg = 10^8$ and $Wo = 100$ resulting in $Re = 1086$ and a large–eddy simulation (LES) at $Hg = 10^9$ and $Wo = 100$ resulting in $Re = 3580$. Both simulations lie within the range of the experiments of [3].

In this contribution, we investigate the temporal behaviour of the superficial velocity and relate it to characteristic events in the instantaneous flow fields. We present instantaneous velocity fields which, despite the strong confinement of the flow, exhibit features that are predominantly found in external bluff body flow. For instance, the flow has a boundary layer structure and shows massive flow separations. The high frequency of the forcing leads to a strongly varying turbulence intensity over the course of the cycle. Based on symmetry- and phase-averaged statistics, we decompose the volume-averaged kinetic energy as well as the volume-averaged dissipation rate into their respective mean flow and turbulence contributions.

C. Marchioli et al. (Eds.): DLES 2023, ERCO 31, pp. 118–123, 2024.
https://doi.org/10.1007/978-3-031-47028-8_18

2 Methodology

2.1 Numerical Method

Our in-house code MGLET [9] solves the incompressible Navier-Stokes equations on a staggered Cartesian grid using a finite volume discretisation with second-order central differencing. A third-order explicit Runge-Kutta scheme is employed for the time integration. The no-slip boundary condition on the spheres is enforced using an immersed boundary method [12]. For the LES the sub-grid stresses are formulated with the WALE viscosity model [11] with a coefficient $C_w^2 = 0.1$.

2.2 Domain and Grid

The domain size was chosen as $L_x = 2\,d$, $L_y = \sqrt{3}\,d$ and $L_z = 2\sqrt{6}/3\,d$ with triple periodic boundary conditions. The domain contains two spheres in every lattice direction and every pore is repeated eight times. For their DNS of stationary turbulent flow, He et al. [4] found that a domain of equal volume "showed little variation in statistics compared to a larger domain". At $Wo = 100$, the flow belongs to the high frequency regime and features very thin boundary layers and high velocities near the contact points of the spheres. Thus, a higher resolution than in stationary flow is required. In order to assess the effect of the grid resolution, the DNS at $Re = 1086$ was simulated at resolutions of 192, 384 and 768 cells per diameter (cpd). We observed good agreement between the simulations at 384 and 768 cpd. The LES at $Re = 3580$ was performed using a resolution of 384 cpd. Table 1 summarises the simulation parameters. In the following, the results at 384 cpd will be analysed.

2.3 Turbulence Statistics

The turbulence statistics are estimated by a phase average of instantaneous velocity fields. As we are only concerned with single-point statistics, the symmetries of the sphere pack are used to generate additional realisations. When the flow is driven by a body force along the x-direction, the velocity field has four spatial symmetries; this leads to an increase of the sample size by a factor of 16. The sampling is started after one cycle, when the transient of the superficial velocity has sufficiently decayed.

Table 1. Summary of computational cases

Re	Hg	Wo	Cells per diameter	Number of cells	Simulated cycles	CPU-h
1073[a]	10^8	100	192	$42 \cdot 10^6$	10	20000
1088[a]	10^8	100	384	$199 \cdot 10^6$	10	138000
1086[a]	10^8	100	768	$1.07 \cdot 10^9$	3.9	661000
3580[b]	10^9	100	384	$199 \cdot 10^6$	10	669000

[a] DNS, [b] LES

3 Results

3.1 Superficial Velocity

The time series of the superficial velocity is plotted in Fig. 1. For both Reynolds numbers, the amplitude of $\langle u \rangle_s$ lies within 2% of the steady state value obtained from the correlations of [8]. This is in line with the observation of [3] that "the Forchheimer unsteady-stationary flow law described the oscillatory measurements well when velocities and energy losses were maximum". Based on the time of the zero crossings, the superficial velocity lags behind the sinusoidal forcing by a phase angle of 0.2π at $Re = 1086$ and of 0.1π at $Re = 3580$. At $Re = 3580$ the superficial velocity shows a strong acceleration followed by a low acceleration plateau. The instantaneous velocity fields indicate that this change is caused by flow separations at the contact points and an increase in turbulence intensity.

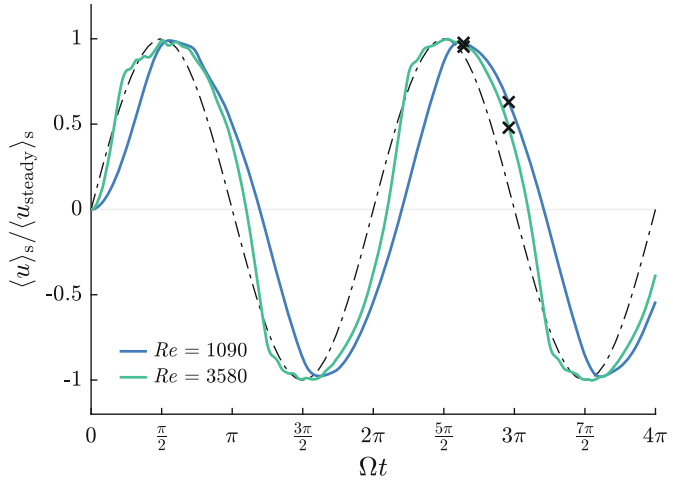

Fig. 1. Time series of the superficial velocity at $Re = 1086$ (blue) and $Re = 3580$ (green). The crosses mark the time of the instantaneous fields presented in Figs. 2 and 3. The reference velocity was obtained from the steady state correlations of [8]. The black dash-dotted curve denotes the sinusoidal body force.

3.2 Instantaneous Velocity Fields

The spatial distribution of the velocity magnitude at the maximum superficial velocity ($\Omega t = 8.3$) and during the deceleration phase ($\Omega t = 9.3$) is displayed in Figs. 2 and 3 for $Re = 1086$ and $Re = 3580$, respectively. At $Re = 1086$, the most prominent feature of the flow is the separation at the contact points between the large pores. Due to the confined pore space, the flow around the separation bubble is concentrated into two jets that are

diverted towards the wake by the spheres bounding the pore. The flow topology appears similar to the results of [14] for stationary turbulent flow. Inside the separation bubble we can observe some complicated vortex structures which disintegrate into turbulence in the course of the cycle. Whereas the velocity field is quite smooth at the end of the acceleration phase, a lot of small vortical structures appear during the deceleration. This behaviour is common in oscillatory flow [1]. At $Re = 3580$, the flow topology is similar to the lower Reynolds number, but the flow at the maximum superficial velocity is already turbulent; this is consistent with the formation of the plateau in the superficial velocity.

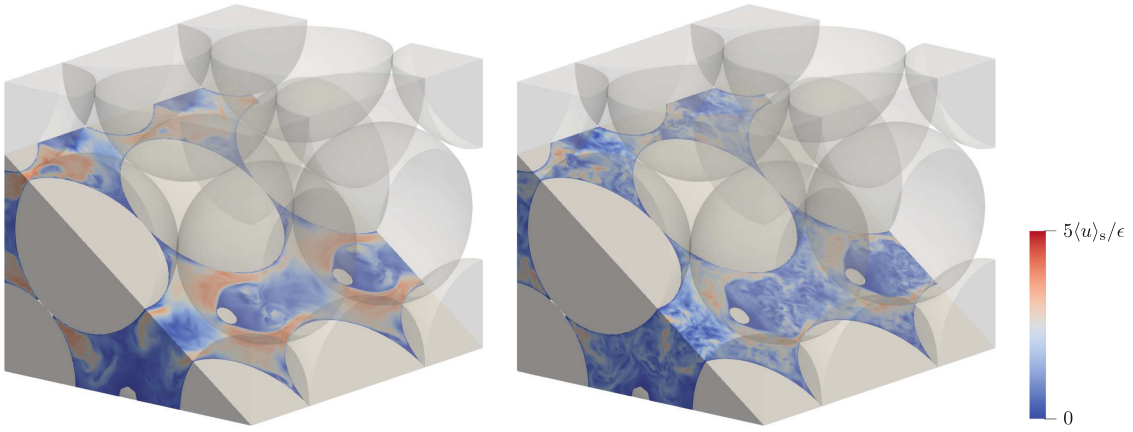

Fig. 2. Velocity magnitude for $Re = 1086$ at the maximum superficial velocity (left) and during deceleration (right). The colourmap is based on the maximum superficial velocity $\langle u\rangle_s$.

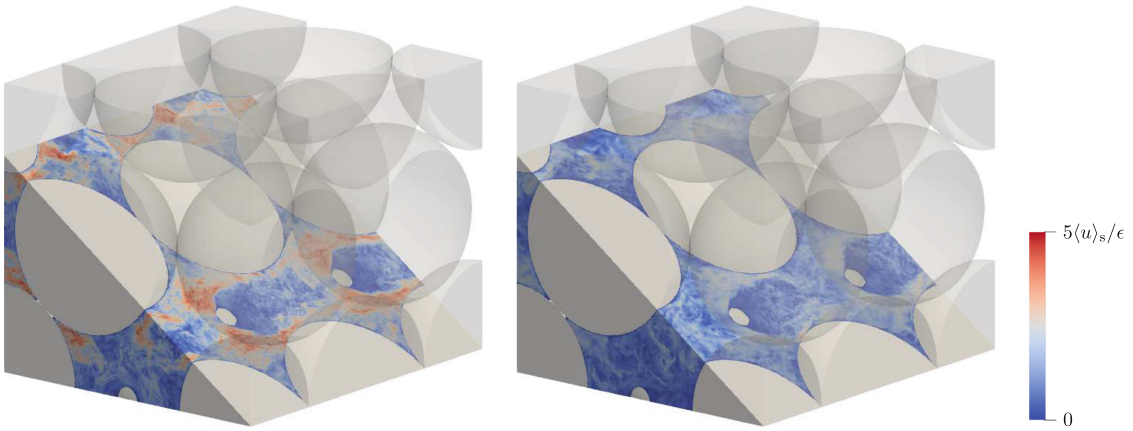

Fig. 3. Velocity magnitude for $Re = 3580$ at the maximum superficial velocity (left) and during deceleration (right). The colourmap is based on the maximum superficial velocity $\langle u\rangle_s$.

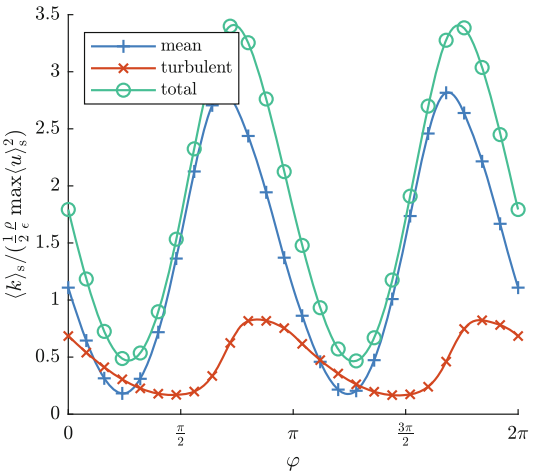

Fig. 4. Volume-averaged MKE, TKE, and sum of MKE and TKE over the cycle for $Re = 1086$.

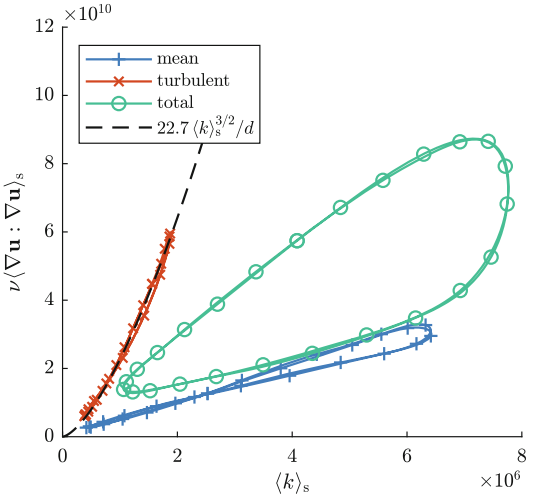

Fig. 5. Volume-averaged dissipation over kinetic energy for $Re = 1086$. The dashed line indicates a fit to the $\mathrm{TKE}^{3/2}$ power law.

3.3 Mean and Turbulent Kinetic Energy

In order to investigate the evolution of the turbulence over the course of a cycle, we analyse the volume-averaged mean and turbulent kinetic energy (MKE and TKE) for $Re = 1086$. It can be seen in Fig. 4 that TKE is present throughout the entire cycle, indicating that no complete relaminarisation occurs. Moreover, a phase shift can be observed between the MKE and the TKE: During the acceleration phase (indicated by rising MKE) the TKE has only a small contribution, whereas during the deceleration phase the TKE attains its maximum of approximately 25% of the total kinetic energy amplitude.

3.4 Relation Between Kinetic Energy and Dissipation Rate

A phase lag between the volume-averaged kinetic energy and the dissipation rate can be observed at $Re = 1086$ which results in the green hysteresis loop in plotted in Fig. 5. When the Reynolds decomposition is introduced, the hysteresis disappears and a nearly one-to-one relation between the TKE and the turbulent dissipation rate emerges (red curve). This matches well to a $\mathrm{TKE}^{3/2}$ power law similar to the ones used by Prandtl [13] and Lilly [6] to model the dissipation rate. This suggests that the length scale of the turbulence production remains relatively constant which could be explained by the dominant flow separation pattern.

The LES at $Re = 3580$ follows approximately the same curve in the acceleration phase, whereas it follows another $\mathrm{TKE}^{3/2}$ power law with a smaller prefactor in the deceleration phase. It will be further investigated whether this discrepancy between DNS and LES is influenced by the WALE model coefficient C_w.

4 Conclusion

We performed DNS and LES of a turbulent oscillatory flow through a hexagonal sphere pack at $Re = 1086$ and 3580 and $Wo = 100$. A separation occurs at the contact points of the spheres that leads to a significant increase in the drag. At $Re = 1086$ turbulence can be observed mainly during the deceleration phase whereas at $Re = 3580$ turbulence can be observed over a longer part of the cycle. The turbulent dissipation rate was shown to depend on the TKE with the well known $\mathrm{TKE}^{3/2}$ relation.

Acknowledgements. We gratefully acknowledge the financial support of the Deutsche Forschungsgemeinschaft (DFG, German Research Foundation) under grant no. MA2062/13-1. Computing time was granted by the Leibniz Supercomputing Centre on its Linux-Cluster.

References

1. Akhavan, R., Kamm, R., Shapiro, A.: An investigation of transition to turbulence in bounded oscillatory stokes flows part 1. Experiments. J. Fluid Mech. **225**, 395–422 (1991)
2. Burcharth, H., Andersen, O.: On the one-dimensional steady and unsteady porous flow equations. Coast. Eng. **24**, 233–257 (1995)
3. Hall, K., Smith, G., Turcke, D.: Comparison of oscillatory and stationary flow through porous media. Coast. Eng. **24**, 217–232 (1995)
4. He, X., Apte, S., Finn, J., Wood, B.: Characteristics of turbulence in a face-centred cubic porous unit cell. J. Fluid Mech. **873**, 608–645 (2019)
5. Polubarinova-Kochina, P., De Wiest, R.: Theory of Ground Water Movement (1962)
6. Lilly, D.: The representation of small-scale turbulence in numerical simulation experiments. In: Proceedings Of IBM Scientific Computing Symposium On Environmental Sciences, Yorktown Heights, New York, pp. 195–210 (1967)
7. Losada, I., Losada, M., Martín, F.: Experimental study of wave-induced flow in a porous structure. Coast. Eng. **26**, 77–98 (1995)
8. Macdonald, I., El-Sayed, M., Mow, K., Dullien, F.: Flow through porous media - the Ergun equation revisited. Ind. Eng. Chem. Fundam. **18**, 199–208 (1979)
9. Manhart, M., Tremblay, F., Friedrich, R.: MGLET: a parallel code for efficient DNS and LES of complex geometries. Parallel Comput. Fluid Dyn. **2000**, 449–456 (2001)
10. Muttray, M.: Wellenbewegung an und in einem geschütteten Wellenbrecher - Laborexperimente im Großmaßstab und theoretische Untersuchungen. Technische Universität Braunschweig (2000)
11. Nicoud, F., Ducros, F.: Subgrid-scale stress modelling based on the square of the velocity gradient tensor. Flow Turbul. Combust. **62**, 183–200 (1999)
12. Peller, N.: Numerische simulation turbulenter Strömungen mit immersed boundaries. Technische Universität München (2010)
13. Prandtl, L.: Über ein neues Formelsystem für die ausgebildete Turbulenz. Nachrichten Akademie Wissenschaften zu Göttingen Mathematisch-Physikalische Klasse **2**, 6–19 (1945)
14. Sakai, Y., Manhart, M.: Consistent flow structure evolution in accelerating flow through hexagonal sphere pack. Flow Turbul. Combust. **105**(2), 581–606 (2020). https://doi.org/10.1007/s10494-020-00168-4
15. van Gent, M.: Stationary and oscillatory flow through coarse porous media. Commun. Hydraul. Geotech. Eng. **9** (1993)
16. van Gent, M.: The modelling of wave action on and in coastal structures. Coast. Eng. **22**, 311–339 (1994)

D.4. Assessment of models in nonlinear oscillatory flow through a hexagonal sphere pack

Division of work between the authors

Lukas Unglehrt performed the review of the models from the literature, implemented the models and analysed the simulation data. Lukas Unglehrt and Michael Manhart both contributed to writing the manuscript.

Reference

Unglehrt, L. & Manhart, M. Assessment of models for nonlinear oscillatory flow through a hexagonal sphere pack. *Manuscript submitted for publication.*

Copyright

Assessment of models for nonlinear oscillatory flow through a hexagonal sphere pack

Lukas Unglehrt[1*] and Michael Manhart[1]

[1*]Professorship for Hydromechanics, Technical University of Munich, Arcisstr. 21, 80333 Munich, Germany.

*Corresponding author(s). E-mail(s): lukas.unglehrt@tum.de;
Contributing authors: michael.manhart@tum.de;

Abstract

We review models for unsteady porous media flow in the volume-averaging framework and we discuss the theoretical relations between the models and the definition of the model coefficients (and the uncertainty therein). The different models are compared against direct numerical simulations of oscillatory flow through a hexagonal sphere pack. The model constants are determined based on their definition in terms of the Stokes flow, the potential flow and steady nonlinear flow. Thus, the discrepancies between the model predictions and the simulation data can be attributed to shortcomings of the models' parametrisation.

We found that an extension of the dynamic permeability model of Pride et al. [Physical Review B 47(9), 1993] with a Forchheimer-type nonlinearity performs very well for linear flow and for nonlinear flow at low and medium frequencies, but the Forchheimer term with a coefficient obtained from the steady-state overpredicts the nonlinear drag at high frequencies. The model reduces to the unsteady Forchheimer equation with an acceleration coefficient based on the static viscous tortuosity for low frequencies.

The unsteady Forchheimer equation with an acceleration coefficient based on the high frequency limit of the dynamic tortuosity has large errors for linear flow at medium and high frequencies, but low errors for nonlinear flow at all frequencies. This is explained by an error cancellation between the inertial and the nonlinear drag.

Keywords: oscillatory porous media flow, unsteady Forchheimer equation, dynamic permeability model, model comparison, direct numerical simulation

Article highlights

- We review models for unsteady porous media flow in the volume-averaging framework and discuss their relationships.
- The model predictions are compared to direct numerical simulations of oscillatory flow through a hexagonal sphere pack.
- Accurate models exist for the linear drag, but the Forchheimer term overpredicts the nonlinear drag at high frequencies.

1 Introduction

Unsteady flow through porous media occurs in a variety of environmental, engineering and industrial applications. For instance, wave-induced flow through coral reefs (Lowe et al, 2008), breakwaters (van Gent, 1994; Losada et al, 1995; Hall et al, 1995; Muttray, 2000) and marine sediment (Gu and Wang, 1991) has been described using the theory of porous media. Oscillatory flow is also present in combustion engines where porous media burners could lead to emission reductions (Aboujafari et al, 2022). Moreover, porous media have been used as regenerator-type heat exchangers in Stirling engines (Simon and Seume, 1988; Trevizoli et al, 2016). In chemical reactors, pulsating flow could be used to enhance mixing and mass transfer (Ni et al, 2003) or to separate substances (Graham and Higdon, 2002). The increasing use of wind energy may also lead to an interest in processes with an intermittent energy supply. Furthermore, the understanding of transient flow behaviour is important for the safety design of nuclear pebble bed reactors (Andreades et al, 2014). Finally, Kahler and Kabala (2019) suggested to use pulsating flow to accelerate groundwater remediation.

The pore scale flow through a porous medium is governed by the laws of continuum mechanics, i.e. the Navier-Stokes equations, or statistical mechanics, i.e. the Boltzmann equation. However, a direct solution of the pore scale flow is often computationally demanding and knowledge of the pore geometry is often not available. Therefore, coarse-grained descriptions have been developed, made possible by the scale separation between the pore size and the extent of the porous medium. These coarse-grained descriptions are based, for example, on the volume-averaging framework (Whitaker, 1967) or homogenisation theory (Ene and Sanchez-Palencia, 1975). A comparison between these approaches can be found in (Davit et al, 2013). Descriptions based on the volume-averaging approach have been used for example by Gu and Wang (1991), who studied gravity waves over a porous seabed, by van Gent (1994), who investigated wave transmission through dikes and breakwaters, by Breugem et al (2006), who studied turbulent channel flow over porous media, and by Iliuta and Larachi (2016, 2017), who simulated oscillating packed-bed reactors for offshore applications. We now give a brief outline of the volume-averaging method. The macroscopic quantities are obtained by performing a (weighted) local average of the quantities defined at the pore scale over a representative volume element. For example, the superficial velocity and the

macroscopic pressure are defined as

$$\langle \boldsymbol{u} \rangle_{\mathrm{s}} = \frac{1}{V} \int_{V_{\mathrm{f}}} \boldsymbol{u} \, \mathrm{d}V \tag{1a}$$

$$\langle p \rangle_{\mathrm{i}} = \frac{1}{V_{\mathrm{f}}} \int_{V_{\mathrm{f}}} p \, \mathrm{d}V \,, \tag{1b}$$

where $\langle . \rangle_{\mathrm{s}}$ and $\langle . \rangle_{\mathrm{i}}$ denote the superficial and intrinsic volume average, respectively, and V and V_{f} are the volumes of the representative volume element and of the fluid contained therein. These quantities are governed by the volume-averaged Navier-Stokes (VANS) equations (Whitaker, 1996)

$$\boldsymbol{\nabla} \cdot \langle \boldsymbol{u} \rangle_{\mathrm{s}} = 0 \tag{2a}$$

$$\rho \frac{\partial \langle \boldsymbol{u} \rangle_{\mathrm{s}}}{\partial t} = \underbrace{-\frac{1}{V} \int_{A_{\mathrm{fs}}} \tilde{p} \, \boldsymbol{n} \, \mathrm{d}A}_{\text{pressure drag}} \underbrace{-\frac{1}{V} \int_{A_{\mathrm{fs}}} \boldsymbol{\tau}_{\mathrm{w}} \, \mathrm{d}A}_{\text{friction drag}} - \epsilon \, \boldsymbol{\nabla} \langle p \rangle_{\mathrm{i}} \tag{2b}$$

where $\tilde{p} = p - \langle p \rangle_{\mathrm{i}}$, $\epsilon = V_{\mathrm{f}}/V$ is the porosity and A_{fs} is the fluid-solid interface. Other works, e.g. (Hsu and Cheng, 1990), have also included convective and diffusive terms in the superficial velocity, but these can be generally neglected if the scale separation between the pore scale and the averaging scale is large enough (Whitaker, 1986, 1996). In the VANS equations the pressure drag and the friction drag are unclosed with respect to the superficial velocity and the macroscopic pressure gradient. In the approach of Whitaker (1986, 1996), the pore scale velocity and pressure are expressed in terms of the superficial velocity by linear mappings. These mappings take the form of tensor and vector fields that satisfy a boundary value problem in the pore space of a representative volume element ("closure problem"). When the mappings are substituted into the pressure drag and friction drag terms, the drag terms take the form of a product of the inverse of a permeability-like tensor with the superficial velocity. In steady linear flow, the closure problem depends only on the geometry of the pore space (Whitaker, 1986), and consequently the permeability tensor of the porous medium is independent of the flow history and the fluid properties. In nonlinear flow, however, the closure problem depends on the velocity field on the pore scale (Whitaker, 1996) and the permeability-like tensor depends on the flow history and the fluid properties. Thus, a direct numerical simulation of the pore scale flow in a representative volume element is required to solve the closure problem. For three-dimensional porous media, these simulations require a large computational effort. Solving the pore scale problem can be avoided by parametrising the nonlinear drag directly in terms of the superficial velocity and the macroscopic pressure gradient. This is based on experiments or numerical simulations of representative volume elements that are performed before solving the macroscale problem. In the following, we refer to these parametrisations as *models*.

The aim of the present work is to compare different models for unsteady porous media flow for the special case of oscillatory flow. We address the following research questions: What is the domain of validity for the different models? How should the model coefficients be chosen? How can the models be improved?

In this contribution, we first describe some of the prominent models that are available in the literature and discuss their interrelations. We then compare the predictions of the different models with a high fidelity direct numerical simulation dataset of oscillatory flow through a hexagonal sphere pack. We make the assumption of constant model coefficients that are defined in terms of the linear and the steady state behaviour and represent properties of the porous medium geometry. For the present flow configuration this information is available with a high fidelity based on the works of Zhu and Manhart (2016); Sakai and Manhart (2020); Unglehrt and Manhart (2022a). This allows us to test the actual predictive capabilities of the models with a negligible ambiguity in the values of the model coefficients. The errors of the predictions therefore represent a shortcoming of the model and suggest the need for a different parametrisation.

2 Review of models for porous media flow

In this section, we give an overview of some of the common models for porous media flow. As discussed in the introduction, we use the term *model* to refer to a parametrisation of the drag in the volume-averaged momentum equation.

2.1 Models for linear flow

2.1.1 Darcy equation

In steady conditions, linear flow can be described using the Darcy equation (Darcy, 1856)

$$-\boldsymbol{\nabla}\langle p\rangle_{\mathrm{i}} = \frac{\mu}{K}\,\langle \boldsymbol{u}\rangle_{\mathrm{s}} \tag{3}$$

The Darcy equation relates the pressure gradient and the superficial velocity linearly using the dynamic viscosity μ and the permeability K. The permeability has units of length squared and is a pure function of the pore geometry. For a given pore geometry, it can be computed directly from the solution to the Stokes equations for a given pore geometry or from empirical correlations, e.g. the Kozeny-Carman equation.

2.1.2 Unsteady Darcy equation

The unsteady Darcy equation arises from the volume-averaged Navier-Stokes equations (2b) if the quasi-steady closure with Darcy's law is employed for the drag forces

$$\rho\,\frac{\mathrm{d}\langle \boldsymbol{u}\rangle_{\mathrm{s}}}{\mathrm{d}t} = -\epsilon\,\boldsymbol{\nabla}\langle p\rangle_{\mathrm{i}} - \frac{\epsilon\,\mu}{K}\,\langle \boldsymbol{u}\rangle_{\mathrm{s}}\ . \tag{4}$$

The solutions to this equation relax to Darcy's law (3) with a time constant $\tau_{\text{vans}} = K/(\epsilon\,\nu)$. This model was applied by Kuznetsov and Nield (2006) to pulsating and by Wang (2008) to transient porous media flow, respectively; in these works the unsteady Darcy equation was extended by the Brinkman term in order to account for wall boundary conditions.

As discussed for example by Nield (1991), an a priori unknown acceleration coefficient needs to be introduced in front of the time derivative. Based on a virtual mass analogy, Sollitt and Cross (1972) and Gu and Wang (1991) used a factor $1 + C_{\text{M}}\frac{1-\epsilon}{\epsilon}$ in front of the acceleration term which results in a time constant $\tau_{\text{vm}} = \left[1 + C_{\text{M}}\frac{1-\epsilon}{\epsilon}\right] K/(\epsilon\,\nu)$. Finally, Hill et al (2001, eq. (20) and (21)) and Zhu et al (2014) derived another time constant $\tau_{\text{en}} = \alpha_0\,\tau_{\text{vans}}$ from the volume-averaged kinetic energy equation assuming self-similar velocity profiles and a quasi-steady dissipation rate where $\alpha_0 = \left\langle \boldsymbol{u}^2_{\text{Stokes}} \right\rangle_{\text{i}} / \left\langle \boldsymbol{u}_{\text{Stokes}} \right\rangle^2_{\text{i}}$ is the static viscous tortuosity that is defined in terms of the velocity field of the Stokes flow (Lafarge, 1993, p.156f). In the literature, the static viscous tortuosity α_0 has been referred to as "inertial factor" (Norris, 1986), "acceleration coefficient" (Nield, 1991), "low-frequency limit of the dynamic tortuosity" (Champoux and Allard, 1991), "low frequency viscous [...] [equivalent] of the tortuosity $[\alpha_\infty]$" (Cortis et al, 2002), "viscous tortuosity" (Kergomard et al, 2013), "time scale ratio" (Zhu and Manhart, 2016), "static viscous tortuosity" (Roncen et al, 2018).

It was shown by Zhu et al (2014); Zhu and Manhart (2016) that the unsteady Darcy equation with the time constant τ_{en}, i.e.

$$\rho\,\alpha_0\,\frac{\mathrm{d}\langle \boldsymbol{u}\rangle_{\text{s}}}{\mathrm{d}t} = -\epsilon\,\boldsymbol{\nabla}\langle p\rangle_{\text{i}} - \frac{\epsilon\,\mu}{K}\,\langle \boldsymbol{u}\rangle_{\text{s}}\ , \tag{5}$$

is the appropriate choice for transient flow and low frequency oscillatory flow whereas for high frequency oscillatory flow a different time constant needs to be employed. This will be further discussed in section 2.3.

2.1.3 Dynamic permeability models

Linear oscillatory flow through porous media has been studied extensively in acoustics. Johnson et al (1987) proposed an important family of models, the dynamic permeability. These are based on a generalisation of the Darcy equation (3) in the frequency domain [1]

$$\mathcal{F}\left\{\langle \boldsymbol{u}\rangle_{\text{s}}\right\}(\omega) = -\frac{\hat{K}(-\omega)}{\mu}\mathcal{F}\left\{\boldsymbol{\nabla}\langle p\rangle_{\text{i}}\right\}(\omega) \tag{8}$$

[1] We define the Fourier transform of a function $g(t)$ and the inverse Fourier transform of a function $\hat{g}(\omega)$ as

$$\mathcal{F}\left\{g(t)\right\}(\omega) = \int_{-\infty}^{\infty} g(t)e^{-\mathrm{i}\omega t}\,\mathrm{d}t \tag{6}$$

$$\mathcal{F}^{-1}\left\{\hat{g}(\omega)\right\}(t) = \frac{1}{2\pi}\int_{-\infty}^{\infty} \hat{g}(\omega)e^{\mathrm{i}\omega t}\,\mathrm{d}\omega \tag{7}$$

where the function $\hat{K}(\Omega)$ is referred to as dynamic permeability and corresponds to the frequency response function in linear systems theory.

Johnson et al (1987) derived high-frequency asymptotics from boundary layer theory (cf. Cortis et al (2003)) and proposed a model for the entire frequency range by blending the high-frequency asymptotics with Darcy's law at low frequencies. The model by Johnson et al (1987) is given in the notation of Pride et al (1993) for a complex frequency Ω as

$$\hat{K}(\Omega) = \frac{K}{\sqrt{1 - \mathrm{i}P\frac{\Omega}{\Omega_0}} - \mathrm{i}\frac{\Omega}{\Omega_0}}\,, \tag{9}$$

with the frequency $\Omega_0 = \epsilon\,\nu/(\alpha_\infty\,K)$ and the dimensionless parameter $P = 4\,\alpha_\infty\,K/(\epsilon\,\Lambda^2)$. The transition frequency Ω_0 "separates viscous-force-dominated flow from inertial-force flow" (Pride et al, 1993). The original parameters introduced by Johnson et al (1987) are the high-frequency limit of the dynamic tortuosity α_∞ (identical to the ratio $\langle \boldsymbol{u}^2 \rangle_\mathrm{i} \,/\, \langle \boldsymbol{u} \rangle_\mathrm{i}^2$ in potential flow) and a length-scale Λ. Both parameters can be computed in terms of the potential flow solution. Smeulders et al (1992) presented a derivation of the model of Johnson et al (1987) from first principles using homogenisation theory. Chapman and Higdon (1992) compared the model predictions to numerical solutions of the unsteady Stokes equations obtained with a least-squares collocation approach and found good agreement. Similarly, in (Unglehrt and Manhart, 2022a) we observed excellent agreement of the model with our simulations. For large frequencies, the model (9) reduces to

$$\hat{K}(\Omega) = \frac{K}{\sqrt{-\mathrm{i}P\frac{\Omega}{\Omega_0}} - \mathrm{i}\frac{\Omega}{\Omega_0}} \tag{10}$$

Using the inverse Fourier transform of equations (8) and (10), we can write the momentum equation in the time domain (Turo and Umnova, 2013)

$$\rho\,\frac{\mathrm{d}\langle \boldsymbol{u} \rangle_\mathrm{s}}{\mathrm{d}t} = -\frac{2\rho\sqrt{\nu}}{\Lambda}\int_{-\infty}^{t} \frac{\mathrm{d}\langle \boldsymbol{u} \rangle_\mathrm{s}}{\mathrm{d}\tau}\,\frac{1}{\sqrt{\pi(t-\tau)}}\,\mathrm{d}\tau - \frac{\epsilon}{\alpha_\infty}\boldsymbol{\nabla}\langle p \rangle_\mathrm{i}\,, \tag{11}$$

where the integral term corresponds to the Caputo fractional derivative of order $\frac{1}{2}$. This term originates from boundary layer theory and is analogous to the Basset history term in the solution for flow around a sphere (Turo and Umnova, 2013). Consequently, the flow state in the dynamic permeability model (9) requires the specification of the entire history of $\langle \boldsymbol{u} \rangle_\mathrm{s}(t)$. This is in contrast to the unsteady Darcy equation where the flow state is completely specified by the instantaneous value of $\langle \boldsymbol{u} \rangle_\mathrm{s}$.

In order to improve the low-frequency behaviour, Pride et al (1993) devised an extended model

$$\hat{K}(\Omega) = \frac{K}{\left(1 - \frac{P}{2\beta} + \sqrt{\frac{P^2}{4\beta^2} - \mathrm{i}P\frac{\Omega}{\Omega_0}}\right) - \mathrm{i}\frac{\Omega}{\Omega_0}} \,. \tag{12}$$

The model of Johnson et al (1987) is obtained in the special case $P = 2\beta$ where the additional non-dimensional parameter $\beta = \frac{\alpha_0}{\alpha_\infty} - 1$ is defined in terms of the static viscous tortuosity α_0 and the high-frequency limit of the dynamic tortuosity α_∞. It is therefore a measure for the difference in time scales of Stokes flow and potential flow.

Another extension of the model of Johnson et al (1987) was developed by Champoux and Allard (1991) to represent thermal dissipation effects occuring for an ideal gas. As we restrict our analyses to incompressible flow, we will not discuss this any further. A comprehensive discussion of the dynamic permeability models (also known as *equivalent fluid model*) can be found in Lafarge (2009).

The dynamic permeability models can also be written in the time domain by performing an inverse Fourier transform. For example, a time domain formulation of the model of Johnson et al (1987) (equation 9) was given by Umnova and Turo (2009). In the same way, we obtained the time domain formulation of the more general model of Pride et al (1993) (equation 12):

$$\begin{aligned} \rho \frac{\mathrm{d}\langle \boldsymbol{u} \rangle_\mathrm{s}}{\mathrm{d}t} = &- \frac{\epsilon}{\alpha_\infty} \boldsymbol{\nabla} \langle p \rangle_\mathrm{i} - \left(\frac{\epsilon}{\alpha_\infty} \frac{\mu}{K} - \frac{2\mu}{\Lambda^2 \beta} \right) \langle \boldsymbol{u} \rangle_\mathrm{s} \\ &- \frac{2\rho\sqrt{\nu}}{\Lambda} \int_{-\infty}^{t} \left(\frac{\nu \langle \boldsymbol{u} \rangle_\mathrm{s}}{\Lambda^2 \beta^2} + \frac{\mathrm{d}\langle \boldsymbol{u} \rangle_\mathrm{s}}{\mathrm{d}\tau} \right) \frac{e^{-\frac{\nu(t-\tau)}{\Lambda^2 \beta^2}}}{\sqrt{\pi(t-\tau)}} \mathrm{d}\tau \,. \end{aligned} \tag{13}$$

Note that we have inserted the definitions of the parameters P and Ω_0 in order to ease the comparison with the other time domain models. The kernel in the convolution integral represents an exponential damping of the fractional derivative kernel and reduces the weight on the history further in the past.

2.2 Models for nonlinear flow

2.2.1 Darcy equation with cubic correction

For steady flow at small Re, Mei and Auriault (1991) showed using a homogenization theory approach that Darcy's law needs to be corrected with a cubic term

$$-\boldsymbol{\nabla} \langle p \rangle_\mathrm{i} = \frac{\mu}{K} \langle \boldsymbol{u} \rangle_\mathrm{s} + \frac{\mu\, b}{K} \langle \boldsymbol{u} \rangle_\mathrm{s}^2 \langle \boldsymbol{u} \rangle_\mathrm{s} \tag{14}$$

where b is a non-negative coefficient with the units T^2/L^2. Koch and Ladd (1997) simulated flow through periodic and random arrays of cylinders and confirmed that the first correction to Darcy's law is cubic with respect to the

bulk velocity. Firdaouss et al (1997) showed that the cubic correction also holds for anisotropic media provided that the modulus of the bulk velocity does not change under a reversal of the driving force. Hill et al (2001) investigated flow through random and ordered arrays of spheres using DNS and concluded that "[a]t all solid volume fractions, the first inertial contribution to the non-dimensional drag force was found to be proportional to the square of the Reynolds number, as predicted by the theory of Mei & Auriault.".

2.2.2 Forchheimer equation

For nonlinear flow at higher Reynolds numbers, Forchheimer (1901) proposed the empirical equation

$$-\boldsymbol{\nabla}\langle p\rangle_{\mathrm{i}} = a\,\langle \boldsymbol{u}\rangle_{\mathrm{s}} + b\,|\langle \boldsymbol{u}\rangle_{\mathrm{s}}|\,\langle \boldsymbol{u}\rangle_{\mathrm{s}} \tag{15}$$

where the coefficients a and b have units of $M/(L^3\,T)$ and M/L^4, respectively. For packed beds of spheres, comprehensive empirical correlations for these coefficients were first given by Ergun (1952). Updated forms of the correlations have been given e.g. by Macdonald et al (1979). When the flow in the pore space becomes turbulent, a different set of coefficients should be chosen (Burcharth and Andersen, 1995); this results in a piecewise description of the drag.

2.2.3 Unsteady Forchheimer equation

For the description of unsteady porous media flow, Polubarinova-Kochina (1962) proposed to extend the Forchheimer equation (15) with an acceleration term

$$-\boldsymbol{\nabla}\langle p\rangle_{\mathrm{i}} = a\,\langle \boldsymbol{u}\rangle_{\mathrm{s}} + b\,|\langle \boldsymbol{u}\rangle_{\mathrm{s}}|\,\langle \boldsymbol{u}\rangle_{\mathrm{s}} + c\frac{\mathrm{d}\langle \boldsymbol{u}\rangle_{\mathrm{s}}}{\mathrm{d}t}\,. \tag{16}$$

Sollitt and Cross (1972) derived a parametrisation of this equation where a and b were chosen according to the steady state equation by Ward (1964) and the form of the acceleration coefficient c was determined based on a virtual mass argument. Their equation reads

$$\rho\,S\,\frac{\mathrm{d}\langle \boldsymbol{u}\rangle_{\mathrm{s}}}{\mathrm{d}t} = -\epsilon\,\boldsymbol{\nabla}\langle p\rangle_{\mathrm{i}} - \frac{\epsilon\,\mu}{K}\,\langle \boldsymbol{u}\rangle_{\mathrm{s}} - \rho\,\frac{\epsilon\,C_{\mathrm{f}}}{\sqrt{K}}\,|\langle \boldsymbol{u}\rangle_{\mathrm{s}}|\,\langle \boldsymbol{u}\rangle_{\mathrm{s}} \tag{17a}$$

where the "inertial coefficient" is defined as

$$S = 1 + \frac{1-\epsilon}{\epsilon}C_{\mathrm{M}}\,. \tag{17b}$$

However, Sollitt and Cross (1972) considered the coefficient C_{M}, which represents the virtual mass of the solid grains, as unknown and set it to zero. In contrast, the experimental investigation of Gu and Wang (1991) resulted in $C_{\mathrm{M}} = 0.46$ for gravel beds with a porosity between 0.35 and 0.38. Also, other parametrisations of the acceleration coefficient have been given in later works (Burcharth and Andersen, 1995).

Another choice for the coefficient c was proposed by Zhu (2016) who suggested to use the time constant $\tau_{\mathrm{en}} = \alpha_0 K/(\epsilon\nu)$ in direct analogy to the unsteady Darcy equation (5).

Burcharth and Andersen (1995) state that "the coefficients [b and c] are not constants and should in principle be treated as instantaneous values, even for oscillatory flow conditions". For example, Hall et al (1995) calculated the instantaneous values of the coefficients a, b and c from oscillatory flow data. However, no explicit parametrisation of the constants was determined. On the other hand, van Gent (1993) considered the coefficients as constants for each flow case and found frequency-dependent correlations for the coefficients b and c. However, this kind of parametrisation is specific to the flow case and is not generally applicable (Burcharth and Andersen, 1995).

Furthermore, it is unclear how the change of the drag behaviour due to the transition to turbulence (see Burcharth and Andersen (1995)) could be incorporated into the unsteady Forchheimer equation. In oscillatory flow the critical Reynolds number of transition depends on the frequency (see section 3.2 or the estimations of Gu and Wang (1991)), ruling out the straightforward way of changing the coefficients a, b, and c depending on the instantaneous Reynolds number.

2.2.4 Extended dynamic permeability model

Turo and Umnova (2013) proposed a model for unsteady nonlinear porous media flow. The model combines the time domain formulation of a dynamic permability model with a Forchheimer-type quadratic term:

$$\begin{aligned}\rho\frac{\mathrm{d}\langle\boldsymbol{u}\rangle_{\mathrm{s}}}{\mathrm{d}t} = &-\frac{\epsilon}{\alpha_\infty}\boldsymbol{\nabla}\langle p\rangle_{\mathrm{i}} - \frac{\epsilon}{\alpha_\infty}\frac{\mu}{K}\left(1+\xi|\langle\boldsymbol{u}\rangle_{\mathrm{s}}|\right)\langle\boldsymbol{u}\rangle_{\mathrm{s}} \\ &-\frac{2\rho\sqrt{\nu}}{\Lambda}\int_{-\infty}^{t}\frac{\mathrm{d}\langle\boldsymbol{u}\rangle_{\mathrm{s}}}{\mathrm{d}\tau}\frac{1}{\sqrt{\pi(t-\tau)}}\,\mathrm{d}\tau\,.\end{aligned} \tag{18}$$

The parameter ξ $[T/L]$ describes the nonlinearity and is related to the Forchheimer coefficient b as $\xi = \frac{bK}{\mu}$. This model can be interpreted as an additive combination of the drag due to the boundary layers (corresponding to the high-frequency asymptotics (10) of Johnson et al (1987)) and of the drag in the steady state described by the Forchheimer equation (15).

2.3 Discussion

2.3.1 Relations among the linear models

The linear models presented in section 2.1 can be understood as various special cases of the dynamic permeability model of Pride et al (1993) given in equation (12). First, by setting $P = 2\beta$, the model of Johnson et al (1987) given in equation (9) is recovered. Thus, the model of Johnson et al (1987) has the

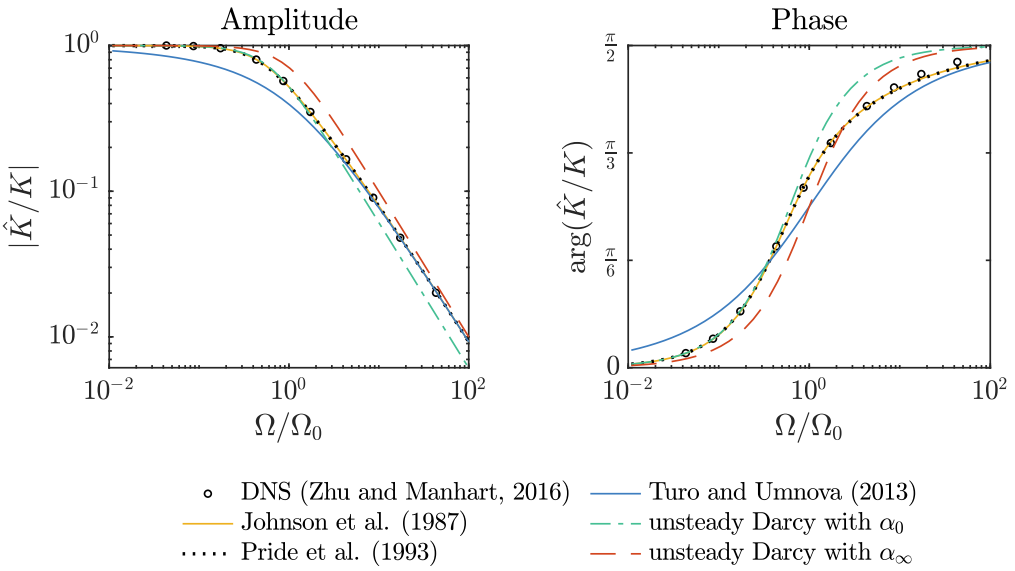

Fig. 1: Comparison of different linear models with the direct numerical simulations of Zhu and Manhart (2016). Amplitude (left) and phase (right) of the dynamic permeability $\hat{K}$ normalised with the permeability. The dynamic permeability functions of the models are given by the equations (9), (12), (22) and (20), respectively.

inherent assumption

$$\alpha_0 = \alpha_\infty \left(1 + \frac{P}{2}\right) = \alpha_\infty \left(1 + \frac{2\,\alpha_\infty\,K}{\epsilon\,\Lambda^2}\right) \tag{19}$$

for the static viscous tortuosity. Second, the unsteady Darcy equation (5) can be recast as a dynamic permeability model by taking the Fourier transform:

$$\mathcal{F}\left\{\langle \boldsymbol{u}\rangle_{\mathrm{s}}\right\}(\omega) = -\frac{1}{\mu}\frac{K}{1 + \frac{\alpha_0}{\alpha_\infty}\,\mathrm{i}\frac{\omega}{\Omega_0}}\mathcal{F}\left\{\boldsymbol{\nabla}\langle p\rangle_{\mathrm{i}}\right\}(\omega)\ . \tag{20}$$

On the other hand, a Taylor expansion of the denominator of the model of Pride et al (1993) (equation 12) at $\omega = 0$ results in

$$\hat{K}(-\omega) = \frac{K}{1 + \frac{\alpha_0}{\alpha_\infty}\,\mathrm{i}\frac{\omega}{\Omega_0} + O\left(\frac{\omega^2}{\Omega_0^2}\right)}\ . \tag{21}$$

By comparison, we see that the Darcy equation and the unsteady Darcy equation represents the zeroth and first order asymptotes to the low frequency behaviour of the frequency response function of the Pride et al (1993) model. This explains the observations of Zhu and Manhart (2016) that the unsteady Darcy equation with α_0 shows excellent agreement with the direct numerical

simulations at low frequencies whereas a different time constant – the high-frequency limit of the dynamic tortuosity α_∞ – has to be employed at high frequencies. Notably, the high-frequency limit of the dynamic tortuosity α_∞ is a consistent choice of coefficient for the unsteady Darcy equation in that it leads to the correct limits for $\Omega \to 0$ and $\Omega \to \infty$.

In figure 1 the dynamic permeabilities implied by the different models are compared to the numerical simulations of Zhu and Manhart (2016) of oscillatory flow through a hexagonal sphere pack. It can be seen that the dynamic permeability models of Johnson et al (1987) and Pride et al (1993) show an excellent agreement with the simulation data. Note that for the hexagonal sphere pack, the assumption (19) is fulfilled with an error of only 1%, rendering the models of Johnson et al (1987) and Pride et al (1993) virtually identical for this geometry. On the other hand, the unsteady Darcy equation departs from the simulation data at medium or high frequencies, depending on the choice of the acceleration coefficient. The model of Turo and Umnova (2013) will be discussed in the next section.

In conclusion, we find that the unsteady Darcy equation and the dynamic permeability model of Johnson et al (1987) can be seen as simplifications of the dynamic permeability model of Pride et al (1993), which is able to accurately describe the simulation data for the hexagonal sphere pack.

2.3.2 Improvement of the model of Turo & Umnova (2013)

In the linear limit, the model (18) corresponds to a dynamic permeability of the following form

$$\hat{K}(\Omega) = \frac{K}{1 + \sqrt{-\mathrm{i}P\frac{\Omega}{\Omega_0}} - \mathrm{i}\frac{\Omega}{\Omega_0}}\,. \tag{22}$$

It can be seen that for $\Omega \to 0$ and for $\Omega \to \infty$ the correct limits (3) and (10) are approached. However, when the dynamic permeability is compared to the models of Johnson et al (1987); Pride et al (1993); Zhu et al (2014) it becomes apparent that the model of Turo and Umnova (2013) severely underestimates the permeability at low and intermediate frequencies. This can be seen clearly in figure 1a.

The analysis of this model deficiency suggests a simple remedy: We replace the underlying dynamic permeability model of equation (18) with the model of Pride et al (1993) which has the correct behaviour at low frequencies. We obtain the following equation:

$$\begin{aligned}\rho\,\frac{\mathrm{d}\langle \boldsymbol{u}\rangle_\mathrm{s}}{\mathrm{d}t} = &-\frac{\epsilon}{\alpha_\infty}\boldsymbol{\nabla}\langle p\rangle_\mathrm{i} - \left[\frac{\epsilon}{\alpha_\infty}\frac{\mu}{K}\left(1+\xi|\langle \boldsymbol{u}\rangle_\mathrm{s}|\right) - \frac{2\mu}{\Lambda^2\,\beta}\right]\langle \boldsymbol{u}\rangle_\mathrm{s} \\ &- \frac{2\rho\sqrt{\nu}}{\Lambda}\int_{-\infty}^{t}\left(\frac{\nu\,\langle \boldsymbol{u}\rangle_\mathrm{s}}{\Lambda^2\,\beta^2} + \frac{\mathrm{d}\langle \boldsymbol{u}\rangle_\mathrm{s}}{\mathrm{d}\tau}\right)\frac{e^{-\frac{\nu(t-\tau)}{\Lambda^2\,\beta^2}}}{\sqrt{\pi(t-\tau)}}\,\mathrm{d}\tau\,.\end{aligned} \tag{23}$$

This model allows us to explore the potential of the basic idea of Turo and Umnova (2013) of combining a dynamic permeability model with the Forchheimer nonlinearity.

2.3.3 Lower bounds for the coefficients of the unsteady Forchheimer equation

In this section, we discuss lower bounds for the coefficients of the unsteady Forchheimer equation that arise from Kelvin's minimum energy theorem, Helmholtz' minimum dissipation theorem and the volume-averaged kinetic energy equation if the coefficients are considered as constants.

First, we multiply the unsteady Forchheimer equation (16) with the superficial velocity such that after some rearrangements the following equation is obtained:

$$\frac{\mathrm{d}}{\mathrm{d}t}\left(\frac{c}{2}\left\langle \boldsymbol{u}\right\rangle_{\mathrm{s}}^{2}\right)=-\left\langle \boldsymbol{u}\right\rangle_{\mathrm{s}}\cdot\boldsymbol{\nabla}\left\langle p\right\rangle_{\mathrm{i}}-a\left\langle \boldsymbol{u}\right\rangle_{\mathrm{s}}^{2}-b\left|\left\langle \boldsymbol{u}\right\rangle_{\mathrm{s}}\right|\left\langle \boldsymbol{u}\right\rangle_{\mathrm{s}}^{2} \tag{24}$$

where the first term on the right hand side is the power added to or removed from the flow by the macroscopic pressure gradient. Comparing this equation to the volume-averaged kinetic energy equation (Zhu et al, 2014)

$$\frac{\mathrm{d}}{\mathrm{d}t}\left(\frac{1}{2}\rho\left\langle \boldsymbol{u}^{2}\right\rangle_{\mathrm{s}}\right)=-\left\langle \boldsymbol{u}\right\rangle_{\mathrm{s}}\cdot\boldsymbol{\nabla}\left\langle p\right\rangle_{\mathrm{i}}-2\mu\left\langle \mathsf{S}:\mathsf{S}\right\rangle_{\mathrm{s}}\,, \tag{25}$$

wherein S is the strain rate tensor, we find that the term on the left hand side of (24) is the time derivative of a positive quantity and can take both signs. Thus it cannot be part of the dissipation. On the other hand, the second and third term on the right hand side of (24) have a definite sign. Hence they cannot be part of the time derivative of the kinetic energy which can take both signs. Consequently, we identify

$$\frac{1}{2}\rho\left\langle \boldsymbol{u}^{2}\right\rangle_{\mathrm{s}}=\frac{c}{2}\left\langle \boldsymbol{u}\right\rangle_{\mathrm{s}}^{2} \tag{26a}$$

$$2\mu\left\langle \mathsf{S}:\mathsf{S}\right\rangle_{\mathrm{s}}=\left(a+b\left|\left\langle \boldsymbol{u}\right\rangle_{\mathrm{s}}\right|\right)\left\langle \boldsymbol{u}\right\rangle_{\mathrm{s}}^{2} \tag{26b}$$

as underlying assumptions of the unsteady Forchheimer equation. Note that the dissipation term is consistent with Nield (2000) who discussed stationary flow.

From Kelvin's minimum energy theorem (Batchelor, 2000, p.384), it is possible to show that the kinetic energy for a given superficial velocity is smallest in the potential flow. This results in the inequality (Lafarge, 1993, p.123)

$$\frac{1}{2}\rho\left\langle \boldsymbol{u}^{2}\right\rangle_{\mathrm{s}}\geq\frac{1}{2}\frac{\rho\,\alpha_{\infty}}{\epsilon}\left\langle \boldsymbol{u}\right\rangle_{\mathrm{s}}^{2} \tag{27}$$

which is valid for an isotropic porous medium. Moreover, according to Helmholtz' minimum dissipation theorem (Batchelor, 2000, pp.227–228), the

dissipation rate for a given superficial velocity is smallest in the Stokes flow. Using the expression of Zhu et al (2014); Paéz-García et al (2017) for the dissipation rate in the Stokes flow, we arrive at the inequality

$$2\mu \langle \mathsf{S} : \mathsf{S} \rangle_{\mathrm{s}} \geq \frac{\mu}{K} \langle \boldsymbol{u} \rangle_{\mathrm{s}}^2 \tag{28}$$

which again is valid for an isotropic porous medium. We therefore obtain the lower bounds

$$a \geq \frac{\mu}{K} \tag{29a}$$

$$b \geq 0 \tag{29b}$$

$$c \geq \frac{\rho\, \alpha_\infty}{\epsilon} \tag{29c}$$

for the coefficients of the unsteady Forchheimer equation.

These inequalities could be interpreted as *realisability conditions* similar to those of Schumann (1977) in the context of Reynolds stress turbulence models, for if these conditions are violated, no pore scale velocity field can be found such that equation (24) describes the evolution of the kinetic energy.

3 Methodology

In this section, we describe the simulation dataset that will be used as a reference for comparing the different models. Moreover, we discuss aspects of the numerical implementation of the models. Finally, we introduce the metrics that will be used for quantifying the model errors.

3.1 Description of the flow solver

The reference simulations were conducted using our in-house code MGLET (Manhart et al, 2001) which solves the incompressible Navier-Stokes equations on a Cartesian block-structured grid with a staggered arrangement of variables. For the spatial discretisation, a symmetry-preserving second-order finite volume scheme (Verstappen and Veldman, 2003) is employed. The no-slip boundary condition on the spheres is imposed by means of a mass-conserving ghost-cell immersed boundary method (Peller et al, 2006; Peller, 2010). For the temporal discretisation, a third-order explicit Runge-Kutta method (Williamson, 1980) is used and a projection step (Chorin, 1968) is performed at every stage.

3.2 Description of the simulation database

The simulation database that will be used as a reference for the model comparison consists of direct numerical simulations of oscillatory flow through a hexagonal sphere pack (Unglehrt and Manhart, 2022a, 2023a,b). The sphere pack is a triply periodic close-packed arrangement of equal spheres of diameter

d. Hence, each sphere is in contact with 12 other spheres and the porosity is given as $\epsilon = 1 - \frac{\pi}{3\sqrt{2}} \approx 0.26$. The flow was driven by a sinusoidally time-varying pressure gradient

$$\boldsymbol{\nabla} \langle p \rangle_{\mathrm{i}} (t) = g_x \sin(\Omega t) \tag{30}$$

and therefore depends on two dimensionless parameters: The Hagen number $Hg = |g_x| \, d^3/(\rho \nu^2)$ determines the amplitude and the Womersley number $Wo = \sqrt{\Omega \, d^2/\nu}$ determines the frequency of the macroscopic pressure gradient. The Reynolds number was defined as

$$Re = \limsup_{t \to \infty} \frac{|\langle \boldsymbol{u} \rangle_{\mathrm{s}}| \, d}{\nu} \tag{31}$$

and was obtained as a result of the simulations. The simulations were performed at the three Womersley numbers $Wo = 10$, 31.62, and 100 that correspond to the low, medium and high frequency regime in linear flow, respectively.[2] The Hagen numbers were set such that the simulations cover linear flow, laminar nonlinear flow, and transitional and turbulence-like flow at each Womersley number. The flow was started from rest and simulated until a recurrent behaviour could be observed in the superficial velocity. The difference in the superficial velocity in the last simulated cycle and the preceding cycle was less than approximately 0.1% of the maximum superficial velocity in the last simulated cycle for the laminar cases and about 2% for the transitional and turbulence-like cases. The simulation parameters can be found in table 1.

Figure 2 shows the dimensionless parameters of our simulation database in the Re–Wo^2 parameter space. We additionally give the frequency ratio Ω/Ω_0 where $\Omega_0 = 930.25 \, \nu/d^2$ is the transition frequency defined in section 2.1.3 that can be used to distinguish between the low and the high frequency regime in linear flow. The parameter region in which linear flow can be observed was determined in (Unglehrt and Manhart, 2022a). The breaking of the geometry-imposed symmetries in the flow was used to distinguish the laminar nonlinear from the transitional and turbulence-like regime (Unglehrt and Manhart, 2022b).

The time series of the superficial velocity for some of the simulation cases is shown in figure 3. The amplitudes of the superficial velocity decrease with increasing Reynolds or Womersley number. The decrease of the amplitude with Womersley number is caused by the inertia of the system, whereas the decrease with Reynolds number can be explained by the increase of the drag. As the Reynolds number increases, the behaviour of the superficial velocity becomes non-sinusoidal. This could be explained by the effect of nonlinearity and turbulence. At high Womersley and Reynolds numbers, we can distinguish phases of strong and weak acceleration that lead to distinctive bends in the superficial velocity. In (Unglehrt and Manhart, 2023a) we could link this to an increase in the convective pressure drag due to flow separation at the contact

[2] The medium frequency regime in linear flow through a hexagonal sphere pack occurs around a Womersley number $Wo_0 = \sqrt{\epsilon \, d^2/(\alpha_\infty \, K)} = 30.5$, where $\Omega_0 = \epsilon \, \nu/(\alpha_\infty \, K)$ is the transition frequency (Pride et al, 1993). The geometric constants are given in table 2.

Table 1: Parameters of the simulations of oscillatory flow through a hexagonal sphere pack.

Case	Hg	Wo	Re	number of simulated cycles	flow regime
LF1 [1]	$1.00 \cdot 10^3$	10	0.171	1.5	linear
LF2 [1]	$1.00 \cdot 10^4$	10	1.7	2.25	linear
LF3 [1]	$1.00 \cdot 10^5$	10	14.8	1.4	laminar nonlinear
LF4 [1]	$1.00 \cdot 10^6$	10	76.7	1.25	laminar nonlinear
LF5 [2]	$3.16 \cdot 10^6$	10	158	2.27	transitional
LF6 [2]	$1.00 \cdot 10^7$	10	307	1.56	turbulence-like
MF1 [1]	$1.00 \cdot 10^4$	31.6	0.857	3	linear
MF2 [1]	$1.00 \cdot 10^5$	31.6	8.57	3	linear
MF3 [1]	$3.16 \cdot 10^5$	31.6	26.9	3	laminar nonlinear
MF4 [1]	$1.00 \cdot 10^6$	31.6	73.1	3	laminar nonlinear
MF5 [2]	$3.16 \cdot 10^6$	31.6	157	6.4	transitional
MF6 [2]	$1.00 \cdot 10^7$	31.6	298	2.26	turbulence-like
HF1 [1]	$1.00 \cdot 10^5$	100	1.3	20.4	linear
HF2 [1]	$1.00 \cdot 10^6$	100	13	19.9	linear
HF3 [1]	$1.00 \cdot 10^7$	100	132	6.32	laminar nonlinear
HF4 [1]	$1.78 \cdot 10^7$	100	252	8	laminar nonlinear
HF5 [2]	$3.16 \cdot 10^7$	100	465	6	transitional
HF6 [3]	$1.00 \cdot 10^8$	100	1090	3.91	turbulence-like
HF7 [3]	$1.00 \cdot 10^9$	100	3620	10	turbulence-like

[1] from Unglehrt and Manhart (2022a)

[2] from Unglehrt and Manhart (2023a)

[3] from Unglehrt and Manhart (2023b)

points. As the Womersley number increases, we observe a phase lag of the superficial velocity with respect to the forcing. This can be seen from the zero-crossings of the superficial velocity which do not coincide with the zeros of the forcing ($\varphi = k\pi$ for $k = 0, 1, 2, \dots$). This is due to the increasing importance of the inertia compared to the drag. On the other hand, the phase lag decreases as the Reynolds number increases. This goes in hand with an increase of the nonlinear drag which advances the inertial term. Overall, these time series demonstrate a distinct effect of nonlinearity and turbulence on the response of the superficial velocity to harmonic excitations.

3.3 Model constants for the hexagonal sphere pack

In this section, we specify the model constants that were used to evaluate the model predictions. The parameters for the linear models have rigorous definitions in terms of the steady Stokes flow (K, α_0) and the potential flow solution (Λ/d, α_∞), respectively. Notably, these quantities are intrinsic properties of the pore geometry. The low frequency properties of the hexagonal sphere pack were determined from direct numerical simulations in the studies of Zhu and Manhart (2016) and Sakai and Manhart (2020); the high frequency properties

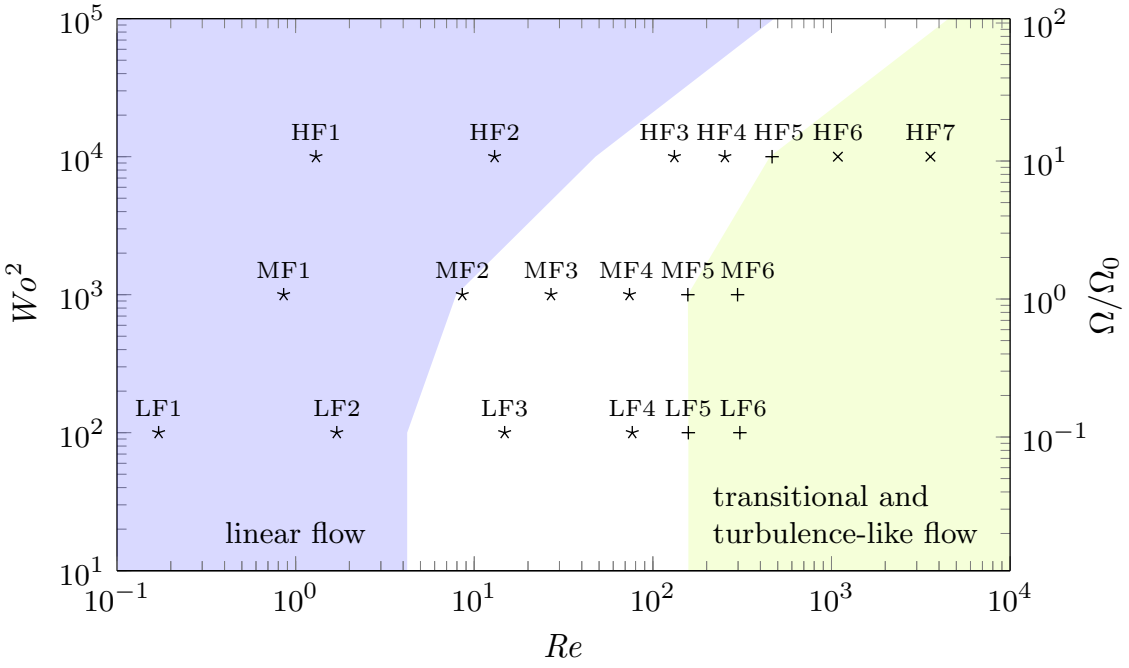

Fig. 2: Simulation parameters. The stars mark the simulations from (Unglehrt and Manhart, 2022a), the pluses mark the simulations from (Unglehrt and Manhart, 2023a) and the crosses mark the simulations from (Unglehrt and Manhart, 2023b). The regions shaded in blue and green corresponds to the linear regime and the transitional and turbulence-like regime, respectively.

were determined by a potential flow calculation in our previous study (Unglehrt and Manhart, 2023a). The parameter values are summarised in table 2.

For the coefficients of the unsteady Forchheimer equation various choices can be found in the literature (see section 2.2.3). Following Sollitt and Cross (1972), we assume that the coefficients a and b are constant and take their steady state values. This choice ensures that the unsteady Forchheimer equation has the correct low frequency limit behaviour. For the acceleration coefficient c, we consider two choices: Either the coefficient is set to the potential flow value $\rho\,\alpha_\infty/\epsilon$ such that the correct high-frequency behaviour is recovered (Zhu and Manhart, 2016), or, following Zhu (2016), the coefficient is set to the Stokes flow value $\rho\,\alpha_0/\epsilon$ such that the unsteady Forchheimer equation reduces to the unsteady Darcy equation with the static viscous tortuosity (Zhu et al, 2014). We do not consider time- or frequency-dependent coefficients as no generally applicable correlations have been given in the literature. Note that the coefficients of the unsteady Forchheimer equation could be adjusted to improve the fit for some simulation cases; however, this comes at the price of high prediction errors behaviour in some of the asymptotic limits, e.g. for slowly varying flow or for linear flow.

The coefficients of the Forchheimer equation (15) are determined based on the simulation results in (Sakai and Manhart, 2020; Unglehrt and Manhart,

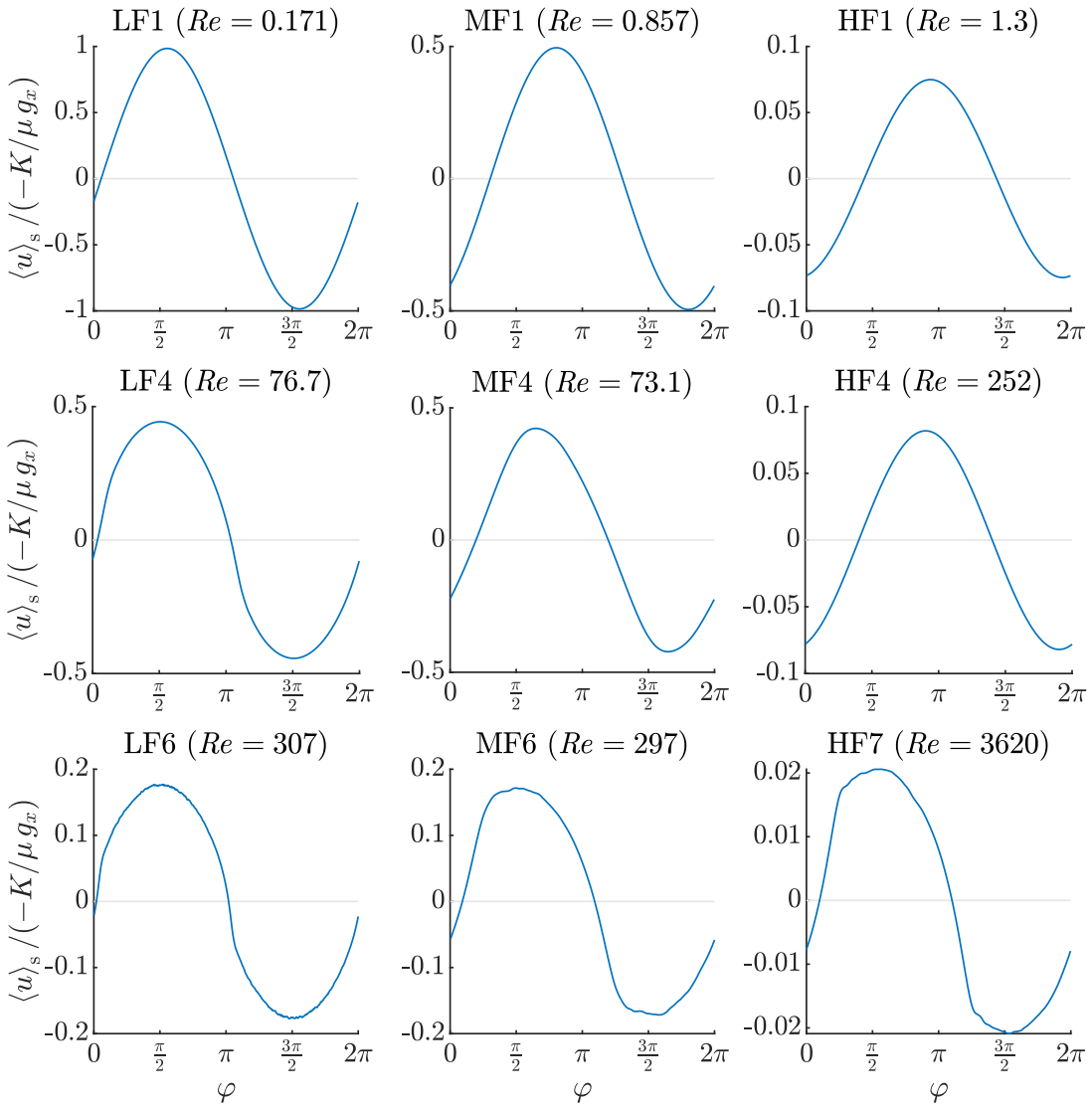

Fig. 3: Variation of the superficial velocity over the cycle from the direct numerical simulations of oscillatory flow through a hexagonal sphere pack. In all cases, the forcing is given by $\boldsymbol{\nabla}\langle p \rangle_{\mathrm{i}} = g_x \sin\varphi$ and the superficial velocity is normalised by the value obtained from Darcy's law at the peak pressure gradient.

2023a). The linear Forchheimer coefficient a is chosen such that the Forchheimer equation approaches Darcy's law for $Re \to 0$. Then, the nonlinear Forchheimer coefficient b is determined from a least squares fit to the ratio of the macroscopic pressure gradient and the superficial velocity. We obtained the following coefficients:

$$a = \frac{\mu}{K} = 5777\,\frac{\mu}{d^2} \tag{32a}$$

$$b = 88.9\,\frac{\rho}{d}\,. \tag{32b}$$

Table 2: Geometric parameters for the hexagonal close-packed arrangement of equal spheres.

Parameter	Symbol	Value
Porosity	ϵ	$1 - \frac{\pi}{3\sqrt{2}} = 0.2595$
Permeability	K	$1.731 \cdot 10^{-4}\, d^2$ [1]
Low-frequency limit of the dynamic tortuosity	α_0	2.657 [2]
High-frequency limit of the dynamic tortuosity	α_∞	1.622 [3]
Boundary layer length scale	Λ	$5.904 \cdot 10^{-2}\, d$ [3]

[1] from Sakai and Manhart (2020)

[2] from Zhu and Manhart (2016)

[3] from Unglehrt and Manhart (2023a)

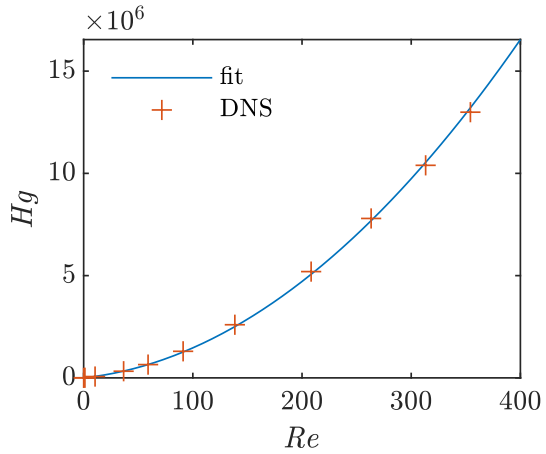

Fig. 4: Forchheimer equation (15) with coefficients (32) and direct numerical simulation data for stationary flow through a hexagonal sphere pack.

It can be seen in figure 4 that these coefficients provide a good fit to the simulation data. Finally, the nonlinear coefficient ξ in the equations (18) and (23) results as $0.0154\, d/\nu$.

3.4 Implementation of the models

3.4.1 Discretisation of the model of Pride et al. (1993)

As we would like to obtain model predictions for transient flow, we discretise the model of Pride et al (1993) in the time domain. We discretise equation (13) using the implicit Euler method and a piecewise linear interpolation of the convolution term. We obtained the following scheme

$$a \langle \boldsymbol{u} \rangle_{\mathrm{s}}^{n+1} = \langle \boldsymbol{u} \rangle_{\mathrm{s}}^{n} - \Delta t \, \frac{\epsilon}{\rho \, \alpha_\infty} \boldsymbol{\nabla} \langle p \rangle_{\mathrm{i}}^{n+1} - \sum_{k=1}^{\infty} c_k \, \langle \boldsymbol{u} \rangle_{\mathrm{s}}^{n-k+1} \tag{33a}$$

with precomputable coefficients

$$a = 1 + h\left(\frac{4\beta^2}{P} - 2\beta\right) + 2\beta\left[\left(\frac{1}{2} + h\right)\operatorname{erf}\left(\sqrt{h}\right) + \sqrt{\frac{h}{\pi}}e^{-h}\right] \tag{33b}$$

$$\begin{aligned} c_k = &-2\beta\left\{\left[\operatorname{erf}\left(\sqrt{\xi}\right)\right]_{(k-1)h}^{kh}\left(\frac{1}{2} + (k-1)h\right) + \left[\sqrt{\frac{\xi}{\pi}}e^{-\xi}\right]_{(k-1)h}^{kh}\right\} \\ &+ 2\beta\left\{\left[\operatorname{erf}\left(\sqrt{\xi}\right)\right]_{kh}^{(k+1)h}\left(\frac{1}{2} + (k+1)h\right) + \left[\sqrt{\frac{\xi}{\pi}}e^{-\xi}\right]_{kh}^{(k+1)h}\right\} \end{aligned} \tag{33c}$$

depending on the dimensionless time step $h = \frac{\nu\Delta t}{\Lambda^2\beta^2}$. Note that the computational effort grows linearly with the number of time steps as the discrete convolution must be performed over a time series of increasing length. Computationally more efficient discretisations could be devised by approximating the tail of the convolution kernel in equation (13) with an exponential function similar to (van Hinsberg et al, 2011).

The correctness of the scheme (33) and its convergence with the time step size is assessed using the method of manufactured solutions. As a test case, we consider the velocity $\langle u\rangle_\mathrm{s} = j_0\,\frac{t^2}{2}\,\theta(t)$ with the Heaviside function $\theta(t)$. The forcing that is necessary to find this velocity as a solution to (13) can be obtained as

$$\begin{aligned} -\boldsymbol{\nabla}\langle p\rangle_\mathrm{i} = &\frac{\rho\,\alpha_\infty}{\epsilon}j_0\,t\,\theta(t) + \left(\frac{\mu}{K} - \frac{\alpha_\infty}{\epsilon}\frac{2\mu}{\Lambda^2\,\beta}\right)j_0\,\frac{t^2}{2}\,\theta(t) \\ &+ \frac{\rho\,\alpha_\infty}{\epsilon}\,\beta\,j_0\,\theta(t)\left[\left(t + \frac{\nu t^2}{\Lambda^2\beta^2} - \frac{1}{4}\frac{\Lambda^2\,\beta^2}{\nu}\right)\operatorname{erf}\left(\sqrt{\frac{\nu t}{\Lambda^2\beta^2}}\right)\right. \\ &\left. + \left(t + \frac{\Lambda^2\,\beta^2}{2\nu}\right)\sqrt{\frac{\nu t}{\Lambda^2\beta^2}}\frac{e^{-\frac{\nu t}{\Lambda^2\beta^2}}}{\sqrt{\pi}}\right]. \end{aligned} \tag{34}$$

We simulated (33) with the forcing defined above for a hexagonal sphere pack. Figure 5a shows the relative error of $\langle u\rangle_\mathrm{s}$ with respect to the analytic solution at $\frac{\nu T}{d^2} = 5$. We observe first order convergence which means that the singularity in the integral kernel is treated with sufficient accuracy.

3.4.2 Discretisation of the model of Turo & Umnova (2013)

Similar to the preceding section, the discretisation of equation (18) was derived using the implicit Euler method and a linear interpolation in the convolution term. This resulted in the following scheme

$$a\,\langle\boldsymbol{u}\rangle_\mathrm{s}^{n+1} + b\left|\langle\boldsymbol{u}\rangle_\mathrm{s}^{n+1}\right|\langle\boldsymbol{u}\rangle_\mathrm{s}^{n+1} = \langle\boldsymbol{u}\rangle_\mathrm{s}^{n} - \Delta t\,\frac{\epsilon}{\rho\,\alpha_\infty}\boldsymbol{\nabla}\langle p\rangle_\mathrm{i}^{n+1} - \sum_{k=1}^{\infty} c_k\,\langle\boldsymbol{u}\rangle_\mathrm{s}^{n-k+1} \tag{35a}$$

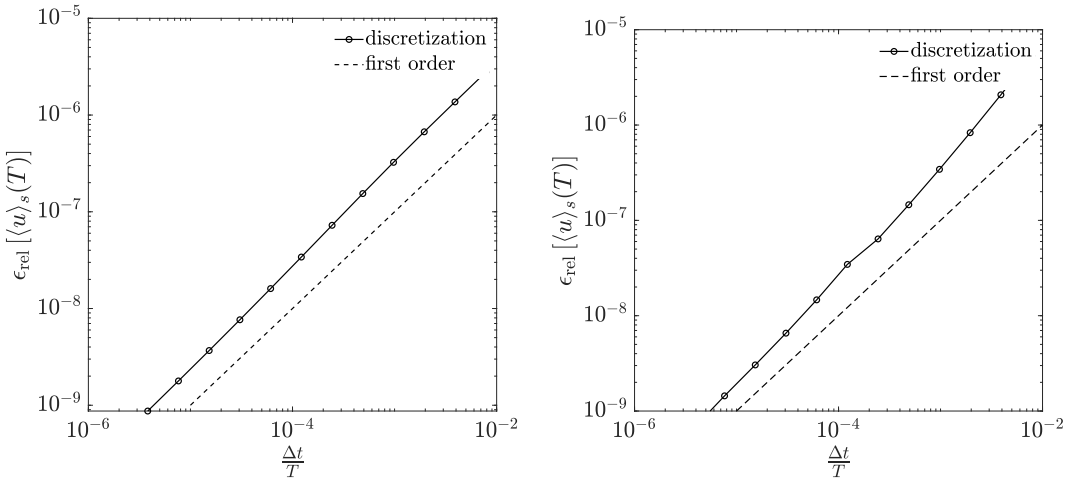

Fig. 5: Verification of the discretisations for (a) the model of Pride et al (1993) and (b) the model of Turo and Umnova (2013) with manufactured solutions (equation (34) and equation (36) with $\frac{\xi}{j_0^{1/5}\nu^{2/5}} = 0.01$, respectively).

with precomputable coefficients

$$a = 1 + \frac{\epsilon}{\alpha_\infty}\frac{\nu\Delta t}{K} + \frac{2\sqrt{\nu\Delta t}}{\Lambda}\frac{2}{\sqrt{\pi}} \tag{35b}$$

$$b = \frac{\epsilon}{\alpha_\infty}\frac{\nu\Delta t}{K}\xi \tag{35c}$$

$$c_k = \frac{2\sqrt{\nu\Delta t}}{\Lambda}\frac{2}{\sqrt{\pi}}\left(\sqrt{k+1} - 2\sqrt{k} + \sqrt{k-1}\right). \tag{35d}$$

The nonlinear equation appearing in every time step was solved with the function `fsolve` in MATLAB where the superficial velocity from the previous time step was taken as an initial guess. Other discretisations of the fractional derivative have been given e.g. by Diethelm et al (2005).

As in the preceding section, we verified the correctness and convergence of our implementation using a manufactured solution for the velocity $\langle u\rangle_{\mathrm{s}} = j_0\,\frac{t^2}{2}\,\theta(t)$. The corresponding forcing results from (18) as

$$\begin{aligned} -\boldsymbol{\nabla}\langle p\rangle_{\mathrm{i}} = &\frac{\rho\alpha_\infty}{\epsilon} j_0\, t\,\theta(t) + \frac{\mu}{K}\left(1 + \xi\,|j_0|\,\frac{t^2}{2}\right) j_0\,\frac{t^2}{2}\,\theta(t) \\ &+ \frac{\rho\alpha_\infty}{\epsilon} j_0\,\frac{\sqrt{\nu}}{\Lambda}\,\frac{8}{3\sqrt{\pi}}\, t^{\frac{3}{2}}\theta(t)\,. \end{aligned} \tag{36}$$

Figure 5b shows the convergence of the numerical solution to the analytical solution at a time $\frac{\nu T}{d^2} = 5$ and for a coefficient of nonlinearity $\frac{\xi}{j_0^{1/5}\nu^{2/5}} = 0.01$. Again, we have used the material properties of the hexagonal sphere pack.

3.4.3 Evaluation of model ODEs

The unsteady Darcy equation (5) and the unsteady Forchheimer equation (16) are simple ordinary differential equations. These were solved using a second order modified Rosenbrock method implemented in the MATLAB routine `ode23s` (Shampine and Reichelt, 1997). The time step size was chosen adaptively according to a relative tolerance of 10^{-6} and an absolute tolerance of $10^{-8}\,\frac{\nu}{d}$ for the superficial velocity.

3.5 Metrics for comparison

In order to compare the different models between the different simulation cases, we define an integral error metric. For two periodic signals $u_1(t)$ and $u_2(t)$ that will represent the model predictions and the reference for the superficial velocity, respectively, the L^2 distance between the signals

$$\|u_1 - u_2\|_2 = \left(\frac{1}{T} \int_{T_{\text{sim}}-T}^{T_{\text{sim}}} |u_1 - u_2|^2 \, \mathrm{d}t \right)^{\frac{1}{2}} . \tag{37}$$

As we are dealing with periodic signals, we can take advantage of their Fourier series to further split this error into an amplitude and a phase contribution. Using Parseval's identity, we can express the squared L^2 distance as

$$\|u_1 - u_2\|_2^2 = \sum_{k=-\infty}^{\infty} |c_k|^2 \tag{38}$$

where c_k are the Fourier series coefficients of $u_1 - u_2$

$$c_k = \frac{1}{T} \int_{T_{\text{sim}}-T}^{T_{\text{sim}}} (u_1 - u_2) e^{-\mathrm{i}k\frac{2\pi}{T}t} \, \mathrm{d}t = a_k - b_k \tag{39}$$

where a_k and b_k are the Fourier series coefficients of u_1 and u_2, respectively. Expressing the complex numbers a_k and b_k in polar form, we obtain

$$\begin{aligned} \|u_1 - u_2\|_2^2 &= \sum_{k=-\infty}^{\infty} \left| |a_k| \, e^{\mathrm{i}\phi_k} - |b_k| \, e^{\mathrm{i}\psi_k} \right|^2 \\ &= \sum_{k=-\infty}^{\infty} \left| |a_k| - |b_k| \right|^2 + \sum_{k=-\infty}^{\infty} 2 \, |a_k| \, |b_k| \, [1 - \cos(\phi_k - \psi_k)] \, . \end{aligned} \tag{40}$$

The first term represents the difference in the magnitude of the Fourier coefficients and the second term represents the difference in the phase of the Fourier coefficients. Since both terms are positive, we can define an amplitude and a

phase distance

$$d_{\text{ampl.}}(u_1, u_2) = \sqrt{\sum_{k=-\infty}^{\infty} \left| |a_k| - |b_k| \right|^2} \tag{41}$$

$$d_{\text{phase}}(u_1, u_2) = \sqrt{\sum_{k=-\infty}^{\infty} 2\,|a_k|\,|b_k|\,[1 - \cos(\phi_k - \psi_k)]} \tag{42}$$

and the L^2 distance can be decomposed into the sum of squares

$$\|u_1 - u_2\|_2^2 = d_{\text{ampl.}}(u_1, u_2)^2 + d_{\text{phase}}(u_1, u_2)^2 \,. \tag{43}$$

Note that $d_{\text{ampl.}}(u_1, u_2)$ and $d_{\text{phase}}(u_1, u_2)$ are not proper distances in that they can be zero also if $u_1 \neq u_2$. Moreover, $d_{\text{phase}}(u_1, u_2)$ does not satisfy the triangle inequality. However, these definitions ensure that two identical waveforms that are shifted with respect to each other only lead to a phase distance, but not to an amplitude distance. Also, a waveform that is a constant multiple of the other only leads to an amplitude distance, but not to a phase distance.

4 Results

4.1 Comparison of model errors

In this section, we compare the accuracy of the model predictions in response to the forcing (30) with respect to the direct numerical simulation dataset. In particular, we look at the model of Turo and Umnova (2013) given in equation (18), the extended Pride et al (1993) model given in equation (23) and the unsteady Forchheimer equation (16). For the unsteady Forchheimer equations, we take the acceleration coefficient as the static viscous tortuosity α_0 and as the high-frequency limit of the dynamic tortuosity α_∞.

The error of the model predictions with respect to the direct numerical simulation results is quantified using the cycle-averaged L^2 error (37); we further decompose this error into an amplitude (41) and a phase contribution (42) using a Fourier series. Table 3 shows the amplitude and phase contribution to the L^2 error of the different model predictions with respect to the direct numerical simulation dataset. Note that the linear models were not applied to the nonlinear cases since they cannot account for the nonlinear drag and thus would produce large errors at high Reynolds numbers. Both the amplitude error and the phase error make significant contributions to the overall error of the models. The two components are weakly correlated, with the phase error being on average about 57% of the amplitude error, but the importance of the two components varies considerably between models and simulation cases.

For linear flow it can be seen that the dynamic permeability models of Johnson et al (1987) and Pride et al (1993) are very accurate over the entire

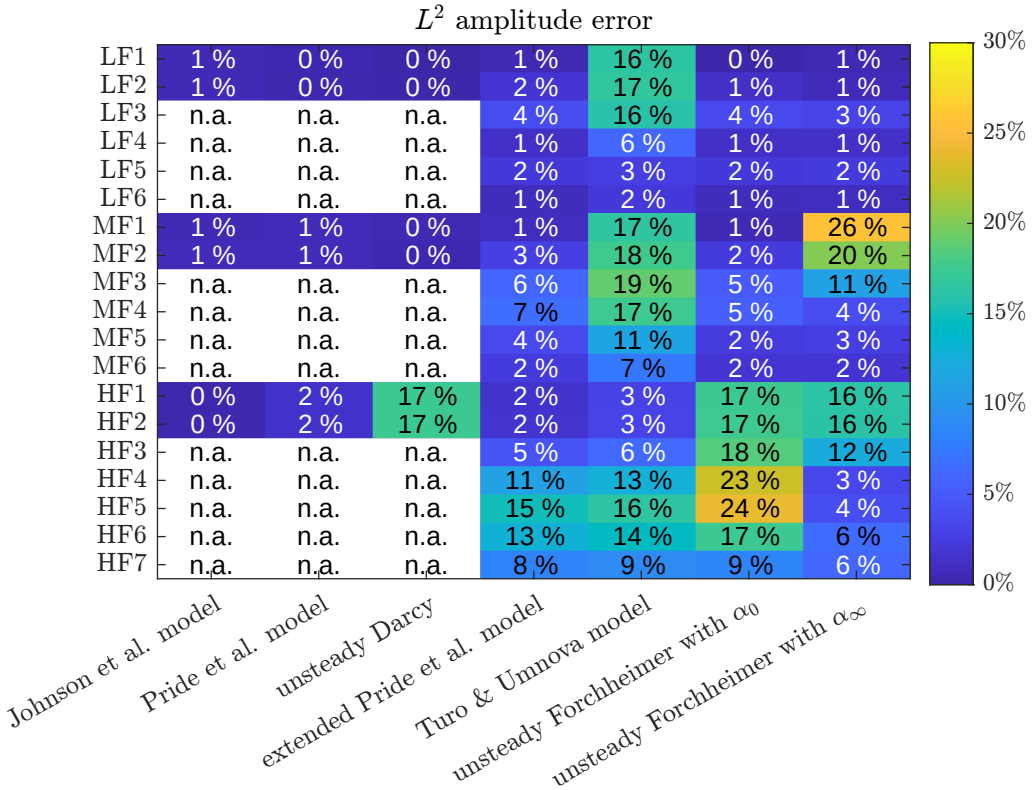

(a)

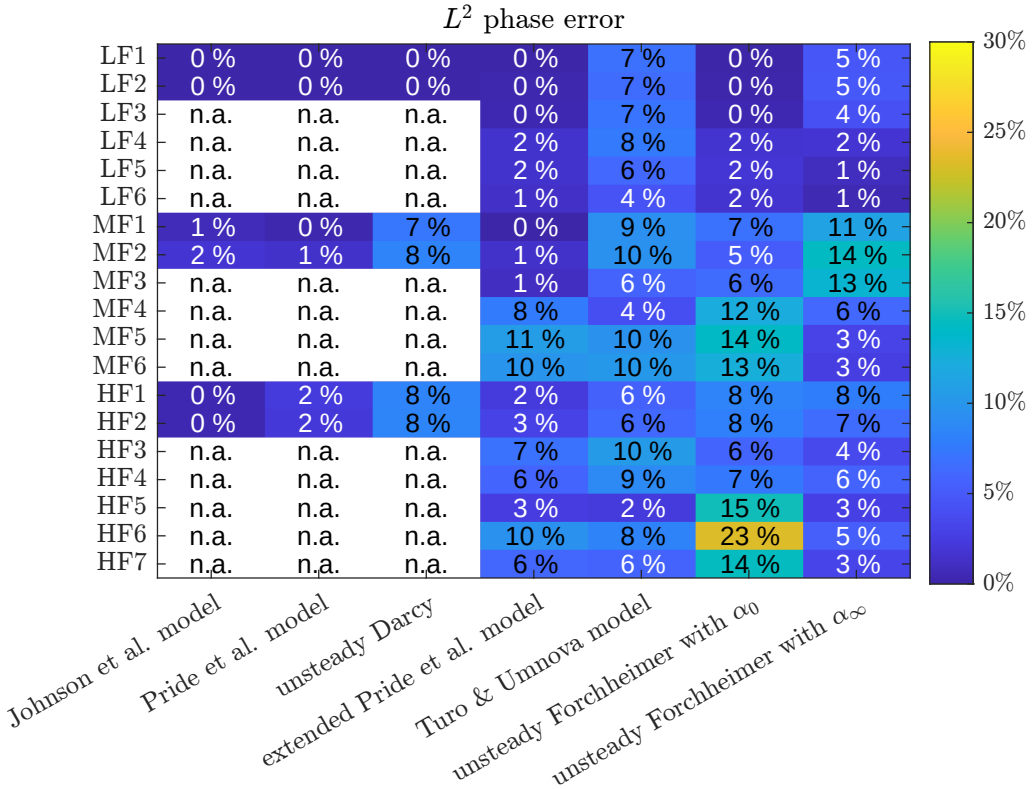

(b)

Table 3: Amplitude and phase contribution to the L^2 error normalised with $\max \langle u \rangle_s$ of the respective flow case. The entries where a linear model would be applied to a nonlinear flow case are marked as n.a. (not applicable).

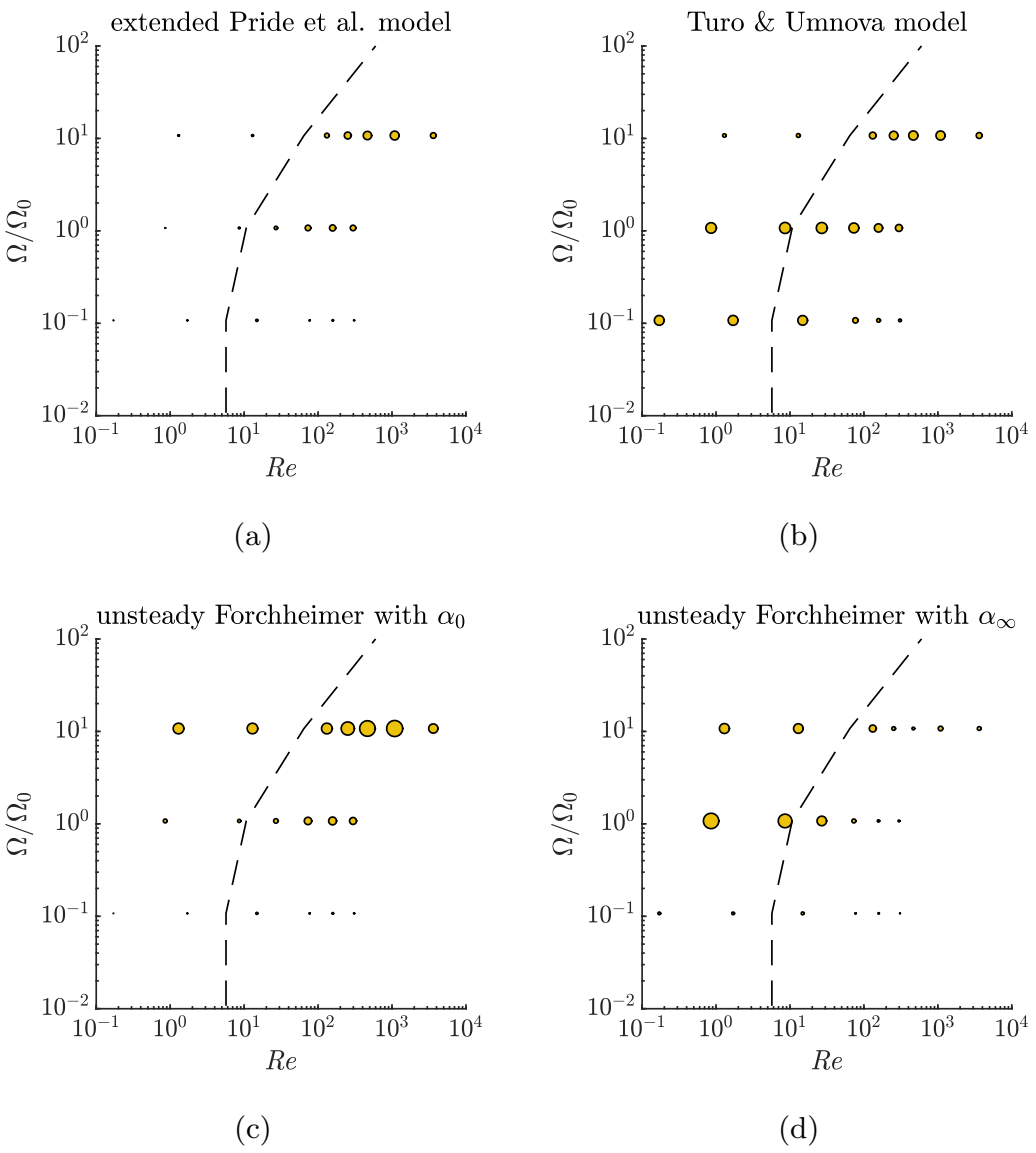

Fig. 6: Distribution of the L^2 model error in the Re–Ω/Ω_0 parameter space. The diameter of the circles is proportional to the L^2 error. The dashed line indicates the approximate boundary between linear and nonlinear flow (Unglehrt and Manhart, 2022a).

frequency range whereas the unsteady Darcy equation of Zhu et al (2014) has very small errors at low frequencies and high errors at high frequencies. Thus, the behaviour of the linear models is consistent with the discussion in section 2.3.

The prediction accuracy of the four nonlinear models shows significant differences depending on the flow case. This is illustrated in figure 6 which shows the variation of the L^2 error of the different nonlinear models over the Re–Wo parameter space.

We find that the extended dynamic permeability model based on the model of Pride et al (1993) has very small errors in linear flow and for flow at low

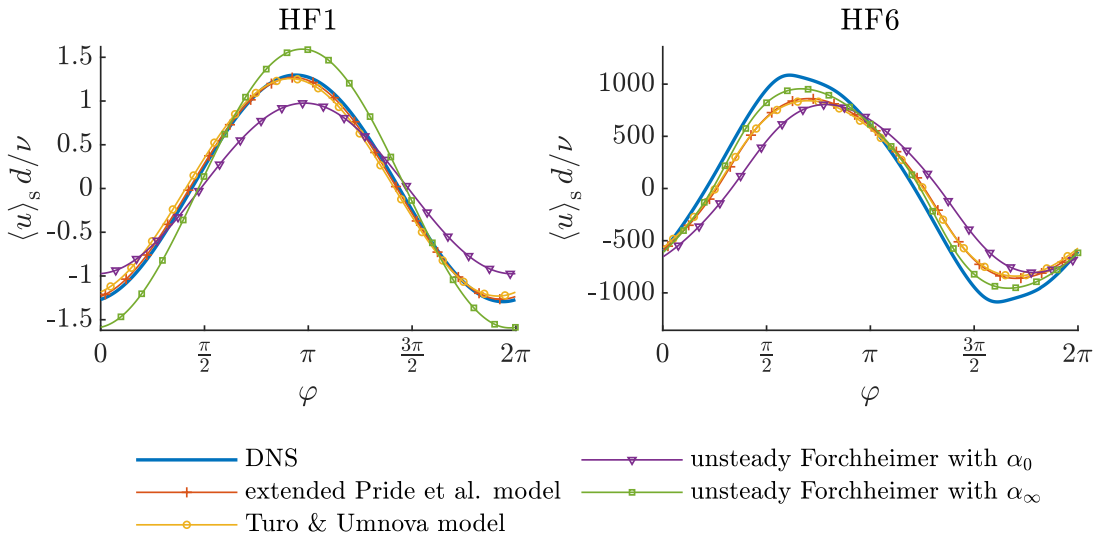

Fig. 7: Comparison of model predictions of the superficial velocity for the cases HF1 and HF6.

frequencies. The reason for this is that the model equation (23) reverts to the model of Pride et al (1993) as $Re \to 0$ and to the steady Forchheimer equation as $\Omega/\Omega_0 \to 0$. The prediction errors are largest for nonlinear flow at high frequencies. Interestingly, the prediction error for the case HF7 ($Re = 3580$) is smaller than for the case HF6 ($Re = 1080$). The model of Turo and Umnova (2013) performs similar to the extended (Pride et al, 1993) model at high frequencies; however, the prediction errors in the medium and low frequency regime are very large. The reason for this is the excessive damping in the linear regime that was discussed in section 2.3. The unsteady Forchheimer equation with the acceleration coefficient based on the static viscous tortuosity α_0 has relatively small errors at low frequencies, moderate errors at medium frequencies and very large errors at high frequencies. The largest errors can be observed in nonlinear flow at high frequencies. In contrast, the unsteady Forchheimer equation with the acceleration coefficient based on the high-frequency limit of the dynamic tortuosity α_∞ has comparably small errors at low frequencies, very large errors in linear flow at medium and high frequencies and small errors for flow at high Reynolds numbers. This somewhat surprising behaviour of the unsteady Forchheimer equation with α_∞ will be investigated in the following section.

4.2 Analysis of prediction errors

In this section, we aim to explain the different error behaviours described above. We first investigate the discrepancies in the linear regime, where the model of Turo and Umnova (2013) (equation 18) and the unsteady Forchheimer equation (16) have large errors at low and high frequencies, respectively. We then proceed to the nonlinear high frequency regime where large discrepancies between the models can be observed and the flow state is characterised by the

interaction between strong accelerations and turbulence. Therefore, we take a closer look at the predictions of the models for the linear case HF1 and for the turbulent case HF6 at $\Omega/\Omega_0 = 10.7$ ($Wo = 100$). Figure 7 shows the predictions of the different models in comparison to the superficial velocity from the simulations.

For the linear case, the model of Turo and Umnova (2013) (equation 18) and the extended Pride et al (1993) model (equation 23) accurately represent the amplitude and phase of the superficial velocity; the errors in the maximum superficial velocity are -3.1% and -2.2%, respectively. This is in agreement with the discussion in section 2.3.1 (figure 1). On the other hand, the unsteady Forchheimer equation (16) with an acceleration coefficient α_0 underpredicts the amplitude of the superficial velocity by 24.8% whereas the unsteady Forchheimer equation with an acceleration coefficient α_∞ overpredicts the amplitude of the superficial velocity by 22.7%.

Since for this case the magnitude of the nonlinear term is only about 1.5% of the linear drag, the unsteady Forchheimer equation is effectively reduced to the unsteady Darcy equation here. Therefore, the behaviour is determined by the acceleration coefficient c and the permeability (contained in the coefficient $a = \mu/K$)). The comparison of the two different choices for the acceleration coefficient c of the unsteady Forchheimer equation thus highlights the effect of the ratio between inertia and linear drag on the superficial velocity. While the choice $c = \rho\,\alpha_\infty/\epsilon$ appears to have too little mass, the choice $c = \rho\,\alpha_0/\epsilon$ appears to have too much mass. Since the behaviour of the case HF1 is sinusoidal, it would be possible to find coefficients for the unsteady Darcy equation that represent the simulation data exactly. However, these best fit coefficients would only be valid at this particular frequency and lead to inconsistent behaviour in the low- and high frequency limit (see also figure 1). Choosing the coefficients as a function of the frequency leads to the frequency domain formulation of the dynamic permeability models (see section 2.1.3). In the time domain, this is reflected in the appearance of a history term.

For the turbulent case, the amplitude of the superficial velocity in the direct numerical simulation is 16% lower than the amplitude of the linear case HF1 scaled by a factor of 10^3 to the same Hagen number. Moreover, the maximum superficial velocity in the case HF6 is attained significantly earlier than in the case HF1 ($\varphi = 0.61\pi$ for HF6 compared to $\varphi = 0.94\pi$ for HF1). It can be seen in figure 7 that all models underpredict the amplitude of the superficial velocity: The error in the maximum superficial velocity is -23% for the model of Turo and Umnova (2013), -21.2% for the extended Pride et al (1993) model, -26.4% for the unsteady Forchheimer equation with α_0 and -12.9% for the unsteady Forchheimer equation with α_∞. The phase is captured satisfactorily by the extended Pride et al (1993) model, the model of Turo and Umnova (2013) and the unsteady Forchheimer equation with α_∞, whereas the unsteady Forchheimer equation with α_0 mispredicts the phase. It can be seen that all models fail to represent the relatively sharp bend at the peak.

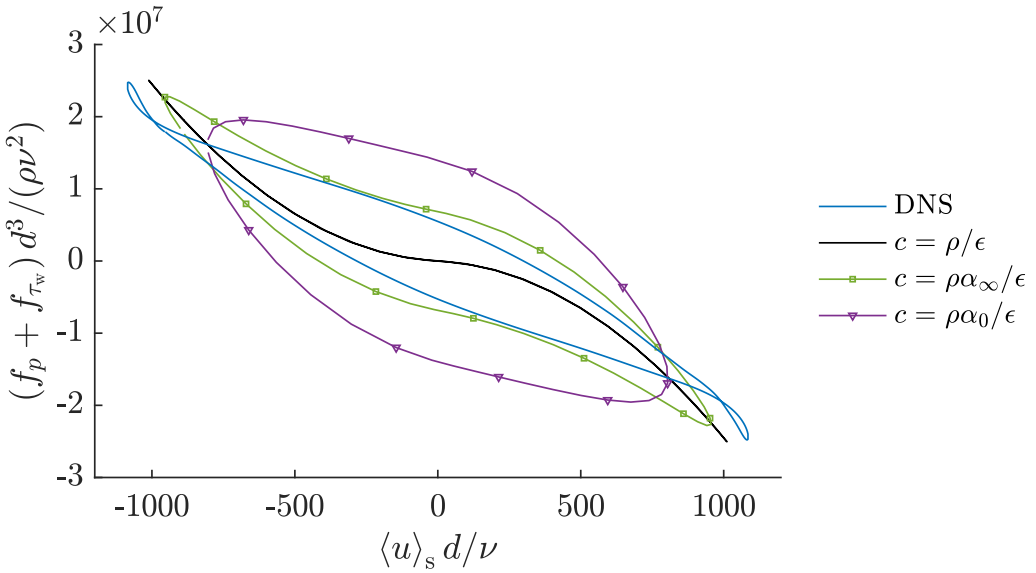

Fig. 8: Comparison of the drag from the direct numerical simulation of the case HF6 with the drag from model solutions to the unsteady Forchheimer equation for the values of the acceleration coefficient $c = \rho/\epsilon$ (quasi-steady closure / zero virtual mass), $c = \rho\,\alpha_\infty/\epsilon$ (high-frequency limit of the dynamic tortuosity) and $c = \rho\,\alpha_0/\epsilon$ (static viscous tortuosity).

It can be seen from the comparison to the linear case that the (identical) nonlinear term in the models causes excessive damping, since even the unsteady Forchheimer equation with an acceleration coefficient $c = \rho\,\alpha_\infty/\epsilon$ underpredicts the amplitude of the simulation. In this sense, the behaviour of the different models could be understood as a compensation or superposition of errors.

This interpretation is supported by figure 8, which compares the drag of the direct numerical simulation of the case HF6 to the drag of model solutions by the unsteady Forchheimer equation for different values of the acceleration coefficient. The drag is determined for each time series according to the volume-averaged momentum equation (2b) as the sum of the acceleration and the pressure gradient. We first consider the curve for the value $c = \rho/\epsilon$, which corresponds to the case of zero virtual mass and was assumed for instance by Sollitt and Cross (1972), Kuznetsov and Nield (2006) or Breugem et al (2006). It can be seen that the drag is a single-valued function of the superficial velocity

$$f_p + f_{\tau_{wx}} = -\epsilon\,(a\,\langle u \rangle_s + b\,|\langle u \rangle_s|\,\langle u \rangle_s)\ . \tag{44}$$

that is identical to the drag in the steady flow (15). For higher values of the acceleration coefficient, the drag becomes a double-valued function of the superficial velocity. Since the drag in the direct numerical simulation is also multi-valued, a nonzero virtual mass ($c > \rho/\epsilon$) is required to represent the correct behaviour. It can be seen that the peak superficial velocity of the model predictions decreases as the acceleration coefficient increases. The peak

superficial velocity of the simulation cannot be reached even for $c = \rho/\epsilon$ for which highest amplitude of the different model predictions is obtained. As $b\,|\langle u \rangle_s| \approx 12a$, this indicates that the nonlinear drag is too large.

It is important to realise that the physical assumptions underlying the different models are not fulfilled in this flow case, for instance:

- The unsteady Forchheimer equation implies an energy equation (see section 2.3.3) in which both the kinetic energy and the dissipation rate are single-valued functions of the instantaneous superficial velocity. This is not the case in the direct numerical simulation: The kinetic energy during acceleration is significantly lower than during deceleration due to the generation of turbulent kinetic energy and the kinetic energy is not in phase with the dissipation rate (Unglehrt and Manhart, 2023b) – as it would have to be if both were single-valued functions of the superficial velocity.
- The model of Turo and Umnova (2013) (and similarly the model of Pride et al (1993)) assume linear Stokes boundary layers at high frequencies that evolve according to an outer potential flow unlimited by convection. However, when the flow separates, the outer flow is modified such that the boundary layers would have to evolve differently, resulting in a different formulation of the history term.

Therefore, different parametrisations of the drag should be explored beyond the models investigated here.

In conclusion, we could explain the mispredictions of the unsteady Forchheimer equation for linear flow at high frequencies. These could be attributed mainly to a mismatch of the ratio between the inertia and the linear drag. A consistent resolution of this issue is provided by the dynamic permeability models that choose this ratio depending on the frequency. The behaviour of the models in nonlinear flow at high frequencies could be partially explained by an overprediction of the nonlinear drag. However, since many intrinsic assumptions of the models are violated in this regime, the overall functional form of the parametrisations should be revisited.

5 Conclusion

In this contribution, we reviewed various models for unsteady porous media flow from the literature and compared their predictions for oscillatory flow through a hexagonal sphere pack. The reference data are direct numerical simulations of Zhu and Manhart (2016); Unglehrt and Manhart (2022a, 2023a,b) for this flow configuration.

The models can be divided into two classes: On the one hand, there are the unsteady variants of the Darcy and Forchheimer equation (Polubarinova-Kochina, 1962); on the other hand, there are the dynamic permeability models (Johnson et al, 1987; Pride et al, 1993) which feature a convolution-type structure in the time domain and nonlinear extensions thereof (Turo and Umnova, 2013).

In linear flow, the dynamic permeability models of Johnson et al (1987); Pride et al (1993) provide an accurate description of the simulation data. The unsteady Darcy equation could be obtained as a special case of these models in which the acceleration coefficient is either based on the static viscous tortuosity α_0 or on the high-frequency limit of the dynamic tortuosity α_∞. The model of Turo and Umnova (2013) is overly dissipative at medium and low frequencies. To alleviate this drawback, we constructed a similar model based on the model of Pride et al (1993).

In nonlinear flow, we compared the unsteady Forchheimer equation for two different choices of the acceleration coefficient, the extended dynamic permeability model of Turo and Umnova (2013) and an analogous formulation based on the model of Pride et al (1993). The unsteady Forchheimer equation with the acceleration coefficient based on the static viscous tortuosity α_0 shows good results in the low frequency regime, but the results deteriorate at higher frequencies and are particularly bad in the high frequency nonlinear regime. On the other hand, the unsteady Forchheimer equation with the acceleration coefficient chosen based on the high-frequency limit of the dynamic tortuosity α_∞ shows very good results at high Reynolds numbers, but incurs large errors in the linear regime. The model of Turo and Umnova (2013) has relatively large errors throughout the entire parameter space. On the other hand, the extension of the model of Pride et al (1993) shows excellent results in the linear regime and at low frequencies numbers, but the results deteriorate for nonlinear flow at high frequencies.

Generally, our proposed extension of the model of Pride et al (1993) along the lines of (Turo and Umnova, 2013) (see section 2.3.2) seems to be a robust choice with accurate results in linear unsteady and nonlinear steady flow and a moderate increase of errors towards strongly accelerated nonlinear flow. The drawback of this model is the additional implementation effort and computational cost caused by the convolution term. For weakly accelerated flow, this model can be simplified to the unsteady Forchheimer equation with an acceleration coefficient $c = \rho\,\alpha_0/\epsilon$ based on the static viscous tortuosity α_0, which is more economical. On the other hand, the unsteady Forchheimer equation with an acceleration coefficient $c = \rho\,\alpha_\infty/\epsilon$ based on the high frequency limit of the dynamic tortuosity α_∞ should be used judiciously since the small errors at large Reynolds numbers must be weighed against large errors for linear unsteady flow.

Further improvements are needed in the parametrisation of the nonlinear drag at high frequencies, as our results indicate that the Forchheimer term leads to an overprediction of the nonlinear drag. Moreover, our previous investigations showed that there is a phase lag between the nonlinear effects in the velocity field and in the drag and the superficial velocity (Unglehrt and Manhart, 2022a, 2023a). It thus seems plausible that introducing a time lag between the nonlinear drag and the superficial velocity could lead to an improved model. Further research should also aim to generalise the present results to different

kinds of porous media, for example random and polydisperse sphere packs, foams, and cylinder arrays.

Declarations

Funding. The authors gratefully acknowledge the financial support of the Deutsche Forschungsgemeinschaft (DFG, German Research Foundation) under grant no. MA2062/13-1. Computing time was granted by the Leibniz Supercomputing Centre on its Linux-Cluster.

Competing Interests. The authors have no relevant financial or non-financial interests to disclose.

Author Contributions. L.U. performed the review of the models from the literature, implemented the models and analysed the simulation data. L.U. and M.M. both contributed to writing the manuscript.

Data Availability. The time series of the superficial velocity and kinetic energy for the simulations LF1–LF4, MF1–MF4 and HF1–HF4 are provided as a supplement to (Unglehrt and Manhart, 2022a). The time series of the superficial velocity and kinetic energy for the simulations LF5, LF6, MF5, MF6 and HF5 are provided as a supplement to (Unglehrt and Manhart, 2023a). The time series of the superficial velocity and kinetic energy for the simulations HF6 and HF7 are provided as a supplement to this work.

References

Aboujafari M, Valipour MS, Hajialimohammadi A, et al (2022) Porous Medium Applications in Internal Combustion Engines: A Review. Transport in Porous Media 141(3):799–824. https://doi.org/10.1007/s11242-022-01750-2

Andreades CH, Cisneros AT, Choi JK, et al (2014) Technical Description of the "Mark 1" Pebble-Bed Fluoride-Salt-Cooled High-Temperature Reactor (PB-FHR) Power Plant. Tech. Rep. UCBTH- 14- 002, Department of Nuclear Engineering University of California, Berkeley, Berkeley

Batchelor GK (2000) An Introduction to Fluid Dynamics. Cambridge University Press, Cambridge, https://doi.org/10.1017/CBO9780511800955

Breugem WP, Boersma BJ, Uittenbogaard RE (2006) The influence of wall permeability on turbulent channel flow. Journal of Fluid Mechanics 562:35. https://doi.org/10.1017/S0022112006000887

Burcharth H, Andersen O (1995) On the one-dimensional steady and unsteady porous flow equations. Coastal Engineering 24(3-4):233–257. https://doi.org/10.1016/0378-3839(94)00025-S

Champoux Y, Allard JF (1991) Dynamic tortuosity and bulk modulus in air-saturated porous media. Journal of Applied Physics 70(4):1975–1979. https://doi.org/10.1063/1.349482

Chapman AM, Higdon JJL (1992) Oscillatory Stokes flow in periodic porous media. Physics of Fluids A: Fluid Dynamics 4(10):2099–2116. https://doi.org/10.1063/1.858507

Chorin AJ (1968) Numerical solution of the Navier-Stokes equations. Mathematics of Computation 22(104):745–762. https://doi.org/10.1090/S0025-5718-1968-0242392-2

Cortis A, Smeulders DMJ, Lafarge D, et al (2002) Geometry Effects on Sound in Porous Media. In: Ehlers W (ed) IUTAM Symposium on Theoretical and Numerical Methods in Continuum Mechanics of Porous Materials, vol 87. Kluwer Academic Publishers, Dordrecht, p 187–192, https://doi.org/10.1007/0-306-46953-7_26

Cortis A, Smeulders DMJ, Guermond JL, et al (2003) Influence of pore roughness on high-frequency permeability. Physics of Fluids 15(6):1766–1775. https://doi.org/10.1063/1.1571545

Darcy H (1856) Les fontaines publiques de la ville de Dijon. Victor Dalmont, Paris

Davit Y, Bell CG, Byrne HM, et al (2013) Homogenization via formal multiscale asymptotics and volume averaging: How do the two techniques compare? Advances in Water Resources 62:178–206. https://doi.org/10.1016/j.advwatres.2013.09.006

Diethelm K, Ford N, Freed A, et al (2005) Algorithms for the fractional calculus: A selection of numerical methods. Computer Methods in Applied Mechanics and Engineering 194(6-8):743–773. https://doi.org/10.1016/j.cma.2004.06.006

Ene H, Sanchez-Palencia E (1975) Equations et phénomènes de surface pour l'écoulement dans un milieu poreux. Journal de Mécanique 14

Ergun S (1952) Fluid Flow Through Packed Columns. Chemical Engineering Progress 48(2):89–94

Firdaouss M, Guermond JL, Le Quéré P (1997) Nonlinear corrections to Darcy's law at low Reynolds numbers. Journal of Fluid Mechanics 343:331–350. https://doi.org/10.1017/S0022112097005843

Forchheimer P (1901) Wasserbewegung durch Boden. Zeitschrift des Vereins deutscher Ingenieure 45:1782–1788

Graham DR, Higdon JJL (2002) Oscillatory forcing of flow through porous media. Part 2. Unsteady flow. Journal of Fluid Mechanics 465. https://doi.org/10.1017/s0022112002001143

Gu Z, Wang H (1991) Gravity waves over porous bottoms. Coastal Engineering 15(5-6):497–524. https://doi.org/10.1016/0378-3839(91)90025-C

Hall KR, Smith GM, Turcke DJ (1995) Comparison of oscillatory and stationary flow through porous media. Coastal Engineering 24(3-4):217–232. https://doi.org/10.1016/0378-3839(94)00017-R

Hill RJ, Koch DL, Ladd AJC (2001) The first effects of fluid inertia on flows in ordered and random arrays of spheres. Journal of Fluid Mechanics 448:213–241. https://doi.org/10.1017/S0022112001005948

Hsu C, Cheng P (1990) Thermal dispersion in a porous medium. International Journal of Heat and Mass Transfer 33(8):1587–1597. https://doi.org/10.1016/0017-9310(90)90015-M

Iliuta I, Larachi F (2016) Three-dimensional simulations of gas-liquid cocurrent downflow in vertical, inclined, and oscillating packed beds. AIChE Journal 62(3):916–927. https://doi.org/10.1002/aic.15071

Iliuta I, Larachi F (2017) CO2 abatement in oscillating packed-bed scrubbers: Hydrodynamics and reaction performances for marine applications. AIChE Journal 63(3):1064–1076. https://doi.org/10.1002/aic.15450

Johnson DL, Koplik J, Dashen R (1987) Theory of dynamic permeability and tortuosity in fluid-saturated porous media. Journal of Fluid Mechanics 176:379–402. https://doi.org/10.1017/S0022112087000727

Kahler DM, Kabala ZJ (2019) Acceleration of Groundwater Remediation by Rapidly Pulsed Pumping: Laboratory Column Tests. Journal of Environmental Engineering 145(1):06018,009. https://doi.org/10.1061/(ASCE)EE.1943-7870.0001479

Kergomard J, Lafarge D, Gilbert J (2013) Transients in Porous Media: Exact and Modelled Time-Domain Green's Functions. Acta Acustica united with Acustica 99(4):557–571. https://doi.org/10.3813/AAA.918635

Koch DL, Ladd AJC (1997) Moderate Reynolds number flows through periodic and random arrays of aligned cylinders. Journal of Fluid Mechanics 349:31–66. https://doi.org/10.1017/S002211209700671X

Kuznetsov AV, Nield DA (2006) Forced Convection with Laminar Pulsating Flow in a Saturated Porous Channel or Tube. Transport in Porous Media 65(3):505–523. https://doi.org/10.1007/s11242-006-6791-6

Lafarge D (1993) Propagation du son dans les matériaux poreux á structure rig ide saturés par un fluide viscothermique: Définition de paramètres géométriques, analogie electromagnétique, temps de relaxation. PhD thesis, Université du Maine, Le Mans

Lafarge D (2009) The Equivalent Fluid Model. In: Bruneau M, Potel C (eds) Materials and Acoustics Handbook. ISTE, London, UK, p 153–204, https://doi.org/10.1002/9780470611609.ch6

Losada I, Losada M, Martín F (1995) Experimental study of wave-induced flow in a porous structure. Coastal Engineering 26(1-2):77–98. https://doi.org/10.1016/0378-3839(95)00013-5

Lowe RJ, Shavit U, Falter JL, et al (2008) Modeling flow in coral communities with and without waves: A synthesis of porous media and canopy flow approaches. Limnology and Oceanography 53(6):2668–2680. https://doi.org/10.4319/lo.2008.53.6.2668

Macdonald IF, El-Sayed MS, Mow K, et al (1979) Flow through Porous Media-the Ergun Equation Revisited. Industrial & Engineering Chemistry Fundamentals 18(3):199–208. https://doi.org/10.1021/i160071a001

Manhart M, Tremblay F, Friedrich R (2001) MGLET: A parallel code for efficient DNS and LES of complex geometries. In: Parallel Computational Fluid Dynamics 2000. North-Holland, Amsterdam, p 449–456, https://doi.org/10.1016/B978-044450673-3/50123-8

Mei CC, Auriault JL (1991) The effect of weak inertia on flow through a porous medium. Journal of Fluid Mechanics 222:647–663. https://doi.org/10.1017/S0022112091001258

Muttray M (2000) Wellenbewegung an und in einem geschütteten Wellenbrecher - Laborexperimente im Großmaßstab und theoretische Untersuchungen. PhD thesis, Technische Universität Braunschweig, Braunschweig

Ni X, Mackley M, Harvey A, et al (2003) Mixing Through Oscillations and Pulsations—A Guide to Achieving Process Enhancements in the Chemical and Process Industries. Chemical Engineering Research and Design 81(3):373–383. https://doi.org/10.1205/02638760360596928

Nield D (1991) The limitations of the Brinkman-Forchheimer equation in modeling flow in a saturated porous medium and at an interface. International Journal of Heat and Fluid Flow 12(3):269–272. https://doi.org/10.1016/0142-727X(91)90062-Z

Nield DA (2000) Resolution of a Paradox Involving Viscous Dissipation and Nonlinear Drag in a Porous Medium. Transport in Porous Media 41(3):349–357. https://doi.org/10.1023/A:1006636605498

Norris AN (1986) On the viscodynamic operator in Biot's equations of poroelasticity. Journal of Wave-material Interaction 1:365–380

Paéz-García CT, Valdés-Parada FJ, Lasseux D (2017) Macroscopic momentum and mechanical energy equations for incompressible single-phase flow in porous media. Physical Review E 95(2). https://doi.org/10.1103/PhysRevE.95.023101

Peller N (2010) Numerische Simulation turbulenter Strömungen mit Immersed Boundaries. PhD thesis, Technische Universität München, München

Peller N, Duc AL, Tremblay F, et al (2006) High-order stable interpolations for immersed boundary methods. International Journal for Numerical Methods in Fluids 52(11):1175–1193. https://doi.org/10.1002/fld.1227

Polubarinova-Kochina PI (1962) Theory of Ground Water Movement. Princeton University Press, Princeton, New Jersey

Pride SR, Morgan FD, Gangi AF (1993) Drag forces of porous-medium acoustics. Physical Review B 47(9):4964–4978. https://doi.org/10.1103/PhysRevB.47.4964

Roncen R, Fellah ZEA, Lafarge D, et al (2018) Acoustical modeling and Bayesian inference for rigid porous media in the low-mid frequency regime. The Journal of the Acoustical Society of America 144(6):3084–3101. https://doi.org/10.1121/1.5080561

Sakai Y, Manhart M (2020) Consistent Flow Structure Evolution in Accelerating Flow Through Hexagonal Sphere Pack. Flow, Turbulence and Combustion 105(2):581–606. https://doi.org/10.1007/s10494-020-00168-4

Schumann U (1977) Realizability of Reynolds-Stress Turbulence Models. Physics of Fluids 20:721–725. https://doi.org/10.1063/1.861942

Shampine L, Reichelt M (1997) The MATLAB ODE Suite. SIAM J Sci Comput https://doi.org/10.1137/S1064827594276424

Simon TW, Seume JR (1988) A Survey of Oscillating Engine Heat Exchangers. Tech. Rep. NASA-CR-182108), University of Minnesota, Minneapolis, Minnesota

Smeulders DMJ, Eggels RLGM, Van Dongen MEH (1992) Dynamic permeability: Reformulation of theory and new experimental and numerical

data. Journal of Fluid Mechanics 245(-1):211. https://doi.org/10.1017/S0022112092000429

Sollitt CK, Cross RH (1972) Wave Transmission through Permeable Breakwaters. In: Coastal Engineering 1972. American Society of Civil Engineers, Vancouver, British Columbia, Canada, pp 1827–1846, https://doi.org/10.1061/9780872620490.106

Trevizoli PV, Peixer GF, Barbosa JR (2016) Thermal–hydraulic evaluation of oscillating-flow regenerators using water: Experimental analysis of packed beds of spheres. International Journal of Heat and Mass Transfer 99:918–930. https://doi.org/10.1016/j.ijheatmasstransfer.2016.03.014

Turo D, Umnova O (2013) Influence of Forchheimer's nonlinearity and transient effects on pulse propagation in air saturated rigid granular materials. The Journal of the Acoustical Society of America 134(6):4763–4774. https://doi.org/10.1121/1.4824969

Umnova O, Turo D (2009) Time domain formulation of the equivalent fluid model for rigid porous media. The Journal of the Acoustical Society of America 125(4):1860–1863. https://doi.org/10.1121/1.3082123

Unglehrt L, Manhart M (2022a) Onset of nonlinearity in oscillatory flow through a hexagonal sphere pack. Journal of Fluid Mechanics 944:A30. https://doi.org/10.1017/jfm.2022.496

Unglehrt L, Manhart M (2022b) Symmetry Breaking and Turbulence in Oscillatory Flow Through a Hexagonal Sphere Pack. In: Proceedings of TSFP-12 (2022) Osaka, Osaka, Japan, p 6

Unglehrt L, Manhart M (2023a) Decomposition of the drag force in steady and oscillatory flow through a hexagonal sphere pack. Journal of Fluid Mechanics 974:A32. https://doi.org/10.1017/jfm.2023.798

Unglehrt L, Manhart M (2023b) Direct and Large–Eddy simulation of turbulent oscillatory flow through a hexagonal sphere pack. In: Marchioli C, Salvetti MV, Garcia-Villalba M, et al (eds) Direct and Large Eddy Simulation XIII: Proceedings of DLES13, 1st edn. No. 31 in ERCOFTAC Series, Springer Cham, p 118–123

van Gent MRA (1993) Stationary and oscillatory flow through coarse porous media. Communications on hydraulic and geotechnical engineering, No 1993-09

van Gent MRA (1994) The modelling of wave action on and in coastal structures. Coastal Engineering 22(3-4):311–339. https://doi.org/10.1016/0378-3839(94)90041-8

van Hinsberg MAT, ten Thije Boonkkamp JHM, Clercx HJH (2011) An efficient, second order method for the approximation of the Basset history force. Journal of Computational Physics 230(4):1465–1478. https://doi.org/10.1016/j.jcp.2010.11.014

Verstappen R, Veldman A (2003) Symmetry-preserving discretization of turbulent flow. Journal of Computational Physics 187(1):343–368. https://doi.org/10.1016/S0021-9991(03)00126-8

Wang CY (2008) The Starting Flow in Ducts Filled with a Darcy–Brinkman Medium. Transport in Porous Media 75(1):55–62. https://doi.org/10.1007/s11242-008-9210-3

Ward JC (1964) Turbulent Flow in Porous Media. Journal of the Hydraulics Division 90(5):1–12. https://doi.org/10.1061/JYCEAJ.0001096

Whitaker S (1967) Diffusion and dispersion in porous media. AIChE Journal 13(3):420–427. https://doi.org/10.1002/aic.690130308

Whitaker S (1986) Flow in porous media I: A theoretical derivation of Darcy's law. Transport in Porous Media 1(1):3–25. https://doi.org/10.1007/BF01036523

Whitaker S (1996) The Forchheimer equation: A theoretical development. Transport in Porous Media 25(1):27–61. https://doi.org/10.1007/BF00141261

Williamson J (1980) Low-storage Runge-Kutta schemes. Journal of Computational Physics 35(1):48–56. https://doi.org/10.1016/0021-9991(80)90033-9

Zhu T (2016) Unsteady porous-media flows. PhD thesis, Technische Universität München, München

Zhu T, Manhart M (2016) Oscillatory Darcy Flow in Porous Media. Transport in Porous Media 111(2):521–539. https://doi.org/10.1007/s11242-015-0609-3

Zhu T, Waluga C, Wohlmuth B, et al (2014) A Study of the Time Constant in Unsteady Porous Media Flow Using Direct Numerical Simulation. Transport in Porous Media 104(1):161–179. https://doi.org/10.1007/s11242-014-0326-3

D.5. A model for the dissipation rate in linear unsteady flow through porous media

Division of work between the authors

Lukas Unglehrt derived the model, performed the simulations and wrote the manuscript. Michael Manhart provided scientific supervision and contributed to writing the manuscript.

Reference

Unglehrt, L. & Manhart, M. 2023 A model for the dissipation rate in linear unsteady flow through porous media. *Journal of Fluid Mechanics* **975**, A42.

Copyright

J. Fluid Mech. (2023), *vol.* 975, A42, doi:10.1017/jfm.2023.889

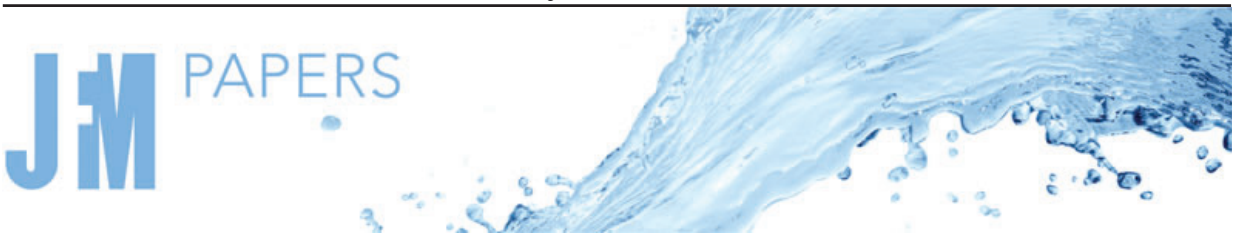

A model for the dissipation rate in linear unsteady flow through porous media

Lukas Unglehrt[1],† **and Michael Manhart**[1]

[1]Professorship of Hydromechanics, Technical University of Munich, Arcisstr. 21, 80333 Munich, Germany

(Received 30 June 2023; revised 24 August 2023; accepted 16 October 2023)

We present a model for the volume-averaged dissipation rate in linear unsteady flow through porous media. The model is derived by blending a new small-time asymptotic expression for the dissipation rate obtained from boundary layer theory with the known large-time asymptotic expression obtained from Darcy's law. The resulting model is a second-order Volterra functional of the volume-averaged acceleration. We validate the model with an analytical solution for transient flow through a porous medium composed of circular tubes and with numerical simulations of transient and oscillatory flow through a cylinder array and through a hexagonal sphere pack.

Key words: porous media

1. Introduction

The theory of unsteady flow through porous media can be applied to a variety of different systems. For example, it can be used to describe wave-induced flow through the seabed (Gu & Wang 1991) or coral reefs (Lowe *et al.* 2008) or the propagation of acoustic and seismic waves through the Earth (Biot 1956*a*,*b*). Furthermore, Cha *et al.* (2007) modelled endovascular coil embolisation, a treatment for aneurysms, as a porous medium interacting with the blood flow. In engineering applications, unsteady flow through porous media can be used to describe regenerator-type heat exchangers (Trevizoli, Peixer & Barbosa 2016) or pulsed flow in chemical reactors (Ni *et al.* 2003).

Using the volume-averaging framework (Whitaker 1966, 1986) or homogenisation theory (Ene & Sanchez-Palencia 1975), a macroscopic description of flow through porous media can be derived from the Navier–Stokes equations. The macroscopic variables are

† Email address for correspondence: lukas.unglehrt@tum.de

the superficial velocity, which is defined as

$$\langle \boldsymbol{u} \rangle_s = \frac{1}{V} \int_{V_f} \boldsymbol{u} \, \mathrm{d}V, \tag{1.1}$$

and the intrinsic pressure, which is defined as

$$\langle p \rangle_i = \frac{1}{V_f} \int_{V_f} p \, \mathrm{d}V, \tag{1.2}$$

where V_f is the volume of fluid contained in the representative volume element or unit cell, which has a combined solid and fluid volume V. The volume averaging gives rise to effective properties of the porous medium, such as the porosity ϵ, which is defined as the ratio V_f/V, and the permeability K, which relates $\langle \boldsymbol{u} \rangle_s$ and $\boldsymbol{\nabla} \langle p \rangle_i$ by Darcy's law $\langle \boldsymbol{u} \rangle_s = K/\mu \, \boldsymbol{\nabla} \langle p \rangle_i$ (Darcy 1856).

Accurate models exist for the superficial velocity in linear flow (Johnson, Koplik & Dashen 1987; Chapman & Higdon 1992; Pride, Morgan & Gangi 1993), which allow the superficial velocity to be calculated in response to an arbitrary forcing. On the other hand, there is no comparably general model for the volume-averaged dissipation rate. Knowledge of the volume-averaged dissipation rate as a functional of the superficial velocity allows computation of the volume-averaged kinetic energy $\langle k \rangle_s = \left\langle \frac{1}{2} \rho \boldsymbol{u}^2 \right\rangle_s$ using the equation (Zhu *et al.* 2014)

$$\frac{\mathrm{d}\langle k \rangle_s}{\mathrm{d}t} = - \langle \boldsymbol{u} \rangle_s \cdot \boldsymbol{\nabla} \langle p \rangle_i - 2\mu \, \langle \boldsymbol{S} : \boldsymbol{S} \rangle_s \,, \tag{1.3}$$

where ρ is the density, μ is the dynamic viscosity and $\boldsymbol{S}$ is the strain rate tensor. The volume-averaged kinetic energy and dissipation rate could be used to model scalar transport in unsteady flow. For instance, the small-time asymptotic descriptions of the dispersion coefficient and the temporal velocity autocorrelation function require knowledge of the volume-averaged kinetic energy and dissipation rate (Brosten 2013, (6.10) and (6.14)). Also, the continuous time random walk description of dispersion involves the volume-averaged kinetic energy of the Stokes flow (Cortis *et al.* 2004, (7) and (8)).

The volume-averaged dissipation rate in a steady linear flow has been given, for example, by Murthy & Singh (1997) or Zhu *et al.* (2014) as

$$2\mu \, \langle \boldsymbol{S} : \boldsymbol{S} \rangle_s = \frac{\mu}{K} \, \langle \boldsymbol{u} \rangle_s^2 \,, \tag{1.4}$$

which was derived by equating the dissipation rate to the power input into the flow and then using Darcy's law. This expression was confirmed by Paéz-García, Valdés-Parada & Lasseux (2017), who applied an upscaling procedure to the mechanical energy equation. On the other hand, no comparable equation has been given for the volume-averaged dissipation rate in unsteady linear flow. A difficulty in modelling the dissipation rate arises from its nonlinear dependence on the velocity field. Thus, unlike the superficial velocity, the dissipation rate therefore cannot be obtained from a superposition of single-frequency modes (for which the dissipation rate has been computed, for example, by Johnson *et al.* (1987)).

In this paper, we present a time domain model for the volume-averaged dissipation rate in linear unsteady flow. The model is derived by blending the steady-state dissipation rate (1.4) with the small-time limit of the dissipation rate obtained from boundary layer theory. The model is validated with an analytical solution of transient flow through a bundle of

circular tubes and with direct numerical simulations (DNS) of flow through a periodic cylinder array and a periodic sphere pack.

2. Derivation of the model

2.1. *Boundary layer theory*

In this section, we derive a new asymptotic expression for the volume-averaged dissipation rate in linear flow that is valid in the small-time or high-frequency limits. Under these circumstances, the local acceleration term of the unsteady Stokes equation is dominant compared with the viscous term and the flow is laminar and has a boundary layer structure (Schlichting & Gersten 2017, pp. 349–350).

For the sake of this derivation, we assume that the flow is at rest at $t = 0$ and that the macroscopic pressure gradient is applied for $t \geq 0$. Then, for small times, the flow can be approximated as a potential core flow and a viscous boundary layer flow (Schlichting & Gersten 2017, pp. 352–353) and the velocity profile in the boundary layer is locally given by the solution to Stokes' first problem (Schlichting & Gersten 2017, pp. 126–128)

$$\boldsymbol{u}(y,t) = \int_0^t \left.\frac{\partial \boldsymbol{U}}{\partial \tau}\right|_{y=0} \operatorname{erf}\left(\frac{y}{2\sqrt{\nu(t-\tau)}}\right) \mathrm{d}\tau. \tag{2.1}$$

Here, $\nu = \mu/\rho$ is the kinematic viscosity and y is the local wall-normal coordinate. The velocity of the potential core flow $\boldsymbol{U}(\boldsymbol{x}, t)$ can be obtained from the theory of unsteady potential flow (Batchelor 2000, pp. 394–409) for a given pore geometry. As will be discussed below, $\boldsymbol{U}(\boldsymbol{x}, t)$ enters the volume-averaged dissipation rate only through the two integral quantities α_∞ and Λ (2.6), which have been tabulated for simple geometries (Chapman & Higdon 1992; Lee, Leamy & Nadler 2009). The volume-averaged dissipation rate is equal to the sum of the dissipation in the boundary layer and the dissipation in the potential core flow (Johnson *et al.* 1987),

$$2\mu \langle \boldsymbol{S} : \boldsymbol{S} \rangle_s = \underbrace{\frac{\mu}{V} \int_{A_{fs}} \int_0^\infty \left(\frac{\partial \boldsymbol{u}}{\partial y}\right)^2 \mathrm{d}y \, \mathrm{d}A}_{\text{boundary layer}} + \underbrace{\frac{\mu}{V} \int_{A_{fs}} \nabla |\boldsymbol{U}|^2 \cdot \boldsymbol{n} \, \mathrm{d}A}_{\text{potential flow } (\approx 0)}, \tag{2.2}$$

where A_{fs} denotes the fluid–solid interface. As observed by Johnson *et al.* (1987), the boundary layer term increases with frequency whereas the potential flow term is independent of frequency and can be neglected. In the boundary layer contribution, we can identify the dissipation integral

$$D = \int_0^\infty \left(\frac{\partial \boldsymbol{u}}{\partial y}\right)^2 \mathrm{d}y = \int_0^\infty \left[\int_0^t \left.\frac{\partial \boldsymbol{U}}{\partial \tau}\right|_{y=0} \exp\left(-\frac{y^2}{4\nu(t-\tau)}\right) \frac{1}{\sqrt{\pi\nu(t-\tau)}} \mathrm{d}\tau\right]^2 \mathrm{d}y. \tag{2.3}$$

Here, we have departed from Johnson *et al.* (1987) in pursuing a time-domain approach. Now, we change the order of spatial and temporal integration. With the integral

$$\int_0^\infty \exp\left(-\frac{y^2}{4\nu(t-\tau_1)}\right) \exp\left(-\frac{y^2}{4\nu(t-\tau_2)}\right) \mathrm{d}y = \sqrt{\frac{\pi\nu(t-\tau_1)(t-\tau_2)}{(t-\tau_1)+(t-\tau_2)}}, \tag{2.4}$$

we can rewrite the dissipation integral as a double convolution,

$$D = \int_0^t \int_0^t \left.\frac{\partial \boldsymbol{U}}{\partial \tau_1}\right|_{y=0} \left.\frac{\partial \boldsymbol{U}}{\partial \tau_2}\right|_{y=0} \frac{1}{\sqrt{\pi\nu\left[(t-\tau_1)+(t-\tau_2)\right]}} \mathrm{d}\tau_1 \, \mathrm{d}\tau_2. \tag{2.5}$$

The spatial integration has thus changed the square of a one-dimensional convolution integral into a two-dimensional convolution integral. For the potential flow, there is a time-independent proportionality between the potential flow velocity at the wall $\boldsymbol{U}|_{y=0}$ and the superficial velocity $\langle \boldsymbol{U} \rangle_s$ of the potential flow. This relationship is expressed by the high-frequency limit of the dynamic tortuosity α_∞ and the characteristic viscous length Λ derived by Johnson *et al.* (1987):

$$\frac{\alpha_\infty}{\epsilon} = \frac{\langle \boldsymbol{U}^2 \rangle_s}{\langle \boldsymbol{U} \rangle_s^2}, \tag{2.6a}$$

$$\frac{2}{\Lambda} = \frac{\dfrac{1}{V}\displaystyle\int_{A_{fs}} |\boldsymbol{U}|^2 \, \mathrm{d}A}{\langle \boldsymbol{U}^2 \rangle_s}. \tag{2.6b}$$

Using these expressions, the surface integral over the dissipation integral in (2.2) can be rewritten in terms of the superficial velocity of the potential flow. Furthermore, the superficial velocity of the potential flow can be approximated with the actual superficial velocity provided that the boundary layer is very thin. This gives the final expression for the volume-averaged dissipation rate in the small-time limit

$$2\mu \langle \boldsymbol{S} : \boldsymbol{S} \rangle_s = \frac{2\mu\alpha_\infty}{\epsilon\Lambda} \int_0^t \int_0^t \frac{\mathrm{d}\langle \boldsymbol{u} \rangle_s}{\mathrm{d}\tau_1} \cdot \frac{\mathrm{d}\langle \boldsymbol{u} \rangle_s}{\mathrm{d}\tau_2} \frac{1}{\sqrt{\pi\nu\,[(t-\tau_1)+(t-\tau_2)]}} \, \mathrm{d}\tau_1 \, \mathrm{d}\tau_2 \,, \tag{2.7}$$

which is a key result of this study.

2.2. *Blending of steady and boundary layer asymptotics*

In this section, we use the expressions for the volume-averaged dissipation rate for small times (2.7) and for the steady state (1.4) to construct a model for the volume-averaged dissipation rate that is valid for linear flow.

We begin by rewriting the steady-state dissipation rate (1.4) as a second-order Volterra integral similar to (2.7):

$$2\mu \langle \boldsymbol{S} : \boldsymbol{S} \rangle_s = \frac{\mu}{K} \langle \boldsymbol{u} \rangle_s^2 = \frac{\mu}{K} \int_0^t \int_0^t \frac{\mathrm{d}\langle \boldsymbol{u} \rangle_s}{\mathrm{d}\tau_1} \cdot \frac{\mathrm{d}\langle \boldsymbol{u} \rangle_s}{\mathrm{d}\tau_2} \, \mathrm{d}\tau_1 \, \mathrm{d}\tau_2. \tag{2.8}$$

This leads us to consider a general model for the dissipation rate in the linear regime of the following form:

$$2\mu \langle \boldsymbol{S} : \boldsymbol{S} \rangle_s = \int_0^t \int_0^t \frac{\mathrm{d}\langle \boldsymbol{u} \rangle_s}{\mathrm{d}\tau_1} \cdot \frac{\mathrm{d}\langle \boldsymbol{u} \rangle_s}{\mathrm{d}\tau_2} \, g(t-\tau_1, t-\tau_2) \, \mathrm{d}\tau_1 \, \mathrm{d}\tau_2, \tag{2.9}$$

where the kernel function $g(t_1, t_2)$ is assumed to be symmetric, $g(t_1, t_2) = g(t_2, t_1)$, and satisfies the limits

$$\lim_{t_1 \to 0} \lim_{t_2 \to 0} g(t_1, t_2) = \frac{2\mu\alpha_\infty}{\epsilon\Lambda} \frac{1}{\sqrt{\pi\nu\,[t_1 + t_2]}}, \tag{2.10a}$$

$$\lim_{t_1 \to \infty} \lim_{t_2 \to \infty} g(t_1, t_2) = \frac{\mu}{K}. \tag{2.10b}$$

The latter condition can be explained as follows: for a function that varies very slowly, only a small part of the history will be affected by the small-time limit of $g(t_1, t_2)$, while most of the history will be weighted with μ/K, thus approaching the steady-state limit.

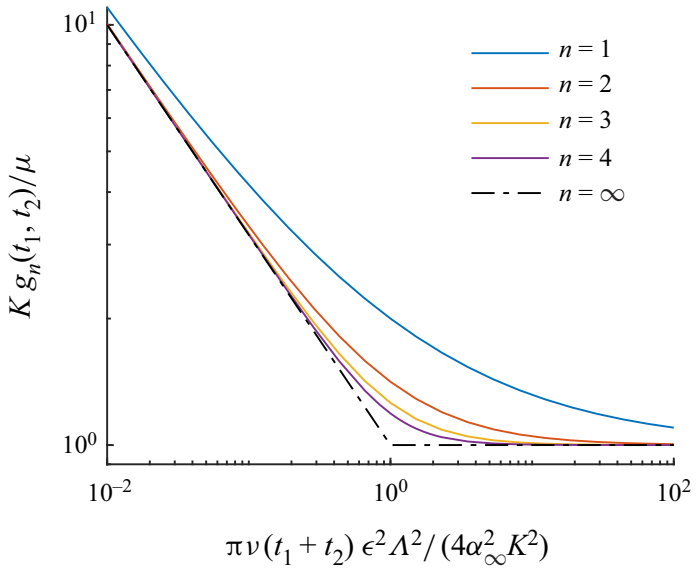

Figure 1. Kernel function $g_n(t_1, t_2)$ for different values of the blending parameter n in logarithmic axes. The kernel function is universal in the chosen normalisation.

Following Churchill & Usagi (1972), we consider the following family of models:

$$g_n(t_1, t_2) = \left[\left(\frac{\mu}{K}\right)^n + \left(\frac{2\mu\alpha_\infty}{\epsilon\Lambda}\frac{1}{\sqrt{\pi\nu\,[t_1 + t_2]}}\right)^n\right]^{1/n}, \tag{2.11}$$

where n is a real number. In this blending, the transition between the small- and large-time behaviour occurs when the limiting expressions (2.10) take the same value. The family parameter n could be determined using additional information about the dissipation rate. Here, the parameter will be estimated empirically based on analytical solutions and numerical simulations. Figure 1 shows the kernel function (2.11) for different values of the parameter n. It can be seen that the width of the transition region between the asymptotes decreases with increasing values of n.

In the remainder of this paper, the proposed model is validated using analytical and numerical solutions to the (Navier–)Stokes equations for unsteady flow through porous media.

3. Analytical validation

In this section, we validate the model for the case of transient flow through a porous medium consisting of cylindrical tubes of radius R that are inclined by an angle θ with respect to the pressure gradient. Johnson *et al.* (1987) reported the exact values for the permeability, the high-frequency limit of the dynamic tortuosity and the characteristic viscous length for this case,

$$K = \tfrac{1}{8}\,\epsilon\,R^2\cos^2\theta, \tag{3.1a}$$

$$\alpha_\infty = \frac{1}{\cos^2\theta}, \tag{3.1b}$$

$$\Lambda = R. \tag{3.1c}$$

In the following, we show that the volume-averaged dissipation rate obtained from the analytical solution agrees with the asymptotic limits (2.7) and (1.4) and we compare our proposed model (2.11) for the volume-averaged dissipation rate with the exact solution.

3.1. *Exact solution for the dissipation rate*

The analytical solution for the streamwise velocity in transient flow through a circular pipe is given as (Pozrikidis 2017, pp. 509–514)

$$u_s(r,t) = \frac{1}{4\mu}\left|\nabla\langle p\rangle_i\right|\cos\theta\left[R^2 - r^2 - 8R^2\sum_{k=1}^{\infty}\frac{1}{\alpha_k^3}\frac{\mathrm{J}_0(\alpha_k r/R)}{\mathrm{J}_1(\alpha_k)}\exp\left(-\alpha_k^2\frac{\nu t}{R^2}\right)\right], \tag{3.2}$$

where $\mathrm{J}_n(z)$ are the Bessel functions of the first kind and α_k denotes the kth zero of the Bessel function J_0. The velocity gradient can be calculated as

$$\frac{\partial u_s}{\partial r} = \frac{1}{4\mu}\left|\nabla\langle p\rangle_i\right|\cos\theta\left[-2r + 8R\sum_{k=1}^{\infty}\frac{1}{\alpha_k^2}\frac{\mathrm{J}_1(\alpha_k r/R)}{\mathrm{J}_1(\alpha_k)}\exp\left(-\alpha_k^2\frac{\nu t}{R^2}\right)\right]. \tag{3.3}$$

We can then obtain the superficial volume-averaged dissipation rate by integration as

$$\begin{aligned}
&2\mu\,\langle \boldsymbol{S}:\boldsymbol{S}\rangle_s \\
&\quad= \frac{\epsilon\mu}{\pi R^2}\int_0^R\left(\frac{\partial u_s}{\partial r}\right)^2 2\pi r\,\mathrm{d}r \\
&\quad= \frac{1}{8\mu}\epsilon R^2\cos^2\theta\left|\nabla\langle p\rangle_i\right|^2\int_0^1\left[-2x + 8\sum_{k=1}^{\infty}\frac{1}{\alpha_k^2}\frac{\mathrm{J}_1(\alpha_k x)}{\mathrm{J}_1(\alpha_k)}\exp\left(-\alpha_k^2\frac{\nu t}{R^2}\right)\right]^2 x\,\mathrm{d}x \\
&\quad= \frac{1}{8\mu}\epsilon R^2\cos^2\theta\left|\nabla\langle p\rangle_i\right|^2\left[\int_0^1 4x^3\,\mathrm{d}x\right. \\
&\qquad - 32\sum_{k=1}^{\infty}\frac{1}{\alpha_k^2\,\mathrm{J}_1(\alpha_k)}\exp\left(-\alpha_k^2\frac{\nu t}{R^2}\right)\int_0^1 x^2\,\mathrm{J}_1(\alpha_k x)\,\mathrm{d}x \\
&\qquad \left. + 64\sum_{k=1}^{\infty}\sum_{l=1}^{\infty}\frac{1}{\alpha_k^2\,\mathrm{J}_1(\alpha_k)\,\alpha_l^2\,\mathrm{J}_1(\alpha_l)}\exp\left(-(\alpha_k^2+\alpha_l^2)\frac{\nu t}{R^2}\right)\int_0^1 x\,\mathrm{J}_1(\alpha_k x)\,\mathrm{J}_1(\alpha_l x)\,\mathrm{d}x\right] \\
&\quad= \frac{1}{8\mu}\epsilon R^2\cos^2\theta\left|\nabla\langle p\rangle_i\right|^2\left[1 - 64\sum_{k=1}^{\infty}\frac{1}{\alpha_k^4}\exp\left(-\alpha_k^2\frac{\nu t}{R^2}\right) + 32\sum_{k=1}^{\infty}\frac{1}{\alpha_k^4}\exp\left(-2\alpha_k^2\frac{\nu t}{R^2}\right)\right] \\
&\quad= \frac{K}{\mu}\left|\nabla\langle p\rangle_i\right|^2\left[1 - 64\sum_{k=1}^{\infty}\frac{1}{\alpha_k^4}\exp\left(-\alpha_k^2\frac{\nu t}{R^2}\right) + 32\sum_{k=1}^{\infty}\frac{1}{\alpha_k^4}\exp\left(-2\alpha_k^2\frac{\nu t}{R^2}\right)\right].
\end{aligned} \tag{3.4}$$

At the starting time $t = 0$, the dissipation vanishes since the zeros of the Bessel function J_0 satisfy

$$\sum_{k=1}^{\infty}\frac{1}{\alpha_k^4} = \frac{1}{32}. \tag{3.5}$$

At large times, the exponential terms tend to zero and we arrive at (1.4) using Darcy's law.

3.2. *Small- and large-time asymptotics*

In this section, we compare the small- and large-time asymptotics of the volume-averaged dissipation rate given by (2.7) and (1.4) with the exact dissipation rate. To evaluate these expressions, we need to determine the superficial velocity and the superficial acceleration. The superficial velocity can be obtained by averaging the velocity (3.2) over

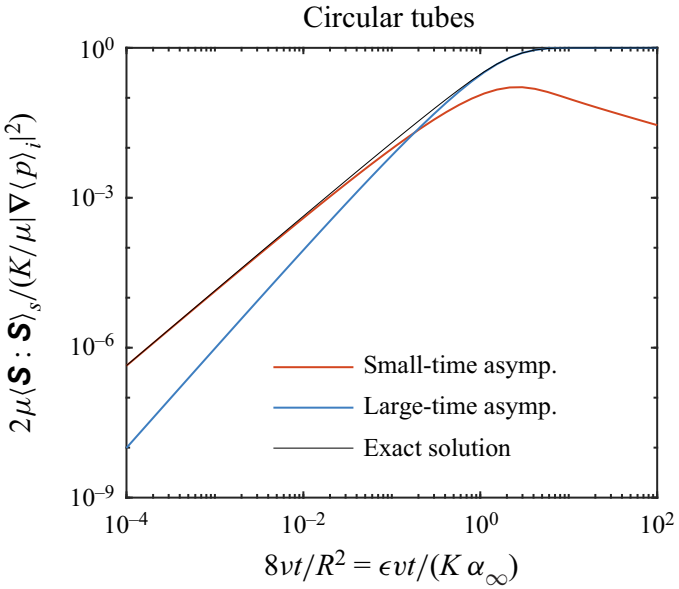

Figure 2. Comparison of the dissipation rate of the analytical solution (3.4) with the small- and large-time asymptotics (2.7) and (1.4) for a porous medium consisting of circular tubes. The dissipation is normalised with the steady-state value $K/\mu|\nabla\langle p\rangle_i|^2$.

the cross-section and then projecting it onto the direction of the pressure gradient (which amounts to a multiplication with $\cos\theta$). Using the permeability (3.1*a*) we get

$$\langle u\rangle_s = \frac{K}{\mu}\left|\nabla\langle p\rangle_i\right|\left[1 - 32\sum_{k=1}^{\infty}\frac{1}{\alpha_k^4}\exp\left(-\alpha_k^2\frac{\nu t}{R^2}\right)\right]. \tag{3.6}$$

By differentiation, the superficial acceleration follows as

$$\frac{\mathrm{d}\langle u\rangle_s}{\mathrm{d}t} = \frac{\epsilon}{\rho\alpha_\infty}\left|\nabla\langle p\rangle_i\right|\left[4\sum_{k=1}^{\infty}\frac{1}{\alpha_k^2}\exp\left(-\alpha_k^2\frac{\nu t}{R^2}\right)\right]. \tag{3.7}$$

We then evaluate the small-time asymptotics (2.7) using adaptive quadrature. Figure 2 shows the exact dissipation rate (3.4) and the small- and large-time asymptotics according to the equations (2.7) and (1.4). It can be seen that the dissipation rate is indeed well approximated by the boundary layer theory for small times and by the steady-state behaviour at large times. Note that if the superficial velocity (3.6) is substituted into the steady-state dissipation (1.4), the first two terms of the exact dissipation rate (3.4) are exactly recovered.

3.3. *Evaluation of model predictions*

Having demonstrated the correctness of the asymptotic limits, we can now evaluate the proposed model for the volume-averaged dissipation rate given by (2.9) and (2.11). Figure 3 shows the exact solution for the dissipation rate (3.4), the large-time asymptotics (1.4) and the modelled dissipation rate. For the blending parameter n, we have chosen the values $n = 2$ and $n = 3$ for which the predictions lie closest to the exact solution. It can be seen that the model accurately predicts the dissipation rate and has the correct limiting behaviour. The maximum relative error with respect to the instantaneous dissipation rate is 7 % for $n = 2$ and 14 % for $n = 3$.

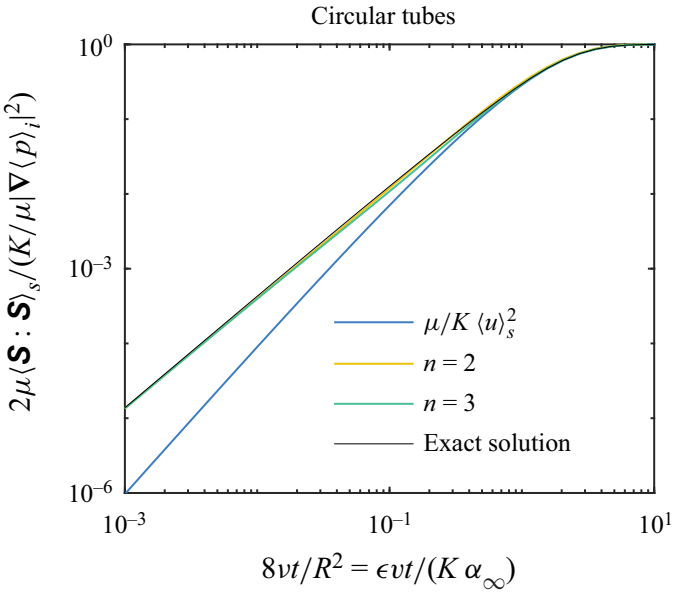

Figure 3. Comparison of the dissipation rate of the analytical solution (3.4), the large-time asymptotics (1.4) and the model given by (2.9), (2.11) for a porous medium consisting of circular tubes. The dissipation is normalised with the steady-state value $K/\mu|\boldsymbol{\nabla}\langle p\rangle_i|^2$.

4. Numerical validation

In this section, we further compare the volume-averaged dissipation rate modelled according to the equations (2.9) and (2.11) with the volume-averaged dissipation rate obtained from the DNS of flow through a cylinder array and a hexagonal sphere pack.

4.1. *Description of the flow solver*

The simulations were performed using our in-house code MGLET (Manhart, Tremblay & Friedrich 2001). The incompressible Navier–Stokes equations are discretised on a Cartesian grid with a second-order symmetry-preserving finite volume method (Verstappen & Veldman 2003). A third-order explicit Runge–Kutta method (Williamson 1980) is employed for time integration of the momentum equation and the continuity equation is enforced using the projection method (Chorin 1968), resulting in a Poisson equation at each stage.

The no-slip and no-penetration boundary conditions at the fluid–solid interface of the porous medium are imposed using a second-order accurate ghost-cell immersed boundary method (Peller *et al.* 2006; Peller 2010). The conservation of mass in the interface cells is ensured by a flux correction procedure that is iteratively coupled to the global pressure correction. The immersed boundary method has been validated for the simulation of porous media flow in Peller (2010), Sakai & Manhart (2020) and Unglehrt & Manhart (2022).

4.2. *Porous medium geometries*

Following Zhu *et al.* (2014), we consider flow through a periodic array of cylinders and through a hexagonal close-packed arrangement of spheres. The corresponding simulation domains are shown in figure 4. These porous media have a considerably different porosity ($\epsilon = 0.56$ and 0.26, respectively) and pore space geometry.

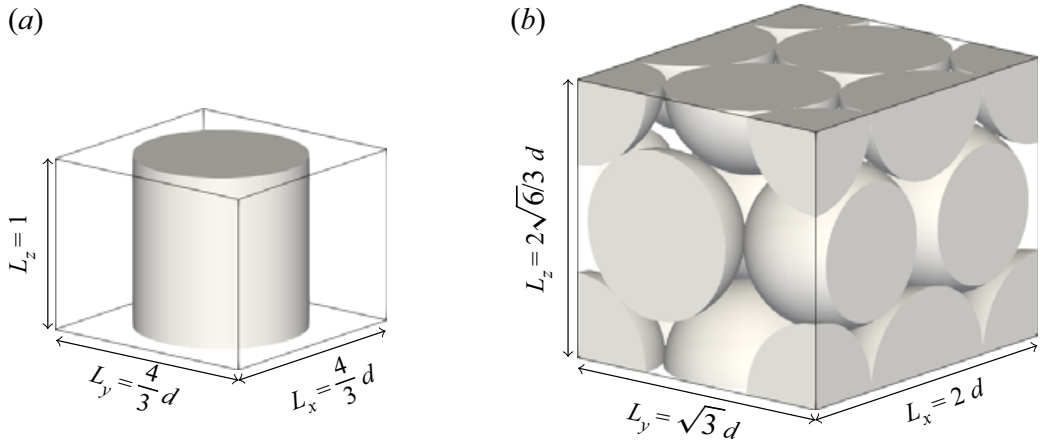

Figure 4. Simulation domains for the cylinder array and for the hexagonal sphere pack. Periodic boundary conditions are applied on all sides of the domain.

Parameter	Symbol	Cylinder array	Hexagonal sphere pack
Porosity	ϵ	$1 - (9\pi/64) = 0.5582$	$1 - (\pi/(3\sqrt{2})) = 0.2595$
Permeability	K	$5.768 \times 10^{-3}\, d^2$	$1.755 \times 10^{-4}\, d^2$
High-frequency limit of the dynamic tortuosity	α_∞	1.461	1.622
Characteristic viscous length	Λ	$0.438\, d$	$5.904 \times 10^{-2}\, d$

Table 1. Geometric parameters for the cylinder array and the hexagonal close-packed arrangement of equal spheres.

Case	Hg	Re	Wo	Ω/Ω_0	$d/\Delta x$
cyl-step	0.1	5.74×10^{-4}	—	—	480
cyl-LF	0.1	5.72×10^{-4}	2.576	0.1	480
cyl-MF	0.1	3.62×10^{-4}	8.146	1.0	480
cyl-HF	0.1	5.08×10^{-5}	25.76	10	480
hcp-step[a]	6.5×10^1	0.0114	—	—	320
hcp-LF[b]	10^3	0.171	10	0.107	384
hcp-MF[b]	10^4	0.857	31.6	1.07	384
hcp-HF[b]	10^5	0.130	100	10.7	384

Table 2. Simulation parameters for flow through a cylinder array and a hexagonal sphere pack.
[a]From Sakai & Manhart (2020), recomputed at a higher resolution in Unglehrt & Manhart (2023).
[b]From Unglehrt & Manhart (2022).

The geometric parameters of these porous media are reported in table 1. The high-frequency limit of the dynamic tortuosity α_∞ and the characteristic viscous length Λ were determined from the potential flow using a finite element calculation (see Unglehrt & Manhart (2023) for the hexagonal sphere pack). The permeability values were obtained from the steady state of the simulations cyl-step and hcp-step (see table 2).

4.3. *Simulation set-up*

The pore scale flow is described by the incompressible Navier–Stokes equations. However, a small Reynolds number is chosen such that the nonlinear terms are insignificant.

No-slip and no-penetration boundary conditions are imposed at the cylinder or spheres and triple periodic boundary conditions are applied at the domain boundaries.

We consider flow started from rest in response to a constant pressure gradient

$$\nabla \langle p \rangle_i(t) = -g_x \, \boldsymbol{e}_x \quad \text{for } t > 0 \tag{4.1}$$

and in response to a sinusoidal pressure gradient

$$\nabla \langle p \rangle_i(t) = -g_x \, \sin(\Omega t) \, \boldsymbol{e}_x \quad \text{for } t > 0 \tag{4.2}$$

that are applied as a body force on the fluid. In the latter case, we have chosen three values of the frequency: $\Omega/\Omega_0 = 0.1$ (low frequency), $\Omega/\Omega_0 = 1$ (medium frequency) and $\Omega/\Omega_0 = 10$ (high frequency) where $\Omega_0 = \epsilon \, \nu/(\alpha_\infty \, K)$ is the transition frequency between the low and the high frequency regime (Pride *et al.* 1993). Note that the high-frequency cases represent behaviour that could be found, for example, in wave-induced flow in a coral reef ($d \sim 2$ cm, period $\sim$4 s, wind velocity $\sim$5 m s^{-1}, wave height $\sim$0.6 m, water depth $\sim$30 m), while the low- and medium-frequency cases would correspond to flow within a sandy seabed.

The flow cases for the cylinder array were simulated at a grid resolution of 480 cells per diameter following Zhu & Manhart (2016). The flow cases for the hexagonal sphere pack were simulated at a resolution of 384 cells per diameter for the oscillatory flow and at a resolution of 320 cells per diameter for the transient flow. They were validated by a grid study in Unglehrt & Manhart (2022) and Sakai & Manhart (2020). The important parameters of the simulations are summarised in table 2.

The time series of the volume-averaged dissipation rate was obtained indirectly from the time series of the superficial velocity and the volume-averaged kinetic energy using the kinetic energy equation (1.3),

$$2\mu \, \langle \boldsymbol{S} : \boldsymbol{S} \rangle_s = - \langle \boldsymbol{u} \rangle_s \cdot \nabla \langle p \rangle_i - \frac{\mathrm{d}\langle k \rangle_s}{\mathrm{d}t}. \tag{4.3}$$

The superficial velocity and the volume-averaged kinetic energy were extracted from the simulation with a high temporal resolution.

4.4. *Results*

We first consider the case of transient flow started from rest and driven by a constant pressure gradient. Figure 5 shows the volume-averaged dissipation rate from the DNS cyl-step and hcp-step, the large-time asymptotics (1.4) and the model evaluated for the values $n = 2$ and $n = 3$ of the blending parameter. It can be seen that the model correctly captures the small-time behaviour of the simulations whereas the dissipation rate clearly cannot be approximated by (1.4) at small times. After the first few time steps, in which the simulations are not fully accurate due to the extremely thin boundary layers, the model errors relative to the simulation lie between $-18\,\%$ and $4\,\%$ for the cylinder array and between $-12\,\%$ and $8\,\%$ for the hexagonal sphere pack. For the cylinder array, the blending parameter $n = 2$ gives better results, while for the hexagonal sphere pack the blending parameter $n = 3$ gives better results.

We then consider the case of transient flow started from rest that is driven by a sinusoidal pressure gradient. The low frequency cases (simulations cyl-LF and hcp-LF) are shown in figure 6. There are almost no differences between the dissipation rate of the DNS, the large-time asymptotics and the model. For the cylinder, all curves agree with the dissipation rate of the simulations. For the hexagonal sphere pack, the dissipation is

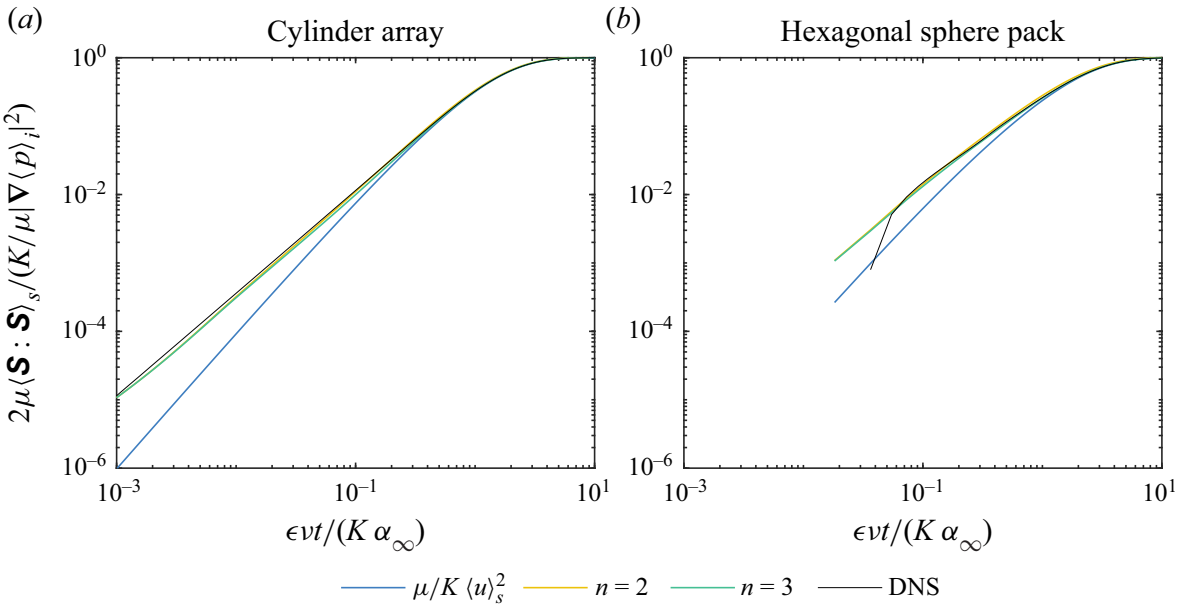

Figure 5. Comparison of the dissipation rate from the DNS, the large-time asymptotics (1.4) and the model given by (2.9), (2.11) for transient flow in response to a constant pressure gradient through the cylinder array (*a*) and the hexagonal sphere pack (*b*). The dissipation is normalised with the steady-state value $K/\mu|\nabla\langle p\rangle_i|^2$.

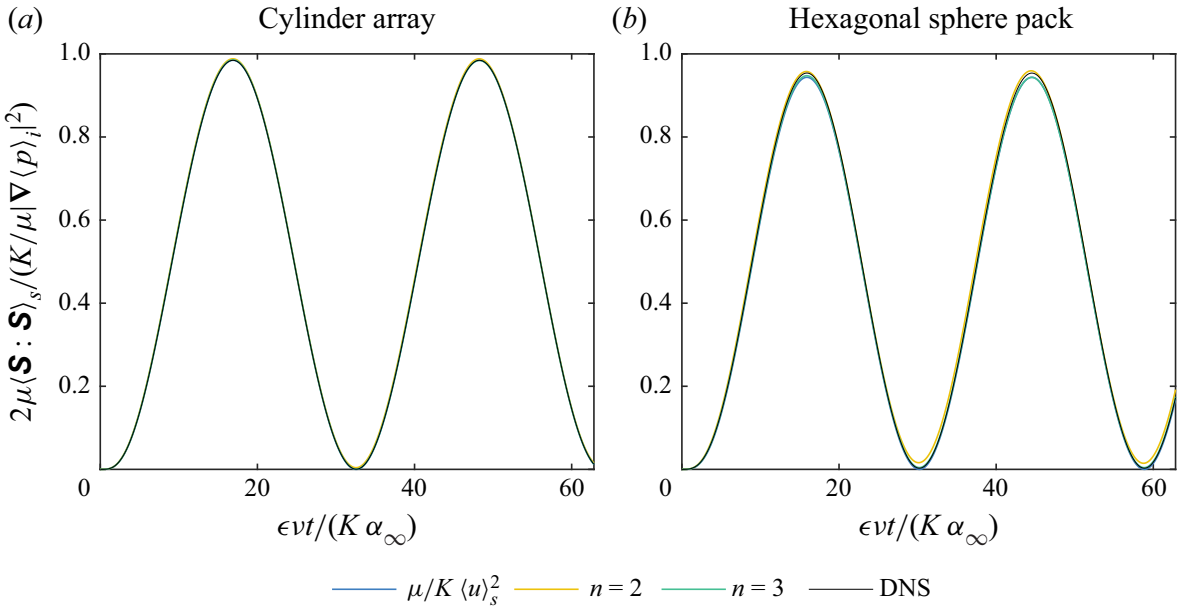

Figure 6. Comparison of the dissipation rate from the DNS, the large-time asymptotics (1.4) and the model given by (2.9), (2.11) for transient flow in response to a sinusoidal pressure gradient with $\Omega/\Omega_0 \approx 0.1$ through the cylinder array (*a*) and the hexagonal sphere pack (*b*). The dissipation is normalised with the steady-state value $K/\mu|\nabla\langle p\rangle_i|^2$.

slightly overestimated by the model for $n = 2$, while it is slightly underestimated by the model for $n = 3$ as well as by the large-time asymptotics.

The medium frequency cases (simulations cyl-MF and hcp-MF) are shown in figure 7. For the cylinder, again the large-time asymptotics agree very well with the dissipation rate of the DNS, while the model slightly overestimates the dissipation rate for both $n = 2$ and $n = 3$. For the hexagonal sphere pack, the model overestimates the dissipation rate for $n = 2$, while it is in close agreement with the simulation for $n = 3$. The large-time asymptotics slightly underestimate the dissipation rate.

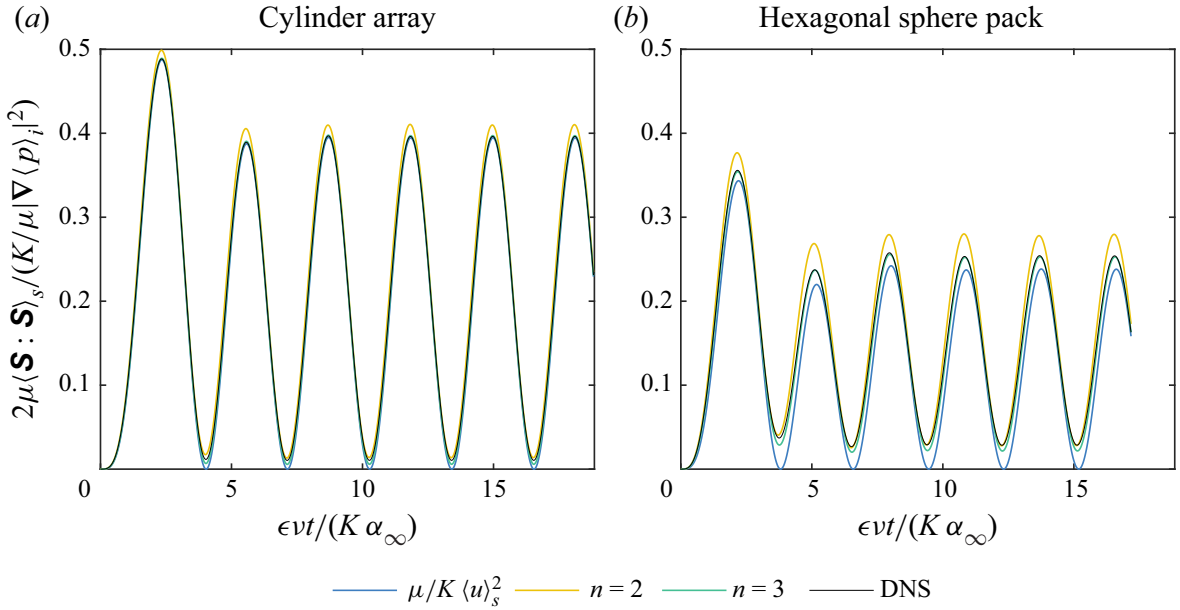

Figure 7. Comparison of the dissipation rate from the DNS, the large-time asymptotics (1.4) and the model given by (2.9), (2.11) for transient flow in response to a sinusoidal pressure gradient with $\Omega/\Omega_0 \approx 1$ through the cylinder array (a) and the hexagonal sphere pack (b). The dissipation is normalised with the steady-state value $K/\mu|\nabla\langle p\rangle_i|^2$.

The high frequency cases (simulations cyl-HF and hcp-HF) are shown in figure 8. It can be seen that the large-time asymptotics (1.4) clearly underestimate the dissipation from the simulations by approximately 30 % and 55 % for the cylinder array and the hexagonal sphere pack, respectively, while the model (2.9), (2.11) provides significantly better predictions. In particular, the model reproduces the evolution of the dissipation rate during the transient oscillation. For the cylinder array, a very good agreement can be observed for the value $n = 2$ of the blending parameter with a relative difference of approximately 3 %; for the sphere pack, an excellent agreement between the dissipation rate from the simulation and the modelled dissipation rate is found for $n = 3$ with a relative difference of approximately 1.5 %. Note that the agreement could be improved by choosing non-integer values of n. However, based on the results above, we expect that the optimal value for n will still depend on the geometry.

5. Conclusion

We have proposed a model for the volume-averaged dissipation rate in linear unsteady flow through a porous medium. The model is derived by blending the steady-state expression for the volume-averaged dissipation rate (Murthy & Singh 1997; Zhu *et al.* 2014) with a small-time asymptotic expression obtained from boundary layer theory for a flow started at rest. The model was first validated against an analytical solution of the Navier–Stokes equations for transient flow through a porous medium consisting of circular tubes. The model was then compared with a DNS dataset comprising transient and oscillatory flow through a cylinder array and through a hexagonal close-packed arrangement of spheres. The model showed significantly better predictions at small times or high frequencies than the large-time asymptotics given by the steady-state expression, while maintaining the accuracy of the large-time asymptotics at large times or low frequencies. In all cases, values of the blending parameter n between 2 and 3 gave good results.

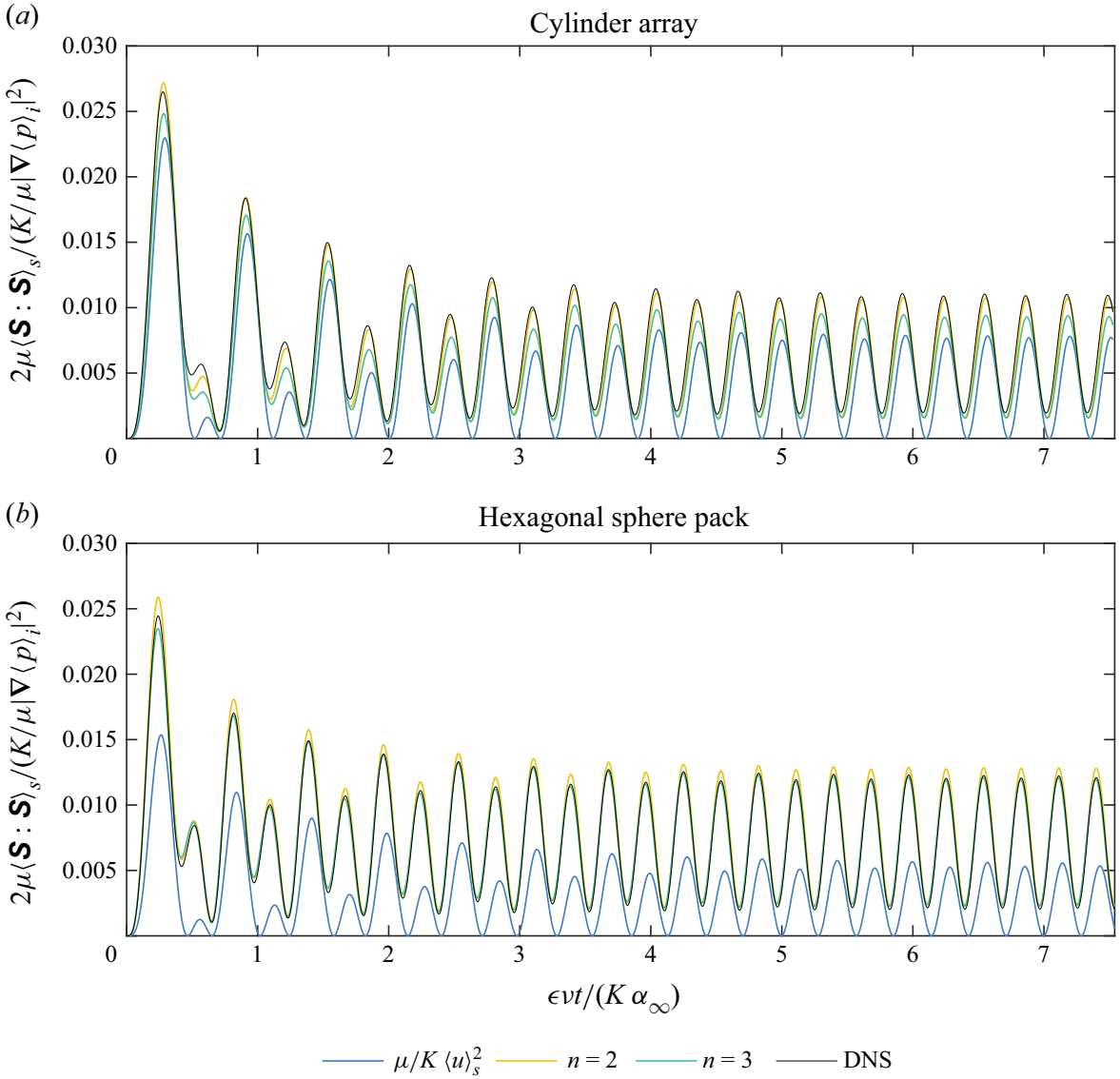

Figure 8. Comparison of the dissipation rate from the DNS, the large-time asymptotics (1.4) and the model given by (2.9), (2.11) for transient flow in response to a sinusoidal pressure gradient with $\Omega/\Omega_0 \approx 10$ through the cylinder array (*a*) and the hexagonal sphere pack (*b*). The dissipation is normalised with the steady-state value $K/\mu|\boldsymbol{\nabla}\langle p\rangle_i|^2$.

Future work could attempt to generalise the model to nonlinear unsteady flow. For this, it might be promising to represent the volume-averaged dissipation rate as a Volterra series in the superficial acceleration. Furthermore, the proposed model could provide a basis for modelling dispersion and mixing in linear unsteady flow through porous media. For instance, Brosten *et al.* (2012) considered the short-time dispersion coefficient defined as $D(t) = E[|\boldsymbol{R}(t) - E[\boldsymbol{R}(t)]|^2]/(6t)$, wherein $E[.]$ is the ensemble average and $\boldsymbol{R}(t)$ is the fluid particle displacement, and derived the following asymptotic expression for small times:

$$D(t) = D_o(t) + \left\langle (\boldsymbol{u} - \langle \boldsymbol{u}\rangle_i)^2 \right\rangle_i t + \frac{\kappa}{18}\left[\frac{\epsilon}{K}\langle \boldsymbol{u}\rangle_i^2\right] t^{3/2} + O(t^{5/2}). \tag{5.1}$$

Here, $D_o(t)$ is the short-time dispersion coefficient without convection and κ is the molecular diffusion constant. The spatial velocity variance in the second term on the right-hand side is closely related to the kinetic energy and the term in brackets can be identified as the steady-state expression (1.4) in intrinsic volume-averaged form. Therefore,

within a frozen field assumption, our model allows the evaluation of these terms for unsteady linear flow.

Funding. The authors gratefully acknowledge the financial support of the Deutsche Forschungsgemeinschaft (DFG, German Research Foundation) under grant no. MA2062/13-1. Computing time was granted by the Leibniz Supercomputing Centre on its Linux-Cluster.

Declaration of interests. The authors report no conflict of interest.

Author ORCIDs.
Lukas Unglehrt https://orcid.org/0000-0002-1299-0430;
Michael Manhart https://orcid.org/0000-0001-7809-6282.

Author contributions. L.U. derived the model, performed the simulations and wrote the manuscript. M.M. provided scientific supervision and contributed to writing the manuscript.

References

Batchelor, G.K. 2000 *An Introduction to Fluid Dynamics*. Cambridge University Press.

Biot, M.A. 1956*a* Theory of propagation of elastic waves in a fluid-saturated porous solid. I. Low-frequency range. *J. Acoust. Soc. Am.* **28** (2), 168–178.

Biot, M.A. 1956*b* Theory of propagation of elastic waves in a fluid-saturated porous solid. II. Higher frequency range. *J. Acoust. Soc. Am.* **28** (2), 179–191.

Brosten, T.R. 2013 Short-time asymptotics of hydrodynamic dispersion in porous media. *J. Fluid Mech.* **732**, 687–705.

Brosten, T.R., Vogt, S.J., Seymour, J.D., Codd, S.L. & Maier, R.S. 2012 Preasymptotic hydrodynamic dispersion as a quantitative probe of permeability. *Phys. Rev.* E **85** (4), 045301.

Cha, K.S., Balaras, E., Lieber, B.B., Sadasivan, C. & Wakhloo, A.K. 2007 Modeling the interaction of coils with the local blood flow after coil embolization of intracranial aneurysms. *Trans. ASME J. Biomech. Engng* **129** (6), 873–879.

Chapman, A.M. & Higdon, J.J.L. 1992 Oscillatory Stokes flow in periodic porous media. *Phys. Fluids* A **4** (10), 2099–2116.

Chorin, A.J. 1968 Numerical solution of the Navier–Stokes equations. *Maths Comput.* **22** (104), 745–762.

Churchill, S.W. & Usagi, R. 1972 A general expression for the correlation of rates of transfer and other phenomena. *AIChE J.* **18** (6), 1121–1128.

Cortis, A., Youjian, C., Scher, H. & Berkowitz, B. 2004 Quantitative characterization of pore-scale disorder effects on transport in 'homogeneous' granular media. *Phys. Rev.* E **70**, 041108.

Darcy, H. 1856 *Les fontaines publiques de la ville de Dijon*. Victor Dalmont.

Ene, H. & Sanchez-Palencia, E. 1975 Equations et phénomènes de surface pour l'écoulement dans un milieu poreux. *J. Méc.* **14**, 73–108.

Gu, Z. & Wang, H. 1991 Gravity waves over porous bottoms. *Coast. Engng* **15** (5–6), 497–524.

Johnson, D.L., Koplik, J. & Dashen, R. 1987 Theory of dynamic permeability and tortuosity in fluid-saturated porous media. *J. Fluid Mech.* **176**, 379–402.

Lee, C.-Y., Leamy, M.J. & Nadler, J.H. 2009 Acoustic absorption calculation in irreducible porous media: a unified computational approach. *J. Acoust. Soc. Am.* **126** (4), 1862–1870.

Lowe, R.J., Shavit, U., Falter, J.L., Koseff, J.R. & Monismith, S.G. 2008 Modeling flow in coral communities with and without waves: a synthesis of porous media and canopy flow approaches. *Limnol. Oceanogr.* **53** (6), 2668–2680.

Manhart, M., Tremblay, F. & Friedrich, R. 2001 MGLET: a parallel code for efficient DNS and LES of complex geometries. In *Parallel Computational Fluid Dynamics 2000* (ed. C.B. Jenssen, T. Kvamsdal, H.I. Andersson, B. Pettersen, A. Ecer, J. Periaux, N. Satofuka & P. Fox), pp. 449–456. North-Holland.

Murthy, P.V.S.N. & Singh, P. 1997 Effect of viscous dissipation on a non-Darcy natural convection regime. *Intl J. Heat Mass Transfer* **40** (6), 1251–1260.

Ni, X., Mackley, M.R., Harvey, A.P., Stonestreet, P., Baird, M.H.I. & Rama Rao, N.V. 2003 Mixing through oscillations and pulsations – a guide to achieving process enhancements in the chemical and process industries. *Chem. Engng Res. Des.* **81** (3), 373–383.

Paéz-García, C.T., Valdés-Parada, F.J. & Lasseux, D. 2017 Macroscopic momentum and mechanical energy equations for incompressible single-phase flow in porous media. *Phys. Rev.* E **95** (2), 023101.

PELLER, N. 2010 Numerische simulation turbulenter Strömungen mit immersed boundaries. PhD thesis, Technische Universität München.

PELLER, N., LE DUC, A., TREMBLAY, F. & MANHART, M. 2006 High-order stable interpolations for immersed boundary methods. *Intl J. Numer. Meth. Fluids* **52** (11), 1175–1193.

POZRIKIDIS, C. 2017 *Fluid Dynamics: Theory, Computation, and Numerical Simulation*, 3rd edn. Springer.

PRIDE, S.R., MORGAN, F.D. & GANGI, A.F. 1993 Drag forces of porous-medium acoustics. *Phys. Rev.* B **47** (9), 4964–4978.

SAKAI, Y. & MANHART, M. 2020 Consistent flow structure evolution in accelerating flow through hexagonal sphere pack. *Flow Turbul. Combust.* **105** (2), 581–606.

SCHLICHTING, H. & GERSTEN, K. 2017 *Boundary-Layer Theory*. Springer.

TREVIZOLI, P.V., PEIXER, G.F. & BARBOSA, J.R. 2016 Thermal–hydraulic evaluation of oscillating-flow regenerators using water: experimental analysis of packed beds of spheres. *Intl J. Heat Mass Transfer* **99**, 918–930.

UNGLEHRT, L. & MANHART, M. 2022 Onset of nonlinearity in oscillatory flow through a hexagonal sphere pack. *J. Fluid Mech.* **944**, A30.

UNGLEHRT, L. & MANHART, M. 2023 Decomposition of the drag force in steady and oscillatory flow through a hexagonal sphere pack. *J. Fluid Mech.* (submitted).

VERSTAPPEN, R.W.C.P. & VELDMAN, A.E.P. 2003 Symmetry-preserving discretization of turbulent flow. *J. Comput. Phys.* **187** (1), 343–368.

WHITAKER, S. 1966 The equations of motion in porous media. *Chem. Engng Sci.* **21**, 291–300.

WHITAKER, S. 1986 Flow in porous media I: a theoretical derivation of Darcy's law. *Transp. Porous Med.* **1** (1), 3–25.

WILLIAMSON, J.H 1980 Low-storage Runge–Kutta schemes. *J. Comput. Phys.* **35** (1), 48–56.

ZHU, T. & MANHART, M. 2016 Oscillatory Darcy flow in porous media. *Transp. Porous Med.* **111** (2), 521–539.

ZHU, T., WALUGA, C., WOHLMUTH, B. & MANHART, M. 2014 A study of the time constant in unsteady porous media flow using direct numerical simulation. *Transp. Porous Med.* **104** (1), 161–179.

D.6. Decomposition of the drag force in steady and oscillatory flow through a hexagonal sphere pack

Division of work between the authors

Lukas Unglehrt performed the simulations advised by Michael Manhart. Lukas Unglehrt derived the theory of the drag decomposition and performed the evaluation of the simulations. Both authors contributed to reaching conclusions and in writing the paper.

Reference

Unglehrt, L. & Manhart, M. 2023 Decomposition of the drag force in steady and oscillatory flow through a hexagonal sphere pack. *Journal of Fluid Mechanics* **974**, A32.

Copyright

J. Fluid Mech. (2023), *vol.* 974, A32, doi:10.1017/jfm.2023.798

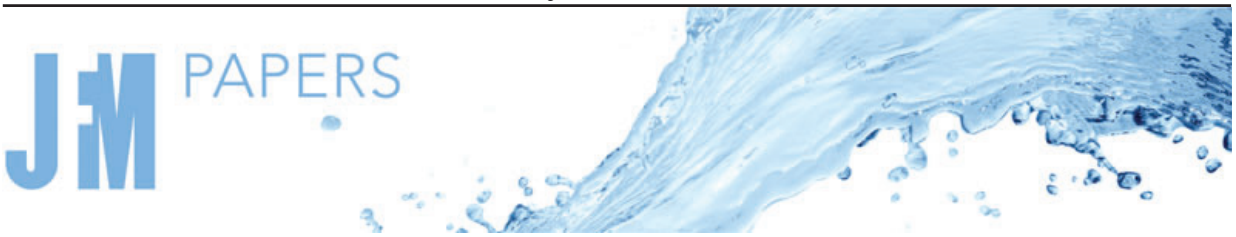

Decomposition of the drag force in steady and oscillatory flow through a hexagonal sphere pack

Lukas Unglehrt[1],† **and Michael Manhart**[1]

[1]Professorship of Hydromechanics, Technical University of Munich, Arcisstr. 21, 80333 Munich, Germany

(Received 16 March 2023; revised 3 August 2023; accepted 19 September 2023)

We investigate steady and oscillatory flow through a hexagonal close-packed arrangement of spheres in the framework of the volume-averaged momentum equation. We quantify the friction and pressure drag based on a direct numerical simulation dataset. Using the pressure decomposition of Graham (*J. Fluid Mech.*, vol. 881, 2019), the pressure drag can be further split up into an accelerative, a viscous and a convective contribution. For the accelerative pressure, a closed-form expression can be given in terms of the potential flow solution. We investigate the contributions of the different drag components to the volume-averaged momentum budget and their Reynolds number scaling. For steady flow, we find that the friction and viscous pressure drag are proportional to Re at low Reynolds numbers and scale with $Re^{1.4}$ for high Reynolds numbers. This is close to the steady laminar boundary layer scaling. For the convective pressure drag, we find a cubic scaling at low and a quadratic scaling at high Reynolds numbers. The Reynolds stresses have a minor contribution to the momentum budget. For oscillatory flow at low and medium Womersley numbers, the amplitudes of the drag components are similar to the steady cases at the same Reynolds number. At high Womersley numbers, the drag components behave quite differently and the friction and viscous pressure drag are relatively insignificant. The drag components are not in phase with the forcing and the superficial velocity; the phase lag increases with the Womersley number. This suggests that new models beyond the current quasisteady approaches need to be developed.

Key words: porous media, general fluid mechanics, Navier–Stokes equations

1. Introduction

In this contribution we investigate the behaviour of the drag in steady and oscillatory flow through a hexagonal sphere pack. The sphere pack can be decomposed into triply periodic

† Email address for correspondence: lukas.unglehrt@tum.de

unit cells of size ℓ and is assumed to have a spatial extent $L \gg \ell$ (figure 1*a*). When the flow is driven by pressure or velocity variations on the macroscale, for example by a pressure wave of wavelength $O(L)$, the flow is locally almost periodic (Ene & Sanchez-Palencia 1975). The pore-scale flow is described in terms of the velocity $\boldsymbol{u}$ and the pressure P. The large-scale flow is described in terms of the macroscopic pressure gradient $\boldsymbol{f}$, which is defined such that the pore-scale pressure deviation $p = P - \boldsymbol{f} \cdot \boldsymbol{x}$ is a periodic function, and in terms of the superficial velocity $\langle \boldsymbol{u} \rangle_s$, which is defined as the volume average of the pore-scale velocity $\boldsymbol{u}$ over the unit cell

$$\langle \boldsymbol{u} \rangle_s = \frac{1}{V} \int_{V_f} \boldsymbol{u} \, \mathrm{d}V. \tag{1.1}$$

Here, V is the volume of the unit cell and V_f is the fluid volume within the unit cell; the porosity ϵ is defined as the ratio V_f/V. Note that depending on the flow regime, the unit cell has to be chosen larger than the primitive unit cell of the geometry (Agnaou, Lasseux & Ahmadi 2016). Here, the unit cell contains four primitive unit cells (figure 1*b*). In the limit $\ell/L \to 0$, the superficial velocity is governed by the continuity equation

$$\boldsymbol{\nabla} \cdot \langle \boldsymbol{u} \rangle_s = 0 \tag{1.2}$$

and a local relation between the superficial velocity and the macroscopic pressure gradient that follows from the solution of the Navier–Stokes equations on the unit cell (Ene & Sanchez-Palencia 1975). The pore-scale velocity $\boldsymbol{u}$ and the pore-scale pressure deviation p are regarded as triply periodic fields on the unit cell. The relation between the superficial velocity and the macroscopic pressure gradient can also be expressed by the volume-averaged Navier–Stokes equations, which are obtained by averaging equation (2.1*b*) over the unit cell. By Gauss' theorem and the periodic boundary conditions, the integrals over the open pore areas cancel; thus we obtain

$$\rho \frac{\partial \langle \boldsymbol{u} \rangle_s}{\partial t} = \underbrace{-\frac{1}{V} \int_{A_{fs}} p \, \boldsymbol{n} \, \mathrm{d}A}_{\textit{pressure drag}} \underbrace{-\frac{1}{V} \int_{A_{fs}} \boldsymbol{\tau}_w \, \mathrm{d}A}_{\textit{friction drag}} - \epsilon \boldsymbol{f}. \tag{1.3}$$

In this equation, the symbol $\boldsymbol{\tau}_w = \mu \, (\boldsymbol{\nabla} \otimes \boldsymbol{u})^{\mathrm{T}}|_w \cdot \boldsymbol{n}$ represents the wall shear stress vector, and A_{fs} denotes the fluid–solid interface, i.e. the surface of the spheres. Note that the force exerted by the fluid onto the spheres also contains a contribution from the macroscopic pressure gradient. While (1.2) and (1.3) have been derived assuming a periodic porous medium, they can also be obtained for non-periodic porous media by the volume-averaging theory of Whitaker (1986, 1996) if the pore scale, the averaging scale and the macroscale are sufficiently separated. A comparison between the homogenisation approach outlined above and the volume-averaging approach can be found in Davit *et al.* (2013). The pressure drag and the friction drag terms appearing in (1.3) are unclosed with respect to $\langle \boldsymbol{u} \rangle_s$ and $\boldsymbol{f}$. In general, they can be obtained only by direct numerical simulation (DNS) of the pore-scale flow. The aim of modelling is to replace the solution to the pore-scale flow problem by an explicit relationship between $\boldsymbol{f}$ and $\langle \boldsymbol{u} \rangle_s$.

In this work, we investigate this relationship and consider the macroscopic pressure gradient as a known quantity. The pore-scale flow is computed numerically in a triply periodic domain of the hexagonal sphere pack (shown in figure 1*b*) for a constant and a sinusoidally oscillating forcing. The pore-scale flow then depends on two dimensionless numbers that are formed with the sphere diameter d, the density ρ and the kinematic viscosity ν: The Hagen number $Hg = |\boldsymbol{f}|d^3/(\rho\nu^2)$ describes the magnitude

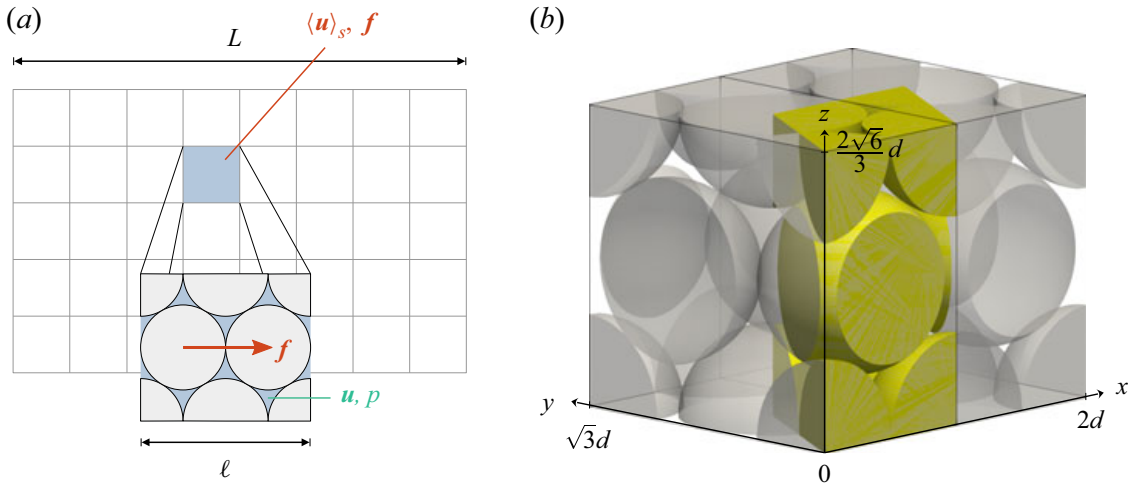

Figure 1. Conceptual sketch of the volume approach for the hexagonal sphere pack. (*a*) The sphere pack consists of triply periodic unit cells. The periodic flow $\boldsymbol{u}, p$ inside the unit cell is driven by the macroscopic pressure gradient $\boldsymbol{f}$. (*b*) The simulation domain of the hexagonal sphere pack consists of four primitive unit cells (one of which is highlighted in yellow).

of the macroscopic pressure gradient relative to the viscous forces. In other work, the Hagen number is referred to as the pressure-gradient-based Reynolds number (Ene & Sanchez-Palencia 1975; Firdaouss, Guermond & Le Quéré 1997; Iervolino, Manna & Vacca 2010; Lasseux, Valdés-Parada & Bellet 2019). The Womersley number is defined as $Wo = \sqrt{\Omega d^2/\nu}$ where Ω is the angular frequency of the forcing. The Womersley number is proportional to the ratio of the sphere diameter to the Stokes layer thickness $\sqrt{2\nu/\Omega}$ and thus determines the region that is affected by the wall friction via diffusive transport. For each parameter combination, a Reynolds number $Re = |\langle \boldsymbol{u} \rangle_s| d/\nu$ for steady flow or

$$Re = \limsup_{t\to\infty} \frac{|\langle \boldsymbol{u} \rangle_s|\, d}{\nu} \tag{1.4}$$

for oscillatory flow results from solving the pore-scale flow problem.

Next, we briefly summarise some important findings on the flow resistance behaviour of steady flow. In this case there are closed-form expressions which allow the pore-scale problem to be bypassed. Figure 2 shows the drag coefficient defined according to (Macdonald *et al.* 1979) as

$$F_k' = \frac{|\boldsymbol{f}|\, d}{\rho \langle u \rangle_s^2} = \frac{Hg}{Re^2} \tag{1.5}$$

as a function of the Reynolds number for the DNSs of Sakai & Manhart (2020) of steady flow through the hexagonal sphere pack. For very small Reynolds numbers, the superficial velocity depends linearly on the macroscopic pressure gradient. This relationship is described by Darcy's law (dotted line) which can be written in dimensionless form as

$$Hg = \frac{d^2}{K} Re \quad \text{or} \quad F_k' = \frac{d^2}{K} Re^{-1}, \tag{1.6}$$

where K denotes the permeability. For Reynolds numbers $\lesssim 10$, Mei & Auriault (1991) derived a cubic correction to Darcy's law of the form

$$Hg = \frac{d^2}{K} Re + \hat{b}\, Re^3 \quad \text{or} \quad F_k' = \frac{d^2}{K} Re^{-1} + \hat{b}\, Re \tag{1.7}$$

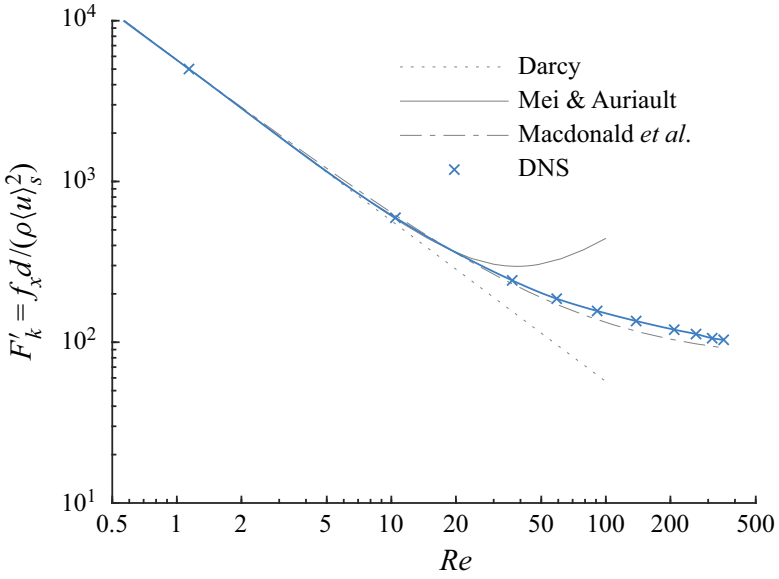

Figure 2. Drag coefficient in steady flow through a hexagonal sphere pack together with Darcy's law, the correction of Mei & Auriault (1991) and the modified Ergun equation (Macdonald *et al.* 1979).

for isotropic porous media (solid line). Firdaouss *et al.* (1997) derived the same law under the condition that 'if the pressure gradient is reversed, the seepage velocity should also be reversed with no change in modulus'. They supported their derivation with numerical simulations of two-dimensional porous media flow and further demonstrated that (1.7) is satisfied for several classical experimental datasets up to Reynolds numbers of approximately 16. Hill, Koch & Ladd (2001) confirmed the theory of Mei & Auriault (1991) for numerical simulations of flow through regular and random sphere packs. For higher Reynolds numbers, the drag is commonly described in terms of the Forchheimer equation (Forchheimer 1901) which is composed of a linear and a quadratic term

$$Hg = a\,Re + b\,Re^2 \quad \text{or} \quad F'_k = a\,Re^{-1} + b. \tag{1.8}$$

It should be noted that the Forchheimer equation is not consistent with (1.7). Ergun (1952) proposed empirical correlations for the coefficients a and b based on packed bed experiments. The correlations were further refined by, for example, Macdonald *et al.* (1979) who aggregated multiple experimental datasets. When the flow becomes turbulent, a change of slope of the resistance curve occurs and a different set of coefficients a', b' must be determined (Fand *et al.* 1987; Burcharth & Andersen 1995).

A major difficulty in describing unsteady and oscillatory flow is that the drag force does not depend solely on the instantaneous Reynolds number, but is generally a function of the history of the flow. For example, figure 3 shows the instantaneous drag force (i.e. the first two terms on the right-hand side of (1.3)) as a function of the instantaneous Reynolds number for two of our oscillatory flow simulations. It can be seen in figure 3(*a*) that for the low frequency case LF5 the instantaneous drag is mostly close to the drag observed in a steady flow at the same instantaneous Reynolds number. Conversely, for the medium frequency case MF5 (figure 3*b*) the instantaneous drag differs significantly from the drag observed in a steady flow at the same instantaneous Reynolds number. Moreover, a hysteresis loop can be observed which suggests a different behaviour of the flow in the acceleration and deceleration phases of the cycle. For linear oscillatory flow the models of Johnson, Koplik & Dashen (1987) and Pride, Morgan & Gangi (1993) provide an accurate description of the history-dependent drag. The models are formulated

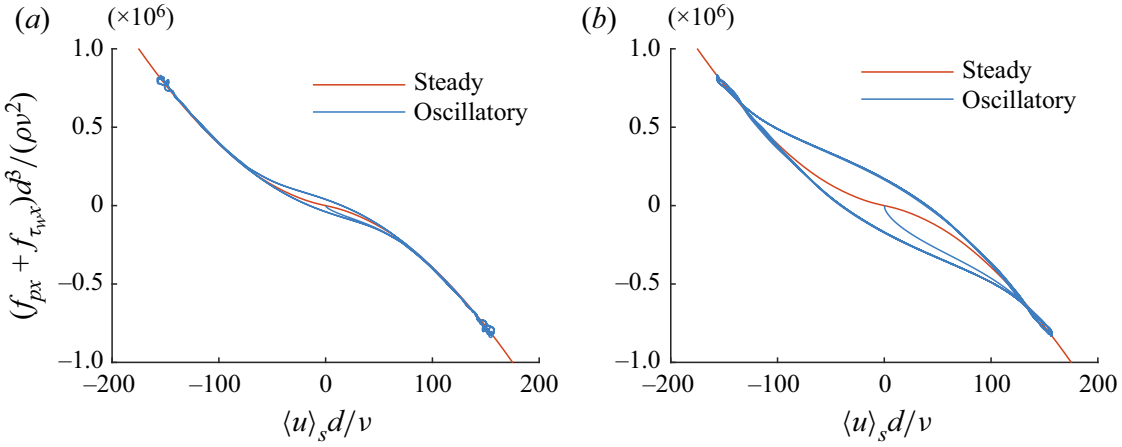

Figure 3. Comparison of the relation between the instantaneous drag force and the superficial velocity for steady and oscillatory flow: (*a*) LF5 ($Re = 158$, $Wo = 10$); (*b*) MF5 ($Re = 157$, $Wo = 31.62$).

in the frequency domain as a non-rational transfer function ('dynamic permeability'). For nonlinear oscillatory flow, the drag has been described by a Forchheimer-type expression (see (1.8)) and variations thereof with frequency- or time-dependent coefficients (van Gent 1993; Hall, Smith & Turcke 1995). However, the inherent assumption of the model is that the nonlinear drag is a function of the instantaneous Reynolds number. As discussed in the above, this assumption is not valid for some flow configurations. Furthermore, we have shown in our previous work (Unglehrt & Manhart 2022*a*) that at medium and large Womersley numbers the nonlinear parts of the flow can be out of phase with the superficial velocity.

Therefore, the objective of the present contribution is to identify and quantify the drag generation processes in steady and oscillatory flow through a sphere pack. In particular, the analysis is guided by the following questions: How large is the contribution of the pressure drag and the friction drag? What effects contribute to the pressure drag? What is the effect of turbulence? How do these contributions scale with the dimensionless numbers governing the flow? What is the phase of these contributions in oscillatory flow?

We adapt the pressure decomposition of Graham (2019) to unsteady incompressible flow through a periodic porous medium. Based on the Poisson equation for the pressure, the pressure is decomposed into three different components: the first component is a reaction force to the imposed macroscopic pressure gradient; the second component represents the displacement of the flow from the wall due to viscosity; and the third component represents the pressure drag induced by vorticity and dissipation. The resulting decomposition of the volume-averaged Navier–Stokes equations is similar to the approach of Aghaei-Jouybari *et al.* (2022) and is also closely related to various decompositions of the force on a moving body (Quartapelle & Napolitano 1983; Howe 1989; Yu 2014; Li & Wu 2018; Menon & Mittal 2021). We comment on the relationship between this decomposition and the theory of Johnson *et al.* (1987) for linear oscillatory porous media flow in Appendix B.2. We then investigate DNS datasets for laminar oscillatory flow (Unglehrt & Manhart 2022*a*) and steady flow (Sakai & Manhart 2020) through a hexagonal sphere pack. In order to establish a baseline, we apply this decomposition to nonlinear steady flow and linear oscillatory flow. We then proceed to analyse nonlinear oscillatory flow. We investigate the evolution of the drag components over the cycle depending on the Reynolds and Womersley number, with particular focus on the Reynolds number scaling of the drag components. Finally, we discuss the implications of our results for the physical understanding and for the modelling of unsteady flow in porous media.

2. Theory

2.1. *Mathematical notation*

The equations are written in vector notation according to the ISO 80000-2:2019 standard. In particular, $\boldsymbol{\nabla} = \boldsymbol{e}_i\, \partial(.)/\partial x_i$ denotes the Nabla operator, where $\boldsymbol{e}_i$ are the Cartesian unit vectors; $\boldsymbol{a} \cdot \boldsymbol{b} = a_i b_i$ denotes the inner product, $\boldsymbol{A} : \boldsymbol{B} = A_{ij} B_{ij}$ denotes the double inner product, $(\boldsymbol{a} \otimes \boldsymbol{b})_{ij} = a_i b_j$ denotes the outer product and $(\boldsymbol{a} \times \boldsymbol{b})_i = \epsilon_{ijk} a_j b_k$ denotes the cross product.

2.2. *Differential equations*

The flow in the pore space is governed by the incompressible Navier–Stokes equations

$$\boldsymbol{\nabla} \cdot \boldsymbol{u} = 0, \tag{2.1a}$$

$$\frac{\partial \boldsymbol{u}}{\partial t} + \boldsymbol{\nabla} \cdot (\boldsymbol{u} \otimes \boldsymbol{u}) = -\frac{1}{\rho} \boldsymbol{\nabla} p + \nu \Delta \boldsymbol{u} + \frac{1}{\rho} \boldsymbol{f}. \tag{2.1b}$$

The flow is driven by a constant force $\boldsymbol{f} = f_x\, \boldsymbol{e}_x$ or a sinusoidal force $\boldsymbol{f} = f_x \sin \Omega t\, \boldsymbol{e}_x$ which is constant in space and represents to the macroscopic pressure gradient. On the spheres, the velocity satisfies no-slip and impermeability boundary conditions and for both the velocity $\boldsymbol{u}$ and the deviation pressure p triply periodic boundary conditions are imposed.

2.3. *Decomposition of the pressure*

In this section, we recall the decomposition of the pressure of Graham (2019) that forms the basis of the discussion in the rest of the article. We start from the Poisson equation for the pressure, which can be derived by taking the divergence of the momentum equation (2.1*b*):

$$\Delta p = -\rho\, \boldsymbol{\nabla} \cdot \boldsymbol{\nabla} \cdot (\boldsymbol{u} \otimes \boldsymbol{u}) = 2\rho Q, \tag{2.2a}$$

where $Q = -\frac{1}{2} (\boldsymbol{\nabla} \otimes \boldsymbol{u}) : (\boldsymbol{\nabla} \otimes \boldsymbol{u})^{\mathrm{T}}$ is the second invariant of the velocity gradient tensor (Chong, Perry & Cantwell 1990) that is frequently used for vortex identification (Hunt, Wray & Moin 1988; Dubief & Delcayre 2000). The pressure satisfies periodic boundary conditions at the open domain boundaries and the Neumann boundary condition

$$\boldsymbol{\nabla} p \cdot \boldsymbol{n} = \mu \Delta \boldsymbol{u} \cdot \boldsymbol{n} + \boldsymbol{f} \cdot \boldsymbol{n} \tag{2.2b}$$

at solid walls where $\mu = \rho\nu$ is the dynamic viscosity. The boundary condition can be obtained by projecting the Navier–Stokes equations onto the normal $\boldsymbol{n}$ and using the no-slip and no-penetration conditions for $\boldsymbol{u}$. Note that this boundary condition is not required to solve for the pressure, but it is a property of any sufficiently smooth solution (Sani *et al.* 2006). Thus, the pressure has three sources with a generally different scaling: the macroscopic pressure gradient; the viscous force; and the convective force. The additive decomposition of Graham (2019) separates these different scalings and results in the following three boundary value problems:

differential equation	wall boundary condition	
$\Delta p^{(a)} = 0,$	$\boldsymbol{\nabla} p^{(a)} \cdot \boldsymbol{n} = \boldsymbol{f} \cdot \boldsymbol{n},$	(2.3*a*)
$\Delta p^{(v)} = 0,$	$\boldsymbol{\nabla} p^{(v)} \cdot \boldsymbol{n} = \mu \Delta \boldsymbol{u} \cdot \boldsymbol{n},$	(2.3*b*)
$\Delta p^{(c)} = 2\rho Q,$	$\boldsymbol{\nabla} p^{(c)} \cdot \boldsymbol{n} = 0.$	(2.3*c*)

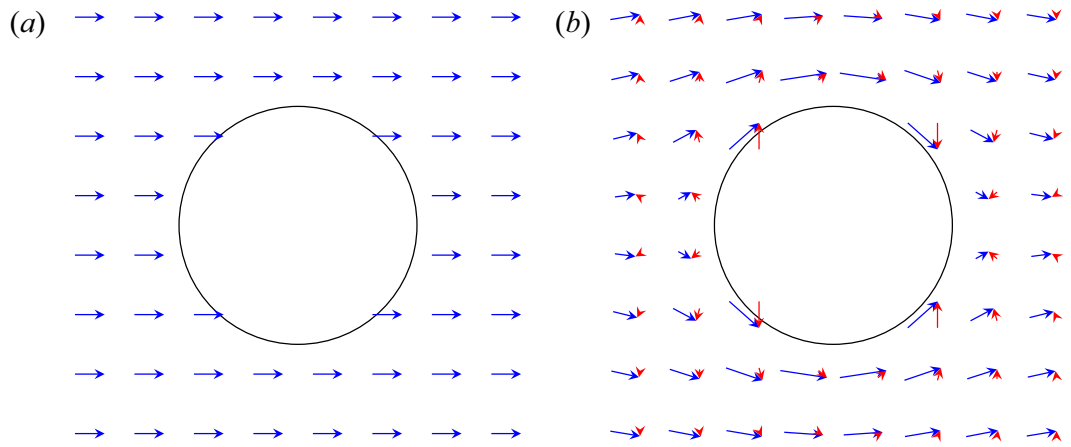

Figure 4. Illustration of the effect of the pressure component $p^{(a)}$. (*a*) External force field $\boldsymbol{f}$. (*b*) Projected force field $\boldsymbol{f} - \boldsymbol{\nabla} p^{(a)}$ (blue) and $-\boldsymbol{\nabla} p^{(a)}$ (red).

By summing up the equations, the pressure Poisson equation and the boundary condition are recovered. The accelerative pressure $p^{(a)}$ counterbalances the wall-normal component of the macroscopic pressure gradient $\boldsymbol{f}$ and therefore ensures that the force field acts tangentially to the wall. This effect is illustrated in figure 4 for flow around a cylinder. Note that Graham (2019) defined the accelerative pressure in terms of the acceleration of a moving body in a stationary frame of reference. Upon changing to a comoving frame of reference, the body becomes stationary and a fictitious force appears in the momentum equation. By identifying the acceleration of the body with $-\boldsymbol{f}/\rho$, we have adapted the decomposition to the present setting. The viscous pressure $p^{(v)}$ arises from unbalanced viscous stresses at the wall (Graham 2019). In particular, we show in Appendix A.1 that the boundary condition of the viscous pressure is given by the divergence of the wall shear stress. Finally, as the Q-invariant is equal to the difference between the rotation rate magnitude and the strain rate magnitude (Dubief & Delcayre 2000), the convective pressure $p^{(c)}$ is caused by vortical ($Q > 0$) and dissipative ($Q < 0$) flow features.

For turbulent flow, we follow Aghaei-Jouybari *et al.* (2022) and take the Reynolds average of the pressure decomposition. Then, the mean convective pressure $\bar{p}^{(c)}$ contains contributions from the mean velocity $\bar{\boldsymbol{u}}$ and the Reynolds stress tensor:

$$\Delta \bar{p}^{(c)} = 2\rho \bar{Q} = -\rho\, \boldsymbol{\nabla} \cdot \boldsymbol{\nabla} \cdot (\overline{\boldsymbol{u} \otimes \boldsymbol{u}}) = -\rho\, \boldsymbol{\nabla} \cdot \boldsymbol{\nabla} \cdot (\bar{\boldsymbol{u}} \otimes \bar{\boldsymbol{u}}) - \rho\, \boldsymbol{\nabla} \cdot \boldsymbol{\nabla} \cdot (\overline{\boldsymbol{u}' \otimes \boldsymbol{u}'}). \quad (2.4)$$

In analogy to the terminology for the dissipation rate, we refer to the former contribution as 'direct' convective pressure $\bar{p}^{(d)}$ and to the latter as 'turbulent' convective pressure $\bar{p}^{(t)}$.

2.4. *Decomposition of the pressure drag*

In this section, we decompose the pressure drag in the volume-averaged momentum equation (1.3) into the components due to the accelerative pressure $p^{(a)}$, the viscous pressure $p^{(v)}$ and the convective pressure $p^{(c)}$. An auxiliary potential field allows the pressure drag components to be directly expressed in terms of the sources in the boundary value problems (2.3). First, we define an auxiliary potential $\boldsymbol{\Phi}$ which satisfies the Laplace equation $\Delta \boldsymbol{\Phi} = 0$ with periodic boundary conditions and $(\boldsymbol{\nabla} \otimes \boldsymbol{\Phi})^{\mathrm{T}} \cdot \boldsymbol{n} = \boldsymbol{n}$ at solid walls (Batchelor 2000, (6.4.11)). This auxiliary potential also forms the basis of other force decompositions (Quartapelle & Napolitano 1983; Howe 1989; Yu 2014; Li & Wu 2018; Menon & Mittal 2021). Then, we apply Green's second identity to the pressure p and the

components of the auxiliary potential $\boldsymbol{\Phi}$:

$$\int_{V_f} \boldsymbol{\Phi}\, \Delta p \,\mathrm{d}V = \underbrace{\int_{V_f} p\, \Delta \boldsymbol{\Phi} \,\mathrm{d}V}_{=0} + \int_{\partial V_f} \boldsymbol{\Phi} (\nabla p \cdot \boldsymbol{n}) \,\mathrm{d}A - \int_{\partial V_f} p\, (\nabla \otimes \boldsymbol{\Phi})^{\mathrm{T}} \cdot \boldsymbol{n} \,\mathrm{d}A. \tag{2.5}$$

By the definition of the auxiliary potential, its Laplacian is zero and its wall-normal gradient can be replaced by the normal vector. Furthermore, the integrals over the pore areas cancel due to the periodic boundary conditions on $\boldsymbol{\Phi}$ and p. We get

$$\int_{V_f} \boldsymbol{\Phi}\, \Delta p \,\mathrm{d}V = \int_{A_{fs}} \boldsymbol{\Phi} (\nabla p \cdot \boldsymbol{n}) \,\mathrm{d}A - \int_{A_{fs}} p\, \boldsymbol{n} \,\mathrm{d}A. \tag{2.6}$$

Finally, we insert the boundary value problems (2.3) and we obtain the components of the pressure drag force per unit volume

$$-\boldsymbol{f}_p^{(a)} := -\frac{1}{V} \int_{A_{fs}} p^{(a)}\, \boldsymbol{n} \,\mathrm{d}A = -\frac{1}{V} \int_{A_{fs}} \boldsymbol{\Phi}\, (\boldsymbol{f} \cdot \boldsymbol{n}) \,\mathrm{d}A, \tag{2.7a}$$

$$-\boldsymbol{f}_p^{(v)} := -\frac{1}{V} \int_{A_{fs}} p^{(v)}\, \boldsymbol{n} \,\mathrm{d}A = -\frac{1}{V} \int_{A_{fs}} \boldsymbol{\Phi}\, (\mu \Delta \boldsymbol{u} \cdot \boldsymbol{n}) \,\mathrm{d}A, \tag{2.7b}$$

$$-\boldsymbol{f}_p^{(c)} := -\frac{1}{V} \int_{A_{fs}} p^{(c)}\, \boldsymbol{n} \,\mathrm{d}A = \frac{1}{V} \int_{V_f} \boldsymbol{\Phi}\, 2\rho Q \,\mathrm{d}V. \tag{2.7c}$$

The auxiliary potential $\boldsymbol{\Phi}$ can be considered as an analogue of the influence line in structural mechanics and represents the effect of a pressure source on the integral pressure drag. *Vice versa*, the components Φ_x, Φ_y and Φ_z of the auxiliary potential can be seen as the pressure fields in response to a unit source $\boldsymbol{e}_x$, $\boldsymbol{e}_y$ or $\boldsymbol{e}_z$ distributed uniformly over the surface. Note that the auxiliary potential $\boldsymbol{\Phi}$ is defined up to a constant, but both Q and $\Delta \boldsymbol{u} \cdot \boldsymbol{n}$ have zero mean for a domain with periodic and no-slip boundary conditions (see Soria, Ooi & Chong (1997) and Appendix A.2, respectively) and the constant does not affect the result. For simplicity, we constrain $\boldsymbol{\Phi}$ to have zero mean. Figure 5 shows the distribution of the x-component of this potential in the hexagonal sphere pack. We can see that Φ_x is an antisymmetric function with respect to the planes $x = 0, x = d/2, x = d, \ldots$, and has periodicity d in the x-direction. The auxiliary potential is largest at the wall and takes its extreme values near the contact points of the spheres.

In the following, we briefly discuss the pressure drag components in (2.7). With the (dimensionless) tensor of virtual inertia

$$\boldsymbol{A} = \frac{1}{V_s} \int_{A_{fs}} \boldsymbol{\Phi} \otimes \boldsymbol{n} \,\mathrm{d}A \tag{2.8}$$

defined in Batchelor (2000, (6.4.15)), we can rewrite the accelerative pressure drag as

$$-\frac{1}{V} \int_{A_{fs}} p^{(a)}\, \boldsymbol{n} \,\mathrm{d}A = -\left(\frac{1}{V} \int_{A_{fs}} \boldsymbol{\Phi} \otimes \boldsymbol{n} \,\mathrm{d}A \right) \cdot \boldsymbol{f} = -(1-\epsilon)\, \boldsymbol{A} \cdot \boldsymbol{f}. \tag{2.9}$$

Consequently, the accelerative pressure drag directly counteracts the macroscopic pressure gradient. The tensor $-(1-\epsilon)\boldsymbol{A}$ is equivalent to the hydrodynamic drag tensor λ_∞ introduced by Lafarge (2009, p. 159) based on the work of Johnson & Sen (1981). Moreover, we demonstrate in Appendix B.1 that the tensor of virtual inertia $\boldsymbol{A}$ can be

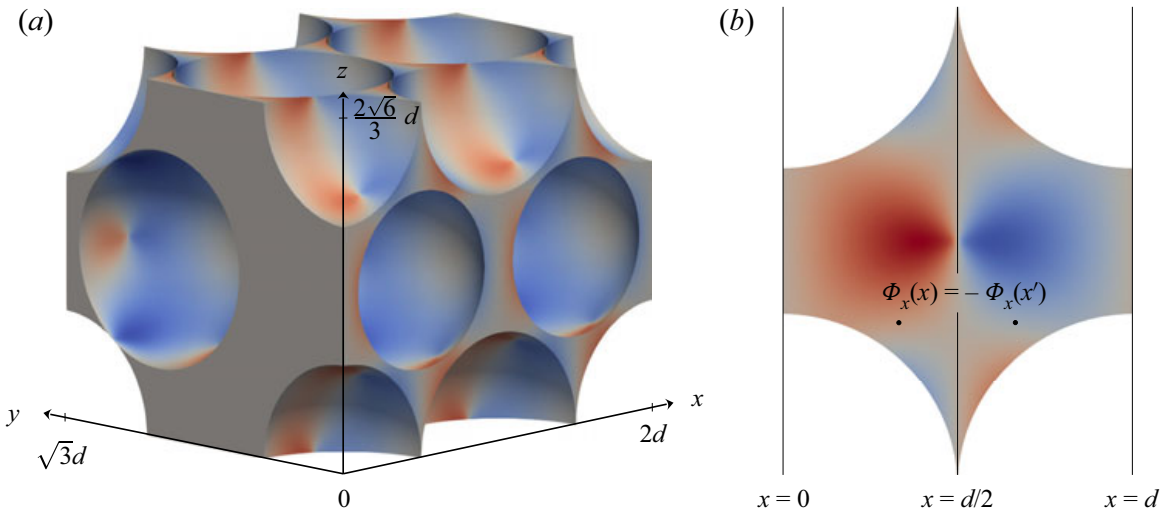

Figure 5. Auxiliary potential Φ_x in the hexagonal sphere pack (*a*) in a three-dimensional view and (*b*) in the plane $\sqrt{3}/3\,y - \sqrt{6}/3\,z = 0$ with the mirror planes $x = 0$, $x = d/2$ and $x = d$ of the hexagonal sphere pack. The auxiliary potential Φ_x is antisymmetric with respect to these mirror planes. The colours range from $-0.15\,d$ (blue) to $0.15\,d$ (red).

related to the well-known 'high-frequency limit of the dynamic tortuosity' α_∞ by Johnson *et al.* (1987). As the tensor of virtual inertia can be precomputed for a given geometry, no further model is necessary to describe the accelerative pressure drag. The viscous pressure drag is a weighted surface integral of the source term of the viscous pressure $p^{(v)}$. As demonstrated in Appendix A.3, the viscous pressure drag can be reformulated in terms of the wall shear stress as

$$-\frac{1}{V}\int_{A_{fs}} p^{(v)}\,\boldsymbol{n}\,\mathrm{d}A = \frac{1}{V}\int_{A_{fs}} (\nabla \otimes \boldsymbol{\Phi})^{\mathrm{T}} \cdot \boldsymbol{\tau}_w\,\mathrm{d}A \tag{2.10}$$

for the present boundary conditions. As both the friction drag and the viscous pressure drag are integrals of the wall shear stress with only geometry-dependent weights, these terms should have the same scaling. The convective pressure drag term (2.7*c*) has also been referred to as 'Q-induced force' (Aghaei-Jouybari *et al.* 2022). Due to the fore–aft antisymmetry of the auxiliary potential Φ_x in the hexagonal sphere pack (figure 5), drag can only be produced from the part of the distribution of the Q-invariant that is antisymmetric with respect to the fore–aft symmetry.

Finally, we can insert the decomposition (2.7) into the volume-averaged momentum equation (1.3):

$$\rho\frac{\mathrm{d}\langle \boldsymbol{u}\rangle_s}{\mathrm{d}t} = \underbrace{-\frac{1}{V}\int_{A_{\mathrm{fs}}} (\boldsymbol{I} - \nabla \otimes \boldsymbol{\Phi})^{\mathrm{T}} \cdot \boldsymbol{\tau}_w\,\mathrm{d}A}_{\textit{friction and viscous pressure drag}} + \underbrace{\frac{1}{V}\int_{V_f} \boldsymbol{\Phi}\,2\rho Q\,\mathrm{d}V}_{\textit{convective pressure drag}} + \underbrace{[\epsilon\boldsymbol{I} - (1-\epsilon)\,\boldsymbol{A}]\cdot\boldsymbol{f}}_{\textit{effective forcing}}. \tag{2.11}$$

In this form, the drag in the porous media flow is separated into a surface contribution due to the viscous term and a volume contribution due to the convective term of the Navier–Stokes equations. It can also be seen that only a fraction of the macroscopic pressure gradient acts onto the flow. In the remainder of the paper, we apply the pressure drag decomposition to a DNS dataset of steady and oscillatory flow in a hexagonal sphere pack. We also show in the Appendices B.2 and B.3 how the drag terms in (2.11) can be used to rederive the results of Johnson *et al.* (1987) for linear oscillatory flow at high

Womersley numbers and to generalise the theory of Mei & Auriault (1991) to oscillatory flow at low Reynolds numbers, respectively.

3. Methodology

3.1. *Description of the flow solver*

The simulation dataset used in this paper was obtained using our in-house code MGLET (Manhart, Tremblay & Friedrich 2001). It employs a block-structured Cartesian grid with a staggered arrangement of variables (Harlow & Welch 1965) on which the incompressible Navier–Stokes equations are discretised by means of a finite volume method with second-order central approximations. A third-order low-storage Runge–Kutta method is used for the time integration. In every stage a projection step is performed to make the stage velocity divergence-free. This requires the solution of a discrete Poisson problem for a correction pressure. The no-slip boundary conditions on the spheres are enforced by a second-order accurate ghost-cell immersed boundary method (Peller *et al.* 2006; Peller 2010). In this approach, the velocity field in the interface cells is approximated by a linear least-squares interpolant that satisfies the no-slip boundary condition. From this the specific volume fluxes are computed for the convective velocities, whereas the point values are computed for the convected velocities. The convective velocities are made divergence-free by a cell-by-cell iterative correction that is coupled to the pressure correction in the field. As a result the immersed boundary method is mass conserving.

3.2. *Description of the porous medium geometry*

A hexagonal close-packed arrangement of spheres (simply referred to as hexagonal sphere pack) is considered as a porous medium geometry. It is triply periodic with the lattice vectors $d\,\boldsymbol{e}_x$, $1/2\,d\,\boldsymbol{e}_x + \sqrt{3}/2\,d\,\boldsymbol{e}_y$ and $2\sqrt{6}/3\,d\,\boldsymbol{e}_z$, and the primitive unit cell (figure 1*b*) contains two spheres of diameter d that are placed at the locations $(0, 0, 0)\,d$ and $(1/2, 2\sqrt{3}/3, \sqrt{6}/3)\,d$ (Conway & Sloane 1999, p. 114). The sphere pack has a porosity $\epsilon = 1 - \pi/(3\sqrt{2}) = 0.26$ which is identical to the porosity of the cubic close-packing studied for example in Hill *et al.* (2001), Hill & Koch (2002) and He *et al.* (2019). The hexagonal close-packing arrangement possesses a total number of 24 symmetries (Cockroft 1999, space group 194), for example mirror symmetries about the planes $x = 1/2\,d$ and $z = \sqrt{6}/3\,d$.

3.3. *Description of the simulation database*

The drag decomposition will be evaluated for a collection of DNSs of steady and oscillatory flow through a hexagonal close-packed arrangement of spheres (Conway & Sloane 1999, p. 114). The simulation parameters of the steady and the oscillatory cases are summarised in tables 1 and 2, respectively. Figure 6 shows the distribution of the simulated cases in the *Hg–Wo* parameter space. Note that since oscillatory flow in the quasisteady limit ($Wo \to 0$) is in equilibrium at every instant, its behaviour is identical to the corresponding steady flow.

For all cases, we used a triply periodic simulation domain with the lengths $L_x = 2\,d$, $L_y = \sqrt{3}\,d$ and $L_z = 2\sqrt{6}/3\,d$ in the x-, y- and z-directions, respectively. The simulation domain thus contains four primitive unit cells. Choosing an appropriate domain size is essential since the flow may otherwise be constrained to a periodic state far from what would be observed in larger domains. Since laminar flow has the same periodicity as the geometry, it would be sufficient to consider one unit cell. Using multiple unit cells allows

Case	Hg	Re	$d/\Delta x$	$T_{sim}\langle u\rangle_i/d$	$T_{avg}\langle u\rangle_i/d$	$N_{samples}$	$(r)_{rms}/\left(f_{px}\right)_{rms}$
L4†	6.50×10^{1}	0.0114	320	0.00158	—	—	1.5 %
L6†	6.50×10^{3}	1.14	320	0.158	—	—	1.5 %
SNL1†	6.50×10^{4}	10.5	320	1.45	—	—	1.4 %
SNL2†	3.25×10^{5}	36.6	320	5.08	—	—	1.0 %
SNL4	6.50×10^{5}	58.9	320	2.04	—	—	0.8 %
UNL1	1.30×10^{6}	91.1	320	10.5	—	—	0.6 %
UNL2	2.60×10^{6}	138	320	19.2	16.8	36	0.6 %
T1	5.20×10^{6}	208	320	12.6	7.22	21	0.8 %
T2	7.80×10^{6}	263	320	16.7	15.2	51	0.9 %
T3	1.04×10^{7}	313	320	17.7	14.9	56	1.2 %
T4	1.30×10^{7}	354	320	11.8	9.33	39	1.2 %

Table 1. Simulation parameters of the steady cases and root mean square of the pressure drag decomposition residual. The simulations marked with † were recomputed at a finer grid resolution compared with Sakai & Manhart (2020). The value $N_{samples}$ denotes the number of snapshots that were collected during the averaging time T_{avg}. The residual $r = f_{px} - f_{px}^{(a)} - f_{px}^{(v)} - f_{px}^{(c)}$ of the pressure drag decomposition was computed for each snapshot.

Case	Hg	Wo	Re	$d/\Delta x$	$T_{sim}\Omega/(2\pi)$	$N_{samples/\mathrm{period}}$	$(r)_{rms}/\left(f_{px}\right)_{rms}$
LF1†	1.00×10^{3}	10	0.171	384	1.5	12.5	0.2 %
LF2†	1.00×10^{4}	10	1.7	384	2.25	25	0.2 %
LF3†	1.00×10^{5}	10	14.8	384	1.4	100	0.1 %
LF4†	1.00×10^{6}	10	76.7	384	1.25	100	0.3 %
LF5	3.16×10^{6}	10	158	384	2.27	100	1.0 %
LF6	1.00×10^{7}	10	307	384	1.56	100	2.3 %
MF1†	1.00×10^{4}	31.6	0.857	384	3	50	1.0 %
MF2†	1.00×10^{5}	31.6	8.57	384	3	50	0.9 %
MF3†	3.16×10^{5}	31.6	26.9	384	3	50	0.8 %
MF4†	1.00×10^{6}	31.6	73.1	384	3	25	0.7 %
MF5	3.16×10^{6}	31.6	157	384	6.4	50	1.1 %
MF6	1.00×10^{7}	31.6	298	384	2.26	50	2.7 %
HF1†	1.00×10^{5}	100	1.3	384	20.4	25	1.6 %
HF2†	1.00×10^{6}	100	13	384	19.9	25	1.6 %
HF3†	1.00×10^{7}	100	132	384	6.32	25	1.1 %
HF4†	1.78×10^{7}	100	252	768	8	50	0.9 %
HF5	3.16×10^{7}	100	465	768	6	25	1.5 %

Table 2. Simulation parameters of the oscillatory cases and root mean square of the pressure drag decomposition residual. The simulations marked with † were taken from Unglehrt & Manhart (2022*a*). The residual $r = f_{px} - f_{px}^{(a)} - f_{px}^{(v)} - f_{px}^{(c)}$ of the pressure drag decomposition was computed for each snapshot.

us to observe the breaking of this periodicity, which is an indicator of a transitional or turbulent flow state. In these regimes, it is plausible that structures spanning multiple pores could form. However, in their study of turbulent flow through a cubic-close packed array of spheres at $Re = 222$, 370 and 740, He *et al.* (2019) found that '[. . .] the integral scales for all Reynolds numbers studied in this work are much smaller than the particle diameter and thus the unit cell domain showed little variation in statistics compared to a larger domain'. Consequently, we would expect only minor changes if the domain size were increased. The findings of Agnaou *et al.* (2016) further support this view; they observed that the

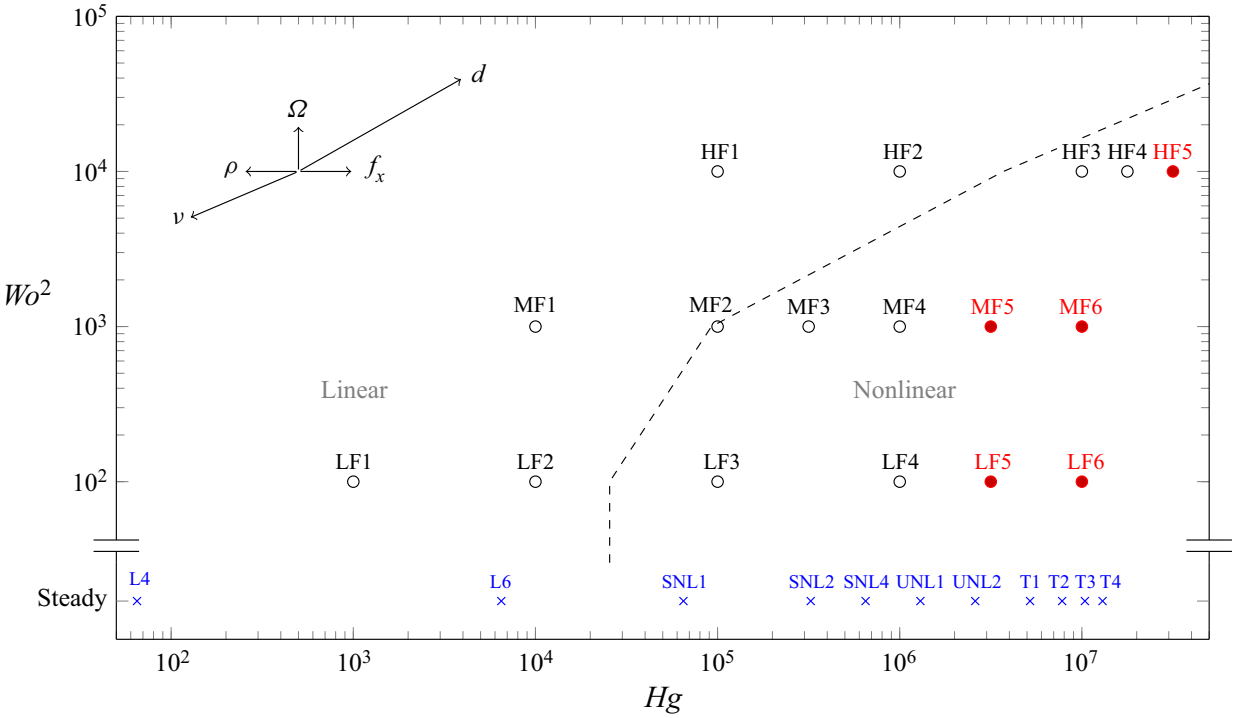

Figure 6. Parameter space for the hexagonal sphere pack. The blue crosses represent the steady simulations in Sakai & Manhart (2020) that correspond to the limit $Wo \to 0$. The open circles denote the simulations in Unglehrt & Manhart (2022*a*) of laminar oscillatory flow and the red filled circles represent simulations of transitional and turbulent oscillatory flow. The dashed line separates the linear regime on the left-hand side from the nonlinear regime on the right-hand side (Unglehrt & Manhart 2022*a*).

critical Reynolds number for the onset of unsteady flow in arrays of cylinders is essentially independent of the domain size if the porosity is small ($\epsilon \lesssim 0.45$).

The steady cases are based on the transient flow simulations by Sakai & Manhart (2020). They classified their flow cases into linear (L), steady nonlinear (SNL), unsteady nonlinear (UNL) and turbulent (T) regimes. For large times, the linear and steady nonlinear cases resulted in a constant flow field, whereas the unsteady nonlinear and turbulent cases resulted in a temporally fluctuating velocity field. The low-Reynolds-number cases were recomputed on a finer grid in order to reduce the errors in the evaluation of the pressure decomposition. Thus, all simulations of steady flow used in the present paper were performed using a resolution of 320 cells per sphere diameter (cpd). The high-Reynolds-number simulations UNL2–T4 were continued in order to collect instantaneous flow fields for a statistical evaluation of the mean and turbulent drag components. When the case UNL1 was continued up to a time $t\,\langle u\rangle_i\,/d = 10.5$, the chaotic oscillations changed into a decaying harmonic oscillation which indicates that the flow converges to a steady state.

The oscillatory cases are based on the simulations in Unglehrt & Manhart (2022*a*) of linear and nonlinear laminar oscillatory flow. The cases are grouped according to their Womersley number into the low frequency regime (LF) at $Wo = 10$, the medium frequency regime (MF) at $Wo = 31.62$ and the high frequency regime (HF) at $Wo = 100$ and numbered consecutively from 1 to 4 with increasing Hagen number. We performed additional simulations of oscillatory flow (cases LF5, LF6, MF5, MF6 and HF5) that were classified as transitional or turbulent based upon their symmetry behaviour (Unglehrt & Manhart 2022*b*). The cases HF4 and HF5 were computed at a resolution of 768 cpd and the other oscillatory flow cases were computed at a resolution of 384 cpd. We found in Unglehrt & Manhart (2022*a*) that the cases LF1, LF2, MF1, MF2, HF1, HF2 show

effectively linear behaviour and the cases LF3, MF3, HF3 and LF4, MF4, HF4 exhibit nonlinear effects of comparable strength, respectively. For all simulations, the time series of the volume-averaged velocity as well as instantaneous velocity and pressure fields were saved. For the simulations LF5, LF6, MF5, MF6 and HF5, which are transitional or turbulent, only the instantaneous values are discussed as it is computationally expensive to obtain converged statistics for an oscillatory flow.

In Sakai & Manhart (2020) and Unglehrt & Manhart (2022*a*), the relationship between the imposed pressure gradient and the superficial velocity in the steady and linear oscillatory cases was validated with results from the literature and the grid resolution was determined based on a grid study. The grid convergence of the new cases LF5, LF6, MF5, MF6 and HF5 was assessed based on simulations with coarser grids at resolutions of 48, 96 and 192 cpd (Appendix C). We found that the differences in the cycle-averaged kinetic energy and in the maximum amplitude of the superficial velocity between the finest and the second finest resolution were less than 1.8 % for all cases.

3.4. *Calculation of the terms in the decomposition*

In this section, we describe the details of the evaluation of the terms in the drag decomposition from our simulation data. Moreover, we quantify the errors introduced by the decomposition and the statistical errors. First, the pressure drag components were determined from snapshots of the flow fields. The accelerative pressure drag $\boldsymbol{f}_p^{(a)}$ could be calculated in closed form using the tensor of virtual inertia (2.8) obtained from the auxiliary potential. The viscous pressure drag $\boldsymbol{f}_p^{(v)}$ was calculated in the form of (2.7*b*). To obtain the second derivative $\Delta\boldsymbol{u}\cdot\boldsymbol{n}$ at the surface, the wall normal velocity v was interpolated to a point at wall distance $h = 1.5\Delta x$. The value of $\Delta\boldsymbol{u}\cdot\boldsymbol{n}|_w$ was then calculated using a Taylor expansion of the wall normal velocity profile

$$v(y) = \underbrace{v|_w}_{=0} + \underbrace{\left.\frac{\partial v}{\partial y}\right|_w}_{=0} y + \left.\frac{\partial^2 v}{\partial y^2}\right|_w \frac{y^2}{2} = \Delta\boldsymbol{u}\cdot\boldsymbol{n}|_w \frac{y^2}{2} \tag{3.1}$$

that satisfies the no-slip, impermeability and incompressibility conditions. The convective pressure drag $\boldsymbol{f}_p^{(c)}$ was determined by the volume integral (2.7*c*). As the integrand $\boldsymbol{\Phi}Q$ can take large positive and negative values, the numerical evaluation of the integral is a delicate task. Due to the symmetry of the hexagonal sphere pack, flow in the positive and negative x-direction should behave the same. To enforce this behaviour, we made the values of the auxiliary potential Φ_x antisymmetric with respect to the mirror planes $x = 0$, $x = d/2$, $x = d$, etc. (figure 5) by setting $\Phi_x(x) := [\Phi_x(x) - \Phi_x(2d - x)]/2$. Note that this is unnecessary in the continuous setting due to the identities $\langle Q\rangle_s = 0$ and (A7), which are, however, not perfectly satisfied in the discrete sense. In addition, the Q-invariant was formulated as the divergence of the convective term in order to be consistent with the projection method used in our flow solver. The interface cells were not included in the integration as $Q = 0$ at no-slip walls.

We determined the residual of the pressure drag decomposition with respect to the pressure drag force that was directly computed from the instantaneous pressure fields. In tables 1 and 2, we report the root mean square residuals over all snapshots; for the steady cases L4, L6, SNL1, SNL2 and SNL4 we report only the residual at the final time. It can be seen that the balance is closed with satisfactory accuracy considering that the total and viscous pressure drag terms have been computed at a ghost-cell immersed boundary. The residual of the decomposition increases with the Womersley number; this can be explained by the formation of boundary layers that increase the error in the evaluation of the source

term for the viscous pressure especially near the contact points of the spheres. A higher residual is also observed for the transitional and turbulent cases.

Second, we determined the friction drag using the volume-averaged momentum balance (1.3). The pressure drag term was computed directly from the instantaneous pressure fields and the superficial acceleration was obtained from the derivative of the time series of the superficial velocity $\langle u \rangle_s$.

Third, for the line plots of the oscillatory cases in § 4 the snapshot values in the last period of each simulation were shifted such that the abscissae $\varphi := \Omega t$ lie in $[0, 2\pi]$. Since the sinusoidal behaviour of the linear cases was misrepresented by a piecewise linear curve due to the relatively low number of samples (table 2), we used a Fourier series interpolation of the snapshot values. For the cases LF5, LF6, MF5 and MF6 a piecewise cubic interpolation (Akima 1974) was used due to high frequency fluctuations during parts of the cycle.

Finally, we averaged the snapshot values for the steady chaotic and turbulent cases UNL2, T1, T2, T3 and T4. For the cases L4–UNL1 we used only the final flow field of the simulation. To decompose the time-averaged convective pressure drag into its direct and turbulent contributions (see § 2.3), we determined the direct convective pressure drag from the time-averaged velocity field and then computed the turbulent convective pressure drag from the difference between the total and the direct contribution. The time-averaged velocity field was estimated from the snapshots. The number of samples is given in table 1. Since our simulation domain contains eight repetitions of the same pore geometry (Unglehrt & Manhart 2022*a*), we included shifted copies of every instantaneous field into the average. This led to a nominal increase of the sample size by a factor of eight.

We estimated the statistical error for each drag component with the Student's t-distribution. In all cases the 95 % confidence interval of the sample average had a half-width smaller than 0.75 % of the average value. While the underlying assumption of a Gaussian distribution of the sample values was not satisfied for some of the cases, we nevertheless expect that the statistical error has in a similar order of magnitude.

3.5. *Calculation of the auxiliary potential field*

As the ghost cell immersed boundary method in MGLET (see 3.1) is tailored towards flow with no-slip boundary conditions, we computed the auxiliary potential field with the finite element method (FEM) using the FEniCS solver framework (Logg, Mardal & Wells 2012). We employed uniform meshes of linear tetrahedral elements with resolutions up to 384 cpd. From the numerical solution for the auxiliary potential $\boldsymbol{\Phi}$, we obtained the tensor of virtual inertia

$$\boldsymbol{A} = \begin{bmatrix} 0.1345 & 0 & 0 \\ 0 & 0.1345 & 0 \\ 0 & 0 & 0.1329 \end{bmatrix} \tag{3.2}$$

where the off-diagonal terms are numerically zero. Furthermore, we computed the length scale tensor $\boldsymbol{L}$ defined in § B.2,

$$\begin{aligned} \boldsymbol{L} &= 2\left[\epsilon\, \boldsymbol{I} - (1-\epsilon)\, \boldsymbol{A}\right] \cdot \left[\frac{1}{V} \int_{A_{fs}} (\boldsymbol{I} - \nabla \otimes \boldsymbol{\Phi})^{\mathrm{T}} \cdot (\boldsymbol{I} - \nabla \otimes \boldsymbol{\Phi})\, \mathrm{d}A \right]^{-1} \\ &= \begin{bmatrix} 0.05886 & 0 & 0 \\ 0 & 0.05922 & 0 \\ 0 & 0 & 0.06011 \end{bmatrix} d \end{aligned} \tag{3.3}$$

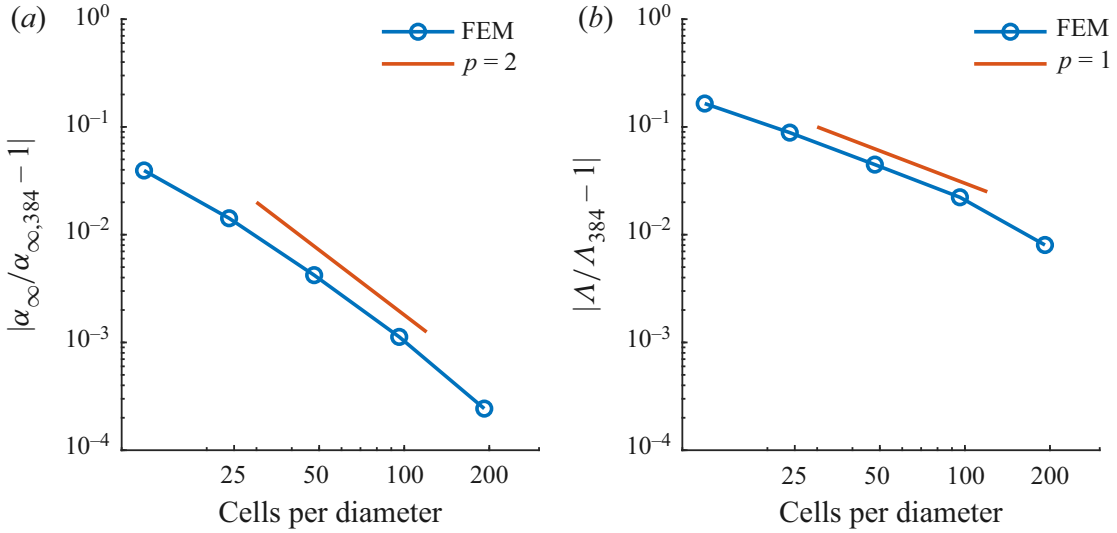

Figure 7. Mesh convergence of the auxiliary potential solution. We give the difference in the high-frequency limit of the dynamic tortuosity α_∞ and the length scale Λ relative to their values at a resolution of 384 cpd.

where the off-diagonal elements are numerically zero, too.

The hexagonal sphere pack is isotropic in the x–y plane and possesses the same arrangement of spheres as the face-centred cubic sphere pack. Therefore, we can compare our results with the values of Chapman & Higdon (1992) who give a value $1/F = 1.612 \times 10^{-1}$ for the 'electrical formation factor' F, corresponding to a value $\alpha_\infty = \epsilon/F = 1.61$ for the high-frequency limit of the dynamic tortuosity, and a value $\Lambda = 0.062\,d$ for the length scale defined by Johnson *et al.* (1987). From (3.2) and (3.3), we obtain the values

$$\alpha_\infty = \left(1 - \frac{1-\epsilon}{\epsilon}\frac{A_{11} + A_{22}}{2}\right)^{-1} = 1.622, \tag{3.4}$$

$$\Lambda = \frac{L_{11} + L_{22}}{2} = 0.05904\,d, \tag{3.5}$$

which show a satisfactory agreement with the results of Chapman & Higdon (1992).

Figure 7 shows the convergence of α_∞ and Λ over the resolution, which was successively doubled starting from 12 cpd. At intermediate resolutions, we observe a second-order convergence for α_∞ and a first-order convergence for Λ. The value of $\boldsymbol{L}$ is uncertain as we expect the velocity potential to behave as $O(r^{\sqrt{2}-1})$ close to the contact point, leading to a singular velocity (Cox & Cooker 2000). Consequently, we observe a decrease in the rate of convergence. Nevertheless, we consider the numerical solution for the auxiliary potential $\boldsymbol{\Phi}$ at a resolution of 384 cpd as well converged.

4. Results

In this section, we apply the decomposition of the pressure drag (2.7) to our DNS dataset of flow through a hexagonal sphere pack. First, we analyse the steady flow (§ 4.1) and linear oscillatory flow cases (§ 4.2). These represent the quasisteady limit $Wo \to 0$ and the small amplitude limit $Re \to 0$ and serve as a baseline for discussing of the effects of the Reynolds number and the Womersley number in nonlinear oscillatory flow. We then analyse the nonlinear oscillatory flow data (§ 4.3).

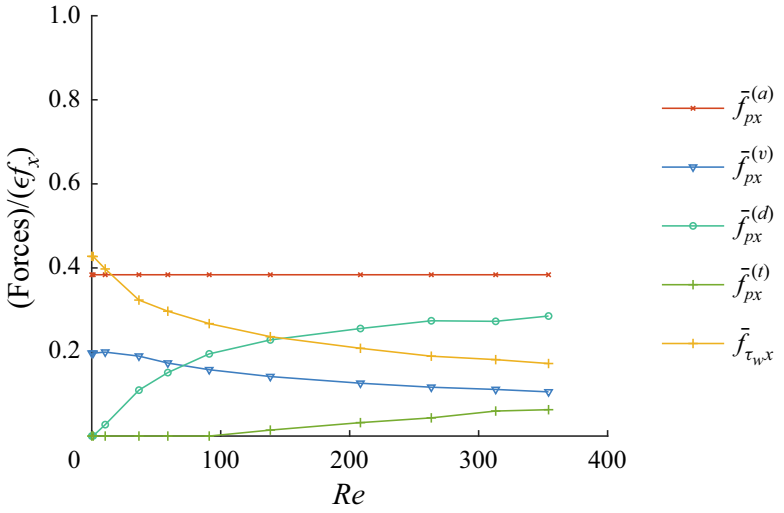

Figure 8. Drag components in steady flow normalised with the imposed macroscopic pressure gradient ϵf_x.

4.1. *Stationary flow*

In this section, we discuss the decomposed drag of our DNS dataset for steady nonlinear flow. In particular, we analyse the dependence of the different drag components on the Reynolds number. Figure 8 shows the contributions of the drag components to the Reynolds-averaged momentum budget in the x-direction:

$$\frac{1}{\epsilon f_x}\left[\underbrace{\rho\frac{\mathrm{d}\langle\bar{u}\rangle_s}{\mathrm{d}t}}_{=0}+\bar{f}_{px}^{(a)}+\bar{f}_{px}^{(v)}\underbrace{+\bar{f}_{px}^{(d)}+\bar{f}_{px}^{(t)}}_{=\bar{f}_{px}^{(c)}}+\bar{f}_{\tau_w x}\right]=1. \tag{4.1}$$

Since we have divided the momentum equation by the magnitude of the macroscopic pressure gradient ϵf_x, the terms represent the fraction of the total drag for each drag component. The accelerative pressure drag $\boldsymbol{f}_p^{(a)}$ is a pure function of the macroscopic pressure gradient and the geometry due to its definition in (2.3*a*); its relative contribution to the total stress balance has a value of 38.4 % independent of the Reynolds number. The viscous pressure drag $\boldsymbol{f}_p^{(v)}$ and the friction drag both decrease with the Reynolds number. At low Reynolds numbers the friction drag is approximately twice as large as the viscous pressure drag. For Reynolds numbers above 36, the ratio between the terms remains almost constant around 1.7. The direct convective pressure drag $\bar{f}_{px}^{(d)}$ caused by the time-averaged velocity field starts at zero and increases with the Reynolds number. It overtakes the friction and pressure drag at a Reynolds number of approximately 250. The drag $\bar{f}_{px}^{(t)}$ caused by the Reynolds stresses is non-zero only for the unsteady nonlinear and turbulent cases. Its share increases with the Reynolds number and reaches 6 % of the total drag at the highest Reynolds number (which is 22 % of the direct convective pressure drag).

In order to investigate the scaling of the drag components with Re, we form a friction factor-like quantity by normalising the drag with ρ, $\langle u\rangle_s$ and d. The result is shown in figure 9. For small Reynolds numbers, especially between the cases L4 and L6, the viscous pressure drag coefficient and the friction drag coefficient decrease with $1/Re$, indicating a linear dependence of these drag components on the Reynolds number. The convective pressure drag coefficient increases proportionally to Re, corresponding to a cubic dependence of the drag on Re. These observations are consistent with the theory of

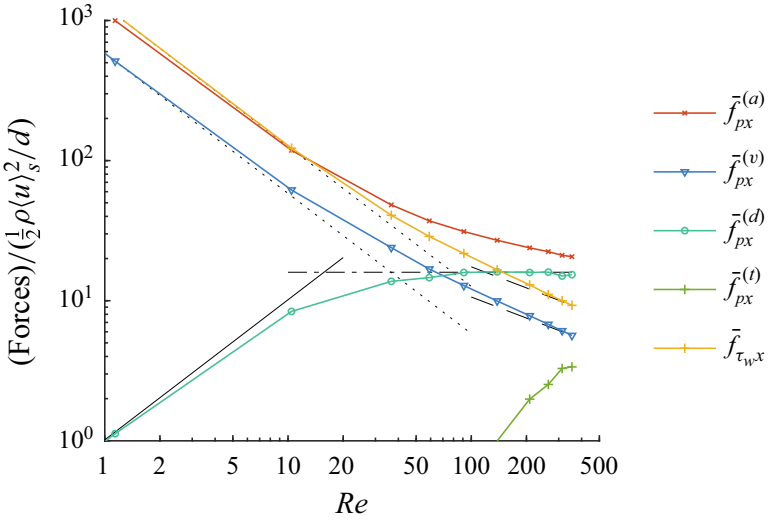

Figure 9. Drag components in steady flow normalised with $\frac{1}{2}\rho\langle u\rangle_s^2/d$. The black lines represent different scalings with the Reynolds number: $1/Re$ (dotted), $1/\sqrt{Re}$ (dashed), 1 (dash-dotted) and Re (solid). The scaling line for Re was anchored at the case L4, the scaling lines for $1/\sqrt{Re}$ were anchored at the case T4, and the scaling line for 1 was set to the mean value of the cases UNL1–T2.

Mei & Auriault (1991). For large Reynolds numbers (T1–T4), the friction drag coefficient and the viscous pressure drag coefficient approach a scaling with exponents -0.63 and -0.61, respectively. This is very close to the classical laminar boundary layer scaling $1/\sqrt{Re}$ of the friction coefficient (dashed line). The direct convective drag due to the mean velocity field shows a nearly perfect scaling with Re^2 for Reynolds numbers between 91 and 263, as indicated by a constant drag coefficient. For higher Reynolds numbers, the direct convective pressure drag coefficient shows a slight decrease. There is no clear scaling for the turbulent convective pressure drag. Although we see neither a quadratic scaling of the convective pressure drag nor a linear scaling of the friction and viscous pressure drag in the steady nonlinear regime ($Re = 10$–59), the total drag can be described by the Forchheimer equation (1.8), i.e. the sum of a linear and a quadratic term (Sakai & Manhart 2020).

4.2. *Linear oscillatory flow*

In this section, we present the results of the drag decomposition for linear oscillatory flow and compare them with theoretical results from the literature. In particular, we discuss the cases LF1 and LF2 at $Wo = 10$, MF1 and MF2 at $Wo = 31.62$, and HF1 and HF2 at $Wo = 100$; all of which have been shown to exhibit linear behaviour in Unglehrt & Manhart (2022*a*).

The theoretical behaviour of linear oscillatory flow is well understood (Landau & Lifshits (1987, pp. 83f); Batchelor (2000, pp. 353f); Lafarge (2009)) and is summarised below. The velocities and forces are directly proportional to the magnitude of the macroscopic pressure gradient, ϵf_x; the velocities and forces normalised by ϵf_x depend only on the Womersley number. At low frequencies ($Wo \to 0$), the velocity is in phase with the forcing and is governed by the steady Stokes equations. At high frequencies, the flow has a boundary layer structure: the bulk flow is irrotational and has a phase lag of 90° with respect to the forcing, and the amplitude of the bulk flow decreases as Wo^{-2}. Near the wall, the flow behaves like the Stokes boundary layer for which the wall shear stress is history

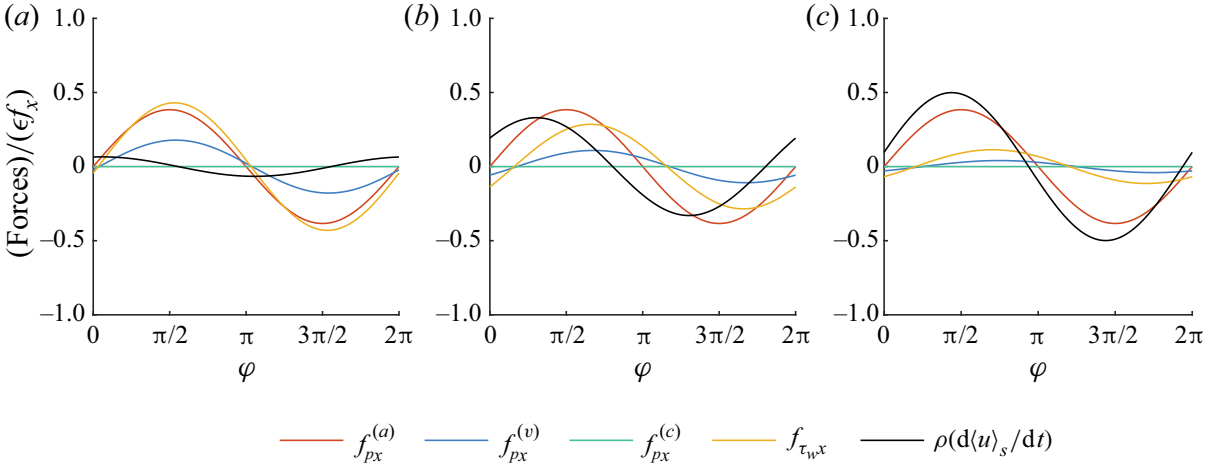

Figure 10. Drag components in linear flow normalised with the amplitude of the imposed macroscopic pressure gradient ϵf_x for $Wo = 10$ (LF1), $Wo = 31.62$ (MF1) and $Wo = 100$ (HF1).

dependent and advances the outer flow velocity by 45° (Schlichting & Gersten 2017, p. 142). The superficial velocity can be predicted by Darcy's law or the unsteady Darcy equation (Zhu & Manhart 2016) for low frequencies and by the asymptotics of Johnson *et al.* (1987) for high frequencies. The well-known model of Johnson *et al.* (1987) blends these asymptotes and predicts the response of the superficial velocity with good accuracy (Chapman & Higdon 1992; Unglehrt & Manhart 2022*a*). Please note that the asymptotics of Johnson *et al.* (1987) can be directly obtained from the drag decomposition (2.11) and the Stokes boundary layer solution (see Appendix B.2). This calculation suggests that the viscous pressure drag and the friction drag have the same time dependence as $Wo \to \infty$.

In the following, we address the question of which processes take up the momentum that is supplied to the flow by the macroscopic pressure gradient. To this end, we rearrange the volume-averaged momentum equation like in (4.1):

$$\frac{1}{\epsilon f_x}\left[\rho\frac{\mathrm{d}\langle u\rangle_s}{\mathrm{d}t} + f_{px}^{(a)} + f_{px}^{(v)} + f_{px}^{(c)} + f_{\tau_w x}\right] = \sin(\Omega t). \tag{4.2}$$

Figure 10 displays the terms of this equation over the course of one period of oscillation ($\varphi := \Omega t \mod 2\pi$) for the simulations LF1, MF1 and HF1. We observe that the acceleration term increases with the Womersley number whereas the viscous pressure and friction drag decrease with the Womersley number. By definition, the accelerative pressure drag remains constant at 38.4 % of the macroscopic pressure gradient. At $Wo = 10$ more than half of the drag is caused by friction and the viscous pressure. On the other hand, at $Wo = 100$ most of the pressure drag is caused by the accelerative pressure and the contributions of the friction and viscous pressure drag decrease. Table 3 summarises the relative amplitudes and the phase lag of the different terms with respect to the macroscopic pressure gradient. It can be seen that both quantities are in line with the theoretical expectations and reflect the change of the velocity field from a Stokes flow to a potential flow with thin boundary layers.

The convective pressure has almost no contribution to the force balance. As in the steady state, the convective pressure drag exhibits a cubic scaling with the Reynolds number. This is demonstrated by the collapse of the suitably normalised $f_{px}^{(c)}$ curves for LF1 and LF2, MF1 and MF2, and HF1 and HF2 in figure 11. The relative intensity of the convective pressure drag decreases strongly with the Womersley number. The cubic scaling follows from the drag decomposition when the symmetries of the flow in the hexagonal sphere

	$Wo \to 0$	$Wo = 10$	$Wo = 31.62$	$Wo = 100$	$Wo \to \infty$
$\rho \dfrac{\mathrm{d}\langle u\rangle_s}{\mathrm{d}t}$	0 % −90°	6.6 % −80°	33.0 % −35.4°	49.9 % −11°	61.6 % 0°
$f_{\tau_{wx}}$	42.8 % 0°	43.0 % 4.2°	28.5 % 26.1°	11.4 % 42.1°	0 % 45°
$f_p^{(v)}$	19.7 % 0°	17.8 % 2.9°	10.9 % 22.8°	4.1 % 34.1°	0 % 45°

Table 3. Relative amplitude and phase lag of the acceleration, the accelerative pressure drag, the friction drag and the viscous pressure drag with respect to to the macroscopic pressure gradient $\epsilon f_x \sin(\Omega t)$ in linear flow. The limits $Wo \to 0$ and $Wo \to \infty$ correspond to Stokes flow (case L4) and potential flow, respectively. Note that the accelerative pressure drag $f_p^{(a)}$ always has a relative amplitude of 38.4 %; the convective pressure drag $f_p^{(c)}$ is negligible in linear flow.

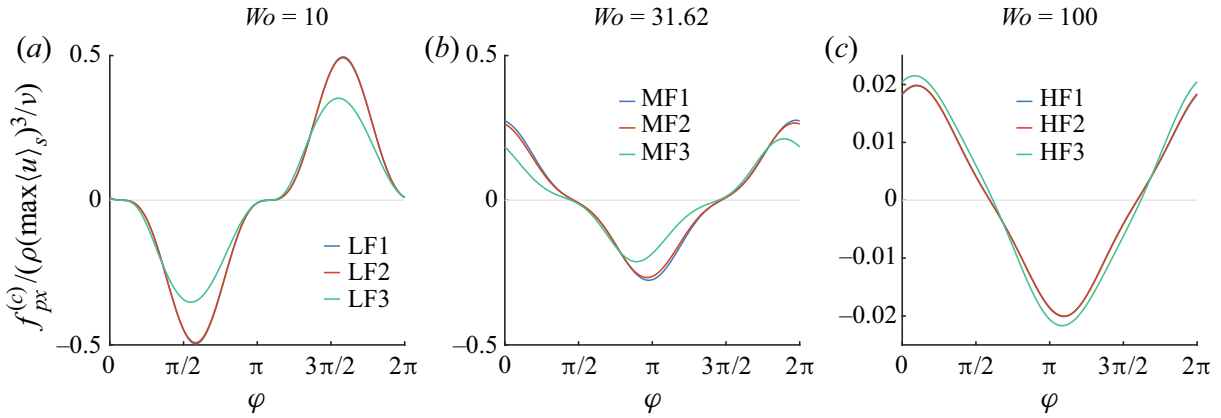

Figure 11. Convective pressure drag normalised with $\rho(\max\langle u\rangle_s)^3/\nu$ corresponding to the scaling of Mei & Auriault (1991).

pack are taken into account (see Appendix B.3). For $Wo = 10$ we can observe a saddle point at the zero crossing of the convective pressure drag, which is consistent with a $\langle u\rangle_s^3$ behaviour of the convective pressure drag. For $Wo = 31.62$ and $Wo = 100$, this saddle point is absent.

4.3. *Nonlinear oscillatory flow*

In this section, we analyse the simulations of nonlinear oscillatory flow. The momentum budgets for the weakly nonlinear cases LF3, MF3 and HF3 are not shown, as they differ only slightly from the linear regime. However, it can be seen in figure 11 that for these cases the convective pressure drag deviates from the cubic Reynolds number scaling.

For the strongly nonlinear cases, figures 12, 13 and 14 show the terms of the momentum equation for $Wo = 10$, $Wo = 31.62$ and $Wo = 100$, respectively. Like in the previous section, the forces are normalised with the amplitude ϵf_x of the macroscopic pressure gradient (cf. (4.2)) such that all terms sum up to $\sin(\Omega t)$ and the accelerative pressure drag appears as $0.384\sin(\Omega t)$.

At the lowest Womersley number (figure 12), the acceleration is very small compared with the drag forces and the drag components are mostly in phase with the macroscopic pressure gradient. Hence, the flow can be considered quasisteady. The acceleration

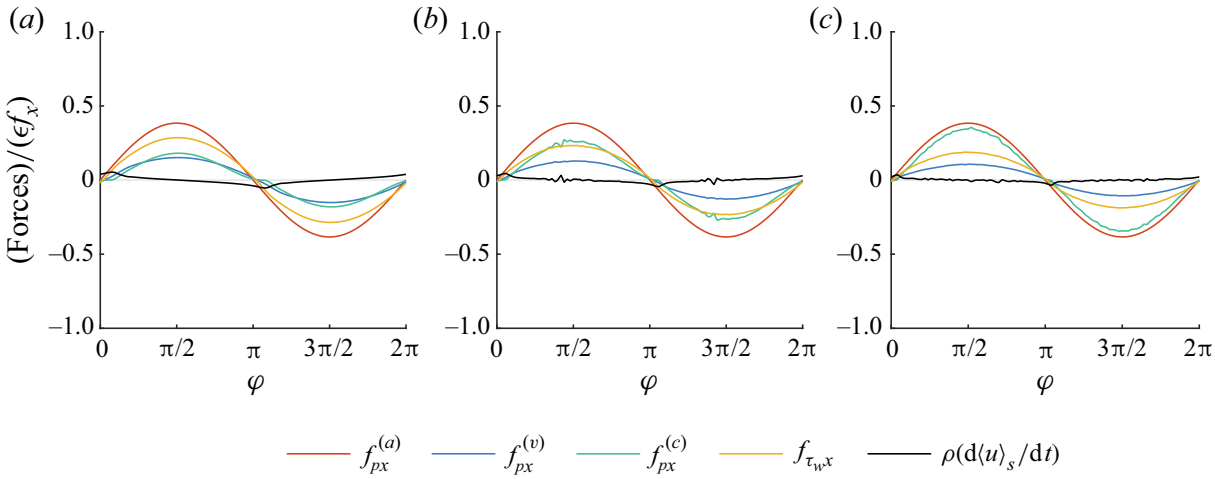

Figure 12. Drag components in nonlinear flow at $Wo = 10$ normalised with the amplitude of the imposed macroscopic pressure gradient ϵf_x for $Re = 77$ (LF4), $Re = 158$ (LF5) and $Re = 306$ (LF6).

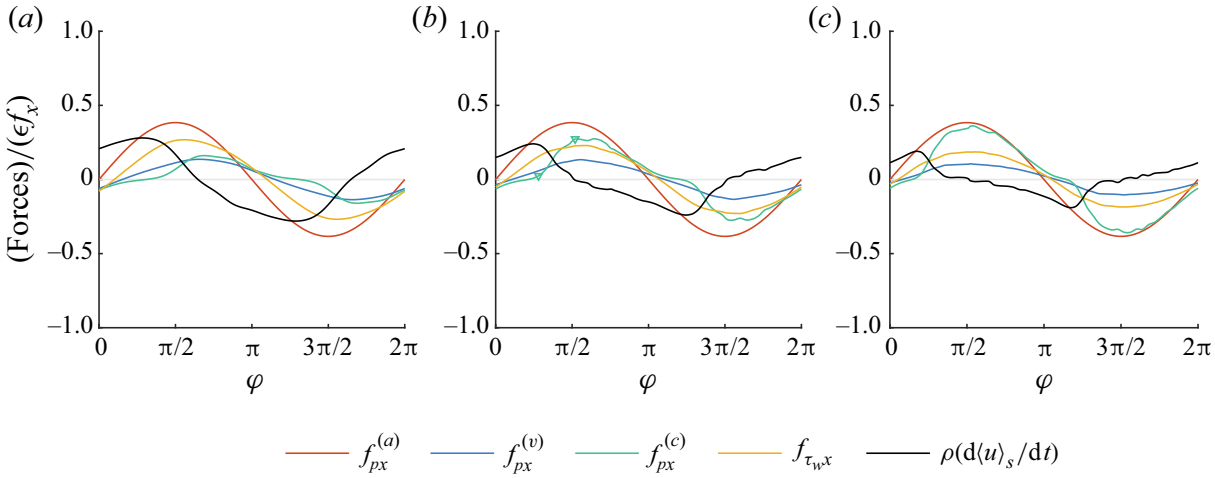

Figure 13. Drag components in nonlinear flow at $Wo = 31.62$ normalised with the amplitude of the imposed macroscopic pressure gradient ϵf_x for $Re = 73$ (MF4), $Re = 157$ (MF5) and $Re = 297$ (MF6).

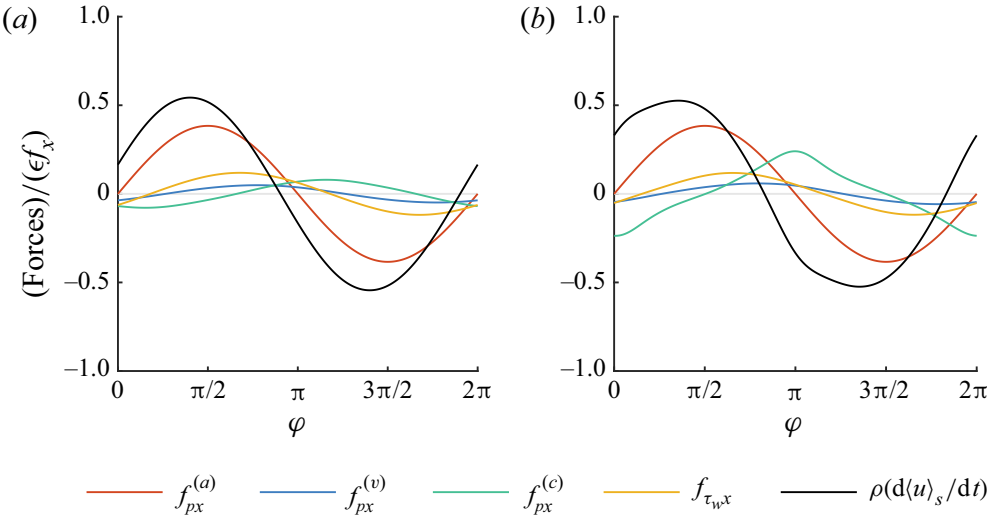

Figure 14. Drag components in nonlinear flow at $Wo = 100$ normalised with the amplitude of the imposed macroscopic pressure gradient ϵf_x for $Re = 252$ (HF4) and $Re = 468$ (HF5).

shows a distinct non-sinusoidal behaviour due to the nonlinear relationship between the macroscopic pressure gradient and the superficial velocity. The convective pressure drag shows a short plateau at the zero crossings; the duration of the plateau decreases with the Reynolds number. As the Reynolds number increases, the friction drag and the viscous pressure drag decrease whereas the convective pressure drag increases. The amplitudes of these components agree well with the results of the steady cases (figure 8). For the cases LF5 and LF6 we can observe fluctuations in the acceleration and in the convective pressure drag, while the friction drag and the viscous pressure drag do not show any fluctuations. These fluctuations could be attributed to vortex shedding and the transition to turbulence.

At the intermediate Womersley number (figure 13), the acceleration is significantly larger than at the lower Womersley number. The amplitudes of the friction drag, viscous pressure drag and convective pressure drag are comparable to $Wo = 10$, but the phases lag behind the macroscopic pressure gradient. The convective pressure drag is close to zero during the acceleration phase of each half-cycle, the duration of which decreases with increasing Reynolds number. This behaviour is similar to the plateaus observed at $Wo = 10$. When the acceleration reaches its maximum, the convective pressure drag starts to increase; the acceleration goes to zero and changes its sign. Consequently, the maximum convective pressure drag occurs later than the maximum of the superficial velocity. This is consistent with the observations in Unglehrt & Manhart (2022*a*) that the maximum kinetic energy of the nonlinear part of the velocity field is delayed with respect to the maximum of the superficial velocity.

At the highest Womersley number (figure 14), the acceleration is the dominant term in the momentum balance. The friction drag and the viscous pressure drag are much smaller than for the other Womersley numbers and have approximately the same magnitude as for linear flow at the same Womersley number. Furthermore, they are shifted in phase with respect to the macroscopic pressure gradient. For the case HF4, the convective pressure drag has a relative magnitude of 8 % and a nearly sinusoidal waveform; for the case HF5, the magnitude increases to 24 % and the waveform becomes triangular. The phase lag between the convective pressure drag and the macroscopic pressure gradient decreases with increasing Reynolds number. Remarkably, the triangular waveform of the convective pressure drag can also be observed at low Reynolds numbers (figure 11).

In the following, we investigate the high-Reynolds-number scaling of the friction drag and the viscous and convective pressure drag components. In particular, do the scalings observed in steady flow extend to oscillatory flow? For this analysis we construct different normalisations for the drag components based on the sphere diameter d, the density ρ, the kinematic viscosity ν and the cycle maximum of the superficial velocity $\max \langle u \rangle_s$. For the inertial scaling, the convective pressure drag $f_{px}^{(c)}$ is normalised with $\rho(\max \langle u \rangle_s)^2/d$, and for the steady laminar boundary layer scaling, the friction drag f_{τ_w} and the viscous pressure drag $f_{px}^{(v)}$ are normalised with $\rho\sqrt{\nu}\,(\max \langle u \rangle_s)^{3/2}/d^{3/2}$.

Figures 15 and 16 show the friction drag and the viscous pressure drag in the steady laminar boundary layer scaling. At $Wo = 10$, the curves of the viscous pressure drag collapse for the cases LF5 and LF6. We do not observe a collapse of the friction drag, but the curves are close. At $Wo = 31.62$, we find an excellent agreement of the friction drag amplitude with the steady boundary layer scaling for the cases MF5 and MF6. The normalised amplitudes of the viscous pressure drag also agree with the scaling, but the shape of the curves is different between the cases. At $Wo = 100$, we do not observe a collapse of the friction drag and the viscous pressure drag in the steady boundary layer scaling.

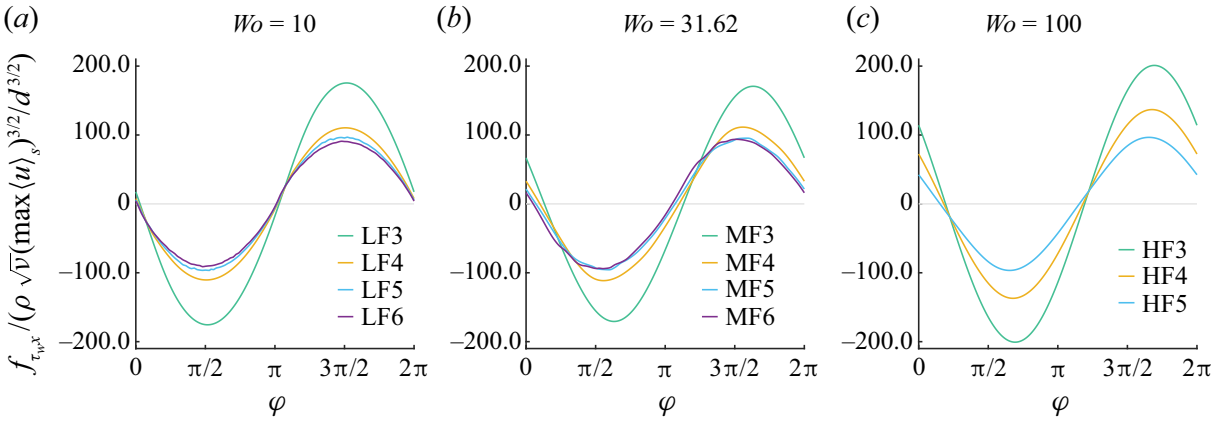

Figure 15. Friction drag normalised with $\rho\sqrt{\nu}(\max\langle u\rangle_s)^{3/2}/d^{3/2}$ corresponding to a steady laminar boundary layer scaling.

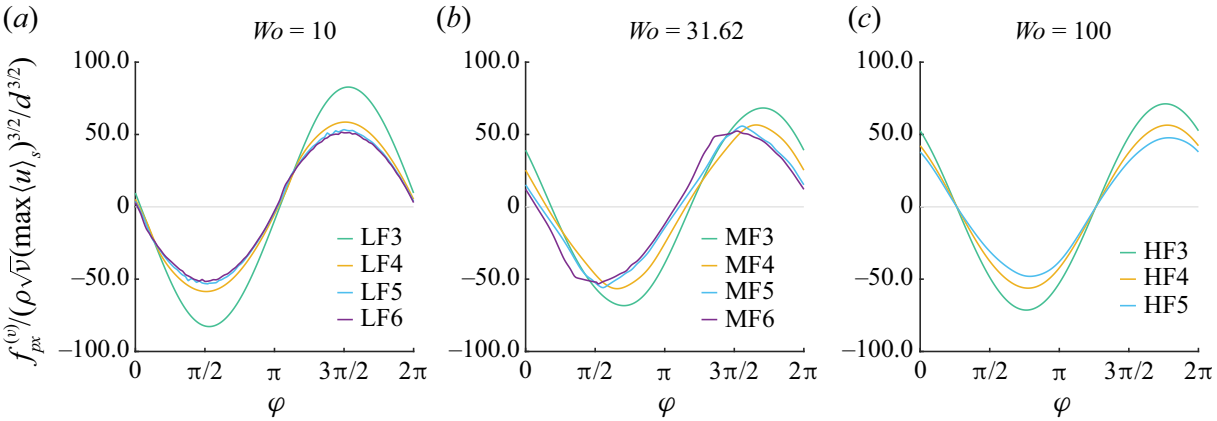

Figure 16. Viscous pressure drag normalised with $\rho\sqrt{\nu}(\max\langle u\rangle_s)^{3/2}/d^{3/2}$ corresponding to a steady laminar boundary layer scaling.

Figure 17 shows the convective pressure drag in the inertial normalisation. We observe similar amplitudes of the convective pressure drag at $Wo = 10$ and $Wo = 31.62$. Moreover, the normalised amplitude of the cases LF6 ($Re = 307$) and MF6 ($Re = 298$) is consistent with the normalised amplitude of the sum of the direct and turbulent convective pressure drag for the cases T2–T4 in the same Reynolds number range ($Re = 263$–354). However, we do not observe a collapse of the curves at neither Womersley number and thus we cannot confirm the inertial scaling of the convective pressure drag for the oscillatory cases. At $Wo = 100$, we do not observe an inertial scaling in the present range of Reynolds numbers ($Re \leqslant 465$). A striking feature in figure 17 is the phase behaviour at $Wo = 31.62$. While at low Reynolds numbers the convective pressure drag is approximately 70° out of phase with the forcing, the phase shift decreases with increasing Reynolds number. At $Wo = 100$, we can also observe a variation of the phase shift, but no clear trend can be identified.

5. Discussion

In this section, we interpret our results with regard to the dynamics of the pore-scale flow. We then discuss the implications of our findings for model descriptions of unsteady porous media flow.

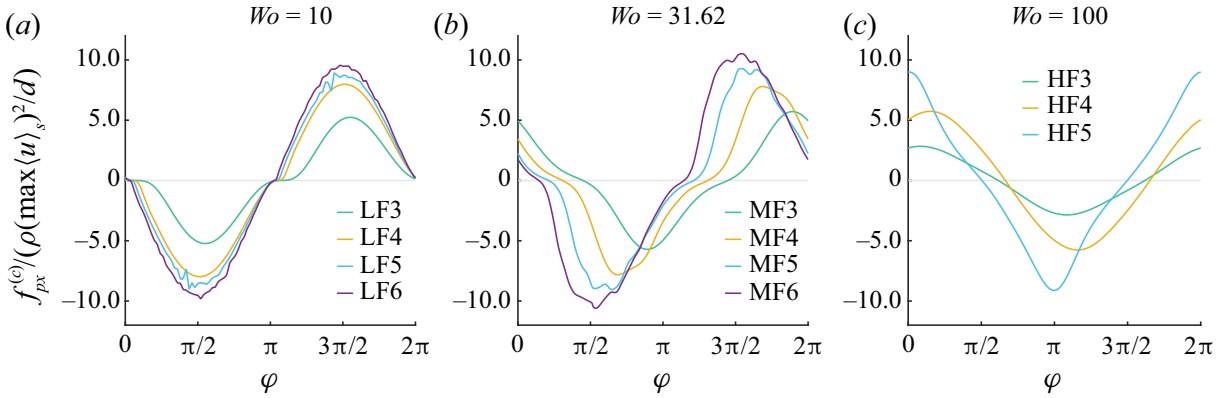

Figure 17. Convective pressure drag normalised with $\rho(\max\langle u\rangle_s)^2/d$ corresponding to an inertial scaling.

5.1. *Steady flow*

For steady flow we observed that the direct convective pressure drag due to the time-averaged velocity field scales approximately with Re^2 for high Reynolds numbers ($Re = 140$–350); the friction drag and the viscous pressure drag scale with $Re^{2–0.6} = Re^{1.4}$ for $Re = 200$–350. Dybbs & Edwards (1984) conducted experiments of steady flow through a hexagonal sphere pack. They reported the emergence of boundary layers and an 'inertial core flow' between $Re = 1$ and 10. A consistent flow pattern has been observed in the DNSs (Sakai & Manhart 2020). Similarly, for a simple cubic sphere pack Horton & Pokrajac (2009) put forward a conceptual division of the velocity field into a high speed 'core flow' and low speed regions near the spheres. Using dye visualisations, Wegner, Karabelas & Hanratty (1971) obtained the skin friction line pattern in a face-centred cubic sphere pack. In a follow-up study, Karabelas, Wegner & Hanratty (1973) hypothesised the presence of boundary layers between the attachment points and the separation lines along the spheres. A simple boundary layer calculation based on a pressure profile resulted in an approximate agreement with the experimental data. Furthermore, Jolls & Hanratty (1969) electrochemically measured the mass transfer rate and the wall shear stress over a sphere inside a packed bed of porosity $\epsilon = 0.41$ at Reynolds numbers between 5 and 1120. 'With the exception of the very rearward portion of the spheres the effect of Reynolds number on the local mass transfer rate and on the local shear stress is what is predicted by boundary layer theory for isolated spheres. This would seem to suggest that flow over most of the surface of the sphere could be described by a three-dimensional boundary layer flow.'

Our results seem to support this conceptual picture in that the observed scaling of the friction drag and viscous pressure drag are consistent with the $Re^{3/2}$ scaling predicted by laminar boundary layer theory under the assumption of a Reynolds number independent core flow. The nearly quadratic scaling of the direct convective pressure drag indeed suggests that the time-averaged core flow varies only weakly with the Reynolds number. Furthermore, He *et al.* (2019, figures 2 and 3) and Sakai & Manhart (2020, figure 15) found that the turbulent kinetic energy is concentrated in the large pores and is low near the walls and where the time-averaged velocity is high. This substantiates the hypothesis of a laminar boundary layer even in the 'turbulent' flow regime.

Future research should attempt to confirm the applicability of the boundary layer concept to the present flow configuration based on velocity profiles or the local momentum budget. The presence of laminar boundary layers would allow us to extrapolate the viscous drag to higher Reynolds numbers and would also imply a scaling for the heat and mass transfer in the vicinity of the wall (Karabelas, Wegner & Hanratty 1971; Schlichting & Gersten 2017, ch. 9). This could be important, for example, in the design of chemical

reactors. It would also be interesting to extend the present analysis to higher Reynolds numbers to investigate the scaling of the turbulent convective pressure drag.

Given that the observed low-Reynolds-number behaviour agrees with the theory of Mei & Auriault (1991) for isotropic porous media and that the experiments in disordered packed beds point to a quadratic scaling of the drag (Macdonald *et al.* 1979) and a boundary layer scaling of the friction drag (Jolls & Hanratty 1969) at high Reynolds numbers, we expect the present scalings to carry over qualitatively also to other kinds of sphere packs.

5.2. *Oscillatory flow*

For oscillatory flow at $Wo = 10$ we found that the amplitudes and scalings of the different drag components are very similar to the steady case. In the cases LF5 and LF6 some fluctuations can be observed in the convective pressure drag and in the acceleration (and thus the superficial velocity); the friction drag and the viscous pressure drag show only small traces of these fluctuations (figure 12). This further supports the above hypothesis that the laminar boundary layers are only weakly influenced by inertial and turbulent effects.

At $Wo = 31.62$, the amplitudes of the drag components are still close to the steady values, but the phases differ considerably from the lower Womersley number. As the Reynolds number increases, the friction drag and viscous pressure drag become increasingly in phase with the macroscopic pressure gradient (figures 10 and 13). Since the Womersley number is relatively high and since the friction and viscous pressure drag approach a steady laminar boundary layer scaling for higher Reynolds numbers, we explain this behaviour using the boundary layer concept. Generally, the boundary layer thickness can be estimated as $\delta \propto \sqrt{\nu t_B}$ where t_B is the time that a fluid particle spends inside the boundary layer (Schlichting & Gersten 2017, p. 141). In an accelerating flow, t_B is just the elapsed time t since the start of the boundary layer formation. When the time reaches the convection time $d/\langle u \rangle_s$, the boundary layer starts to become steady and its thickness is $\delta \propto \sqrt{\nu d/\langle u \rangle_s}$ or $\delta/d \propto Re^{-1/2}$. In this case, the drag is in phase with the superficial velocity. If the period of oscillation is shorter than the convection time, the flow never becomes steady and the boundary layer thickness is $\delta \propto \sqrt{\nu/\Omega}$ or $\delta/d \propto Wo^{-1}$. In this case, the boundary layer flow is essentially linear and the drag is out of phase with the superficial velocity (cf. § 4.2). When the Womersley number is fixed, the Reynolds number determines if the boundary layer flow reaches a quasisteady state. The process outlined above can be seen in the case MF5 (figure 18*a*). In the acceleration phase, the boundary layer is thinner than in the steady case; consequently, the drag is higher than in the steady case. Then, the boundary layer growth reaches the steady state value and during the deceleration, the boundary layer remains quasisteady. Thus, the drag coincides with the steady state curve. For the convective pressure drag (figure 18*b*) we observe a non-sinusoidal time evolution with a plateau around the zero crossings and a high magnitude in between. The shape and phase of the waveform vary considerably with the Reynolds number (figure 17).

In order to extend our understanding of the convective pressure drag, we look at the instantaneous velocity fields of the case MF5 at the beginning and at the end of the steep increase of the convective pressure drag (the times are highlighted by the markers in figure 13). At the first time ($\varphi = 0.28\pi$), the flow has an instantaneous Reynolds number of 85 and the convective pressure drag in the x-direction is $-3\,\%$ of the instantaneous macroscopic pressure gradient ($f_{px}^{(c)}/(\epsilon f_x) = -0.03\sin(0.28\pi)$). At the second time ($\varphi = 0.52\pi$), the instantaneous Reynolds number is at its peak value 157 and the convective

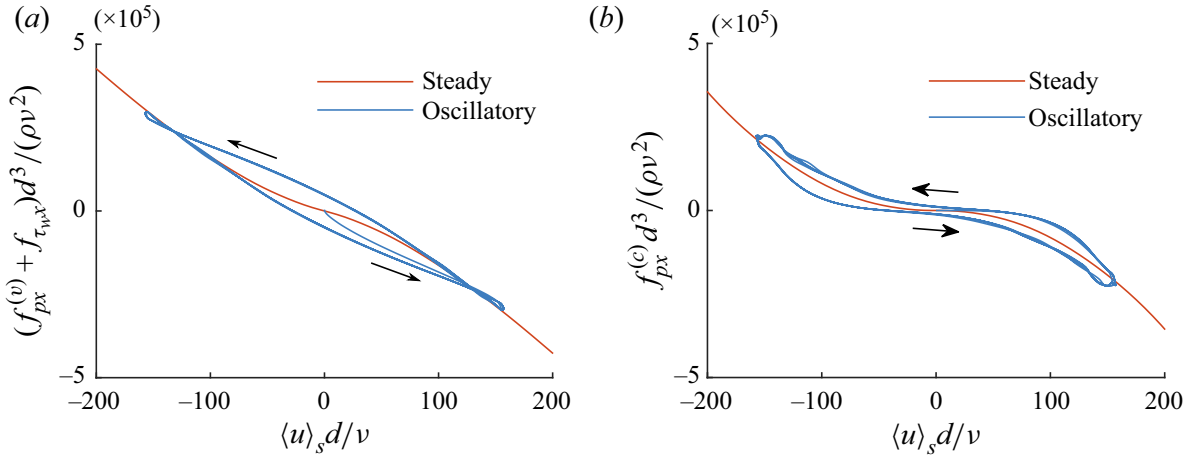

Figure 18. Comparison of the relation between the instantaneous drag components and the superficial velocity for steady and oscillatory flow in the case MF5 ($Re = 157$, $Wo = 31.62$). (*a*) Sum of friction and viscous pressure drag; (*b*) convective pressure drag.

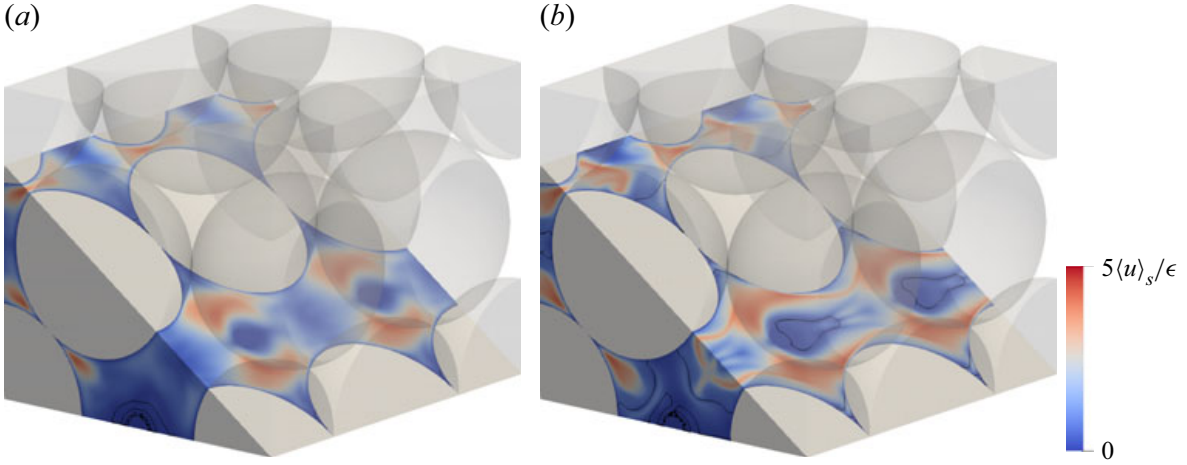

Figure 19. Instantaneous velocity magnitude $|\boldsymbol{u}|$ and $u = 0$ contour of the case MF5 at the times marked in figure 13. The colours are normalised with respect to the instantaneous superficial velocity. (*a*) Beginning of the steep increase of the convective pressure drag ($\varphi = 0.28\pi$, $Re(t) = 85$). (*b*) End of the steep increase of the convective pressure drag ($\varphi = 0.52\pi$, $Re(t) = 157$).

pressure drag in the x-direction is $-27\,\%$ of the instantaneous macroscopic pressure gradient ($f_{px}^{(c)}/(\epsilon f_x) = -0.26\sin(0.52\pi)$). It can be seen in figure 19 that at the beginning of the increase the distribution of the velocity magnitude is roughly fore–aft symmetric with respect to the planes $x = d/2$ and $x = 3d/2$. Since a symmetric velocity field has a symmetric distribution of the Q-invariant, which is then multiplied with the antisymmetric auxiliary potential Φ_x, a relatively low convective pressure drag is produced. On the other hand, a non-symmetric velocity magnitude distribution can be observed at the end of the increase of the convective pressure drag. The zero contour of the streamwise velocity component ($u = 0$) indicates that the latter field exhibits a large separation region behind the contact points in the oblique cut plane. The comparison of the two velocity fields shown in figure 19 suggests that the steep increase in convective pressure drag is caused by the emergence of the flow separation regions. The plateaus near the zero crossings of the convective pressure drag could thus be seen as attached flow whereas the parts of the cycle with a large convective pressure drag would correspond to separated flow.

At $Wo = 100$, the drag components do not follow the same scalings as at the lower Womersley numbers and clear phase differences between the drag components can be observed. A possible explanation for these discrepancies is that at low Womersley numbers the boundary layers are quasisteady if the Reynolds number is high enough, whereas the boundary layers do not become steady at the highest Womersley number in the considered Reynolds number range. The convective pressure drag has an almost triangular waveform at low Reynolds numbers (figure 11) and at high Reynolds numbers (figure 17). This qualitatively different behaviour of the convective pressure drag in comparison with the lower Womersley numbers could be understood if one assumes a finite formation time for the drag producing structures. Then, at $Wo = 10$ the formation time would be small compared with the period of oscillation, resulting in a small phase lag of the convective pressure drag. At $Wo = 31.62$, the formation time would be relatively large compared with the period of oscillation (similar to the duration of the plateaus at the zero crossings), resulting in a larger phase lag of the convective pressure drag. Figure 17(b) suggests that the formation time would decrease with increasing Reynolds numbers. Finally, at $Wo = 100$ the frequency of oscillation is so high that the formation and destruction in subsequent half-cycles overlaps in time. Thus, the plateau would disappear.

5.3. *Implications for modelling*

We have presented a new form (2.11) of the volume-averaged momentum equation for a spatially constant macroscopic pressure gradient $\boldsymbol{f}$ where we can express the drag in terms of the wall shear stress and the second invariant of the velocity gradient tensor. The auxiliary potential $\boldsymbol{\Phi}$ (and derived from it the tensor of virtual inertia $\boldsymbol{A}$) only depends on the geometry of the porous medium. In this formulation, the components of the pressure drag with a viscous scaling, an inertial scaling and a direct proportionality to the macroscopic pressure gradient are separated. We have shown in Appendix B.2 how this form of the volume-averaged momentum equation can be used to directly derive the asymptotic drag behaviour at high Womersley numbers of Johnson *et al.* (1987).

For steady flow, we found that the friction drag and the viscous pressure drag depend linearly on Re at low Reynolds numbers and scale with $Re^{1.4}$ at high Reynolds numbers. The convective pressure drag scales with Re^3 at low Reynolds numbers and with Re^2 at high Reynolds numbers. At low Reynolds numbers, these results are in line with Darcy's law (1.6) and its correction (1.7) by Mei & Auriault (1991). However, the Forchheimer equation (1.8) is incompatible with the low-Reynolds-number behaviour of the convective pressure drag and with the high-Reynolds-number behaviour of the friction drag and of the viscous pressure drag.

In nonlinear oscillatory flow at $Wo = 10$ the drag components show the same scaling as in steady flow. Moreover, the momentum balance indicates that the flow is quasisteady. This flow can thus be modelled by extending the steady state drag law with an acceleration term (Zhu *et al.* 2014; Zhu & Manhart 2016). At $Wo = 31.62$ the Reynolds number scalings of the drag components are similar to the steady case, but the drag components are out of phase with the superficial velocity (figure 18). To model the friction and viscous pressure drag, a promising approach could be to blend the parametrisation of Johnson *et al.* (1987) with the $Re^{3/2}$ behaviour of the laminar boundary layer. As the convective pressure drag cannot be expressed as a function of the instantaneous superficial velocity alone and, furthermore, scales with Re^3 at low Reynolds numbers, it seems necessary to think beyond the traditional parametrisation in terms of $\langle u \rangle_s^2$. In particular, we could observe a smaller hysteresis between the convective pressure drag and a time-lagged superficial

velocity or the instantaneous kinetic energy. For the simulation cases at $Wo = 100$ no clear high-Reynolds-number scalings could be identified; thus, further research is required in this direction. As a starting point for the development of improved models, we provide the time series of the superficial velocity and the drag components from our simulations as supplementary material available at https://doi.org/10.1017/jfm.2023.798.

Finally, our decomposition provides a new point of view on the time constant in the volume-averaged momentum equation. In most model equations for unsteady porous media flow, the resistance of the bulk flow to acceleration has been incorporated with the *ad hoc* addition of a 'virtual mass coefficient' (Sollitt & Cross 1972; Burcharth & Andersen 1995) or 'acceleration coefficient tensor' (Nield 1991) to the volume-averaged momentum equation. This was done by analogy to the added-mass effect in inviscid flow. For example, Nield (1991) suggested an unsteady extension to Darcy's law (1.6),

$$\rho \boldsymbol{C}_a \cdot \frac{\mathrm{d}\langle \boldsymbol{u} \rangle_s}{\mathrm{d}t} = -\frac{\mu}{K} \langle \boldsymbol{u} \rangle_s + \boldsymbol{f} \tag{5.1}$$

where the acceleration coefficient tensor is assumed to be of the form $\boldsymbol{C}_a = \epsilon^{-1}\boldsymbol{I} + \boldsymbol{N}$; the tensor $\boldsymbol{N}$ representing 'the contribution from "fractures"'. The volume-averaged momentum equation (2.11) can also be brought to such a form by multiplying the equation with $\boldsymbol{C}_a := [\epsilon \boldsymbol{I} - (1-\epsilon)\boldsymbol{A}]^{-1}$. Then, the accelerative pressure drag is absorbed into the prefactor of the acceleration and all other drag terms are rescaled:

$$\rho \boldsymbol{C}_a \cdot \frac{\mathrm{d}\langle \boldsymbol{u} \rangle_s}{\mathrm{d}t} = \boldsymbol{C}_a \cdot \left[-\frac{1}{V} \int_{A_{fs}} (\boldsymbol{I} - \nabla \otimes \boldsymbol{\Phi})^{\mathrm{T}} \cdot \boldsymbol{\tau}_w \, \mathrm{d}A + \frac{1}{V} \int_{V_f} \boldsymbol{\Phi} \, 2\rho Q \, \mathrm{d}V \right] + \boldsymbol{f}. \tag{5.2}$$

The term $-\mu/K \, \langle \boldsymbol{u} \rangle_s$ in (5.1) can be identified as a parametrisation of the first term on the right-hand side of (5.2) with the Darcy expression for the drag. Our decomposition thus gives a new interpretation to the 'virtual mass' in a porous medium in terms of the accelerative pressure drag, which possesses a clear physical meaning also for viscous flow. As discussed in Appendix B.1, this definition of the acceleration coefficient reduces to the 'high-frequency limit of the dynamic tortuosity' by Johnson *et al.* (1987) in the isotropic case, i.e. $\boldsymbol{C}_\mathrm{a} = \alpha_\infty/\epsilon \, \boldsymbol{I}$.

6. Conclusion

In this paper, we studied the behaviour of the drag force in steady and oscillatory flow through a hexagonal sphere pack. Based on the pressure decomposition of Graham (2019) we derived a new form of the volume-averaged momentum equation in which the pressure drag force is split into three contributions. The accelerative pressure drag is a reaction force directly proportional the macroscopic pressure gradient. It prevents the macroscopic pressure gradient from accelerating the fluid normal to the wall. The viscous pressure drag results from unbalanced viscous stresses and can be expressed to a weighted integral of the wall shear stress. The convective pressure drag can be expressed as a weighted volume integral of the Q-invariant of the velocity gradient tensor representing effects like vortices, shear layers and flow separation.

Using this decomposition, the drag law for high Womersley numbers (Johnson *et al.* 1987) and the Re dependence of the drag for low Reynolds numbers could be derived using relatively simple arguments (see §§ B.2 and B.3). Moreover, we could provide a new theoretical basis for the virtual mass coefficient commonly employed in models for unsteady porous media flow (see § 5.3).

We then applied the drag decomposition to a DNS dataset of steady and oscillatory flow through a hexagonal sphere pack. We investigated the contributions of the different drag terms to the volume-averaged momentum budget. The accelerative pressure drag is proportional to the macroscopic pressure gradient and thus has a fixed contribution of 38.4 % to the momentum budget. For steady flow, the remaining drag is dominated by the friction and viscous pressure drag at low Reynolds numbers and by the convective pressure drag at high Reynolds numbers. For the considered Reynolds numbers, the Reynolds stresses only have a minor effect on the drag. For oscillatory flow at low and medium Womersley numbers, the friction drag, viscous pressure drag and convective pressure drag have a similar magnitude as in the steady case. At high Womersley numbers, the friction and viscous pressure drag are significantly smaller than in the steady case. Thus, the drag at high Womersley numbers is made up mostly by the accelerative and the convective pressure drag. An important feature of the drag in oscillatory flow is that the drag components are not in phase with the body force and the superficial velocity. The phase differences increase with the Womersley number.

We investigated the Reynolds number scalings of the friction drag, the viscous pressure drag and the convective pressure drag. In the steady case, the friction and viscous pressure drag are proportional to Re at small Reynolds numbers and scale with $Re^{1.4}$ for Reynolds numbers between 200 and 350. The convective pressure drag of the time-averaged velocity field scales with Re^3 up to a Reynolds number of 10 and with Re^2 for $Re = 140$–350. For oscillatory flow, the same amplitude scalings can be observed at $Wo = 10$ and $Wo = 31.62$, whereas no clear high Re scaling could be found for the cases at $Wo = 100$.

These scalings support the picture of Dybbs & Edwards (1984) who divided the flow at higher Reynolds numbers into an inertial core flow and viscous boundary layers, where we linked the former with the convective pressure drag and the latter with the friction and viscous pressure drag. The visualisation of instantaneous velocity fields suggests that the convective pressure drag in the hexagonal sphere pack is caused by large flow separations. Moreover, the clear scalings of the friction and viscous pressure drag and of the convective pressure drag indicate that the inertial core and the boundary layers are only weakly affected by the turbulence for $Re = 200$–350.

In future work, the present theory for periodic porous media could be extended to non-periodic porous media. This might be realised by rewriting the identity

$$\langle \boldsymbol{\Phi}\, \Delta P\rangle_s = \langle \boldsymbol{\nabla} \cdot (\boldsymbol{\nabla} P \otimes \boldsymbol{\Phi})\rangle_s - \langle \boldsymbol{\nabla} \cdot [(\boldsymbol{\nabla} \otimes \boldsymbol{\Phi}) P]\rangle_s \tag{6.1}$$

with the spatial averaging theorem (Whitaker 1985); together with the volume-averaged Navier–Stokes equations (Whitaker 1986, 1996) a generalisation of (2.11) would be obtained.

Supplementary material. The time series of the volume-averaged momentum budget terms are provided for all simulation cases. Moreover, the time series of the superficial velocity and kinetic energy components are provided for the cases LF5, LF6, MF5, MF6 and HF5. Supplementary material is available at https://doi.org/10.1017/jfm.2023.798.

Acknowledgements. We would like to express our thanks to Y. Sakai for providing the complete simulation dataset for the steady flow cases. We further thank Y. Sakai, U. Jenssen, J. Brosda and S. Wenczowski for helpful and interesting discussions and we thank H.I. Andersson for reading the manuscript and providing valuable feedback. Finally, we thank the anonymous reviewers for their thorough and constructive criticism.

Funding. The authors gratefully acknowledge the financial support of the DFG under grant no. MA2062/13-1. Computing time was granted by the Leibniz Supercomputing Centre on its Linux-Cluster.

Declaration of interests. The authors report no conflict of interest.

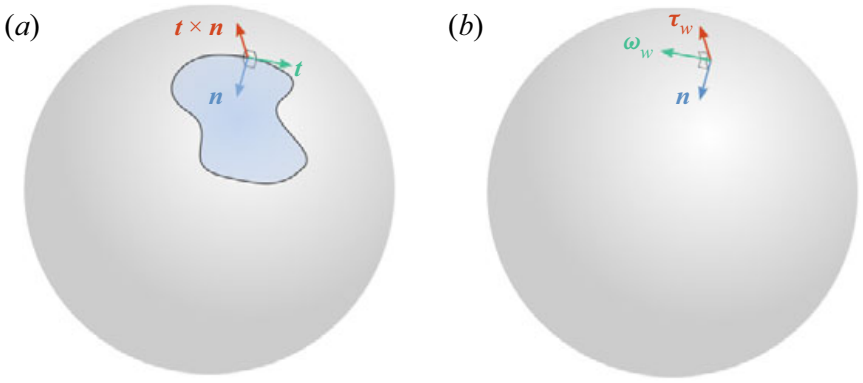

Figure 20. (*a*) Orientation of the normal vector $\boldsymbol{n}$, the tangent vector $\boldsymbol{t}$ and their cross product $\boldsymbol{t} \times \boldsymbol{n}$ with respect to the surface patch A. The normal vector points from the fluid outside into the sphere. (*b*) Orientation of the normal vector $\boldsymbol{n}$, the wall shear stress $\boldsymbol{\tau}_w$ and the wall vorticity $\boldsymbol{\omega}_w$ with respect to the surface.

Author ORCIDs.
Lukas Unglehrt https://orcid.org/0000-0002-1299-0430;
Michael Manhart https://orcid.org/0000-0001-7809-6282.

Author contributions. L.U. performed the simulations advised by M.M. L.U. derived the theory of the drag decomposition and performed the evaluation of the simulations. Both authors contributed to reaching conclusions and in writing the paper.

Appendix A. Notes on the viscous pressure drag

This appendix discusses some aspects of the relationship between the viscous pressure and the wall shear stress. In § A.1, we show that the boundary condition of the viscous pressure $p^{(v)}$ can be expressed in terms of the wall shear stress divergence. In § A.2, we show that the mean value of the viscous pressure source term is zero for a periodic domain. Finally, in § A.3 we derive an alternative expression for the viscous pressure drag as a weighted integral of the wall shear stress.

A.1. *Relationship between the viscous pressure and the wall shear stress divergence*

The boundary condition of the viscous pressure (2.3*b*) can be rewritten using the identity $\Delta \boldsymbol{u} = -\nabla \times (\nabla \times \boldsymbol{u})$ and Stokes' theorem as

$$\nabla p^{(v)} \cdot \boldsymbol{n} = \mu \Delta \boldsymbol{u} \cdot \boldsymbol{n} = -\mu \left[\nabla \times (\nabla \times \boldsymbol{u})\right] \cdot \boldsymbol{n} = -\mu \lim_{A \to 0} \frac{1}{A} \int_{\partial A} (\nabla \times \boldsymbol{u}) \cdot \boldsymbol{t} \, \mathrm{d}s, \quad \text{(A1)}$$

where $\boldsymbol{n}$ is the normal vector pointing from the fluid towards the wall, A is an small surface patch on the wall and $\boldsymbol{t}$ represents the tangent vector on its boundary ∂A. The vorticity on the wall is related to the wall shear stress by the equation

$$\boldsymbol{\omega}_w = \nabla \times \boldsymbol{u}|_w = \frac{\boldsymbol{\tau}_w}{\mu} \times \boldsymbol{n} \quad \text{(A2)}$$

where the cross product expresses a clockwise rotation of the wall shear stress by 90° around the normal. Figure 20 shows the orientation of the vectors with respect to a single sphere.

Using Lagrange's identity for the cross product (Bronstein *et al.* 1991, p. 556), we can establish the relation

$$[(\nabla \times \boldsymbol{u}) \times \boldsymbol{n}] \cdot [\boldsymbol{t} \times \boldsymbol{n}] = [(\nabla \times \boldsymbol{u}) \cdot \boldsymbol{t}] \underbrace{[\boldsymbol{n} \cdot \boldsymbol{n}]}_{=1} - \underbrace{[(\nabla \times \boldsymbol{u}) \cdot \boldsymbol{n}]}_{=0} \underbrace{[\boldsymbol{n} \cdot \boldsymbol{t}]}_{=0} = (\nabla \times \boldsymbol{u}) \cdot \boldsymbol{t} \tag{A3}$$

and by combining the two expressions, we obtain

$$(\nabla \times \boldsymbol{u}) \cdot \boldsymbol{t} = \left[\left(\frac{\boldsymbol{\tau}_w}{\mu} \times \boldsymbol{n} \right) \times \boldsymbol{n} \right] \cdot [\boldsymbol{t} \times \boldsymbol{n}] = -\frac{\boldsymbol{\tau}_w}{\mu} \cdot (\boldsymbol{t} \times \boldsymbol{n}). \tag{A4}$$

Finally, we arrive at the boundary condition

$$\nabla p^{(v)} \cdot \boldsymbol{n} = \lim_{A \to 0} \frac{1}{A} \int_{\partial A} \boldsymbol{\tau}_w \cdot (\boldsymbol{t} \times \boldsymbol{n}) \, \mathrm{d}s \tag{A5}$$

where the right-hand side can be understood as the divergence of the wall shear stress, since the vector $\boldsymbol{t} \times \boldsymbol{n}$ represents the outward normal vector on the boundary ∂A of the surface patch along the wall. Consequently, the viscous pressure $p^{(v)}$ is caused by imbalances in the wall shear stress. For example, a stagnation point represents a source of the wall shear stress, hence $\nabla p^{(v)} \cdot \boldsymbol{n} > 0$ and the viscous pressure increases towards the wall. This is indeed observed in the analytical solution (Graham 2019).

A.2. *Zero-mean property of the wall-normal friction force for a periodic domain*

We apply Gauss's integral theorem to the vector field $\Delta \boldsymbol{u}$:

$$\int_{\partial V_f} \Delta \boldsymbol{u} \cdot \boldsymbol{n} \, \mathrm{d}A = \int_{V_f} \nabla \cdot (\Delta \boldsymbol{u}) \, \mathrm{d}V = \int_{V_f} \Delta (\nabla \cdot \boldsymbol{u}) \, \mathrm{d}V = 0. \tag{A6}$$

As the velocity field is periodic, we can further simplify this to

$$\int_{A_{fs}} \Delta \boldsymbol{u} \cdot \boldsymbol{n} \, \mathrm{d}A = 0, \tag{A7}$$

where A_{fs} represents the fluid–solid interface.

A.3. *Alternative expression for the viscous pressure drag*

We can rewrite viscous pressure drag (2.7*b*) using the periodic boundary conditions and Gauss's theorem as

$$\begin{aligned} -\frac{1}{V} \int_{A_{fs}} p^{(v)} \boldsymbol{n} \, \mathrm{d}A &= -\frac{1}{V} \int_{A_{fs}} \boldsymbol{\Phi} \, (\mu \Delta \boldsymbol{u} \cdot \boldsymbol{n}) \, \mathrm{d}A = -\frac{1}{V} \int_{\partial V_f} \boldsymbol{\Phi} \, (\mu \Delta \boldsymbol{u} \cdot \boldsymbol{n}) \, \mathrm{d}A \\ &= -\frac{1}{V} \int_{V_f} \nabla \cdot (\mu \Delta \boldsymbol{u} \otimes \boldsymbol{\Phi}) \, \mathrm{d}V \\ &= \underbrace{\frac{1}{V} \int_{V_f} \boldsymbol{\Phi} \, \mu \Delta (\nabla \cdot \boldsymbol{u}) \, \mathrm{d}V}_{=0} - \frac{1}{V} \int_{V_f} \mu \Delta \boldsymbol{u} \cdot (\nabla \otimes \boldsymbol{\Phi}) \, \mathrm{d}V. \end{aligned} \tag{A8}$$

The first term vanishes due to incompressibility. For the second term, we can apply Green's second identity componentwise to move the Laplacian onto the auxiliary potential $\boldsymbol{\Phi}$,

which satisfies the Laplace equation. We obtain

$$-\frac{1}{V}\int_{V_f}\mu\Delta\boldsymbol{u}\cdot(\boldsymbol{\nabla}\otimes\boldsymbol{\Phi})\,\mathrm{d}V=-\frac{1}{V}\int_{A_{fs}}(\boldsymbol{\nabla}\otimes\boldsymbol{\Phi})^{\mathrm{T}}\cdot\left[\mu\,(\boldsymbol{\nabla}\otimes\boldsymbol{u})^{\mathrm{T}}\cdot\boldsymbol{n}\right]\mathrm{d}A + \frac{1}{V}\int_{A_{fs}}\mu\,\boldsymbol{u}\cdot[\boldsymbol{n}\cdot(\boldsymbol{\nabla}\otimes(\boldsymbol{\nabla}\otimes\boldsymbol{\Phi}))]\,\mathrm{d}A. \tag{A9}$$

With the no-slip condition $\boldsymbol{u}=0$ and the definition of the wall shear stress, we arrive at

$$-\frac{1}{V}\int_{A_{fs}}p^{(v)}\,\boldsymbol{n}\,\mathrm{d}A=\frac{1}{V}\int_{A_{fs}}(\boldsymbol{\nabla}\otimes\boldsymbol{\Phi})^{\mathrm{T}}\cdot\boldsymbol{\tau}_w\,\mathrm{d}A. \tag{A10}$$

This equation expresses the viscous pressure drag as a weighted integral of the wall shear stress. As the function $(\boldsymbol{\nabla}\otimes\boldsymbol{\Phi})^{\mathrm{T}}$ solely depends on the geometry, we expect that the viscous pressure drag has the same scaling as the wall shear stress and the friction drag.

Appendix B. Asymptotic behaviour of oscillatory flow

This appendix contains a discussion of the behaviour of oscillatory flow in potential flow (§ B.1), at high Womersley numbers (§ B.2) and at low Reynolds numbers (§ B.3). In particular, §§ B.1 and B.2 establish a link between our pressure drag decomposition and the established theory of Johnson *et al.* (1987) for oscillatory porous media flow. Section B.3 generalises the theory of Mei & Auriault (1991) and Firdaouss *et al.* (1997) to oscillatory flow.

B.1. *Potential flow*

In this section, we derive the potential flow solution in response to a spatially constant macroscopic pressure gradient $\boldsymbol{f}$ using the pressure decomposition (2.3). By comparing the boundary value problems for $\boldsymbol{\Phi}$ and $p^{(a)}$ (2.3*a*) we find that $p^{(a)}=\boldsymbol{\Phi}\cdot\boldsymbol{f}$. Since the flow is inviscid, the pressure $p^{(v)}$ is zero. It can be shown that for a potential flow the Q-invariant can be computed as $4Q=-\Delta|\boldsymbol{u}|^2$. Therefore, we have $p^{(c)}=-\frac{1}{2}\rho|\boldsymbol{u}|^2$. Note that $p^{(c)}$ satisfies different boundary conditions due to the slip walls where only $\boldsymbol{u}\cdot\boldsymbol{n}=0$. We can now use the momentum equation to determine the velocity:

$$\frac{\partial\boldsymbol{u}}{\partial t}+\boldsymbol{\nabla}\left(\frac{1}{2}|\boldsymbol{u}|^2\right)=-\frac{1}{\rho}\boldsymbol{\nabla}p^{(a)}-\frac{1}{\rho}\boldsymbol{\nabla}p^{(c)}+\frac{1}{\rho}\boldsymbol{f}. \tag{B1}$$

The convective term and $\boldsymbol{\nabla}p^{(c)}$ cancel and we are left with

$$\frac{\partial\boldsymbol{u}}{\partial t}=-\frac{1}{\rho}\boldsymbol{\nabla}p^{(a)}+\frac{1}{\rho}\boldsymbol{f}=\frac{1}{\rho}\,(\boldsymbol{I}-\boldsymbol{\nabla}\otimes\boldsymbol{\Phi})\cdot\boldsymbol{f}. \tag{B2}$$

From (B2), the volume-averaged momentum equation in potential flow follows as

$$\rho\frac{\mathrm{d}\langle\boldsymbol{u}\rangle_s}{\mathrm{d}t}=\langle\boldsymbol{I}-\boldsymbol{\nabla}\otimes\boldsymbol{\Phi}\rangle_s\cdot\boldsymbol{f}=\left[\epsilon\boldsymbol{I}-\frac{1}{V}\int_{V_f}\boldsymbol{\nabla}\otimes\boldsymbol{\Phi}\,\mathrm{d}V\right]\cdot\boldsymbol{f} \tag{B3}$$

which we can transform using Gauss's theorem and the periodic boundary conditions of $\boldsymbol{\Phi}$ into

$$\rho\frac{\mathrm{d}\langle\boldsymbol{u}\rangle_s}{\mathrm{d}t}=\left[\epsilon\boldsymbol{I}-\frac{1}{V}\int_{A_{fs}}\boldsymbol{n}\otimes\boldsymbol{\Phi}\,\mathrm{d}A\right]\cdot\boldsymbol{f}. \tag{B4}$$

With the tensor of added mass (which is symmetric), we can simplify the volume-averaged momentum equation (1.3) to

$$\rho \frac{\mathrm{d}\langle \boldsymbol{u} \rangle_s}{\mathrm{d}t} = [\epsilon \boldsymbol{I} - (1-\epsilon)\boldsymbol{A}] \cdot \boldsymbol{f}. \tag{B5}$$

On the other hand, if the porous medium is isotropic, the theory of Johnson *et al.* (1987) gives

$$\rho \frac{\alpha_\infty}{\epsilon} \frac{\mathrm{d}\langle \boldsymbol{u} \rangle_s}{\mathrm{d}t} = \boldsymbol{f} \tag{B6}$$

in inviscid flow. Consequently, we have $\boldsymbol{A} = \epsilon(1-\alpha_\infty^{-1})/(1-\epsilon)\boldsymbol{I}$ with the high-frequency limit of the dynamic tortuosity α_∞ (Johnson *et al.* 1987).

B.2. *Behaviour in the high Womersley number limit*

In this section, we show how the pressure decomposition can be used to derive the high-frequency asymptotics of oscillatory flow in a porous medium (Johnson *et al.* 1987). These can be written in the time domain as

$$\rho \frac{\mathrm{d}\langle \boldsymbol{u} \rangle_s}{\mathrm{d}t} = -\rho\sqrt{\nu}\,\frac{2}{\Lambda}\int_0^t \frac{\mathrm{d}\langle \boldsymbol{u} \rangle_s}{\mathrm{d}\tau}\,\frac{1}{\sqrt{\pi(t-\tau)}}\,\mathrm{d}\tau + \frac{\epsilon}{\alpha_\infty}\boldsymbol{f}. \tag{B7}$$

We begin the derivation from the volume-averaged momentum equation (1.3) in which we insert the decomposition (2.11) to get

$$\rho \frac{\mathrm{d}\langle \boldsymbol{u} \rangle_s}{\mathrm{d}t} = -\frac{1}{V}\int_{A_{fs}} (\boldsymbol{I} - \boldsymbol{\nabla} \otimes \boldsymbol{\Phi})^{\mathrm{T}} \cdot \boldsymbol{\tau}_w \,\mathrm{d}A + \underbrace{\frac{1}{V}\int_{V_f} \boldsymbol{\Phi}\, 2\rho Q \,\mathrm{d}V}_{\approx 0} + [\epsilon \boldsymbol{I} - (1-\epsilon)\boldsymbol{A}] \cdot \boldsymbol{f}. \tag{B8}$$

For linear flow, the convective pressure drag can be neglected as it contains the square of the velocity.

In the high-frequency limit, the flow has a boundary layer character and the boundary layer is locally identical to a Stokes boundary layer (Schlichting & Gersten 2017, pp. 352f, pp. 126f). The wall shear stress in the Stokes boundary layer can be written as

$$\boldsymbol{\tau}_w = \rho\sqrt{\nu}\int_0^t \left.\frac{\partial \boldsymbol{u}_p}{\partial \tau}\right|_w \frac{1}{\sqrt{\pi(t-\tau)}}\,\mathrm{d}\tau, \tag{B9}$$

where $\boldsymbol{u}_p$ is the potential flow velocity in the core flow. Combining (B2) and (B5), we can establish a one-to-one correspondence between the velocity field in potential flow and its superficial average:

$$\rho \frac{\partial \boldsymbol{u}_p}{\partial t} = (\boldsymbol{I} - \boldsymbol{\nabla} \otimes \boldsymbol{\Phi}) \cdot [\epsilon \boldsymbol{I} - (1-\epsilon)\boldsymbol{A}]^{-1} \cdot \rho \frac{\mathrm{d}\langle \boldsymbol{u}_p \rangle_s}{\mathrm{d}t}. \tag{B10}$$

With this relation, the wall shear stress can be expressed in terms of the superficial velocity of the potential flow:

$$\boldsymbol{\tau}_w = \rho\sqrt{\nu}\,(\boldsymbol{I} - \boldsymbol{\nabla} \otimes \boldsymbol{\Phi}) \cdot [\epsilon \boldsymbol{I} - (1-\epsilon)\boldsymbol{A}]^{-1} \cdot \int_0^t \frac{\mathrm{d}\langle \boldsymbol{u}_p \rangle_s}{\mathrm{d}\tau}\,\frac{1}{\sqrt{\pi(t-\tau)}}\,\mathrm{d}\tau. \tag{B11}$$

Using (2.10), we can compute the total viscous drag force as

$$-\frac{1}{V}\int_{A_{fs}}(p^{(v)}\,\boldsymbol{n}+\boldsymbol{\tau}_w)\,\mathrm{d}A=-\rho\sqrt{\nu}\,2\,\boldsymbol{L}^{-1}\cdot\int_0^t\frac{\mathrm{d}\langle\boldsymbol{u}_p\rangle_s}{\mathrm{d}\tau}\,\frac{1}{\sqrt{\pi(t-\tau)}}\,\mathrm{d}\tau \tag{B12}$$

with the tensor

$$2\boldsymbol{L}^{-1}=\frac{1}{V}\int_{A_{fs}}(\boldsymbol{I}-\nabla\otimes\boldsymbol{\Phi})^{\mathrm{T}}\cdot(\boldsymbol{I}-\nabla\otimes\boldsymbol{\Phi})\,\mathrm{d}A\cdot[\epsilon\,\boldsymbol{I}-(1-\epsilon)\,\boldsymbol{A}]^{-1}\,. \tag{B13}$$

Finally, when the potential flow velocity is replaced with the actual fluid velocity, we obtain the volume-averaged momentum equation

$$\rho\frac{\mathrm{d}\langle\boldsymbol{u}\rangle_s}{\mathrm{d}t}=-\rho\sqrt{\nu}\,2\,\boldsymbol{L}^{-1}\cdot\int_0^t\frac{\mathrm{d}\langle\boldsymbol{u}\rangle_s}{\mathrm{d}\tau}\,\frac{1}{\sqrt{\pi(t-\tau)}}\,\mathrm{d}\tau+[\epsilon\,\boldsymbol{I}-(1-\epsilon)\,\boldsymbol{A}]\cdot\boldsymbol{f}. \tag{B14}$$

Comparing this result with the high-frequency asymptotics of Johnson *et al.* (1987) given in (B7), it is readily apparent that the former is just a tensorial generalisation of the latter.

B.3. *Behaviour at finite Reynolds numbers*

In this section, we derive the Re^3 dependence of the first nonlinear correction to the linear drag behaviour from the fore–aft symmetry of the hexagonal sphere pack for oscillatory flow in the x-direction. The derivation is based on our new representation of the drag in the volume-averaged momentum equation (2.11) and assumes a macroscopic pressure gradient along the x-direction. This extends the results of Mei & Auriault (1991) and Firdaouss *et al.* (1997) for steady flow at finite Reynolds numbers (see (1.7)) to oscillatory flow.

The viscous pressure drag in the x-direction is given by (2.10)

$$f_{px}^{(v)}=-\frac{1}{V}\int_{A_{fs}}p^{(v)}\,n_x\,\mathrm{d}A=\frac{1}{V}\int_{A_{fs}}\nabla\Phi_x\cdot\boldsymbol{\tau}_w\,\mathrm{d}A, \tag{B15}$$

the friction drag is given by the integral of the wall shear stress

$$f_{\tau_w x}=-\frac{1}{V}\int_{A_{fs}}\tau_{wx}\,\mathrm{d}A \tag{B16}$$

and the convective pressure drag is given by (2.7*c*)

$$-\frac{1}{V}\int_{A_{fs}}p^{(c)}\,n_x\,\mathrm{d}A=\frac{1}{V}\int_{V_f}\Phi_x\,2\rho Q\,\mathrm{d}V. \tag{B17}$$

The auxiliary potential Φ_x is fore–aft antisymmetric with respect to the planes $x=0, x=d/2, x=d, \ldots$, i.e. an odd function with respect to x. Therefore, the partial derivative $\partial\Phi_x/\partial x$ is an even function whereas $\partial\Phi_x/\partial y$ and $\partial\Phi_x/\partial z$ are odd functions. Thus, the friction and viscous pressure drag are generated by the even part of τ_{wx} and by the odd part of τ_{wy} and τ_{wz}; the convective pressure drag is generated by the odd part of the Q-invariant. Below we discuss how these parts depend on the Reynolds number.

Like in our previous work (Unglehrt & Manhart 2022*a*), we decompose the velocity field into a symmetric part $\boldsymbol{u}_{sym}=\frac{1}{2}(\boldsymbol{u}+\mathcal{S}\boldsymbol{u})$ and an antisymmetric part $\boldsymbol{u}_{anti}=\frac{1}{2}(\boldsymbol{u}-\mathcal{S}\boldsymbol{u})$

with respect to the fore–aft symmetry

$$\mathcal{S}\boldsymbol{u}(\boldsymbol{x},t) = \begin{bmatrix} u(2d-x,y,z,t) \\ -v(2d-x,y,z,t) \\ -w(2d-x,y,z,t) \end{bmatrix} \tag{B18}$$

with respect to the plane $x = d$. In laminar flow, the velocity field is d-periodic in the x-direction. Consequently, this symmetry operation also expresses the fore–aft symmetries with respect to the planes $x = 0$, $x = d/2$, $x = 3/2\,d$ and $x = 2\,d$.

The wall shear stress points in the direction of the velocity vector near the wall. Consequently, the x-component of the wall shear stress of the symmetric part $\boldsymbol{u}_{sym}$ of the velocity field is an even function whereas the y- and z-components are odd functions. The wall shear stress components of the antisymmetric part $\boldsymbol{u}_{anti}$ of the velocity field behave in the opposite way. So we find that the friction and viscous pressure drag arise solely from the symmetric part $\boldsymbol{u}_{sym}$.

Using the decomposition of the velocity field the Q-invariant can be rewritten as

$$Q = \underbrace{-\tfrac{1}{2}(\nabla \otimes \boldsymbol{u}_{sym}) : (\nabla \otimes \boldsymbol{u}_{sym})^{\mathrm{T}}}_{\textit{fore–aft symmetric}} \underbrace{-(\nabla \otimes \boldsymbol{u}_{sym}) : (\nabla \otimes \boldsymbol{u}_{anti})^{\mathrm{T}}}_{\textit{fore–aft antisymmetric}} \underbrace{-\tfrac{1}{2}(\nabla \otimes \boldsymbol{u}_{anti}) : (\nabla \otimes \boldsymbol{u}_{anti})^{\mathrm{T}}}_{\textit{fore–aft symmetric}}. \tag{B19}$$

We find that the quadratic contributions in $\boldsymbol{u}_{sym}$ and $\boldsymbol{u}_{anti}$ lead to a fore–aft symmetric distribution of Q and hence do not cause any convective pressure drag. On the other hand, the interaction between $\boldsymbol{u}_{sym}$ and $\boldsymbol{u}_{anti}$ is fore–aft antisymmetric and can cause a convective pressure drag.

For small Reynolds numbers, the velocity field can be described by as the sum of the velocity field in linear flow and corrections proportional to powers of the Reynolds number:

$$\boldsymbol{u}_{sym} = \boldsymbol{u}_{1|sym}\,Re + \boldsymbol{u}_{2|sym}\,Re^2 + O(Re^3), \tag{B20a}$$

$$\boldsymbol{u}_{anti} = \boldsymbol{u}_{1|anti}\,Re + \boldsymbol{u}_{2|anti}\,Re^2 + O(Re^3). \tag{B20b}$$

Since the velocity field in linear flow is fore–aft symmetric (Unglehrt & Manhart 2022*a*), the antisymmetric first-order contribution $\boldsymbol{u}_{1|anti}$ is zero. The self-interaction of the symmetric first-order contribution $(\boldsymbol{u}_{1|sym} \cdot \nabla)\boldsymbol{u}_{1|sym}$ creates the antisymmetric second-order contribution $\boldsymbol{u}_{2|anti}$ whereas the symmetric second-order contribution $\boldsymbol{u}_{2|sym}$ is zero. Then, we have that the symmetric part $\boldsymbol{u}_{sym}$ is proportional to Re and causes a friction drag and viscous pressure drag proportional to Re with a higher-order contribution of order Re^3. The antisymmetric part $\boldsymbol{u}_{anti}$ is proportional to Re^2 and does not cause any friction and viscous pressure drag. The convective pressure drag arises from the part of the Q-invariant due to the interaction of $\boldsymbol{u}_{sym}$ and $\boldsymbol{u}_{anti}$ and is therefore proportional to Re^3. In conclusion, like in steady flow (Mei & Auriault 1991) the drag in oscillatory flow at small Reynolds numbers consists of a linear and a cubic part in Re.

Appendix C. Grid resolution of the simulations

In this appendix, we discuss the grid resolution of the simulation cases LF5, LF6, MF5, MF6 and HF5. For the other oscillatory cases LF1–LF4, MF1–MF4, HF1–HF4 and for the steady cases, convergence with respect to grid resolution was demonstrated in the previous publications, Unglehrt & Manhart (2022*a*) and Sakai & Manhart (2020), respectively.

C.1. *Estimate of the required grid resolution*

For turbulent flow driven by a constant pressure gradient, the required grid resolution can be estimated following Finn (2013) and He *et al.* (2019). It is assumed that a grid spacing in wall units

$$\Delta x^+ = \frac{u_\tau \, \Delta x}{\nu} \approx 1\text{–}3 \tag{C1}$$

is necessary to resolve all scales in the flow, where the friction velocity $u_\tau = \sqrt{\langle \tau_{wx} \rangle_{A_{fs}} / \rho}$ is defined in terms of the wall shear stress $\langle \tau_{wx} \rangle_{A_{fs}}$ averaged over the fluid–solid interface. He *et al.* (2019) approximate the average wall shear stress as a fraction $\beta \approx 0.25$ of the total stress $\langle \sigma_{wx} \rangle_{A_{fs}}$ which they find from equilibrium as

$$\langle \sigma_{wx} \rangle_{A_{fs}} = f_x \frac{d}{6} \frac{\epsilon}{1-\epsilon}. \tag{C2}$$

Combining (C1) and (C2), the required grid resolution for turbulent flow at a given Hagen number can be estimated as

$$\frac{d}{\Delta x} = \frac{1}{\Delta x^+} \sqrt{\frac{\beta}{6} \frac{\epsilon}{1-\epsilon} Hg}. \tag{C3}$$

For the cases LF6 and MF6, the acceleration is close to zero when the convective pressure drag is large. Therefore, it seems plausible that these cases behave similar to a flow with a constant pressure gradient. Taking a dimensionless grid spacing $\Delta x^+ = 1$ and setting $\beta = 0.2$ (which was taken from the momentum budgets in the figures 12 and 13), the estimate results in a required grid resolution of 342 cpd for the cases LF6 and MF6 ($Hg = 10^7$). Consequently, the employed grid resolution of 384 cpd for the cases LF6 and MF6 seems to be sufficient. For the case HF5, the estimate is not applicable, as the flow is far from an equilibrium with the imposed pressure gradient and the wall shear stress is out of phase with the convective pressure drag (figure 14).

C.2. *Grid study*

In this section, we present a grid study for the cases LF5, LF6, MF5, MF6 and HF5. For each case the simulations were conducted at the resolutions 48 cpd, 96 cpd, 192 cpd and 384 cpd; for the case HF5 an additional simulation at 768 cpd was performed.

For consistency, the discretisation error is assessed using the same procedure as in our previous publication (Unglehrt & Manhart 2022*a*). We first consider the Reynolds number based on the maximum superficial velocity in the last cycle and the sphere diameter, which is defined in (1.4). As can be seen in table 4, for every case the Reynolds numbers differ less than 1 % between the two finest grid resolutions. We then consider the space–time L^2-norm of the velocity field over the last simulated period,

$$\|\boldsymbol{u}\|_{L^2}^2 = \int_{V_f} \int_T |\boldsymbol{u}|^2 \, \mathrm{d}t \, \mathrm{d}V, \tag{C4}$$

corresponding to the signal energy of the velocity field. For all cases the relative difference of the space–time L^2-norm between the second-finest grid to the finest grid is below 1.8 % (cf. table 4). Consequently, we consider the simulations at the finest grid resolution as converged.

Case	$T_{sim}\Omega/(2\pi)$	e_{48}	e_{96}	e_{192}	e_{384}	Re_{48}	Re_{96}	Re_{192}	Re_{384}	Re_{768}
LF5	2.274	−10.66 %	2.46 %	1.79 %	—	138	157	159	157.7	—
LF6	1.562	−18.62 %	−8.26 %	1.43 %	—	255.4	282.6	310.5	306.6	—
MF5	6.397	−13.95 %	−0.91 %	0.04 %	—	133.6	154.5	157.3	157.1	—
MF6	2.261	−18.49 %	−6.61 %	0.37 %	—	252.3	277.2	297.1	297.6	—
HF5	6	−22.47 %	−14.11 %	−2.55 %	−1.02 %	375.1	415.9	459.6	464	465

Table 4. Grid convergence of the velocity field $\boldsymbol{u}(\boldsymbol{x}, t)$ in steady oscillation. The relative error in $\|\boldsymbol{u}\|_{L^2}^2$ is defined as $e_{res} = (\|\boldsymbol{u}_{res}\|_{L^2}^2 - \|\boldsymbol{u}_{384}\|_{L^2}^2)/\|\boldsymbol{u}_{384}\|_{L^2}^2$ and as $e_{res} = (\|\boldsymbol{u}_{res}\|_{L^2}^2 - \|\boldsymbol{u}_{768}\|_{L^2}^2)/\|\boldsymbol{u}_{768}\|_{L^2}^2$ for HF5. The Reynolds number Re is defined according to (1.4).

References

Aghaei-Jouybari, M., Seo, J.-H., Yuan, J., Mittal, R. & Meneveau, C. 2022 Contributions to pressure drag in rough-wall turbulent flows: insights from force partitioning. *Phys. Rev. Fluids* **7** (8), 084602.

Agnaou, M., Lasseux, D. & Ahmadi, A. 2016 From steady to unsteady laminar flow in model porous structures: an investigation of the first Hopf bifurcation. *Comput. Fluids* **136**, 67–82.

Akima, H. 1974 A method of bivariate interpolation and smooth surface fitting based on local procedures. *Commun. ACM* **17** (1), 18–20.

Batchelor, G.K. 2000 *An Introduction to Fluid Dynamics*. Cambridge University Press.

Bronstein, I.N., Semendjajew, K.A., Grosche, G., Ziegler, V. & Ziegler, D. 1991 *Taschenbuch Der Mathematik*, 25th edn. Teubner.

Burcharth, H.F. & Andersen, O.K. 1995 On the one-dimensional steady and unsteady porous flow equations. *Coast. Engng* **24** (3–4), 233–257.

Chapman, A.M. & Higdon, J.J.L. 1992 Oscillatory Stokes flow in periodic porous media. *Phys. Fluids* A **4** (10), 2099–2116.

Chong, M.S., Perry, A.E. & Cantwell, B.J. 1990 A general classification of three-dimensional flow fields. *Phys. Fluids* A **2** (5), 765–777.

Cockroft, J.K. 1999 *A Hypertext Book of Crystallographic Space Group Diagrams and Tables*. Birkbeck College.

Conway, J.H. & Sloane, N.J.A. 1999 *Sphere Packings, Lattices and Groups*, Grundlehren Der Mathematischen Wissenschaften, vol. 290. Springer.

Cox, S.J. & Cooker, M.J. 2000 Potential flow past a sphere touching a tangent plane. *J. Engng Maths* **38** (3), 355–370.

Davit, Y., *et al.* 2013 Homogenization via formal multiscale asymptotics and volume averaging: how do the two techniques compare? *Adv. Water Resour.* **62**, 178–206.

Dubief, Y. & Delcayre, F. 2000 On coherent-vortex identification in turbulence. *J. Turbul.* **1**, N11.

Dybbs, A. & Edwards, R.V. 1984 A new look at porous media fluid mechanics—Darcy to turbulent. In *Fundamentals of Transport Phenomena in Porous Media* (ed. J. Bear & M.Y. Corapcioglu), NATO ASI Series, vol. 82, pp. 199–256. Springer.

Ene, H. & Sanchez-Palencia, E. 1975 Equations et phénomènes de surface pour l'écoulement dans un milieu poreux. *J. Méc.* **14**, 73–108.

Ergun, S. 1952 Fluid flow through packed columns. *Chem. Engng Prog.* **48** (2), 89–94.

Fand, R.M., Kim, B.Y.K., Lam, A.C.C. & Phan, R.T. 1987 Resistance to the flow of fluids through simple and complex porous media whose matrices are composed of randomly packed spheres. *Trans. ASME J. Fluids Engng* **109** (3), 268–273.

Finn, J.R. 2013 A numerical study of inertial flow features in moderate Reynolds number flow through packed beds of spheres. PhD thesis, Oregon State University, Corvallis, Oregon.

Firdaouss, M., Guermond, J.-L. & Le Quéré, P. 1997 Nonlinear corrections to Darcy's law at low Reynolds numbers. *J. Fluid Mech.* **343**, 331–350.

Forchheimer, P. 1901 Wasserbewegung durch Boden. *Z. Verein. Deutsch. Ing.* **45**, 1782–1788.

van Gent, M.R.A. 1993 Stationary and oscillatory flow through coarse porous media. *Communications on Hydraulic and Geotechnical Engineering*, No. 1993-09. TU Delft.

GRAHAM, W.R. 2019 Decomposition of the forces on a body moving in an incompressible fluid. *J. Fluid Mech.* **881**, 1097–1122.

HALL, K.R., SMITH, G.M. & TURCKE, D.J. 1995 Comparison of oscillatory and stationary flow through porous media. *Coast. Engng* **24** (3–4), 217–232.

HARLOW, F.H. & WELCH, J.E. 1965 Numerical calculation of time-dependent viscous incompressible flow of fluid with free surface. *Phys. Fluids* **8** (12), 2182–2189.

HE, X., APTE, S.V., FINN, J.R. & WOOD, B.D. 2019 Characteristics of turbulence in a face-centred cubic porous unit cell. *J. Fluid Mech.* **873**, 608–645.

HILL, R.J. & KOCH, D.L. 2002 The transition from steady to weakly turbulent flow in a close-packed ordered array of spheres. *J. Fluid Mech.* **465**, 59–97.

HILL, R.J., KOCH, D.L. & LADD, A.J.C. 2001 The first effects of fluid inertia on flows in ordered and random arrays of spheres. *J. Fluid Mech.* **448**, 213–241.

HORTON, N.A. & POKRAJAC, D. 2009 Onset of turbulence in a regular porous medium: an experimental study. *Phys. Fluids* **21** (4), 045104.

HOWE, M.S. 1989 On unsteady surface forces, and sound produced by the normal chopping of a rectilinear vortex. *J. Fluid Mech.* **206**, 131–153.

HUNT, J.C.R., WRAY, A.A. & MOIN, P. 1988 Eddies, streams, and convergence zones in turbulent flows. In *Studying Turbulence Using Numerical Simulation Databases, 2. Proceedings of the 1988 Summer Program, Stanford*, pp. 193–208. Center for Turbulence Research.

IERVOLINO, M., MANNA, M. & VACCA, A. 2010 Pulsating flow through porous media. In *Turbulence and Interactions* (ed. E.H. Hirschel, W. Schröder, K. Fujii, W. Haase, B. Leer, M.A. Leschziner, M. Pandolfi, J. Periaux, A. Rizzi, B. Roux, Y.I. Shokin, M. Deville, T.-H. Lê & P. Sagaut), vol. 110, pp. 167–173. Springer.

JOHNSON, D.L., KOPLIK, J. & DASHEN, R. 1987 Theory of dynamic permeability and tortuosity in fluid-saturated porous media. *J. Fluid Mech.* **176**, 379–402.

JOHNSON, D.L. & SEN, P.N. 1981 Multiple scattering of acoustic waves with application to the index of refraction of fourth sound. *Phys. Rev.* B **24** (5), 2486–2496.

JOLLS, K.R. & HANRATTY, T.J. 1969 Use of electrochemical techniques to study mass transfer rates and local skin friction to a sphere in a dumped bed. *AIChE J.* **15** (2), 199–205.

KARABELAS, A.J., WEGNER, T.H. & HANRATTY, T.J. 1971 Use of asymptotic relations to correlate mass transfer data in packed beds. *Chem. Engng Sci.* **26** (10), 1581–1589.

KARABELAS, A.J., WEGNER, T.H. & HANRATTY, T.J. 1973 Flow pattern in a close packed cubic array of spheres near the critical Reynolds number. *Chem. Engng Sci.* **28** (3), 673–682.

LAFARGE, D. 2009 The equivalent fluid model. In *Materials and Acoustics Handbook* (ed. M. Bruneau & C. Potel), pp. 153–204. ISTE.

LANDAU, L.D. & LIFSHITS, E.M. 1987 *Fluid Mechanics*, 2nd edn. Course of Theoretical Physics, vol. 6. Pergamon.

LASSEUX, D., VALDÉS-PARADA, F.J. & BELLET, F. 2019 Macroscopic model for unsteady flow in porous media. *J. Fluid Mech.* **862**, 283–311.

LI, J. & WU, Z.-N. 2018 Vortex force map method for viscous flows of general airfoils. *J. Fluid Mech.* **836**, 145–166.

LOGG, A., MARDAL, K.-A. & WELLS, G. (Ed.) 2012 *Automated Solution of Differential Equations by the Finite Element Method: The FEniCS Book*. Lecture Notes in Computational Science and Engineering, vol. 84. Springer.

MACDONALD, I.F., EL-SAYED, M.S., MOW, K. & DULLIEN, F.A.L. 1979 Flow through porous media–the Ergun equation revisited. *Ind. Engng Chem. Fundam.* **18** (3), 199–208.

MANHART, M., TREMBLAY, F. & FRIEDRICH, R. 2001 MGLET: a parallel code for efficient DNS and LES of complex geometries. In *Parallel Computational Fluid Dynamics 2000* (ed. C.B. Jenssen, T. Kvamsdal, H.I. Andersson, B. Pettersen, A. Ecer, J. Periaux, N. Satofuka & P. Fox), pp. 449–456. North-Holland.

MEI, C.C. & AURIAULT, J.-L. 1991 The effect of weak inertia on flow through a porous medium. *J. Fluid Mech.* **222**, 647–663.

MENON, K. & MITTAL, R. 2021 On the initiation and sustenance of flow-induced vibration of cylinders: insights from force partitioning. *J. Fluid Mech.* **907**, A37.

NIELD, D.A. 1991 The limitations of the Brinkman–Forchheimer equation in modeling flow in a saturated porous medium and at an interface. *Intl J. Heat Fluid Flow* **12** (3), 269–272.

PELLER, N. 2010 Numerische simulation turbulenter Strömungen mit immersed boundaries. PhD thesis, Technical University of Munich, Munich.

PELLER, N., LE DUC, A., TREMBLAY, F. & MANHART, M. 2006 High-order stable interpolations for immersed boundary methods. *Intl J. Numer. Meth. Fluids* **52** (11), 1175–1193.

PRIDE, S.R., MORGAN, F.D. & GANGI, A.F. 1993 Drag forces of porous-medium acoustics. *Phys. Rev.* B **47** (9), 4964–4978.

QUARTAPELLE, L. & NAPOLITANO, M. 1983 Force and moment in incompressible flows. *AIAA J.* **21** (6), 911–913.

SAKAI, Y. & MANHART, M. 2020 Consistent flow structure evolution in accelerating flow through hexagonal sphere pack. *Flow Turbul. Combust.* **105** (2), 581–606.

SANI, R.L., SHEN, J., PIRONNEAU, O. & GRESHO, P.M. 2006 Pressure boundary condition for the time-dependent incompressible Navier–Stokes equations. *Intl J. Numer. Meth. Fluids* **50** (6), 673–682.

SCHLICHTING, H. & GERSTEN, K. 2017 *Boundary-Layer Theory*. Springer.

SOLLITT, C.K. & CROSS, R.H. 1972 Wave transmission through permeable breakwaters. In *Coastal Engineering 1972*, pp. 1827–1846. American Society of Civil Engineers.

SORIA, J., OOI, A. & CHONG, M.S. 1997 Volume integrals of the QA-RA invariants of the velocity gradient tensor in incompressible flows. *Fluid Dyn. Res.* **19** (4), 219–233.

UNGLEHRT, L. & MANHART, M. 2022*a* Onset of nonlinearity in oscillatory flow through a hexagonal sphere pack. *J. Fluid Mech.* **944**, A30.

UNGLEHRT, L. & MANHART, M. 2022*b* Symmetry breaking and turbulence in oscillatory flow through a hexagonal sphere pack. In *Proceedings of TSFP-12 (2022), Osaka, Japan*. Available at: http://www.tsfp-conference.org/proceedings/proceedings-of-tsfp-12-2022-osaka.html.

WEGNER, T.H., KARABELAS, A.J. & HANRATTY, T.J. 1971 Visual studies of flow in a regular array of spheres. *Chem. Engng Sci.* **26** (1), 59–63.

WHITAKER, S. 1985 A simple geometrical derivation of the spatial averaging theorem. *Chemical Engineering Education* **19** (1), 18–21 and 50–52.

WHITAKER, S. 1986 Flow in porous media I: a theoretical derivation of Darcy's law. *Transp. Porous Med.* **1** (1), 3–25.

WHITAKER, S. 1996 The Forchheimer equation: a theoretical development. *Transp. Porous Med.* **25** (1), 27–61.

YU, Y. 2014 The virtual power principle in fluid mechanics. *J. Fluid Mech.* **744**, 310–328.

ZHU, T. & MANHART, M. 2016 Oscillatory Darcy flow in porous media. *Transp. Porous Med.* **111** (2), 521–539.

ZHU, T., WALUGA, C., WOHLMUTH, B. & MANHART, M. 2014 A study of the time constant in unsteady porous media flow using direct numerical simulation. *Transp. Porous Med.* **104** (1), 161–179.